Crystallography Reports, Vol. 45, No. 3, 2000, pp. 349–355. Translated from Kristallografiya, Vol. 45, No. 3, 2000, pp. 391–397.

CRYSTALLOGRAPHIC SYMMETRY

Complete Normalizer for a Direct Product of Three-Dimensional Rotation Groups

V. I. Burdina

Shubnikov Institute of Crystallography, Russian Academy of Sciences, Leninskiĭ pr. 59, Moscow, 117333 Russia

Received June 19, 1996; in final form, December 1, 1999

Abstract—A normalizer of the symmetry group defined on a three-dimensional sphere S^3 of rotation is considered in the four-dimensional Euclidean space E^4. The sphere S^3 is treated as the first approximation of the three-dimensional crystallographic space. The analysis of the normalizer $\mathcal{N}$ of the direct product $\mathcal{G} = G_1 \times G_2$ of space crystallographic rotation groups G_1 and G_2 is reduced to the study of transformations characterized by the positive determinants of the subgroups $\mathcal{N}^+(G_1)$ and $\mathcal{N}^+(G_2)$. These subgroups correspond to the Euclidean normalizers $\mathcal{N} = \mathcal{N}^+(G_1) \times \mathcal{N}^+(G_2)$ of the components of the direct product. We derived a table including the groups of automorphisms induced by the transformations corresponding to the normalizers under study. Analyzing the general operation of multiplication of three-dimensional rotations in E^4, we refined the distribution of the supersymmetry operators of the three-dimensional sphere of rotations, S^3, for the symmetry groups considered earlier. © *2000 MAIK "Nauka/Interperiodica".*

INTRODUCTION

A normalizer $\mathcal{N}$ of the symmetry group $\mathcal{G}$ is widely used in crystallography [1, 2] alongside with a more general concept of symmetrizer. In [3, 4], this normalizer was used to interpret the additional symmetry (supersymmetry) arising in the regular divisions of three-dimensional sphere S^3 of rotation (which involves the center of inversion). The normalizer is defined in a purely algebraic manner [5] as a group of isometric transformations of a sphere of rotation, which induces automorphisms $\mathcal{N}\mathcal{G}\mathcal{N}^{-1} = \mathcal{G}$ of the symmetry group $\mathcal{G}$. By definition, a normalizer can lead to the continuous spectrum of transformations, and hence to the reduced dimension of the minimum domain of parameters. The normalizer operators not belonging to the symmetry group of the space under study can be related to the medium "dissymmetry" that causes symmetrization of some lattices formed by the sets of regular, or homological, points (in full accordance with the generalized Curie–Shubnikov principle [6–9]).

Developing [4], we consider the general problem of the determination of the normalizer $\mathcal{N}(\mathcal{G})$ for the direct product $\mathcal{G} = G_1 \times G_2$ of the crystallographic rotation groups G_1 and G_2. The group G is a symmetry group on the three-dimensional manifold belonging to the sphere of rotation S^3 immersed into the four-dimensional Euclidean space E^4. We prove the completeness of this normalizer in the sense of the full involvement into it of various automorphisms of the symmetry groups. The information contained in the normalizer allows us to construct the minimum parameter domain, and to indicate the exact location of the symmetrized lattices of regular points. This allows us to refine the structures of computer-calculated regular divisions. The procedure is illustrated by two examples.

GENERAL INFORMATION

The transformation

$$p = \mathbf{p}_1 \times \mathbf{p}_2 \tag{1}$$

of the direct product of three-dimensional rotations $\mathbf{p}_1 = \mathbf{P}(\mathbf{l}_1, \varphi_1)$ and $\mathbf{p}_2 = \mathbf{P}(\mathbf{l}_2, \varphi_2)$ on the sphere S^3 about the unit vectors $\mathbf{l}_1$ and $\mathbf{l}_2$ through angles φ_1 and φ_2 in the four-dimensional Euclidean space $E^4(u_0, u_1, u_2, u_3)$ acts as a linear orthogonal transformation, which can be written in the quaternion form [10] as

$$\mathbf{u}' = \mathbf{sut}, \tag{2}$$

where $\mathbf{u} = u_0 + u_1\mathbf{i} + u_2\mathbf{j} + u_3\mathbf{k}$ and $\mathbf{u}' = u_0' + u_1'\mathbf{i} + u_2'\mathbf{j} + u_3'\mathbf{k}$ are the arbitrary and the transformed quaternions, respectively; $\mathbf{s} = \cos(\varphi_1/2) + \mathbf{l}_1\sin(\varphi_1/2)$ and $\mathbf{t} = \cos(\varphi_2/2) + \mathbf{l}_2\sin(\varphi_2/2)$ are the unit quaternions of rotations $\mathbf{p}_1$ and $\mathbf{p}_2$. In the vector–matrix form, we can write

$$\mathbf{u}' = \mathbf{Zu}, \tag{2'}$$

where the orthogonal 4×4 matrix $\mathbf{Z} = \mathbf{ST} = \mathbf{TS}$ is equal to the product of the commuting matrices

$$\mathbf{S} = \begin{pmatrix} s_0 & -s_1 & -s_2 & -s_3 \\ s_1 & s_0 & -s_3 & s_2 \\ s_2 & s_3 & s_0 & -s_1 \\ s_3 & -s_2 & s_1 & s_0 \end{pmatrix} \text{ and } \mathbf{T} = \begin{pmatrix} t_0 & -t_1 & -t_2 & -t_3 \\ t_1 & t_0 & t_3 & -t_2 \\ t_2 & -t_3 & t_0 & t_1 \\ t_3 & t_2 & -t_1 & t_0 \end{pmatrix}$$

1063-7745/00/4503-0349$20.00 © 2000 MAIK "Nauka/Interperiodica"

constructed with the use of the elements of the quaternions $\mathbf{s} = s_0 + s_1\mathbf{i} + s_2\mathbf{j} + s_3\mathbf{k}$ and $\mathbf{t} = t_0 + t_1\mathbf{i} + t_2\mathbf{j} + t_3\mathbf{k}$.

To each rotation $\mathbf{P}(\mathbf{l}, \varphi)$ there corresponds, in addition to quaternion $\cos(\varphi/2) + \mathbf{l}\sin(\varphi/2)$, also the quaternion of the opposite sign, which arises upon the change of the rotation angle φ by $\varphi + 360°$ not changing the rotation. Therefore, to the direct product (1) of rotations there correspond $\pm\mathbf{s}$, $\pm\mathbf{t}$, $\pm\mathbf{Z}$, $\pm\mathbf{S}$, and $\pm\mathbf{T}$ and two transformations, (2) and (2'), related by inversion, which transform the point $\mathbf{u} \in E^4$ either into $\mathbf{u}'$ or $-\mathbf{u}'$, and a pair of diametric points $\mathbf{u}$ and $-\mathbf{u}'$ either into $\mathbf{u}'$ and $-\mathbf{u}'$ or $-\mathbf{u}'$ and $\mathbf{u}'$, i.e., into the same pair. Therefore, a unique transformation of the sphere of rotation S^3 and one transformation of tangential space $T^3(1, x_1, x_2, x_3)$ correspond to product (1). Here, $x_i = u_i/u_0$, $i = 1–3$. The diametric points at this sphere are assumed to be symmetrically identical, because in the transition from S^3 to the tangential space, the diametric points $\mathbf{u}$ and $-\mathbf{u}$ are projected to a single point.

The multiplication of $pq = (\mathbf{p}_1 \times \mathbf{p}_2)(\mathbf{q}_1 \times \mathbf{q}_2)$ of operators $p = \mathbf{p}_1 \times \mathbf{p}_2$ and $q = \mathbf{q}_1 \times \mathbf{q}_2$ is performed from right to left; the corresponding double quaternion transformation has the form: $\mathbf{u}' = \mathbf{s}_p(\mathbf{s}_q\mathbf{u}\mathbf{t}_q)\mathbf{t}_p = (\mathbf{s}_p\mathbf{s}_q)\mathbf{u}(\mathbf{t}_q\mathbf{t}_p)$.

Since the multiplication of two quaternions corresponds to the multiplication of rotations described by these quaternions, then the direct product is written as $\mathbf{p}_1\mathbf{q}_1 \times \mathbf{q}_2\mathbf{p}_2$. Thus, the multiplication of direct products of rotations

$$(\mathbf{p}_1 \times \mathbf{p}_2)(\mathbf{q}_1 \times \mathbf{q}_2) = \mathbf{p}_1\mathbf{q}_1 \times \mathbf{q}_2\mathbf{p}_2$$

reduces to the multiplication of left-hand factors in the same direction, whereas the right-hand factors are multiplied in the opposite direction. The product of transformations (2') and matrices $\mathbf{Z} = \mathbf{Z}_1$ and $\mathbf{Z} = \mathbf{Z}_2$ reduces to the linear transformation corresponding to the matrix $\mathbf{Z} = \mathbf{Z}_2\mathbf{Z}_1$.

In addition to individual multiplications of transformations (1), we also consider the group

$$\mathcal{P} = P_1 \times P_2$$

of direct multiplication of three-dimensional rotation groups P_1 and P_2. Let Φ be the automorphism, that is, the one-to-one mapping of group $\mathcal{P}$ onto itself retaining the multiplication operation

$$\Phi(pq) = \Phi(p)\Phi(q), \text{ where } p, q \in \mathcal{P}.$$

Here, $\Phi(e) = e$, e is the unity element of the group ($e = \mathbf{E} \times \mathbf{E}$) which is transformed into itself. For the element $p = \mathbf{p}_1 \times \mathbf{p}_2$ in the direct product, we have $\Phi(\mathbf{p}_1 \times \mathbf{p}_2) = \mathbf{p}_1' \times \mathbf{p}_2'$, where $\mathbf{p}_i'$, $\mathbf{p}_i \in \mathbf{P}_i\,\mathbf{p}_{i,\,i=1,2}$. Assuming that $\mathbf{p}_1' = \Phi_1(\mathbf{p}_1)$ and $\mathbf{p}_2' = \Phi_2(\mathbf{p}_2)$, we have

$$\Phi(\mathbf{p}_1 \times \mathbf{p}_2) = \Phi_1(\mathbf{p}_1) \times \Phi_2(\mathbf{p}_2).$$

It is easy to check that the transformations Φ_1 and Φ_2 acting onto the elements of left and right groups P_1 and P_2 of the direct product preserve the multiplication operation, i.e., they also are automorphisms. As a consequence, we have $\Phi(\mathbf{E} \times p) = \Phi_1(\mathbf{E}) \times \Phi_2(\mathbf{p}) = \mathbf{E} \times \Phi_2(\mathbf{p})$ and $\Phi(\mathbf{p} \times \mathbf{E}) = \Phi_1(\mathbf{p}) \times \Phi_2(\mathbf{E}) = \Phi_1(\mathbf{p}) \times \mathbf{E}$. In the Euclidean space E^4, the matrix $\mathbf{Z} = \mathbf{S}$ of the linear transformation (2') is transformed into the matrix s by automorphism Φ, whereas the matrix $\mathbf{Z} = \mathbf{T}$ is transformed into the matrix t. Coming back to direct product (1) of rotations, we consider some geometrical characteristics of the resulting operator in E^4 [11]. The existence of the linear orthogonal transformation of the four-dimensional Euclidean space corresponding to direct product $\mathbf{P}(\mathbf{l}_1, \varphi_1) \times \mathbf{P}(\mathbf{l}_2, \varphi_2)$ of rotations corresponds to the existence of two invariant orthogonal two-dimensional subspaces, or planes π and π' of rotation through angles $(\varphi_1 - \varphi_2)/2$ and $(\varphi_1 + \varphi_2)/2$, which are equal to the half-difference and the half-sum of initial rotation angles, respectively, determined by the directions

$$\pi\colon \mathbf{L}_1 = \mathbf{l}_1 - \mathbf{l}_2,\ \mathbf{L}_2 = 1 + \frac{2}{|\mathbf{l}_1 - \mathbf{l}_2|^2}[\mathbf{l}_1, \mathbf{l}_2] \qquad (3)$$

and

$$\pi'\colon \mathbf{L}_1' = \mathbf{l}_1 + \mathbf{l}_2,\ \mathbf{L}_2' = 1 - \frac{2}{|\mathbf{l}_1 + \mathbf{l}_2|^2}[\mathbf{l}_1, \mathbf{l}_2], \qquad (4)$$

whose locations are independent of the initial rotation angles φ_1 and φ_2. If one of the latter angles changes by 360°, the rotations themselves remain unchanged, but the rotation angles in the invariant planes π and π' change by 180°, and the transformation in E^4 is complemented with inversion.

In the general case, the first invariant plane π (see (3)) in the projective tangential space T^3 is represented by the line of intersection passing through the point $A(2[\mathbf{l}_1, \mathbf{l}_2]/|\mathbf{l}_1 - \mathbf{l}_2|^2)$ along the $\mathbf{l}_1 - \mathbf{l}_2$ direction, whereas the second plane π' (see (4)) is represented by the point $B(-2[\mathbf{l}_1, \mathbf{l}_2]/|\mathbf{l}_1 + \mathbf{l}_2|^2)$ and by the $(\mathbf{l}_1 + \mathbf{l}_2)$ direction.

In the particular case of direct product $\mathbf{P}(\mathbf{l}_1, \varphi) \times \mathbf{P}(\mathbf{l}_2, \varphi)$ of the rotations of the same order, $\varphi_1 = \varphi_2 = \varphi$, the first plane π remains stationary, since the rotation angle in this plane is $(\varphi_1 - \varphi_2)/2 = 0$, whereas the rotation angle in the plane π' is equal to $(\varphi_1 + \varphi_2)/2 = \varphi$, i.e., to the common angle of the initial rotations. In T^3, we have the fixed "rotation axis" of the order of $360°/\varphi$. If, in addition, the initial axes differ only in signs, $\mathbf{l}_2 = -\mathbf{l}_1$, then the vector product becomes zero $[\mathbf{l}_1, \mathbf{l}_2] = -[\mathbf{l}_2, \mathbf{l}_1] = 0$, the point A is displaced to the origin of coordinates in the tangential hyperplane T^3, i.e., the point A coincides with the pole (1, 0, 0, 0) of the sphere S^3. The fixed direction of the axis, $\mathbf{l}_1 - \mathbf{l}_2 = 2\mathbf{l}_1$, is characterized by the unit vector $\mathbf{l}_1$. Thus, we have the Hamiltonian rotation $\mathbf{P}(\mathbf{l}, \varphi) \times \mathbf{P}^{-1}(\mathbf{l}, \varphi)$ coinciding with the rotation $\mathbf{P}(\mathbf{l}, \varphi)$ in T^3 and in three-dimensional coordinate space $E^3(u_1, u_2, u_3)$.

As is seen from (3) and (4), the invariant planes π and π' are orthogonal, but otherwise they can be located

arbitrarily in E^4 depending on the choice of the directions of the unit vectors $\mathbf{I}_1$ and $\mathbf{I}_2$ for the initial rotations. The rotation angles for the invariant planes can also be specified arbitrarily. This picture corresponds to the general case of the orthogonal transformation with the positive determinant equal to +1 in the Euclidean space E^4 [12–14].

NORMALIZER FOR DIRECT PRODUCT $G_1 \times G_2$ OF SPACE ROTATION GROUPS G_1 AND G_2

Consider the symmetry group $\mathcal{G}$ of the three-dimensional sphere S^3 of rotations in the four-dimensional Euclidean space $E^4(u_0, u_1, u_2, u_3)$ specified by the direct product $\mathcal{G} = G_1 \times G_2$ of three-dimensional rotation groups G_1 and G_2.

The isometric transformation n of the rotation sphere S^3 meeting the operator condition

$$ngn^{-1} = g', \tag{5}$$

where g is an arbitrary transformation of the symmetry,

$$g, g' \in \mathcal{G},$$

and defining the mapping of the group $\mathcal{G}$ onto itself with retaining the multiplication operation (the so-called automorphism (5) of the symmetry group $\mathcal{G}$) generates, in turn, a group or normalizer $\mathcal{N}(\mathcal{G})$ of the symmetry group $\mathcal{G}$. The latter forms a part or a subgroup of the normalizer, $\mathcal{G} \subset \mathcal{N}(\mathcal{G})$.

In accordance with the above consideration, there are two linear orthogonal transformations corresponding to an arbitrary operator $g \in \mathcal{G}$ in E^4 related by the inversion

$$\mathbf{u}' = \pm\mathbf{Z}(g)\mathbf{u}.$$

To the product gg' of the elements g and $g' \in \mathcal{G}$, there correspond two such transformations or the transformation with the matrix $\pm\mathbf{Z}(gg') = \pm\mathbf{Z}(g)\mathbf{Z}(g')$. The relationship $\mathbf{Z}(e) = \pm\mathbf{E}$ corresponds to the unit element e. The set of the orthogonal matrices $\pm\mathbf{Z}(g)$, $g \in \mathcal{G}$ forms the group $\mathcal{Z}$ or the two-valued representation of the fourth-order group $\mathcal{G}$.

The isometric transformation $n \in \mathcal{N}(\mathcal{G})$ of the normalizer in E^4 corresponds to two linear orthogonal transformations related by inversion:

$$\mathbf{u}' = \pm\mathbf{N}\mathbf{u}. \tag{6}$$

Condition (5) of the automorphism can be rewritten in the form of the automorphism for the group $\mathcal{Z}$ of the two-valued representation

$$\mathbf{N}\mathbf{Z}(g)\mathbf{N}^{-1} = \pm\mathbf{Z}(g'). \tag{7}$$

Let us show that the determinant of the 4×4 matrix $\pm\mathbf{N}$ of the linear orthogonal transformation (6) is positive. Since $\det(-\mathbf{N}) = (-1)^4 \det\mathbf{N} = \det\mathbf{N}$, it is sufficient to show that

$$\det\mathbf{N} > 0. \tag{8}$$

If we assume that the opposite condition is valid; i.e., that there exists an orthogonal 4×4 matrix $\mathbf{N} = \eta$ with the negative determinant $\det\eta < 0$, then assuming also that $\eta = \mu\mathbf{Z}$, where $\mu = \begin{pmatrix} -1 & 0 & 0 & 0 \\ 0 & 1 & 0 & 0 \\ 0 & 0 & 1 & 0 \\ 0 & 0 & 0 & 1 \end{pmatrix}$ and $\det\mathbf{Z} > 0$,

and using the expansion $\mathbf{Z} = \mathbf{S}\mathbf{T}$ proved in the previous section, we have $\eta = \mu\mathbf{S} \cdot \mathbf{T}$. Using the parentheses, we can rewrite transformation (7) of the automorphism as

$$\mu(\mathbf{S}(\mathbf{T}\mathbf{Z}(g)\mathbf{T}^{-1})\mathbf{S}^{-1}) \quad \mu^{-1} = \pm\mathbf{Z}(g'). \tag{9}$$

In the particular case of the left-hand transformation $g = \mathbf{g} \times \mathbf{E}$, the matrix $\mathbf{Z}(g) = \mathbf{Z}(\mathbf{g} \times \mathbf{E}) = S(g)T(E) = S(g)$ is reduced to the matrix s, because $T(E) = E$. In virtue of the properties of the automorphism for the direct product, we should have in the right-hand side of (9) $g' = g' \times E$. Hence, we find that $\mathbf{Z}(g') = \mathbf{S}(\mathbf{g}')\mathbf{T}(\mathbf{E}) = \mathbf{S}(\mathbf{g}')$ is also the s matrix. Since matrices s and t permutable, the left-hand threefold product retains $\mathbf{S}(\mathbf{g})$ unchanged and, thus, $\mathbf{T}\mathbf{S}(\mathbf{g})\mathbf{T}^{-1} = \mathbf{S}(\mathbf{g})\mathbf{T}\mathbf{T}^{-1} = \mathbf{S}(\mathbf{g})$. Then, taking into account that the product of similar matrices retains its type, we conclude that the threefold product of the s-matrices, $\mathbf{S}\mathbf{S}(\mathbf{g})\mathbf{S}^{-1} = \mathbf{S}_1$, is also a certain s-matrix. The further multiplication by μ on the left and by $\mu^{-1} = \mu$ on the right reduces to the change of the sign for the first column and the first line of the matrix. This leads to the change of the matrix type, $\mu\mathbf{S}_1\mu^{-1} = \mathbf{T}_1$. As a result, (9) reduces to the relationship $\mathbf{T}_1 = \mathbf{S}(\mathbf{g}')$ involving the matrices of different types. The latter situation is possible only for the case of $\pm E$ matrices, i.e., if $\mathbf{g}' = E$, $g' = \mathbf{E} \times \mathbf{E}$, and, thus, if $g = e$. Similarly, the assumption that $g = \mathbf{E} \times \mathbf{g}$ leads to the relationship $g = e$. Hence, it follows that the group of direct product $\mathcal{G} = \mathbf{G}_1 \times \mathbf{G}_2$ can contain only the unit element, that is, this group is the trivial one. Thus, we proved statement (8) for the nontrivial group $\mathcal{G}$.

Since the determinant of transformation (6) is positively defined, one can expand the transformation n into the direct product of two space rotations $\mathbf{n}_1$ and $\mathbf{n}_2$

$$n = \mathbf{n}_1 \times \mathbf{n}_2.$$

Substituting the last expression and relationships $g = \mathbf{g}_1 \times \mathbf{g}_2$, $g' = \mathbf{g}'_1 \times \mathbf{g}'_2$ in (5), we can reduce the automorphism under study to the two following automorphisms:

$$\begin{aligned} \mathbf{n}_1\mathbf{g}_1\mathbf{n}_1^{-1} &= \mathbf{g}'_1, \\ \mathbf{n}_2^{-1}\mathbf{g}_2\mathbf{n}_2 &= \mathbf{g}'_2 \end{aligned} \tag{10}$$

for the left and right groups of the direct product $\mathcal{G} = \mathbf{G}_1 \times \mathbf{G}_2$.

The set of space rotations $\mathbf{n}_1$ and $\mathbf{n}_2$ generating left and right automorphisms (10) is characterized by the positive determinants for orthogonal 3×3 matrices; therefore three-dimensional groups of normalizers $\mathcal{N}_1$ and $\mathcal{N}_2$ should also be positively defined $\mathcal{N}_1 = \mathcal{N}^+(\mathbf{G}_1)$ and $\mathcal{N}^+(\mathbf{G}_2)$.

The normalizer of the symmetry group is split into the direct products of two positive definite normalizers

$$\mathcal{N}(\mathcal{G}) = \mathcal{N}^+(\mathbf{G}_1) \times \mathcal{N}^+(\mathbf{G}_2).$$

Thus, in the case of the $\mathbf{3} \times \mathbf{23}$ group, the normalizer can be written as $\mathcal{N}(\mathbf{3} \times \mathbf{23}) = \mathcal{N}^+(\mathbf{3}) \times \mathcal{N}^+(\mathbf{23})$. According to [1], the subgroups of the rotation group in the general normalizers of groups **3** and **23** are $\mathcal{N}^+(\mathbf{3}) = \mathbf{P}_\infty\mathbf{/2}$ and $\mathcal{N}^+(\mathbf{23}) = \mathbf{432}$. Hence, the normalizer sought is $\mathcal{N}(\mathbf{3} \times \mathbf{23}) = \mathbf{P}_\infty\mathbf{/2} \times \mathbf{432}$.

Similarly, the normalizer of the direct product $\mathbf{3} \times \mathbf{432}$ appears to be $\mathcal{N}(\mathbf{3} \times \mathbf{432}) = \mathbf{P}_\infty\mathbf{/2} \times \mathbf{432}$, that is, it fully coincides with the previous one.

The symmetry group remains invariant with respect to the normalizer operators. Thus, the symmetry group plays the role of the normal divisor of this normalizer. Automorphism condition (5) is equivalent to the equality $ng = g'n$, where g and $g' \in \mathcal{G}$. Two operators, m and n, of the normalizer generating the same automorphism, $mgm^{-1} = ngn^{-1}$, $g \in \mathcal{G}$, differ by a factor $n = m\zeta$, where $\zeta = m^{-1}n$. One can readily see that this factor commutes with an arbitrary g, and, therefore, it belongs to the centralizer [5] CEN($\mathcal{G}$) of the group $\mathcal{G}$. The centralizer CEN($\mathcal{G}$) $\subset \mathcal{N}(\mathcal{G})$ leaves the group $\mathcal{G}$ at its place ($\zeta g\zeta^{-1} = g$, $g \in \mathcal{G}$) and possesses the properties of the normal divisor [5].

It is possible to bring in correspondence to each element $n \in \mathcal{N}(\mathcal{G})$ of the normalizer the automorphism generated by this element, (5). We denote this automorphism by Φ_n. In such a way, we arrive at homomorphic mapping $n \longrightarrow \Phi_n$ of the normalizer onto the group $\mathcal{F}$ of automorphisms corresponding to the symmetry group $\mathcal{G}$. In this case, to the elements ζ of the centralizer there corresponds the identical or unit automorphism $\Phi_\zeta = \mathrm{E}$. To the elements $n\zeta$ of the class $n \cdot$ CEN($\mathcal{G}$), there corresponds the automorphism $\Phi_{n\zeta} = \Phi_n\Phi_\zeta = \Phi_n$. Considering the cosets as "enlarged elements," we come to the factor group of the normalizer with respect to the centralizer. This factor group is isomorphous to the group of automorphisms

$$\mathcal{N}(\mathcal{G})/\mathrm{CEN}(\mathcal{G}) \backsim \mathcal{F}(\mathcal{G}). \qquad (11)$$

In contrast to $\mathcal{N}(\mathcal{G})$ and CEN($\mathcal{G}$), the group $\mathcal{F}(\mathcal{G})$ of automorphisms is always finite, since the symmetry group in our problem is finite. This can simplify the analysis of the normalizer structure. Since the groups $\mathcal{G}$ and $\mathcal{N}(\mathcal{G})$ are direct products, each individual automorphism Φ_n, $n = n_1 \times n_2$, is split into the product $\Phi = \Phi_{n1} \times \Phi_{n2}$ of independent automorphisms corresponding to the left and right groups G_1 and G_2 generated by the elements $\mathbf{n}_1$ and $\mathbf{n}_2$, respectively. The group of automorphisms splits into the direct product $\mathcal{F}(\mathcal{G}) = \mathcal{F}(\mathcal{G}_1) \times \mathcal{F}(\mathcal{G}_2)$ of the three-dimensional groups $\mathcal{F}(G_1)$ and $\mathcal{F}(G_2)$ corresponding to the automorphisms of the left and right components of the symmetry group $\mathcal{G} = G_1 \times G_2$.

The groups of automorphisms for crystallographic rotation groups calculated with the use of the positive definite normalizers [1] are listed in the table in the conventional notation and settings. The dots indicate the common products of the complemented subgroups. The groups of automorphisms are described either in terms of the normalizer subgroup (upon the reduction of the fraction in (11) by CEN($\mathcal{G}$), resulting in the decomposition of the normalizer into the semidirect product, [15]) or in terms of the isomorphous equivalents.

The direct exhaustion of the substitutions for the G_i group elements shows that the automorphisms presented in the table cover all the automorphisms of the group. In contrast to the purely algebraic construction of the group automorphism with the aid of the holomorph [5], the revealed possibility of describing an arbitrary automorphism of the rotation group G_i in terms of the rotation in E^3 (the Bieberbach theorem [16]) allows one (with due regard for our results) to describe an arbitrary automorphism of the direct product $G_1 \times G_2$ in terms of the positively defined transformation n in S^3 [5].

APPENDIX

The operator n of the normalizer transforms the operation m into the equivalent or conjugated operation $m = nmn^{-1}$ (the geometrical element $\hat{m}' = n\hat{m}$). Similar to the diagram, the partition of the crystallographic space into the unit cells with respect to the symmetry group, the points and the operators of the sphere S^3 independent or nonequivalent with respect to the normalizer form the minimum or fundamental domain of parameters.

As an example, consider the action of the symmetry group $\mathbf{3} \times \mathbf{23}$ onto the sphere S^3 of rotation. The normalizer of this group $\mathcal{N}(\mathbf{3} \times \mathbf{23}) = \mathbf{P}_\infty(001)\mathbf{/2} \times \mathbf{432}$ was determined in the previous section. Among the normalizer transformations, there are the independent rotations in S^3 and T^3 described by the direct products of the similar rotations. It is quite clear that all the similar three- and fourfold rotation axes in the right-hand component **432** of the normalizer group are equivalent and transformed into each other by the group operations. Let us assume that the rotations $\mathbf{4}(00\bar{1}) = \mathbf{4}^{-1}(001)$ and $\mathbf{3}(1\bar{1}\bar{1})$ are independent. Arbitrary rotations around the twofold axes can be considered as two independent

Groups of automorphisms of three-dimensional crystallographic rotation groups

i	G_i	CEN(G_i)	$\mathcal{N}^+(G_i)$	$\mathcal{N}^+(G_i)$/CEN(G_i) ~ $\mathcal{F}(G_i)$
1	**E**	∞	∞	**E**
2	**2**	$\mathbf{P}_\infty \times \mathbf{2}(100)$	$\mathbf{P}_\infty \times \mathbf{2}(100)$	**E**
3	**3**, **4**, **6**	$\mathbf{P}_\infty$	$\mathbf{P}_\infty \times \mathbf{2}(100)$	**2**(100)
4	**222**	**222**	**432** = **222** × **322**	$\mathbf{3}(111) \times \mathbf{2}(\bar{1}10)$ ~ **322**
5	**322**	**2**(001)	**622** = **2** × **322**	**322**
6	**422**	**2**(001)	$\mathbf{P}_8(001) \times \mathbf{2}(100)$	~**422**
7	**622**	**2**(001)	$\mathbf{P}_{12}(001) \times \mathbf{2}(100)$	~**622**
8	**23**, **432**	**E**	**432**	**432**

rotations: vertical one **2**(001) and diagonal one **2**(110). Combining these rotations with the similar independent rotations of the left-hand group $\mathbf{P}_\infty(001)/\mathbf{2}$ of the normalizer, we find six products:

$$\begin{aligned}
&(1)\ \mathbf{4}(001) \times \mathbf{4}^{-1}(001),\\
&(2)\ \mathbf{3}(001) \times \mathbf{3}(1\bar{1}\bar{1}),\\
&(3)\ \mathbf{2}(001) \times \mathbf{2}(001),\\
&(4)\ \mathbf{2}(100) \times \mathbf{2}(001),\\
&(5)\ \mathbf{2}(001) \times \mathbf{2}(110),\\
&(6)\ \mathbf{2}(100) \times \mathbf{2}(110).
\end{aligned} \qquad (12)$$

The presented domain of parameters for the group under study was used in the schematic form [17] for attaining uniform scanning.

The full diagram of the fundamental domain within the minimum boundaries in T^3 is shown in Fig. 1. The diagram includes the rotation axes of the normalizer distributed at its periphery. All the independent geometric loci of the rotation axes listed in (12) are presented in this figure.

The point group 422 of the Hamiltonian rotation axis located at the origin of coordinates is characterized by the vertical fourfold axis $\mathbf{4}(001) = \mathbf{4}(001) \times \mathbf{4}^{-1}(001)$ coinciding with the rotation axis from row 1 of product (12), by the twofold axis $\mathbf{2}(100) = \mathbf{2}(100) \times \mathbf{2}(100)$ parallel to the horizontal axis and apparently equivalent to the rotation axis from row 4 of product (12) with respect to transformation $\mathbf{E} \times \mathbf{3}(111)$ of the normalizer, and finally, by the diagonal twofold axis $\mathbf{2}(110) \times \mathbf{2}(110) = \mathbf{2}(110)$ transformed to the dyad of row 6 by the automorphism, generated by the one-side transformation $\mathbf{P}_8^{-1} \times \mathbf{E}$ of the normalizer.

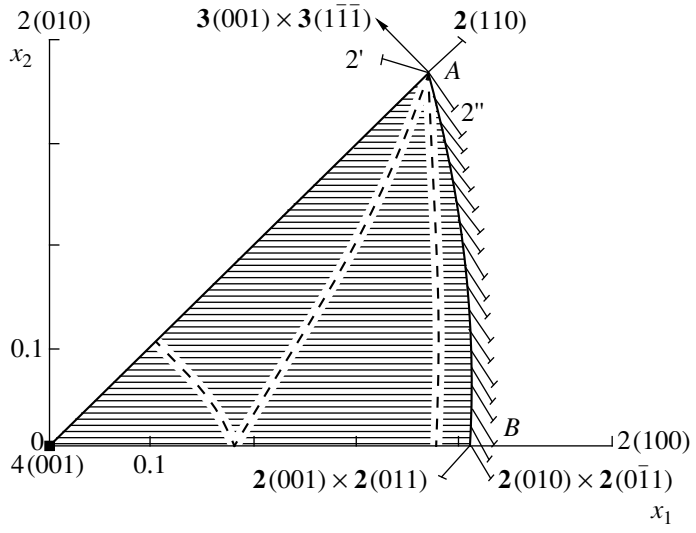

Fig. 1. Arrangement of point operators corresponding to the normalizer of the symmetry group $\mathbf{3} \times \mathbf{23}$ along the boundary of the planar minimum domain of parameters in T^3.

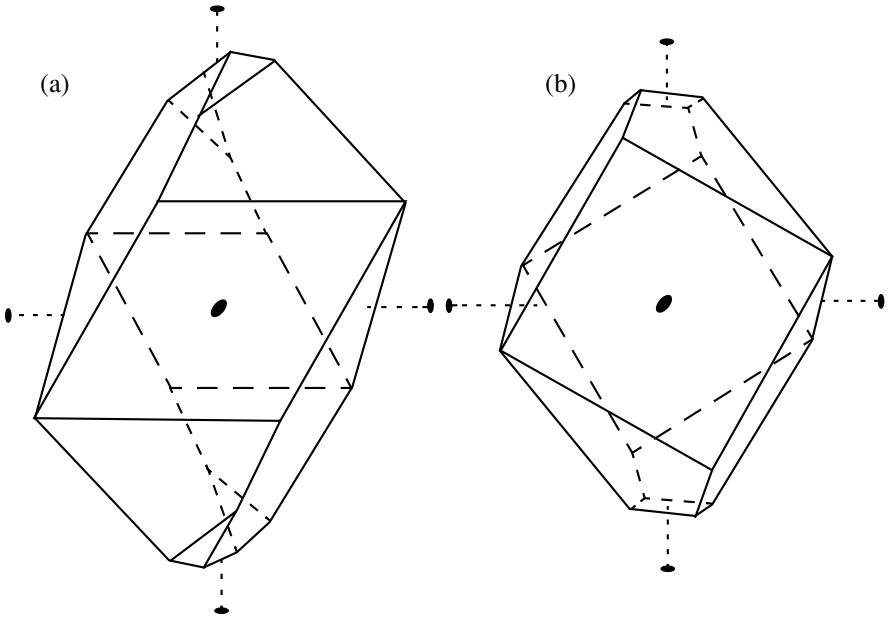

Fig. 2. Stereohedra corresponding to the regular partition of the fundamental domain of parameters for two symmetry groups at the general extremum point $B(0.414, 0, 0)$: (a) $\mathbf{3} \times \mathbf{23}$, $p_2/p_0 = 14/20$ and (b) $\mathbf{3} \times \mathbf{432}$, $p_2/p_0 = 12/16$, where p_2 is the number of faces and p_0 is the number of vertices in the polyhedron of the **222**-type symmetry (supersymmetry).

Among the rotations of the point group **322** located at the upper corner point A (0.366, 0.366) of the minimum domain of parameters, we have the threefold axis, which is simultaneously a symmetry axis $\mathbf{3}(001) \times \mathbf{3}(1\bar{1}\bar{1})$ and coincides with the rotation axis corresponding to row 2 in product (12). Twofold axis $\mathbf{2}(110)$ orthogonal to the latter and passing along the bisector of the coordinate angle was mentioned above. Two other axes, 2' and 2", are obtained from the first one by counterclockwise rotations about the threefold symmetry axis in the same way as in the $\mathbf{2}(110)$ dyad. As a result, they are equivalent to the item 6 rotation.

Each point of the boundary line between A and B has its own equivalent of twofold axis **2**" corresponding to the point group **322** of the normalizer. This equivalent is obtained using one-side operator $\mathbf{P}_\alpha(001) \times \mathbf{E}$ corresponding to the "descent" at different values of the parameter α. As a result, we obtain a continuous array of inclined twofold supersymmetry axes beginning at point A by the 2" axis and ending with the dyad $\mathbf{2}(010) \times \mathbf{2}(011)$ at point B (0.414, 0, 0) on the horizontal axis. The third twofold axis $\mathbf{2}(001) \times \mathbf{2}(011)$ of the supersymmetry group **222** at point B is equivalent to the rotation indicated in row 5 according to transformation $\mathbf{E} \times \mathbf{3}(111)$ of the normalizer.

At the computer scanning [17] of the independent domain, the point B is overlapped from the left and the right sides by two neighboring nodal points. The existence of the supersymmetry group **222** was indirectly confirmed being as a nonisometric homology group [8] in divisions corresponding to the nearest nodal points retaining the same combinatorial and topological type. The stereohedron corresponding to the regular partition of the parameter domain at point B is shown in Fig. 2a.

The results obtained can be extended, without any modifications, to the diagram describing the boundaries of the fundamental parameter domain of the symmetry group $\mathbf{3} \times \mathbf{432}$ [18] having the same normalizer as the group $\mathbf{3} \times \mathbf{23}$. The configuration of the limiting stereohedron corresponding to point B of the parameter domain is shown in Fig. 2b.

ACKNOWLEDGMENTS

The author is grateful to V.A. Koptsik for his valuable remarks.

REFERENCES

1. *International Tables for Crystallography. Vol. A. Space-Group Symmetry*, Ed. by T. Hahn (Reidel, Dordrecht, Holland, 1983), p. 869.
2. E. Koch and V. Fischer, Acta Cryst., Sect. A: Cryst. Phys., Diffr., Theor. Gen. Crystallogr. **31**, 88 (1975).
3. V. I. Burdina, Dokl. Akad. Nauk **350**, 78 (1996) [Phys. Dokl. (1996)].
4. V. I. Burdina, Dokl. Akad. Nauk **328**, 459 (1993) [Phys. Dokl. **38**, 49 (1993)].
5. A. G. Kurosh, *The Theory of Groups* (Nauka, Moscow, 1967, 3rd ed.; Chelsea, New York, 1960, 2nd ed.).
6. P. Curie, *Selected Works* (Nauka, Moscow, 1960).
7. A. V. Shubnikov and V. A. Koptsik, *Symmetry in Science and Art* (Nauka, Moscow, 1972; Plenum Press, New York, 1974).

8. B. K. Vaĭnshteĭn, *Modern Crystallography. Vol. 1. Symmetry of Crystals. Methods of Structural Crystallography*, Ed. by B. K. Vaĭnshteĭn (Nauka, Moscow, 1979; Springer, Berlin, 1994, 2nd ed.).
9. A. V. Shubnikov, Usp. Fiz. Nauk **59**, 591 (1956).
10. V. I. Burdina, Dokl. Akad. Nauk SSSR **204**, 338 (1972) [Sov. Phys. Dokl. **17**, 428 (1972)].
11. V. I. Burdina, Dokl. Akad. Nauk SSSR **222**, 841 (1975) [Sov. Phys. Dokl. **20**, 378 (1975)].
12. L. S. Pontryagin, *Topological Groups* (Nauka, Moscow, 1988, 4th ed.; Gordon and Breach, New York, 1966).
13. G. A. Korn and T. M. Korn, *Mathematical Handbook for Scientists and Engineers* (McGraw-Hill, New York, 1961; Nauka, Moscow, 1970).
14. P. S. Aleksandrov, *Course of Analytical Geometry and Linear Algebra* (Nauka, Moscow, 1979).
15. M. Gubler, Z. Kristallogr. **158**, 1 (1982).
16. Z. Bieberbach, Math. Ann. **72**, 400 (1912).
17. V. I. Burdina, Dokl. Akad. Nauk SSSR **250**, 854 (1980) [Sov. Phys. Dokl. **25**, 62 (1980)].
18. V. I. Burdina, Dokl. Akad. Nauk SSSR **246**, 96 (1979) [Sov. Phys. Dokl. **24**, 317 (1979)].

Translated by K.I. Kugel

Crystallography Reports, Vol. 45, No. 3, 2000, pp. 356–359. Translated from Kristallografiya, Vol. 45, No. 3, 2000, pp. 398–401.

DIFFRACTION AND SCATTERING OF X-RAY AND SYNCHROTRON RADIATION

Normalization of Intensity Curves in X-ray Diffraction by Disordered Systems

V. É. Sokol'skiĭ, V. P. Kazimirov, V. A. Shovskiĭ, and Ya. I. Stetsiv*

Kiev State University, ul. Glushkova 6, Kiev, 252127 Ukraine

** University L'vivs'ka Politekhnika, L'viv, Ukraine*

Received November 21, 1995; in final form, February 10, 1998

Abstract—The application of the method of graphic construction of the background line (widely used in electron diffraction analysis of amorphous films) to the normalization of X-ray intensity curves obtained by the "reflection" method has been considered. © *2000 MAIK "Nauka/Interperiodica".*

The present study is devoted to the normalization of experimental scattering curves by the method suggested earlier by one of the authors for the X-ray study of disordered materials (melts, glasses, solutions, amorphous substances) [1–3]. Despite the fact that this method was initially developed and used in the electron diffraction study of amorphous films, it can also be successfully applied to X-ray diffraction studies of disordered systems [4].

The major goal of the primary processing of the experimental diffraction data for disordered materials is the reliable separation of the coherent component from the intensity curve of the scattered radiation. With this aim, the experimental curve is first normalized to the absolute values. This procedure is most often based on the law of intensity conservation, within which the normalization coefficient K is determined from the equation [5]

$$K = \int_{s_1}^{s_m} [I_{in}(s)/f^2(s) + 1]s^2 ds / \int_{s_1}^{s_m} [I(s)/Pf^2(s)]s^2 ds, \quad (1)$$

where $I(s)$ is the experimental value of the intensity of the scattered radiation in arbitrary units, $f^2(s)$ is the atomic scattering factor, $I_{in}(s)$ is the intensity of incoherent scattering, P is the polarization correction, $s = 4\pi\sin\theta/\lambda$ is the diffraction vector, θ is the scattering half-angle, and λ is the wavelength of the radiation used. Constructing the X-ray $I_{in}(s)$ curve, one most often uses the tabulated intensity values for the Compton scattering calculated within a certain approximation [6].

Strictly speaking, equation (1) is applicable only to a system of independently scattering particles, because the curve is normalized to the sum of atomic amplitudes of coherent ($f^2(s)$) and incoherent ($I_{in}(s)$) scattering. However, in condensed systems, there are also some additional scattering mechanisms introducing certain contributions to the total intensity of the scattered radiation. These are single and multiple scattering, scattering by phonons, plasma scattering, etc. Therefore, the experimental intensities of the radiation scattered by condensed systems should be normalized to the total sum of the atomic amplitudes of all types of scattering taking place in such systems [2]. This important fact should be necessarily taken into account when normalizing the experimental data, because it is one of the main sources of nonuniqueness of such structural parameters as the shortest interatomic distances, coordination numbers, etc.

In connection with the above stated, the process of separation of the coherent component in electron diffraction of amorphous materials includes the stage of constructing a background line for the experimental scattering curve. This procedure was considered in detail elsewhere [1] and, therefore, we skip it here. If one uses the "reflection" method in X-ray diffraction, then, depending on the nature and composition of the sample and the beam monochromatization, one can encounter a situation in which incoherent scattering (or, using an analogy with electron diffraction, background) cannot be reduced to the Compton scattering alone. Such materials are those consisting of chemical elements with small atomic numbers characterized by low values of the atomic scattering factors and absorption coefficients. In this case, the penetration depth of X-rays considerably increases and "reflection" is provided not only by the surface layer, but also by deeper ones, which results in partial beam defocusing, multiple scattering, and the action of other scattering mechanisms which are difficult to take into account when normalizing the intensity curve of the scattered radiation. In this situation, it is expedient to use the normalization method suggested in [1].

Many of the above problems can be eliminated by placing the monochromator into a diffracted beam, although the technical implementation of the method often dictates the use of the conventional variant of beam monochromatization.

1063-7745/00/4503-0356$20.00

The efficiency of the procedure of constructing the background line used in electron diffraction [1] is determined by the fact that the nature of incoherent scattering (which, as was indicated above, can be rather complicated and cannot be estimated theoretically) in this case becomes unimportant. The only requirement to be met is that the intensity curve should uniformly oscillate about the background line, following in turn, from the requirement of uniform oscillation of the structure factor around the unity ($a(s) = I'(s)/f^2(s)$, where $I'(s)$ is the intensity of coherent scattering in electron units). For a more convenient construction of the background line, the experimental scattering curve is reduced to the form $I(s)/Pf^2(s)$ with much more pronounced oscillations, which provides their more reliable separation at large scattering angles.

The initial criterion for drawing of an appropriate background line ($I_b(s)/f^2(s)$) is the fulfillment of the equality

$$\int_{s_1}^{s_2} \frac{I(s)}{Pf^2(s)} ds = \int_{s_1}^{s_2} \frac{I_b(s)}{f^2(s)} ds. \quad (2)$$

Then

$$a(s) - 1 = \frac{I'(s) - f^2(s)}{f^2(s)} = K\left[\frac{I(s)}{Pf^2(s)} - \frac{I_b(s)}{f^2(s)}\right] \quad (3)$$

and the normalization coefficient can be determined in the following way [1–2]:

(i) as the average between the maximum and minimum values of the functions $I(s)/Pf^2(s)$ and $I_b(s)/f^2(s)$, namely

$$K_{av} = \frac{1}{2}\left[\left(\frac{I_b(s)}{f^2(s)} - \frac{I(s)}{Pf^2(s)}\right)_{max} + \left(\frac{I_b(s)}{f^2(s)}\right)_{min}\right]; \quad (4)$$

(ii) from the curve of the radial distribution of atoms in the range $R < R_1$, where R_1 is the shortest interatomic distance

$$4\pi R^2[\rho(R) - \rho_0] = \frac{2R}{\pi}K \times \int_{s_1}^{s_2} s\left[\frac{I(s)}{Pf^2(s)} - \frac{I(s)}{f^2(s)}\right]\sin(sR)ds = KF(R). \quad (5)$$

It follows from (5) that at $R < R_1$ $\rho(R) = 0$, we have $-4\pi R^2\rho_0$, and the curve $KF(R)$ should become a parabola described as $-4\pi R^2\rho_0$. However, the $F(R)$ curve in the range of small R values have some spurious oscillations caused by the measurement errors and experimental-data processing a result, the $F(R)$ curve oscillates around the parabola $-4\pi R^2\rho_0$. Therefore, the areas limited by the curves $KF(R)$ and $-4\pi R^2\rho_0$ should be equal to

$$K\int_0^{R_0} F(R)dR = -\int_0^{R_0} 4\pi R^2\rho_0 dR, \quad (6)$$

whence one can readily calculate the normalization coefficient. In (6), R_0 is the radius in the vicinity of the first coordination maximum, where the function $F(R)$ is still negative.

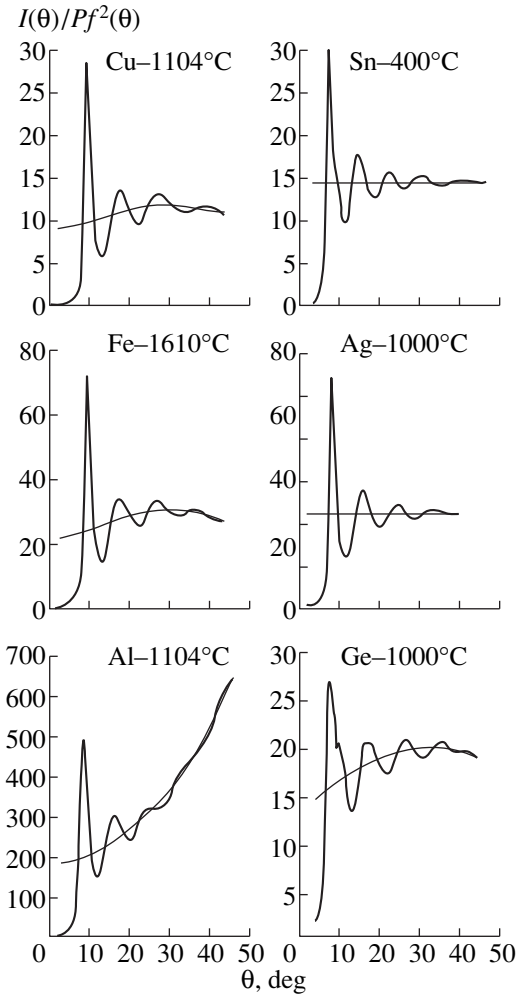

Fig. 1. $I(s)/Pf^2(s)$ curves and the background lines, $I_b(s)/f^2(s)$, constructed by (2) for some liquid metals.

Structural parameters of liquid silver obtained by the graphic and analytic* methods of normalization

K	$a(s_1)$	R_1, Å	Z_1
0.03507	2.45	2.85	7.3
0.03437	2.50	2.85	7.3
0.03370	2.55	2.86	7.3
0.03722*	2.55*	2.86*	7.3*

* Parameters obtained using (1).

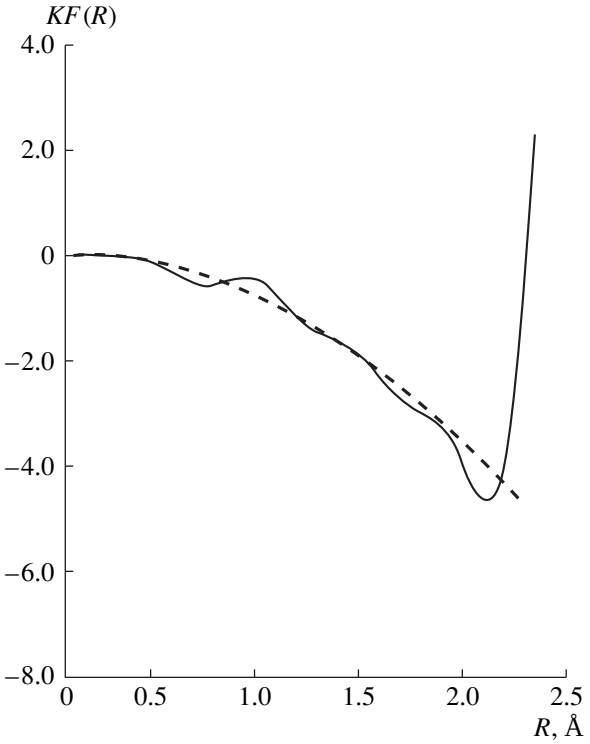

Fig. 2. $KF(R)$ (solid line) and $-4\pi R^2\rho_0$ (dashed line) curves for liquid Fe in the range $R < R_1$ at the optimum value of the normalization coefficient.

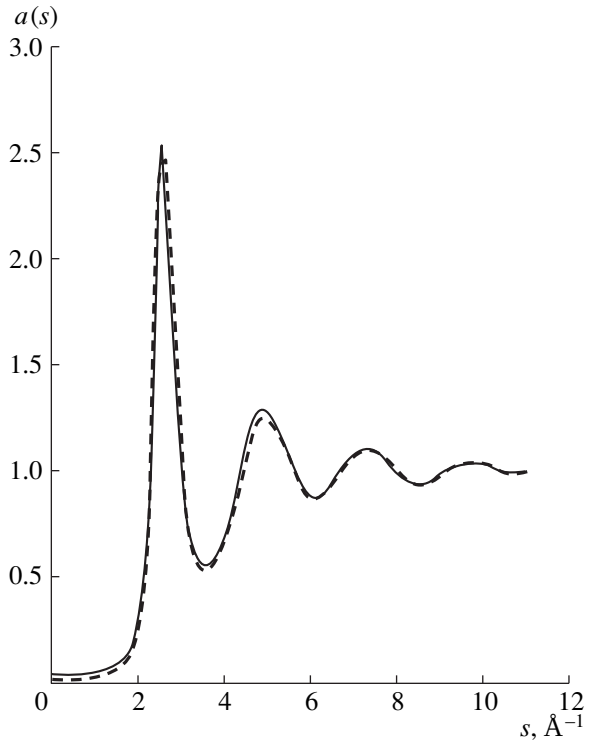

Fig. 3. Structure-factor curves for liquid silver; the dashed line indicates normalization by (1); the solid line is obtained by the graphical method of normalization.

In practice, the normalization coefficient is determined by the method of successive approximations from equations (4)–(6). As the first approximation, one uses the value obtained from (4), whereas the subsequent corrections are obtained from equations (5) and (6) under the requirement of uniform oscillations of the curve $KF(R)$ around the parabola $-4\pi R^2\rho_0$. In the second case, the control is performed visually by displaying the $KF(R)$ and $-4\pi R^2\rho_0$ curves on the display screen. Thus, one cycle of the calculations includes the setting of the normalization coefficient and the calculation of the structure factor and the radial distribution function (RDF) of atoms in the range where $R < R_1$. This procedure is repeated until the optimum K value satisfying all the above criteria is attained.

The application of the method to liquid metals is illustrated by Fig. 1, which shows the experimental curves $I(s)/Pf^2(s)$ and the background line constructed using (2). Figure 2 shows the portion of the RDF for liquid iron at $R < R_1$, which corresponds to the optimum value of the normalization coefficient. We also studied the influence of the error deliberately introduced into the normalization coefficient on the structural parameters such as the height of the first maximum of the structure factor ($a(s_1)$), the shortest interatomic distance, R_1, and the coordination number, Z_1. These data for liquid silver together with the corresponding data obtained by the conventional normalization method (1) suggested by Vainshtein are listed in table. The Z_1 values were determined by the "symmetrical resolution" of the first maximum of the Gaussian RDF curve whose position is set by R_1 with the left-hand branch coinciding with the experimental data. The symmetric resolution of the maximum performed manually yielded $Z_1 = 7.5$.

It is seen from table that in the vicinity of the optimum normalization coefficient (0.03437 ± 0.00070), the structural parameters determined by both methods coincide. The relationship between the structure-factor curves for liquid silver are shown in Fig. 3. The atomic radial distribution curves are not shown in Fig. 3, because they are exactly the same. For six liquid metals studied (with the exception of aluminum) (Fig. 1), both methods yield the identical results, whence it follows that the incoherent background is determined by the Compton scattering alone. For aluminum the lightest of these elements), the Vainshtein method fails to yield the appropriate structure-factor curve, despite the fact that, in our experiments, the differential filters were located in the diffracted beam and that the use of the MoK_α-radiation provided a smooth "cutting-off" of the Compton scattering intensity beginning with the value $s \approx 6$ Å^{-1} [7]. Nevertheless, the Compton scattering at $\theta = 30°$–$40°$ is responsible for half of the coherent scattering intensity. It is most probable that in this case, some additional scattering mechanisms indicated

above also work. The method of graphical normalization provides the adequate calculation and yields the structural parameters ($a(s_1) = 2.45$, $R_1 = 2.82$ Å, $Z_1 = 7.5$) corresponding to the published data.

Thus, the use of the above method should include the performance of the following operations:

1. The preliminary processing of the experimental data, i.e., interpolation, smoothing, introduction of the polarization correction, the calculation and displaying on the display of the curve $I(s)/Pf^2(s)$ screen.

2. The graphical construction of the background line in accordance with (2).

3. The computation of the normalization coefficient by (4), with its subsequent refinement by (6), with an allowance made for the requirement of one-dimensional oscillations of the $KF(R)$ curve around the parabola $-4\pi R^2\rho(R)$. The optimum value of the normalization coefficient is then used for reducing the experimental scattering curve $I(s)$ to electron units and calculating the atomic radial distribution function.

The above graphic method is a simple and physically justified method, which is more universal then all the other normalization methods, in particular, the Vainshtein method.

REFERENCES

1. I. D. Nabitovich, Ya. I. Stetsiv, and Ya. V. Voloshchuk, Kristallografiya **12** (6), 584 (1967) [Sov. Phys. Crystallogr. **12** (4), 513 (1967)].
2. Ya. I. Stetsiv and R. Ya. Yurechko, in *Proceedings of IV All-Union Conference on Stucture and Properties of Metal and Slag Melts, Sverdlovsk, Russia, 1980* (Sverdlovsk, 1988), Part 2.
3. Ya. I. Stetsiv and R. Ya. Yurechko, in *Proceedings of V All-Union Conference on Stucture and Properties of Metal and Slag Melts, Sverdlovsk, Russia, 1983* (Sverdlovsk, 1983), Part 2.
4. A. K. Dorosh, *Structure of Condensed Systems* (Vishcha Shkola, L'vov, 1981).
5. N. A. Vatolin and É. A. Pastukhov, *X-ray Diffraction Studies of High-Temperature Melts* (Nauka, Moscow, 1980).
6. D. T. Cromer, J. Chem. Phys. **50**, 4857 (1969).
7. W. Bol, Rev. Sci. Instrum. **44**, 736 (1967).

Translated by L. Man

Crystallography Reports, Vol. 45, No. 3, 2000, pp. 360–364. Translated from Kristallografiya, Vol. 45, No. 3, 2000, pp. 402–407.

DIFFRACTION AND SCATTERING OF X-RAY AND SYNCHROTRON RADIATION

X-ray Diffraction from Ideal Mosaic Crystals in External Fields of Certain Types. I. Atomic Displacements and the Corresponding Diffraction Patterns

E. N. Treushnikov

Moscow State Academy of Geological Prospecting, Moscow, Russia

Received July 8, 1998; in final form, July 10, 1999

Abstract—The problem of the theoretical description of X-ray diffraction from ideal mosaic crystals under the effect of various external fields has been formulated. Electric, magnetic, electromagnetic, and acoustic perturbations are considered. The atomic displacements in crystals under the effect of external fields and the types of the corresponding diffraction patterns are analyzed for various types of perturbations. The crystal classes are determined in which atomic displacements can be recorded experimentally. Diffraction patterns formed under the effect of various external factors are considered on the basis of the derived dependence of the structure factor on the characteristics of an applied force field. © *2000 MAIK "Nauka/Interperiodica".*

INTRODUCTION

The experimental studies of X-ray diffraction in crystals in various external fields attract ever growing attention [1–9]. It is clear that under certain external fields, the traditional kinematic theory of X-ray diffraction becomes invalid. In order to be able to study the changes in the crystal structure and the electron-density distribution under the effect of various external perturbations, one has, first of all, to consider and describe X-ray diffraction for ideal mosaic crystals in external fields. The present study is aimed to solve this problem for crystals in electric, magnetic, electromagnetic, and acoustic fields weak in comparison with the corresponding fields inside the crystals.

The study is addressed to scientists studying the crystal structure and electron-density distributions by the X-ray diffraction methods, because these scientists may encounter the effect of the external perturbations in their work. Earlier, the author described in detail almost all the major problems of the kinematical theory of diffraction [10]. Here, the author considers only some of the results important for understanding the essence of the above formulated problem.

ATOMIC DISPLACEMENTS IN A CRYSTAL UNDER THE EFFECT OF EXTERNAL PERTURBATIONS

There is a widespread opinion that under the effect of external fields, atoms in a crystal are displaced to so small distances that they cannot be recorded in diffraction experiments. However, the analysis performed below allows one to choose objects that allow the reliable record of atomic displacements in precision X-ray diffraction experiments.

Atomic displacements under the effect of an external field $\mathbf{E}^{ext}$. A linear dielectric in a magnetic field acquires the macroscopical polarization $\mathbf{P} = \varepsilon_0\kappa\mathbf{E}$ (where ε_0 is the dielectric constant, κ is the dielectric susceptibility, and $\mathbf{E}$ is the macroscopic field inside the crystal). Since $\mathbf{P}$ is proportional ($\backsim$) to the average atomic displacements $\langle\Delta\mathbf{r}\rangle$, we can state that $\langle\Delta\mathbf{r}\rangle \backsim \mathbf{E}$ (it is assumed that these vectors are parallel). For piezoelectrics, this effect is enhanced, because the inverse piezoeffect gives rise to the following atomic displacements $r_{ij} = d_{mij}E_m$ (where i, j, and m takes the values from 1 to 3 and d_{mij} and r_{ij} are the components of the tensor of piezomodules and strains, respectively) [11, p. 165]. The relationship $\langle\Delta\mathbf{r}\rangle \backsim \mathbf{E}$ is valid not only for polarization due to ionic displacements, but also for polarization due to electron displacements.

In practice, it is more convenient to measure not the field inside a crystal, but the external field $\mathbf{E}^{ext}$ (or the potential difference U between the crystal faces). The relationship between these fields is established from the boundary conditions. If the applied field $\mathbf{E}^{ext}$ is normal to the face of a crystal in vacuum, then $\mathbf{E}^{ext} = \varepsilon\mathbf{E}$ (where ε is the dielectric constant of the crystal), we have $\langle\Delta\mathbf{r}\rangle \backsim \mathbf{E}^{ext}$.

It can readily be shown that in the transition from the average, $\langle\Delta\mathbf{r}\rangle$, to the local, $\Delta\mathbf{r}_s$, displacements (where s is the atomic number), we have $\Delta\mathbf{r}_s = \hat{a}_s\mathbf{E}^{ext}(\mathbf{r}_s)$. In this case, $\hat{a}_s$ depends on the kind of an atom and its position and should be considered as a second-rank tensor relating the vectors $\mathbf{E}^{ext}(\mathbf{r}_s)$ and $\Delta\mathbf{r}_s$. In the general case, the values of the components $a_{lm}^{(s)}$ of the tensor $\hat{a}_s$ depend on the orientation of the vector

$\mathbf{E}^{\mathbf{ext}}$ with respect to the crystallographic coordinate system. Hereafter, we assume that $\mathbf{E}^{\mathbf{ext}} \parallel \mathbf{a}$. Then

$$\Delta x_{s,l} = a_{l1}^{(s)} E^{\text{ext}}(\mathbf{r}_s), \quad (1)$$

where $l = 1$–3; $\Delta x_{s,1} \equiv \Delta x$; $\Delta x_{s,2} \equiv \Delta y$; and $\Delta x_{s,3} \equiv \Delta z$. Following the conventional X-ray diffraction studies, it is natural to consider $a_{l1}^{(s)}$ as parameters that can be refined by the least squares method. If the field $\mathbf{E}^{\mathbf{ext}}$ is inhomogeneous, then the periodicity of the atomic structure is disturbed, and the traditional kinematic theory should be modified.

We should like to emphasize that it is very important to choose appropriately the objects for the experimental recording of the atomic displacements under the effect of an electric field. Consider, e.g., the contribution of the piezoelectric component (having the largest value) to the total average atomic displacement. For linear dielectrics, the piezomodulus d is usually of the order of 10^{-6}–10^{-8} CGSE units (we do not use here the tensor notation). Therefore, applying the potential difference $U \sim 10$ CGSE units = 3 kV to the opposite crystal faces (which corresponds to the field $\mathbf{E} \approx 3 \times 10^6$ V/m at the crystal dimension $l \approx 1$ mm), we obtain the deformation of $\Delta l/l \approx 10^{-4}$–$10^{-6}$. The maximum $\Delta l/l$ value is at the accuracy limit in recording the changes in the heavy-atom positions. However, the piezoelectric constants for ferroelectrics considerably exceed the corresponding values for conventional linear dielectric. Thus, for the tetragonal $BaTiO_3$ modification, the coefficient d is equal to $d \approx (10^{-5}$–$10^{-6})$ CGSE units ([11], p.192). Therefore, at $U \approx 10$ CGSE units, the average relative atomic displacement equals $\sim 10^{-3}$–10^{-4}, i.e., has the value that can be detected by the X-ray diffraction method. Close estimates can also be obtained for other ferroelectrics, e.g., for Seignette salt, triglycine sulfate, lithium niobate, etc.

Atomic displacements under the effect of a magnetic field $\mathbf{H}^{\mathbf{ext}}$. In most cases, magnetostriction in para- and diamagnetics is rather low, $\Delta l/l \sim 10^{-6}$–10^{-7}. However, recent studies recorded anomalously high (gigantic) magnetostriction in paramagnetics of rare-earth metals and in some alloys [12, p. 117]. Thus, magnetostriction of the $TmLiF_4$ paramagnetic in a field of about ~10 kOe equals $\sim 2 \times 10^{-4}$, and in the field of ~30 kOe, it attains the value of $\sim 10^{-3}$ (at low temperatures), and, therefore, can be recorded by the X-ray diffraction method. The functional dependence of magnetostriction in the paraprocess on the field $\mathbf{H}$ is given in [12, p. 35]. This dependence shows that $\Delta l/l$ is proportional to H^2 (and, therefore also to $(H^{\text{ext}})^2$), because the magnetic susceptibility for paramagnetics is $\mu \approx 1$. This was confirmed experimentally [12, p. 35]. Passing from the average displacements to the local atomic displacements $\Delta x_{s,l}$, one can write

$$\Delta x_{s,l} = c_l^{(s)} (H^{\text{ext}}(\mathbf{r}_s))^2, \quad (2)$$

where the proportionality coefficients $c_l^{(s)}$ are independent of the field H^{ext}, but, because of anisotropy in magnetostriction, depend on the field orientation.

For ferro- and ferrimagnetics, magnetostriction can also attain gigantic values of the order of $\sim 10^{-4}$–10^{-2} [12, Chs. 3 and 4], and, therefore, can be studied in the X-ray diffraction experiment. However, because of the specific behavior of the spontaneous-magnetization vector $\mathbf{I}_s$ in a magnetic field $\mathbf{H}^{\text{ext}}$, in the general case, the dependence of magnetostriction on $\mathbf{H}^{\text{ext}}$ is of a complicated nonlinear nature and cannot be described analytically. The numerous graphic dependences of magnetostriction $\Delta l/l$ on $\mathbf{H}^{\text{ext}}$ [12, Chs. 3, 4] are rather intricate. Therefore, it is expedient to write the dependence of the atomic displacements $\Delta x_{s,l}$ on the field $\mathbf{H}^{\text{ext}}$ as

$$\Delta x_{s,l} = b_{l1}^{(s)} H^{\text{ext}}(\mathbf{r}_s), \quad (3)$$

under the assumption that the coefficients $b_{l1}^{(s)}$ are the functions of $\mathbf{H}^{\text{ext}}$. The chemical formulas for a number of compounds possessing gigantic magnetostriction and the corresponding values of the field intensities and temperature are given in [12, Chs. 3 and 4].

As to the effect of harmonic perturbations (electromagnetic and acoustic fields), it is clear that, except for some particular cases, the time-averaged displacements $\Delta \mathbf{r}_s$ are equal to zero, i.e., $\Delta x_{s,l} = 0$.

The estimation of the changes $|\Delta I|$ in the integrated intensity I presents no difficulty either. At $\langle \Delta x \rangle \sim 10^{-4}$–$10^{-2}$, these changes are $|\Delta I| \sim I \times 10^{-3}$–0.8 for the far reflections, where I is the intensity of the diffraction peak in the absence of any external factors. The error in the intensities measured on diffractometers is $\sigma I \sim \sqrt{I}$, therefore, $\sigma I/I \sim \sqrt{1/I}$ and, for rather strong reflections, we have $I \sim (10^3$–$10^4)$ pulse/min, $\sigma I/I \sim (3$–$1) \times 10^{-2}$. The latter value dictates a very thorough selection of the experimental strategy in order to reveal the effect.

In the general case, in addition to the contribution into the change of the integrated intensity due to atomic displacements (the changes in their coordinates), one can also observe the contributions due to the variation in the temperature and extinction parameters and the deformation of the electron density of the outer valence shells. However, it is rather difficult and, in some cases, even impossible to estimate these contributions. We indicate here only that, in some cases, these contributions would increase the value of $|\Delta I|/I$, and the above estimates should be considered as the lower limit of the relative change in the intensity under the effect of the above external factors.

EXPRESSION FOR A STRUCTURE FACTOR AND ANALYSIS OF DIFFRACTION PATTERNS

The expression for the structure factor $F(\mathbf{S})$ is one of the basic relationships of the traditional theory. There-

fore, it is expedient to consider the changes in the expression for $F(\mathbf{S})$ and to analyze the diffraction pattern obtained from crystals in external fields. Hereafter, $\mathbf{S}$ is the reciprocal-lattice vector, whose components s_l (l = 1–3) can take any values; the vector $\mathbf{H}$ has its conventional meaning, and the components h_l are integers.

Let A^{ext} be the amplitude of an external homogeneous force field resulting in the displacement of atoms by a value $\Delta x_{s,l}$. These fields can be induced, e.g., by some electric, magnetic, and mechanical factors. The periodicity of the crystal in a homogeneous field is preserved, therefore the expressions for $F_1(\mathbf{H})$ (hereafter, the subscript 1 indicates the presence of external perturbations) can be obtained from the traditional $F(\mathbf{H})$ by expanding $\exp 2\pi i\mathbf{H}(\mathbf{r}_s + \Delta\mathbf{r}_s)$ into series within the accuracy of the linear term (because of the smallness of $\Delta x_{s,l}$). Then

$$F_1(\mathbf{H}) = F(\mathbf{H}) + 2\pi i A^{\text{ext}} \times \sum_{s,l} f_s(\mathbf{H}) h_l a_{l1}^{(s)} \exp(2\pi i \mathbf{H}\mathbf{r}_s). \quad (4)$$

In the above expression, we used the expressions of types (1) and (3) and assume that $f_{1,s}(\mathbf{H}) \approx f_s(\mathbf{H})$. Relationship (4) yields the dependence $F_1(\mathbf{H})$ on the applied field, A^{ext}. The unknown quantities $a_{l1}^{(s)}$ can be considered as the parameters to be refined.

General expression for structure factor in inhomogeneous external fields. In this situation, the initial crystal periodicity is disturbed, and, therefore, it is natural to introduce the concept of the structure scattering amplitude by the whole crystal, $F_{\text{cr}}(\mathbf{S})$. Let $\mathbf{R}_{mnp}$ be a translation vector determining the origin of a certain (mnp)th averaged unit cell of a prismatic crystal (m, n, and p are integers ranging from 0 to M_1, M_2, M_3, respectively). At small displacements $\Delta\mathbf{r}_{s,mnp}$, one can expand $F_{\text{cr}}(\mathbf{S})$ into a Taylor series:

$$F_{\text{cr}}(\mathbf{S}) = \sum_{mnp} \exp(2\pi i \mathbf{S}\mathbf{R}_{mnp}) \times \left[F(\mathbf{H}) + \sum_{s,l} \frac{\partial F(\mathbf{H})}{\partial x_{s,l}} \Delta x_{l,mnp}^{(s)} \right], \quad (5)$$

where, within the diffraction peak, we have $F(\mathbf{S}) \approx F(\mathbf{H})$. The latter quantity is the structure factor which describes scattering by only one unit cell, where atoms are located in the positions $\mathbf{r}_s$. To pass from the sum $\sum_{mnp} \exp(2\pi i \mathbf{S}\mathbf{R}_{mnp})$ to the integral form, we have to introduce a new vector $\boldsymbol{\varepsilon} \equiv \mathbf{S} - \mathbf{H}$. For a specimen in the shape of a parallelepiped with the linear dimensions $L_1 = M_1 a_1$, $L_2 = M_2 b_1$, and $L_3 = M_3 c_1$, we obtain

$$\sum_{mnp} \exp(2\pi i \mathbf{S}\mathbf{R}_{mnp}) \approx \frac{1}{V}\int_V \exp(2\pi i \boldsymbol{\varepsilon}\mathbf{r}) dv = \prod_{l=1}^{3} \frac{\sin \pi \varepsilon_l M_l}{\pi \varepsilon_l}, \quad (6)$$

where integration is performed over the crystal volume v, V is the unit cell volume, and $\varepsilon_l = s_l - h_l$. Assuming that $a_{l1}^{(s)}$ is independent of A^{ext} and taking into account (5) and (6), we can write $F_{\text{cr}}(\mathbf{S})$ in the form

$$F_{\text{cr}}(\mathbf{S}) = \prod_{l=1}^{3} \frac{\sin \pi \varepsilon_l M_l}{\pi \varepsilon_l} F(\mathbf{H}) + \int_{-M_1/2}^{+M_1/2} A^{\text{ext}}(x) \exp(2\pi i \varepsilon_1 x) dx \times \prod_{l=2}^{3} \frac{\sin \pi \varepsilon_l M_l}{\pi \varepsilon_l} \sum_{s,l} \frac{\partial F(\mathbf{H})}{\partial x_{s,l}} a_{l1}^{(s)}. \quad (7)$$

Relationship (7) describes the diffraction pattern in the space of structure factors as a function of $A^{\text{ext}}(x)$. The first term describes discrete peaks localized at the reciprocal-lattice points $\mathbf{H}$ characteristic of the periodic crystal. Their shapes (angular dependence) are described by the function $\prod_{l=1}^{3} (\sin \pi \varepsilon_l M_l)/\pi \varepsilon_l$, and the amplitude is equal to $F(\mathbf{H})$ [13, p. 47]. The second term characterizes the deviation of the diffraction pattern from the pattern predicted by the kinematic theory. It depends on the form of the external factor $A^{\text{ext}}(x)$. The shape of the peaks formed along the axis $\mathbf{a}^*$ is determined by the integral in (7). Here, broadening of the diffraction peak because of the finite value of the spectral interval $\Delta\lambda$, crystal mosaicity, and incident-beam divergence is ignored. The shapes of the peak along $\mathbf{b}^*$ and $\mathbf{c}^*$ remain the same. To predict the form of the diffraction pattern, consider several characteristic cases.

Homogeneous perturbations as a particular case of general expression (7). At A^{ext} = const, the integral in (7) equals $A^{\text{ext}}(\sin \pi \varepsilon_l M_l)/\pi \varepsilon_1$. In this case, the diffraction pattern is a set of discrete peaks localized at the reciprocal-lattice points $s_l = h_l$. Their shapes are described by the function $\prod_{l=1}^{3} (\sin \pi \varepsilon_l M_l)/\pi \varepsilon_l$, and the amplitude depends on A^{ext}. Naturally, this result also correlates with (4).

External factor of the type $A^{\text{ext}}(x) = A_0^{\text{ext}} \cos 2\pi k_1 x$. It should be remembered that in the X-ray diffraction, x is a dimensionless quantity, and, therefore, the "wave number" is $k_1 = a/\lambda_1$. The role of the external factor can be played by inhomogeneous electric and magnetic fields and electromagnetic or

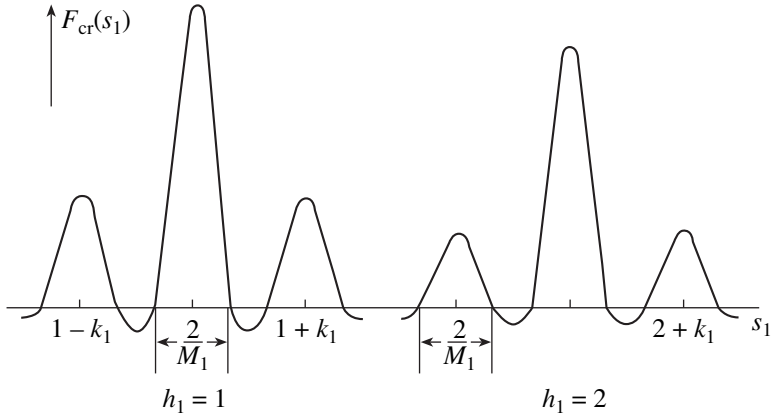

Fig. 1. Schematic view of the one-dimensional section of the peaks of the function $F_{cr}(\mathbf{S})$ for two reciprocal-lattice points, $h_1 = 1$ and $h_1 = 2$, under the applied external fields of the form $A^{ext}(x) = A_0^{ext}\cos 2\pi k_1 x$. The case where $\lambda_1 < L_1/2$. Only the real values of $F_{cr}(\mathbf{S})$ are considered.

acoustic standing waves, whose amplitudes are characterized by the above dependence. The integral in (7) is equal to $A_0^{ext}\sum_{\pm}\sin[\pi(k_1 \pm \varepsilon_1)M_1]/2\pi(k_1 \pm \varepsilon_1)$. Therefore, in addition to the main peak at $s_l = h_l$, there are two additional (auxiliary) peaks at $s_1 = h_1 \pm k_1$, $s_2 = h_2$, and $s_3 = h_3$ (Fig. 1). Their shape along the **a***-axis is described by the function $\sin[\pi(k_1 \pm \varepsilon_1)M_1]/2\pi(k_1 \pm \varepsilon_1)$ with the amplitude $A_0^{ext}\sum_{s,l}(\partial F(\mathbf{H})/\partial x_{s,l})a_{l1}^{(s)}$. Equation (7) also yields the overlapping condition of the main and the auxiliary peaks. These peaks overlap if $\lambda_1 > (L_1/2)$. At $\lambda_1 = L_1$, the center of the auxiliary maximum coincides with the edge of the major peak (Fig. 2). It is the case of the maximum peak overlapping, because, at $\lambda_1 > L_1$, the periodic effect of external perturbation has no physical sense. It should be indicated that the allowance for primary beam divergence, nonmonochromaticity, etc. broadens both main and auxiliary peaks, so that some peaks on the experimental diffraction pattern are not resolved. However, the above analysis should necessarily be performed, because the integrated intensities of the measured reflections are independent of the above experimental conditions and are determined by the interference function under consideration. Moreover, it is clear that the diffraction theory describes most completely the "ideal experiment", because the main quantities used in the theory are independent of the details of the experimental setup.

The case considered above allows one to analyze the diffraction pattern from the crystal in an external field of a more general form as well. Indeed, if $A^{ext}(x)$ is a superposition of perturbations of different frequencies, it can be expanded into a Fourier series, namely, $A^{ext}(x) = \sum_n A_{0n}^{ext}\cos 2\pi n k_1 x$, where A_{0n}^{ext} is the amplitude of the nth harmonic. Then, in accordance with (7), to each frequency (wave number), there correspond two additional maxima located at the points $s_1 = h_1 \pm nk_1$, $s_2 = h_2$, and $s_3 = h_3$. Figure 3 shows the diffraction pattern at $n = 1, 2$.

External factor of the type $A^{ext}(x) = (A_0^{ext}/2\pi)\exp(-\alpha x^2)$. We assume that the constant α allows to extend the integration limits in (7) to infinity. Therefore, this integral is equal to $(A_0^{ext}/2\sqrt{\pi\alpha})\exp(-\pi^2\varepsilon_1^2/\alpha)$. As a result, the diffraction peaks on the diffraction pattern are not broadened along the **a***-axis and their heights remain constant (Fig. 4). The above transformation depends on the parameters α and A_0^{ext} of the external field.

External factor of the type $A^{ext}(x) = A_0^{ext}\exp(-2\pi\alpha x)$. Choosing the constant α in such a way that $A^{ext}(x)$ rapidly decreases within the crystal, we can use the integration limits from zero to infinity. Then, the integral in (7) equals $A_0^{ext}(\alpha + i\varepsilon_1)/2\pi(\alpha^2 + \varepsilon_1^2)$. The

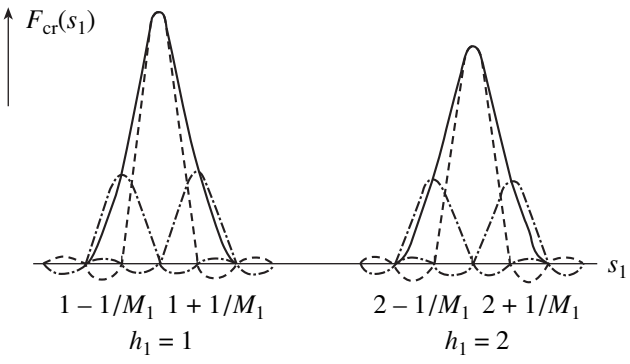

Fig. 2. The same as in Fig.1 for the case $\lambda_1 = L_1$. The dashed and dashed-dotted lines represent individual terms in (7), the solid line shows their sum.

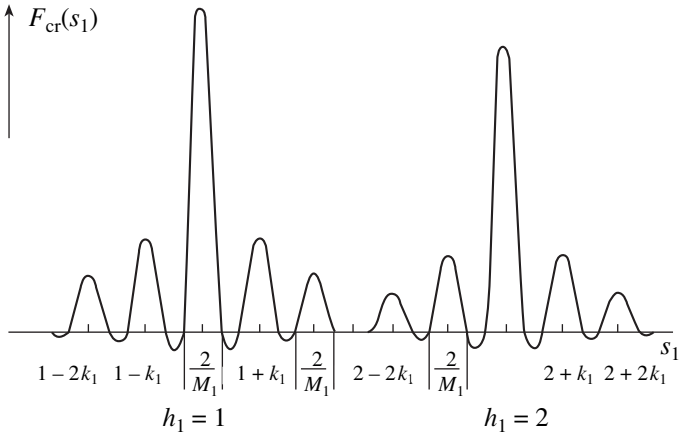

Fig. 3. Schematic form of one-dimensional section of the peaks of the function $F_{cr}(\mathbf{S})$ for two reciprocal-lattice points $h_1 = 1$ and $h_1 = 2$ under the effect of an applied field of the form $A^{ext}(x) = \sum_{n=1}^{2} A_{0n}^{ext} \cos 2\pi n k_1 x$. Only the real values of $F_{cr}(\mathbf{S})$ are considered.

modulus of this function has the maximum at the peak center and provides a broadening of the diffraction line and a change of its height. These changes are determined by the parameters of the external factor, α and A_0^{ext}.

The transformations occurring in the diffraction pattern can also be analyzed for other forms of external factors in a similar way.

Now, estimate the intensities of auxiliary maxima I^{aux} with respect to the intensity of the main peak I^{main} under the effect of a periodic external factor. The corresponding relationships are determined by the atomic displacements $\Delta x_{s,l}$. For the averaged $\langle \Delta x \rangle$ value (averaging is performed over the subscript l and the number of independent atoms s), we obtain the ratio $I^{aux}/I^{main} \sim (\langle \Delta x \rangle \pi \sum_l h_l)^2$. As a result, if $\langle \Delta x \rangle \sim 10^{-3}$–$10^{-2}$ (the above estimates), we have $I^{aux} \sim 2 \times (10^{-3}$–$10^{-1}) I^{main}$; for the high-angle reflections, $\sum_l h_l \sim 14$.

It should be indicated that the changes in the diffraction pattern can also be observed in the transitions from the ideal to a real single crystal because of certain modulations of their lattices in the process of crystal formation. The above description can be useful in this case as well.

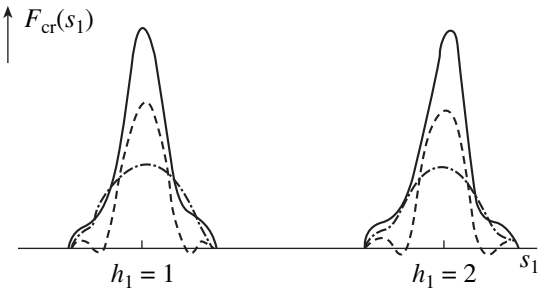

Fig. 4. The same as in Fig. 3 under the field of the form $A^{ext}(x) = (A_0^{ext}/2\pi)\exp(-\alpha x^2)$. The dashed and dashed-dotted lines represent individual terms in (7), the solid line shows their sum.

REFERENCES

1. J. Fujumoto, Acta Crystallogr., Seet. A: Cryst. Phys., Diffr., Theor. Gen. Crystallogr. **38**, 337 (1982).
2. M. Mikami-Kido and M. Konno, J. Magn. Magn. Mater. **31–34**, 775 (1983).
3. T. Tamegai, K. Tsutsumi, S. Kagoshima, *et al.*, Solid State Commun. **56**, 13 (1985).
4. V. N. Trushin, E. V. Chuprunov, and A. F. Khokhlov, Pis'ma Zh. Tekh. Fiz. **14**, 307 (1988) [Sov. Tech. Phys. Lett. **14**, 136 (1988)].
5. A. A. Zholudev, V. N. Trushin, E. V. Chuprunov, and A. F. Khokhlov, Pis'ma Zh. Tekh. Fiz. **17**, 90 (1991).
6. V. A. Shuvaev, M. Yu. Antipin, O. E. Fesenko, *et al.*, Kristallografiya **37**, 1033 (1992) [Sov. Phys. Crystallogr. **37** (4), 551 (1992)].
7. V. A. Shuvaeva, M. Yu. Antipin, S. V. Lindeman, *et al.*, Kristallografiya **37**, 1502 (1992) [Sov. Phys. Crystallogr. **37** (6), 814 (1992)].
8. A. A. Zholudev, V. N. Trushin, E. V. Chuprunov, and A. F. Khokhlov, Kristallografiya **38** (3), 140 (1993) [Crystallogr. Rep. **38** (3), 364 (1993)].
9. B. A. Maksimov, M. I. Sirota, S. Verner, and G. Shul'ts, Vestn. Nizhegorodskogo Univ., Ser. Fiz. Tverd. Tela **1**, 82 (1998).
10. E. N. Treushnikov, Doctoral Dissertation in Phys.-Math. Sci. (Nizhniĭ Novgorod State University, Nizhniĭ Novgorod, 1995).
11. L. A. Shuvalov, A. A. Urusovskaya, I. S. Zheludev, *et al.*, Modern Crystallography, Vol. 4. Physical Properties of Crystals (Nauka, Moscow, 1981; Springer, Berlin, 1984).
12. K. P. Belov, *Magnetostriction Phenomena and Their Technical Applications* (Nauka, Moscow, 1987).
13. L. A. Aslanov and E. N. Treushnikov, *Fundamentals of Diffraction Theory* (Izd. Moskovskogo Gos. Univ., Moscow, 1985).

Translated by L. Man

Crystallography Reports, Vol. 45, No. 3, 2000, pp. 365–373. Translated from Kristallografiya, Vol. 45, No. 3, 2000, pp. 408–416.

DIFFRACTION AND SCATTERING OF X-RAY AND SYNCHROTRON RADIATION

X-ray Diffraction by Polydomain Crystals Modulated by Transverse Waves of Atomic Displacements. 1. Single-Wave Modulation in Crystals

A. I. Ustinov*, L. A. Olikhovskaya*, and I. M. Shmyt'ko**

** Institute for Metal Physics, National Academy of Sciences of Ukraine, ul. Vernadskogo 36, Kiev, 252680 Ukraine*

*** Institute of Solid State Physics, Russian Academy of Sciences, Chernogolovka, Moscow oblast, 142432 Russia*

Received June 18, 1997; in final form, March 10, 1998

Abstract—The intensity distributions of diffuse X-ray scattering caused by domains characterized by the transverse wave of atomic displacements polarized in the (010) plane and propagating along the [001] direction are calculated by numerical methods analyzed in the kinematical approximation. The regular changes in the intensity and half-width of the satellite peaks are revealed as functions of the wave amplitude and the average domain size. The characteristic features of diffraction are considered in the case where the defect-density wave in the crystal affects the parameters of the displacement wave. *© 2000 MAIK "Nauka/Interperiodica".*

INTRODUCTION

The static waves of atomic displacements arise in some crystals due to changes of the thermal parameters (temperature, pressure) or the composition [1–9]. Such modulated states of the crystals are usually related to the changes in the magnetic [1–3] or electron [4–6] subsystems or in the characteristic features of atomic interactions in dielectric (ferroelectric) crystals [7–9]. Therefore, the experimental measurement of such structural characteristics in the modulated state (wavevector, amplitude, polarization plane, temperature range, etc.) provides an additional insight into the changes in the electron and magnetic properties of the crystal or the interactions between its structural components.

The state of the crystal characterized by the incommensurate displacement wave can arise as an intermediate state accompanying the transitions between the commensurate phases or between the nonmodulated paraelectric phase and the phase with the commensurate modulation [9]. Two types of changes of the diffraction patterns are observed in such cases. In the first one, the displacements of the satellite peaks to the positions characteristic of the commensurate displacement wave (position $\mathbf{q}$ of the satellite peak with respect to the nearest reflection is determined by wavelength λ of the displacement wave). In the other one, new peaks appear in the positions typical of the commensurate phase, whereas the transformation process is accompanied by the redistribution of intensities among the peaks characterizing the commensurate and incommensurate phases [10]. In some experiments, in the region of the two-phase state [11], the additional satellite peaks are observed between the peaks, corresponding to wavevectors $\mathbf{q}_1$ and $\mathbf{q}_2$ of the phases with the commensurate modulation.[1] These additional peaks appear in the positions corresponding to the sum $(\mathbf{q}_1 + \mathbf{q}_2)$ and the difference $(\mathbf{q}_2 - \mathbf{q}_1)$ of the wavevectors corresponding to the coexisting phases. The formation of these additional peaks is also observed under the long-term thermal treatment of thiourea at a fixed temperature within the existence range of the incommensurate phase [12]. In the first case, the formation of the "sum" and "difference" peaks can be explained either by certain synchronization of the displacement waves in the correlating phases or by the superposition of these waves in the crystal. According to [11, 12], the additional peaks arising after the preliminary thermal treatment at a fixed temperature within the existence range of the incommensurate phase are explained by the formation of the defect density wave [13–20] and pinning of the structure modulation at these waves.

The theoretical analysis of the X-ray diffraction in crystals modulated by the displacement waves was first reported in [4–9]. The estimates [4] of the relationship between the intensities of the main peak and the first-order satellite peak demonstrate that their values differ by two orders of magnitude. The allowance for the Debye–Waller factor leads to an additional decrease in the predicted intensity of the satellite peak. Therefore, it was proposed to study the modulated crystals by X-ray methods and measure only the intensity variations of the main peaks or to use electron diffraction. In the latter case, in is possible to fulfil the conditions of dynamic scattering [5]. However, the experimental

[1] Below, the satellite peaks of the peaks due to the displacement wave with vector q are referred to as additional peaks.

1063-7745/00/4503-0365$20.00 © 2000 MAIK "Nauka/Interperiodica"

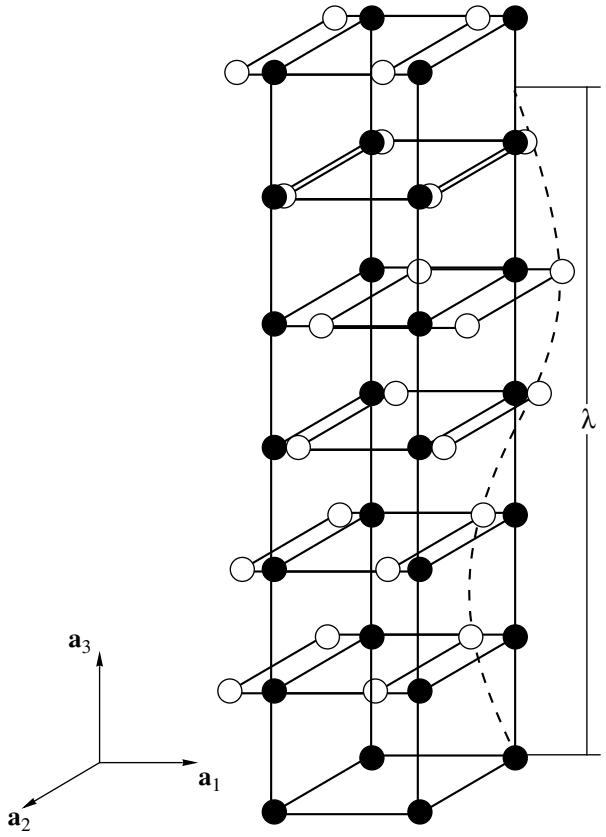

Fig. 1. Schematic picture of atomic positions in the initial crystal (filled circles) and in the crystal with a transverse displacement wave (empty circles).

studies of real crystals by the X-ray diffraction methods show that, in some cases, the intensities of the satellite peaks can be comparable with the intensity of the main peak [11, 12] or even can considerably exceed this intensity [10].

The above discussion demonstrate that the further theoretical analysis of X-ray scattering in crystals with unusual distribution of the structure defects and in crystals with several types of displacement waves is quite a burning problem.

In this paper, we present the model calculation of X-ray scattering in crystals with different types of fragmentation in the direction of the modulation wave (domains, twins, phase boundaries) and with the defect density waves. An emphasis is made on the conditions supporting the formation of additional peaks within the reciprocal lattice period.

In the first part of this article, we analyze the X-ray intensity distributions in the case of a single-wave modulation in crystals. In the second part of the article, the case of the two-wave modulation in crystals is discussed.

CALCULATION TECHNIQUE

To calculate the intensity of diffracted radiation, we used the numerical method based on the kinematical approximation. An orthorhombic crystal modulated by the by the transverse wave of atomic displacements along the [001] direction and polarized in the (010) plane (Fig. 1) was considered as a model object. In this case, the displacements of atoms along the [100] direction can be represented as $\boldsymbol{\delta}_n = \mathbf{A}\sin\left(\frac{2\pi n}{\lambda} + \varphi\right)$, where $\mathbf{A} = A \cdot \mathbf{a}_1$. Here, A is the amplitude of the displacement wave, λ is its wavelength in the units of the interlayer distance along the [001] direction, n is the number of the atomic layer, and φ is the initial phase of the displacement wave. The transverse displacement wave causes the changes in the mutual relative positions of atomic layers, and, hence, it disturbs the atomic-layer packing along the [001] direction. Therefore, the scattering intensity can be written as

$$I(\mathbf{S}) = |C|^2 \sum_{n=-N_3}^{N_3} \sum_{n'=-N_3}^{N_3} \exp[2\pi i \mathbf{S}(\mathbf{r}_n - \mathbf{r}_{n'})], \quad (1)$$

where $|C|^2$ is the structure factor for scattering by an atomic layer (the two-dimensional Laue function), N_3 is the number of atomic layers along the [001] direction, $\mathbf{S} = H \cdot \mathbf{a}_1^* + K \cdot \mathbf{a}_2^* + L \cdot \mathbf{a}_3^*$ is the reciprocal-lattice vector of the crystal with the basis vectors $\mathbf{a}_1$, $\mathbf{a}_2$, and $\mathbf{a}_3$, and $\mathbf{r}_{n'}$ is the position of the "zeroth" atom in the nth atomic plane. Within the framework of the statistical approach to intensity calculation, relationship (1) can be rewritten as

$$I(\mathbf{S}) = |C|^2 \sum_{m=-N_3}^{N_3} (N_3 - |m|) \langle \exp[2\pi i \mathbf{S}(\mathbf{r}_n - \mathbf{r}_{n'})] \rangle, \quad (2)$$

where the angular brackets denote averaging over all the pairs of atomic layers separated by $m = n' - n$ other atomic layers, $N - |m|$ is the number of pairs of atomic layers located at the interlayer distances m from one another. Taking into account that $\mathbf{r}_n = n \cdot \mathbf{a}_3 + \boldsymbol{\delta}_n$ and that the interlayer distances remain unchanged along the [001] direction (transverse displacement wave), we can write (2) as

$$I(L) = |C|^2 \sum_{m=-N_3}^{N_3} (N_3 - |m|) \exp(2\pi i L) \times \langle \exp\{2\pi i \mathbf{S}[\boldsymbol{\delta}_n - \boldsymbol{\delta}_{n+m}]\} \rangle, \quad (3)$$

where $\boldsymbol{\delta}_n$ and $\boldsymbol{\delta}_{n+m}$ are the projections of the position of the zeroth atoms in the nth and $(n + m)$th atomic layers onto the zeroth atomic layer.

With due regard for the fact that the factor $|C|^2$ has the nonzero value only at the integer values of H and K and that at $H = 0$, the expression in angular brackets is unity, it follows from (3) that diffuse scattering caused by the transverse displacement wave (or waves) should be localized along the reciprocal-lattice rods with $H \neq 0$.

We calculated the values of the expression in the angular brackets at different m for a crystal consisting of 100000 atomic layers. The crystal was "grown" by the Monte Carlo method. We assumed that the crystal is divided into domains with the planar boundaries normal to the wavevector crossing the whole crystal. A polydomain crystal modulated by a single displacement wave can be represented as alternation of domains with equal amplitudes and wavelengths, but with different initial phases. The boundaries between such domains can be considered as "antiphase" boundaries. The formation of these boundaries can be the consequence of non-correlated nucleation and growth of modulated regions. In modeling, we assumed that the domain size has an arbitrary value which is not less than the wavelength.

Substituting the values of the vectors determining the positions of atomic layers in the (001) plane into the expression in angular brackets, we find

$$\langle \exp\{2\pi i \mathbf{S}[\boldsymbol{\delta}_n - \boldsymbol{\delta}_{n+m}]\}\rangle = \left\langle \exp\left\{2\pi i A H\left[\sin\left(\frac{2\pi n}{\lambda} + \varphi_n\right) - \sin\left(\frac{2\pi(n+m)}{\lambda} + \varphi_{n+m}\right)\right]\right\}\right\rangle. \quad (4)$$

It should be noted that the amplitude A of the displacement wave enters expression (4) for the scattered intensity via the product $A \cdot H$. Therefore, at the same value of A, the diffuse scattering by the reciprocal-lattice rods can have different intensities and different H values. Taking this into account, we consider here only two limiting situations: small and large displacement "amplitudes" (low and high values of the product $A \cdot H$).

SMALL DISPLACEMENT "AMPLITUDES"

The small displacement "amplitudes" are understood as those amplitudes that have such $A \cdot H$ values that the intensity ratio of the satellite of the first and the higher order considerably exceeds the value of ten. In the experiment, such ratios are observed rather often, and, as will be shown below, such values are preferable for the analysis of the domain structure in the crystal based on the satellite-peak profile.

Let us consider the crystal in which the initial phase of the displacement wave in each domain is the random value from the set $\{2\pi n/\lambda\}$, where $n = 0, 1, \ldots$.

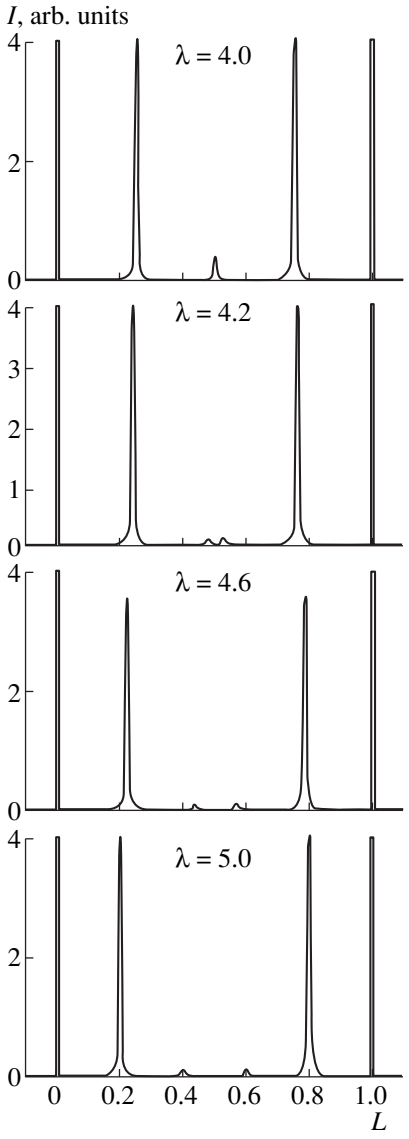

Fig. 2. Intensity distributions calculated for various wavelengths λ of the displacement waves at the $A \cdot H = 0.1$ and the average domain thickness equal to $D = 30$ atomic layers.

The intensity distributions for such a crystal calculated at $A \cdot H = 0.1$ and at different values of the displacement wavelength for the fixed average number of atomic layers in domains are shown in Fig. 2. The intensity distribution has two first-order satellite peaks and two low-intensity satellite peaks (the second-order satellites). The diffraction pattern is symmetric with respect to points $L \pm 0.5$, where L are the coordinates of the reciprocal-lattice points in the unmodulated crystal. The positions of satellite peaks with respect to the nearest peak if the initial crystal is determined by the wavelength $\mathbf{q} = 1/\lambda$ as for a single-domain crystal. In other words, the domain ("antiphase") boundaries do not affect the satellite-peak positions. It follows from Fig. 2 that for the structural transition of the crystal from the state modulated by one displacement wave to the state

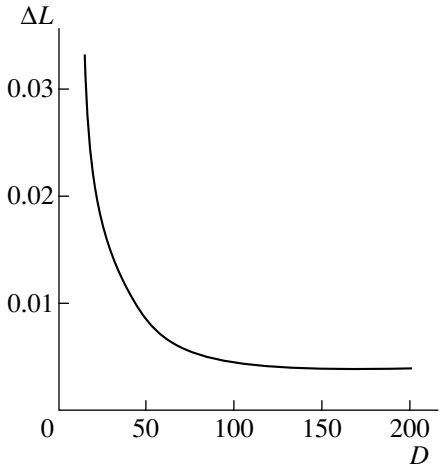

Fig. 3. Half width ΔL of the first-order satellite peak versus domain thickness.

modulated by another displacement wave through some intermediate states with different degrees of incommensurability, the positions of satellite peaks should continuously vary without the formation of any additional intensity peaks.

An increase of the mean domain thickness gives rise to the monotonic decrease of the half-width of the satellite peaks. It was established that the half-width of the satellite peaks is almost independent of the displacement wavelength, and, therefore, the average domain thickness (D) can be determined from the experimentally measured intensity distribution with the use of the calculated dependence of the half-width of the satellite peak on D (Fig. 3).

LARGE DISPLACEMENT "AMPLITUDES"

The large displacement "amplitudes" are understood as such amplitudes in which the intensity of at least one satellite of the order higher than the first differs from the intensity of the last satellite by a factor less than ten. In the framework of the model of a modulated crystal under study (with random values of the initial phases of the waves in different domains), the second-order satellite peaks attain this intensity value at $A \cdot H$ values approximately larger than 0.15.

An increase of the peak intensity for the higher-order satellites with an increase of the displacement "amplitude" is accompanied by a decrease in the intensity of the Bragg peaks for the initial crystal. The intensity ratios of the satellite peaks for satellites of different orders also undergo some changes (Fig. 4). The latter fact can be used to determine the amplitude A of the displacement wave by comparing the measured intensity ratios for satellites of various orders for a specified reciprocal-lattice rod (with the given H value) with the

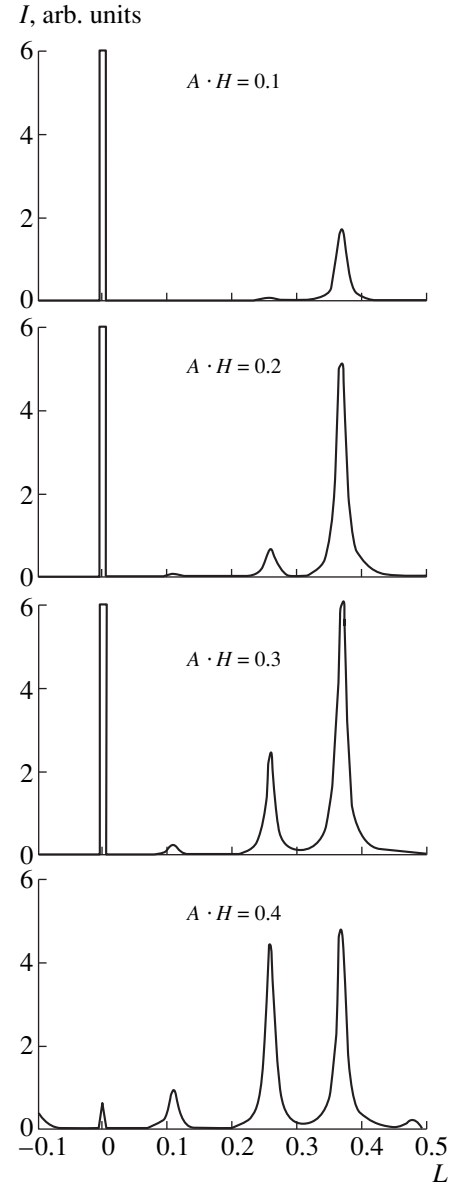

Fig. 4. Intensity distributions calculated for various values of $A \cdot H$ at the wavelength of the displacement wave $\lambda = 2.7$ and the average domain thickness $D = 30$ atomic layers.

calculated values of these ratios corresponding to the same H.

The aforementioned features of the diffraction pattern at large $A \cdot H$ values lead to the qualitative differences in the transformation of the intensity distribution in the transition from one modulated structures to another at the continuous variation of λ (Fig. 5) in comparison with the case of small displacement "amplitudes." The intensity distributions shown in Figs. 2 and 5 show that the transition from the state of the crystal modulated by a commensurate displacement wave with a large "amplitude" to the incommensurate modulation is accompanied by the changes in the peak location in

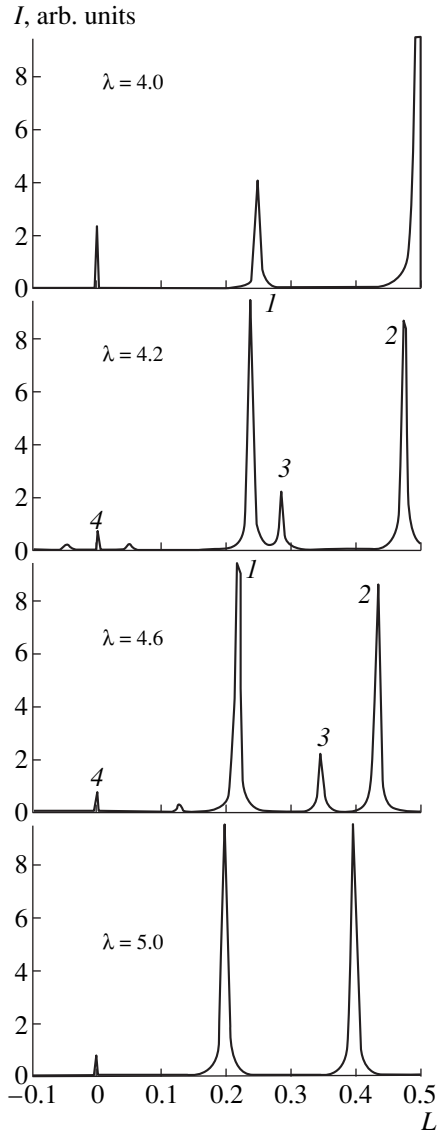

Fig. 5. Intensity distributions calculated for various wavelengths λ of the displacement wave at $A \cdot H = 0.4$ and the average domain thickness $D = 60$ atomic layers. Numbers *1–4* denote the satellite peaks of the corresponding order.

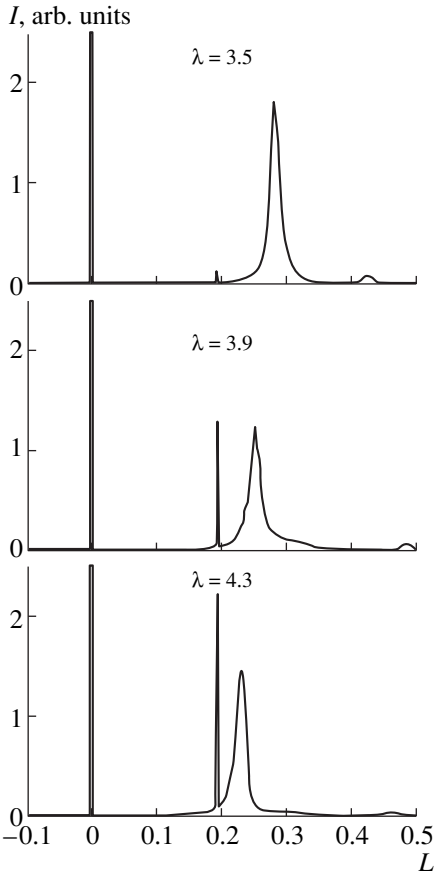

Fig. 6. Intensity distributions calculated for the case where the initial phase of displacement wave λ is determined in each domain by the phase of the defect-density wave equal to $\lambda_d = 5.1$ passing through the whole crystal.

accordance with the wavelength and also by the formation of "additional" peaks.

DEFECT DENSITY WAVE

The theory predicts that if the crystal is modulated by an incommensurate displacement wave, the mobile defects can redistribute and form the defect-density [13–16, 20–22]. The formation of the defect-density wave at the thermal treatment at a fixed temperature within the range of existence of an incommensurate phase gives rise to the anomalies in the physical characteristics in the range of existence of the commensurate phase [11, 12]. This gives ground to believe that the defect-density wave is stable and can exist for some time also in the range of existence of the commensurate phase. Therefore, one can assume at the repeated passages of the range of the incommensurate phase, the formation of modulated domains in the crystal and their parameters would depend on the existing defect density wave.

Currently, there are no theoretically verified concepts of the "interaction" between the defect-density wave and the displacement waves. Therefore, we consider the effect produced by the defect density wave on each of the parameters characterizing the displacement wave.

Synchronization of the initial phase of the displacement waves. In contrast to the case discussed above, now we assume that the initial phase of the displacement wave in each domain is determined by the phase of the defect density wave λ_d propagating through the whole crystal. As a result, the initial phases of the displacement waves in all the domains are synchronized and obey the relationship

$$\varphi_i = \frac{2\pi n_i}{\lambda_d}, \qquad (5)$$

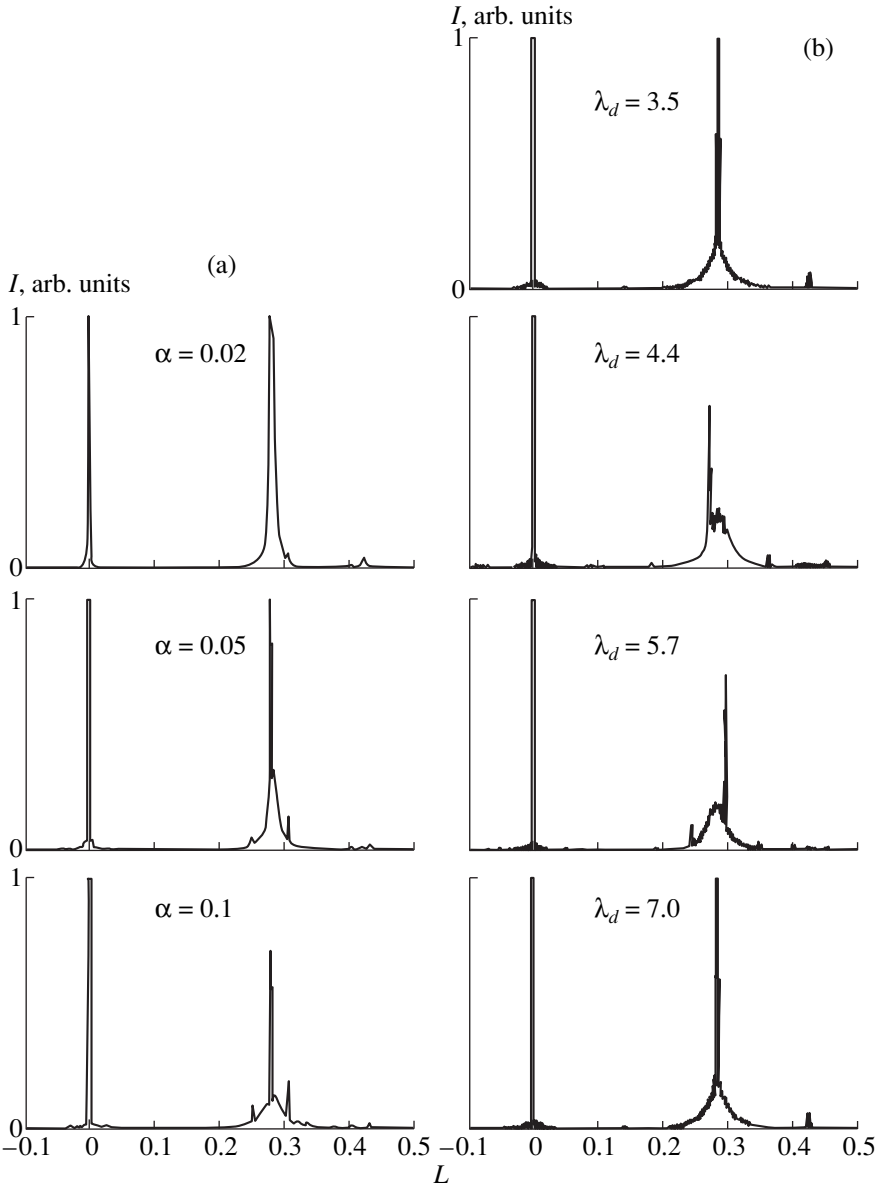

Fig. 7. Intensity distributions calculated for the case where the defect-density wave λ_d determines the spatial arrangement of domains and synchronizes the initial phases of the displacement wave $\lambda = 3.5$ in them. The curves are calculated at different values of α (a) and λ_d (b).

where n_i is the number of the initial atomic layer which "begins" the ith domain. Figure 6 shows the intensity distributions calculated for such a crystal at different values of the displacement wavelength. It is seen that the synchronization of initial phase gives rise to the formation of a δ-function-like additional peak with the intensity increasing with a decrease in the difference $\mathbf{q} - \mathbf{q}_d$ (where $\mathbf{q}_d$ is the wavevector of the defect density wave).

Spatial synchronization. If the probability of nucleation of a displacement wave is related in some way to the value of defect density at the given site of the crystal, then the waves of atomic displacements are synchronized not only with respect to the initial phase, but also with respect to their positions as well.

Let α be the probability that the beginning from a certain atomic layer n_j (where n_j are the numbers of the atomic layers with the extremum value of the defect density, for example, with the minimum value) crystal has a modulation wave. In the limiting case (at $\alpha \longrightarrow 1$), the crystal consists of alternating domains modulated by the displacement waves with the equal initial phases and arranged orderly with respect to one another, that is, the spacing between the front part of

each domain is spaced from the front part of the previous one by a distance multiple of λ_d.

The results of calculations illustrating the evolution of intensity distribution with an increase of α are shown in Fig. 7a. It is seen that the spatial correlation in the domain positions introduced in addition to the synchronization of the initial phases of the displacement waves provides, the formation of additional peaks whose intensities increase with α. Note that the correlation only in the positions of domains (with random values of the initial phases) does not cause any qualitative changes in the intensity distribution in comparison with the case of uncorrelated domain positions. However, in the limiting case, where the distribution of domain thicknesses tends to the δ-function-like distribution, the domain arrangement should acquire the long-range order. As a result, additional peaks are formed whose number and positions are determined by the period of this superlattice [23].

Similar to the case of the phase synchronization alone, the diffraction effects caused by both phase and spatial modulations are strongly dependent on the degree of incommensurability of the waves with λ_d and λ. It is seen (Fig. 7b) that the additional peaks in the presence of both phase and spatial synchronization between the defect density wave and the displacement wave are observed only in the case where $\lambda_d/\lambda \neq n$ with $n = 0, 1, 2, \ldots$. The intensities of additional peaks are also sensitive to this ratio.

Phase modulation. Let a defect density wave modulate the phase of the displacement wave. From the formal viewpoint, this model is similar to the existence of a "phason" in the crystal. The only difference is that the phase modulation in our case is not caused by phonons, in contrast to the situation discussed, e.g., in [4]. If such a "phason" really exists in the crystal, then the atomic displacements can be described as

$$\boldsymbol{\delta}_n = \mathbf{A}\sin\left[\frac{2\pi n}{\lambda} + \varphi + \Phi\sin\left(\frac{2\pi n}{\lambda_d}\right)\right], \qquad (6)$$

where Φ is the amplitude of the phase modulation.

It is seen from Fig. 8 that the phase modulation gives rise to the formation of additional peaks located at $\mathbf{q} + \mathbf{q}_d$ and $\mathbf{q} - \mathbf{q}_d$, whose intensities increase with both amplitude of phase modulation, Φ, and displacement "amplitude," $A \cdot H$. At a certain ratio between Φ and $A \cdot H$, some additional peaks can also arise in the positions corresponding to the sum and difference of the vectors $\mathbf{q}_d$ and $\mathbf{q}/2$ (second-order satellites). Another characteristic feature of the intensity distribution in the presence of "phasons" is the diffuse peak in the vicinity of the peaks corresponding to the initial structure.

Amplitude modulation. Assuming that the displacement of atoms under the effect of the defect density wave is proportional to the defect density, we can write the following expression for the atomic displacements

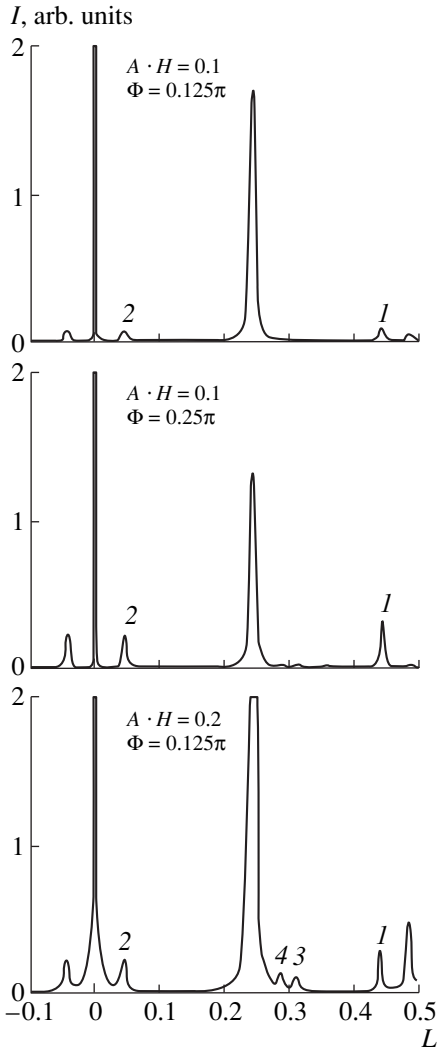

Fig. 8. Intensity distributions for the case where the phase of the displacement wave with wavevector q ($\lambda = 4.1$) is modulated in the domains by a defect density wave with the wavevector q_d ($\lambda = 5.0$ atomic layers). The curves are calculated at different values of $A \cdot H$ and amplitude Φ of the phase modulation by the defect-density wave: (*1*) the additional peak corresponding to $q + q_d$; (*2*) $q - q_d$; (*3*) $1 - (2q + q_d)$; and (*4*) $2q - q_d$.

$$\boldsymbol{\delta}_n = \mathbf{A}\left|\sin\left(\frac{2\pi n}{\lambda_d} + \varphi\right)\right|\sin\left(\frac{2\pi n}{\lambda} + \varphi\right). \qquad (7)$$

It is seen Fig. 9 that the amplitude modulation gives rise to the formation of additional peaks symmetric with respect to the satellite peak **q**. The distance between the satellite and additional peaks is proportional to qq_d. The number of the peaks and their relative positions are strongly dependent on the degree of incommensurabil-

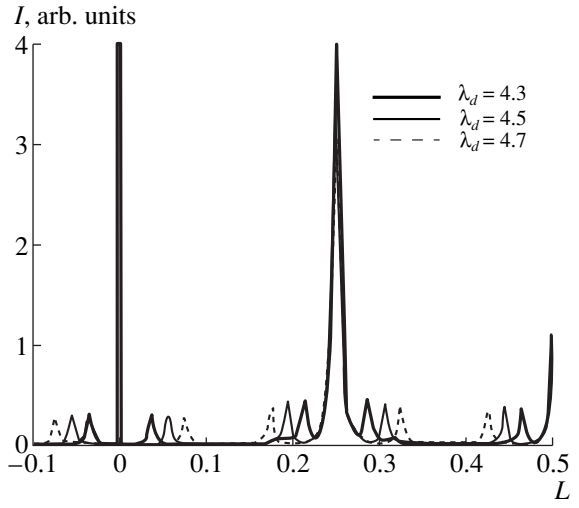

Fig. 9. Intensity distributions for the case where the amplitude of the displacement wave ($A = 0.1$, $\lambda = 4.0$) is modulated by the defect-density wave.

ity q_d with respect to the initial lattice and the relationship between **q** and q_d.

DISCUSSION AND CONCLUSIONS

The results obtained above demonstrate that, in the general case, the diffraction pattern from a polydomain crystal modulated by a single wave of atomic displacements can be rather complicated. Even in the simplest situation corresponding to "independent" domains, it is useful to measure the intensity distributions for two types of reciprocal lattice rods with H indices satisfying the conditions imposed on large and small displacement amplitudes $A \cdot H$, respectively. In order to determine the average domain size, it is preferable to consider the reciprocal-lattice rods, which are responsible for the formation of first-order satellite peaks. This provides the determination of their profiles with sufficient accuracy. On the other hand, in order to determine the amplitudes of displacement wave, it is necessary to use the intensity distributions along the reciprocal-lattice rods satisfying the condition of the large $A \cdot H$ values.

If in addition to the static wave of atomic displacements, another type wave propagates in the crystal, e.g., the defect density wave, then both waves can "interact" in some way. The calculations showed that, in this case, the additional peaks in the intensity distribution can appear at any type of the correlation between the defect density wave and the parameters of the displacement wave. These additional peaks are arranged with respect of the satellite ones differently in all the cases under study. This fact can be used for determining the type of the "interaction" between the defect-density wave and the displacement wave. Another important feature is the possibility to determine in the experiment the wavelength of the defect density wave.

In addition to the results of the earlier theoretical studies obtained by many authors also showed, we demonstrated that the domain structure corresponding to the single-wave modulation does not influence the positions of the main satellites, but can change their half-widths. The correlation between the parameters characterizing the displacement wave in each domain or the correlation between the domain positions provide the formation of additional peaks. The additional peaks appear also if the parameters of the displacement waves are influenced by the modulation of another type (the waves of defect density, chemical composition, etc.). Within the framework of a rather simple model, we showed that the characteristic features of the arrangement of additional peaks with respect to the main satellites are uniquely determined by the type of the "interaction" between the displacement wave and the waves of other types.

The results obtained open new vistas for the diffraction methods in the studies not only of the parameters characterizing the wave of atomic displacements, but also in the studies of the microstructure of modulated crystals.

ACKNOWLEDGMENTS

The work was supported by INTAS, grant INTAS-93-3230-ext.

REFERENCES

1. I. E. Dzyaloshinskiĭ, Zh. Éksp. Teor. Fiz. **46** (4), 1420 (1964) [Sov. Phys. JETP **19**, 960 (1964)].
2. I. E. Dzyaloshinskiĭ, Zh. Éksp. Teor. Fiz. **47**, 336 (1964) [Sov. Phys. JETP **20**, 223 (1964)].
3. I. E. Dzyaloshinskiĭ, Zh. Éksp. Teor. Fiz. **47**, 992 (1964) [Sov. Phys. JETP **20**, 665 (1964)].
4. A. W. Overhauser, Phys. Rev. B: Solid State **3** (10), 3173 (1971).
5. J. A. Wilson, F. J. Di Salvo, and S. Mahajan, Adv. Chem. Phys. **24** (2), 1 (1975).
6. W. L. McMillan, Phys. Rev. B: Condens. Matter **14** (4), 1496 (1976).
7. A. P. Levanyuk and D. G. Sannikov, Fiz. Tverd. Tela (Leningrad) **18** (2), 423 (1976) [Sov. Phys.-Solid State **18** (2), 245 (1976)].
8. A. P. Levanyuk and D. G. Sannikov, Fiz. Tverd. Tela (Leningrad) **18** (7), 1927 (1976) [Sov. Phys.-Solid State **18** (7), 1122 (1976)].
9. A. D. Bruce, R. A. Cowley, and A. F. Murray, J. Phys. C: Solid State Phys. **11** (17), 3591 (1978).
10. I. K. Bdikin, N. C. Afonikova, *et al.*, Physica C (Amsterdam) **196**, 191 (1992).
11. B. Sh. Bagautdinov and I. M. Shmyt'ko, Pis'ma Zh. Éksp. Teor. Fiz. **59** (3), 171 (1994) [JETP Lett. **59** (3), 182 (1994)].

12. B. Sh. Bagautdinov, V. V. Gladkiĭ, S. N. Kallaev, *et al.*, Pis'ma Zh. Éksp. Teor. Fiz. **59** (2), 113 (1994) [JETP Lett. **59** (2), 119 (1994)].
13. J. P. Jamet and P. J. Lederer, Phys. Lett. **44**, L257 (1983).
14. P. Lederer, G. Montambaux, J. P. Jamet, and M. Chauvin, Phys. Lett. A **45**, L627 (1984).
15. J. P. Jamet, Phase Transitions **11**, 335 (1988).
16. H.-G. Unruh, Physica C (Amsterdam) **16**, 3245 (1983).
17. M. J. Tello, C. L. Folcia, J. M. Pérez-Mato, *et al.*, Solid State Commun. **60**, 581 (1986).
18. V. S. Vikhnin, in *Proceedings of Int. Symposium Synergetics and Cooperation Phenomena in Solids and Macromolecules, Tallinn, Estonia, 1983*, p. 91.
19. V. S. Vikhnin, *Dielectrics and Semiconductors* (Vysshaya Shkola, Kiev, 1983).
20. V. S. Vikhnin, Kristallografiya **31** (4), 635 (1986) [Sov. Phys. Crystallogr. **31** (4), 374 (1986)].
21. G. Errandonea, Phys. Rev. B: Condens. Matter **33** (9), 6261 (1986).
22. C. L. Folcia, F. J. Zúiga, G. Madariaga, *et al.*, Phys. Rev. B: Condens. Matter **40** (16), 11037 (1989).
23. R. A. Cowley, Adv. Phys. **29** (1), 1 (1980).

Translated by K.I. Kugel

Crystallography Reports, Vol. 45, No. 3, 2000, pp. 374–379. Translated from Kristallografiya, Vol. 45, No. 3, 2000, pp. 417–422.

DIFFRACTION AND SCATTERING OF X-RAY AND SYNCHROTRON RADIATION

X-ray Diffraction in Polydomain Crystals Modulated by Transverse Waves of Atomic Displacements. 2. Two-Wave Modulation of Crystals

A. I. Ustinov*, L. A. Olikhovskaya*, and I. M. Shmyt'ko**

** Institute for Metal Physics, National Academy of Sciences of Ukraine, ul. Vernadskogo 36, Kiev, 252680 Ukraine*

*** Institute of Solid State Physics, Russian Academy of Sciences, Chernogolovka, Moscow oblast, 142432 Russia*

Received June 18, 1997; in final form, March 10, 1998

Abstract—X-ray diffraction in an orthorhombic crystal modulated by two transverse-displacement waves propagating along one of the crystallographic directions has been numerically studied within the framework of the kinematic approximation. Crystal models are considered that allow the superposition of the displacement waves or the coexistence of domains modulated by the displacement waves with different parameters. It is shown that the formation of peaks additional to the satellite ones is possible not only due to the superposition of the displacement waves, but also due to a certain correlation of the displacement waves in each domain.

INTRODUCTION

In the transition from one modulated structure of a crystal to another, one can expect the appearance of two static waves of atomic displacements propagating along one of the crystallographic directions. The diffraction pattern, which can be interpreted as a consequence of this modulated state in the crystal, was first observed in [1]. In addition to the satellite reflections corresponding to the displacement waves with wavevectors $\mathbf{q}_1$ and $\mathbf{q}_2$, some additional peaks were observed at positions corresponding to $\mathbf{q}_1 + \mathbf{q}_2$ and $\mathbf{q}_2 - \mathbf{q}_1$. These additional peaks can be caused, in particular, by the superposition of displacement waves in the presence of two modulation modes in the crystal [1]. Within the framework of the single-wave model, it was shown [2] that such additional peaks could also arise on the diffraction patterns from modulated crystals with polydomain structures in which the displacement waves in domains are synchronized in a certain way.

The multiwave modulation for the displacement waves propagating along three different directions in a single crystal was analyzed earlier [3]. In this paper, we consider X-ray diffraction from a polydomain crystal modulated by two displacement waves along one of the crystallographic direction. Taking into account the results obtained in [2], we paid special attention to the effect of modulations synchronization in domains on the form of the diffraction pattern. Such a synchronization can be caused either by the coherency of the domain boundaries or by the "interaction" of the displacement waves, e.g., with the defect-density wave.

Modeling of the intensity distributions in the reciprocal space was performed numerically in the framework of kinematic approximation according to the computation scheme described in [2], in which the intensity of the scattered radiation was expressed in terms of the "layer–layer" pair correlation functions calculated for the given crystal structure. The crystal was "grown" by the Monte Carlo method under the assumption of a random arrangement of domain boundaries. Similar to the case of the single-wave modulation, the planar domain boundaries were take to be normal to the wavevector and propagating through the whole crystal.

UNCORRELATED DISPLACEMENT WAVES

As a starting model, we consider the case where the domains and static displacement waves in these domains do not "interact."

Let each domain have only one of two possible displacement waves with the parameters, which do not correlate with the corresponding parameters of the waves in the neighboring domains. Then, the atomic displacements in the crystal can be represented as

$$\boldsymbol{\delta}_n = \mathbf{A}_i \sin\left(\frac{2\pi n}{\lambda_i} + \varphi_i\right), \quad (1)$$

where n is the ordinal number of the atomic layer in the direction of the wavevector, $\mathbf{A}_i$ is the amplitude, λ_i is

the wavelength corresponding to the displacement wave polarized in the (010) plane measured in the units of the interlayer spacing in [100] and [001] directions, respectively; $i = 1$ or $i = 2$ depending on the domain type, and φ_i is the initial phase of the wave in the ith domain. The phase φ_i takes random values from the set determined by all the possible atomic positions in a crystal modulated by the displacement wave λ_i corresponding to $\varphi_i = 0$.

Figure 1 shows the fragments of the intensity distributions calculated within the framework of the "noninteracting" domain model. They illustrate the evolution of the diffraction pattern with the change of the relative volume content of the domains with the waves of two different types. The intensity distributions are plotted for a reciprocal-lattice half-period along the 10L rod because the distributions constructed for the whole period have the symmetry point $L = 0.5 \pm M$, where $M = 0, 1, 2, \ldots$ (see [2]). These diffraction patterns are, in fact, the superpositions of two intensity distributions characteristic of a crystal modulated by waves of each type (denoted hereafter as λ_1 and λ_2). The redistribution of the volume fractions of the domains with the λ_1 and λ_2 waves results in the corresponding changes in the intensities of the satellite peaks characteristic of these waves. It was shown [2] that the half-widths of the satellite peaks are determined by the average domain thickness. At the random location of domain boundaries within the crystal, the average thicknesses D_1 and D_2 for domains of two types are related to their volume fractions W_1 and W_2: $D_1/D_2 = W_1/W_2$. Therefore, an increase of the volume fraction of a certain component results in an increase of the average size of domains giving rise to a decrease of the half-widths of the corresponding satellite peaks. The change in the amplitude of one displacement wave or the change in the average thickness of domains corresponding to this wave produce no effect on the intensity and the position of the satellite peaks corresponding to the crystal modulation by the other wave.

COHERENT DOMAIN BOUNDARIES

In a crystal consisting of "noninteracting" domains, their boundaries can include the regions, where the displacements of the atomic planes considerably exceed the displacement amplitude of each of the waves. Then, one can expect that the crystal would tend to relaxation of these "defects" by "correlating" the modulations in different domains.

One of the methods for attaining such a correlation is the "adjustment" of the initial phases in the neighboring domains in a way to minimize the relative displacements of the atomic layers at the domain boundary (a "coherent" boundary). Thus, passing from the ith to

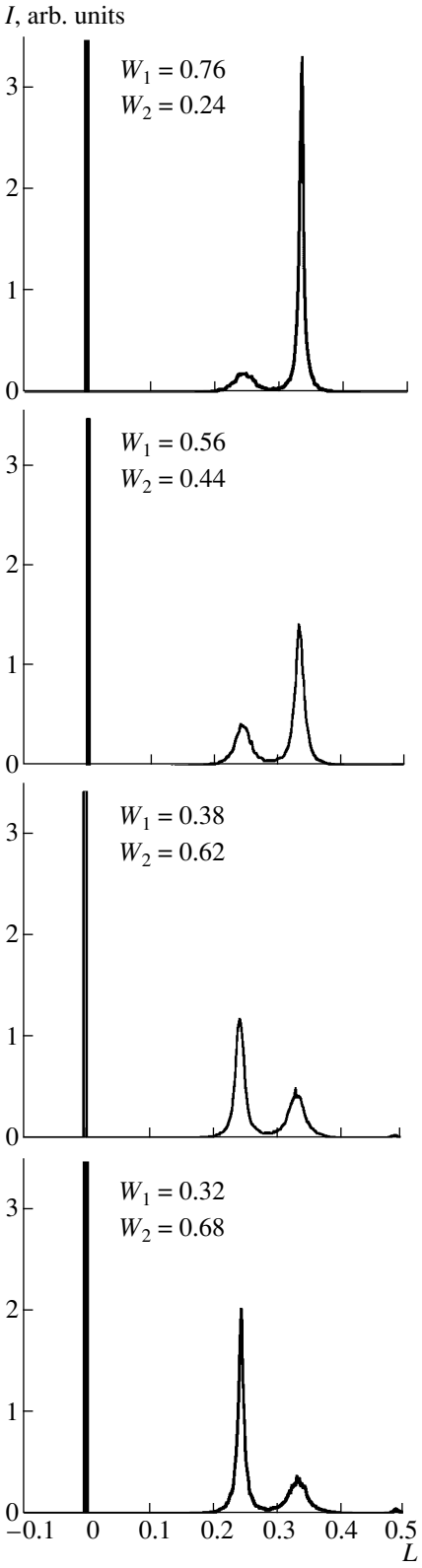

Fig. 1. Intensity distributions for a crystal consisting of domains with the displacement waves $\lambda_1 = 3.0$ and $\lambda_2 = 4.1$ and with the initial phases being random numbers. The distributions are calculated for different ratios of volume fractions W of these domains in the crystal, with the modulation "amplitude" being constant, $A_1 \cdot H = A_2 \cdot H = 0.1$.

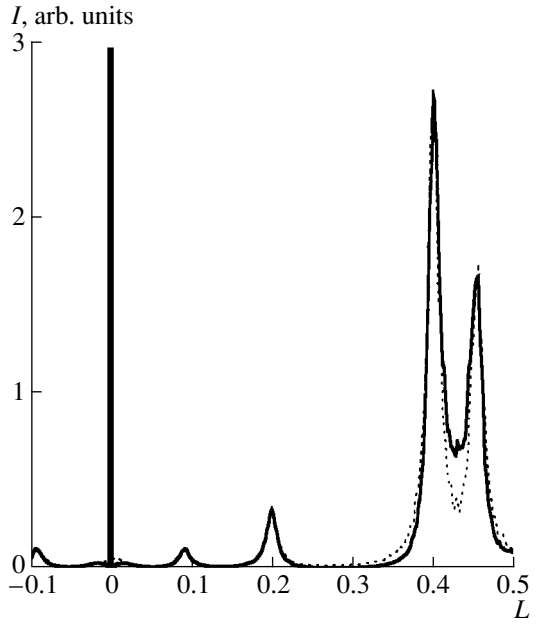

Fig. 2. Intensity distributions calculated at $\lambda_1 = 2.2$, $\lambda_2 = 2.5$, $A_1 = 0.15$, $A_2 = 0.2$, and $D_1 = D_2 = 30$ for the case of independent displacement waves in domains (dashed line) and the case of phase correlation at the domain boundaries (solid line).

the *j*th domain, we can determine the initial phase φ_j in the *j*th domain by minimizing the following expression:

$$\left|\mathbf{A}_i \sin\left(\frac{2\pi n_0}{\lambda_i} + \varphi_i\right) - \mathbf{A}_j \sin\left(\frac{2\pi(n_0+1)}{\lambda_j} + \varphi_j\right)\right|, \quad (2)$$

where n_0 is the ordinal number of the last atomic layer in the *i*th domain, $i \neq j$.

An example of the intensity distribution for this case is shown in Fig. 2 alongside with the intensity distribution calculated for the "noninteracting" domains, with the parameters of the displacement wave being the same. It is seen that the half-widths of the satellite peaks are almost the same in both cases, but the diffuse background between the peaks is more pronounced for the "coherent" boundary. The calculations for different λ_1 and λ_2 demonstrate that the background intensity depends on the spacing between the satellites: the closer the satellites, the higher the intensity. If the relation between λ_1 and λ_2 provides the close location within the reciprocal-lattice period of the second-order satellites, then the diffuse background is enhanced between these satellites and is absent between the first-order satellites. Similar to the case of "noninteracting" domains, the coherent "correlation" of the waves in the neighboring domains does not result in the formation of any additional peaks.

PHASE CORRELATION OF THE WAVES

The correlation of displacements in the domains can be also determined by the long-range forces. For example, one can imagine the situation where the initial phases of the displacement waves in each domain are "dictated" by the defect-density wave (hereafter called "the correlating wave").

It was shown [2] that an additional peak is formed in the vicinity of the satellite peak on the intensity distribution, if the crystal with the single displacement wave has the domain structure and if the initial phase φ_i in each domain is determined by the phase of correlating wave. The number of additional peaks increases in addition to the initial phase correlation for the displacement wave there also exists a certain correlation between the domain positions also dependent on the correlating wave. Similar diffraction phenomena are also observed in the case of two displacement waves.

The intensity distributions in Fig. 3 are obtained for a crystal consisting of randomly located domains with the displacement waves λ_1 and λ_2 and the initial phases determined by the phase of the correlating wave. It is seen that the correlation between the initial phases of the modulation waves in different domains provides the formation of an additional peak in the position corresponding to wavevector $\mathbf{q}_d$ of the defect-density wave, whereas its intensity depends on the distance to the nearest satellite peak: the less the distance, the higher the peak intensity.

SUPERPOSITION OF THE DISPLACEMENT WAVES

The existence of a defect density wave in a crystal can hinder the formation of the displacement waves with the wavelengths different from the wavelength of the defect-density wave. In this case, the transition from one modulated structure to another can occur via a continuous decrease in the amplitude of the displacement wave stabilized by the defect-density wave and an increase in the amplitude of the displacement wave characteristic of the equilibrium state at the given temperature. Then, two displacement waves coexist in each domain at the intermediate stages of the structural phase transition. An atomic displacement under the action of these two waves can be written as

$$\boldsymbol{\delta}_n = \mathbf{A}_1 \sin\left(\frac{2\pi n}{\lambda_1} + \varphi_1\right) + \mathbf{A}_2 \sin\left(\frac{2\pi n}{\lambda_2} + \varphi_2\right), \quad (3)$$

where λ_1, λ_2, $\mathbf{A}_1$, and $\mathbf{A}_2$ are the wavelengths and the amplitudes of the displacement waves, φ_1 and φ_2 are the initial phases of the displacement waves, which are chosen for each domain from the set of the values obeying the condition $\varphi_1 = \varphi_2 = 0$ at $n = 0$.

The intensity distributions shown in Fig. 4 were calculated for the different ratios of the amplitudes $\mathbf{A}_1$ and

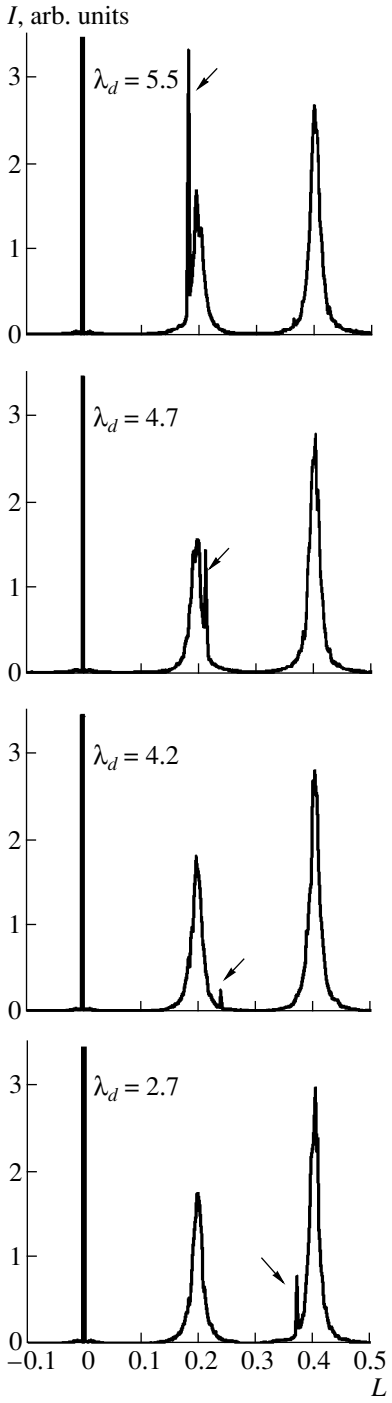

Fig. 3. Intensity distributions for the case when the initial phases of the displacement waves with $\lambda_1 = 2.5$ and $\lambda_2 = 5.1$ domains are dictated by the phase of correlating wave λ_d ($D_1 = D_2 = 30, A_1 = 0.2, A_2 = 0.15$). The peak corresponding to the wavevector of the correlating wave is indicated by an arrow.

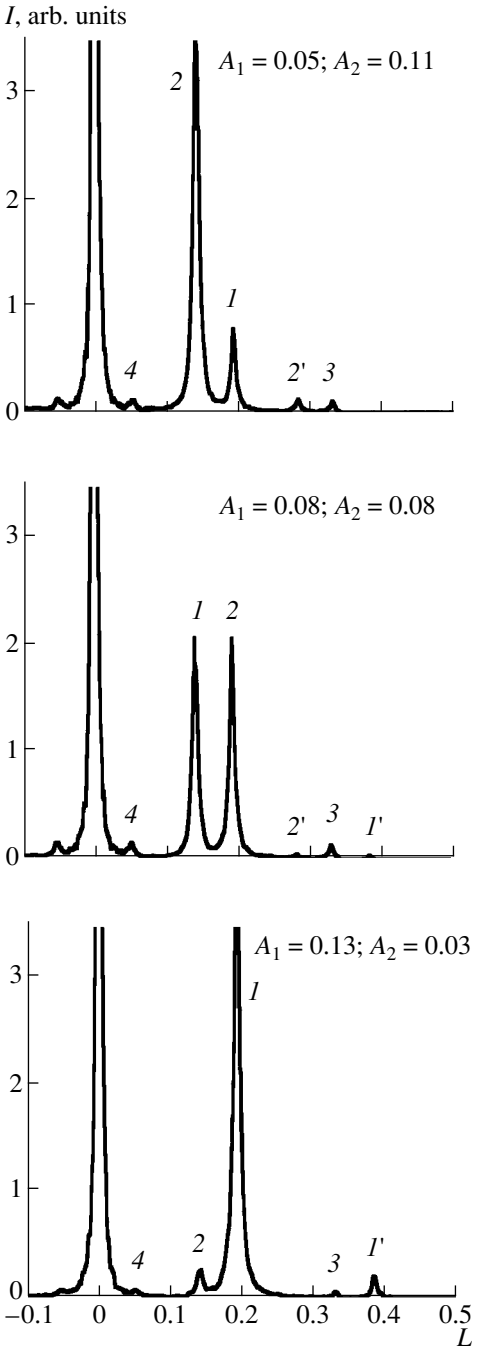

Fig. 4. Intensity distributions calculated for the superposition of two waves with $\lambda_1 = 5.2$ and $\lambda_2 = 7.1$ in one domain at different ratios of their amplitudes A_1 and A_2 ($D = 30$): *1* and *1'*, *2* and *2'* are first- and second-order satellites for the waves of the first and the second type, *3* and *4* are the additional peaks corresponding to $\mathbf{q}_1 + \mathbf{q}_2$ and $\mathbf{q}_1 - \mathbf{q}_2$.

$\mathbf{A}_2$ corresponding to two displacement waves present in one domain. On the corresponding diffraction pattern, in addition to the satellite peaks in the positions $\mathbf{q}_1 = 1/\lambda_1$ and $\mathbf{q}_2 = 1/\lambda_2$ (which correspond to the modulation of the crystal by the displacement waves with λ_1 and λ_2), there are also the peaks at the positions $\mathbf{q}_1 + \mathbf{q}_2$ and $\mathbf{q}_1 - \mathbf{q}_2$. The intensities of these additional peaks are equal, with their values being dependent not only on the

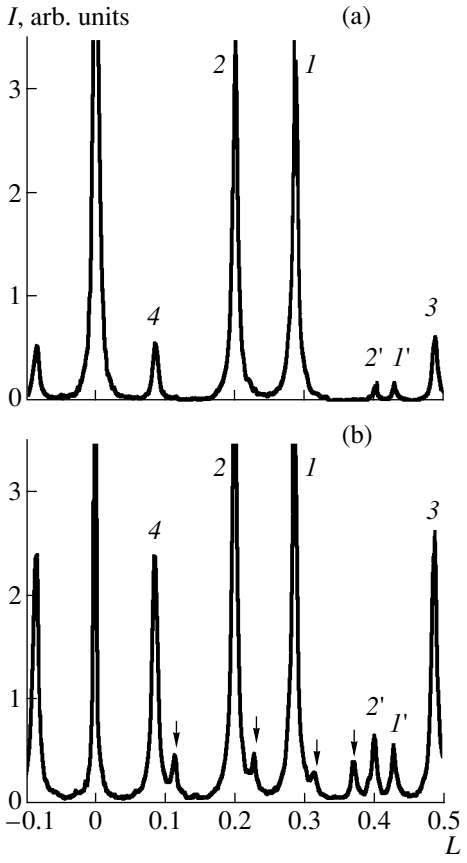

Fig. 5. Intensity distributions for the superposition of two displacement waves with $\lambda_1 = 5.2$ and $\lambda_2 = 7.1$ at (a) $A_1 = A_2 = 0.1$ and (b) $A_1 = A_2 = 0.2$. For notation see Fig. 4. Arrows indicate the peaks with the positions corresponding to multiples of $\mathbf{q}_1 \cdot \mathbf{q}_2$.

absolute values of the amplitudes $\mathbf{A}_1$ and $\mathbf{A}_2$, but also on their ratio.

Considering the large amplitudes (with increasing $A \cdot H$ value for each of the displacement waves), we see that alongside with the additional peaks at positions $\mathbf{q}_1 + \mathbf{q}_2$ and $\mathbf{q}_1 - \mathbf{q}_2$, there are also some peaks located at the distance from the main and the satellite peaks multiple of $\mathbf{q}_1 \cdot \mathbf{q}_2$ (Fig. 5b). These additional peaks were observed for the intensity distributions calculated for the displacement wave with the modulated amplitude [2]. This is not surprising, because expression (3) can be represented as a product of two harmonic functions. If $\mathbf{A}_1 = \mathbf{A}_2$ and $\varphi_1 = \varphi_2$, this transformation has a rather simple form

$$\boldsymbol{\delta}_n = \mathbf{A}\sin\left[\pi n\left(\frac{1}{\lambda_1} + \frac{1}{\lambda_2}\right)\right]\cos\left[\pi n\left(\frac{1}{\lambda_1} - \frac{1}{\lambda_2}\right)\right].$$

Comparing this expression with the relationship determining the position of atomic layers in the case of the amplitude modulation (equation (7) in [2]), we see that they are similar, and, therefore, we may expect the manifestation of analogous diffraction effects also in the case under consideration.

DISCUSSION

One of the characteristic features of the intensity distributions for two-wave modulation is an increase of the background intensity between the nearest satellite peaks in the presence of coherent interdomain boundaries. This fact can be used to confirm the existence of a similar state in a crystal. On the other hand, this distortion of the intensity profile should also be taken into account in the full-profile analysis for determining the average domain size and the volume fractions of domains having different types of modulation.

The peaks additional to satellites are formed on the diffraction pattern at the correlation of the phases of the waves and at the superposition of the displacement waves. In the former case, the intensity distribution has a δ-function-like peak whose position is independent of the wavevectors $\mathbf{q}_1$ and $\mathbf{q}_2$ of the displacement waves is determined only by wavevector $\mathbf{q}_d$ of the correlating wave. Similar to the case of the single-wave modulation in a polydomain crystal [2], the intensity of this peak increases with a decrease of the distance to the nearest satellite peak (Fig. 3). The superposition of the displacement waves also leads to the formation of additional peaks, but the positions of these peaks are determined by the sum and the difference of the wavevectors $\mathbf{q}_1$ and $\mathbf{q}_2$ (Fig. 4).

A special attention should be paid to the models that lead to qualitatively similar intensity distributions. For example, the single-wave model for "noninteracting" domains at certain values of $A \cdot H$ leads to two intensity peaks (first- and second-order satellites) within a half-period of the reciprocal lattice. In general, the spacing between these peaks cannot be multiple of the wavevector. Therefore, qualitatively, the corresponding diffraction pattern can be considered as a pattern with two first-order satellite peaks with different $\mathbf{q}$ values (Fig. 1 in this paper and Fig. 4 in [2]).

The models in which the correlating wave (e.g., a defect density wave) modulates the phase of the waves in the domains in the case of one wave and the model providing the superposition of the waves in the two-wave case can also give similar diffraction patterns. The effect of the correlating wave on the phase of the displacement wave manifests itself in the formation of peaks additional to the satellite on the intensity distributions. The positions of these additional peaks are determined by the sum and the difference of the wavevectors $\mathbf{q}_d$ and $\mathbf{q}$ characterizing the correlating and the displacement waves, respectively (see Fig. 9 in [2]). If the intensity distribution for a crystal modulated by a single displacement $A \cdot H$ is large enough to detect a second-order satellite, then, the diffraction pattern obtained at certain values of $\mathbf{q}$ and $\mathbf{q}_d$ can also be inter-

preted as a result of the superposition of two displacement waves.

Therefore, a model providing the adequate description of the structure of a modulated crystals in such cases can be constructed only upon the quantitative analysis of the intensity distributions in the reciprocal space. Here, of great importance are the experimental data obtained for the reciprocal-lattice rods with different *H* indices.

ACKNOWLEDGMENTS

The work was supported by INTAS, grant INTAS-93-3230-ext.

REFERENCES

1. B. Sh. Bagautdinov, V. V. Gladkiĭ, S. N. Kallaev, *et al.*, Pis'ma Zh. Éksp. Teor. Fiz. **59** (2), 113 (1994) [JETP Lett. **59** (2), 119 (1994)].
2. A. I. Ustinov, L. A. Olikhovskaya, and I. M. Shmyt'ko, Kristallografiya **45** (3), 408 (2000) [Crystallogr. Rep. **45** (3), 365 (2000)].
3. J. A. Wilson, F. J. Di Salvo, and S. Mahajan, Adv. Phys. **24** (2), 1 (1975).

Translated by K.I. Kugel

Crystallography Reports, Vol. 45, No. 3, 2000, pp. 380–385. Translated from Kristallografiya, Vol. 45, No. 3, 2000, pp. 423–428.

STRUCTURE OF INORGANIC COMPOUNDS

Synthesis, Atomic Structure, and Properties of Crystals in the $RbTiOPO_4$–$CsTiPO_5$ System

Liu Wen*, V. I. Voronkova*, V. K. Yanovskiĭ*, N. I. Sorokina, I. A. Verin**, and V. I. Simonov****

** Moscow State University, Vorob'evy gory, Moscow, 119899 Russia*

*** Shubnikov Institute of Crystallography, Russian Academy of Sciences, Leninskiĭ pr. 59, Moscow, 117333 Russia*

Received November 4, 1998

Abstract—The subsolidus region of the phase diagram of the $RbTiOPO_4$–$CsTiPO_5$ system has been studied in the temperature range 700–1000°C, and the boundaries between the stability fields of the orthorhombic phase with the $KTiOPO_4$-type structure and the cubic phase with the pyrochlore-type structure have been determined. Single crystals of the $RbTiOPO_4$ and $CsTiPO_5$ based solid solutions were synthesized by crystallization from flux. The crystal structure and the physical properties of the first members of the series were studied. © *2000 MAIK "Nauka/Interperiodica".*

INTRODUCTION

At present, single crystals of the compounds of the potassium titanyl phosphate family, such as $KTiOPO_4$ (KTP), $RbTiOPO_4$ (RTP), $TlTiOPO_4$ (TTP) and of similar arsenates attract much attention as promising materials for nonlinear optics [1] and new ferroelectrics and superionic conductors [2]. The alkaline metal ions play an important role in the crystals with the KTP-type structure, since they participate in ionic conductivity and in the formation of spontaneous polarization [2, 3]. As a result, mutual substitution of alkaline ions can significantly affect the physical properties of these crystals. The $K_{1-x}Rb_xTiOPO_4$ [1], $K_{1-x}Tl_xTiOPO_4$, and $Rb_{1-x}Tl_xTiOPO_4$ [4, 5] form a continuous series of solid solutions, whereas the $K_{1-x}Na_xTiOPO_4$ and $Rb_{1-x}Cs_xTiOPO_4$ systems form solid solutions only within the limited range [5].

The $RbTiOPO_4$–$CsTiPO_5$ system is of special interest, because the RTP and $CsTiPO_5$ (CTP) phases form different crystal structures at room temperature: the RTP phase has a KTP-type orthorhombic structure [6], and the CTP phase has a pyrochlore-type disordered cubic structure [5, 7]. The RTP, TTP, and $CsTiOAsO_4$ (CTA) crystals undergo, in addition to the ferroelectric phase transition, also the structural transition into the same cubic phase at higher temperatures [8]. Since the CTP-type cubic structure can be considered as an original structure for the crystals of the KTP family, the detailed studies of the RTP–CTP system can shed the light on the specific features of the crystal structure and the physical properties of all the compounds of the KTP family. The present study is focused on some details of the phase diagram of the $RbTiOPO_4$–$CsTiPO_5$ system and the structure and properties of crystals with mixed compositions.

SYNTHESIS OF SPECIMENS AND EXPERIMENTAL PROCEDURE

The studies of phase relationships in the subsolidus region of the RTP–CTP system were performed on ceramic specimens obtained as a result of two-stage annealing in the temperature range 700–1000°C (with the temperature step of 50°) followed by quick cooling. The relative content of rubidium and cesium in the specimens was changed with a step of 5 at. %. The extra-pure grade Rb_2CO_3, Cs_2CO_3, TiO_2, and $NH_4H_2PO_4$ reagents were used. The phase composition of the specimens was checked by the X-ray diffraction analysis on a DRON-2.0 diffractometer.

The structural features and the physical properties of the crystalline phases of different compositions were studied in more detail on single crystals grown by crystallization from flux in the quaternary Rb_2O–Cs_2O–TiO_2–P_2O_5 system. The starting compositions of some melts, the temperature modes of crystallization, and the experimental results obtained are listed in Table 1. In these experiments, the reagents were mixed for 2–3 h in an agate ball mill, annealed in a muffle furnace at 600°C, and then were loaded into 50 ml-large platinum crucibles. Then, they were heated for 24 hours at the maximum temperatures specified in Table 1 and cooled at a rate of 0.5–2.0 deg/h. Upon the attainment of the lower temperature limit, the solution was poured out, and the crystals grown on the crucible walls were cooled down to room temperature at a rate of 50 deg/h.

Note that the crystallization fields in the solid solutions with the KTP-type ($Rb_{1-x}Cs_xTiOPO_4$, RTP : Cs)

Table 1. Results of the experiments on crystal growth from flux in the Cs_2O–Rb_2O–TiO_2–P_2O_5 system

Experiment	Melt composition, mol %				Temperature mode, °C	Crystal type
	Cs_2O	Rb_2O	TiO_2	P_2O_5		
1	15	30	20	35	920–620, 1 deg/h	RTP : Cs; 1 mm
2	15	30	25	30	1000–650, 1 deg/h	RTP : Cs; 2–3 mm
3	23.3	10	33.3	33.3	1140–950, 1 deg/h	CTP : Rb; 1–2 mm
4	25	13	25	37	1000–750, 2 deg/h	CTP : Rb; 0.5 mm
5	20	20	30	30	1100–850, 2 deg/h	CTP : Rb; 0.5 mm
6	22	22	22.5	33.5	950–600, 2 deg/h	RTP : Cs; 1 mm
7	7	33	20	40	1100–800, 2 deg/h	RTP : Cs; 4–5 mm
8	7	35	25	33	1050–900, 2 deg/h	RTP : Cs; 6–7 mm
9	21	21	25	33	950–800, 1 deg/h	RTP : Cs; 1 mm
10	19	19	25	37	1050–870, 0.5 deg/h	CTP : Rb; 1 mm
11	23.5	11.5	25	40	1050–900, 1 deg/h	$Rb_3Ti_3P_5O_{20}$: Cs
12	27	13	20	40	950–750, 1 deg/h	$Rb_3Ti_3P_5O_{20}$: Cs
13	30	15	20	35	1050–710, 2 deg/h	$Cs_2TiP_2O_8$: Rb
14	25	10	20	45	1000–800, 1 deg/h	$RbTi_2(PO_4)$: Cs
15	28	14	25	33	1100–700, 1 deg/h	Glass
16	30	15	25	30	1050–650, 2 deg/h	Glass
17	25	20	25	30	1100–70, 1 deg/h	Glass
18	30	5	30	35	1000–800, 1 deg/h	$Cs_2TiP_2O_8$: Rb

and pyrochlore-type ($Cs_{1-x}Rb_xTiPO_5$, CTP : Rb) structures in the quaternary system are relatively narrow and are located in the direct vicinity of the broad crystallization fields of the $Rb_3Ti_3P_5O_{20}$ [9, 10], $Cs_2TiP_2O_8$ [11], and $RbTi_2(PO_4)_3$ [12] compounds and the solid solutions on their basis, which considerably hinders the preparation of RTP : Cs and CTP : Rb single crystals.

The X-ray data for the structural refinement of the crystals obtained were collected on a CAD-4F automated diffractometer (MoK_α radiation, graphite monochromator, room temperature). The crystal density was determined by hydrostatic weighing in toluene; the morphology was studied on a ZRG-3 goniometer. The chemical composition of the solid solution crystals was checked by X-ray microanalysis on a Camebax SX50 analyzer. The $RbTiOPO_4$ and $CsNb_3O_8$ single crystals served as the standards.

The temperature dependences of permittivity and electric conductivity were measured on a Tesla BM-431E bridge at a frequency of 1 MHz; optical diagnostics of the crystals was performed on a polarization microscope.

$RbTiOPO_4$–$CsTiPO_5$ SYSTEM

The study of the phase relationships on ceramic specimens in the RTP–CTP system revealed that, in the subsolidus region, this system is binary and forms a limited series of solid solutions with the KTP-type (RTP : Cs) and CTP-type (CTP : Rb) structures (Fig. 1). The width of the existence region of the former compound was $0 < x < 0.2$ at 700°C and decreased at higher annealing temperatures. At higher Cs concentrations

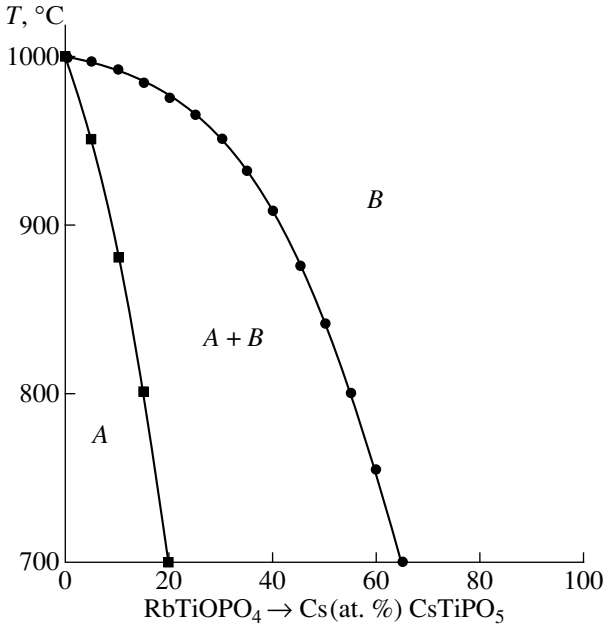

Fig. 1. Phase diagram of the subsolidus region in the $RbTiOPO_4$–$CsTiPO_5$ system: (*A*) RTP : Cs and (*B*) CTP : Rb solid solutions.

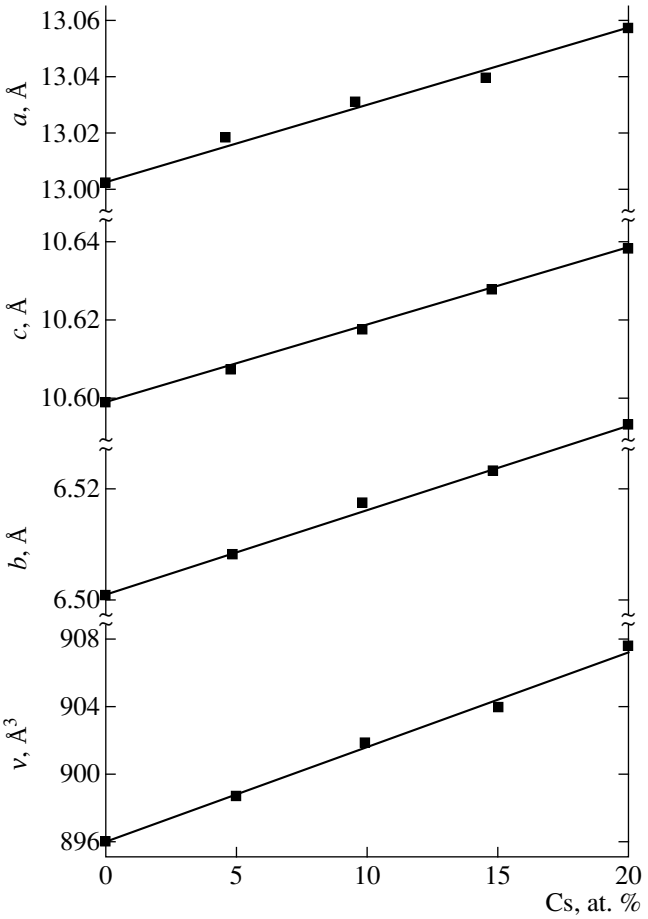

Fig. 2. Parameters and volume of the orthorhombic unit cell for the RTP : Cs solid solutions. Ceramic specimens upon annealing at 700°C.

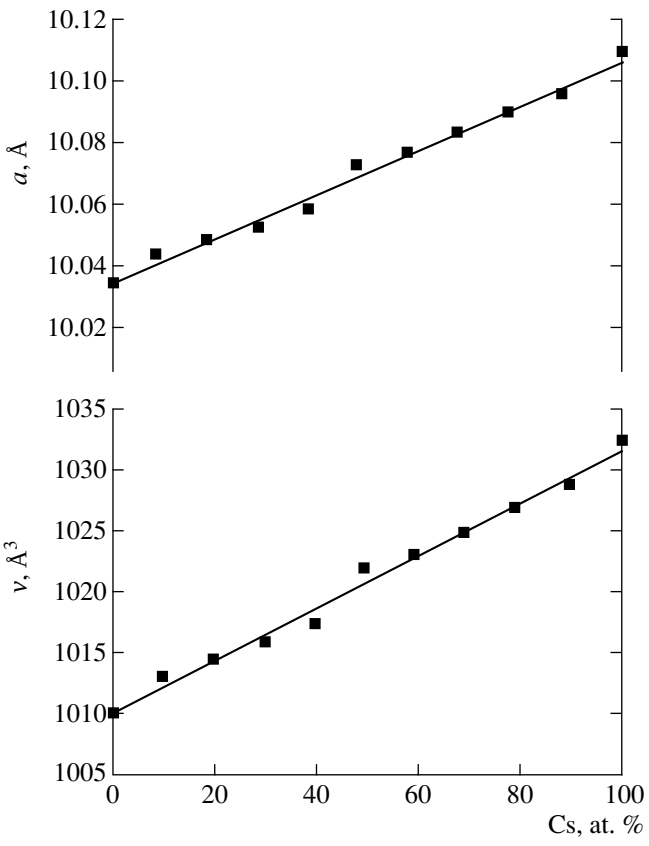

Fig. 3. The *a*-parameter and volume of the cubic unit cell for the CTP : Rb solid solutions. Ceramic specimens upon annealing at 1000°C.

and temperatures, the pyrochlore-type structure becomes stable. The change in the unit-cell parameters of the RTP : Cs and CTP : Rb solid solutions caused by the change of their composition follows Vegard's law (Figs. 2, 3). According to the chemical analysis, the distribution coefficients of Cs and Rb during growth were 0.3 for RTP : Cs and ~1.1 for CTP : Rb.

STRUCTURE AND PROPERTIES OF CRYSTALS GROWN

The crystals of the solid solutions with the KTP-type structure were transparent, colorless, and well-faceted; however, their growth forms were of two types: one was characteristic of pure RTP crystals (the absence of the {100} and {110} faces), and the other was conventional for KTP [13] but with poorly developed {100} faces. The crystals of the cubic CTP : Rb solid solutions had the shape of the octahedra with the {111} faces. The violet color of the crystals indicated partial reduction of titanium and nonstoichiometry. The observations in the polarized light showed that the crystals were considerably stressed and inhomogeneous, which prevented their detailed X-ray study.

Table 2. Unit-cell parameters of $RbTiOPO_4$ (1), $Rb_{0.95}Cs_{0.05}TiOPO_4$ (2), and $Rb_{0.89}Cs_{0.11}TiOPO_4$ (3) crystals

Parameter	1*	2	3
a	12.948(2)	12.959(1)	12.982(1)
b	6.494(3)	6.501(1)	6.512(1)
c	10.551(1)	10.544(1)	10.545(1)

* See [14].

The preliminary X-ray studies of the RTP : Cs crystals obtained in experiments 8 and 9 revealed their orthorhombic symmetry (Table 2). The *a* and *b* unit-cell parameters increase with the Cs content, whereas the *c*-parameter remains almost constant. The best small $Rb_{1-x}Cs_xTiOPO_4$ single crystals of two compositions ($x \approx 0.05$ and $x \approx 0.10$) were subjected to the detailed X-ray diffraction analysis. The crystals were rolled to the spherical shape. The specimens thus prepared were first subjected to the preliminary X-ray study. As a result, two single crystals of different compositions

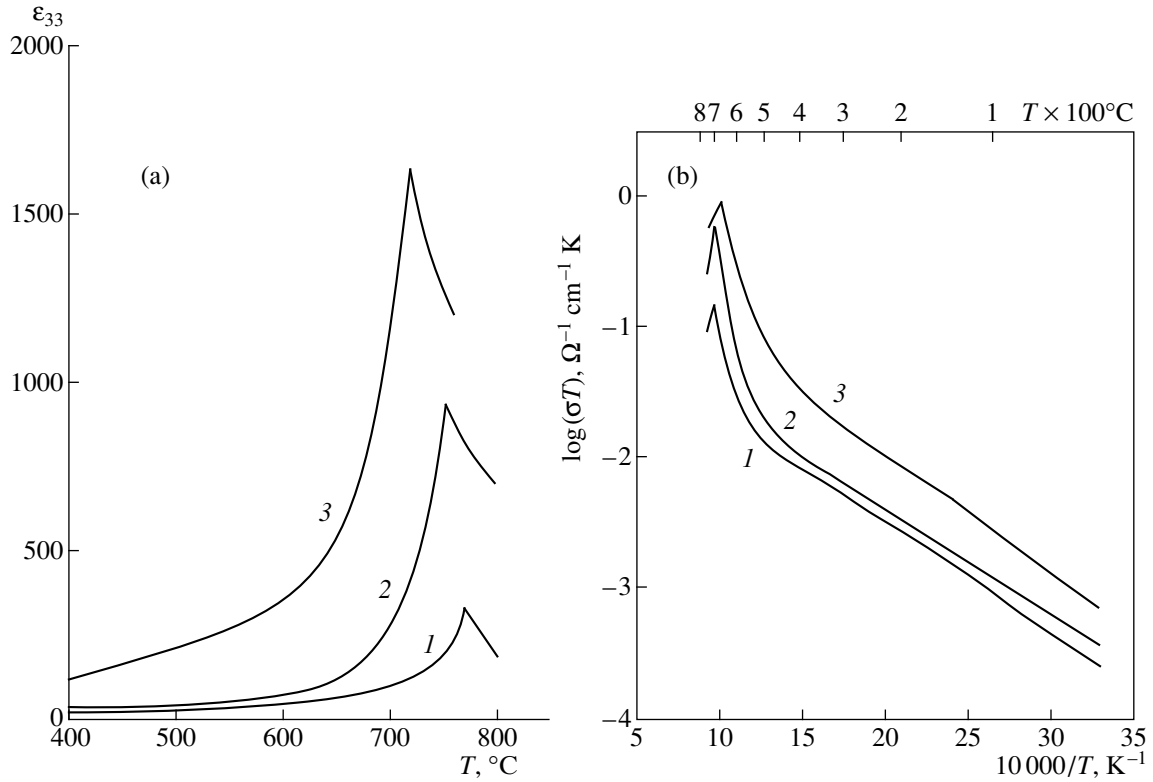

Fig. 4. Temperature behavior of (a) permittivity ε_{33} and (b) electric conductivity σ_{33} of (*1*) $RbTiOPO_4$, (*2*) $Rb_{0.96}Cs_{0.04}OPO_4$, and (*3*) $Rb_{0.93}Cs_{0.07}OPO_4$ single crystals.

characterized by the best diffraction-peak profiles and the closest correspondence of the intensities of symmetrically equivalent diffraction reflections were selected for the further detailed analysis.

The characteristics of the data collection for the complete X-ray structure studies of the $Rb_{1-x}Cs_xTiOPO_4$ crystals with $x \approx 0.05$ and $x \approx 0.10$ and the details of the least-squares refinement of the

Table 3. Characteristics of the experiments and the crystallographic data for $(Rb_{0.95}Cs_{0.05})TiOPO_4$ and $(Rb_{0.89}Cs_{0.11})TiOPO_4$ single crystals

Compound	$(Rb_{0.95}Cs_{0.05})TiOPO_4$	$(Rb_{0.89}Cs_{0.11})TiOPO_4$
Radiation	MoK_α	MoK_α
Diffractometer	Enraf-Nonius	Enraf-Nonius
Monochromator	Graphite	Graphite
Scan mode	ω/θ	ω/θ
$(\sin\theta/\lambda)_{max}$	1.0	1.0
Total number of reflections	9477	10142
Number of independent reflections	2820	2853
R_{av} ($\|F\|$)	0.026	0.023
Radius of the specimen, mm	0.131	0.144
Sp. gr.	$Pna2_1$	$Pna2_1$
a, Å	12.9591(11)	12.9821(8)
b, Å	6.5005(6)	6.5124(4)
c, Å	10.5441(18)	10.5447(5)
V, Å^3	888.2(2)	891.5(2)
μ, cm^{-1}	143.7	148.9
Reliability factors R/R_ω	0.037/0.020	0.026/0.018

Table 4. Interatomic distances (Å) in the $(Rb_{0.95}Cs_{0.05})TiOPO_4$ (**I**) and $(Rb_{0.89}Cs_{0.11})TiOPO_4$ (**II**) structures

Distances	I	II	Distances	I	II
Ti(1)–O(9)	1.705(1)	1.715(1)	Rb, Cs(1)–O(1)	2.765(2)	2.774(2)
O(2)	1.936(1)	1.948(1)	O(10)	2.810(2)	2.811(2)
O(10)	1.981(1)	1.968(1)	O(5)	2.862(2)	2.873(2)
O(6)	2.031(1)	2.027(1)	O(7)	3.013(2)	3.024(2)
O(5)	2.089(1)	2.088(1)	O(2)	3.058(2)	3.120(1)
O(1)	2.151(1)	2.143(1)	O(4)	3.088(2)	3.048(2)
Ti(2)–O(10)	1.728(1)	1.737(1)	O(8)	3.085(2)	3.136(2)
O(7)	1.949(1)	1.956(1)	O(3)	3.037(2)	3.116(2)
O(4)	2.011(1)	2.016(1)	O(9)	3.058(2)	3.110(2)
O(8)	2.000(1)	1.984(1)			
O(3)	2.061(1)	2.064(1)	Rb, Cs(2)–O(1)	2.990(2)	3.033(2)
O(9)	2.098(1)	2.089(1)	O(5)	2.929(2)	2.994(2)
P(1)–O(1)	1.522(1)	1.513(1)	O(10)	3.128(2)	3.159(2)
O(2)	1.552(1)	1.550(1)	O(8)	2.864(2)	2.853(2)
O(3)	1.540(1)	1.540(1)	O(7)	3.172(2)	3.193(2)
O(4)	1.541(1)	1.539(1)	O(2)	2.755(2)	2.744(2)
P(2)–O(5)	1.532(1)	1.537(1)	O(3)	2.768(2)	2.780(2)
O(6)	1.527(1)	1.534(1)	O(9)	2.805(2)	2.790(2)
O(7)	1.554(1)	1.550(1)			
O(8)	1.532(1)	1.537(1)			

structural models are summarized in Table 3. All the calculations were performed using the AREN and the PROMETHEUS program packages. The occupancies of the (Rb,Cs) positions were refined along with the atomic structural parameters under the restriction that the positional and thermal parameters of Rb(1), Cs(1), Rb(2), and Cs(2) atoms coincide and that the total occupancy of each position (1 and 2) by the Rb and Cs atoms is unity. In the crystal of $Rb_{1-x}Cs_xTiOPO_4$ with $x \approx 0.05$, the refinement of the occupancy of position 1 soon yielded 0.933(3) for Rb(1) and 0.067 for Cs(1). The values for position 2 were 0.970(3) for Rb(2) and 0.030 for Cs(2). In other words, Cs atoms populate the two positions of rubidium atoms with different probabilities. A similar arrangement of Cs atoms is observed in the second structure studied—$Rb_{1-x}Cs_xTiOPO_4$ with $x \approx 0.10$. The refinement of the structural model of this compound resulted in the following position occupancies: 0.822(4) for Rb(1), 0.178 for Cs(1), 0.956(4) for Rb(2), and 0.044 for Cs(2) atoms. Thus, according to the occupancies *q* obtained, the chemical formulas of the specimens studied should be written as $Rb_{0.95}Cs_{0.05}TiOPO_4$ and $Rb_{0.89}Cs_{0.11}TiOPO_4$. The table of atomic coordinates and thermal parameters is available from the authors. The selected interatomic distances in the structures are listed in Table 4.

Crystals of $Rb_{0.95}Cs_{0.05}TiOPO_4$ and $Rb_{0.89}Cs_{0.11}TiOPO_4$ are isostructural to the KTP crystals. The three-dimensional framework formed by apex-sharing TiO_6-octahedra and PO_4-tetrahedra is characterized by wide helical channels along the *c*-axis which accommodate weakly bound Rb and Cs cations. It is seen from Table 4 that Cs atoms tend to occupy the more "spacious" position 1. Substitution of cesium for rubidium results in an increase of the mean Me–O distance for positions with the coordination numbers equal to nine (from 2.975 to 3.001 Å) and eight (from 2.929 to 2.943 Å). It is assumed that one of the factors providing a considerable increase of the nonlinear-optical susceptibility is the distortion of the TiO_6 octahedra. Substitution of cesium for rubidium is accompanied by less distortion of these octahedra (Table 4).

The temperature behavior of permittivity ε_{33} and ionic conductivity σ_{33} in $RbTiOPO_4$ single crystals and two solid solutions on its basis with different Cs-content are illustrated by Fig. 4. It is seen that small amounts of cesium substituting for rubidium reduce the temperature of the ferroelectric phase transition and enhance the ionic conductivity. This can be explained by a loosening of the crystal structure due to incorporation into it of large Cs^+ cations.

ACKNOWLEDGMENTS

This study was supported by the Russian Foundation for Basic Research (project no. 00-02-16059) the Leading Scientific Schools, project no. 00-15-96633, and the Ministry of Higher Education of Russia (grant no. 5017 within the program "Russian Universities").

REFERENCES

1. F. C. Zumsteg, J. D. Bierlein, and T. D. Gier, J. Appl. Phys. **47** (11), 4980 (1976).
2. V. K. Yanovskiĭ and V. I. Voronkova, Phys. Status Solidi A **93**, 665 (1986).
3. J. D. Bierlein and C. B. Arweiler, Appl. Phys. Lett. **49**, 917 (1986).
4. M. Jannin, C. Kolinsky, G. Godefroy, *et al.*, Eur. J. Solid State Inorg. Chem. **33**, 607 (1996).
5. V. I. Voronkova, E. S. Shubentsova, and V. K. Yanovskiĭ, Neorg. Mater. **26** (1), 143 (1990).
6. I. Tordjman, R. Masse, and J. C. Guetel, Z. Kristallogr. **139**, 103 (1974).
7. M. Kunz, R. Dinnebier, L. K. Cheng, *et al.*, J. Solid State Chem. **120**, 299 (1995).
8. L. K. Cheng and J. D. Bierlein, Ferroelectrics **142**, 209 (1993).
9. R. Duhlev, Acta Crystallogr., Sect. C: Cryst. Struct. Commun. **50**, 1523 (1994).
10. I. N. Geĭfman, N. G. Furmanova, P. G. Nagornyĭ, and I. S. Golovina, Kristallografiya **41** (1), 109 (1996) [Crystallogr. Rep. **41** (1), 101 (1996)].
11. J. Protas, B. Menaert, G. Marnier, and B. Boulanger, Acta Crystallogr., Sect. C: Cryst. Struct. Commun. **47**, 698 (1991).
12. M. R. Masse, Bull. Soc. Fr. Mineral. Crystallogr. **93**, 300 (1970).
13. V. I. Voronkova and V. K. Yanovskiĭ, Kristallografiya **31** (1), 207 (1986) [Sov. Phys. Crystallogr. **31**, 123 (1986)].
14. J. A. Kaduk and R. H. Jahrman, Z. Kristallogr. **204**, 285 (1993).

Translated by I. Polyakova

Crystallography Reports, Vol. 45, No. 3, 2000, pp. 386–388. Translated from Kristallografiya, Vol. 45, No. 3, 2000, pp. 429–431.

STRUCTURE OF INORGANIC COMPOUNDS

Crystal Structure of $KTi_{0.93}Sn_{0.07}OPO_4$

Liu Wen*, N. I. Sorokina, V. I. Voronkova*, V. K. Yanovskiĭ*, I. A. Verin**, A. G. Vigdorchik**, and V. I. Simonov****

** Moscow State University, Vorob'evy gory, Moscow, 119899 Russia*

*** Shubnikov Institute of Crystallography, Russian Academy of Sciences, Leninskiĭ pr. 59, Moscow, 117333 Russia*

Received July 19, 1999

Abstract—To reveal correlations between the atomic structure and properties of the $KTi_{1-x}Sn_xOPO_4$ solid solutions, single crystals of the $KTi_{0.93}Sn_{0.07}OPO_4$ composition were synthesized and their structure was determined. The crystals belong to the $KTiOPO_4$ family; orthorhombic, sp. gr. $Pna2_1$. The unit-cell parameters are $a = 12.831$, $b = 6.410$, and $c = 10.584$ Å. The partial substitution of Sn atoms for Ti atoms results in the formation of more symmetric coordination polyhedra in the structure framework and the change of the physical properties of the crystals. *© 2000 MAIK "Nauka/Interperiodica".*

At present, single crystals of potassium titanyl phosphate (KTP), which exhibit both ferroelectric and superionic properties, attract the attention of researchers as a promising material for nonlinear optics. The numerous crystals of the KTP family have different compositions [1]. In distinction from KTP crystals possessing unique properties, the crystals in which Ge or Sn substitute for Ti show an almost zero signal of the second-harmonic generation [1, 2]. It was found that the structures of these compounds are closer to the structure of the corresponding paraelectric phases [3, 4].

Single crystals of $KSnOPO_4$ were first synthesized in a narrow concentration range of the K_2O–P_2O_5–SnO_2 system with the $K_2O : P_2O_5$ ratio ranging within 1.30–1.46) [5]. The conditions for preparing the $KTi_{1-x}Sn_xOPO_4$ solid solutions were reported in [2]. It was also established a significant decrease in the intensity of the second harmonic upon the substitution of Sn for Ti.

We aimed to continue our studies of the structural characteristics and the ferroelectric and nonlinear-optical properties of the crystals of the $KTi_{1-x}Sn_xOPO_4$ solid solutions and to establish correlations between the structure and physical properties for this family of compounds. A number of single crystals with different tin contents were grown. Below, we reported the determination of the atomic structure of a single crystal with ~10% substitution of tin for titanium.

Single crystals of $KTi_{0.93}Sn_{0.07}OPO_4$ were obtained by spontaneous crystallization from the flux of the K_2O–TiO_2–SnO_2–P_2O_5 quaternary system by the method described elsewhere [6]. The colorless crystals obtained had a platelike shape with the developed {100} faces. The crystal density measured by hydrostatic weighing in toluene was 3.04 g/cm^3.

Small perfect single crystals chosen for X-ray structure analysis were rolled into a spherical shape. The specimens, thus, prepared were subjected to the preliminary X-ray study. As a result, a single crystal, 0.12 mm in radius with the best diffraction-peak profiles and the

Table 1. Characteristics of the experiment and crystallographic data for $KTi_{0.93}Sn_{0.07}OPO_4$ single crystals

Parameter	Value
Radius of the specimen, mm	0.12
μ, cm^{-1}	42.085
ρ_{obs}, g/cm^3	3.04
Diffractometer	CAD-4F Enraf Nonius
Radiation	MoK_α
Monochromator	Graphite
Scan mode	ω/θ
$(\sin\theta/\lambda)_{max}$	1.0
Space group	$Pna2_1$
a, Å	12.831
b, Å	6.410
c, Å	10.584
V, Å^3	870.50
Total number of reflections	13036
Number of unique reflections	3564
R_{av} ($\|F\|$)	0.029
Structure type	$KTiOPO_4$
Programs used	PROMETHEUS, AREN
Weighting scheme	$\omega = 1/\sigma^2$
Number of parameters refined	147
Discrepancy factors R/R_ω	0.0331/0.0355

Table 2. Atomic coordinates, site-occupation factors (q), and equivalent (isotropic) parameters of thermal motion (B_{eq}) in the $KTi_{0.93}Sn_{0.07}OPO_4$ crystal structure

Atom	x/a	y/b	z/c	q	B_{eq}
Ti(1)	0.37244(2)	0.50013(5)	0.0000	0.978(2)	0.461(5)
Sn(1)	0.37244	0.50013	0.0000	0.022	0.461
Ti(2)	0.24635(2)	0.26558(4)	0.25115(5)	0.893(2)	0.461(5)
Sn(2)	0.24635	0.26558	0.25115	0.107	0.461
P(1)	0.49815(4)	0.33689(7)	0.25812(7)	1	0.447(5)
P(2)	0.18055(4)	0.50250(9)	0.51012(6)	1	0.468(6)
K(1)	0.10545(5)	0.69973(11)	0.06399(8)	1	1.626(9)
K(2)	0.37801(5)	0.78033(9)	0.30955(8)	1	1.548(9)
O(1)	0.4853(2)	0.4873(3)	0.1481(2)	1	0.77(2)
O(2)	0.5102(1)	0.4663(3)	0.3808(2)	1	0.76(2)
O(3)	0.4008(1)	0.1998(3)	0.2771(2)	1	0.68(2)
O(4)	0.5933(1)	0.1939(3)	0.2375(2)	1	0.72(2)
O(5)	0.1118(1)	0.3119(3)	0.5375(2)	1	0.72(2)
O(6)	0.1116(1)	0.6924(3)	0.4850(2)	1	0.82(2)
O(7)	0.2526(1)	0.5376(3)	0.6252(2)	1	0.79(2)
O(8)	0.2525(2)	0.4628(3)	0.3967(2)	1	0.79(2)
O(9)	0.2241(1)	0.0422(3)	0.3869(2)	1	0.74(2)
O(10)	0.2251(1)	−0.0317(3)	0.6397(2)	1	0.70(2)

closest correspondence of the intensities of the symmetrically equivalent diffraction reflections, was chosen. A complete X-ray structure study was performed on an Enraf–Nonius CAD-4F automated diffractometer using the MoK_α radiation.

The main crystallographic parameters of the specimen, the characteristics of the X-ray diffraction study, and the details of the least-squares refinement of the structural model are summarized in Table 1. The atomic coordinates, site occupancies factors (q), and equivalent (isotropic) thermal parameters (B_{eq}) are listed in Table 2.

The $KTi_{0.93}Sn_{0.07}OPO_4$ crystals are isostructural to $KTiOPO_4$ [3] and $KSnOPO_4$ [3] crystals. The unit-cell parameters of these compounds are given in Table 3.

Table 3

Compound	a, Å	b, Å	c, Å	V, Å^3
$KTiOPO_4$	12.819(1)	6.399(1)	10.584(1)	868.19
$KTi_{0.93}Sn_{0.07}OPO_4$	12.831(1)	6.410(1)	10.584(1)	870.50
$KSnOPO_4$	13.145(1)	6.526(1)	10.738(1)	921.15

The changes in the a and b parameters and the unit-cell volume correlate with the ratio of the ionic radii of Sn^{4+} (0.71 Å) and Ti^{4+} (0.68 Å) cations, whereas the c parameter is independent of the type of the tetravalent cations. Since the ionic radius of Sn^{4+} ions is larger than that of Ti^{4+} ions, the partial substitution of Sn^{4+} for Ti^{4+} ions results in an increase of almost all bond lengths in both $Ti(1)O_6$- and $Ti(2)O_6$-octahedra. The longest Ti,Sn(1)–O(1) and Ti,Sn(2)–O(9) bonds are an exception: the Ti(1)–O(1) distance shortens from 2.154 to 2.135 Å, and the Ti(2)–O(9) distance shortens from 2.099 to 2.048 Å. The complete substitution of Sn^{4+} for Ti^{4+} ions breaks the alternation of long and short Sn–O bonds in the chains of octahedra [3]. The tendency of Sn^{4+} ions to surround themselves with less distorted oxygen octahedra provides the location of Sn^{4+} ions mainly in less distorted $Ti(2)O_6$-octahedra (Table 2) upon partial substitution of Sn^{4+} for Ti^{4+} ions in the $KTi_{0.93}Sn_{0.07}OPO_4$ structure. It is reasonable to assume that if is the less distortion of the $Ti(Sn)O_6$-octahedra in the structure under study that is responsible for a decrease of the signal of the second-harmonic generation in this crystal.

ACKNOWLEDGMENTS

The authors from the Institute of Crystallography acknowledge the support of the Russian Foundation for Basic Research and the Leading Scientific Schools no. 00-15-96633 (project no. 00-02-16059). The authors from Moscow University acknowledge the support of the Ministry of Higher Education of the Russian Federation (grant no. 5017 within the program "Russian Universities").

REFERENCES

1. G. D. Stucky, M. L. F. Phillips, and T. E. Gier, Chem. Mater., No. 1, 492 (1989).
2. R. H. Jarman and S. G. Grubb, Proc. SPIE Int. Soc. Opt. Eng. **968**, 108 (1988).
3. P. A. Thomas, A. M. Glazer, and B. E. Watts, Acta Crystallogr., Sect. B: Struct. Sci. **46**, 333 (1990).
4. V. I. Voronkova, V. K. Yanovskiĭ, N. I. Sorokina, *et al.*, Kristallografiya **38** (5), 147 (1993) [Crystallogr. Rep. **38**, 662 (1993)].
5. N. S. Slobodyanik, N. G. Nagornyĭ, V. V. Skopenkov, and E. S. Lugovskaya, Zh. Neorg. Khim. **32**, 1724 (1987).
6. V. I. Voronkova and V. K. Yanovskiĭ, Neorg. Mater. **24** (2), 273 (1988).

Translated by I. Polyakova

Crystallography Reports, Vol. 45, No. 3, 2000, pp. 389–394. Translated from Kristallografiya, Vol. 45, No. 3, 2000, pp. 432–437.

STRUCTURE OF INORGANIC COMPOUNDS

Crystal Structure of Double Vanadates $Ca_9R(VO_4)_7$. II. R = Tb, Dy, Ho, and Y

A. A. Belik*, V. A. Morozov*, R. N. Kotov*, S. S. Khasanov, and B. I. Lazoryak***

** Chemistry Department, Moscow State University, Vorob'evy gory, Moscow, 119899 Russia*

*** Institute of Solid State Physics, Russian Academy of Sciences, Chernogolovka, Moscow oblast, 142432 Russia*

Received August 7, 1997; in final form, March 16, 1999

Abstract—Crystal structures of the compounds $Ca_9R(VO_4)_7$ (R = Tb (**I**), Dy (**II**), Ho (**III**), and Y (**IV**) have been studied by the method of the full-profile analysis. All the compounds are crystallized in the trigonal system (sp. gr. $R3c$, $Z = 6$) with the unit-cell parameters (**I**) a = 10.8592(1), c = 38.035(1), V = 3884.2(2) Å^3; (**II**) a = 10.8564(1), c = 38.009(1) Å, V = 3879.6(2) Å^3, (**III**) a = 10.8565(1) and c = 37.995(1) Å, V = 3878.3(2) Å^3, and (**IV**) a = 10.8588(1), c = 37.995(1) Å, V = 3879.9(2) Å^3. In structures **I**–**IV**, rare earth and calcium cations occupy three positions—$M(1)$, $M(2)$, and $M(5)$. Rare earth cations occupy the R^{3+} positions almost in the same way: 2.7–2.6(2) cations in the $M(1)$ position; 2.7–2.3(2) cations in the $M(2)$ position, and 0.6–1.0(1) cation in the $M(5)$ position. At the same time, the occupancy of the $M(5)$ position regularly increases with a decrease of the R^{3+} radius. © *2000 MAIK "Nauka/Interperiodica".*

INTRODUCTION

This study continues our investigation of the $Ca_9R(VO_4)_7$ (R = RE, Y) structures and determination of the distribution of R^{3+}-cations over the positions of the initial $Ca_3(VO_4)_2$ structure [1]. The $Ca_3(VO_4)_2$ [1] and β-$Ca_3(PO_4)_2$ [2] compounds are often used as the matrices for the synthesis of materials with the valuable optical valuable properties [3–6]. The data on the distribution of R^{3+} cations over the positions of the $Ca_3(VO_4)_2$ structure [1] allows the purposeful modification of the optical (luminescence) properties of the materials, in particular, to appropriate choice of the cations–diluters in order to reduce the concentration-induced quenching of the active cation.

Depending on the character of the variation in the unit-cell parameters depending on the radius R^{3+} [7], the $Ca_9R(VO_4)_7$ (R = RE, Y) compounds can be divided into two groups. The a- and c- parameters of the first group of compounds (RE = La–Eu) decrease almost linearly with the radius of R^{3+}. The a-parameter of the second group of compounds (RE = Tb–Lu and Y) is almost independent of the radius, whereas the c-parameter decreases with the radius of R^{3+} quite dramatically. The study of the compounds of the first group (R = La, Pr, Eu) showed that the R^{3+} cations occupy three positions, $M(1)$, $M(2)$, and $M(3)$, of the initial $Ca_3(VO_4)_2$ structure [8]. The $M(5)$ position in these compounds is filled with Ca^{2+} cations, whereas the $M(4)$ position is empty. Each of the compounds with R = La, Pr, Eu is characterized by its own distribution of the R^{3+} cations over the $M(1)$–$M(3)$ positions. The occupancy of the $M(3)$ position with R^{3+} cations decreases, and occupancies of the $M(1)$ and $M(2)$ positions increase with a decrease of the R^{3+} radius [8].

Below, we describe the study of the compounds $Ca_9R(VO_4)_7$ with R = Tb (**I**), Dy (**II**), Ho (**III**), and Y (**IV**) belonging to the second group.

EXPERIMENTAL

Compounds **I**–**IV** were synthesized from the solid phase by the method described elsewhere [7]. The X-ray diffraction data were obtained on a SIEMENS D500 powder diffractometer with a BRAUN position-sensitive detector at 297 K (Cu$K_{\alpha 1}$-radiation, λ = 1.5406 Å, SiO_2-monochromator). The effective exposure at each point was ~30 min, the 2θ-scan was performed at a step of 0.01°. Other experimental conditions are indicated in Table 1. The structures were refined by the Rietveld method [9] using the RIETAN-94 program [10, 11].

The structure was refined with the use of the f-curves for Ca^{2+}, R^{3+}, V^{5+}, and O^-. The peak profiles were described by the modified pseudo-Voight function (Mod-TCH pV) [9]). The background profile was described by the polynomial of degree five. The occupancies of the vanadium and oxygen positions have not been refined.

The initial model for the structure refinement was based on the coordinates of the $Ca_3(VO_4)_2$ structure [1]. At the first stage of the model-parameter refinement, the cations were set using the f-curve of Ca^{2+} cations. The analysis of the thus obtained occupancies (Table 2, $n_{f\text{-Ca}}$) showed that the R^{3+} cations are distributed over the $M(1)$, $M(2)$, and $M(5)$ positions. The occupancy of the $M(4)$ position was close to zero, and that of the $M(3)$

Table 1. Experimental conditions and results of the refinement of the $Ca_9R(VO_4)_7$ structures (R = Tb (**I**), Dy (**II**), Ho (**III**) and Y (**IV**))

Parameter	Compound			
	I	**II**	**III**	**IV**
Range of angles 2θ, deg	10–110	10–110	10–110	10–140
I_{max} (pulse)	23805	24443	25040	32759
Unit-cell parameters (sp. gr. $R3c$, z = 6)				
a, Å	10.8592(1)	10.8564(1)	10.8565(1)	10.8588(1)
c, Å	38.035(1)	38.009(1)	37.995(1)	37.995(1)
V, Å^3	3884.2(2)	3879.6(2)	3878.3(2)	3879.9(2)
Number of reflections	548	546	546	745
Number of refined parameters*	17 + 63	17 + 61	17 + 63	17 + 64
Reliability factors**				
R_{WP}; R_P	4.25; 3.18	3.97; 2.90	4.08; 3.08	4.42; 3.36
R_I; R_F	2.28; 1.43	2.46; 1.48	1.72; 1.10	2.60; 1.59
S	1.71	1.67	1.50	1.49
D–Wd	0.77	0.78	0.91	0.93

* The first figure indicates the total number of the parameters describing the background and the profile, the scale factor, and the unit-cell parameters; the second figure indicates the total number of the positional and thermal parameters, and the position occupancies.

** Calculated by the formulas [10]:

$$R_{WP} = [(\Sigma w_i[y_i(\text{obs}) - y_i(\text{calc})]^2)/(\Sigma w_i[y_i(\text{obs})]^2)]^{1/2},$$

$$R_p = (\Sigma|y_i(\text{obs}) - y_i(\text{calc})|)/(\Sigma y_i(\text{obs})),$$

$$R_I = (\Sigma|I(\text{obs}) - I(\text{calc})|)/(\Sigma I(\text{obs})),$$

$$R_F = (\Sigma|[I(\text{obs})]^{1/2} - [I(\text{calc})]^{1/2}|)/(\Sigma[I(\text{obs})]^{1/2}),$$

$S = [(\Sigma w_i[y_i(\text{obs}) - y_i(\text{calc})]^2)/(N - P)]^{1/2}$ (N is the number of the experimental points, P is the number of the refined parameters), D–Wd (Durbin–Watson statistic): $d = \Sigma(\Delta y_i - \Delta y_{i-1})^2/\Sigma(\Delta y_i)^2$, $\Delta y_i = y_i(\text{obs}) - y_i(\text{calc})$.

Table 2. Occupancies of the $M(1)$, $M(2)$, and $M(5)$ positions in structures **I**–**IV** and the number of R^{3+} cations in each position

Position		Compound (radius r_{VIII} (Å) [15])			
		I; 1.04	**II**; 1.03	**III**; 1.02	**IV**; 1.015
$M(1)$	n_{Ca}	0.85(1)	0.85(1)	0.86(1)	0.85(1)
	m_R	0.15(1)	0.15(1)	0.14(1)	0.15(1)
	Number of R^{3+} cations	2.7(2)	2.7(2)	2.6(2)	2.6(2)
	$n_{f\text{-Ca}}$	1.28(3)	1.29(3)	1.27(2)	1.15(1)
$M(2)$	n_{Ca}	0.85(1)	0.86(1)	0.85(1)	0.87(1)
	m_R	0.15(1)	0.14(1)	0.15(1)	0.13(1)
	Number of R^{3+} cations	2.7(2)	2.6(2)	2.6(2)	2.3(2)
	$n_{f\text{-Ca}}$	1.28(3)	1.29(3)	1.26(2)	1.13(1)
$M(5)$	n_{Ca}	0.90(1)	0.87(1)	0.87(1)	0.83(1)
	m_R	0.10(1)	0.13(1)	0.13(1)	0.17(1)
	Number of R^{3+} cations	0.6(1)	0.8(1)	0.8(1)	1.0(1)
	$n_{f\text{-Ca}}$	1.23(3)	1.31(3)	1.26(2)	1.20(2)

Note: n_{Ca} and m_R are the occupancies of the positions with Ca^{2+} and R^{3+} cations in the model structure, respectively; $n_{f\text{-Ca}}$ is the occupancy of the position in the structure model obtained using only f-curves of Ca^{2+}.

position, to unity. At the second stage of the refinement, we studied the distribution of the R^{3+} cations over the $M(1)$, $M(2)$, and $M(5)$ positions with due regard for position multiplicities ($n_{Ca} + m_R = 1$). The $M(4)$ position was taken to be empty. For the cations in the $M(3)$ positions, the f-curve of Ca^{2+} was used. The thus refined number of R^{3+} cations in the unit cell was close to six (Table 2) and corresponded to the composition $Ca_9R(VO_4)_7$ (Z = 6).

At the final stage of the refinement, the f-curves for each position were set proceeding from the cation distribution obtained at the previous stage of the refinement, and then all the model parameters (including the occupancy of the cation positions) were refined again. The thermal parameters of some oxygen atoms (those which had negative values) were fixed and were not refined. The occupancies (n) of the $M(1)$–$M(3)$, and $M(5)$ positions in the refined models were close to unity (Table 3). The experimental and the calculated X-ray diffraction patterns (Fig. 1) were quite consistent. The electron-density maps $\rho(xyz)$ and $\Delta\rho(xyz)$ (calculated using the GSAS program) showed no additional peaks with intensities exceeding $> \pm 1$ eÅ^{-3}. The refined unit-cell parameters and the reliability factors R are indicated in Table 1. The atomic coordinates, the thermal

Table 3. Structural parameters in the $Ca_9R(VO_4)_7$ compounds (R = Tb (**I**), Dy (**II**), Ho (**III**), Y (**IV**))

Atom	R^{3+}	n**	x	y	z	B_{iso}, Å^2
M(1)***	**I**	0.98(2)	0.723(2)	0.860(2)	0.4301(8)	1.1(2)
	II	1.00(2)	0.727(2)	0.862(2)	0.4303(9)	1.0(2)
	III	1.02(2)	0.725(1)	0.861(1)	0.4308(6)	1.1(2)
	IV	1.00(1)	0.7249(7)	0.8606(8)	0.4310(4)	0.6(2)
M(2)***	**I**	0.98(2)	0.613(1)	0.824(2)	0.2334(8)	0.4(2)
	II	0.99(2)	0.615(1)	0.823(1)	0.2336(8)	0.1(2)
	III	1.01(2)	0.615(1)	0.825(1)	0.2340(6)	0.9(2)
	IV	0.99(1)	0.6134(7)	0.8223(8)	0.2341(4)	0.5(2)
Ca(3)	**I**	1.02(2)	0.125(2)	0.267(1)	0.3238(8)	0.7(2)
	II	0.99(2)	0.124(2)	0.267(1)	0.3249(9)	1.4(2)
	III	1.02(2)	0.122(1)	0.2678(8)	0.3250(6)	0.6(2)
	IV	1.02(1)	0.1238(8)	0.2686(6)	0.3244(4)	0.9(2)
M(5)***	**I**	1.01(3)	0	0	0	1.0(2)
	II	1.02(3)	0	0	0	1.5(2)
	III	1.01(2)	0	0	0	0.7(2)
	IV	1.01(1)	0	0	0	0.7(2)
V(1)	**I**	1	0	0	0.2670(8)	0.2(3)
	II	1	0	0	0.2679(8)	0.7(4)
	III	1	0	0	0.2672(6)	1.4(3)
	IV	1	0	0	0.2666(4)	1.1(2)
V(2)	**I**	1	0.683(1)	0.858(2)	0.1336(8)	0.7(3)
	II	1	0.686(1)	0.859(2)	0.1341(8)	0.4(4)
	III	1	0.6834(9)	0.857(1)	0.1334(5)	1.1(3)
	IV	1	0.6827(6)	0.8558(7)	0.1334(4)	0.6(2)
V(3)	**I**	1	0.655(2)	0.847(2)	0.0318(8)	0.5(3)
	II	1	0.657(2)	0.849(2)	0.0321(9)	0.8(4)
	III	1	0.655(1)	0.848(1)	0.0317(6)	0.7(3)
	IV	1	0.6550(8)	0.8486(7)	0.0319(4)	0.3(1)
O(11)	**I**	1	0	0	0.315(2)	0.5(4)
	II	1	0	0	0.315(2)	0.2(5)
	III	1	0	0	0.312(1)	0.5*
	IV	1	0	0	0.314(1)	1.6(4)
O(12)	**I**	1	0.012(6)	0.855(4)	0.267(2)	1.6(5)
	II	1	0.017(5)	0.857(4)	0.259(1)	0.4(5)
	III	1	0.012(4)	0.858(3)	0.257(1)	1.6(5)
	IV	1	0.013(2)	0.857(2)	0.2572(7)	0.(4)
O(21)	**I**	1	0.699(5)	0.895(5)	0.179(2)	1.2(5)
	II	1	0.693(6)	0.899(6)	0.176(2)	3.3(5)
	III	1	0.705(4)	0.902(4)	0.177(1)	3.4(5)
	IV	1	0.708(3)	0.903(3)	0.1785(9)	2.6(5)
O(22)	**I**	1	0.760(5)	0.752(5)	0.125(1)	0.5*
	II	1	0.765(6)	0.763(6)	0.124(2)	1.6(5)
	III	1	0.758(4)	0.762(5)	0.124(1)	1.8(5)
	IV	1	0.760(3)	0.757(3)	0.1237(9)	1.5(5)

Table 3. (Contd.)

Atom	R^{3+}	*n***	*x*	*y*	*z*	B_{iso}, Å^2
O(23)	**I**	1	0.729(6)	0.023(5)	0.112(2)	0.6(4)
	II	1	0.724(6)	0.019(5)	0.113(2)	0.5*
	III	1	0.725(4)	0.015(4)	0.113(1)	0.7(5)
	IV	1	0.722(2)	0.019(2)	0.1125(7)	0.2(4)
O(24)	**I**	1	0.497(5)	0.753(6)	0.127(1)	0.6(4)
	II	1	0.505(5)	0.759(6)	0.126(1)	0.4(5)
	III	1	0.505(3)	0.755(5)	0.126(1)	1.3(5)
	IV	1	0.501(2)	0.751(3)	0.1232(9)	1.5(4)
O(31)	**I**	1	0.589(6)	0.953(5)	0.048(2)	0.9(5)
	II	1	0.588(5)	0.953(5)	0.047(2)	0.5*
	III	1	0.595(4)	0.953(4)	0.046(1)	0.5*
	IV	1	0.594(2)	0.953(2)	0.0450(8)	0.5*
O(32)	**I**	1	0.566(5)	0.682(5)	0.052(2)	0.5*
	II	1	0.574(6)	0.684(5)	0.052(2)	0.5*
	III	1	0.563(4)	0.681(4)	0.050(1)	1.5(5)
	IV	1	0.567(3)	0.679(3)	0.0484(8)	1.4(4)
O(33)	**I**	1	0.824(4)	0.913(6)	0.047(1)	0.6(5)
	II	1	0.834(4)	0.915(7)	0.050(1)	0.5*
	III	1	0.832(3)	0.920(5)	0.048(1)	1.2(5)
	IV	1	0.828(2)	0.921(3)	0.0425(9)	0.4(4)
O(34)	**I**	1	0.633(4)	0.831(5)	0.991(1)	0.1(5)
	II	1	0.633(4)	0.829(6)	0.990(1)	0.5(5)
	III	1	0.634(3)	0.828(4)	0.989(1)	0.5(5)
	IV	1	0.631(2)	0.828(2)	0.9893(6)	0.2(4)

Note: Notation for oxygen atoms: the first number in parentheses indicates the ordinal number of the vanadium atom, the second number in parentheses indicates the ordinal number of the oxygen atom in the oxygen tetrahedron.

* The fixed value of B_{iso}.

** The position occupancy.

*** The *M*(1), *M*(2), and *M*(5) positions are filled with Ca^{2+} and R^{3+} cations in the ratios indicated in Table 1.

parameters, and the position occupancies are listed in Table 3.

DISCUSSION OF THE RESULTS

Compounds **I**–**IV** are isostructural to $Ca_3(VO_4)_2$ [1] and belong to the structure type of the mineral whitlockite [12]. Similar to $Ca_3(VO_4)_2$ [1] and $Ca_9R(VO_4)_7$ (R = La, Pr, Eu) [8], the VO_4^{3-}-tetrahedra in compounds **I**–**IV** are considerably distorted (the V–O distances range within 1.57–1.84 Å). The analysis of the interatomic distances in these structures showed that the substitution of Ca^{2+} by RE cations only slightly affects the framework of the $Ca_3(VO_4)_2$ structure. Most interatomic distances in the $M(1)O_7$ and $M(2)O_8$ polyhedra in the $Ca_3(VO_4)_2$ structure and **I**–**IV** structures are equal. Some changes are observed in the *M*(3)-polyhedron. The O(21) atom enters the polyhedron of the *M*(3) position; the *M*(3)–O(21) distances in structures **I**–**IV** [2.97(5), 2.87(6), 2.85(4), and 2.87(3) Å] are longer in comparison with the analogous distance in $Ca_3(VO_4)_2$ [2.687(1) Å]. The O(12) atom is not a necessary element of the polyhedron of the *M*(3) position. The *M*(3)–O(12) distance for structures **I**–**IV** [2.87(6), 2.81(4), 2.92(4), and 2.88(2) Å) decreases in comparison with the analogous distance in $Ca_3(VO_4)_2$ [2.999(8) Å] and is comparable with the *M*(3)–O(21) distance. Most of the other *M*(3)–O distances in structures **I**–**IV** and $Ca_3(VO_4)_2$ are the same within the experimental error. Thus, the coordination number for the *M*(3) positions in structures **I**–**IV** is nine. Similar variations in the distances in the $M(3)O_9$ polyhedron are also recorded for the compounds with R = La, Pr, and Eu [8]. Since the interatomic distances in the $M(1)O_7$, $M(2)O_8$, and $M(3)O_9$-polyhedra are almost the same for all the $Ca_9R(VO_4)_7$ compounds (R = La, Pr, Eu, Tb, Dy, Ho,

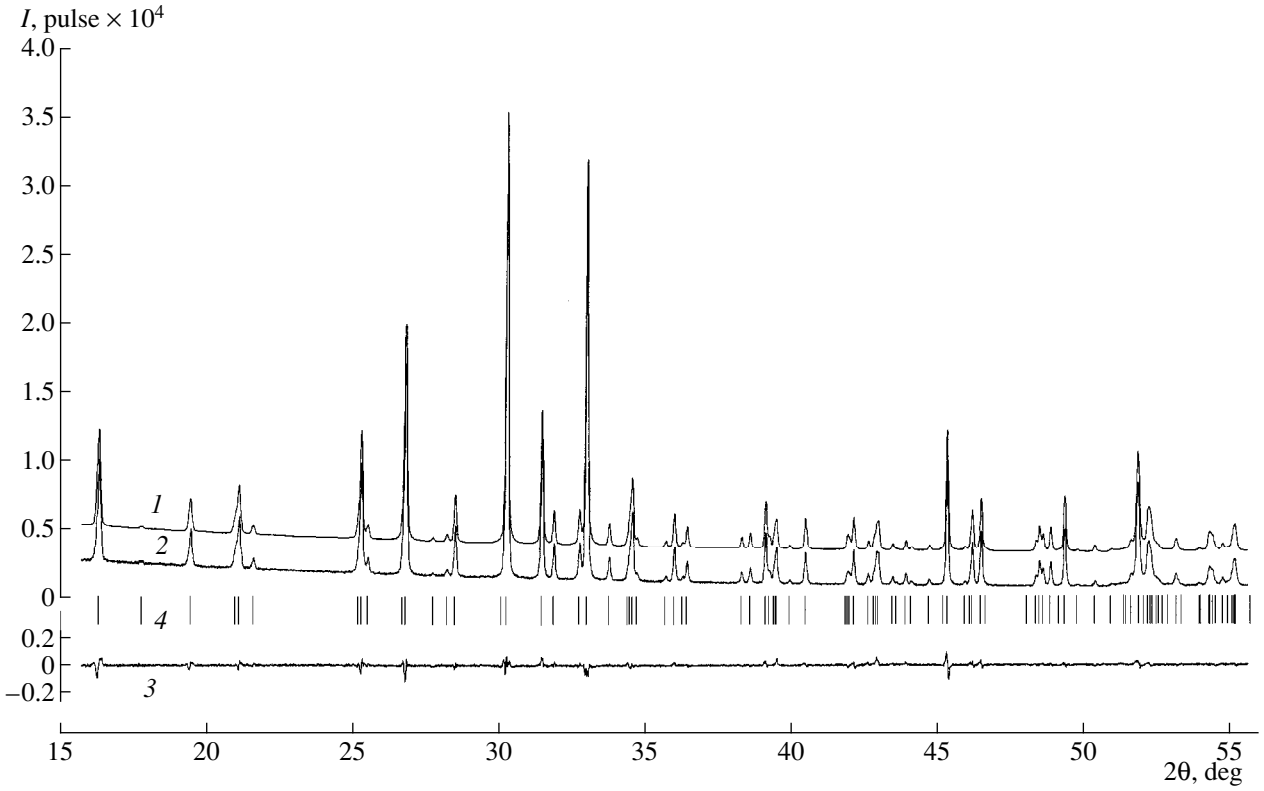

Fragments of the (*1*) calculated, (*2*) observed, (*3*) "difference" X-ray patterns, and (*4*) X-ray diffraction diagram for $Ca_9Y(VO_4)_7$.

and Y) and are independent of the character of the R^{3+}-cation distribution over the structure positions, the distortion of the $M(3)O_9$-polyhedron in comparison with the analogous distortion in the $Ca_3(VO_4)_2$ structure seems to be associated with the existence of the vacant $M(4)$ position surrounded with the oxygen atoms O(21) and O(12). In $Ca_3(VO_4)_2$, the $M(4)$ position is filled by 50% [1]. It should also be indicated that the thermal parameter of the O(21) atom in compounds **I–IV** and in $Ca_9R(VO_4)_7$ (R = La, Pr, Eu) has relatively high values [8].

The Madelung constants for whitlockite-like compounds (as has already been indicated, the phases studied here belong to this structure type) indicate that trivalent cations are most probably located in the $M(1)$ and $M(2)$ positions [13]. The analysis of the interatomic distances in the polyhedra of the whitlockite-type structure shows that rare earth cations occupy the $M(1)$, $M(2)$, and $M(3)$ positions [14]. The $M(5)$-polyhedron in the initial $Ca_3(VO_4)_2$ structure is geometrically distorted, because the sum of the ionic radii $r_{VI}(Ca^{2+}) + r(O^{2-}) = 2.4$ Å [15] exceeds the average ⟨Ca(5)–O⟩ distance (2.3 Å) [1]. Filling of this position with cations having radii less than 0.9 Å in the $M(5)$ position should eliminate this distortion. In the compounds $Ca_9R(PO_4)_7$ (R = Fe [16]; Al, Cr [17]), the trivalent R^{3+} cations fully occupy the $M(5)$ position. Unlike the compounds with R = La, Pr, Eu, where the R^{3+} cations are distributed over the $M(1)$, $M(2)$, and $M(3)$ positions [8], the R^{3+} cations in structures **I–IV** are distributed over the $M(1)$, $M(2)$, and $M(5)$ positions. The $M(5)$ position in the $Ca_9R(VO_4)_7$ compounds (R = RE, Y) is most readily filled with Tb [$r_{VI}(Tb^{3+})$] = 0.923 Å], which is consistent with the optimum size of the cation calculated on the basis of the geometrical criteria (0.9 Å) [14].

The R^{3+} cations in structures **I–IV** almost equally occupy the $M(1)$, $M(2)$, and $M(5)$ positions: ~2.7–2.6(2) of R^{3+} cations in the $M(1)$ position; ~2.7–2.3(2), in the $M(2)$ position; and ~0.6–1.0(1), in the $M(5)$ position. This differs from the situation in $Ca_9R(VO_4)_7$ (R = La, Pr, Eu), where the $M(3)$ position is filled with ~4 La^{3+} cations and only ~0.8 of a Eu^{3+} cation [8]. At the same time, it should be emphasized that in structures **I–IV**, a regular increase of the number of R^{3+} cations in the $M(5)$ position and the corresponding decrease of their number in the $M(1)$ and $M(2)$ positions are observed with a decrease of the R^{3+} radius. This fact is consistent with the above statement on the elimination of the distortion of the $M(5)$ polyhedron.

ACKNOWLEDGMENTS

This study was supported by the Russian Foundation for Basic Research, project no. 97-03-33224a.

REFERENCES

1. R. Gopal and C. Calvo, Z. Kristallogr. **137**, 67 (1973).
2. B. Dickens, L. W. Schroeder, and W. E. Brown, J. Solid State Chem. **10**, 232 (1974).
3. L. H. Brixner and P. A. Flournoy, J. Electrochem. Soc. **112**, 303 (1965).
4. V. Pelova, K. Kynev, and G. Gochev, J. Mater. Sci. Lett. **14**, 330 (1995).
5. B. I. Lazoryak, V. N. Golubev, E. A. Vovk, *et al.*, Zh. Prikl. Spektrosk. **53** (5), 754 (1990).
6. A. A. Fotiev, B. V. Shul'gin, A. S. Moskvin, and F. F. Gavrilov, *Vanadium Crystal Phosphors* (Nauka, Moscow, 1976).
7. B. I. Lazoryak, L. O. Dmitrienko, and S. V. Grechkin, Zh. Neorg. Khim. **35** (5), 1095 (1990).
8. A. A. Belik, V. A. Morozov, S. S. Khasanov, and B. I. Lazoryak, Kristallografiya **42** (5), 818 (1997).
9. H. M. Rietvield, Acta Crystallogr. **22**, 151 (1967).
10. F. Izumi, *The Rietveld Method*, Ed. by R. A. Young (Oxford Univ., Oxford, 1993), Ch. 13.
11. Y.-I. Kim and F. Izumi, J. Ceram. Soc. Jpn. **102**, 401 (1994).
12. C. Calvo and R. Gopal, Am. Mineral. **60**, 120 (1975).
13. B. N. Viting, Candidate's Dissertation in Chemistry (Moscow, Moscow State Univ., 1990).
14. B. I. Lazoryak, Usp. Khim. **65** (4), 307 (1996).
15. R. D. Shannon, Acta Crystallogr., Section B: Struct. Crystallogr. Cryst. Chem. **32**, 751 (1976).
16. B. I. Lazoryak, V. A. Morozov, A. A. Belik, *et al.*, J. Solid State Chem. **122** (1), 15 (1996).
17. V. A. Morozov, Candidate's Dissertation in Chemistry (Moscow, Moscow State Univ., 1996).

Translated by L. Man

Crystallography Reports, Vol. 45, No. 3, 2000, pp. 395–397. Translated from Kristallografiya, Vol. 45, No. 3, 2000, pp. 438–440.

STRUCTURE OF INORGANIC COMPOUNDS

Model of the Crystal Structure of Np(VI) Sulfate with Dimethyl Sulfoxide, $NpO_2SO_4 \cdot 2SO(CH_3)_2 \cdot H_2O$

R. K. Rastsvetaeva*, A. V. Barinova, N. A. Budantseva***, and A. M. Fedoseev*****

** Shubnikov Institute of Crystallography, Russian Academy of Sciences, Leninskiĭ pr. 59, Moscow, 117333 Russia*
e-mail: rast@nsa. crystal.msk.su

*** Moscow State University, Vorob'evy gory, Moscow, 119899 Russia*

**** Institute of Physical Chemistry, Russian Academy of Sciences, Leninskiĭ pr. 31, Moscow, 117915 Russia*

Received June 23, 1999

Abstract—A new complex compound, neptunium(VI) sulfate, was grown from aqueous solutions and studied by the methods of X-ray structure analysis. The model of the crystal structure was determined by direct methods within the sp. gr. $P2_1$ and was refined in the anisotropic approximation (R = 6.2%, 1044 independent reflections). The structure is built by tetragonal and hexagonal Np bipyramids. A hexagonal bipyramid can be considered as a polyhedron derived from a pentagonal bipyramid, in which one equatorial O atom is replaced by two atoms located above and below the equatorial plane. The polyhedra are linked in chains through S-tetrahedra. The chains are linked into a three-dimensional framework by hydrogen bonds with the participation of *DMSO* groups. *© 2000 MAIK "Nauka/Interperiodica".*

The polycrystals of complex compounds of the $AnO_2TO_4 \cdot 2SO(CH_3)_2 \cdot H_2O$ type (*An* = Np or Pu; *T* = S, Se, or Cr) were grown from aqueous solutions and described in [1]. According to the results of X-ray phase analysis, these compounds are isostructural to their uranyl analogues [2], whose unit cell parameters and the sp. gr. ($P2_1/m$) are known. The structural model consists of pentagonal U-bipyramids, linked by tetrahedra sharing the S(Se,Cr) vertices and forming chains parallel to the [100] direction. Therefore, it was expedient to determine experimentally the structures of such complexes also in single crystals.

We grew well-faceted small greenish crystals from aqueous solutions of the Np(VI)–$SO(CH_3)_2$–H_2O system. The structural model of the $NpO_2SO_4 \cdot 2SO(CH_3)_2 \cdot H_2O$ compound was established by direct methods within the acentric sp. gr. $P2_1$. Using the fragment consisting of two heavy Np atoms, four O atoms of the neptunyl groups, and two sulfate sulfur atoms, we managed to identified the remaining atoms of the structure, from the Fourier syntheses (no localization of H atoms were made). Because of a number of reasons, it was impossible to perform an accurate refinement of the structure. The major reason was the low quality of the data set associated with instability of the crystal due to X-ray radiolysis. However, it is believed that the resulting model is reliable. The principal parameters and characteristics of single-crystal X-ray diffraction study are given in Table 1. The atomic coordinates are listed in Table 2.

The structure consists of polyhedral chains parallel to the [100] direction (Figs. 1, 2). Unlike the chains described in [2], these chains, consist of Np bipyramids of two types (tetragonal and "hexagonal"). In both polyhedra, the distances to two O atoms are shortened (1.75 and 1.82 Å in the first polyhedron and 1.71 and 1.82 Å in the second polyhedron), whereas the remaining distances range within 2.12–2.59 and 2.11–2.48 Å, respectively. The eight-vertex polyhedron has the shape uncharacteristic of dioxo cations of actinides and can be considered as a polyhedron derived from the pentagonal bipyramid in which one equatorial O atom is replaced by two atoms located above and under the equatorial plane. Earlier, this polyhedron was found in the Np(V) compound $(NpO_2)_2SO_4 \cdot H_2O$ [3]. In the hexavalent actinide compounds, this polyhedron is observed for the first time. A combination of six- and

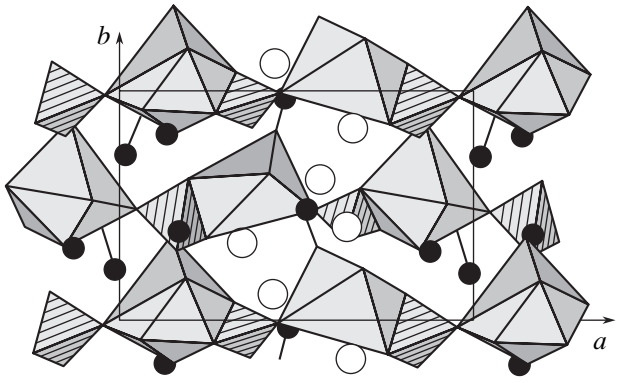

Fig. 1. Projection of the structure onto the (001) plane. The linear hatching indicates S tetrahedra and dotted hatching indicates NpO_2 polyhedra. Sulfur atoms of *DMSO* groups and water molecules are represented by solid and empty circles, respectively.

1063-7745/00/4503-0395$20.00 © 2000 MAIK "Nauka/Interperiodica"

Table 1. Structural data and details of X-ray data collection

Characteristic	Value
Formula	$NpO_2SO_4 \cdot 2SO(CH_3)_2 \cdot H_2O$
Unit-cell parameters, Å, deg	$a = 12.13(1)$
	$b = 7.96(1)$
	$c = 12.99(3)$
	$\beta = 95.5(2)$
Unit-cell volume, Å^3	1249.2
Sp. gr., Z	$P12_11$; 2
Radiation, λ, Å	MoK_α, 0.71073
Linear absorption coefficient, mm^{-1}	6.1
Density, g/cm^3	2.87
Crystal dimensions, mm	$0.15 \times 0.1 \times 0.07$
Diffractometer	SYNTEX $P\bar{1}$
Scanning mode	θ/2θ
$\sin\theta/\lambda$, Å^{-1}	<1.08
Range of data collection	$0 < h < 16$, $0 < k < 11$, $-18 < l < 17$
Total number of reflections	1065 $I > 2\sigma(I)$
Number of independent reflections	1044 $\|F\| > 4\sigma(F)$
R-factor of the refinement	0.062
Program used in computations	AREN [5]
Absorption correction	DIFABS [6]

Table 2. Atomic coordinates and equivalent thermal parameters

Atom	x/a	y/b	z/c	B_{iso}, Å^2	Atom	x/a	y/b	z/c	B_{iso}, Å^2
Np(1)	0.8638(2)	0.5861(1)	0.2123(1)	3.52(7)*	O(3)	0.430(9)	0.650(9)	0.350(9)	5.0(9)
Np(2)	0.3723(1)	0.6104(5)	0.2234(1)	2.52(5)*	O(4)	0.307(1)	0.732(1)	0.115(9)	1.8(9)
S(1)	0.638(9)	0.430(2)	0.259(2)	2.7(7)*	O(5)	0.676(4)	0.579(9)	0.274(3)	5(2)
S(2)	0.148(9)	0.465(9)	0.262(8)	1.1(3)*	O(6)	0.631(2)	0.356(5)	0.353(2)	2.2(9)
S(3)	0.986(2)	0.221(4)	0.156(2)	5.2(5)	O(7)	0.552(4)	0.484(6)	0.178(3)	6(2)
S(4)	0.886(9)	0.307(2)	0.421(9)	3.9(4)	O(8)	0.734(2)	0.400(3)	0.191(2)	0.6(6)
S(5)	0.480(9)	0.990(9)	0.165(9)	2.2(9)	O(9)	0.045(2)	0.473(5)	0.207(4)	5(1)
S(6)	0.833(2)	0.885(3)	0.410(9)	3.3(4)	O(10)	0.195(2)	0.620(4)	0.301(2)	0.3(7)
C(1)	0.907(3)	0.120(6)	0.064(3)	1(1)	O(11)	0.241(5)	0.352(4)	0.211(3)	3.5(8)
C(2)	0.102(9)	0.025(9)	0.155(6)	5.7(9)	O(12)	0.134(9)	0.289(9)	0.340(7)	5(1)
C(3)	0.919(3)	0.088(7)	0.436(3)	3.1(8)	O(13)	0.940(3)	0.409(4)	0.120(3)	1.9(8)
C(4)	0.099(9)	0.916(9)	0.444(9)	4.1(8)	O(14)	0.856(3)	0.870(4)	0.269(3)	3(1)
C(5)	0.736(6)	0.237(7)	0.454(6)	2(1)	O(15)	0.844(3)	0.318(6)	0.303(2)	0.2(8)
C(6)	0.489(4)	0.214(6)	0.183(2)	1(1)	O(16)	0.438(1)	0.810(1)	0.140(9)	0.7(9)
C(7)	0.616(3)	0.000(6)	0.120(4)	2.1(8)	$H_2O(1)$	0.344(3)	0.337(8)	0.369(8)	4(1)
C(8)	0.721(4)	0.990(9)	0.421(4)	1.9(9)	$H_2O(2)$**	0.440(9)	0.111(9)	0.437(6)	5(1)
O(1)	0.922(4)	0.506(5)	0.327(2)	0.5(9)	$H_2O(3)$**	0.359(4)	0.912(7)	0.409(4)	0.1(8)
O(2)	0.812(2)	0.686(3)	0.091(2)	0.6(8)					

* B_{eq}.
** The position occupancy equals 0.5.

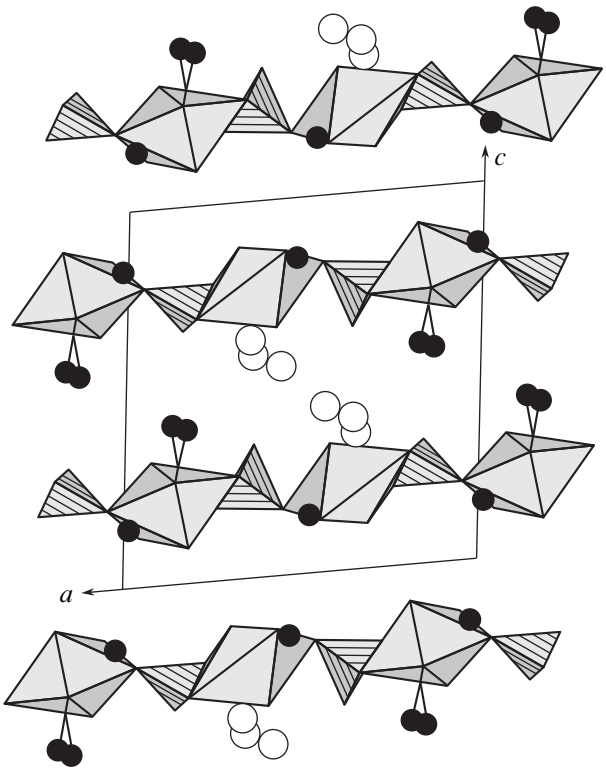

Fig. 2. Projection of the structure onto the (010) plane. For notation, see Fig. 1.

eight-vertex polyhedra in the structure under consideration is also unique for actinides with tetrahedral anions.

Unlike the hypothetical structure described in [2], two independent sulfur tetrahedra (the average S–O distances are 1.42 and 1.54 Å) are tridentate and shared the edge and the vertex, with the Np-polyhedra. The shared edges of small sulfur tetrahedra and rather bulky Np(V) polyhedra were also observed in a number of structures, in particular, in $Cs_3[NpO_2(SO_4)_2 \cdot 2H_2O$ [4]. Free vertices of both Np(VI) polyhedra (one vertex in the tetragonal bipyramid and three vertices in the "hexagonal" bipyramid) are occupied by the O atoms of the *DMSO* groups participating in hydrogen bonding between adjacent chains. The chains are additionally linked by the H atoms of the crystallization water molecules. One of these molecules statistically occupies two equally probable positions between the chains.

ACKNOWLEDGMENTS

We thank D.Yu. Pushcharovskiĭ for his assistance in the X-ray data collection and helpful discussion.

This study was supported by the Russian Foundation for Basic Research, project no. 99-05-65035.

REFERENCES

1. A. Fedoseev, N. Budantseva, A. Bessonov, *et al.*, J. Alloys Compd. **271/273**, 154 (1998).
2. V. N. Serezhkin and L. B. Serezhkina, Zh. Neorg. Khim. **30**, 2039 (1985).
3. M. S. Grigor'ev, N. A. Baturin, N. A. Budantseva, *et al.*, Radiokhimiya, No. 2, 29 (1993).
4. M. S. Grigor'ev, A. I. Yanovskiĭ, A. M. Fedoseev, *et al.*, Radiokhimiya, No. 2, 17 (1991).
5. V. I. Andrianov, Kristallografiya **32**, 228 (1987) [Sov. Phys. Crystallogr. **32**, 130 (1987)].
6. N. Walker and D. Stuart, Acta Cryst., Sect. A: Cryst. Phys., Deltr., Theor. Gen. Crystallogr. **39**, 158 (1983).

Translated by T. Safonova

Crystallography Reports, Vol. 45, No. 3, 2000, pp. 398–404. Translated from Kristallografiya, Vol. 45, No. 3, 2000, pp. 441–447.

STRUCTURE OF INORGANIC COMPOUNDS

Alkali-Metal Hydrogen Selenate–Phosphates $M_2H_3(SeO_4)(PO_4)$ (M = Rb or K) and $M_4H_5(SeO_4)_3(PO_4)$ (M = K or Na)

S. I. Troyanov*, I. V. Morozov*, V. B. Rybakov*, and É. Kemnitz**

** Chemistry Department, Moscow State University, Vorob'evy gory, Moscow, 119899 Russia*
e-mail: troyanov@thermo.chem.msu.ru

*** Institut für Chemie, Humboldt Universität, Berlin, Germany*

Received December 30, 1998

Abstract—Crystalline hydrogen selenate–phosphates $M_2H_3(SeO_4)(PO_4)$ [M = Rb (**I**) or K (**II**)] and $M_4H_5(SeO_4)_3(PO_4)$ [M = K (**III**) or Na (**IV**)] were obtained by reactions of Rb, K, and Na carbonates with mixtures of selenic and phosphoric acid solutions. The X-ray structure study of single crystals revealed that **I** and **II** are isostructural (sp. gr. *Pn*). In these structures, SeO_4 and H_3PO_4 tetrahedra are linked by hydrogen bonds to form corrugated layers. Structures **III** and **IV** (sp. gr. *P*1) have similar arrangements of non-hydrogen atoms but different hydrogen-bond systems. In **III** = $K_4(HSeO_4)_2\{H[H(Se,P)O_4]_2\}$, the $HSeO_4$ groups branch from the infinite anionic $\{H[H(Se,P)O_4]_2\}$ chains. In **IV** = $Na_4[(SeO_4)_2]\{H[H_{1.5}(Se,P)O_4]_2\}$, the anionic $\{H[H_{1.5}(Se,P)O_4]_2\}$ chains are crosslinked by hydrogen bonds formed by the $[H(SeO_4)_2]$ dimers. *© 2000 MAIK "Nauka/Interperiodica".*

INTRODUCTION

Alkali-metal hydrogen sulfates and selenates attract the considerable interest of researchers, because some of these compounds undergo phase transitions into the states with high protonic conductivity [1]. No particular attention has been given to combined-anion potassium [2] and ammonium [3] hydrogen sulfate–phosphates, although they have already been known for more than 15 years. However, the superionic phase transitions [4–6] were observed in cesium hydrogen sulfate–phosphates of the compositions $Cs_3(HSO_4)_2(H_2PO_4)$ [4] and $Cs_5(HSO_4)_3(H_2PO_4)_2$ [5]. Continuing the study of the synthesis and structures of these compounds, we prepared rubidium derivatives with S/P ratio equal to 1 : 1 and 3 : 1 [7].

In view of the close analogy in the chemical behavior of sulfates and selenates, we also studied alkali-metal hydrogen selenate–phosphates. Three compounds with the selenate-to-phosphate ratios 3 : 2; 2 : 1; and 3 : 1 were isolated for cesium derivatives [8]. Later, hydrogen selenate–phosphates of other alkali metals (sodium, potassium, and rubidium) and ammonium were also found. Below, we report the results of our studies of hydrogen selenate–phosphates with the Se/P ratio equal to 1 : 1 and 3 : 1. The compositions and structures of the compounds $M_2(SeO_4)(H_3PO_4)$, where M = Rb (**I**) or K(**II**), $K_4(HSeO_4)_2\{H[H(Se,P)O_4]_2\}$ (**III**), and $Na_4[H(SeO_4)_2]\{H[H_{1.5}(Se,P)O_4]_2\}$ (**IV**) were determined by single-crystal X-ray diffraction analysis.

EXPERIMENTAL

Synthesis. Alkali-metal carbonates M_2CO_3 (*Fluka*), 85% orthophosphoric acid, and 72% selenic acid served as starting materials for preparing hydrogen selenate–phosphates. The simplest method of synthesizing these compounds consisted in dissolving the appropriate carbonate in the stoichiometric mixture of acids. The subsequent slow concentration of the solution resulted in the formation of the crystalline phases. The drawbacks of this approach are the difficulties associated with carbonate dosing. As is well known, they are highly hygroscopic and their first portions are violently dissolve with possible splashing at the initial stages of the process.

An alternative procedure consists in a preliminary preparation of neutral selenates M_2SeO_4 by neutralization of selenic acid with a carbonate and crystallization of the salt by evaporating solution. Then, M_2SeO_4 is dissolved in a mixture of selenic and phosphoric acids. Hydrogen selenate–phosphates were crystallized during slow evaporation of water in air at room temperature (**I**; 3 weeks), in an exsiccator under P_4O_{10} (**II**; 7 days), or on heating (**III**; 24 h at 65°C). Thus, single-phase crystalline specimens of compounds **I** and **II** were obtained. Compound **III** was obtained in the form of 3–4-mm-long crystals. All the three compounds were stable in air.

All the attempts to isolate the rubidium compound with the Se/P ratio equal to 3 : 1 by varying the reagent ratios, acidity, temperature, and the rate of crystallization have failed. The corresponding solutions of the stoichiometric composition always provided the mixture of **I** and $RbHSeO_4$.

1063-7745/00/4503-0398$20.00 © 2000 MAIK "Nauka/Interperiodica"

Table 1. Crystallographic characteristics and details of X-ray data collection and structure refinement for **I–IV**

Parameter	**I**	**II**	**III**	**IV**
Formula	$Rb_2(SeO_4)(H_3PO_4)$	$K_2(SeO_4)(H_3PO_4)$	$K_4(HSeO_4)_3(H_2PO_4)$	$Na_4(HSeO_4)_3(H_2PO_4)$
Crystal system	Monoclinic	Monoclinic	Triclinic	Triclinic
Sp. gr.	*Pn*	*Pn*	$P\bar{1}$	$P\bar{1}$
a, Å	7.546(3)	7.260(2)	7.412(3)	7.029(4)
b, Å	7.697(3)	7.520(2)	7.662(3)	7.089(4)
c, Å	7.744(3)	7.558(2)	7.735(3)	7.130(4)
α, deg	90	90	71.92(3)	79.84(4)
β, deg	101.19(3)	100.11(3)	87.98(3)	85.57(4)
γ, deg	90	90	86.03(3)	80.34(4)
V, Å^3	441.2(3)	406.2(2)	416.5(3)	344.3(3)
Z	2	2	1	1
ρ_{calc}, g cm^{-3}	3.110	2.609	2.732	2.994
$\mu(MoK_\alpha)$, cm^{-1}	154.03	58.50	77.94	83.43
Crystal dimensions, mm	$0.6 \times 0.5 \times 0.2$	$0.4 \times 0.4 \times 0.2$	$0.4 \times 0.3 \times 0.1$	$0.4 \times 0.4 \times 0.2$
θ_{max}, deg	30	35	30	27
Number of independent reflections	2574	1795	2423	1496
Number of reflections with $I > 2\sigma(I)$	1650	1527	1682	1013
Number of reflections/number of parameters	1743/121	1586/121	1908/124	1231/122
R_1/wR_2	0.0421/0.1093	0.0238/0.0633	0.0316/0.0641	0.0444/0.0935

It was found that sodium hydrogen selenate–phosphate, **IV**, can be prepared by crystallization from solutions with a considerable H_3PO_4 excess. Otherwise, Na_2SeO_4 was formed. At room temperature a solution of Na_2SeO_4 in 100% H_3PO_4 yielded only crystalline $NaHSeO_4$, whereas the hot solution provided the formation of $Na_2Se_2O_7$ pyroselenate [9], partly decomposing into Na_2SeO_4 and SeO_2 at 100°C (a sublimate above the solution). Platelike sodium hydrogen selenate–phosphate crystals are formed only in the course of slow crystallization from a viscous solution. The crystals grown were placed into sealed capillaries (to avoid water absorption) for further studies.

X-ray diffraction study. The X-ray data for the structure analysis were collected on a STADI-4 four-circle diffractometer (Stoe) at room temperature (MoK_α radiation, graphite monochromator, and ω-2θ scan). The crystal data collected for compounds **I–IV** are listed in Table 1. Since the compounds contain Se and Rb, they are characterized by high linear absorption coefficients. Therefore, the data were collected on regularly shaped crystals installed symmetrically with respect to the φ-axis of the diffractometer. The empirical collection for absorption was introduced on the basis of φ scans of 5–8 reflections. The numerical allowance for absorption yielded the similar values.

The structures were solved by the direct method (SHELXS86 [10]). The positional and the anisotropic thermal parameters of all non-hydrogen atoms were refined by the SHELXL93 Program [11]. The Se and P atoms in the structures could unambiguously be distinguished due to the large difference in the scattering power of these atoms. The ambiguity in the distribution of the S and P atoms is typical of the structures of sulfate–phosphates [7]. In structure **II**, there are some positions statistically occupied by Se and P atoms in the 9 : 1 and the 1 : 9 ratios. In structures **III** and **IV**, one of the tetrahedral positions is fully occupied by selenium, whereas the other position is shared by selenium and phosphorus atoms in the equal proportions. All hydrogen atoms were located from the difference Fourier maps and were refined in the isotropical approximation; soft geometrical restraints were used for some of these atoms. The atomic coordinates and the equivalent thermal parameters for structures **I–IV** are deposited in the Karlsruhe Fachinformationszentrum under the CDS registration nos. 411 002–411 005. The selected interatomic distances are listed in Table 2.

RESULTS AND DISCUSSION

Numerous attempts to synthesize alkali-metal hydrogen selenate–phosphates varying the ratios of the reagents and the crystallization conditions allow us to conclude that the systems containing different kinds of alkaline metals essentially are different. Also, they allow one to compare the selenate–phosphate and sul-

Table 2. Interatomic distances (Å) in $Rb_2(SeO_4)(H_3PO_4)$ (**I**), $K_2(SeO_4)(H_3PO_4)$ (**II**), $K_4(HSeO_4)_3(H_2PO_4)$ (**III**), and $Na_4(HSeO_4)_3(H_2PO_4)$ (**IV**) structures

Distance	**I**	**II***	Distance	**III**	**IV**
Se–O(1)	1.606(7)	1.608(3)	Se(1)–O(1)	1.608(3)	1.619(5)
Se–O(2)	1.648(6)	1.640(3)	Se(1)–O(2)	1.603(3)	1.667(5)
Se–O(3)	1.637(8)	1.633(3)	Se(1)–O(3)	1.607(3)	1.618(5)
Se–O(4)	1.649(8)	1.636(3)	Se(1)–O(4)	1.715(3)	1.625(5)
P–O(5)	1.490(8)	1.497(3)	(Se,P)–O(5)	1.572(3)	1.624(6)
P–O(6)	1.557(8)	1.562(3)	(Se,P)–O(6)	1.587(3)	1.572(5)
P–O(7)	1.575(9)	1.570(3)	(Se,P)–O(7)	1.590(3)	1.560(5)
P–O(8)	1.545(8)	1.562(3)	(Se,P)–O(8)	1.585(3)	1.564(6)
M(1)–O	2.882–3.397	2.719–3.010	*M*(1)–O	2.733–2.975	2.376–2.814
M(2)–O	2.876–3.351	2.728–2.979	*M*(2)–O	2.659–2.918	2.393–2.571

* Distances for the atoms located mainly in the Se and P positions.

fate–phosphate systems of the same alkaline metal. The largest number of selenate–phosphate phases (three compounds with the Se/P ratio equal to 3 : 2, 2 : 1, and 3 : 1) was found in the system with cesium [8]. In this case, the analogy with the sulfate–phosphates [4–6] consists in that the compounds with *X*/P = 2 : 1 are isostructural and the compounds with *X*/P = 3 : 2 can exist in both systems, but show different hydrogen bonding. In the rubidium selenate–phosphate system, a single compound with Se/P = 1 : 1 was isolated, whereas in the rubidium sulfate–phosphate [7] and the potassium sulfate– and selenate–phosphate [2, 12] systems, the phases with *X*/P = 1 : 1 and 3 : 1 were revealed.

In this study, we managed to isolate a single compound with the Se/P ratio equal to 3 : 1 from the sodium selenate–phosphate system, whereas in the sulfate–phosphate system, no compounds with the empirical formula corresponding to a sodium hydrogen sulfate–phosphate were revealed. Instead, the adduct of sodium hydrogen sulfate to phosphoric acid $NaHSO_4 \cdot H_3PO_4$ was isolated [12].

The positions of the non-hydrogen atoms in structures **I**–**IV** were determined by single-crystal X-ray diffraction analysis with a high accuracy. The considerable difference between the scattering powers of the Se and P atoms provides the establishment of the population of the positions: the Se or P atoms in the tetrahedral positions (**I**), the occupation of such positions mainly by the atoms of one kind (**II**), and their equally probable filling with both Se and P atoms (**III** and **IV**). The modes of position occupation observed correlate with the average *X*–O distances (Table 2) characteristic of the SeO_4 and PO_4-tetrahedra and intermediate values in the $(Se,P)O_4$-tetrahedra.

If the position is occupied mainly with one of the two kinds of atoms (~90%), the average *X*–O distances become only slightly shorter (Se in structure **II**) or longer (P in structure **II**).

In some cases, the difference between the distances within a tetrahedron allowed us to establish the *X*–O and *X*–OH bonds, whereas the consideration of the O··O distances provided the reconstruction of the hydrogen-bond system in all the structures. The positions of H atoms confirmed the validity of our description of the hydrogen-bond systems.

The distribution of the *X*–O bond lengths in structures **I** and **II** (the absence of elongated distances in the SeO_4-tetrahedron and three elongated distances in the PO_4-tetrahedron) indicate that all of the three hydrogen atoms are attached to the PO_4 tetrahedron (Table 2). This assumption was confirmed by H atoms spaced by 0.8–0.9 Å from three oxygen atoms of the PO_4 groups. This result allows one to consider compounds **I** and **II** as adducts of rubidium and potassium selenates to the phosphoric acid $M_2(SeO_4)(H_3PO_4)$ and not as hydrogen selenate–phosphates $M_2(HSeO_4)(H_2PO_4)$. "Migration" of a proton from hydrogen selenate to dihydrogen phosphate group was also observed earlier in $Cs_4(SeO_4)(HSeO_4)_2(H_3PO_4)$ and in ammonium hydrogen selenate–phosphate $(NH_4)_2SeO_4(H_3PO_4)$ [13], whereas no such migration was ever observed in other cesium hydrogen selenate–phosphates [8]. Despite the above examples, we refer (somewhat loosely) to all the compounds obtained in the hydrogen selenate (sulfate)–phosphate systems as to *hydrogen selenate (sulfate)–phosphates*. At the same time, we also indicate the actual hydrogen position in all the cases where it could be determined from the experiment.

The systems of hydrogen bonding in structures **I** and **II** are similar. These bonds link anions into slightly corrugated networks parallel to $(\bar{1}01)$. Each tetrahedral group forms three bonds: H_3PO_4 provides three H atoms, and the SeO_4 group serves as their acceptor (Fig. 1). The O–H··O distances of lengths 2.50–2.57 Å correspond to strong hydrogen bonds.

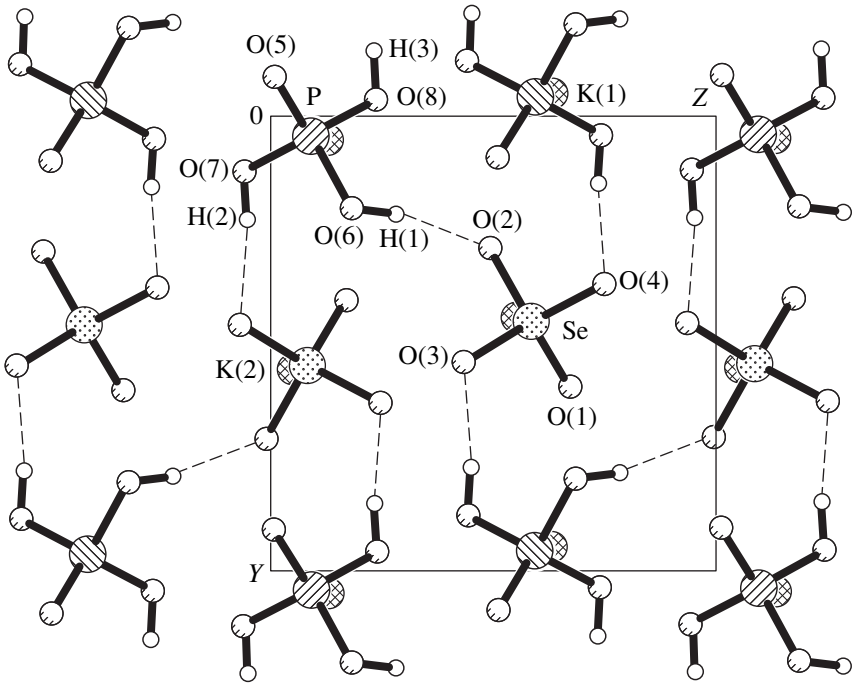

Fig. 1. $K_2(SeO_4)(H_3PO_4)$ (**II**) structure projected along the *x*-axis.

Coordination of the M^+ ions with oxygen atoms is characterized by large coordination numbers (9 for Rb and 7–8 for K) and, in accord with the ionic radii, longer Rb–O distances (Table 2).

Considering similar ratios of the linear parameters for the triclinic unit cells in **III** and **IV** we could draw a conclusion about their isostructurality. Although the arrangements of the M^+-cations and the tetrahedral

Table 3. Hydrogen bonds in structures **I**–**IV**

D–H···*A* bond	*D*–H, Å	H···*A*, Å	*D*···*A*, Å	∠*D*–H···*A*, deg
$Rb_2(SeO_4)(H_3PO_4)$, **I**				
O(6)–H(1)···O(2)	0.80(3)	1.79(5)	2.566(7)	162(11)
O(7)–H(2)···O(3)	0.84(3)	1.75(3)	2.566(11)	166(11)
O(8)–H(3)···O(4)	0.79(3)	1.72(4)	2.501(10)	170(12)
$K_2(SeO_4)(H_3PO_4)$, **II**				
O(6)–H(1)···O(2)	0.82(3)	1.75(3)	2.552(3)	166(6)
O(7)–H(2)···O(3)	0.81(3)	1.77(3)	2.567(4)	167(7)
O(8)–H(3)···O(4)	0.82(3)	1.69(3)	2.511(4)	173(7)
$K_4(HSeO_4)_3(H_2PO_4)$, **III**				
O(4)–H(1)···O(5)	0.84(7)	1.72(7)	2.556(4)	171(7)
O(6)–H(2)···O(7)	0.83(3)	1.74(3)	2.528(4)	158(8)
O(7)–H(3)···O(6)	0.85(10)	1.71(10)	2.528(4)	160(10)
O(8)–H(4)···O(8')	0.81(3)	1.76(3)	2.561(4)	171(12)
$Na_4(HSeO_4)_3(H_2PO_4)$, **IV**				
O(2)–H(1)···O(2)	0..80(3)	1.81(5)	2.601(11)	170(20)
O(5)–H(2)···O(4)	0.79(3)	1.85(5)	2.619(8)	164(10)
O(6)–H(3)···O(7)	0.88(3)	1.87(3)	2.747(8)	173(16)
O(8)–H(4)···O(8')	0.82(3)	1.69(6)	2.481(11)	163(2)

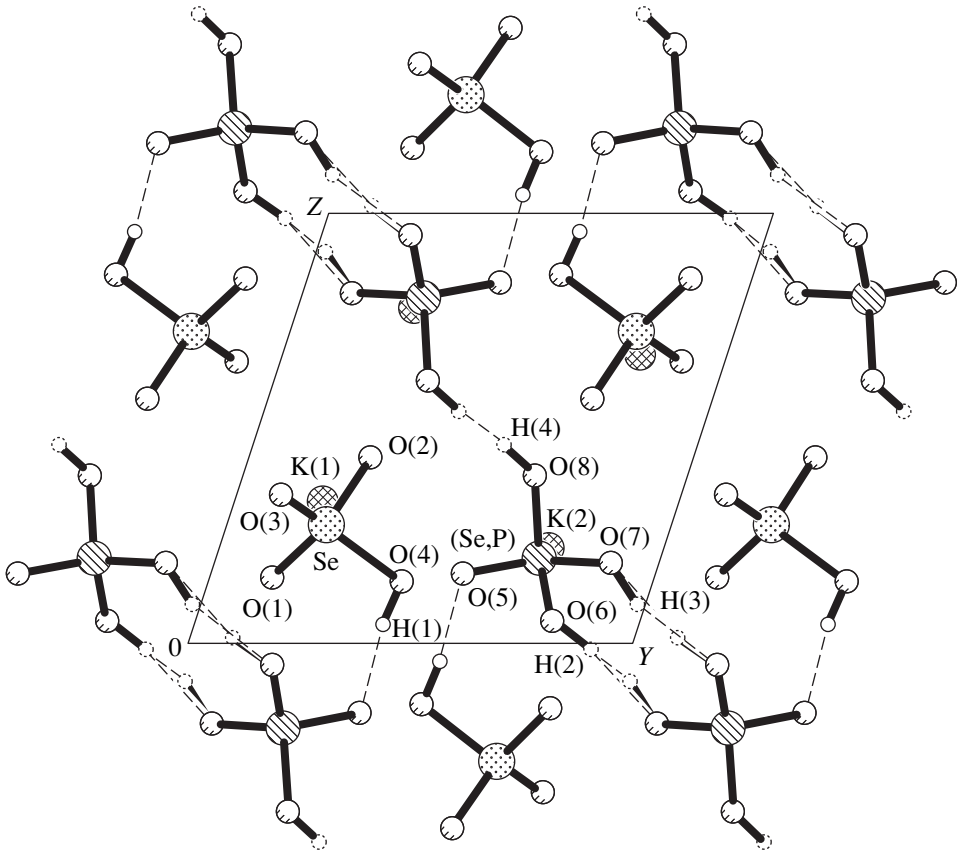

Fig. 2. $K_4(HSeO_4)_2\{H[H(Se,P)O_4]_2\}$ (**III**) structure projected along the *x*-axis.

XO_4-groups are similar, the essential differences in the systems of hydrogen bonding make **III** and **IV** isostructural only to some extent. Both structures contain two independent M^+ cations [K(1) with c.n. = 8 and K(2) with c.n. = 6 in **III**; Na(1) with c.n. = 7 and Na(2) with c.n. = 6 in **IV**; Table 2], one SO_4-group, and one $(Se,P)O_4$-group with the statistical filling of the tetrahedral site. In structure **III**, one of the bonds in the SeO_4-tetrahedron is elongated to a value characteristic of a Se–OH bond [Se–O(4) is 1.715 Å]. At the same time, no obvious differences in the distances within the $(Se,P)O_4$-tetrahedron were observed. The analysis of the O··O distances revealed hydrogen bonds confirmed by the location of hydrogen atoms (Table 3). The only asymmetric (characterized by a single maximum) hydrogen bond in the structure is O(4)–H(1)··O(5). Two other bonds, O(6)··O(7) and O(8)··O(8'), have two maxima each. These maxima correspond to the positions of H atoms populated only by 0.5. The H(2) and H(3) atoms involved in the O(6)··O(7) interaction are symmetrically independent, whereas the H(4) and H(4') atoms involved in the O(8)··O(8') hydrogen bonding are related by a center of inversion. The system of hydrogen bonding is shown in Fig. 2. The dimeric structural units $[H(Se,P)O_4]_2$ are linked by symmetrical hydrogen bonds O(8)H(4)O(8') into infinite chains $\{H[H(Se,P)O_4]_2\}$ running along the $[\bar{1}01]$ direction. The $HSeO_4$-groups are bound to the chains by the O(4)–H(1)··O(5) hydrogen bonds and form terminal branches. Therefore, the formula of compound **III** reflecting the existence of the H atoms attached to tetrahedra should be written as $K_4(HSeO_4)_2\{H[H(Se,P)O_4]_2\}$.

The non-hydrogen atoms in structure **IV** (Fig. 3) are designated as in **III**. This facilitates the comparison of pseudoisostructural compounds. The structures of such compounds differ mainly in the participation of the H atoms in the system of hydrogen bonding. The Se–O(4) bond length of 1.625 Å shows that the O(4) atom of the SeO_4-tetrahedron in **IV** is no more a hydrogen donor. The Se–O(2) bond is slightly elongated (1.667 Å) due to formation of the O(2)–H(1)··O(2) hydrogen bond (2.60 Å), in which the H(1) atom is disordered over two positions related by a center of inversion. The O(4) atom is an acceptor in the 2.62 Å-long O(5)–H(2)··O(4) hydrogen bond. The elongation of the O(6)–H(3)··O(7) hydrogen bond to 2.75 Å allows us to assume that the position of the H(3) atom is half occupied, which is consistent with the composition of the compound. Pairs of such bonds form weakly bound $[H_{1.5}(Se,P)O_4]_2$ dimers which, in turn, are linked by the short symmetrical O(8)H(4)O(8') hydrogen bond

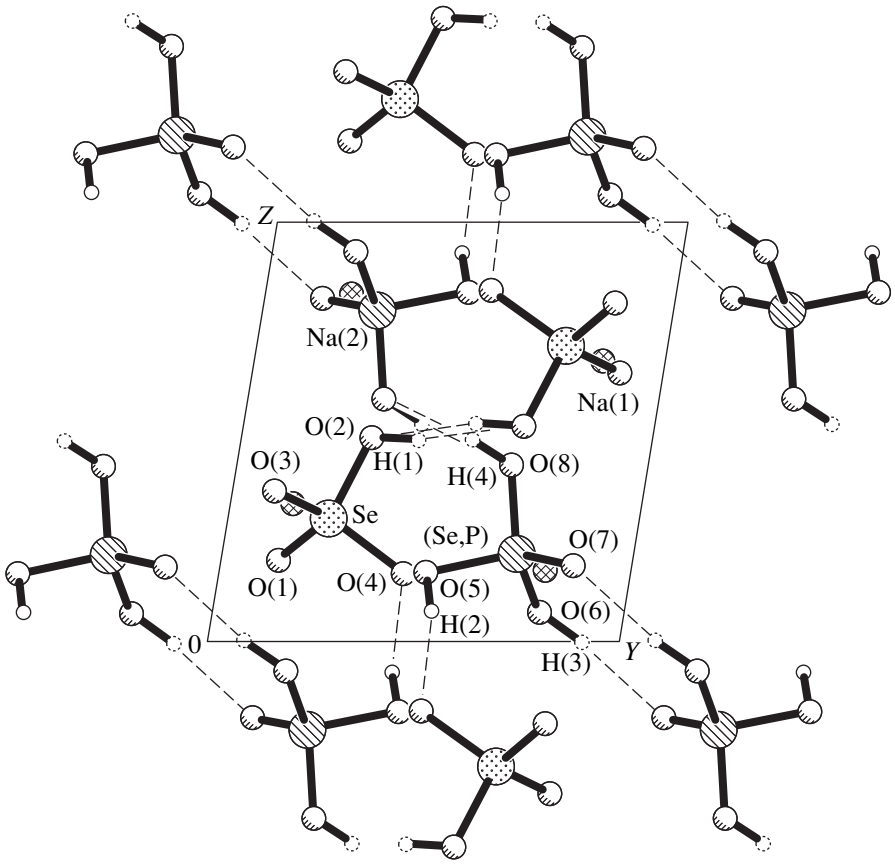

Fig. 3. $Na_4[H(SeO_4)_2]\{H[H_{1.5}(Se,P)O_4]_2\}$ (**IV**) structure projected along the *x*-axis.

2.48 Å to form infinite chains (Fig. 3). As a result, the chains observed in structure **III** are characteristic, to a certain extent, of structure **IV**. In **IV**, the chains are crosslinked by hydrogen bonds involving the dimeric $[H(SeO_4)_2]$ groups. Hence, the formula of compound **IV** should be written as $Na_4[H(SeO_4)_2]\{H[H_{1.5}(Se,P)O_4]_2\}$.

Comparing the projections of structures **III** (Fig. 2) and **IV** (Fig. 3) we see that, in the latter structure, the SeO_4-tetrahedra are shifted toward the unit-cell center and linked by a hydrogen bond. In **III**, no similar bond between the considerably spaced SeO_4-tetrahedra exist. A higher density of the sodium compound than of the potassium compound of the same stoichiometry is apparently associated with the above difference.

Thus, the data of the X-ray structure analysis of the alkali-metal hydrogen selenate–phosphates reported in this paper for Na, K, and Rb derivatives together with the data on cesium derivatives [8] allow us to conclude that the distribution of hydrogen atoms between SeO_4 and PO_4 groups in the structure corresponds either to the coexistence of $HSeO_4^-$ and $H_2PO_4^-$ monoanions, or coexistence of the SeO_4^{2-} dianion and the neutral H_3PO_4 molecule. This versatility corresponds to the $K_2(H_2SeO_4)/K_1(H_3PO_4)$ ratio of the constants of hydrogen dissociation slightly exceeding unity. It should also be noted that in the known structures of Rb and Cs hydrogen sulfate–phosphates only the combination of HSO_4^- and $H_2PO_4^-$ ions was revealed [2–7]. Apparently, this difference is explained by stronger acidic functions of selenic acid in comparison with sulfuric acid.

ACKNOWLEDGMENTS

This study was supported by the Russian Foundation for Basic Research and Deutsche Forschungsgemeinschaft within the joint initiative project no. 96-03-0084.

REFERENCES

1. A. I. Baranov, L. A. Shuvalov, and N. M. Shchagina, Pis'ma Zh. Éksp. Teor. Fiz. **36**, 381 (1982) [JETP Lett. **36**, 459 (1982)].
2. M. T. Averbuch-Pouchot and A. Durif, Mat. Res. Bull. **15**, 427 (1980).
3. M. T. Averbuch-Pouchot, Mat. Res. Bull. **16**, 407 (1981).
4. S. M. Haile, K. D. Kreuer, and J. Maier, Acta Crystallogr., Sect. B: Struct. Sci. **51**, 680 (1995).

5. G. Staneff, S. Calkins, and S. M. Haile, in *Proceedings of 17th IUCr Congress, Seattle, 1997,* P.S11.05.46.
6. S. M. Haile, S. Calkins, and D. Boysen, Solid State Ionics **97**, 145 (1997).
7. A. Stiewe, R. Sonntag, S. Troyanov, *et al.*, J. Solid State Chem. **149**, 9 (2000).
8. S. I. Troyanov, I. V. Morozov, V. B. Rybakov, *et al.*, J. Solid State Chem. **141**, 317 (1998).
9. I. V. Morozov, S. I. Troyanov, A. Stiewe, and E. Kemnitz, Zh. Neorg. Khim. **44** (10), 16 (1999).
10. G. M. Sheldrick, *SHELXS 86: Program for the Solution of Crystal Structures* (Univ. of Göttingen, Germany, 1986).
11. G. M. Sheldrick, *SHELXL 93: Program for the Refinement of Crystal Structures* (Univ. of Göttingen, Germany, 1993).
12. S. Stiewe, S. Troyanov, and E. Kemnitz, Anorg. Allg. Chem. (in press).
13. S. I. Troyanov, I. V. Morozov, M. Reehuis, and E. Kemnitz, Zh. Neorg. Khim. **44** (12), 1810 (1999).

Translated by I. Polyakova

Crystallography Reports, Vol. 45, No. 3, 2000, pp. 405–409. Translated from Kristallografiya, Vol. 45, No. 3, 2000, pp. 448–451.

STRUCTURE OF INORGANIC COMPOUNDS

New Boron–Oxygen Layer in the Structure of Barium Hydrodecaborate $Ba_5[B_{20}O_{33}(OH)_4] \cdot H_2O$

A. V. Arakcheeva*, S. A. Vinogradova, D. Yu. Pushcharovskiĭ**, M. Hostettler***, G. Chapuis***, and O. V. Dimitrova****

** Baikov Institute of Metallurgy and Materials Technology, Russian Academy of Sciences, Leninskiĭ pr. 49, Moscow, 117334 Russia*
e-mail: arakchee@uttra.imet.ac.ru
*** Moscow State University, Vorob'evy gory, Moscow, 119899 Russia*
**** University of Lausanne, Switzerland*
Received March 1, 1999

Abstract—The crystal structure of the new synthetic compound $Ba_5[B_{20}O_{33}(OH)_4] \cdot H_2O$ was established by the methods of X-ray diffraction (a Stoe IPDS diffractometer, λMoK_α, 1860 independent reflections, anisotropic refinement, $R = 1.95\%$, localization of hydrogen atoms): $a = 9.495(2)$ Å, $b = 6.713(1)$ Å, $c = 11.709(2)$ Å, $\beta = 95.09(1)°$, sp. gr. $P2$, $Z = 1$. The structure is based on double pseudohexagonal layers consisting of BO_4-tetrahedra and BO_3 triangles linked into three-membered rings in two mutually perpendicular directions. The double layers adjacent along the [100] direction are linked together through the Ba-polyhedra and hydrogen bonds with the participation of the OH-groups occupying the "end" vertices of two B-triangles. The interlayer space is also filled with a sheet of Ba-polyhedra. The structure of the compound is compared to the structures of topologically similar Ba and Ca borates and hydroborates. © *2000 MAIK "Nauka/Interperiodica"*.

INTRODUCTION

The interest in growth and study of borates is stimulated by search for materials possessing nonlinear optical properties. The relationship between the crystal structure and the optical properties of borates in general and, in particular, of alkali and alkaline-earth borates has been extensively studied in recent years. A considerable number of publications describe the attempts to establish the correlation between the structure and the nonlinear optical properties of the BaB_2O_4 (*BBO*) and LiB_3O_5 crystals. These crystals are characterized by a wide transparency range, large values of nonlinear the optical coefficients, a high destruction threshold, and high temperature stability and are successfully used for the second-harmonic generation of YAG : Nd lasers [1]. Recently, several Ba-borates have been synthesized, including α-BaB_2O_4 [2], β-BaB_2O_4 [3], $Ba[B(OH)_4]_2 \cdot H_2O$ [4], $Ba[B(OH)_4]_2$ [5], and BaB_4O_7 [6]. Although these compounds have close compositions, their structural characteristics show considerable variations. Thus they have different configurations of anionic complexes, different dimensions of Ba-polyhedra, different coordination numbers of Ba atoms, different types of distortions of B-tetrahedra and B-triangles. In this connection, the structural study of a new representative of this group was of a considerable interest, because it would allow further study of the correlation between the composition and the structure in these closely related compounds.

EXPERIMENTAL

Crystals of the new barium hydroborate were grown by the hydrothermal method when studying the characteristic features of the phase formation in the BaO–$PbCO_3$–B_2O_3–H_2O system. The 20 day-synthesis was performed in standard fluoroplastic-lined autoclaves under a pressure of 100 atm at temperature 250°C. The charge was a mixture of BaO and B_2O_3 oxides in a ratio of 1 : 2. The incorporation of Ba atoms into the structure is confirmed by the results of the electron probe analysis (a Cameka SX 50 microprobe, a 20 mA-current at the accelerating voltage of 15 kV).

The transparent colorless crystals were up to 0.2 mm in size and had a pseudohexagonal pyramidal habit. A single crystal of dimensions $0.17 \times 0.1 \times 0.1$ mm was chosen for an X-ray structure study. The X-ray diffraction data were collected on an automated Stoe IPDS diffractometer equipped with a position-sensitive detector. The absorption correction was introduced in the course of data processing by the FACIET (Stoe) program.

All the subsequent computations necessary for the structure solution were performed by the AREN program package [7]. The structure was solved by the direct method. Three Ba-atoms were localized from the *E* synthesis with the lowest *R* factor being attained

Table 1. Crystallographic and experimental data

Formula	$Ba_5[B_{20}O_{33}(OH) \cdot H_2O]$
Unit-cell parameters, Å	$a = 9.495(2)$
	$b = 6.716(1)$
	$c = 11.709(2)$
	$\beta = 95.09(1)°$
Sp. gr.	$P2$
Unit-cell volume V, Å^3	743.4(2)
Number of formula units, Z	1
Calculated density ρ, g/cm^3	3.388
Absorption coefficient μ, mm^{-1}	6.675
Molecular weight	1516.96
F_{000}	690
Diffractometer	Stoe IPDS
Radiation, wavelength	MoK_α, 0.71073 Å
Temperature of data collection, K	293(2)
Total number of reflections	7123
Number of independent reflections with $I > 2\sigma(I)$	1860
R_{int}, %	4.47
R_F in the isotropic approximation, %	4.05
R_F in the anisotropic approximation, %	1.95
Flack factor	1.07(2)
Extinction coefficient, E	0.00081(8)
Maximum and minimum values on the difference electron density map, e/Å^3	$\Delta\rho_{max} = 0.732$
	$\Delta\rho_{min} = 0.737$

within the sp. gr. $P2$. The positions of B- and O-atoms were established from a series of successive difference electron density syntheses. The model determined was refined anisotropically by the full-matrix least-squares method using the SHELXL93 program [8]. The calculation of the valence balance [9] allowed us to establish O-atoms belonging to OH groups and H_2O molecules. The H atoms of the hydroxyl groups were localized from the difference electron density syntheses. The H atoms of water molecules were not localized. The choice of the acentric sp. gr. $P2$ was confirmed by the enantiomorph parameter (the Flack factor) [10]. The crystallographic data and the characteristics of the structure refinement are given in Table 1. The coordinates of the basis atoms are listed in Table 2. The final R factor obtained upon the refinement of the positional and isotropic thermal parameters of hydrogen atoms corresponds to the composition $Ba_5[B_{20}O_{33}(OH)_4] \cdot H_2O$ ($Z = 1$, $d_{calcd} = 3.388$ g/cm^3).

RESULTS AND DISCUSSION

The crystal structure of barium hydroborate consists of double pseudohexagonal boron–oxygen $[B_{20}O_{33}(OH)_4]$ layers perpendicular to the [100]-direction. These layers are formed by five crystallographically independent B-tetrahedra (the average B–O distances are 1.474, 1.481, 1.482, 1.472, and 1.472 Å) and five B-triangles (the average B–O distances are 1.363, 1.367, 1.372, 1.373, and 1.367 Å). The are three types of rings in the boron–oxygen layers of the structure (Fig. 1). The rings of the first type are formed by two B-tetrahedra and one B-triangle (I in Fig. 1). Analogous isolated rings were found in the structures of inyoite $Ca[B_3O_3(OH)_5] \cdot 4H_2O$ [11], inderite $Mg[B_3O_3(OH)_5] \cdot 5H_2O$ [12], inderborite $CaMg[B_3O_3(OH)_5] \cdot 6H_2O$ [13], meyerhofferite $Ca[B_3O_3(OH)_5] \cdot H_2O$ [14], and synthetic Ca-borate $Ca[B_3O_3(OH)_5] \cdot 2H_2O$ [15]. In the structures of colemanite and hydroboracite, these rings are directly linked to form chains. On the contrary, the

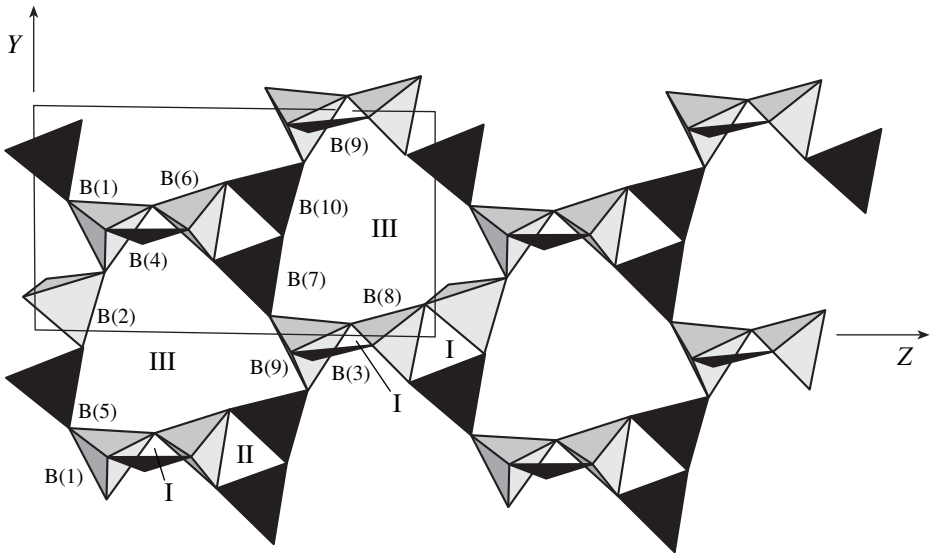

Fig. 1. Boron–oxygen layers in the $Ba_5[B_{20}O_{33}(OH)_4] \cdot H_2O$ structure. Boron triangles are shown by black color. The unit cell is shown by solid lines.

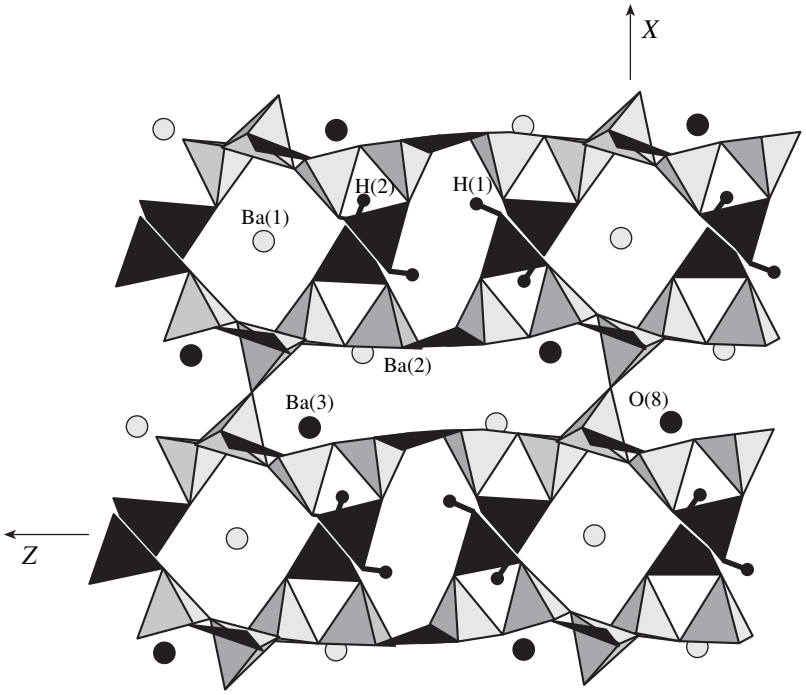

Fig. 2. Structure projection along the [010] direction.

rings of the second type consist of two triangles and one tetrahedron (II in Fig. 1). Analogous isolated rings were also observed in the structure of the synthetic crystals of metaboric acid β-$H_2[B_3O_4(OH)_3]$. In the boron–oxygen layers of the structure under consideration, one can separate the columns along the [010] direction. In these layers, the rings of both types are linked via two additional B-tetrahedra and two B-triangles. The columns containing rings of the either the first type or of the second type alternate along the [001]-direction (Fig. 1). The columns are linked by two additional B tetrahedra, which are not involved in the three-membered rings, and two B triangles whose terminal vertices are occupied by the OH groups and thus form layers which contain nine (III in Fig. 1) and three-membered rings. The configuration of the networks thus formed is very close to the boron–oxygen layers in gowerite $Ca[B_5O_8(OH)][B(OH)_3] \cdot 3H_2O$ [16]. The boron–oxy-

Table 2. Coordinates and thermal parameters ($Å^2 \times 10^3$) of the basis atoms

Atom	*x*/*a*	*y*/*b*	*z*/*c*	U_{eq}
Ba(1)	0.0	0.0003(1)	0.0	12(1)
Ba(2)	0.6159(1)	0.7669(1)	0.6976(1)	9(1)
Ba(3)	0.3822(1)	0.2503(1)	0.8246(1)	8(1)
B(1)	0.7162(3)	0.2692(4)	0.8569(2)	8(1)
B(2)	0.6331(3)	0.9393(4)	0.9653(2)	11(1)
B(3)	0.0456(3)	0.7859(4)	0.6893(2)	11(1)
B(4)	0.9299(3)	0.2827(4)	0.7532(2)	16(1)
B(5)	0.6788(3)	0.5756(4)	0.9916(2)	5(1)
B(6)	0.7019(3)	0.3074(4)	0.6421(2)	6(1)
B(7)	0.3443(3)	0.0753(4)	0.5165(2)	9(1)
B(8)	0.2435(3)	0.8074(4)	0.8450(2)	9(1)
B(9)	0.2873(3)	0.7742(4)	0.6389(2)	11(1)
B(10)	0.3289(3)	0.4255(4)	0.5544(2)	10(1)
O(1)	0.8732(2)	0.2813(3)	0.8565(1)	17(1)
O(2)*	0.9027(2)	0.7796(3)	0.6553(1)	23(1)
O(3)	0.6335(2)	0.7299(3)	0.9222(1)	12(1)
O(4)	0.0881(2)	0.7995(3)	0.8025(1)	10(1)
O(5)	0.6499(2)	0.3583(2)	0.7515(1)	7(1)
O(6)	0.3138(2)	0.2287(2)	0.5908(1)	11(1)
O(7)	0.2559(2)	0.9562(2)	0.9358(1)	9(1)
O(8)	0.5	0.0085(4)	0.0	12(1)
O(9)	0.6740(2)	0.0615(2)	0.8671(1)	14(1)
O(10)	0.1364(2)	0.7699(3)	0.6067(1)	14(1)
O(11)*	0.0777(2)	0.2676(4)	0.7557(1)	28(1)
O(12)	0.8560(2)	0.2848(3)	0.6512(1)	16(1)
O(13)	0.6714(2)	0.3795(2)	0.9571(1)	12(1)
O(14)	0.2828(2)	0.6061(2)	0.8934(1)	10(1)
O(15)	0.6646(2)	0.4660(2)	0.5570(1)	12(1)
O(16)	0.6378(2)	0.1187(2)	0.5948(1)	11(1)
O(17)	0.3573(2)	0.8806(2)	0.5495(1)	8(1)
O(18)	0.3271(2)	0.8584(2)	0.7507(1)	7(1)
O(19)	0.3436(2)	0.5617(2)	0.6409(1)	11(1)
O(20)**	0.0	0.5998(5)	0.0	54(1)
H(1)	0.886(3)	0.769(5)	0.578(2)	27(5)***
H(2)	0.101(3)	0.271(6)	0.690(3)	56(6)***

* OH, ** H_2O, *** U_{iso}.

gen frameworks, which are related by a twofold rotation axis along the *b* axis, form double layers sharing a vertex [O(8) of the B(2) tetrahedron] (Fig. 2).

The above-described double layers are as a new type of boron–oxygen complexes. They complement the classification schemes of natural and synthetic borates developed earlier. According to Strunz's classification scheme [17], barium hydroborate described by the formula of the borate complex 20(10△ + 10*T*) belongs to megaborates and is an intermediate compound between dodecaborate 12(12*T*) rhodizite $(K, Cs)Al_4Be_4[B_{11}BeO_{24}O_4]$ [18] and dimorphs 26(12△ + 14*T*) $Ca_9[B_{26}O_{34}(OH)_{24}]Cl_4 \cdot 13H_2O$ (pringleite and ruitenbergite) [19].

Barium hydroborate contains three types of Ba-atoms, which have different oxygen environment. The Ba(1) atoms are located within the hexagonal pyramids (the Ba(1)–O distances range within 2.623–2.864 Å), which link the double boron–oxygen layers. The H_2O molecule is located in the O(20) vertex of the Ba(1) seven-vertex polyhedron. These interlayer contacts are strengthened via hydrogen bonds with the participation of the protons from OH groups occupying the "end" vertices of the $BO_2(OH)$ triangles. The ten-vertex polyhedra of Ba(2) (the Ba(2)–O distances range within 2.632–3.025 Å) and the eleven-vertex polyhedra of Ba(3) (the Ba(3)–O distances range within 2.703–3.153 Å) form the polyhedral layers parallel to the [100]-direction with the polyhedra sharing their edges. Analogous ten-vertex polyhedra of Ba(2) were observed in the structures of synthetic BaB_4O_7 crystals [6] (in which the Ba–O distances range within 2.718–3.122 Å) and $Ba[B(OH)_4] \cdot H_2O$ [4]. An eleven-vertex Ba(3) polyhedron is formed as a result of the attachment of one more oxygen atom spaced by 3.153 Å from the central Ba-atom.

ACKNOWLEDGMENTS

This study was supported by the Swiss National Science Foundation (grant no. 7SUPJ048718), the Russian Foundation for Basic Research (project no. 97-05-64000), the Foundation for Leading Scientific Schools (project no. 96-15-96427), and by the Program "Russian Universities."

REFERENCES

1. D. N. Nikogosyan, Élektron. Tekh., Ser. Lazer. Tekh. Optoélektron. **2**, 3 (1990).
2. K. H. Hubner, Neues Jahrb. Mineral. Monatsh. **8**, 335 (1969).
3. J. Liebertz and S. Stahr, Z. Kristallogr. **165**, 91 (1983).
4. L. Kutschabsky, Acta Crystallogr., Sect. B: Struct. Crystallogr. Cryst. Chem. **25** (9), 1811 (1969).
5. V. B. Kravchenko, Zh. Strukt. Khim. **6** (5), 724 (1965).
6. S. Block and A. Perloff, Acta Crystallogr. **19**, 297 (1965).

7. V. I. Andrianov, Kristallografiya **32** (1), 228 (1987) [Sov. Phys. Crystallogr. **32** (1), 130 (1987)].
8. G. M. Sheldrick, *SHELXL 93: Program for the Refinement of Crystal Structures* (Univ. of Göttingen, Germany, 1993).
9. I. D. Brown and R. D. Shanon, Acta Crystallogr., Sect. A: Cryst. Phys., Diffr., Theor. Gen. Crystallogr. **29** (3), 226 (1973).
10. H. D. Flack, Acta Crystallogr., Sect. A: Found. Crystallogr. **39** (6), 876 (1983).
11. I. M. Rumanova and E. A. Genkina, Izv. Akad. Nauk Latv. SSR, Ser. Khim., No. 6, 643 (1981).
12. E. Corazza, Acta Crystallogr., Sect B: Struct. Crystallogr. Cryst. Chem. **32** (5), 1329 (1976).
13. E. N. Kurkutova, I. M. Rumanova, and N. V. Belov, Dokl. Akad. Nauk SSSR **164** (1), 90 (1965) [Sov. Phys. Dokl. **10**, 808 (1965)].
14. C. L. Christ and J. R. Clark, Z. Kristallogr. **114**, 321 (1960).
15. J. R. Clark and C. L. Christ, Z. Kristallogr. **112**, 213 (1959).
16. J. A. Konnert, J. R. Clark, and C. L. Christ, Am. Mineral. **57** (3–4), 381 (1972).
17. H. Strunz, Eur. J. Mineral. **9**, 225 (1997).
18. K. J. Taxer and M. J. Buerger, Z. Kristallogr. **125**, 423 (1967).
19. J. D. Grice, P. C. Burns, and F. C. Hawthorne, Can. Mineral. **32**, 1 (1994).

Translated by T. Safonova

Crystallography Reports, Vol. 45, No. 3, 2000, pp. 410–415. Translated from Kristallografiya, Vol. 45, No. 3, 2000, pp. 452–457.

STRUCTURE OF INORGANIC COMPOUNDS

Crystal Structure of Strontium Hilgardite

O. Ferro*, D. Yu. Pushcharovskiĭ, S. Teat***, S. A. Vinogradova**, E. V. Lovskaya**, and I. V. Pekov****

** University of Pisa, Pisa, Italy*

*** Moscow State University, Vorob'evy gory, Moscow, 119899 Russia*

**** SERC Daresbury Laboratory, Daresbury, Warrington WA4 4AD, Cheshire, England*

Received December 29, 1998

Abstract—The crystal structure of strontium hilgardite, $CaSr[B_5O_9]Cl \cdot H_2O$, was established by the method of X-ray diffraction analysis (synchrotron radiation; diffractometer equipped with a position-sensitive detector; $\lambda = 0.688$ Å; 3191 reflections with $F > 4\sigma(F)$; $R = 0.045$ in the anisotropic approximation). The triclinic unit-cell parameters are as follows: $a = 6.5732(6)$ Å, $b = 6.4445(6)$ Å, $c = 6.3693(6)$ Å, $\alpha = 60.995(2)°$, $\beta = 61.257(2)°$, $\gamma = 77.191(2)°$, sp. gr. $P1$; $Z = 1$. The Ca and Sr atoms were found to be disordered over two positions. The structures of strontium hilgardite and hilgardite-1*A* differ in the configurations of the seven-vertex Sr- and Ca(2)-polyhedra. The structure solved in this work is consistent with two series of borates studied previously. One of these groups involves pentaborates with different degrees of hydration of borate complexes, and the second group includes Sr-containing borates. © *2000 MAIK "Nauka/Interperiodica".*

The crystal structures of aqueous calcium pentaborates, namely, monoclinic hilgardite-4*M* and triclinic hilgardite-3*A* (parahilgardite), with the triple unit cells contain the anionic $[B_5O_9]$-frameworks consisting of three B-tetrahedra and two B-triangles [1, 2]. According to Ghose [3], these frameworks are formed by linked pentaborate $[B_5O_{12}]$ complexes with two configurations. In the complexes of the first type (the *l* configuration), two BO_3-triangles are located on the same side (in the *cis* positions) of three BO_4-tetrahedra sharing vertices, whereas in the complexes of the second type (the *d* configuration), the BO_3-triangles are located on each side (in the *trans* positions) of three BO_4-tetrahedra. In terms of stereoisomerism, the structure of monoclinic hilgardite-4*M* can be considered as the alternation of bulky packets along the *a*-axis. In turn, these packets are formed by chains either of *l*- or of *d*-complexes parallel to the *c*-axis. The algorithm of this alternation can be written as *ld*… The triclinic structure of hilgardite-3*A* consists of two packets formed by the *l*-complexes separated by single packets formed by *d*-complexes along the [100] direction and forming the *lld*… sequence.

Recently, the topological analysis of boron–oxygen frameworks in minerals of the hilgardite family, in which the *l*- and *d*-layered complexes were established, was supplemented with the results of structure determination of the centrosymmetric monoclinic $Pb_2[B_5O_9](OH)H_2O$ [4]. In hilgardite-4*M* and synthetic $Ca_2[B_5O_9]Br$ crystals, whose structures were solved earlier [5], the complexes are related to each other by the *a* planes and twofold rotation axes, respectively. Unlike these structures, the $Pb_2[B_5O_9](OH)H_2O$ structure contains the complexes related by a center of inversion.

In addition to hilgardite-4*M* and hilgardite-3*A*, one more representative (1*A*) of this mineral group has been structurally studied [6]. This mineral has a triclinic unit cell, whose volume is three times less than that of hilgardite-3*A*. Using the above-considered notation, we can write the algorithm of repeated packets containing the borate $[B_5O_{11}]$-chains in this structure can be written as *l*… The parameters, the volume, and the content of the unit cell of this mineral fully correspond to yet another natural calcium borate—tyretskite, which differs from hilgardite-1*A* by the substitution of Cl atoms OH groups. Based on this similarity, the authors [6] suggested that hilgardite-1*A* may be a structural analogue of tyretskite.

The unit-cell parameters of strontium hilgardite, whose chemical composition and X-ray characteristics were reported in [7], are close to those of hilgardite-1*A* and tyretskite. The X-ray diffraction study of strontium hilgardite [8] demonstrated that the Debye patterns obtained from two samples were somewhat different, which was attributed to slightly different compositions of these samples. A discovery of strontium hilgardite in the Nepskoe deposit of potassium salts (Irkutskaya oblast, East Siberia) gave an impetus to the structure study of this mineral. The major objective was to establish the character of the distribution of Ca and Sr atoms over two crystallographically independent positions and the structural changes in strontium hilgardite in comparison with hilgardite-1*A* caused by the replacement of half of Ca atoms by Sr.

The borate mineralization from the Nepskoe deposit (where strontium hilgardite occur in dolomite, dolo-

1063-7745/00/4503-0410$20.00 © 2000 MAIK "Nauka/Interperiodica"

Table 1. Crystallographic characteristics and details of X-ray diffraction study

Formula	$CaSr(B_5O_9)Cl \cdot H_2O$
Unit-cell parameters, Å, deg	$a = 6.5732(6)$
	$b = 6.4445(6)$
	$c = 6.3693(6)$
	$\alpha = 60.995(2)$
	$\beta = 61.257(2)$
	$\gamma = 77.191(2)$
Unit-cell volume, V, Å^3	206.88
Sp. gr.	$P1$
Number of formula units, Z	1
Calculated density ρ, g/cm^3	3.044
Molecular weight	379.22
Absorption coefficient μ, mm^{-1}	7.48
F_{000}	182.0
Diffractometer	Brucker AXS SMART CCD
Wavelength, Å	0.6883
Range of data collection	Reflection sphere
θ Scanning range, deg	3.41–33.83
Total number of reflections	4243
Number of independent reflections	3211
R_{int}	0.0205
Number of reflections with $\|F\| > 4\sigma(F)$	3191
R_{hkl} in the anisotropic approximation	0.045
wR	0.1095
Enantiomorph parameter, x	0.028(5)
$\Delta\rho_{max}$, e/Å^3	1.59
$\Delta\rho_{min}$, e/Å^3	–0.81

mite–anhydrite, and sylvinite beds. In this mineralization, strontium hilgardite forms associations with magnesite, quartz, boracite, and conventional low-strontium hilgardite [9]. The chemical composition of this mineral (electron probe microanalysis; Camebax microbeam; analyst I.M. Kulikova, Institute of Mineralogy, Geochemistry, and Crystal Chemistry of Rare Elements, Moscow) is as follows: CaO, 14.99; SrO, 23.62; B_2O_3, 42.45; Cl, 9.58; $–O=Cl_2$, 2.16; the total 88.49 (wt %). No direct determination of the water content was made. Hence, the empirical formula of the mineral was first written as $Ca_{1.09}Sr_{0.94}B_{5.02}O_9Cl_{1.12}$ ($\times n H_2O$). The mineral is characterized by high Sr-content and a constant Sr : Ca ratio equal to ~1.0. According to the IR spectral data and the X-ray powder pattern, this mineral considerably differs from low-strontium hilgardite.

The X-ray diffraction study of the mineral was performed on a single crystal of linear dimensions $0.32 \times 0.26 \times 0.24$ mm^3. The X-ray diffraction data were collected with the use of synchrotron radiation (9.8 synchrotron station at the Daresbury Laboratory Center, England) on an automated diffractometer equipped with a position-sensitive detector (rotation around ω; 0.15°-rotation frames were exposed for 1 s each) [10]. The data obtained were processed according to [11]. The coefficient of reduction to the absolute scale and the absorption correction were calculated by the SADABS program written by G.M. Sheldrick on the basis of the procedure reported in [12]. The crystallographic characteristics and the main characteristics of X-ray diffraction study and structure refinement are given in Table 1. The axial unit vectors were chosen according to [7]. The unit cell of hilgardite-1*A* reported in [6] was transformed into the unit cell of strontium hilgardite by the matrix 0 1 –1/1 0 0/0 0 –1.

The structure solution and all the computations including the correction for anomalous scattering were performed by the SHELXL program package [13]. The absolute configuration of the structure was determined from the results of the calculations of the *x*-parameter (0.028(5)) [14]. The calculations of the valence balance at anions confirmed the presence of a water molecule in

Table 2. Atomic coordinates and displacement parameters

Atom	*x*/*a*	*y*/*b*	*z*/*c*	U^*_{eq}, Å^2
Ca	0.2599(1)	0.8359(1)	0.3075(1)	0.077(1)
Sr	0.72040(2)	0.36847(2)	0.97888(2)	0.01346(9)
Cl	0.7945(2)	0.8832(2)	0.5199(2)	0.0179(2)
B(1)	0.3788(5)	0.3553(5)	0.6547(6)	0.0038(4)
B(2)	0.1679(6)	0.5044(5)	0.0034(6)	0.0048(5)
B(3)	0.2266(6)	0.2754(5)	0.4104(6)	0.0043(4)
B(4)	0.2690(6)	0.9448(6)	0.7901(7)	0.0064(5)
B(5)	0.8304(6)	0.4002(6)	0.4421(7)	0.0057(5)
O(1)	0.6746(5)	0.9274(6)	0.0496(6)	0.0167(5)
O(2)	0.6074(4)	0.3889(5)	0.6228(5)	0.0082(4)
O(3)	0.3038(4)	0.1053(4)	0.8521(5)	0.0076(4)
O(4)	0.3902(4)	0.4086(4)	0.3970(5)	0.0049(4)
O(5)	0.2124(4)	0.5149(4)	0.7549(4)	0.0051(3)
O(6)	0.2388(5)	0.7181(4)	0.9832(5)	0.0095(4)
O(7)	0.9063(4)	0.4802(4)	0.1735(5)	0.0080(4)
O(8)	0.2799(1)	0.3053(4)	0.1504(54)	0.0047(3)
O(9)	0.2509(5)	0.0164(4)	0.5618(5)	0.0079(4)
O(10)	0.9881(4)	0.3429(4)	0.5458(5)	0.0074(4)
H(1)	0.62(5)	0.83(7)	0.247(16)	0.3(2)
H(2)	0.81(3)	0.87(4)	–0.07(4)	0.12(7)

* For H atoms, the U_{iso} values are given; $U_{eq} = \frac{1}{3}\sum_i\sum_j U_{ij}\, a^*_i\, a^*_j\, a_i a_j$.

the O(1) position. The difference electron density synthesis revealed the positions of two protons located at distances of 1.00(4) and 1.00(3) Å from the O(1) atom of the H_2O molecule (∠H(1)–O(1)–H(2) is ~118°). The O–H distances determined are consistent with the data obtained from X-ray diffraction studies. The final coordinates of the basis atoms, the atomic displacements (which were calculated with the use of anisotropic thermal corrections for all non-hydrogen atoms), and the interatomic distances for Ca- and Sr-polyhedra are given in Tables 2 and 3. The atomic coordinates in the structure of hilgardite-1*A* can be related to those in the structure of strontium hilgardite by the relationships *X* = *y*, *Y* = *x*, *Z* = –(*y* + *z*) with the corresponding displacement of the origin of coordinates by a vector with the components ~0.260, ~0.836, ~0.307 along the unit cell axes (where *X*, *Y*, and *Z* are the atomic coordinates in the structure of hilgardite-1*A*). The experimental and theoretical [15] X-ray powder patterns (Table 4) are very close. Different projections and the stereoview of the structure (the ATOMS program [16]) are shown in Figs. 1–4. It should also be noted that the projection of the triclinic structure of hilgardite-1*A* along the [001]-direction [6] is somewhat distorted because the authors neglected the nonorthogonality of the three axes.

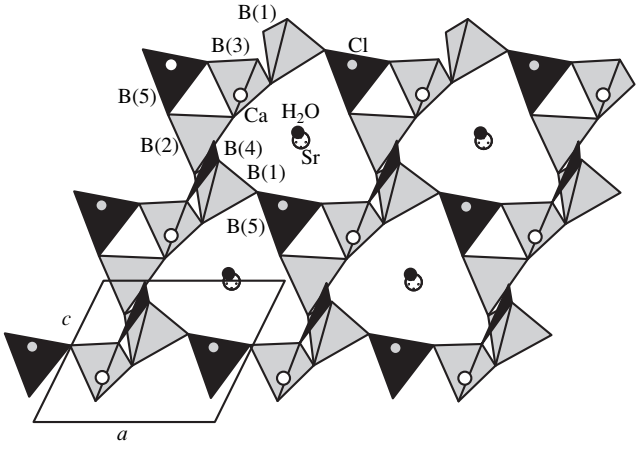

Fig. 1. Structure of strontium hilgardite projected along [010].

The structure of strontium hilgardite is essentially similar to that of hilgardite-1*A*. It is based on the zeolite-like boron–oxygen $[B_2^{\triangle}B_3^{t}O_9]$-framework consisting of tetrahedral $[B_3O_9]$-chains parallel to the [001]-direction (Fig. 1). The links of these chains are formed

by three tetrahedra. The contacts between the tetrahedra are strengthened by two (B,O)-triangles. The interatomic B–O distances (⟨1.470⟩ and ⟨1.362⟩ Å for the tetrahedra and the triangles, respectively) have standard values. The Ca- and Sr-cations, water molecules, and Cl-anions are orderly located in the framework cavities, whereas Cl atoms and water molecules are located in the channels parallel to the [001]-direction (Fig. 2) and Sr- and Ca-atoms, in the channels parallel to the [010]- and [100]-directions, respectively (Fig. 2) (Fig. 3).

The main difference between these structures is associated with the rearrangement of Ca(2)-polyhedra in the structure of hilgardite-1*A* (in strontium hilgardite they are occupied by the Sr atoms) (Fig. 4). In both structures, these polyhedra are formed by seven anions but have essentially different configurations. The Ca(2)-polyhedron is a distorted pentagonal bipyramid, one axial vertex of which is occupied by a Cl atom. The Sr-polyhedron is a hexagonal pyramid, and a Cl atom located at a distance 3.134(1) Å cannot be inclined into the nearest environment of the Sr atom. Therefore, unlike all the other structurally studied minerals of this group, in which Cl atoms are involved in both cationic polyhedra, the Cl atoms in the structure of strontium hilgardite are involved only in the Ca polyhedra and cannot act as ligands in the Sr polyhedra. However, taking into account the standard average distances (~2.65 Å) in the seven- and eight-vertex Sr polyhedra, it is reasonable to complete the coordination polyhedron of the Sr atom with the O(5) atom located at a distance of 3.007 Å from the central cation. The corresponding distance in the structure of hilgardite-1*A* (3.13 Å) led the authors [6] to a conclusion that the O(5) atom cannot be included into the polyhedron of the Ca(2) atom. The seven-vertex polyhedra of Sr atoms were observed earlier in the structures of $SrB_{12}H_{12} \cdot 7H_2O$ [17], $Sr_2LiInB_4O_{10}$ [18], $Sr_2B_2O_5$ [19], etc.

Table 3. Interatomic distances (Å) for the Ca and Sr polyhedra in the structure of strontium hilgardite

Ca-polyhedron		Sr-polyhedron	
Ca–O(1)	2.438(3)	Sr–O(1)	2.694(3)
O(3)	2.459(2)	O(2)	2.636(2)
O(4)	2.558(2)	O(4)	2.604(2)
O(5)	2.492(2)	O(5)	3.007(2)
O(6)	2.590(3)	O(7)	2.517(2)
O(8)	2.669(2)	O(8)	2.602(2)
O(9)	2.384(3)	O(10)	2.515(3)
Cl	2.700(1)		⟨2.654⟩
	⟨2.536⟩	Sr–Cl	3.134(1)

The structure under study is consistent with two series of borates studied previously. One of these groups involves pentaborates with different degrees of hydration of borate complexes, and the second group includes Sr-containing borates. The main building blocks of zeolite-like borate frameworks of minerals of the hilgardite group are two triangles and three tetrahedra. The borate layers of similar composition, $[B_5O_8(OH)]$, which are characterized by the replacement of one O^{2-} anion by the OH^- group, are formed with the participation of three triangles and two tetrahedra. These layers were found in the structures of nasinite $Na_2[B_5O_8(OH)] \cdot 2H_2O$ [20], veatchite

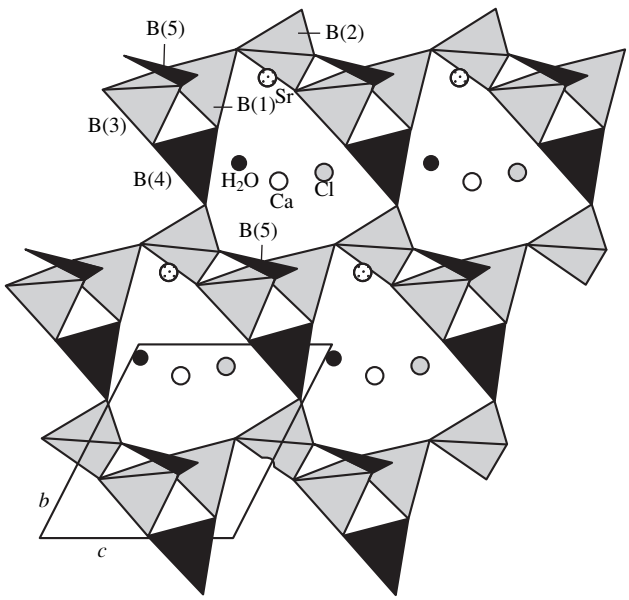

Fig. 2. Structure of strontium hilgardite projected along [100].

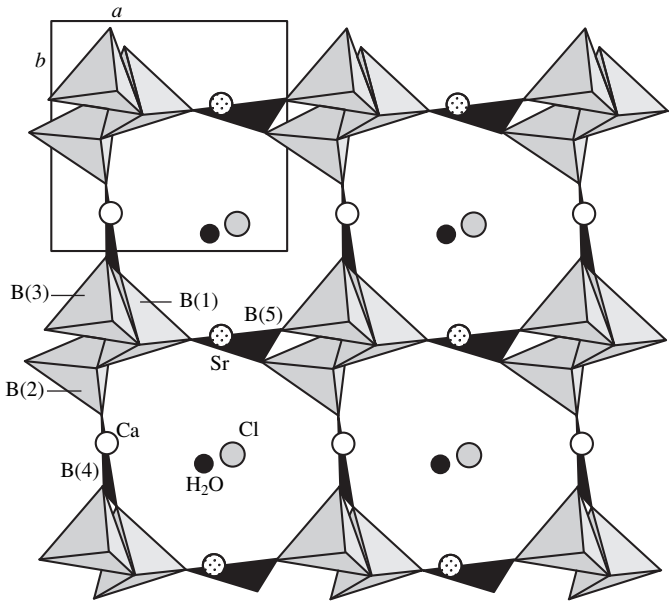

Fig. 3. Structure of strontium hilgardite projected along [001].

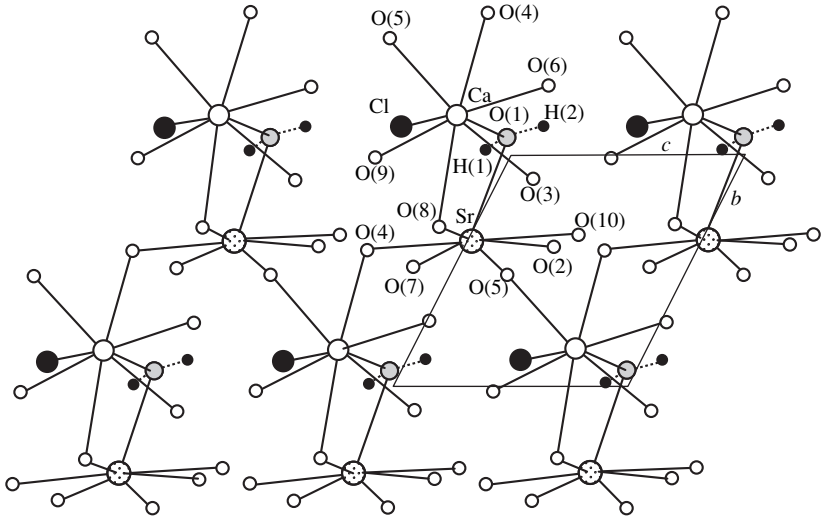

Fig. 4. The Ca- and Sr-polyhedra in the strontium hilgardite structure.

$Sr_2[B_5O_8(OH)]_2[B(OH)_3] \cdot H_2O$ [21], high-calcium *p*-veatchite $Sr(Ca_{0.8}Sr_{0.2})[B_5O_8(OH)][B(OH)_3] \cdot H_2O$ [22], gowerite $Ca[B_5O_8(OH)][B(OH)_3] \cdot 3H_2O$ [23], biringuccite $Na_4[B_5O_8(OH)OB_3O_7(OH)] \cdot 2H_2O$ [24], and the synthetic crystals of $K_2[B_5O_8(OH)] \cdot 2H_2O$ [25].

The involvement of one more OH^- group into the pentaborate complex of tuzlaite $Na,Ca[B_5O_8(OH)_2] \cdot 3H_2O$ [26] provides the preservation of the layers whose major building units are two triangles and three tetrahedra. A further increase in the number of hydroxyl groups in the pentaborate complexes is accompanied by a successive change of their configuration in passing to probertite $NaCa[B_5O_7(OH)_4] \cdot 3H_2O$ [27] containing the (B,O) chains and further to ulexite $NaCa[B_5O_6(OH)_6] \cdot 5H_2O$ [28] containing the isolated (B,O) groups.

On the whole, a small group of natural strontium borates is characterized by a high degree of condensation of borate complexes forming the layers in the structures of pentaborate veatchite $Sr_2[B_5O_8(OH)]_2[B(OH)_3] \cdot H_2O$ [21], hexaborates tunellite $Sr[B_6O_9(OH)_2] \cdot 3H_2O$ [29], strontioborite $Sr[B_6O_9OHOB_2O(OH)_3]$ [30] and strontioginorite $SrCa[Sr_{14}O_{20}(OH)_6] \cdot 5H_2O$ [31] and also a zeolite-like framework in the structure of strontium hilgardite under study.

Table 4. X-ray diffraction powder pattern from strontium hilgardite (an RKD camera, λFe K_α)

hkl	d_{exp}	d_{calc}	I_{exp}	I_{calc}
010	5.71	5.64	9	6.5
101, 001, 011	5.09	5.02, 5.01, 5.00	7	2.7, 0.6, 2
1-10, 110	4.07	4.06, 4.01	5	3.8, 1.3
112, 1-1-1, 201	3.24	3.18	9	6.8
200	2.93	2.89	10	10
020	2.83	2.82	9	9
2-10	2.56	2.58	6	1.4
210	2.53	2.55	4	2.8
222	2.47	2.48	2	0.5
2-1-1, 312, 20-1	2.15	2.14, 2.13, 2.12	9	1.9, 1.9, 2
1-21, 132	2.10	2.10	6	3.1
113	2.07	2.06	6	3.6
322, 032	1.90	1.94	3	3.8
232, 2-2-1	1.88	1.90	4	3.3
21-1, 321, 231	1.85	1.87, 1.85	6	1.6, 1.4
3-12	1.70	1.72	3	1.2

ACKNOWLEDGMENTS

We are grateful to V.N. Zaĭtsev (SERC Daresbury Laboratory) for his assistance in data collection and useful discussion.

This study was supported by the Russian Foundation for Basic Research, (project no. 97-05-64000), the Foundation for Leading Scientific Schools (project no. 96-15-96427), and the Competition Research Center (Geology Grant, Moscow State Geological Prospecting Academy (MGRA)).

REFERENCES

1. S. Chose and C. Wan, Am. Mineral. **64**, 187 (1979).
2. C. Wan and S. Chose, Am. Mineral. **68**, 604 (1983).
3. S. Chose, Am. Mineral. **67**, 1265 (1982).
4. E. L. Belokoneva, O. V. Dimitrova, T. A. Korchemkina, and S. Yu. Stefanovich, Kristallografiya **43** (5), 864 (1998) [Crystallogr. Rep. **43** (5), 810 (1998)].

5. D. J. Lloyd, A. Levasseur, and C. Fouassier, J. Solid State Chem. **6**, 179 (1973).
6. I. M. Rumanova, Z. I. Iorysh, and N. V. Belov, Dokl. Akad. Nauk SSSR **236** (1), 91 (1977) [Sov. Phys. Dokl. **22**, 460 (1977)].
7. O. Braitsch, Beitr. Mineral. Petrogr. **6**, 233 (1959).
8. V. V. Kondrat'eva, Rentgenogr. Miner. Syr'ya, No. 4, 10 (1964).
9. V. N. Appolonov, G. A. Galkin, D. G. Koshchug, *et al.*, Geol. Geofiz., No. 3, 24 (1988).
10. R. J. Cernik, W. Clegg, C. R. A. Catlow, *et al.*, J. Synchrotron Radiat. **4**, 279 (1997).
11. W. Clegg, M. R. J. Elsegood, S. J. Teat, *et al.*, J. Chem. Soc. Dalton Trans. 3037 (1998).
12. R. H. Blessing, Acta Crystallogr., Sect. A: Foundam. Crystallogr. **51**, 33 (1995).
13. G. M. Sheldrick, *SHELXL 93: Program for the Refinement of Crystal Structures* (Univ. of Göttingen, Germany, 1993).
14. H. D. Flack, Acta Crystallogr., Sect. A: Found. Crystallogr. **39**, 876 (1983).
15. K. Yvon, W. Jeitschko, and E. Parthe, J. Appl. Crystallogr. **10**, 73 (1977).
16. E. Dowty, *Atoms 3.2: A Computer Program for Displaying Atomic Structures, Kingsport, TN 37663* (1995).
17. K. A. Solntsev and N. T. Kuznetsov, Dokl. Akad. Nauk SSSR **232**, 1366 (1977).
18. K. I. Schaffers and D. A. Keszler, Acta Crystallogr., Sect. C: Cryst. Struct. Commun. **49**, 211 (1993).
19. H. Bartl and W. Schuckmann, Neues Jahrb. Mineral., Monatsh. **8**, 253 (1966).
20. E. Corazza, Acta Crystallogr., Sect. B: Struct. Crystallogr. Cryst. Chem. **31**, 2405 (1975).
21. J. R. Clark and C. L. Crist, Am. Mineral. **50**, 1934 (1971).
22. R. K. Rastsvetaeva, A. P. Khomyakov, and T. N. Sokolova, Kristallografiya **38** (2), 86 (1993) [Crystallogr. Rep. **38** (2), 180 (1993)].
23. J. A. Konnert, J. R. Clark, and C. L. Christ, Am. Mineral. **57**, 381 (1972).
24. E. Corazza, S. Menchetti, and C. Sabelli, Am. Mineral. **59**, 1005 (1974).
25. M. Marezio, Acta Crystallogr., Sect. B: Struct. Crystallogr. Cryst. Chem. **25**, 1811 (1969).
26. V. Bermanec, T. Armbruster, D. Tibljas, *et al.*, Am. Mineral. **79**, 562 (1994).
27. S. Menchetti, C. Sabelli, and R. Trosti-Ferroni, Acta Crystallogr., Sect. B: Struct. Crystallogr. Cryst. Chem. **38**, 3072 (1982).
28. S. Chose, Ch. Wan, and J. R. Clark, Am. Mineral. **63**, 160 (1978).
29. J. R. Clark, Am. Mineral. **49**, 1549 (1964).
30. A. A. Brovkin, N. V. Zayakina, and V. S. Brovkina, Kristallografiya **20** (5), 911 (1975) [Sov. Phys. Crystallogr. **20** (5), 563 (1975)].
31. J. R. Konnert, J. R. Clark, and C. L. Christ, Am. Mineral. **55** (11–12), 1911 (1970).

Translated by T. Safonova

Crystallography Reports, Vol. 45, No. 3, 2000, pp. 416–421. Translated from Kristallografiya, Vol. 45, No. 3, 2000, pp. 458–464.

STRUCTURES OF COORDINATION COMPOUNDS

Crystal and Molecular Structure of Complex Compound $[Fe_3O(CH_3COO)_6(H_2O)_3]_2[ZnCl_4] \cdot 2H_2O$

S. G. Shova*, I. G. Cadelnic*, M. Gdaniec, Ya. A. Simonov*, T. C. Jovmir***, G. Filoti****, I. I. Bulhac***, and C. I. Turta*****

** Institute of Applied Physics, Academy of Sciences of Moldova, Academiei 5, Chisinau, 20-28 Moldova*
*** Mickiewicz University, Grunwaldzka 6, Poznan, 60-780 Poland*
**** Institute of Chemistry, Academy of Sciences of Moldova, Academiei 3, Chisinau, 20-28 Moldova*
***** National Institute of Physics and Technology of Materials, P.O. Box MG-7, Bucharest, 76900 Romania*

Received December 26, 1997; in final form, April 24, 1999

Abstract—The X-ray crystal structure of trinuclear iron acetate $[Fe_3O(CH_3COO)_6(H_2O)_3]_2[ZnCl_4] \cdot 2H_2O$ was determined. The crystal has a ionic structure. It is monoclinic, $a = 25.363(7)$, $b = 14.533(4)$, $c = 15.692(4)$ Å, $\beta = 103.11(2)°$, space group $C2/c$, and $R = 0.0685$. The structure of the cationic complex $[Fe_3O(CH_3COO)_6(H_2O)_3]^+$ is typical of trinuclear iron(III) compounds containing a μ_3-O bridge: the iron atoms are situated at the vertices of an almost equilateral triangle with the O atom at the center. Each Fe atom is coordinated by four O atoms of bridging carboxy groups, the μ_3-bridging O atom, and the water molecule in the *trans* position to the latter O atom. Mössbauer spectroscopy evidence indicates the high-spin state ($S = 5/2$) of the iron(III) ions. © *2000 MAIK "Nauka/Interperiodica".*

INTRODUCTION

Extensive studies of 3*d*-metal carboxylates are due to their specific structural features, which determine specific physicochemical properties important for fundamental and applied chemistry [1, 2]. Literature data [2–5] suggest possible applications of 3*d*-metal carboxylates in catalysis and analytical chemistry; they can also be used as precursors for preparation of magnetic materials, etc. Polynuclear iron carboxylates, which mimic different metalloprotein centers [6–8] (ferritin, hemerythrin, and others), are of particular interest. The first structural study of iron(III) acetate $[Fe_3O(CH_3COO)_6(H_2O)_3]ClO_4$ dates back to 1969 [9]. Since then, data on the syntheses and structures of bi-, tri-, tetra-, hexa-, octa-, nona-, deca-, undeca-, dodeca-, hexadeca-, heptadeca-, and nonadecanuclear-containing iron complexes with carboxylate bridging anions have been reported [6, 10–13].

The problem of the packing of trinuclear clusters in a crystal is of special interest. Such molecules (or cations) are bulky; thus, their packing contains cavities, which accommodate anions or solvent molecules, in particular, water. It was shown that the compounds $[Fe_3O(CH_3COO)_6(H_2O)_3]NO_3 \cdot 4H_2O$ [14] and $[Cr_2FeO(CH_3COO)_6(H_2O)_3] \cdot NO_3 \cdot CH_3COOH$ [15] crystallize in the same space group with close unit cell parameters. The compounds differ only in dimensions of solvation molecules. Four H_2O molecules in the former compound and a molecule of acetic acid in the latter compound occupy the same volume. The rearrangement of hydrogen bonds in the crystal does not change the mutual arrangement of anions and cations. In this case, the large organometallic cation determines the crystal packing. In [14, 16–18], we tried to reveal the role of an anion and a solvation molecule in the packing of trinuclear cations in a crystal.

In this paper, along with the data on the structure of $[Fe_3O(CH_3COO)_6(H_2O)_3]_2[ZnCl_4] \cdot 2H_2O$, we report the results of its Mössbauer and IR spectroscopic studies.

EXPERIMENTAL

X-ray diffraction study. A prismatic single crystal, $0.2 \times 0.2 \times 0.6$ mm, was chosen for the X-ray study. To prevent the crystal from decomposition during data collection, it was sealed in a capillary containing vapor of the mother liquor. The experimental data were obtained on a KUMA KM-4 diffractometer with graphite-monochromated MoK_α radiation. The unit-cell parameters were determined by a least-squares procedure using 25 reflections in the range $15° \le \theta \le 20°$. The intensities were measured by the $\omega/2\theta$ scan technique up to $\theta_{max} = 25.07°$. The intensities of three standard reflections measured every 100 reflections varied within ±2%.

The structure was solved by direct methods. The non-hydrogen atoms were refined by a least-squares procedure in the anisotropic approximation. All calculations were performed with the SHELXS86 [19] and SHELXL93 [20] program packages. The positional parameters of the hydrogen atoms of the CH_3 groups were calculated geometrically. The hydrogen atoms of the coordinated water molecules were located from difference Fourier syntheses and verified by the geometric

Table 1. Crystallographic characteristics of compound $[Fe_3O(CH_3COO)_6(H_2O)_3]_2[ZnCl_4] \cdot 2H_2O$

Empirical formula	$C_{12}H_{24}Cl_2Fe_3O_{17}Zn_{0.50}$
Molecular weight	711.45
Temperature, K	293(2)
Wavelength, Å	0.71073
Space group	*C*2/*c*
Unit cell parameters:	
a, Å	25.363(7)
b, Å	14.533(4)
c, Å	15.692(4)
β, deg	103.11(2)
V, Å^3	5633(3)
Z	8
ρ_{calcd}, g/cm^3	1.678
Absorption coefficient, mm^{-1}	2.196
F(000)	2872
Crystal size, mm	$0.2 \times 0.2 \times 0.6$
Range of θ angles, deg	1.63–25.05
Index range	$-29 \le h \le 29$, $0 \le k \le 17$, $0 \le l \le 18$
Number of reflections:	
measured	5180
unique	4990 [R_{int} = 0.0277]
Method of refinement	Full-matrix least-squares procedure
Ratio of the number of reflections to the number of parameters	4318/341
Goodness-of-fit on F_2	1.007
R factors [$I > 2\sigma(I)$]	$R1$ = 0.0685, $wR2$ = 0.2013
R factors (for all reflections)	$R1$ = 0.1012, $wR2$ = 0.2537
The highest peak and deepest minima on the zero difference synthesis, e Å^{-3}	1.471 and –0.702

parameters of hydrogen bonds. The values of the isotropic thermal parameters of the hydrogen atoms were fixed equal to $1.2U_{eq}$ of the corresponding C or O atoms.

In the process of structure solution, it was found out that the $[ZnCl_4]^{2-}$ anion is disordered over two systems of points in the vicinity of the twofold axis in space group *C*2/*c*. One of the chlorine atoms, Cl(1), lies on the twofold axis, and the remaining three chlorine atoms and the Zn atom occupy general positions. This disordering is apparently due to the formation of large cavities in the crystal. The refinement revealed that the positions of Zn, Cl(2), Cl(3), and Cl(4) atoms are populated by less than 50%. This suggested that, along with the $[ZnCl_4]^{2-}$ anions, the crystal contains Cl^- ions. The final occupancies with due regard for the multiplicity of the special position are 0.40 for $[ZnCl_4]^{2-}$ anions and 0.10 for Cl^- anions.

Main crystallographic parameters and structure refinement details are summarized in Table 1. The atomic coordinates are listed in Table 2.

Synthesis of $[Fe_3O(CH_3COO)_6(H_2O)_3]_2[ZnCl_4] \cdot 2H_2O$ (I). Weighed portions of $FeCl_3 \cdot 6H_2O$ (5.40 g, 20 mmol) and CH_3COONa (3.3 g, 40 mmol) were dissolved in 15 ml of water at room temperature. A portion of solid $(NH_4)_2ZnCl_4$ (6.0 g, 25 mmol) was added to the solution obtained, and the mixture was allowed to stand at room temperature until the solid salt completely dissolved. The solution was filtered and allowed to stand in an open crystallization basin at room temperature. Within 2–3 weeks, the crystals precipitated in the form of "rosettes" composed of red-brown sticks.

Table 2. Atomic coordinates ($\times 10^4$) and equivalent isotropic thermal parameters U_{eq} ($Å^2 \times 10^3$)

Atom	*x*	*y*	*z*	U_{eq}	Atom	*x*	*y*	*z*	U_{eq}
Fe(1)	7303(1)	3681(1)	3202(1)	27(1)	C(1*F*)	6386(3)	2554(5)	3559(4)	36(4)
Fe(2)	6848(1)	5803(1)	3161(1)	25(1)	C(2*F*)	6236(4)	1779(5)	4097(6)	50(2)
Fe(3)	6022(1)	4116(1)	2327(1)	26(1)	O(1)	6725(2)	4537(3)	2889(3)	25(1)
Zn	4570(1)	1217(2)	7536(2)	70(1)	O(1*W*)	7970(2)	2807(4)	3555(3)	47(1)
Cl(1)	5000	–196(4)	7500	110(3)	O(2*W*)	6946(2)	7199(3)	3409(3)	34(1)
Cl(2)	3843(3)	1191(5)	6382(4)	66(2)	O(3*W*)	5267(2)	3678(4)	1651(3)	39(1)
Cl(3)	5151(3)	2273(6)	7317(8)	107(4)	O(4*W*)	4805(4)	–1926(7)	8769(10)	141(5)
Cl(4)	4206(5)	1538(8)	8739(6)	115(4)	O(1*A*)	7880(2)	4497(4)	2920(4)	43(1)
Cl	4711(6)	968(9)	6680(9)	34(3)	O(2*A*)	7599(2)	5930(3)	2964(4)	43(1)
C(1*A*)	7950(3)	5345(5)	2930(4)	30(1)	O(1*B*)	7500(2)	4126(4)	4440(3)	51(2)
C(2*A*)	8510(3)	5690(6)	2920(6)	53(2)	O(2*B*)	7166(2)	5538(3)	4424(3)	42(1)
C(1*B*)	7390(3)	4843(5)	4809(4)	33(2)	O(1*C*)	6579(2)	6163(4)	1877(3)	38(1)
C(2*B*)	7549(4)	4869(6)	5796(5)	55(2)	O(2*C*)	5922(2)	5131(4)	1428(3)	40(1)
C(1*C*)	6205(3)	5799(5)	1315(5)	37(2)	O(1*D*)	6137(2)	6043(3)	3462(4)	41(1)
C(2*C*)	6079(5)	6199(8)	405(6)	81(4)	O(2*D*)	5613(2)	4821(3)	3107(3)	34(1)
C(1*D*)	5739(3)	5556(5)	3499(4)	31(1)	O(1*E*)	6294(2)	3293(4)	1500(3)	41(1)
C(2*D*)	5382(4)	5895(6)	4092(7)	58(2)	O(2*E*)	7185(2)	3145(3)	1961(3)	32(1)
C(1*E*)	6748(3)	3060(4)	1392(4)	30(1)	O(1*F*)	6012(2)	3061(4)	3164(3)	43(1)
C(2*E*)	6767(3)	2615(6)	536(4)	42(2)	O(2*F*)	6880(2)	2645(3)	3545(3)	40(1)

Note: $U_{eq} = 1.3\Sigma_i\Sigma_j U_{ij} a_i a_j a_i^* a_i^*$.

The crystalline precipitate was quickly filtered off and washed with ethanol and diethyl ether (the yield was 47%). The crystals were kept in a closed vessel, because they lost water in air.

We failed to prepare the target product (**I**) by the reaction of $[Fe_3O(CH_3COO)_6(H_2O)_3]Cl \cdot 5H_2O$ with $(NH_4)_2ZnCl_4$. This mixture gave a brown gelatinous substance.

RESULTS AND DISCUSSION

Structure of the cationic complex. The structure of the cation (Fig. 1) is typical of μ_3-oxo carboxylate complexes of transition metals [5, 9]. Three iron atoms are situated at the corners of an almost regular triangle: Fe(1)–Fe(2) is 3.288(2), Fe(1)–Fe(3) is 3.287(2), and Fe(2)–Fe(3) is 3.295(2) Å. These distances are close to those observed in $[Fe_3O(CH_3COO)_6(H_2O)_3][FeCl_4] \cdot 2CH_3COOH$ (3.296–3.302 Å) [16], $[Fe_3O(CH_3COO)_6(H_2O)_3]NO_3 \cdot 4H_2O$ (av. Fe–Fe is 3.29 Å) [14], $[Fe_3O(CH_3COO)_6(H_2O)_3]Cl \cdot 6H_2O$ (3.285–3.295 Å) [17, 21], $[Fe_3O(C_6H_5COO)_6(H_2O)_3] \cdot 3ClPyH \cdot (CH_3C_6H_4SO_4)_2 \cdot 2H_2O$ (3.283–3.324 Å) [18], and other compounds containing either three Fe atoms or the Fe_2Cr or Fe_2Co nuclei [9, 22–26].

Trinuclear clusters in the compounds of this type owe their formation mainly to the bridges of two types: The μ_3-oxo atom is situated at the center of an almost regular triangle and connects three Fe atoms. The Fe–O(1) distances range between 1.897 and 1.903 Å. Three iron atoms and the O(1) oxygen atom are coplanar. The sum of bond angles at the O(1) atom is 360.0(2)°.

Six acetate ions act as bidentate *syn-syn* bridges [1] and link pairs of iron atoms in the cluster. The Fe–O distances are within 1.991–2.054 Å. Note that the participation of carboxylate oxygens in the hydrogen-bond system as acceptors (see below) naturally increases the Fe–O bond lengths. Thus, the average Fe–O distance for these atoms is 2.049 Å; for the remaining atoms, 2.005 Å.

Water molecules complete the coordination of iron atoms; the Fe–O(H_2O) distances are 2.068–2.087 Å. Thus, the coordination polyhedron of iron is an octahedron, and the coordination number is six. The Fe atoms deviate from the equatorial plane of their octahedra formed by four oxygen atoms by 0.159–0.182 Å toward the μ_3-O atom. The C–O distances in the carboxylate groups have close values and range between 1.241 and 1.263 Å. The C–C(methyl) bond lengths are 1.514 Å.

The $ZnCl_4$ anion has a tetrahedral structure. The angles at the Zn atom range from 104.4(4)° to

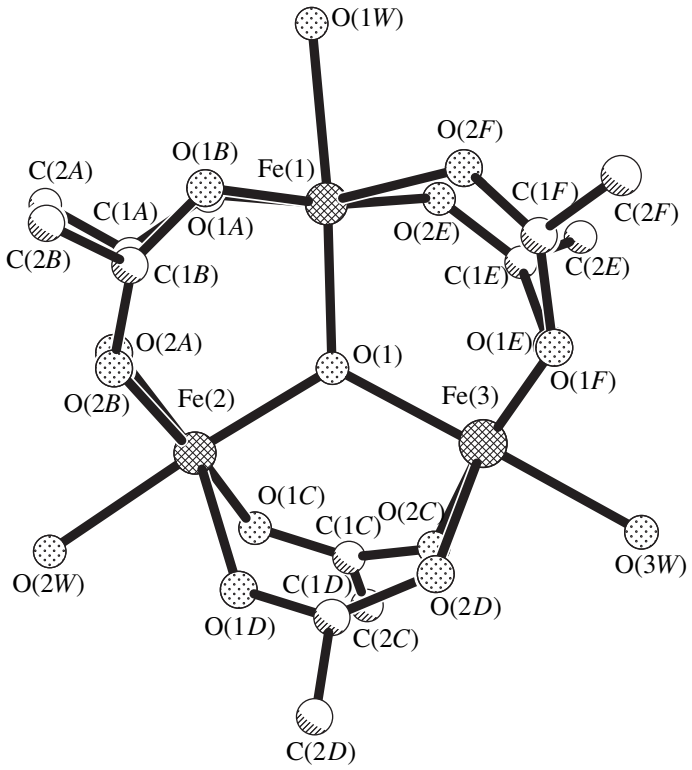

Fig. 1. Cationic complex $[Fe_3O(CH_3COO)_6(H_2O)_3]^+$.

118.0(3)°, and the range of Zn–Cl distances is 2.208–2.331 Å.

System of hydrogen bonds in the crystal. The system of hydrogen bonds (Table 3) interlinks $[Fe_3O(CH_3COO)_6(H_2O)_3]^+$ cations, $[ZnCl_4]^{2-}$ anions, and outer-sphere water molecules in the 2 : 1 : 2 ratio into corrugated layers parallel to the *xy* plane of the crystal (Fig. 2). All of the three coordinated H_2O molecules act as proton donors. The cations are linked through double O(3*W*)–H··O(2*D*) bridges of 2.875 Å into dimers. The reference and symmetry-equivalent (with coordinates $1-x, y, 0.5-z$) cations that form such associates are related by twofold axes parallel to the *y* direction of the crystal. The dimers are linked into layers through hydrogen bonds O(1*W*)–H··O(1*C*) and O(2*W*)–H··O(2*E*) 2.798 and 2.768 Å long, respectively. The $[ZnCl_4]^{2-}$ anions and the O(4*W*) water molecule play specific roles in the association of cations within the layer. The O(1*W*)–Cl(4) and O(2*W*)–Cl(2) bonds (Table 3) additionally link the neighboring cations within the layer. The Cl(1) atom of the anion performs a similar function with the difference that it does not contact the cations directly but is involved in the O(3*W*)–H··O(4*W*)–H··Cl(1) scheme. One of the H atoms of the O(4*W*) molecule is not involved in hydrogen bonding. This, apparently, results from the disordering of the $[ZnCl_4]^{2-}$ anion over two sites and its partial replacement by the Cl^- anion. The Cl^- anions are not involved in the hydrogen-bond system. Probably, the competition of the Cl^- and $[ZnCl_4]^{2-}$ anions during the crystal growth is responsible for the disordering of the latter ions. We cannot exclude that, along with Cl^- ions, some water amount is included in the packing.

Mössbauer spectra. The Mössbauer spectra of the complex represent a doublet. The parameters of its components are given in Table 4. The analysis of these data allows us to conclude that the iron(III) ions in the complex are in the high-spin state ($S = 5/2$) [27].

Table 3. Characteristics of possible hydrogen bonds

Donor (D) ... Acceptor (A)	D ... A, Å	D–H ... A angle, deg
O(1*W*)···O(1*C*) (1)	2.798(8)	134
O(1*W*)···Cl(4) (2)	3.226(8)	141
O(2*W*)···O(2*E*) (3)	2.768(8)	142
O(2*W*)···Cl(2) (4)	3.145(8)	153
O(3*W*)···O(2*D*) (5)	2.875(8)	161
O(3*W*)···O(4*W*) (6)	2.617(8)	158

Symmetry transformations for A: (1) $1.5-x, -0.5+y, 0.5-z$; (2) $0.5+x, 0.5-y, -0.5+z$; (3) $1.5-x, 0.5+y, 0.5-z$; (4) $1-x, 1-y, 1-z$; (5) $1-x, y, 0.5-z$; and (6) $1-x, -y, 1-z$.

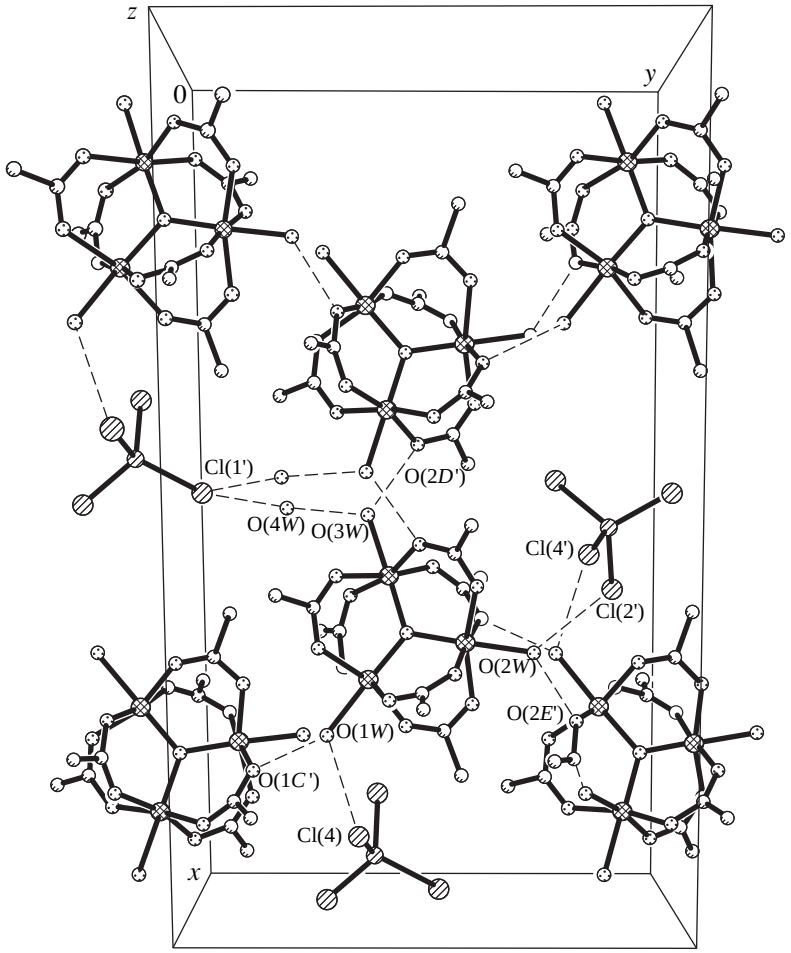

Fig. 2. A fragment of the crystal structure of compound $[Fe_3O(CH_3COO)_6(H_2O)_3]_2[ZnCl_4] \cdot 2H_2O$.

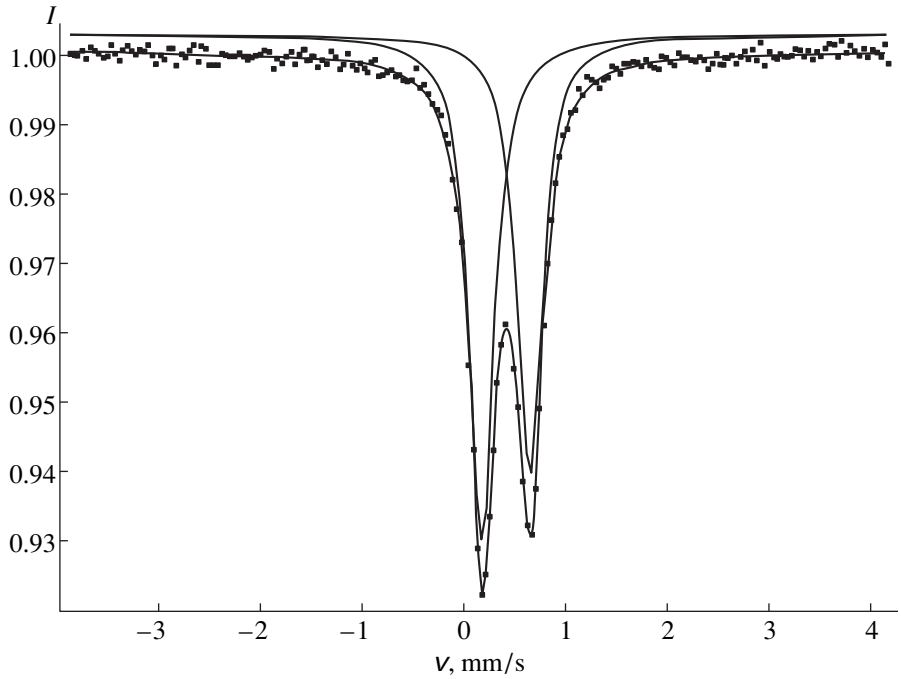

Fig. 3. Mössbauer spectra of a complex powder at different temperatures.

Table 4. Parameters of the Mossbauer spectra of the complex, mm/s

T, K	Isomer shift of ^{57}Fe	Quadrupole splitting	I_{left}/I_{right}
300	0.48	0.47	0.30/0.31
77	0.49	0.57	0.84/0.84
13.5	0.51	0.56	0.85/0.85

Lowering temperature results in the increase in isomer shift due to the second-order Doppler effect, which is usual for the ^{57}Fe isotope [28]. No distinct change in the value of the quadrupole splitting and, hence, in the electric-field gradient, is observed upon substitution of a $[ZnCl_4]^{2-}$ anion for chlorine counterions. Apparently, as predicted by quantum-chemical calculations [29, 30], the major contribution to the value of quadrupole splitting is made by valence electrons rather than by the lattice.

At room temperature, the doublet Mössbauer spectrum (Fig. 3) is distinctly asymmetric (the ratio of peak intensities I_{left}/I_{right} is 1.14), apparently, because of relaxation processes [31].

IR spectra. In the IR spectrum of the complex considered, very broad absorption bands are observed in the 3600–3000 cm^{-1} region. They are assigned to the ν_{OH} stretching vibrations of the coordinated and crystallization water molecules that are involved in hydrogen bonding. The intense absorption bands characteristic of the acetate groups appear at ca. 1575 and 1440 cm^{-1}. They are assigned to $\nu_{as}(COO^-)$ and $\nu_s(COO^-)$, respectively [5]. The moderate band assigned to the $\delta(OCO)$ vibrations is observed at ca. 665 cm^{-1}. The vibrations characteristic of the Fe_3O fragment [$\nu_{as}(Fe_3O)$] [5] give rise to a moderate band at 600–610 cm^{-1}.

REFERENCES

1. M. A. Poraĭ-Koshits, Itogi Nauki Tekh., Ser.: Kristallokhim. **15**, 3 (1981).
2. B. O. West, Polyhedron **4**, 219 (1989).
3. E. L. Muettertis, Catal. Rev. **23** (2), 69 (1981).
4. R. C. Mehrota and R. Bohra, *Metal Carboxylates* (Academic Press, London, 1983).
5. R. D. Cannon and R. P. White, Progr. Inorg. Chem. **36**, 196 (1988).
6. S. I. Lippard, Angew. Chem. Int. Ed. Engl. **27**, 344 (1988).
7. B. Vincent, G. L. Oliver-Lilley, and B. A. Averill, Chem. Rev. **90** (8), 1447 (1990).
8. R. R. Crichton, *Inorganic Biochemistry of Iron Metabolism* (Harvard, New York, 1991).
9. K. Anzenhofer and J. J. de Boer, Rec. Trav. Chim. Pays-Bas **88** (3), 286 (1969).
10. K. Wieghardt, K. Pohl, I. Jibril, and C. Huttner, Angew. Chem. **96**, 66 (1984).
11. K. L. Taft, G. C. Papaefthymiou, and S. J. Lippard, Science **259**, 1302 (1993).
12. W. Micklitz and S. J. Lippard, J. Am. Chem. Soc. **111** (17), 6856 (1989).
13. A. K. Powell, S. L. Heath, and D. Gatteschi, J. Am. Chem. Soc. **117** (9), 2491 (1995).
14. C. I. Turta, S. G. Shova, and F. A. Spatar', Zh. Strukt. Khim. **35** (2), 112 (1994).
15. T. Glowiak, M. Kubiak, T. Szymanska-Buzar, and B. Jezowska-Tyzebiatowska, Acta Crystallogr., Sect. B **33**, 3106 (1977).
16. S. Shova, C. Turta, I. Cadelńic, and V. Meriacre, in *Proceedings of the Conference on Chemistry and Chemical Technology, Bucharest, Romania, 1997* (Bucharest, 1997), Vol. 1, p. 1.
17. S. G. Shova, I. G. Cadelńic, and M. Gdaniec, Zh. Strukt. Khim. **39** (5), 917 (1999).
18. I. Cadelńic, S. Shova, and Yu. A. Simonov, Pol. J. Chem. **71**, 501 (1997).
19. G. M. Sheldrick, Acta Crystallogr., Sect. A **46**, 467 (1990).
20. G. M. Sheldrick, *SHELXL93: Program for the Refinement of Crystal Structures* (Univ. of Göttingen, Göttingen, 1993).
21. C. E. Anson, J. P. Bourke, and R. D. Cannon, Inorg. Chem. **36**, 1265 (1997).
22. V. M. Lynch, J. M. Sibert, J. L. Sessler, and B. E. Davis, Acta Crystallogr., Sect. C **47** (4), 866 (1991).
23. T. Sato and F. Ambe, Acta Crystallogr., Sect. C **52**, 3005 (1996).
24. S. G. Shova, I. G. Cadelńic, and T. C. Jovmir, Koord. Khim. **23** (9), 672 (1997) [J. Coord. Chem. **23**, 629 (1997)].
25. C. I. Turta, A. G. Lézéresku, and Yu. A. Simonov, Koord. Khim. **22** (1), 45 (1996) [J. Coord. Chem. **22**, 42 (1996)].
26. F. Degang, W. Guoxiong, T. Wenxia, and Y. Kaibei, Polyhedron **12** (20), 2459 (1993).
27. *Chemical Applications of Mössbauer Spectroscopy*, Ed. by V. I. Goldanskiĭ and R. H. Herber (Academic Press, New York, 1968; Mir, Moscow, 1970).
28. R. V. Pound and G. A. Rebka, Phys. Rev. Lett. **4** (5–6), 274 (1960).
29. F. A. Spatar', A. T. Lézéresku, and C. I. Turta, Zh. Obshch. Khim. **66** (1), 12 (1996).
30. F. A. Spatar', V. M. Meriakre, and V. E. Zubareva, Koord. Khim. **22** (3), 188 (1996) [J. Coord. Chem. **22**, 176 (1996)].
31. G. Filotti, V. Meriacre, and A. Avramescu, in *Proceedings of ICAME-95* (Rimini, Italy, 1995), O1–D9.

Translated by I. Polyakova

Crystallography Reports, Vol. 45, No. 3, 2000, pp. 422–423. Translated from Kristallografiya, Vol. 45, No. 3, 2000, pp. 465–466.

STRUCTURES OF COORDINATION COMPOUNDS

Crystal Structure of *catena*-Poly[diaqua(μ-iminodiacetato-N,O,O' : O'')cobalt(II)]

I. F. Burshteĭn* and A. L. Poznyak**

** Analytical X-ray Instrumentation Department, Siemens Energy and Automation Inc., 6300 Enterprise Lane, Madison, Wisconsin, USA*

*** Institute of Molecular and Atomic Physics, Belarussian Academy of Sciences, pr. F. Skoriny 70, Minsk, 220072 Belarus*

Received April 13, 1998

Abstract—The crystal structure of the $[Co(C_4H_5NO_4)(H_2O)_2]$ complex has been determined by X-ray diffraction analysis (λMo, $R = 0.0237$ for 768 reflections). The crystals are orthorhombic, $a = 14.345(1)$ Å, $b = 5.234(1)$ Å, $c = 9.780(1)$ Å, $Z = 4$, $d_{calcd} = 2.045$ g cm^{-3}, and space group $Pca2_1$. The donor atoms (one N and two O atoms) of the iminodiacetate ion (*Ida*) are located on the same octahedron face around the Co atom [Co–N, 2.120(3) Å; Co–O, 2.063(3) and 2.151(3) Å]. The O atoms of two water molecules are in the *trans* positions relative to the O atoms of the carboxylate groups [Co–O, 2.126(3) and 2.157(3) Å]. The sixth coordination site is occupied by the O atom of the adjacent *Ida* ion [Co–O, 2.054(3) Å], which results in the formation of infinite chains in the structure. © *2000 MAIK "Nauka/Interperiodica".*

EXPERIMENTAL

X-ray diffraction analysis of the cobalt(II) complex with the iminodiacetate ion (*Ida*) was carried out. The compound $[Co(Ida)(H_2O)_2]$ (**I**) was prepared upon slow cooling of a hot solution of equimolar amounts of $Co(CH_3CO_2)_2 \cdot 4H_2O$ and $HN(CH_2CO_2H)_2$. Crystals **I** are orthorhombic, $a = 14.345(1)$ Å, $b = 5.234(1)$ Å, $c = 9.780(1)$ Å, $V = 734.30(9)$ Å^3, $Z = 4$ (the formula unit is $C_4H_9CoNO_6$), $d_{calcd} = 2.045$ g cm^{-3} and space group $Pca2_1$. The intensities of reflections were measured on a Siemens P4 automated diffractometer (λMoK_α, graphite monochromator, $2\theta_{max} = 50°$). The structure was solved by the direct method and then was refined by the full-matrix least-squares procedure in the anisotropic approximation to $R_1 = 0.0237$ and $wR_2 = 0.0607$ for 768 reflections with $I > 2\sigma(I)$. The positions of the hydrogen atoms were determined at the final stage of calculations. All the calculations were performed with the use of the XP [1] and SHELXTL [2, 3] software packages. The atomic coordinates and the equivalent thermal parameters are listed in the table.

RESULTS AND DISCUSSION

The Co atom adopts a distorted octahedral coordination formed by three donor atoms (one N and two O atoms located on the same octahedron face) of the *Ida* ligand, the O(1*w*) and O(2*w*) oxygen atoms (in the *trans* positions relative to the carboxylate O atoms) of two water molecules, and the O(4*A*) atom of the adjacent *Ida* ion. Thus, the *Ida* ligand is bonded to two Co(II) ions, and, each of them, in turn, coordinates two *Ida* ligands, which results in the formation of the infinite chains $[Co(Ida)(H_2O)_2]_n$ (figure). Therefore, crystals **I** have a polymeric structure. Each chain involves the hydrogen bonds O(1*w*)–H··O(3') $(1 - x, 1 - y, 1/2 + z)$ 2.932(5) Å, and particular chains are linked together into a three-dimensional network through the hydrogen bonds O(2*w*)–H··O(2') $(1/2 + x, 1 - y, z)$ 2.659(4) Å and O(2*w*)–H··O(4') $(1 - x, -y, 1/2 + z)$ 2.931(5) Å.

The completely deprotonated ion *Ida* acts as a tridentate ligand virtually in all the known complexes with metal ions (the bidentate coordination of the *Ida* ion was described, for example, in [4]). To the best of our knowledge, among the *M*(*Ida*)-type complexes containing no additional ligands (except water mole-

Atomic coordinates (×10^4) and equivalent isotropic thermal parameters (×10^3, Å^2)

Atom	*x*	*y*	*z*	U_{eq}
Co	4356(1)	3782(1)	5045(1)	19(1)
O(1)	3444(2)	6683(5)	5540(4)	28(1)
O(2)	2088(2)	8403(5)	5026(6)	37(1)
O(3)	4672(2)	5363(5)	3068(3)	25(1)
O(4)	4586(2)	4104(5)	896(3)	26(1)
O(1*w*)	3946(3)	1399(7)	6698(4)	31(1)
O(2*w*)	5302(2)	783(7)	4441(4)	28(1)
N	3202(2)	2598(7)	3850(4)	20(1)
C(1)	2477(3)	4575(9)	3908(5)	28(1)
C(2)	2686(2)	6695(6)	4913(5)	25(1)
C(3)	3574(3)	2137(8)	2466(5)	24(1)
C(4)	4332(2)	4035(7)	2138(5)	20(1)

1063-7745/00/4503-0422$20.00

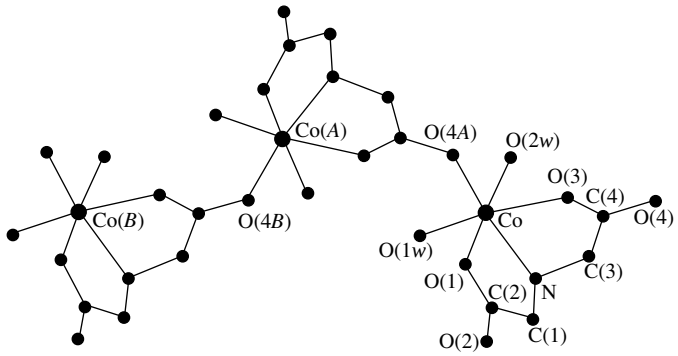

A fragment of the $[Co(Ida)(H_2O)_2]_n$ chain. Bond lengths (Å): Co–O(1*w*), 2.126(3); Co–O(2*w*), 2.157(3); Co–O(1), 2.063(3); Co–O(3), 2.151(3); Co–O(4*A*), 2.054(3); and Co–N, 2.120(3). Bond angles: O(3)CoN, 77.4(1)° and O(1)CoN, 81.3(1)°. Symmetry transformation for the O(4*A*) atom: $1 - x, 1 - y, z + 1/2$.

cules or hydroxyl ions), only the crystals of $[Cu(Ida)(H_2O)_2]$ [5, 6] and $[Al_2(\mu\text{-}OH)_2(Ida)_2(H_2O)_2] \cdot 2H_2O$ [7] have hitherto been characterized structurally. The former crystals, like **I**, involve chain polymers, whereas the latter crystals consist of the hydroxo-bonded dimers. As regards the Co(II) complexes with the *Ida* ion, only the structure containing the discrete ions $[Co(Ida)_2]^{2-}$ was described in the literature [8]. The bond lengths and angles in the coordination octahedron of the Co(II) ion in structure **I** are comparable to those in the $[Co(Ida)_2]^{2-}$ ion [8] or complexes with a related ligand—the nitrilotriacetate ion [9].

ACKNOWLEDGMENTS

This work was supported in part by the Belarussian Republican Foundation for Basic Research, project no. F96-92.

REFERENCES

1. *XP: Interactive Molecular Graphics Program, Version 5.03* (Siemens Analytical X-ray Instrumentation Inc., Madison, Wis., 1994).
2. G. M. Sheldrick, *SHELXL93: Program for the Refinement of Crystal Structures* (Univ. of Göttingen, Göttingen, 1993).
3. G. M. Sheldrick, *SHELXTL: Version 5.0, Reference Manual* (Siemens Analytical X-ray Instrumentation Inc., Madison, Wis., 1994).
4. I. V. Kuz'menko, T. N. Polynova, M. A. Poraĭ-Koshits, and A. L. Poznyak, Koord. Khim. **19** (2), 138 (1993).
5. F. G. Kramarenko, T. N. Polynova, M. A. Poraĭ-Koshits, *et al.*, Zh. Strukt. Khim. **14** (4), 744 (1973).
6. A. Podder, J. K. Dattagupta, N. N. Saha, and W. Saenger, Acta Crystallogr., Sect. B **35** (1), 53 (1979).
7. S. P. Petrosyants, S. P. Malyarik, and A. B. Ilyukhin, Zh. Neorg. Khim. **40** (5), 769 (1995).
8. Ya. M. Nesterova, T. N. Polynova, M. A. Poraĭ-Koshits, *et al.*, Zh. Strukt. Khim. **20** (5), 960 (1979).
9. L.-P. Battaglia, A. B. Corradi, and M. E. Vidoni Tani, Acta Crystallogr., Sect. B **31** (4), 1160 (1975).

Translated by O. Borovik-Romanova

Crystallography Reports, Vol. 45, No. 3, 2000, pp. 424–431. Translated from Kristallografiya, Vol. 45, No. 3, 2000, pp. 467–474.

STRUCTURES OF COORDINATION COMPOUNDS

Crystal Structure of Calcium (Ornithinato-$N_{(\alpha)}$,$N_{(\delta)}$,$N_{(\delta)}$-triacetato)cobaltate(III) Octahydrate Ca[Co(*Orntra*)]$_2 \cdot 8H_2O$

A. S. Antsyshkina*, G. G. Sadikov, A. L. Poznyak, and V. S. Sergienko***

** Kurnakov Institute of General and Inorganic Chemistry, Russian Academy of Sciences, Leninskiĭ pr. 31, Moscow, 117907 Russia*

e-mail: asants@ionchran.rinet.ru

*** Institute of Molecular and Atomic Physics, Belarussian Academy of Sciences, pr. F. Skoriny 70, Minsk, 220072 Belarus*

Received April 6, 1998

Abstract—The X-ray crystal structure of calcium (ornithinato-$N_{(\alpha)}N_{(\delta)}N_{(\delta)}$-triacetato)cobaltate(III) octahydrate Ca[Co(*Orntra*)]$_2 \cdot 8H_2O$ has been determined. The crystals are orthorhombic, a = 21.163(4) Å, b = 8.391(2) Å, c = 19.101(4) Å, V = 3391.9(9) Å^3, Z = 4, and space group $Pca2_1$. In the trinuclear linear molecule [Co(μ-*Orntra*)]$_2$Ca(H_2O)$_5$, two independent anions [Co(*Orntra*)]$^-$ are joined with the Ca^{2+} cation by the bridging bonds through the terminal O atoms. In each [Co(*Orntra*)]$^-$ anion, the Co atom occurs in the octahedral environment of two N atoms and four O atoms of the *Orntra* ligand and closes four five-membered and one seven-membered chelate rings. Two O atoms of two anions occupy axial vertices in a pentagonal bipyramid of the Ca^{2+} ion. Five O(H_2O) atoms are located in the equatorial plane. The asymmetric C atoms in the anions bound to the same Ca^{2+} cation have an identical absolute configuration. The crystal involves the molecules belonging to both configurations. The coordinated and outer-sphere H_2O molecules participate in an extended system of hydrogen bonds. *© 2000 MAIK "Nauka/Interperiodica".*

The most abundant chelating compound—ethylenediaminetetraacetic acid H_4*Edta*—is comprised of 1,2-ethanediamine with two carbon atoms between nitrogen atoms. There exist *Edta* analogues based on 1,3-propanediamine (1,3-*Pdta*) and 1,4-butanediamine (1,4-*Bdta*), in which the bridge between nitrogen atoms consists of three or four carbon atoms. Ornithine $H_2N_{(\delta)}$–$(CH_2)_3$–CH(COOH)$N_{(\alpha)}H_2$ (H*Orn*), which belongs to the natural amino acids, involves two nitrogen atoms linked by a chain of four carbon atoms. This amino acid can be used in synthesis of the diaminopolycarboxylate ligands. In order to obtain an *Edta* analogue, i.e., a hexadentate ligand, three carboxyalkyl groups should be attached to the nitrogen atoms. The synthesis of the cobalt(III) complex with the ornithinetriacetate (*Orntra*) ion was described in [1]. The *Orntra* ion can occur in two isomer forms differing in the distribution of three acetate groups over two nonequivalent nitrogen atoms of the ornithine fragment. Reasoning from the ^{1}H NMR spectrum, it was assumed that two acetate groups are attached to the $N_{(\alpha)}$ atom [1]. In the present work, we attempted to verify this assumption and to reveal the general structural features of the *Orntra* ligand in the octahedral complex. For this purpose, we prepared single crystals of Ca[Co(*Orntra*)]$_2 \cdot 8H_2O$ (**I**) and determined their structure by the X-ray diffraction analysis.

EXPERIMENTAL

Synthesis of compound I. Complex **I** was synthesized from the Ba[Co(*Orntra*)]ClO_4 compound according to the procedure described in [1]. A solution of Ba[Co(*Orntra*)]ClO_4 was passed through a column with a cation in the H^+ form, and the eluate was neutralized by calcium carbonate. A slow evaporation of the obtained solution resulted in the precipitation of crystals **I**.

X-ray diffraction analysis. Compound **I** crystallizes in the orthorhombic crystal system. The unit cell parameters are as follows: a = 21.163(4) Å, b = 8.391(2) Å, c = 19.101(4) Å, V = 3391.9(9) Å^3, M = 906.5, F(000) = 1880, d_{calcd} = 1.775 g/cm^3, $\mu_{(Mo)}$ = 1.23 mm^{-1}, Z = 4, and space group $Pca2_1$.

A set of experimental data for X-ray structure analysis was collected on a Syntex $P2_1$ automated diffractometer (λMoK_α, graphite monochromator, $\theta/2\theta$ scan mode, $2\theta \le 60°$). A total of 6454 reflections were measured, of which 6433 reflections with $F \ge 4\sigma(F)$ were used in the structure refinement.

The structure was solved by the heavy-atom method. Hydrogen atoms of the ligand were specified from geometric considerations at a distance of 0.96 Å from the corresponding basis atoms and refined with them according to the riding-atom model with the same isotropic thermal parameter equal to 0.08 Å^2. The

Table 1. Atomic coordinates and thermal parameters U_{eq} in structure **I**

Atom	*x*	*y*	*z*	U_{eq}, Å^2
Ca	0.1827(1)	0.4228(2)	0	0.0417(3)
Co(1)	0.35977(4)	0.0049(1)	0.1834(1)	0.0317(2)
Co(2)	−0.06418(4)	0.4845(1)	−0.1681(1)	0.0327(2)
N(1*a*)	0.3794(3)	0.0068(8)	0.0834(3)	0.038(1)
N(2*a*)	0.4012(3)	−0.1916(7)	0.2125(3)	0.036(1)
O(1*a*)	0.4346(3)	0.1211(7)	0.1978(3)	0.041(1)
O(2*a*)	0.5070(3)	0.264(1)	0.1420(4)	0.059(2)
O(3*a*)	0.3128(3)	0.1914(6)	0.1608(3)	0.039(1)
O(4*a*)	0.2544(4)	0.2930(8)	0.0757(4)	0.058(2)
O(5*a*)	0.3404(3)	0.0357(6)	0.2787(3)	0.039(1)
O(6*a*)	0.3681(4)	−0.038(1)	0.3852(4)	0.064(2)
O(7*a*)	0.2852(2)	−0.1180(6)	0.1738(3)	0.041(1)
O(8*a*)	0.2475(3)	−0.3608(8)	0.1945(4)	0.054(1)
C(1*a*)	0.4604(4)	0.178(1)	0.1416(4)	0.044(2)
C(2*a*)	0.4293(4)	0.132(1)	0.0727(4)	0.046(2)
C(3*a*)	0.2916(4)	0.195(1)	0.0972(4)	0.041(1)
C(4*a*)	0.3189(4)	0.064(1)	0.0502(4)	0.042(1)
C(5*a*)	0.3707(4)	−0.0527(9)	0.3226(4)	0.042(1)
C(6*a*)	0.4121(5)	−0.179(1)	0.2892(4)	0.047(2)
C(7*a*)	0.2914(4)	−0.2679(9)	0.1884(5)	0.044(1)
C(8*a*)	0.3601(4)	−0.3267(8)	0.1916(5)	0.043(2)
C(9*a*)	0.3780(5)	−0.396(1)	0.1207(6)	0.053(2)
C(10*a*)	0.3641(5)	−0.294(1)	0.0571(6)	0.058(2)
C(11*a*)	0.4034(4)	−0.143(1)	0.0470(5)	0.048(2)
N(1*b*)	−0.1325(3)	0.4505(8)	−0.2353(3)	0.037(1)
N(2*b*)	−0.0104(3)	0.3056(7)	−0.1887(4)	0.040(1)
O(1*b*)	−0.0236(3)	0.6069(7)	−0.2372(3)	0.042(1)
O(2*b*)	−0.0401(3)	0.7333(9)	−0.3379(4)	0.058(2)
O(3*b*)	−0.1157(3)	0.6587(7)	−0.1385(3)	0.046(1)
O(4*b*)	−0.2183(4)	0.716(1)	−0.1263(5)	0.072(2)
O(5*b*)	−0.0020(3)	0.5444(7)	−0.1024(3)	0.043(1)
O(6*b*)	0.0958(4)	0.4996(9)	−0.0680(4)	0.061(2)
O(7*b*)	−0.1003(3)	0.3539(7)	−0.0975(3)	0.040(1)
O(8*b*)	−0.0958(3)	0.1134(7)	−0.0508(3)	0.052(1)
C(1*b*)	−0.0574(4)	0.645(1)	−0.2903(4)	0.043(2)
C(2*b*)	−0.1240(4)	0.574(1)	−0.2921(5)	0.047(2)
C(3*b*)	−0.1754(4)	0.634(1)	−0.1494(4)	0.044(2)
C(4*b*)	−0.1906(4)	0.490(1)	−0.1946(5)	0.043(1)
C(5*b*)	0.0503(4)	0.471(1)	−0.1063(5)	0.045(2)
C(6*b*)	0.0541(3)	0.3450(9)	−0.1614(5)	0.046(2)
C(7*b*)	−0.0802(4)	0.210(1)	−0.0959(4)	0.041(1)
C(8*b*)	−0.0370(4)	0.1588(9)	−0.1569(4)	0.041(1)
C(9*b*)	−0.0777(4)	0.066(1)	−0.2074(5)	0.047(2)
C(10*b*)	−0.1424(2)	0.140(1)	−0.2252(5)	0.048(2)
C(11*b*)	−0.1406(4)	0.290(1)	−0.2724(5)	0.044(2)
O(*w*1)	0.1064(4)	0.224(1)	0.0386(5)	0.070(2)
O(*w*2)	0.2039(3)	0.2211(8)	−0.0850(4)	0.056(1)
O(*w*3)	0.2786(4)	0.4950(9)	−0.0611(5)	0.067(2)
O(*w*4)	0.1954(5)	0.723(1)	−0.0086(5)	0.078(2)
O(*w*5)	0.1449(4)	0.543(1)	0.1099(4)	0.065(2)
O(*w*6)	0.2038(3)	0.3795(9)	−0.2142(4)	0.059(2)
O(*w*7)	−0.0900(5)	0.607(1)	0.5304(6)	0.088(3)
O(*w*8)	0.0071(6)	0.639(2)	0.4433(7)	0.103(3)

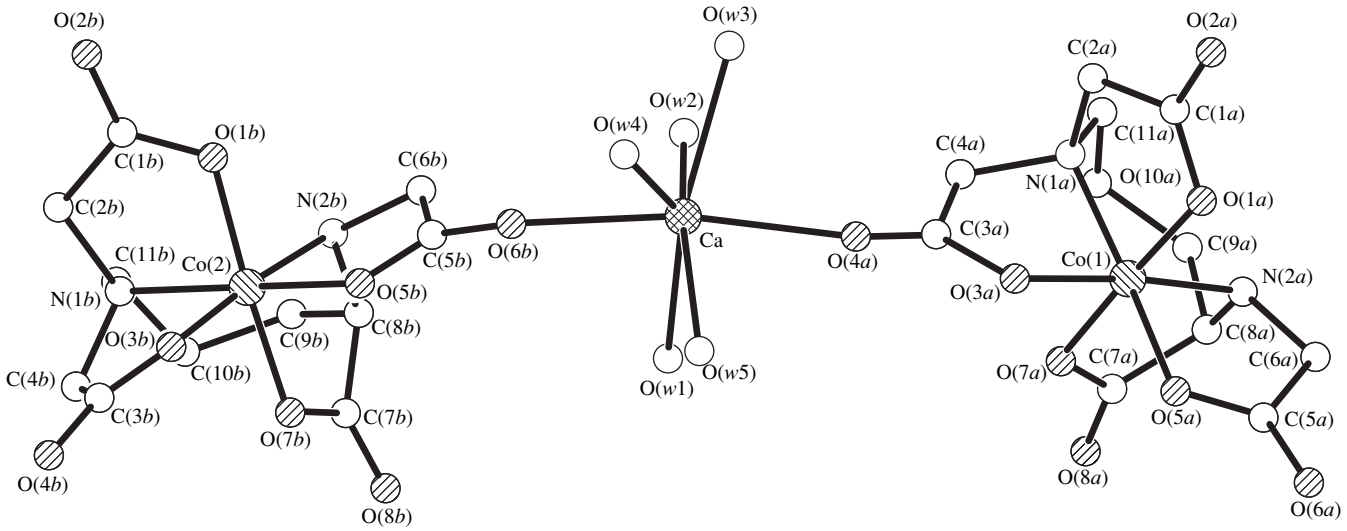

Fig. 1. A general view of neutral molecule **I**.

hydrogen atoms of H_2O molecules were not located. The non-hydrogen atoms were refined by the full-matrix least-squares procedure in the anisotropic approximation. The final values were as follows: $R1$ = 0.0408 (0.045 for 6454 reflections), $wR2$ = 0.099, and $GOOF$ = 1.046.

The calculations were performed on a Pentium-75 IBM computer according to the SHELXL93 [2] software package.

Table 1 lists the atomic coordinates.

RESULTS AND DISCUSSION

The trinuclear linear molecules [Co(μ-*Orntra*)]$_2$Ca$(H_2O)_5$ (Fig. 1) and the crystallization water molecules are the structural units of the crystals. In the molecular complex, the two independent anions [Co(*Orntra*)]$^-$ are joined with the Ca^{2+} cation by the bridging bonds through the terminal O atoms. Five H_2O molecules are coordinated to the Ca^{2+} cation. In each [Co(*Orntra*)]$^-$ anion, the Co atom occurs in the octahedral environment of two N atoms and four O atoms of the *Orntra* ligand, thus closing four five-membered and one seven-membered chelate rings. In both anions, two acetate groups are attached to the $N_{(\delta)}$ (N(1*a*,1*b*)) atom, and one acetate group is bound to the $N_{(\alpha)}$ (N(2*a*,2*b*)) atom. These findings disprove the assumption on the distribution of these groups, which was made in [1] from the analysis of the ^{1}H NMR spectra of [Co(*Orntra*)]$^-$ ions in acid solutions.

In both anions, the seven-membered chelate rings formed upon chelation of the *Orntra*$^{4-}$ ligand are completely identical. In each chelate ring (Fig. 2), it is possible to distinguish a triangular fragment involving the central metal atom and the N atoms bonded to it. The rest of the chelate ring, i.e., the N(1)N(2)C(8)C(9)C(10)C(11) fragment, represent a certain invariant of seven-membered rings, because this fragment retains its configuration from compound to compound. The six-membered fragment with the approximate C_2 symmetry involves the planar trapezoid N(1)N(2)C(9)C(10) depicted by dashed lines in Fig. 2. The C(8) and C(11) atoms in the ring deviate from the trapezoid plane in opposite directions by approximately the same distances. The most essential difference in conformations of the seven-membered rings in different compounds is the deviation of the six-membered fragment (and its trapezoid part) from the plane of the central NCoN core. Table 3 presents the selected parameters characterizing the seven-membered chelate rings in compounds: *cis*-[Co$(NO_2)_2$(*Tmd*)$_2$](NO_3) · nH$_2$O (**II**) and *trans*-[Co$(NO_2)_2$(*Tmd*)$_2$](NO_3) · nH$_2$O

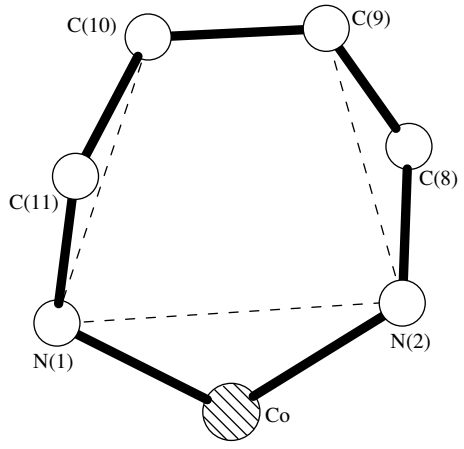

Fig. 2. Projection of the seven-membered ring onto the plane of characteristic trapezoid (depicted by dashed lines). The C(8) and C(11) atoms are deviated from the figure plane in opposite directions (see Table 3).

Table 2. Parameters characterizing the conformation of seven-membered chelate rings in cobalt(III) compounds

Compound	C–C, Å	N···N, Å	ΔÅ	ΔC(8)	ΔC(11)	ΔCo	∠NCoN	Reference
II*a*	1.52	2.84	0.01	0.76	–0.76	0.00	93°	[3]
II*b**	1.508	2.88	0.01	0.75	–0.75	0.02	92°	[3]
II*c*	1.51	2.85	0.03	0.78	–0.78	0.08	92°	[3]
II*d*	1.515	2.84	0.02	0.75	–0.79	0.12	93°	[3]
IV*	1.517	3.16	0.05	0.62	–0.70	0.17	105°	[4]
III*a*	1.524	2.87	0.02	0.63	–0.77	0.57	93°	[3]
III*b**	1.525	2.87	0.03	0.60	–0.75	0.69	93°	[3]
V*a*	1.567	2.91	0.01	0.75	–0.79	0.79	95°	[5]
V*b*	1.581	2.905	0.04	0.81	–0.82	0.73	96°	[5]
I*a**	1.512	3.01	0.02	0.69	–0.74	0.83	101°	This work
I*b*	1.504	2.99	0.03	0.68	–0.74	0.82	101°	This work

Note: Δ is the root-mean-square deviation of atoms of the central trapezoid N(1)C(9)C(10)N(2); and ΔC(8), ΔC(11), and ΔCo are the deviations of atoms (or their analogues taken from the cited works) from the trapezoid plane (in Å).

* The data correspond to Fig. 3.

Table 3. Conformations of the chelate rings in the $[Co(Orntra)]^-$ anions

$[Co(1)(Orntra)]^-$				
Parameter	$N_{(\delta)}$		$N_{(\alpha)}$	
	G ring	*R* ring	*G* ring	*R* ring
	Co(1)N(1)C(4)C(3)O(3)	Co(1)N(1)C(2)C(1)O(1)	Co(1)N(2)C(6)C(5)O(5)	Co(1)N(2)C(8)C(7)O(7)
Q, Å	0.48	0.20	0.23	0.26
φ, deg	22.7	24.4	21.8	242.1
Conformation	T_{12}	T_{12}	T_{12}	$T_{23} \longrightarrow -E_3$
$[Co(2)(Orntra)]^-$				
	G ring	*R* ring	*G* ring	*R* ring
	Co(2)N(1)C(4)C(3)O(3)	Co(2)N(1)C(2)C(1)O(1)	Co(2)N(2)C(6)C(5)O(5)	Co(2)N(2)C(8)C(7)O(7)
Q, Å	0.48	0.21	0.23	0.23
φ, deg	22.3	23.0	30.9	229.9
Conformation	T_{12}	T_{12}	$-E_2 \longrightarrow T_{12}$	$T_{23} \longrightarrow E_2$

(**III**) (where *Tmd* is 1,4-butanediamine) [3], $[Co(Dbata)][Mg(H_2O)_6]$ (**IV**) (where *Dbata* is the 1,4-butanediamine *N*,*N*,*N*',*N*'-tetraacetate) [4], and the $[Co(Orn)_2]^+$ cation (where H*Orn* is ornithine) [5]. Figure 3 demonstrates the structures of the known Co(III) complexes in the same aspect, which permits one to visually assess the degree of deviation of the six-membered fragment from the conventionally equatorial plane of the corresponding octahedral complexes. In the aforementioned compounds, the tilt angle τ of the invariant fragment of the ring, i.e., the angle of folding along the N(1)··N(2) straight line, varies from 0° to 42°. Until presently, all attempts to reveal the regularity of variations in this parameter have failed, because no correlation is observed even with such a seemingly characteristic parameter as the N(1)CoN(2) angle. Hence, a pronounced correlation between the τ angle and the type of complexing metal cannot be expected as well. Most likely, this parameter is affected by external factors such as steric hindrances (for example, the effect of van der Waals interactions of the axial NO_2 groups in the *trans*-$[Co(NO_2)_2(Tmd)_2]^+$ cation [3]). The largest angles τ = 42.2° and 41.5° are observed in both cationic complexes of the studied compound **I** (Fig. 3), which is apparently due to the participation of the C(8) atom in the formation of the adjacent "rigid" five-membered ring. As follows from Table 3, the five-membered ring, in turn, undergoes a strong deformation. In all the compounds presented in Table 2, the six-membered fragment of the seven-membered chelate ring adopts the conformation of a slightly distorted chair, which, probably, is the most appropriate for the relaxation of

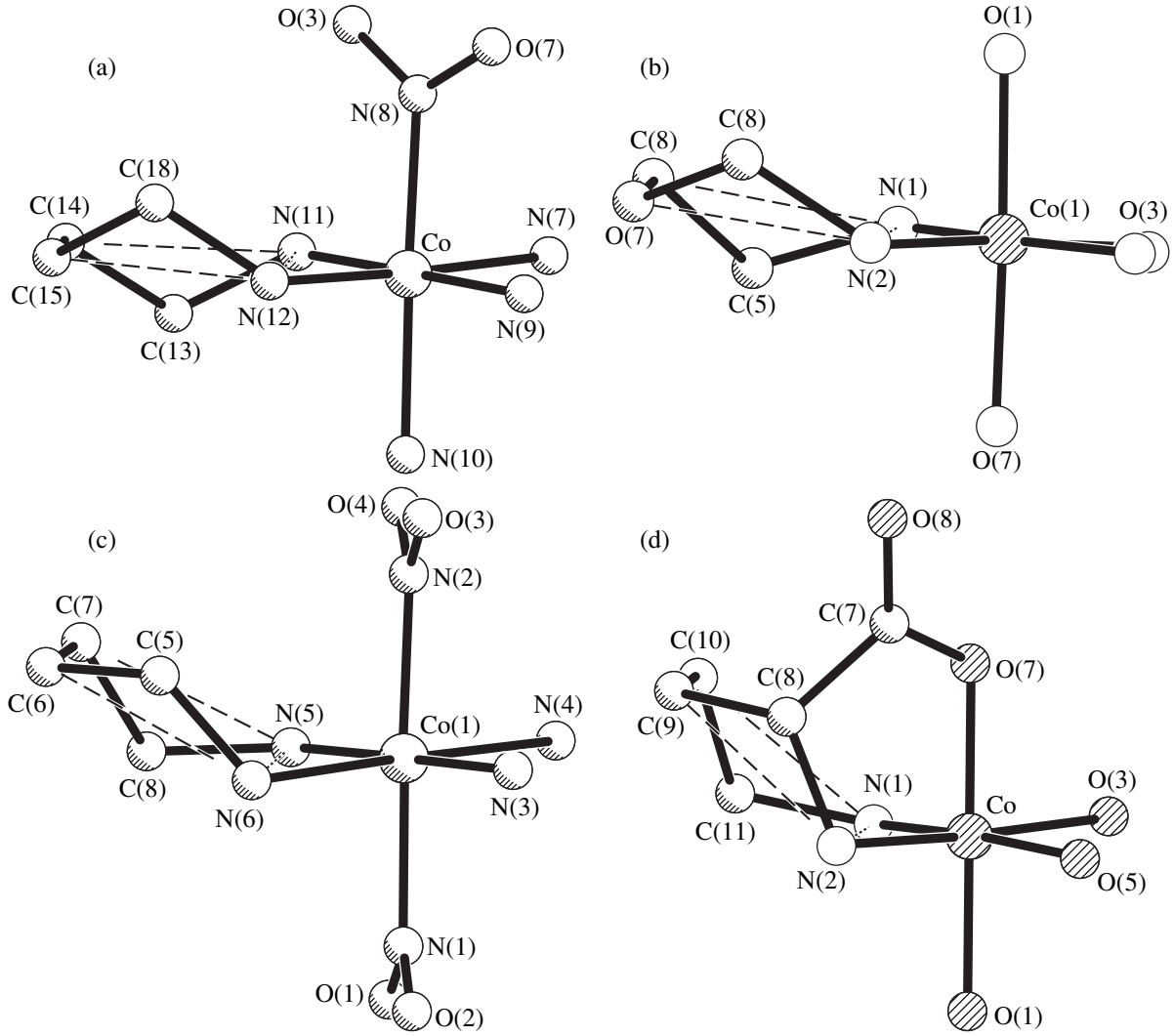

Fig. 3. Evolution of the conformation of the seven-membered chelate rings in cobalt(III) compounds. Fragments of the complexes: (a) *cis*-$[Co(NO_2)_2(Tmd)_2]^{2+}$ (*Tmd* is 1,4-butanediamine) [3], (b) $[Co(Dbata)]^{2-}$ (*Dbata* is the 1,4-butanediamine *N*,*N*,*N*',*N*'-tetraacetate) [4], (c) *trans*-$[Co(NO_2)_2(Tmd)_2]^{2+}$ [3], and (d) $[Co(Orn)_2]^{+}$ (H*orn* is ornithine) [5] and this work.

thermal vibrations and the van der Waals interactions of the adjacent complexes. A similar situation is also observed in seven-membered rings with a different composition, for example, CaOCNCCO in the calcium compound with oxamidediacetic acid $[Ca(Oada)(H_2O)_2] \cdot 2H_2O$ [6].

Table 3 lists the Q and φ parameters characterizing the ring conformation according to Cremer and Pople [7], which were calculated for the $[Co(1)(Orntra)]^-$ and $[Co(2)(Orntra)]^-$ anions. It is evident that the glycinate rings at the $N_{(\delta)}$ atom in both anions correspond in the degree of deformation to the rings in the $[Co(Edta)]^-$ complexes [8]: Q = 0.40–0.49 Å for the equatorial G rings (in the N–Co–N plane) and 0.07–0.19 Å for the axial R rings. Although the glycinate rings at the $N_{(\alpha)}$ atom correspond in their position to the G rings in the $[Co(Edta)]^-$ ion, they are distorted to a considerably lesser extent. As expected, the C atoms in the chelate rings are located on the same side of the NCoO plane. The conformations of the chelate rings can be more rigorously described with the use of the φ coefficient and the conformations of the five-membered rings from the table given in [9]. The ideal values of φ for the T_{12}, T_{23}, E_2, and E_3 conformations are equal to 18°, 234°, 216°, and 252°, respectively.

For both anions, the endocyclic angles in the glycinate rings at the $N_{(\delta)}$ atom are not identical to each other, which is characteristic of the $[Co(Edta)]^-$ complexes. For example, the endocyclic angles in the G rings are somewhat less than those in the R rings (83.3° and 87.6°, respectively). In the other part of the complex (the rings involving the $N_{(\alpha)}$ atom), this difference is not observed, and all the angles fall in the range 86.1°–86.6°.

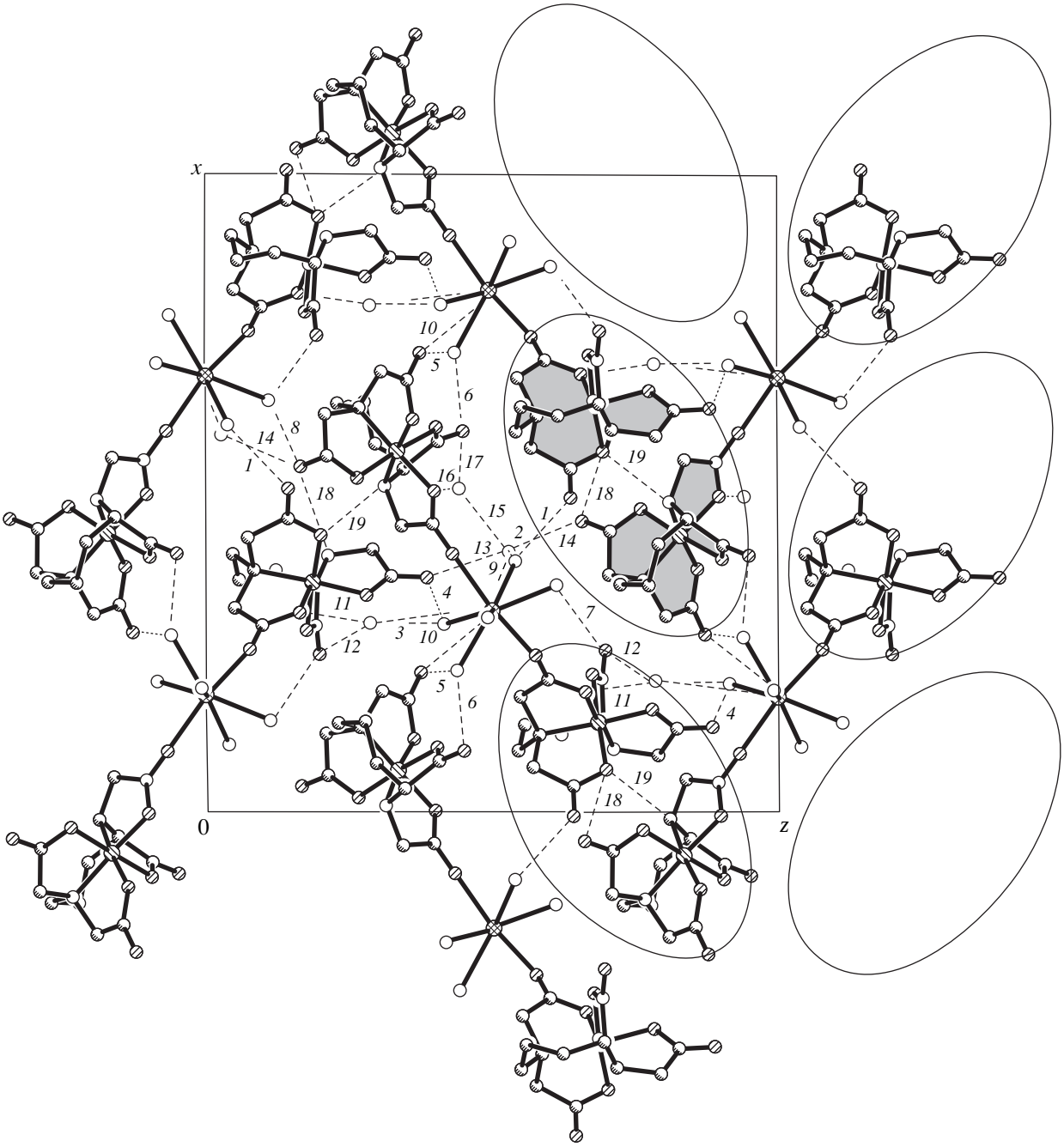

Fig. 4. Projection of structure **I** onto the (010) plane. The double column (consisting of the complexes with different absolute configurations) perpendicular to the figure plane is shaded. The numbering of hydrogen bonds corresponds to that in Table 4.

The lengths of the bonds Co–N (1.925–1.955 Å) and Co–O (1.880–1.904 Å) in structure **I** correspond to the normal values. There is a difference in lengths of the C–O bonds for the oxygen atoms involved and not participating in the cobalt coordination: the mean length of the $C–O_{coord}$ bonds is equal to 1.29 Å, and the mean length of the $C–O_{terminal}$ bonds is 1.22 Å. Note also a certain decrease in the difference between the C–O bond lengths for one group bound to the Ca^{2+} ion [C(5*b*)–O(5*b*), 1.23 Å and C(5*b*)–O(6*b*), 1.27 Å].

As already mentioned, in the trinuclear molecular unit $\{[Co(\mu\text{-}Orntra)]_2Ca(H_2O)_5\}$ (Fig. 1), the two independent anionic complexes are joined together through the central Ca^{2+} cation. These anions are bound to the Ca^{2+} cation through the terminal oxygen atoms of the glycinate rings. These are the O(4*a*) oxygen atom of the acetate group attached to the $N_{(\delta)}$ atom in the $[Co(1)(Orntra)]^-$ anion and the O(6*b*) oxygen atom of the acetate group attached to the $N_{(\alpha)}$ atom in the

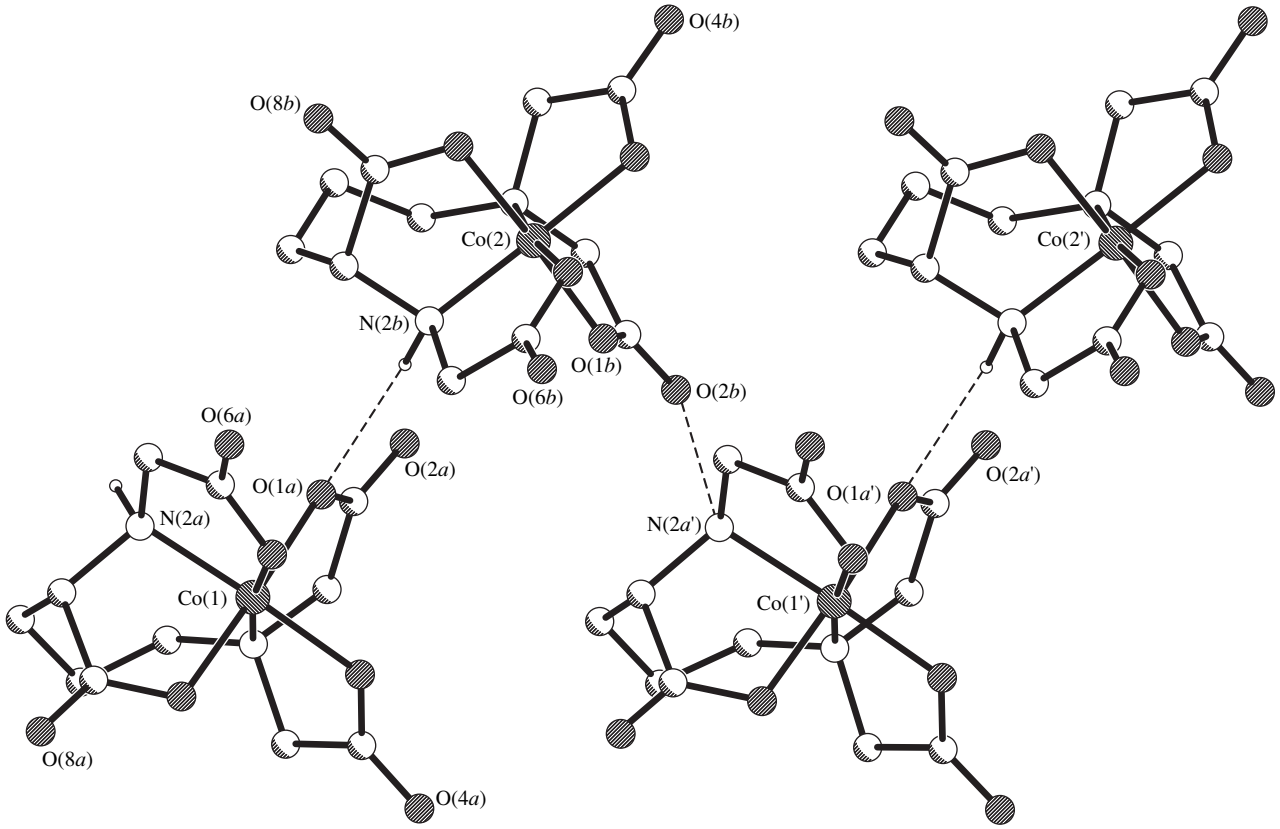

Fig. 5. Structure of the column (along its axis) in projection onto the central plane passing through the Co(1) and Co(2) atoms.

$[Co(2)(Orntra)]^-$ anion. Therefore, each $Orntra^{4-}$ ligand fulfills a heptadentate (2N + 5O) function—the hexadentate (2N + 4O) function with respect to the relevant Co atom and the bridging (μ-O) function relative to the Ca atom. The O(4*a*) and O(6*b*) atoms occupy the axial positions in the coordination polyhedron of the Ca^{2+} ion, which has the shape of a pentagonal bipyramid with the equatorial plane formed by the oxygen atoms of five H_2O molecules. The deviations of the equatorial oxygen atoms from the mean plane fall in the range from –0.52 to 0.63 Å. The Ca atom lies in this mean plane. The bipyramid axis is somewhat bent: the O(4)CaO(6) angle is equal to 166°. The Ca–O(*Orntra*) distances to the axial oxygen atoms (2.342 and 2.364 Å) are somewhat shorter than the equatorial Ca–$O(H_2O)$ bonds (the mean length is 2.449 Å). A similar structure of the Ca polyhedron with about the same ratio between lengths of the axial and equatorial Ca–O bonds is observed in the compounds $Ca[Mo_2O_4(Edta)] \cdot 9H_2O$ [10] and $[Ca(H_2O)_7][Co(Edta)]$ [8]. In the former compound, the axial Ca–O bonds are equal to 2.300 and 2.334 Å, and the equatorial Ca–O bonds are, on average, 2.402 Å. In the latter compound, the corresponding values are equal to 2.350, 2.344, and 2.422 Å, respectively.

The asymmetric C(8) carbon atoms in both anions bound to the same Ca^{2+} cation adopts an identical absolute configuration (either *S* or *R*). In the crystal, the number of molecules belonging to the *S* configuration is equal to that of the *R* configuration, which corresponds to the racemic ornithine employed in the synthesis.

Figure 4 shows the packing of the neutral dumbbell-like molecules $Ca(H_2O)_5[Co(Orntra)]_2$. If we visualize that the Ca^{2+} cations (they form chains along the coordinate *y*-axis aligned perpendicular to the figure plane) are isolated from the structure, then the columns consisting of double complexes and lying along the same direction will clearly manifest themselves in the remaining anionic part. One of these columns is shaded in Fig. 4. Two crystallographically independent anions take part in the formation of columns. Figure 5 depicts the projection of the column onto the plane passing through the Co(1) and Co(2) atoms and lying parallel to the *y*-axis. This plane (perpendicular to the plane of Fig. 4) is rather arbitrarily oriented in the unit cell. It can be seen from Fig. 5 that the anions in the column are related by the glide reflection pseudoplane; i.e., the crystallographically independent anionic complexes $[Co(1)(Orntra)]^-$ and $[Co(2)(Orntra)]^-$ belonging to different molecules are the geometrical isomers and, as mentioned above, have different absolute configura-

tions. The hydrogen bonds N–H··O(1)[O(2)] (Table 4, nos. 18, 19) are primarily responsible for the column formation. It seems likely that, under the external action associated with the cations, the H atom at the $N_{(\alpha)}$ atom [the distance to the terminal atom N(2*b*)··O(2*b*) is equal to 3.11 Å] is switched to the interaction with another (less convenient for this purpose) coordinated O(1) atom of the carboxyl group of the adjacent complex in the chain [the distance N(2*a*)··O(1*a*) is 3.16 Å].

All the other hydrogen bonds are formed with the participation of at least one oxygen atom located outside the column associates (Table 4, nos. 1–17), and none of the hydrogen bonds acts directly between the columns. This indicates that all the water molecules, including the molecules surrounding the Ca^{2+} cations, are located in cavities (channels) between four different columns of the anionic complexes. The water molecules have a rather random arrangement, so that the molecules with quite similar bonds and functions cannot be distinguished. All the water molecules are interlinked by the hydrogen bonds. The strongest hydrogen bond [O(*w*7)··O(*w*8), 2.65 Å] is realized between the molecules located outside the coordination sphere of the Ca^{2+} cation. These H_2O molecules, together with the Ca^{2+} cations, form original aquacationic channels penetrating the structure along the *y*-axis between rather symmetrically arranged anionic columns. Actually, the columns of oval cross-section are slightly rotated with respect to each other (at the right of Fig. 4) and exhibit a close packing with a quadratic motif. The motif of aquacationic channels more closely resembles a hexagonal one. The structure, as a whole, is intermediate between these two radically different structures.

There are good grounds to believe that the formation of column associates is the first stage of forming crystals **I**, followed by the cocrystallization (together with the Ca^{2+} cations) of the neutral product from an aqueous solution. Owing to their sufficient mass and shape (extension in a certain direction), the associates constitute the basis of the crystal. The cations surrounding by water molecules form the aquacationic channels, move the columns apart, rotate them relative to each other, and partially affect the internal structure of the associates (the aforementioned redistribution of hydrogen bonds), thus breaking the possible higher symmetry of the crystal. These mutual effects are responsible for the formation of the neutral molecular structure of crystals **I**.

Table 4. Hydrogen bonds in structure **I**

No.	*A*··*B* bond	*d*(Å)	No.	*A*··*B* bond	*d*(Å)
1	O(*w*1)····O(2*a*)	2.89	11	O(*w*6)····O(3*a*)	2.89
2	O(*w*1)····O(*w*7)	2.81	12	O(*w*6)····O(8*a*)	2.98
3	O(*w*2)····O(*w*6)	2.81	13	O(*w*7)····O(6*a*)	2.97
4	O(*w*2)····O(6*a*)	2.72	14	O(*w*7)····O(2*b*)	2.93
5	O(*w*3)····O(4*b*)	2.73	15	O(*w*7)····O(*w*8)	2.65
6	O(*w*3)····O(8*b*)	2.82	16	O(*w*8)····O(5*b*)	2.80
7	O(*w*5)····O(8*a*)	2.82	17	O(*w*8)····O(8*b*)	2.83
8	O(*w*5)····O(2*b*)	3.07	18	N(2*a*)····O(2*b*)	3.16
9	O(*w*4)····O(*w*7)	2.75	19	N(2*b*)····O(1*a*)	3.11
10	O(*w*4)····O(4*b*)	2.94			

ACKNOWLEDGMENTS

This work was supported in part by the Belarussian Republican Foundation for Basic Research, project no. F96-92.

REFERENCES

1. A. L. Poznyak, Koord. Khim. **17** (9), 1261 (1991).
2. G. M. Sheldrick, *SHELXL93: Program for the Refinement of Crystal Structures* (Univ. of Göttingen, Göttingen, 1993).
3. M. Shimoi, Yu. Fujinava, H. Ogino, *et al.*, Bull. Chem. Soc. Jpn. **61** (10), 3491 (1988).
4. L. M. Shkol'nikova, G. V. Polyanchuk, A. L. Poznyak, *et al.*, Koord. Khim. **17** (5), 626 (1991).
5. Y. Nakayama, S. Ooi, and H. Kuroya, Bull. Chem. Soc. Jpn. **49** (1), 151 (1976).
6. K. D. Suyarov, L. M. Shkol'nikova, A. L. Poznyak, *et al.*, Koord. Khim. **17** (5), 635 (1991).
7. D. Cremer and J. A. Pople, J. Am. Chem. Soc. **97** (6), 1354 (1975).
8. L. A. Zasurskaya, A. L. Poznyak, T. N. Polynova, *et al.*, Zh. Neorg. Khim. **41** (10), 1647 (1996).
9. A. S. Antsyshkina, G. G. Sadikov, V. S. Sergienko, *et al.*, Zh. Neorg. Khim. **41** (12), 2018 (1996).
10. L. A. Zasurskaya, T. N. Polynova, I. B. Zastenker, *et al.*, Kristallografiya **41** (3), 471 (1996) [Crystallogr. Rep. **41** (3), 445 (1996)].

Translated by O. Borovik-Romanova

Crystallography Reports, Vol. 45, No. 3, 2000, pp. 432–438. Translated from Kristallografiya, Vol. 45, No. 3, 2000, pp. 475–481.

STRUCTURES OF COORDINATION COMPOUNDS

An Unusual Function of the Anion of 1-Hydroxyethane-1,1-Diphosphonic Acid (H_4L): Crystal Structure of $[Ni(Phen)_3](H_7L_2)_{0.5}(H_5L_2)_{0.5} \cdot 2H_2O$

V. S. Sergienko*, G. G. Aleksandrov*, and E. G. Afonin**

** Kurnakov Institute of General and Inorganic Chemistry, Russian Academy of Sciences, Leninskiĭ pr. 31, Moscow, 117907 Russia*

*** State Enterprise "Chemical Engineering Laboratory," Kaluga, Russia*

Received April 1, 1998; in final form, April 1, 1999

Abstract—Crystals of $[Ni(Phen)_3](H_3L)_2 \cdot 2H_2O$ (H_4L is 1-hydroxyethane-1,1-diphosphonic acid) have been synthesized, and their structure has been determined by X-ray diffraction analysis. The cationic complexes $[Ni(Phen)_3]^{2+}$, the centrosymmetric dimeric anions $H_7L_2^-$ and $H_5L_2^{3-}$, and the molecules of crystallization water are the structural units of the crystal. The outer-sphere function of the H_4L anions in transition metal compounds and also the presence of differently charged dimeric anions are revealed for the first time. The structural units are joined together by an extended system of hydrogen bonds, including symmetric (or pseudosymmetric) hydrogen bonds in dimeric anions (O···O, 2.436 and 2.466 Å). The Ni–N(*Phen*) bond lengths fall in the range 2.074–2.107 Å. The compound has the structural formula $[Ni(Phen)_3](H_7L_2)_{0.5}(H_5L_2)_{0.5} \cdot 2H_2O$. © *2000 MAIK "Nauka/Interperiodica".*

The crystal structures of a number of 3*d*-metal complexes have been determined in the systematic investigation into the properties and structure of the compounds based on 1-hydroxyethane-1,1-diphosphonic acid $CH_3C(OH)(PO_3H_2)_2$ (H_4L). The metal-to-ligand ratio, specific features of the central atom (*M*) and the outer-sphere cation, and the presence (or absence) of the second ligand are responsible for the realization of a particular structural type, coordination modes of the $H_{4-n}L^{n-}$ ligand, geometric isomers, a certain degree of distortion of six-vertex polyhedron, etc. Specifically, the monomeric complexes with the ratio $M : L = 1 : 2$ have a *trans* octahedral structure both in complexes of the isostructural series $[(C_2H_5)_2NH_2]_2[M(H_2O)_2(H_2L)_2]$ (where *M* = Cu [1], Co [1], Zn [2], Mg [2], Ni* [2], and Mn* [2]) and in the compound β-$[Cu(H_2O)_2(H_3L)_2] \cdot 3H_2O$ [3] and also a *cis* octahedral structure both in complexes of the isostructural series $[(HOCH_2CH_2)_3NH][M(H_2O)_2(H_{2.5}L)_2] \cdot 5H_2O$ (where *M* = Cu [4], Mn* [4], Mg* [4], Zn [5], Co* [5], and Ni* [5]) and in the compound $(NH_4)_2[Ni(H_2O)_2(H_2L)_2] \cdot 7H_2O$ [6].[1] In all these complexes, the $H_{4-n}L^{n-}$ ligands fulfill a bidentate-chelating function. However, two compounds of the general formula $Cat_2Cu(H_2L)_2 \cdot 2H_2O$ (where $Cat_2 = (NH_4)_2$ [7] and $(H_5O_2)Rb$ [8]), which are similar in composition to the aforementioned monomeric complexes, exhibit a polymeric chain structure, such as $[Cu(\mu_2\text{-}H_2L)_2]$, with a tridentate chelate–bridging function of the H_2L^{2-} ligands. The same polymeric chain structure, but with a different (tetradentate chelate–bridging) function of the H_2L^{2-} ligand was revealed for two copper(II) compounds with the ratio $Cu : L = 1 : 1$. In this case, the presence of the second ligand determines the coordination number of the metal. In the $Na[Cu(H_2L)Cl] \cdot 3H_2O$ structure [9], the chlorine atom is the bridging ligand, and the copper atom is located at the center of a (4 + 2) elongated tetragonal bipyramid in the anionic complex $[Cu(\mu_2\text{-}H_2L)(\mu_2\text{-}Cl)]_\infty^-$. In the $[Cu(H_2O)(H_2L)] \cdot 3.5H_2O$ structure [10], the H_2O terminal ligand completes the copper(II) five-vertex polyhedron [a (4 + 1) tetragonal pyramid] in the neutral complex $(Cu(H_2O)(\mu_2\text{-}H_2L)]_\infty$.

In aqueous solutions at low pH, nickel(II) and 1-hydroxyethane-1,1-diphosphonic acid form protonated complexes [11–14], specifically the $[Ni(H_2L)_2]^{2-}$ ($\log K_{st} = = 4.03$) [14]. It is evident that the introduction of 1,10-phenanthroline (*Phen*) into these solutions in the molar ratio Ni(II) : *Phen* = 1 : 3 and more leads to the formation of the thermodynamically stable cationic complex $[Ni(Phen)_3]^{2+}$ ($\log K_{st} = 23.9$), and the H_4L anion is displaced into the outer sphere of the complex.

In this work, we synthesized the $Ni(Phen)_3(H_3L)_2 \cdot 2H_2O$ compound (**I**), which was isolated from an aque-

[1] For six compounds marked by an asterisk, only the unit cell parameters have been determined.

ous solution, and determined its structure by the X-ray diffraction analysis. According to the X-ray diffraction data, the structural formula of **I** is represented as $[Ni(Phen)_3](H_7L_2)_{0.5}(H_5L_2)_{0.5} \cdot 2H_2O$.

EXPERIMENTAL

Synthesis. A weighed portion of $H_4L \cdot H_2O$ (2.24 g, 0.01 mol) was dissolved in water (10 ml), and nickel(II) carbonate hydroxide tetrahydrate (0.62 g, 0.0025 mol; Ni content, 47.00%) was added portionwise with stirring. The suspension was heated to the complete dissolution of the precipitate:

$$4H_4L + Ni(OH)_2 \cdot NiCO_3 \longrightarrow 2Ni(H_3L)_2 + 3H_2O + CO_2\uparrow.$$

The obtained solution was added to a green solution of $Phen \cdot H_2O$ (2.97 g, 0.015 mol) and then was heated to the complete dissolution of 1,10-phenanthroline:

$$Ni(H_3L)_2 + 3Phen \longrightarrow Ni(Phen)_3(H_3L)_2.$$

Prismatic crystals of complex **I** precipitated upon slow evaporation of the red solution. The solution was poured out, crystals were quickly washed with cooled water, wrung out using a paper filter, and dried in air at room temperature to a constant weight. Crystals suitable for X-ray structure analysis were chosen from the resulting crystal samples.

According to the chemical analysis, polycrystalline compound **I** has the composition $Ni(Phen)_3(H_3L)_2 \cdot 2H_2O$, which coincides with the composition determined by X-ray diffraction analysis for the single crystal.

For $C_{40}H_{42}N_6NiO_{16}P_4$ anal. calcd. (%): C, 45.96; H, 4.05; Ni, 5.61; L^{4-}, 38.65.

Found (%): C, 46.3; H, 4.2; Ni, 5.4; L^{4-}, 38.5.

Chemical analysis. The carbon and hydrogen contents in complex **I** were determined on a CHN analyzer. The nickel content was found by the chelatometric technique after the thermal decomposition of the complex at 800°C.

The anion in the nickel(II) complexes with H_4L can be quantitatively determined using the modified procedure, which was described in [15], with 1,10-phenanthroline as a reagent masking nickel(II) [16]. Nickel(II) 1-hydroxyethane-1,1-diphosphonate (50–100 mg) was dissolved in water (20 ml). 1,10-Phenanthroline monohydrate was added in such amounts that the molar ratio Ni(II) : *Phen* was equal to 1 : 3.5–4, and the solution was heated for 5 min to weak boiling. After the cooling to room temperature, a 1 M HCl solution (2 ml) and a 0.05 M $LaCl_3$ solution (10.00 ml) were added to the reaction mixture. The solution was heated for 10 min to weak boiling and then was diluted to 40 ml. After the dilution, two drops of a 0.1% Xylenol Orange solution and hexamethylenetetramine were added until the color changed from yellow to violet. The solution was heated for 5 min to a weak boiling. Then, the hot solution was titrated with a 0.05 M ethylenediaminetetraacetic acid solution with the use of a microburette until the color changed from violet to yellow.

The correctness and reproducibility of the analysis were checked against the reference compound $(C_2H_5)_2NH_2(H_3L)$ with addition of a $NiCl_2$ solution (molar ratio, 2 : 1). Found: 99.3 ± 1.0%, $S_r = 0.012$ at $n = 8$.

Complex I was analyzed for the L^{4-} content according to the above procedure by adding 10 mg of $Phen \cdot H_2O$ per 100 mg of the complex.

X-ray diffraction analysis. Crystals **I** are triclinic, $a = 9.926(2)$ Å, $b = 13.359(3)$ Å, $c = 18.132(4)$ Å, $\alpha = 103.25(3)°$, $\beta = 103.33(3)°$, $\gamma = 102.80(3)°$, $V = 2179.6(8)$ Å^3, $\rho_{calcd} = 1.593$ g/cm^3, $\mu_{Mo} = 6.73$ cm^{-1}, $M = 1045.4$, $F(000) = 1080$, $Z = 2$, and space group $P\bar{1}$.

The experimental data were collected at room temperature on a Syntex $P2_1$ four-circle automated diffractometer (λMoK_α, graphite monochromator, $\theta/2\theta$ scan mode, $2\theta_{max} = 60°$). A total of 7600 independent reflections was measured, of which 7134 reflections with $I \geq 2\sigma(I)$ were used in the structure determination.

The structure was solved by the direct method and refined by the least-squares procedure (for F^2) in the anisotropic approximation for the non-hydrogen atoms. The hydrogen atoms of the water molecules and the H_3L^- anions (except the hydrogen atoms of the methyl groups) were located from the difference Fourier synthesis and refined in the isotropic approximation under the constraint that similar bonds O–H(H_2O) and O–H(H_3L^-) are identical to within ±0.05 Å. The positions of the hydrogen atoms in the *Phen* molecules and the H(*Me*) atoms in the H_3L^- anions were calculated geometrically (C–H, 0.96 Å). These hydrogen atoms were used in the refinement at the fixed positions ($U_H = 0.08$ Å^2). A total of 655 positional and thermal parameters were refined.

The final refinement parameters were as follows: $R = 0.0357$ and $wR = 0.0880$ for the reflections with $I \geq 2\sigma(I)$; $R = 0.0369$ and $wR = 0.0895$ for all the reflections; $GOOF = 1.076$; the extinction coefficient was 0.0037(4); and the maximum and minimum peaks in the "zero" electron density distribution were equal to 0.431 and –0.402 eÅ^{-3}, respectively.

All the calculations were carried out according to the SHELXS86 [17] and SHELXL93 [18] software packages.

Table 1 lists the atomic coordinates and the thermal parameters U_{eq}/U_H.

Table 1. Atomic coordinates and thermal parameters in structure **I***

Atom	*x*	*y*	*z*	U_{eq}/U_H, Å^2
Ni	0.17554(4)	–0.04075(3)	0.27589(2)	0.0223(1)
P(1)	0.48017(8)	0.41597(6)	0.35599(5)	0.0303(2)
P(2)	0.76703(9)	0.52676(6)	0.49074(5)	0.0310(2)
P(3)	0.61661(8)	0.49925(6)	0.11268(4)	0.0262(2)
P(4)	0.92621(8)	0.48091(6)	0.11388(4)	0.0273(2)
O(1)	0.4246(3)	0.3397(2)	0.3990(2)	0.0408(5)
O(2)	0.4366(3)	0.3644(2)	0.2665(2)	0.0456(6)
O(3)	0.4370(3)	0.5208(2)	0.3731(2)	0.0428(6)
O(4)	0.7317(3)	0.4580(2)	0.5432(1)	0.0404(5)
O(5)	0.9275(3)	0.5625(2)	0.4985(2)	0.0465(6)
O(6)	0.7192(4)	0.6297(2)	0.5071(2)	0.0412(5)
O(7)	0.7375(3)	0.5160(2)	0.3436(2)	0.0438(6)
O(8)	0.6457(3)	0.5365(2)	0.2004(1)	0.0411(5)
O(9)	0.4612(2)	0.4355(2)	0.0667(1)	0.0381(5)
O(10)	0.6654(3)	0.5969(2)	0.0814(1)	0.0323(4)
O(11)	1.0082(3)	0.4000(2)	0.1214(2)	0.0396(5)
O(12)	0.9431(3)	0.5350(2)	0.0501(2)	0.0436(6)
O(13)	0.9695(3)	0.5752(2)	0.1923(2)	0.0378(5)
O(14)	0.7231(3)	0.3442(2)	0.1454(2)	0.0401(5)
N(1)	0.0798(3)	0.0810(2)	0.2659(1)	0.0242(4)
N(2)	0.0319(3)	–0.1103(2)	0.1612(1)	0.0267(5)
N(3)	0.2799(3)	–0.1607(2)	0.2645(2)	0.0277(5)
N(4)	0.3350(3)	0.0248(2)	0.2272(2)	0.0290(5)
N(5)	0.0436(3)	–0.1159(2)	0.3328(2)	0.0281(5)
N(6)	0.2983(3)	0.0372(2)	0.3942(1)	0.0268(5)
C(1)	0.1034(3)	0.1752(2)	0.3191(2)	0.0301(6)
C(2)	0.0491(4)	0.2573(2)	0.2998(2)	0.0376(7)
C(3)	–0.0293(4)	0.2425(2)	0.2235(2)	0.0372(7)
C(4)	–0.0566(3)	0.1438(2)	0.1658(2)	0.0287(5)
C(5)	–0.1384(4)	0.1200(3)	0.0843(2)	0.0366(7)
C(6)	–0.1663(4)	0.0227(3)	0.0320(2)	0.0370(6)
C(7)	–0.1125(3)	–0.0606(2)	0.0557(2)	0.0293(5)
C(8)	–0.1417(4)	–0.1649(3)	0.0044(2)	0.0375(7)
C(9)	–0.0852(4)	–0.2382(3)	0.0324(2)	0.0400(7)
C(10)	0.0017(4)	–0.2081(2)	0.1111(2)	0.0341(6)
C(11)	–0.0278(3)	–0.0380(2)	0.1341(2)	0.0246(5)
C(12)	–0.0003(3)	0.0650(2)	0.1902(2)	0.0233(5)
C(13)	0.2508(4)	–0.2521(2)	0.2832(2)	0.0344(6)
C(14)	0.3250(4)	–0.3292(3)	0.2671(2)	0.0448(9)
C(15)	0.4304(4)	–0.3111(3)	0.2313(2)	0.0465(9)
C(16)	0.4648(4)	–0.2149(3)	0.2108(2)	0.0386(7)
C(17)	0.5730(4)	–0.1884(4)	0.1727(3)	0.052(1)
C(18)	0.6000(4)	–0.0954(4)	0.1535(3)	0.054(1)
C(19)	0.5212(4)	–0.0195(3)	0.1710(2)	0.0400(7)
C(20)	0.5436(4)	0.0788(3)	0.1522(2)	0.0491(9)

Table 1. (Contd.)

Atom	*x*	*y*	*z*	U_{eq}/U_H, Å^2
C(21)	0.4644(4)	0.1461(3)	0.1715(2)	0.0434(8)
C(22)	0.3610(4)	0.1173(3)	0.2094(2)	0.0355(6)
C(23)	0.4138(3)	–0.0433(2)	0.2085(2)	0.0312(6)
C(24)	0.3853(3)	–0.1419(2)	0.2285(2)	0.0299(6)
C(25)	–0.0820(4)	–0.1925(3)	0.3010(2)	0.0373(7)
C(26)	–0.1537(4)	–0.2422(3)	0.3468(3)	0.0491(9)
C(27)	–0.0928(5)	–0.2144(3)	0.4263(3)	0.056(1)
C(28)	0.0400(4)	–0.1336(3)	0.4626(2)	0.0450(8)
C(29)	0.1137(6)	–0.0961(4)	0.5464(3)	0.060(1)
C(30)	0.2372(6)	–0.0165(5)	0.5774(2)	0.061(1)
C(31)	0.3039(4)	0.0345(3)	0.5279(2)	0.0423(7)
C(32)	0.4316(5)	0.1210(4)	0.5568(2)	0.054(1)
C(33)	0.4872(4)	0.1631(3)	0.5052(2)	0.0518(9)
C(34)	0.4192(4)	0.1179(3)	0.4234(2)	0.0367(7)
C(35)	0.2393(3)	–0.0029(2)	0.4458(2)	0.0289(6)
C(36)	0.1038(3)	–0.0865(2)	0.4128(2)	0.0303(6)
C(37)	0.6778(3)	0.4486(2)	0.3861(2)	0.0279(5)
C(38)	0.7205(4)	0.3435(3)	0.3699(2)	0.0414(7)
C(39)	0.7328(3)	0.4115(2)	0.0932(2)	0.0268(5)
C(40)	0.6751(5)	0.3368(3)	0.0083(2)	0.0493(9)
O(1*W*)	0.2802(4)	0.4008(4)	0.1547(2)	0.067(1)
O(2*W*)	1.0260(5)	0.5512(5)	0.3351(2)	0.080(1)
H(O2)	0.389(6)	0.386(5)	0.236(3)	0.13(2)
H(O3)	0.402(5)	0.529(4)	0.403(3)	0.09(2)
H(O5)	1.0000(0)	0.5000(0)	0.5000(0)	0.13(4)
H(O6)	0.650(4)	0.622(4)	0.514(4)	0.07(2)
H(O7)	0.690(5)	0.506(4)	0.302(2)	0.06(1)
H(O10)	0.623(5)	0.588(4)	0.039(2)	0.06(1)
H(O12)	1.0000(0)	0.5000(0)	0.0000(0)	0.10(2)
H(O13)	0.976(5)	0.557(4)	0.228(2)	0.06(1)
H(O14)	0.715(6)	0.379(4)	0.182(3)	0.07(2)
H(1*W*1)	0.213(4)	0.409(4)	0.148(3)	0.06(1)
H(2*W*1)	0.327(6)	0.412(6)	0.133(4)	0.09(3)
H(1*W*2)	0.962(4)	0.541(5)	0.345(3)	0.06(2)
H(2*W*2)	1.087(5)	0.554(5)	0.364(3)	0.10(2)

* The coordinates of the H(*Phen*) and H(*Me*) atoms are available from the authors.

RESULTS AND DISCUSSION

Ruby-red crystals of **I** are soluble in water, mineral acids, acetic acid, alkalis, ammonia water (with decomposition), and glycerol and poorly soluble in dimethyl sulfoxide, dimethylformamide, ethanol, acetone, dioxane, carbon tetrachloride, and benzene. The pH value of 0.01 M aqueous solution is equal to 2.45, which corresponds to the dissociation of the compound according to the following scheme:

$$[\mathrm{Ni}(Phen)_3](\mathrm{H_3}L)_2 \longrightarrow [\mathrm{Ni}(Phen)_3]^{2+} + 2\mathrm{H_3}L^-,$$

$$\mathrm{H_3}L^- \rightleftharpoons \mathrm{H_2}L^{2-} + \mathrm{H}^+.$$

The compound is nonhygroscopic and does not lose crystallization water on keeping in air.

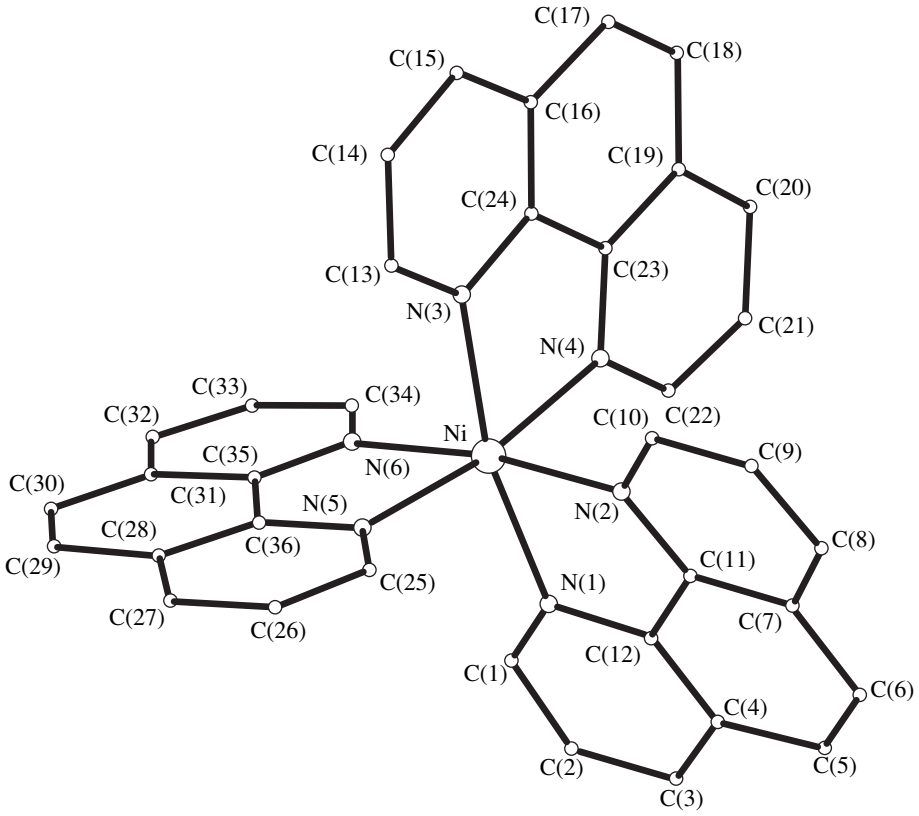

Fig. 1. Structure of the $[Ni(Phen)_3]^{2+}$ cationic complex.

The structural units of crystal **I** are the $[Ni(Phen)_3]^{2+}$ cationic complexes, anions of 1-hydroxyethane-1,1-diphosphonic acid, and molecules of crystallization water.

In the cationic complex (Fig. 1), the nickel atom is bonded to six nitrogen atoms (in vertices of the octahedron) of three bidentate–chelating phenanthroline molecules. The Ni–N(*Phen*) bond lengths fall in the range 2.074–2.107 Å. For each phenanthroline molecule, either of the Ni–N(*Phen*) bonds is shorter than the other bond: the Ni–N(1), Ni–N(3), and Ni–N(5) bond lengths are equal to 2.074–2.089 Å [the mean bond length is 2.081(3) ± 0.008 Å]; and the Ni–N(2), Ni–N(4), and Ni–N(6) bond lengths are 2.093–2.107 Å [the mean bond length is 2.098(2) ± 0.008 Å]. The NNiN angles in the five-membered metallocycles (79.8°–80.0°) are considerably less than the NNiN exocyclic angles (89.1–97.6°). Similar to the Ni–N bonds, the pairs of the N–C bonds for all six nitrogen atoms N(1), N(2), N(3), N(4), N(5), and N(6) in phenanthroline molecules are asymmetric: one bond is short [1.325–1.334 Å; mean bond length, 1.331(4) ± 0.006 Å] and the other bond is long [1.359–1.366 Å; mean bond length, 1.361(4) ± 0.005 Å] The C–C(*Phen*) bond lengths lie in the range 1.334–1.443 Å.

One of three five-membered metallocycles NiN_2C_2 [with the N(1) and N(2) atoms] adopts an envelope conformation, in which a "flap" (the Ni atom) deviates from the plane of the remaining atoms by 0.325 Å. Two other chelate rings are substantially flatter [to within ±0.016–0.032 Å for the ring with the N(3) and N(4) atoms and ± 0.010–0.039 Å for the ring with the N(5) and N(6) atoms]. However, their conformations can be more correctly represented as a flattened envelope with deviations of flaps (Ni atoms) by 0.122 and 0.134 Å, respectively.

Three NiN_2C_2 metallocycles in the cationic complex are approximately perpendicular to each other: the angles between their mean planes are equal to 96.5°, 76.9°, and 93.5°.

Structure **I** exhibits an unusual feature—the anions of 1-hydroxyethane-1,1-diphosphonic acid fulfill the function of the outer-sphere ions. In all the transition metal complexes studied earlier, the $H_{4-n}L^{n-}$ ions enter as ligands into the coordination sphere of the central atom. Particularly, in the mixed-ligand complex $[Cu(Bipy)(H_2O)(H_2L)] \cdot 2H_2O$ [19], the metal atom is located inside the tetragonal pyramid with the oxygen atom of water molecule in the apical position. Two $O(H_2L^{2-})$ atoms and two N(*Bipy*) atoms are bonded to the Cu atom by the bidentate–chelating mode to form the equatorial plane of the pyramid. The $[Co(H_2O)_6](trans\text{-}HO_3PCH{=}CHPO_3H) \cdot 2H_2O$ complex [20] is the sole example of the structure, in which

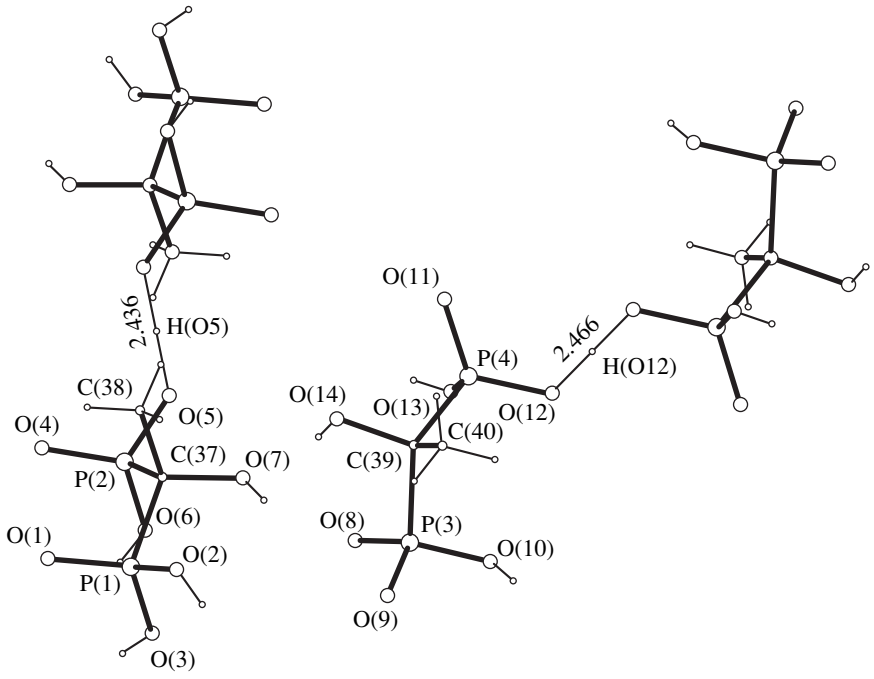

Fig. 2. Centrosymmetric dimeric anions (a) $H_7L_2^-$ and (b) H_5 .

the anion of diphosphonic acid is not bonded to the transition metal atom.

In structure **I**, there are two independent differently charged anions: formally, $H_{3.5}L^{0.5-}$ and $H_{2.5}L^{1.5-}$. Each anion forms the centrosymmetric dimer with the adjacent anion of the same kind via the strong linear hydrogen bond (Fig. 2). The interionic contacts O··H··O in both dimers $H_7L_2^-$ and $H_5L_2^{3-}$ are the strongest in the structure [O··O, 2.436(4) and 2.466(4) Å and H··O, 1.22 and 1.23 Å, respectively].

Therefore, the structural formula of compound **I** can be written as $[Ni(Phen)_3](H_7L_2)_{0.5}(H_5L_2)_{0.5} \cdot 2H_2O$.

A similar dimer, namely, $H_5L_2^{3-}$, in which the $H_{2.5}L^{1.5-}$ "halves" are related by the crystallographic axis 2 (O··O, 2.508 Å; H··O, 1.28 Å; and OHO angle, 160°), was found in the $(NH_4)_3(H_5L_2) \cdot 2H_2O$ compound (**II**) [21]. It should be mentioned that the presence of highly symmetric hydrogen bonds in the $H_7L_2^-$ and $H_5L_2^{3-}$ anions of structures **I** and **II** is most likely due to a superposition of two equally probable orientations of the statistically disordered fragments H_4L and H_3L^- for $H_7L_2^-$ and the H_3L^- and H_2L^{2-} fragments for $H_5L_2^{3-}$. In this case, the structural formula of compound **I** can be represented as

$$[Ni(Phen)_3](H_3L)(H_2L)_{0.5} \cdot 0.5H_4L \cdot 2H_2O.$$

Note also that the identification of dimers in structure **I** is sufficiently conventional. Actually, the structure additionally involves at least three short interionic contacts O(*L*)–H··O(*L*): O··O, 2.482–2.578 Å and H··O, 1.84–1.90 Å (Table 2). Moreover, the outer-sphere anions are joined with the water molecules by hydrogen bonds with the participation of all active protons (O··O, 2.468–2.912 Å and H··O, 1.69–2.22 Å). On the other hand, the interionic contacts C–H··O, which join the cationic complexes and the $H_{4-n}L^{n-}$ anions together, are appreciably weaker (C··O, 3.019–3.463 Å; H··O, 2.36–2.74 Å; and CHO angles, 101°–169°).

In the $H_{4-n}L^{n-}$ anions, the P–O distances, as is often the case, are divided into three groups: short distances to the terminal oxygen atoms [1.491–1.517 Å; mean distance, 1.505(3) ± 0.014 Å], intermediate distances to the oxygen atoms linked by the bridging proton [P–$OH_{0.5}$, 1.519 and 1.521 Å; mean distance, 1.520(3) ± 0.001 Å], and the longest distances to the terminal OH groups (P–OH, 1.525–1.566 Å). However, the last-named distances are clearly subdivided into two subgroups depending on the strength of donor hydrogen bonds involving a given OH group. Indeed, the P(1)–O(2) (1.525 Å), P(1)–O(3) (1.539 Å), and P(2)–O(6) (1.540 Å) bonds [mean bond length, 1.535(3) ± 0.010 Å], on the average, are 0.030 Å shorter than the P(3)–O(10) (1.563 Å) and P(4)–O(13) (1.566 Å) bonds [mean bond length, 1.565(3) ± 0.002 Å]. Note that the O–H··O hydrogen bonds for the former P–O bonds (O··O, 2.468–2.524 Å and H··O, 1.69–1.90 Å) are somewhat stronger than those for the latter bonds (O··O, 2.578 and 2.629 Å and H··O, 1.84 and 1.92 Å). The other mean distances in the $H_{4-n}L^{n-}$ anions are as

Table 2. Geometric parameters of the shortest intermolecular, intraionic, and interionic contacts O–H··O in structure **I**

A–H··*B** bond	Distance, Å			*AHB* angle, deg
	A··*B*	H··*B*	*A*–H	
O(2)–H(O2)···O(1*W*)[a]	2.468(5)	1.69(5)	0.80(6)	165(6)
O(3)–H(O3)···O(4)[b]	2.524(4)	1.84(5)	0.71(5)	165(5)
O(5)···H(O5)···O(5)[c]	2.436(4)	1.22	1.22	180
O(6)–H(O6)···O(1)[c]	2.482(4)	1.90(6)	0.72(5)	138(6)
O(7)–H(O7)···O(8)[a]	2.644(4)	1.95(4)	0.76(4)	153(5)
O(10)–H(O10)···O(9)[d]	2.578(3)	1.84(4)	0.75(4)	173(5)
O(12)···H(O12)···O(12)[e]	2.466(4)	1.23	1.23	180
O(13)–H(O13)···O(2*W*)[a]	2.629(5)	1.92(4)	0.73(4)	164(5)
O(14)–H(O14)···O(8)[a]	2.870(4)	2.33(6)	0.74(5)	130(5)
O(1*W*)–H(1*W*1)···O(11)[a]	2.625(5)	1.95(4)	0.69(4)	168(6)
O(1*W*)–H(2*W*1)···O(9)[a]	2.699(5)	2.01(7)	0.69(7)	176(8)
O(2*W*)–H(1*W*2)···O(7)[a]	2.843(6)	2.18(5)	0.69(5)	163(6)
O(2*W*)–H(2*W*2)···O(4)[b]	2.912(5)	2.22(5)	0.69(5)	172(6)

* The superscripts correspond to the following coordinates of the atoms: (a) *x*, *y*, *z*; (b) 1 – *x*, 1 – *y*, 1 – *z*; (c) 2 – *x*, 1 – *y*, 1 – *z*; (d) 1 – *x*, 1 – *y*, –*z*; (e) 2 – *x*, 1 – *y*, –*z*.

follows: P–C, 1.842(3) ± 0.011 Å; C–O, 1.442(4) ± 0.011 Å; and C–C, 1.533(5) ± 0.006 Å.

REFERENCES

1. V. S. Sergienko, G. G. Aleksandrov, and E. G. Afonin, Zh. Neorg. Khim. **42** (8), 1291 (1997).
2. V. S. Sergienko, E. G. Afonin, and G. G. Aleksandrov, Zh. Neorg. Khim. **43** (6), 1002 (1998).
3. E. G. Afonin, G. G. Aleksandrov, and V. S. Sergienko, Koord. Khim. **23** (11), 846 (1997).
4. V. S. Sergienko, E. G. Afonin, and G. G. Aleksandrov, Koord. Khim. **25** (2), 133 (1999).
5. V. S. Sergienko, G. G. Aleksandrov, and E. G. Afonin, Kristallografiya **44** (1999) (in press).
6. V. S. Sergienko, E. G. Afonin, and G. G. Aleksandrov, Koord. Khim. **24** (4), 293 (1998).
7. V. S. Sergienko, G. G. Aleksandrov, and E. G. Afonin, Koord. Khim. **24** (6), 455 (1998).
8. G. G. Aleksandrov, V. S. Sergienko, and E. G. Afonin, Zh. Neorg. Khim. **43** (11), 1811 (1998).
9. G. G. Aleksandrov, V. S. Sergienko, and E. G. Afonin, Zh. Neorg. Khim. **42** (8), 1287 (1997).
10. G. G. Aleksandrov and V. S. Sergienko, Kristallografiya, **44** (1999) (in press).
11. R. Rautschke, G. Lux, and U. Schlosser, Acta Chim. Hung. **88** (1), 19 (1976).
12. E. N. Rizkalla, M. T. Zaki, and M. I. Ismail, Talanta **27** (9), 715 (1980).
13. R. R. Amirov and Z. A. Saprykova, Zh. Neorg. Khim. **29** (8), 2138 (1984).
14. R. R. Amirov and Z. A. Saprykova, Zh. Obshch. Khim. **57** (7), 1526 (1987).
15. E. G. Afonin, Zh. Prikl. Khim. (S.-Peterburg) **68** (8), 1275 (1995).
16. I. M. Yurist and M. M. Talmud, *Selective Chelatometric Titration* (Nauka, Moscow, 1993).
17. G. M. Sheldrick, Acta Crystallogr., Sect. A **46** (6), 467 (1990).
18. G. M. Sheldrick, *SHELXL93: Program for the Refinement of Crystal Structures* (Univ. of Göttingen, Göttingen, 1993).
19. L. M. Shkol'nikova, A. A. Masyuk, G. V. Polyanchuk, *et al.*, Koord. Khim. **15** (10), 1424 (1989).
20. E. B. Chuklanova, T. N. Polynova, M. A. Poraĭ-Koshits, *et al.*, Koord. Khim. **8** (2), 236 (1982).
21. V. S. Sergienko, E. O. Tolkacheva, and A. B. Ilyukhin, Zh. Neorg. Khim. **38** (7), 1129 (1993).

Translated by O. Borovik-Romanova

Crystallography Reports, Vol. 45, No. 3, 2000, pp. 439–443. Translated from Kristallografiya, Vol. 45, No. 3, 2000, pp. 482–486.

STRUCTURES OF COORDINATION COMPOUNDS

Crystal and Molecular Structures of a Samarium Complex with the 3,5-Di-*tert*-Butyl-1,2-Quinone-1-(2-Hydroxy-3,5-Di-*tert*-Butylphenyl)imine Ligand

N. G. Furmanova*, S. N. Lyubchenko, V. A. Kogan**, and L. P. Olekhnovich****

** Shubnikov Institute of Crystallography, Russian Academy of Sciences, Leninskiĭ pr. 59, Moscow, 117333 Russia*
e-mail: furm@rsa.crystal.msk.su

*** Chemistry Department, Rostov State University, ul. Zorge 7, Rostov-on-Don, 344071 Russia*

Received October 26, 1998

Abstract—X-ray structure analysis of $Sm(C_{28}H_{40}NO_2)_3$ is performed. The crystals are monoclinic, a = 13.490(2) Å, b = 27.955(5) Å, c = 23.000(6) Å, β = 105.30(2)°, Z = 4, space group $P2_1/c$, and R = 0.0332 for 9670 reflections. The coordination number of the Sm atom is nine (tricapped trigonal prism with the O atoms in the base and the N atoms at the caps). The approximate symmetry of the complex is D_3. The mean C–O and C–N bond lengths (1.266 and 1.342 Å, respectively) correspond to the monoanion redox form of the ligands. In distinction to the earlier studied complexes ML_2 with the same ligands, the six-membered rings in the ligands of this complex are essentially noncoplanar: the dihedral angles between them are 42.8°, 34.0°, and 41.1°.

Recently [1], a series of complexes between Group III metals and lanthanides with the tridentate 3,5-di-*tert*-butyl-1,2-quinone-1-(2-hydroxy-3,5-di-*tert*-butylphehyl)imine ligand (**I**), which is able to provide the utmost ninefold coordination of a trivalent metal in its trischelates, have been obtained for the first time by the template synthesis. Due to the symmetry of the structure and the electronic mesomerism of deprotonated ligand **I**, the trischelates (**II**) of the above metals are promising as active dyes in the long-wavelength regions of the spectrum (visible 730–770 nm and infrared 820–825 nm), magnetic materials (with lanthanide metals) for microelectronics, and catalysts of hydration, oxidation–reduction, and polymerization [2, 3].

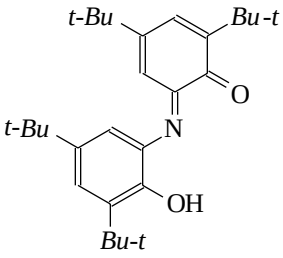

I

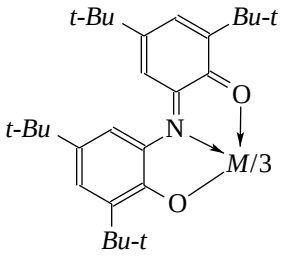

II

M^{3+} = Al, Sc, Ga, Y, In, La, Ce, Pr, Nd, Sm, Eu, Gd, Tb, Dy, Ho, Er, Tm, Yb, Lu

The goal of this study was to directly determine the structure of metal chelates **II** by X-ray diffraction analysis in order to reveal the following regularities and specific features of their structure: (1) the type and geometry of the coordination polyhedron, including ninefold metal coordination ($M^{III}O_6N_3$), (2) the specific structural features of the tridentate chelate moiety of ligand **I** in complexes **II**, (3) the conformation of three ligands and their mutual orientation about the complexing metal with respect to the steric shielding by *tert*-butyl groups and the van der Waals repulsion of the atoms in the *ortho* positions of the six-membered rings closely approaching each other, and (4) the dependence of the above characteristics on the type of complexing metal.

A large group of 19 new metal complexes **II** [1] consists of the complexes with all lanthanides and five Group III metals. Slow evaporation of benzene solutions afforded single crystals of X-ray quality only for the samarium trischelate.

EXPERIMENTAL

A single crystal ($0.18 \times 0.32 \times 0.44$ mm in size) was used for the X-ray diffraction study. The unit cell parameters were determined using 24 reflections measured on an Enraf–Nonius CAD-4F automated X-ray diffractometer (λMoK_α, graphite monochromator). The crystals are monoclinic, a = 13.490(2) Å, b = 27.955(5) Å, c = 23.000(6) Å, β = 105.30(2)°, d_{calcd} = 1.125 g/cm^3, $\mu(MoK_\alpha)$ = 7.656 cm^{-1}, Z = 4, and space group $P2_1/c$.

The intensities of 16 062 reflections, of which 9670 reflections had $I > 3\sigma(I)$ were measured on the same diffractometer by the ω-scan technique in the region $\theta \le 25°$. All the calculations necessary for structure determination and refinement were performed with the AREN program package [4].

Coordinates ($\times 10^5$ for Sm and $\times 10^4$ for the remaining atoms) and equivalent isotropic thermal parameters of non-hydrogen atoms

Atom	*x*/*a*	*y*/*b*	*z*/*c*	B_{eq}, Å^2	Atom	*x*/*a*	*y*/*b*	*z*/*c*	B_{eq}, Å^2
Sm	5464(1)	30 298(1)	67 968(1)	2.48(2)	C(13*B*)	4344(3)	4257(1)	9052(2)	4.4(3)
O(1*A*)	1248(2)	2869(1)	5954(1)	3.5(2)	C(14*B*)	4570(4)	4798(2)	9130(2)	6.8(4)
O(2*A*)	–752(3)	3600(1)	6826(1)	3.6(2)	C(15*B*)	4078(4)	4074(2)	9619(2)	7.4(4)
N(*A*)	–212(2)	3513(1)	5815(1)	2.8(2)	C(16*B*)	5301(4)	4003(2)	8982(3)	7.7(4)
C(1*A*)	1163(2)	3161(1)	5527(1)	2.9(3)	C(17*B*)	3101(3)	4450(1)	6772(1)	3.4(3)
C(2*A*)	355(2)	3527(1)	5414(1)	3.0(3)	C(18*B*)	2093(3)	4683(1)	6420(2)	4.9(3)
C(3*A*)	321(3)	3890(1)	4970(1)	3.6(3)	C(19*B*)	3939(3)	4841(1)	6902(2)	4.6(3)
C(4*A*)	1032(3)	3896(1)	4646(2)	4.0(3)	C(20*B*)	3417(3)	4052(1)	6392(2)	5.0(3)
C(5*A*)	1744(3)	3506(1)	4717(1)	3.9(3)	C(21*B*)	–355(4)	3888(1)	9539(2)	5.3(3)
C(6*A*)	1826(2)	3143(1)	5117(1)	3.4(3)	C(22*B*)	–96(5)	3637(2)	10 153(2)	7.7(4)
C(7*A*)	–1372(2)	3763(1)	6351(1)	3.2(2)	C(23*B*)	235(6)	4350(2)	9588(3)	9.4(4)
C(8*A*)	–1122(2)	3724(1)	5774(1)	3.0(2)	C(24*B*)	–1547(5)	3979(2)	9372(3)	9.0(5)
C(9*A*)	–1871(2)	3851(1)	5229(1)	3.3(3)	C(25*B*)	–1178(3)	2309(1)	8411(2)	4.2(3)
C(10*A*)	–2817(3)	4015(1)	5246(2)	3.6(3)	C(26*B*)	–409(4)	1908(1)	8395(2)	6.2(3)
C(11*A*)	–2989(2)	4110(1)	5826(2)	4.0(3)	C(27*B*)	–1686(5)	2203(2)	8924(2)	7.1(4)
C(12*A*)	–2313(3)	4007(1)	6365(2)	3.7(3)	C(28*B*)	–2021(3)	2317(2)	7818(2)	5.5(3)
C(13*A*)	1136(4)	4320(1)	4238(2)	5.6(3)	O(1*C*)	2184(1)	2702(1)	7317(1)	3.7(2)
C(14*A*)	1316(7)	4121(2)	3635(3)	10.8(5)	O(2*C*)	–950(1)	2590(1)	6248(1)	3.4(2)
C(15*A*)	281(8)	4647(4)	4140(6)	20.0(5)	N(*C*)	723(2)	2105(1)	6772(1)	2.9(2)
C(16*A*)	2148(8)	4569(3)	4540(4)	14.3(6)	C(1*C*)	2448(2)	2279(1)	7229(1)	3.4(3)
C(17*A*)	2593(3)	2729(1)	5171(2)	4.3(3)	C(2*C*)	1680(2)	1930(1)	6919(1)	3.3(2)
C(18*A*)	1997(4)	2255(1)	5087(3)	6.8(4)	C(3*C*)	1993(3)	1470(1)	6763(2)	4.2(3)
C(19*A*)	3169(4)	2761(2)	4675(3)	7.4(4)	C(4*C*)	3013(3)	1348(1)	6921(2)	4.8(3)
C(20*A*)	3395(3)	2750(2)	5781(2)	6.3(3)	C(5*C*)	3732(3)	1673(1)	7281(2)	4.9(3)
C(21*A*)	–3713(3)	4079(1)	4683(2)	4.4(3)	C(6*C*)	3511(3)	2124(1)	7440(1)	3.8(3)
C(22*A*)	–4165(4)	4584(2)	4659(2)	6.3(4)	C(7*C*)	–1056(2)	2145(1)	6314(1)	2.9(2)
C(23*A*)	–3402(4)	3999(2)	4108(2)	6.3(3)	C(8*C*)	–162(2)	1853(1)	6600(1)	2.9(3)
C(24*A*)	–4562(4)	3718(2)	4719(3)	8.0(4)	C(9*C*)	–293(3)	1360(1)	6719(1)	3.5(3)
C(25*A*)	–2519(3)	4117(1)	6978(2)	4.8(3)	C(10*C*)	–1222(3)	1147(1)	6536(2)	4.1(3)
C(26*A*)	–1636(4)	4421(2)	7356(2)	6.5(4)	C(11*C*)	–2080(3)	1429(1)	6209(2)	4.1(3)
C(27*A*)	–3507(4)	4410(2)	6898(2)	7.9(4)	C(12*C*)	–2039(3)	1903(1)	6092(1)	3.4(3)
C(28*A*)	–2619(5)	3651(2)	7312(2)	6.8(4)	C(13*C*)	3411(4)	882(2)	6711(3)	7.0(4)
O(1*B*)	1618(1)	3722(1)	6943(1)	3.3(2)	C(14*C*)	4024(8)	613(2)	7232(4)	13.6(6)
O(2*B*)	–66(2)	2707(1)	7614(1)	3.4(2)	C(15*C*)	2564(6)	565(3)	6389(6)	15.6(6)
N(*B*)	1130(2)	3465(1)	7833(1)	2.8(2)	C(16*C*)	4112(8)	1015(3)	6294(5)	14.4(6)
C(1*B*)	2150(2)	3898(1)	7336(1)	2.7(2)	C(17*C*)	4321(3)	2462(1)	7831(2)	4.7(2)
C(2*B*)	1933(2)	3764(1)	7906(1)	3.0(2)	C(18*C*)	3986(4)	2593(2)	8392(2)	7.0(3)
C(3*B*)	2624(3)	3897(1)	8467(1)	3.5(3)	C(19*C*)	5381(4)	2203(2)	8051(3)	8.6(3)
C(4*B*)	3469(3)	4167(1)	8477(1)	3.5(3)	C(20*C*)	4437(4)	2913(2)	7475(2)	6.8(3)
C(5*B*)	3587(2)	4353(1)	7916(1)	3.4(3)	C(21*C*)	–1418(4)	624(1)	6666(2)	5.5(2)
C(6*B*)	2966(2)	4242(1)	7362(1)	3.0(2)	C(22*C*)	–1827(5)	356(1)	6061(3)	7.3(3)
C(7*B*)	–38(2)	2942(1)	8089(1)	3.1(3)	C(23*C*)	–441(6)	369(2)	7010(3)	9.2(3)
C(8*B*)	598(2)	3370(1)	8235(1)	3.0(2)	C(24*C*)	–2218(6)	608(2)	7032(3)	9.3(3)
C(9*B*)	514(3)	3669(1)	8720(1)	3.6(3)	C(25*C*)	–2978(3)	2191(1)	5738(2)	4.1(2)
C(10*B*)	–128(3)	3551(1)	9067(1)	3.9(3)	C(26*C*)	–2742(4)	2405(2)	5174(2)	6.2(3)
C(11*B*)	–641(3)	3095(1)	8963(1)	4.0(3)	C(27*C*)	–3935(4)	1876(2)	5549(3)	7.2(3)
C(12*B*)	–613(3)	2789(1)	8513(1)	3.3(3)	C(28*C*)	–3223(3)	2596(2)	6127(2)	5.7(2)

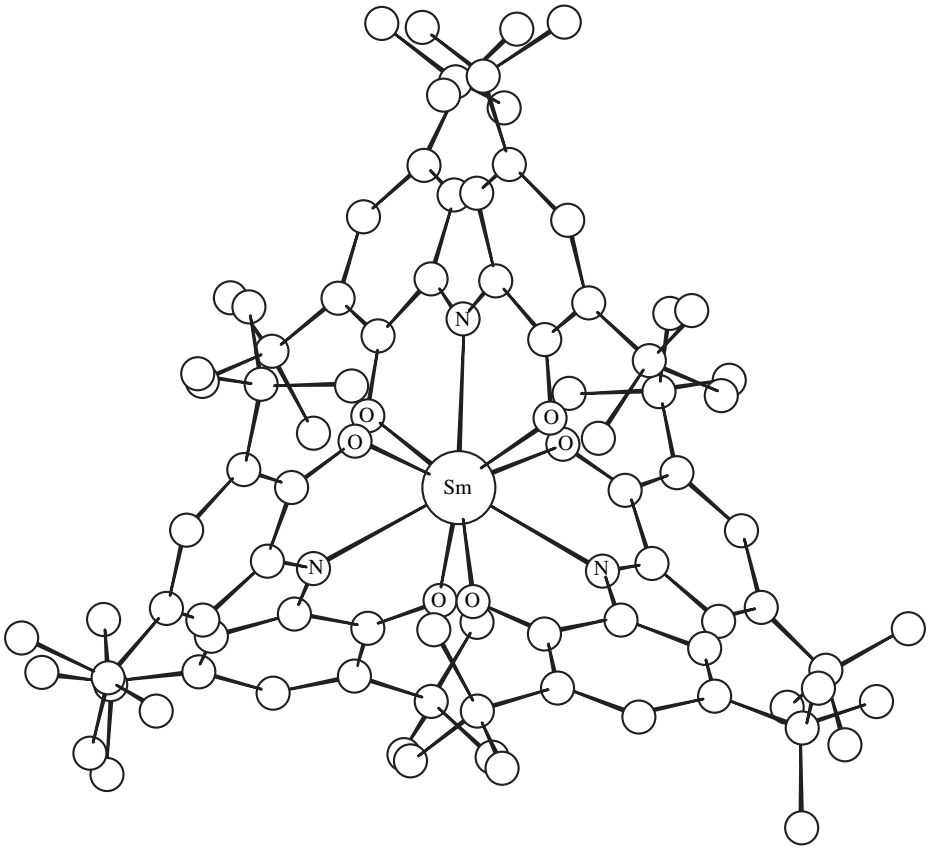

Fig. 1. A general view of the molecule (H atoms are omitted).

The coordinates of the Sm atom were found from the Patterson function, and the light non-hydrogen atoms were revealed in two successive syntheses of electron density. The structure was refined by the least-squares procedure first in the isotropic approximation ($R = 0.0715$) and then in the anisotropic approximation ($R = 0.0470$). Next, two successive difference syntheses revealed 116 H atoms; the coordinates of the remaining four atoms were calculated. The refinement of the positional parameters of the H atoms at fixed thermal parameters ($B_j = 7$ Å^2 for the *tert*-butyl groups and 5 Å^2 for the remaining atoms) resulted in the final value of $R = 0.0332$. The coordinates and thermal parameters of the non-hydrogen atoms are listed in the table (the table of the coordinates of the H atoms is available from the authors).

RESULTS AND DISCUSSION

A general view of the molecule is displayed in Fig. 1. The structure of an isolated ligand and the atomic numbering are shown in Fig. 2. The arrangement of ligands about the samarium atom follows a propeller pattern so that the coordination polyhedron of samarium has the shape of a slightly twisted (by ~15°) tricapped trigonal prism (the coordination number is nine) with the O atoms at the vertices of the prism and the N atoms at the caps over its side faces. The basal planes of the prism are almost parallel: the angle between them is 1.8°. The plane defined by the N atoms forms angles of 0.9° with both bases. The Sm–N distances (2.597–2.605 Å) are longer than the Sm–O distances (2.383–2.417 Å).

A similar coordination of the Sm atom is observed in its complex with another tridentate ligand, namely, 2'-[α-(2-pyridyl)benzylidene]salicylhydrazide [5]. However, in this case, the coordination of the Sm atom is less symmetric: one base of the prism is built up of a pyridyl N atom and two O atoms, and the other base is built up of an O atom and two pyridyl N atoms; the N atoms of the azo groups form the caps. The interatomic distances are close to those in the compound reported in this paper: Sm–O, 2.345–2.392 Å; Sm–N(pyridyl), 2.632–2.659 Å; and Sm–N(azo), 2.572–2.583 Å.

Unlike the latter complex, the triaqua-tris(3-aminobenzoato)samarium complex [6] has a high symmetry: in the crystal, it is located in the threefold rotation axis. The bidentate aminobenzoate ligands occupy the base of the prism and the caps, and the second base is occupied by water molecules.

The complex under study occupies a general position in the crystal. However, its approximate symmetry is 32 (D_3), and the symmetry of each ligand is close to

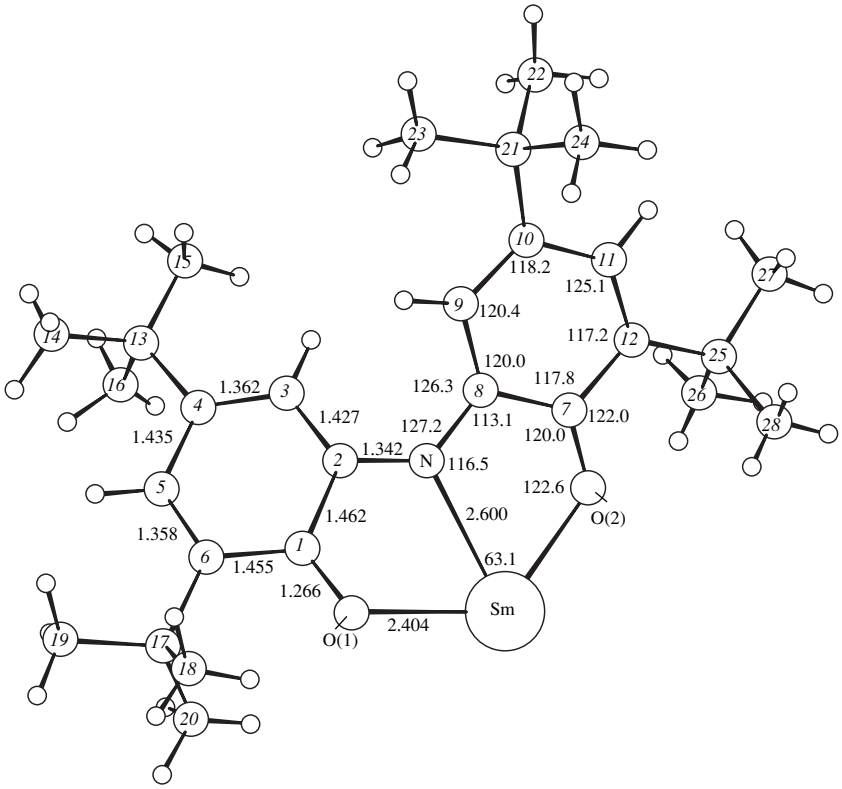

Fig. 2. Structure of an isolated ligand and its bonds with the Sm atom. The atomic numbering and the bond lengths and angles averaged over all ligands and two halves of each ligand are shown.

2 (C_2). Thus, both six-membered rings in each ligand have the same electronic structure, which is intermediate between the aromatic and purely quinoid types.

Earlier, we studied a series of complexes of this ligand (L) with the ML_2 composition, in which L exists in two anionic redox forms, namely, an anion or a dianion radical

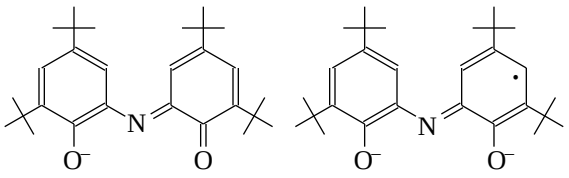

Cat-N-BQ *Cat-N-SQ*

Depending on the valence of the metal, the formula of these complexes can be written as M^{II}(*Cat-N-BQ*)$_2$, M^{III}(*Cat-N-BQ*)(*Cat-N-SQ*), or M^{IV}(*Cat-N-SQ*)$_2$. The summary table of the main geometric parameters of the structures studied by then is represented in [7]. In 1996, the structure of CuL_2 was reported in [8], and the structure of ZnL_2 [9] was also cited in this paper. The most characteristic features of the compounds with all the above formulas are the C–O and C–N bond lengths in the ligands. In the complexes of bivalent metals, the mean C–O bond lengths are 1.264 Å for NiL_2 [10], 1.254 Å for CuL_2 [8], and 1.264 Å for ZnL_2 [9]; and the mean C–N bond lengths are 1.344, 1.347, and 1.331 Å, respectively. In the complexes of trivalent metals, the formally different ligands are equivalent in the crystal; and the mean C–O bond lengths are equal to 1.305 Å for CoL_2 [11] and 1.287 Å for FeL_2 [10], and the mean C–N bond lengths are 1.361 and 1.357 Å, respectively. In the complexes of tetravalent metals, these bonds lengthen further; the mean C–O distances become 1.325 Å in MnL_2 [11], 1.324 Å in VL_2 [7], and 1.337 Å in TiL_2 [12], and the mean C–N distances are 1.380, 1.380, and 1.363 Å, respectively.

To our knowledge, the structures of the complexes with the ML_3 composition have not been studied earlier. As already noted, in the Sm complex under study, the Sm–O and Sm–N bond lengths agree with the values observed in the Sm(III) complexes. Hence, all three ligands should be singly charged, that is, exist in the *Cat-N-BQ* form. Actually, the C–O and C–N bond lengths in these ligands are close to those found in $M^{II}L_2$: the mean values are 1.266 and 1.342 Å, respectively. The shortest C–O and C–N bonds in the complexes of *Cat-N-BQ* are attended with the most pronounced *o*-quinoid structure of their six-membered rings. The rings in SmL_3 are essentially nonplanar: the atomic deviations from the corresponding planes are up

to 0.075 Å, and the torsion angles about the bonds in these rings are up to 11.5°.

The coordination of the N atoms is planar trigonal: the maximum atomic deviation from the SmNC(2)C(8) plane is 0.008 Å. The five-membered chelate rings adopt an envelope conformation, and the Sm atom deviates from the OCCN planes by 0.58–0.68 Å.

An increase in the atomic radius of Sm (0.97 Å) in comparison with those of the metals in the ML_2 complexes studied (0.52–0.80 Å) results in a significant increase in the Sm–O and Sm–N distances and, as a consequence, a decrease in the O–Sm–O angles to ~126° compared to 151°–171° in ML_2. This allows the location of three *L* ligands in the coordination sphere of the Sm atom. However, the conformations of the ligands in SmL_3 and ML_2 differ fundamentally: in the ML_2 complexes, the six-membered rings in the ligands are approximately coplanar (the angles between them are within 13.4°), whereas in SmL_3, the angles are 42.8°, 34.0°, and 41.4° for ligands *A*, *B*, and *C*, respectively. Apparently, this difference is caused by large steric hindrances, which arise if three, not two, ligands *L* are coordinated to a metal atom.

REFERENCES

1. S. N. Lyubchenko, V. A. Kogan, and L. P. Olekhnovich, Koord. Khim. **22**, 569 (1996).
2. T. N. Gerasimova and A. V. Shelkovnikov, Usp. Khim. **61** (1), 102 (1992).
3. T. N. Maptynova, T. M. Polyanskaya, Yu. V. Gatilov, *et al.*, Zh. Obshch. Khim. **63** (8), 1692 (1993).
4. V. I. Andrianov, Kristallografiya **32** (1), 228 (1987) [Sov. Phys. Crystallogr. **32** (1), 130 (1987)].
5. J. Dan, S. Seth, and S. Chakraborty, Acta Crystallogr. C **45**, 1018 (1989).
6. A. E. Koziol, B. Klimek, K. Stepniak, *et al.*, Z. Kristallogr. **200**, 25 (1992).
7. S. Bruni, A. Caneschi, F. Cariati, *et al.*, J. Am. Chem. Soc. **116**, 1388 (1994).
8. G. Speier, J. Csihony, A. M. Whalen, *et al.*, Inorg. Chem. **35**, 3519 (1996).
9. C. S. Scotto, *PhD Thesis* (Univ. of Colorado, Boulder, 1992).
10. C. L. Simpson, S. R. Boone, and C. G. Pierpont, Inorg. Chem. **28**, 4379 (1989).
11. S. K. Larsen and C. G. Pierpont, J. Am. Chem. Soc. **110**, 1827 (1988).
12. A. Caneschi, A. Dei, and D. Gatteschi, J. Chem. Soc., Chem. Commun. 630 (1992).

Translated by I. Polyakova

Crystallography Reports, Vol. 45, No. 3, 2000, pp. 444–448. Translated from Kristallografiya, Vol. 45, No. 3, 2000, pp. 487–491.

STRUCTURES OF ORGANIC COMPOUNDS

Molecular and Crystal Structures of 3-Benzoyl-4-Hydroxy-4-Phenyl-(*N*-Methyl)piperidine and 5-Hydroxymethylene-4-Phenyl-*N*-Methyl-1,2,5,6-Tetrahydropyridine

L. N. Kuleshova and V. N. Khrustalev

Nesmeyanov Institute of Organoelement Compounds, Russian Academy of Sciences, ul. Vavilova 28, Moscow, 117813 Russia

Received January 18, 1999

Abstract—The crystal structures of two compounds—3-benzoyl-4-hydroxy-4-phenyl-(*N*-methyl)piperidine (**I**) [orthorhombic crystals, space group $P2_12_12_1$, $Z = 4$] and 5-hydroxymethylene-4-phenyl-(*N*-methyl)-1,2,5,6-tetrahydropyridine (**II**) [monoclinic crystals, space group $P2_1/n$, $Z = 4$]—are determined by X-ray diffraction. In **I**, the weak intermolecular OH···N hydrogen bonds link the molecules related by the *a* translation into homochiral chains. In **II**, the OH···N hydrogen bonds link the molecules into infinite homochiral chains twisting about the crystallographic screw axes $2_1(y)$. The helices are additionally strengthened by the short CH···O contacts.

Continuing our studies of the molecular structures of hydropyridine hydroxy derivatives [1–5] and the role of intermolecular hydrogen bonds in the formation of their packing [5], we determined the X-ray crystal structures of two compounds in this series: 3-benzoyl-4-hydroxy-4-phenyl-(*N*-methyl)piperidine (**I**) and 5-hydroxymethylene-4-phenyl-(*N*-methyl)-1,2,5,6-tetrahydropyridine (**II**).[1]

EXPERIMENTAL

The unit-cell parameters and intensities of reflections were measured on a Siemens P3/PC automated four-circle diffractometer ($T = 20°C$, λMoK_α, graphite monochromator, $\theta/2\theta$ scan mode, $\theta_{max} = 27°$).

Crystals **I** ($C_{19}H_{21}NO_2$, $M = 295.37$) are orthorhombic, space group $P2_12_12_1$; at $T = 20°C$: $a = 5.830(1)$, $b = 10.377(2)$, and $c = 25.856(8)$ Å; $V = 1564.4(7)$ Å^3; $Z = 4$; and $d_{calcd} = 1.254$ g/cm^3.

Crystals **II** ($C_{13}H_{17}NO$, $M = 203.28$) are monoclinic, space group $P2_1/n$; at $T = 20°C$: $a = 9.793(4)$, $b = 7.178(2)$, and $c = 16.508(5)$ Å; $\beta = 101.08(3)°$; $V = 1138.9(7)$ Å^3; $Z = 4$; and $d_{calcd} = 1.186$ g/cm^3.

The structures were solved by the direct method. The non-hydrogen atoms were refined by the full-matrix least-squares procedures in the anisotropic approximation. The hydrogen atoms were located from difference Fourier syntheses and refined in the isotropic approximation. The final discrepancy factors are as follows: $R_1 = 0.043$ for 1428 reflections with $I > 2\sigma(I)$ and $wR_2 = 0.103$ for all the 2046 unique reflections for compound **I**; $R_1 = 0.044$ for 1538 reflections with $I > 2\sigma(I)$ and $wR_2 = 0.109$ for all the 2238 unique reflections for compound **II**. Atomic coordinates and thermal parameters are listed in Tables 1 and 2. All the calculations were performed with the SHELXTL PLUS (PC Version 5.0) program package on an IBM PC/AT-486.

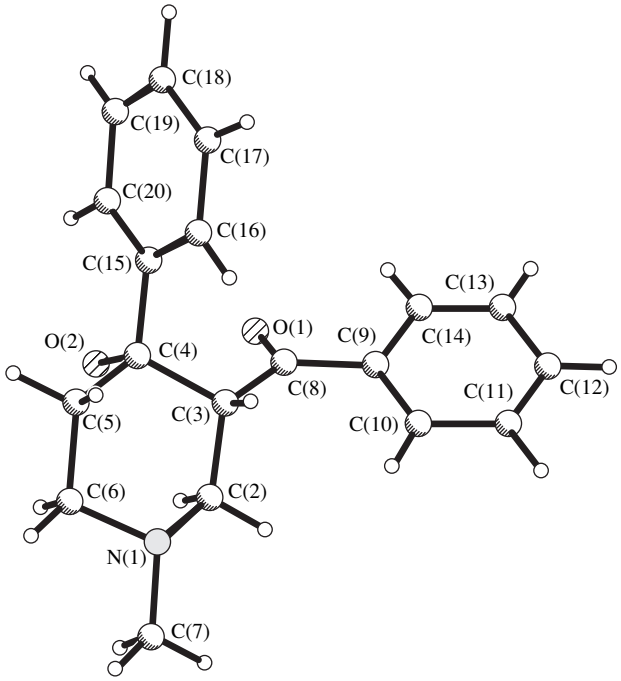

Fig. 1. A general view of molecule **I**.

[1] The compounds were synthesized in the Department of Organic Chemistry of the Peoples' Friendship University.

Table 1. Atomic coordinates ($\times 10^4$) and isotropic (equivalent for non-hydrogen atoms) thermal parameters ($Å^2 \times 10^3$) in structure **I**

Atom	*x*	*y*	*z*	U_{iso}
O(1)	6646(4)	1086(2)	1456(1)	68(1)
O(2)	7627(4)	3442(2)	1916(1)	45(1)
N(1)	12979(5)	2375(2)	2356(1)	45(1)
C(2)	11123(6)	1520(3)	2195(1)	43(1)
C(3)	10433(6)	1817(3)	1635(1)	36(1)
C(4)	9579(5)	3230(3)	1591(1)	36(1)
C(5)	11445(6)	4112(3)	1813(1)	41(1)
C(6)	12183(7)	3717(3)	2350(1)	45(1)
C(7)	13844(10)	2025(4)	2866(2)	67(1)
C(8)	8692(6)	865(3)	1428(1)	40(1)
C(9)	9472(5)	−371(3)	1182(1)	38(1)
C(10)	11611(6)	−917(3)	1274(1)	44(1)
C(11)	12142(7)	−2107(3)	1053(1)	50(1)
C(12)	10609(7)	−2722(3)	735(1)	55(1)
C(13)	8527(7)	−2162(3)	630(1)	59(1)
C(14)	7946(6)	−997(3)	857(1)	47(1)
C(15)	9089(5)	3606(3)	1030(1)	40(1)
C(16)	10664(7)	3346(3)	640(1)	50(1)
C(17)	10233(8)	3714(4)	132(1)	62(1)
C(18)	8246(8)	4351(3)	8(2)	64(1)
C(19)	6692(7)	4618(4)	390(2)	66(1)
C(20)	7113(6)	4261(3)	900(1)	54(1)
H(2*A*)	9755(60)	1644(30)	2427(11)	50(9)
H(2*B*)	11738(52)	644(28)	2226(10)	43(8)
H(3)	11836(54)	1753(27)	1446(10)	40(8)
H(5*A*)	12824(59)	4110(26)	1583(11)	42(8)
H(5*B*)	10754(52)	5029(29)	1812(9)	46(8)
H(6*A*)	10850(49)	3859(25)	2604(10)	37(8)
H(6*B*)	13437(55)	4259(28)	2475(11)	45(8)
H(7*A*)	12716(69)	2139(34)	3144(14)	72(12)
H(7*B*)	15327(79)	2618(41)	2928(16)	104(15)
H(7*C*)	14207(74)	1150(42)	2898(14)	90(13)
H(10)	12786(63)	−525(29)	1475(11)	55(9)
H(11)	13660(66)	−2512(31)	1132(12)	64(10)
H(12)	10989(63)	−3571(36)	581(13)	71(10)
H(13)	7480(65)	−2572(33)	398(13)	72(11)
H(14)	6492(58)	−571(29)	791(11)	49(9)
H(16)	12180(59)	2926(29)	717(10)	51(9)
H(17)	11310(71)	3489(38)	−113(14)	79(13)
H(18)	7838(66)	4603(31)	−355(13)	72(11)
H(19)	5320(66)	5049(33)	306(11)	62(11)
H(20)	5990(64)	4501(32)	1175(12)	65(11)

Table 2. Atomic coordinates ($\times 10^4$) and isotropic (equivalent for non-hydrogen atoms) thermal parameters ($Å^2 \times 10^3$) in structure **II**

Atom	*x*	*y*	*z*	U_{iso}
O(1)	2722(1)	−4359(2)	2120(1)	59(1)
N(1)	2585(2)	510(2)	1178(1)	45(1)
C(2)	3786(2)	1559(3)	1005(1)	54(1)
C(3)	5087(2)	455(3)	1130(1)	47(1)
C(4)	5168(2)	−1387(2)	1230(1)	39(1)
C(5)	3849(2)	−2483(2)	1229(1)	40(1)
C(6)	2577(2)	−1370(3)	832(1)	48(1)
C(7)	1306(3)	1511(4)	822(2)	65(1)
C(8)	6525(2)	−2378(2)	1350(1)	40(1)
C(9)	7748(2)	−1525(3)	1752(1)	52(1)
C(10)	9026(2)	−2394(3)	1816(1)	60(1)
C(11)	9111(2)	−4150(3)	1497(1)	59(1)
C(12)	7921(2)	−5031(3)	1120(1)	60(1)
C(13)	6637(2)	−4178(3)	1050(1)	49(1)
C(14)	3820(2)	−3086(2)	2111(1)	41(1)
H(10)	2593(24)	−4402(32)	2633(15)	83(8)
H(2*A*)	3922(19)	2745(30)	1357(12)	68(6)
H(2*B*)	3601(19)	2051(28)	424(13)	70(6)
H(3)	5930(20)	1149(26)	1121(11)	56(5)
H(5)	3856(16)	−3632(23)	908(10)	40(4)
H(6*A*)	2542(17)	−1279(23)	196(11)	51(5)
H(6*B*)	1725(19)	−1976(25)	924(10)	51(5)
H(7*A*)	1194(20)	1529(28)	195(14)	75(6)
H(7*B*)	1367(22)	2816(35)	1046(14)	82(7)
H(7*C*)	493(24)	874(30)	961(13)	75(7)
H(9)	7689(19)	−322(29)	1999(12)	61(6)
H(10)	9848(20)	−1754(28)	2111(12)	65(6)
H(11)	10053(23)	−4736(30)	1539(13)	76(7)
H(12)	7954(21)	−6278(32)	906(13)	78(7)
H(13)	5792(20)	−4792(26)	781(11)	54(5)
H(14*A*)	3738(15)	−1942(22)	2454(10)	36(4)
H(14*B*)	4768(18)	−3687(25)	2372(10)	50(5)

RESULTS AND DISCUSSION

A general view of molecule **I** is shown in Fig. 1. The central piperidine ring of the molecule adopts the classical chair conformation: the C(2), C(3), C(5), and C(6) atoms are coplanar within 0.016 Å; the N(1) and C(4) atoms deviate from this plane by 0.696 and –0.678 Å, respectively. In the 2-hydroxytetrahydro derivatives studied earlier [1–5], the conformation of the hydropyridine ring is either a distorted chair or a sofa, and the environment of the nitrogen atom in the heterocycle has a planar trigonal configuration. In molecule **I**, the environment of the nitrogen atom in the heterocycle has a pyramidal configuration; the bond angles about the N(1) atom are close to the tetrahedral angles: 109.9(3)°, 110.3(3)°, and 110.7(3)°. The hydroxyl group at the C(4) atom is axial relative to the plane of the heterocycle; the C(2)–C(3)–C(4)–O(2) torsion angle is equal to –60°. This conformation is favorable for the formation of the intermolecular OH···N hydrogen bond (O···N is 3.14 Å, H···N is 2.54 Å, and the O–H–N angle is 127.7°) in the crystal (Fig. 2). The phenyl group at the C(4) atom and the benzoyl substituent at the C(3) atom of the heterocycle are equatorially oriented; the torsion angles C(2)–C(3)–C(4)–C(15) and C(8)–C(3)–C(4)–C(5) are equal to 174.6° and –179.6°, respectively. The plane of the phenyl ring forms an angle of 77.9° with the mean plane of the piperidine ring; the plane of the benzoyl phenyl ring is rotated by 121.7° relative to the

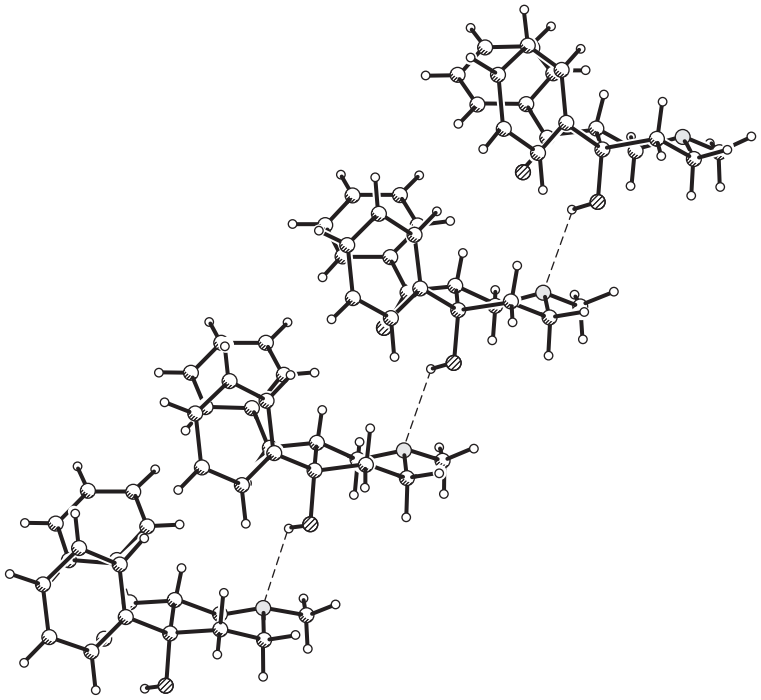

Fig. 2. A homochiral molecular chain in structure **I**.

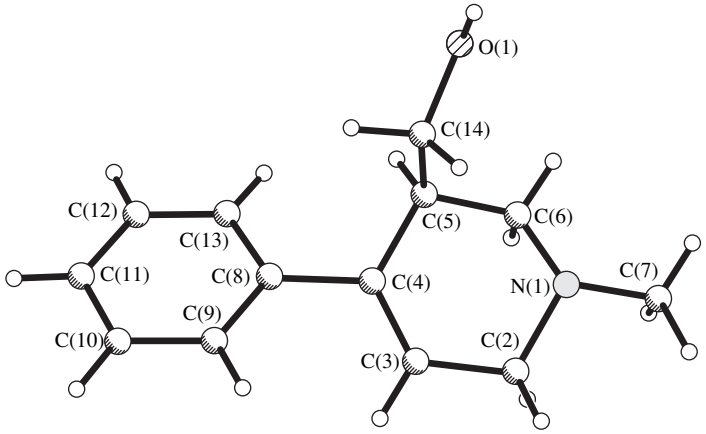

Fig. 3. A general view of molecule **II**.

latter plane. The bond lengths and angles have the normal values [6, 7].

In crystal structure **I**, molecules related by the *a* translation are linked by the weak intermolecular OH··N hydrogen bonds into homochiral chains (Fig. 2). In the crystal, these chains are closely packed in a herringbone fashion, resulting in the chiral space group $P2_12_12_1$ and, consequently, the spontaneous separation of enantiomers in the process of crystallization.

A general view of molecule **II** is shown in Fig. 3. The length of the C(3)–C(4) double bond in the heterocycle is 1.333(2) Å. Similar to molecule **I**, the environment of the N(1) atom in molecule **II** has a pyramidal configuration; the C–N–C bond angles are close to the tetrahedral angles: 109.9(1)°, 109.0(2)°, and 110.8(2)°. As in the case of the 2-hydroxytetrahydro derivatives studied earlier [1–5], the conformation of the central heterocycle is a distorted half-chair: the C(2), C(3), C(4), and C(5) atoms are coplanar (the rms atomic deviation is 0.002 Å), and the N(1) and C(6) atoms deviate from this plane by 0.281 and –0.448 Å, respectively. The orientation of the phenyl ring at the C(4) atom is pseudoequatorial. The C(8) atom lies in the plane of the planar part of the heterocycle; the C(8)–C(4)–C(3)–C(2) torsion angle is 179.9°. However, the plane of the phenyl ring is rotated relative to that of the

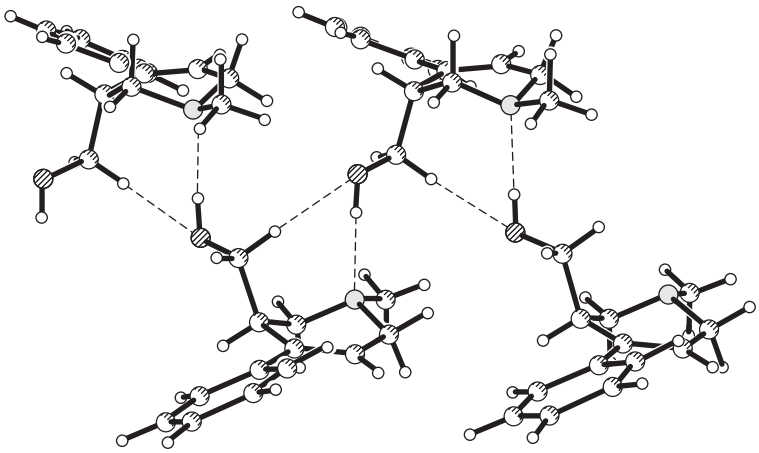

Fig. 4. A homochiral molecular chain in structure **II**.

heterocycle by 32.9°. The hydroxymethylene group at the C(5) atom is pseudoequatorial; the C(3)–C(4)–C(5)–C(14) angle is –106.4°. The bond lengths and angles in molecule **II** have the normal values.

In the crystal, the molecules are linked by the OH··N hydrogen bonds (O··N is 2.88 Å, H··N is 2.00 Å, and the O–H–N angle is 140.6°) into infinite homochiral chains twisting about the crystallographic screw axes $2_1(y)$ (Fig. 4). The chains are additionally strengthened by the short CH··O contacts (H··O is 2.52 Å, and the C–H–O angle is 149.8°). In the crystal, the double homochiral layers formed by these chains are clearly distinguished. The crystal as a whole is built by the alternation of homochiral layers of opposite chirality resulting in the centrosymmetric space group.

ACKNOWLEDGMENTS

This work was supported by the Russian Foundation for Basic Research, project nos. 97-03-33783 and 96-15-97367 (in support of scientific schools).

REFERENCES

1. L. N. Kuleshova, V. N. Khrustalev, Yu. T. Struchkov, *et al*., Kristallografiya **41** (4), 673 (1996) [Crystallogr. Rep. **41** (4), 636 (1996)].
2. L. N. Kuleshova, V. N. Khrustalev, Yu. T. Struchkov, *et al*., Kristallografiya **41** (4), 755 (1996) [Crystallogr. Rep. **41** (4), 717 (1996)].
3. L. N. Kuleshova, V. N. Khrustalev, Yu. T. Struchkov, *et al*., Zh. Strukt. Khim. **37** (5), 957 (1996).
4. A. T. Soldatenkov, I. V. Bekro, S. A. Soldatova, *et al*., Izv. Akad. Nauk, Ser. Khim. 11, 2020 (1997).
5. L. N. Kuleshova and V. N. Khrustalev, Kristallografiya **45** (1), 84 (2000) [Crystallogr. Rep. **45** (1), 78 (2000)].
6. F. H. Allen, O. Kennard, D. G. Watson, *et al*., J. Chem. Soc., Perkin Trans. **2** (1), 1 (1987).
7. A. G. Orpen, L. Bramer, F. H. Allen, *et al*., J. Chem. Soc., Dalton Trans., No. 1, 1 (1989).

Translated by I. Polyakova

Crystallography Reports, Vol. 45, No. 3, 2000, pp. 449–452. Translated from Kristallografiya, Vol. 45, No. 3, 2000, pp. 492–495.

STRUCTURES OF ORGANIC COMPOUNDS

Molecular and Crystal Structure of 4'-Cyanobenzo-15-Crown-5

S. A. Talipov*, Z. Karimov, B. T. Ibragimov*, A. K. Tashmukhamedova***, N. Zh. Saĭfullina***, and T. F. Aripov***

** Institute of Bioorganic Chemistry, Tashkent, Uzbekistan*

*** Institute of Agricultural Irrigation and Mechanization, Tashkent, Uzbekistan*

**** Chemistry Faculty, Tashkent State University, Tashkent, Uzbekistan*

Received April 1, 1997; in final form, October 18, 1998

Abstract—The crystal structure of 4'-cyanobenzo-15-crown-5 is determined by X-ray diffraction. The crystallographic parameters of single crystals are as follows: a = 40.479(6) Å, b = 8.821(2) Å, c = 8.484(2) Å, β = 93.94(2)°, V = 3022.2 Å^3, Z = 8, d_{calcd} = 1.27 g/cm^3, and space group $C2/c$. The structure is solved by the direct method and refined by the least-squares procedure to R = 0.068. The conformation of the macrocycle in 4'-cyano-B15C5 is described by the *a–a–g⁻–a–a–g–g⁻–a–a–g–a–g–a–a–s* sequence of torsion angles. © *2000 MAIK "Nauka/Interperiodica".*

Earlier [1–3], we revealed that the selectivity and membrane properties of a benzo crown ether are affected by a substituent in the benzene ring. The study on membrane activity of the compounds we synthesized showed that acyl substituents with 3–5 carbon atoms in the side chain increase the conductivity of the crown ethers through the Ca^{2+} and Mg^{2+} ions [1]. At the same time, diacetyl-DB18C6[1] exhibits no ionophoric activity. Moreover, it is a blocker of calcium ion-conductivity channels formed by phospholipids of sarcoma-45 cells [2, 3]. The *tert*-butyl and *sec*-butyl substituents endow the DB18C6 molecule with the properties of K^+-ionophore [4] and Mg^{2+}-ionophore [5], respectively. Apparently, one of the factors affecting the complex formation is a change in the conformation of the macrocycle, which depends on the nature of the substituent introduced. Conformational studies of different substituted benzo crown ethers make it possible to obtain further insight into the problem of the substituent effect. For this purpose, we synthesized 4'-cyanobenzo-15-crown-5 and determined its X-ray crystal structure. The cyano derivative of benzo-15-crown-5 (B15C5) was obtained from 4'-B15C5-thiocarbamide, which was synthesized by the procedure developed in our earlier work [6]: thioamidation of benzo crown ethers with potassium thiocyanate in polyphosphoric acid. Methylation of 4'-B15C5-thiocarbamide in an alkaline medium yields 4'-cyano-B15C5.

[1] DB18C6 is dibenzo-18-crown-6.

Table 1. Coordinates (×10^4) and thermal parameters (Å^2 × 10^3) of non-hydrogen atoms in the structure of 4'-cyanobenzo-15-crown-5

Atoms	*x/a*	*y/b*	*z/c*	U_{eq}
N(1)	–285(1)	3257(6)	–878(6)	83(2)
O(1)	1167(1)	525(4)	2149(4)	56(1)
O(2)	1838(1)	219(5)	2045(5)	78(2)
O(3)	2161(1)	2894(6)	3709(6)	99(2)
O(4)	1468(1)	5409(4)	3274(4)	65(1)
O(5)	967(1)	3110(4)	3105(4)	57(1)
C(1)	758(1)	2397(5)	2006(5)	46(2)
C(2)	460(1)	2980(6)	1413(6)	51(2)
C(3)	276(1)	2181(6)	237(6)	55(2)
C(4)	389(1)	823(6)	–330(6)	59(2)
C(5)	685(1)	224(6)	306(6)	53(2)
C(6)	871(1)	1000(5)	1468(5)	45(2)
C(7)	1308(1)	–833(6)	1556(7)	63(2)
C(8)	1639(1)	–1016(7)	2405(7)	74(2)
C(9)	2149(2)	225(9)	2956(10)	102(3)
C(10)	2301(2)	1707(9)	2880(10)	109(3)
C(11)	1846(2)	3427(9)	3093(9)	118(4)
C(12)	1773(2)	4792(11)	3753(10)	123(4)
C(13)	1208(1)	5283(6)	4300(6)	63(2)
C(14)	905(1)	4681(6)	3446(6)	54(2)
C(15)	–37(2)	2790(6)	–388(7)	64(2)

1063-7745/00/4503-0449$20.00 © 2000 MAIK "Nauka/Interperiodica"

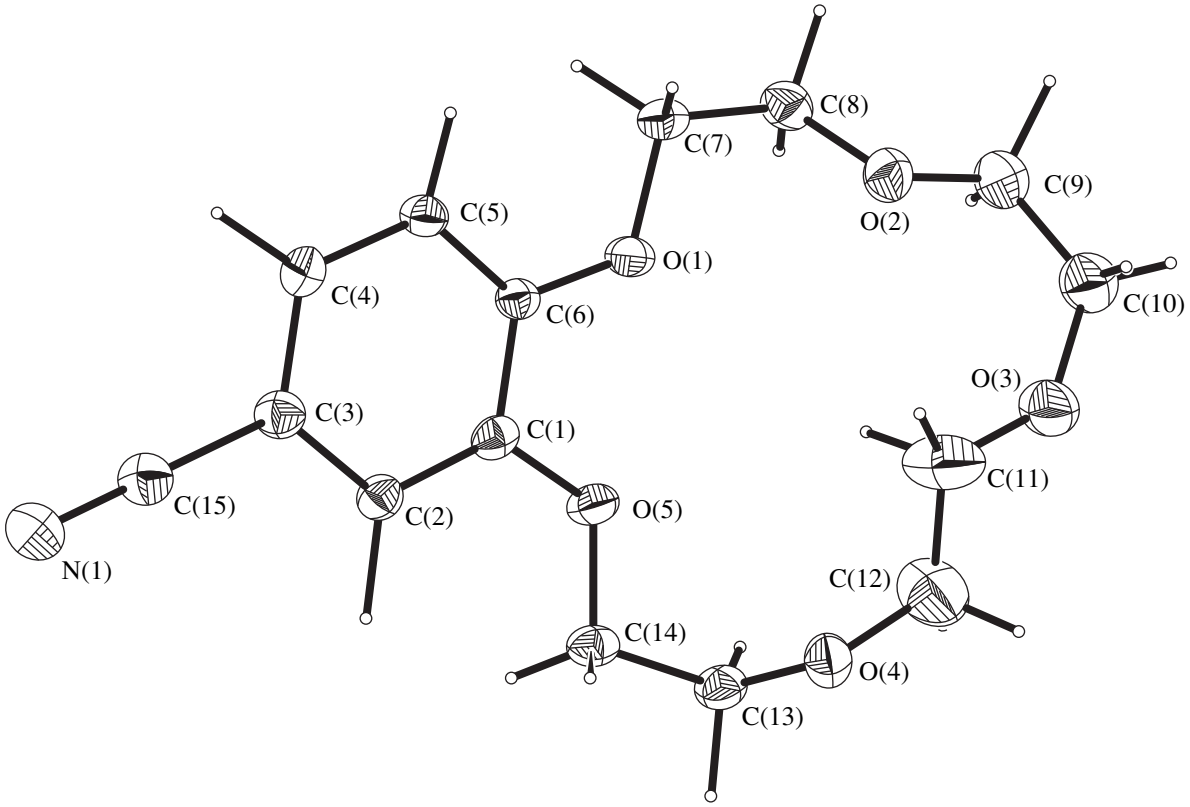

Fig. 1. Molecular structure of 4'-cyanobenzo-15-crown-5.

EXPERIMENTAL

Single crystals of 4'-cyanobenzo-15-crown-5 (T_{melt} = 86–88°C) were grown by slow evaporation of a dilute solution in the hexane : acetone (10 : 1) mixture. The crystallographic parameters of a single crystal were determined and refined on a Syntex $P2_1$ automated four-circle diffractometer using 15 reflections. These parameters are a = 40.479(6) Å, b = 8.821(2) Å, c = 8.484(2) Å, β = 93.94(2)°, V = 3022.2 Å^3, Z = 8, M = 293, d_{calcd} = 1.27 g/cm^3, and space group $C2/c$.

The integrated intensities of 2162 reflections were measured by the $\theta/2\theta$ scan technique with graphite-monochromated CuK_α radiation. After the Lorentz and polarization factors were introduced and the weak reflections with $F < 4\sigma(F)$ were rejected, the data set contained 1498 reflections. The structure was solved by the direct method with the SHELXS86 program package on an IBM-386 personal computer [7] and refined with the SHELX76 programs [8]. The hydrogen atoms were located from the difference Fourier syntheses, and their coordinates were not refined. After the final cycle of refinement of the positional and anisotropic thermal parameters for the non-hydrogen atoms the discrepancy factor is R = 0.068. The atomic coordinates are listed in Table 1.

RESULTS AND DISCUSSION

The molecular structure of 4'-cyano-B15C5 is shown in Fig. 1. The benzene ring is planar. The mean atomic deviation from the rms plane is 0.008 Å. The dihedral angle between the planes passing through the atoms of the benzene ring and those of the macrocycle is 31.6°. A comparison between the torsion angles in the molecule of 4'-cyanobenzo-15-crown-5 and torsion angles for three related compounds is shown in Table 2. The macrocycle exhibits the *gauche* conformation relative to three bonds, namely, C(7)–C(8), C(9)–C(10), and C(13)–C(14), and the *trans* conformation relative to the C(11)–C(12) bond. A similar conformation is observed in the molecule of 4'-hexanoylbenzo-15-crown-5 [9]. In the molecules of unsubstituted benzo-15-crown-5 [10], 4',5'-dibromobenzo-15-crown-5 [11], and a sodium-containing complex of 4'-benzo-15-crown-5-sulfonate [12], the C(11)–C(12) part has the *gauche* conformation. The O(2)···C(11) fragment of the macrocyclic chain in the molecule studied forms an angular fragment with the *a*–*g*–*g*$^-$–*a* bond sequence resulting in the intramolecular C(11)···O(2) contact (2.97 Å). The C–C–O–C dihedral angles in the fragments of the macrocycle adjacent to the benzene ring deviate from the ideal value (180°) by 5°–14°. The C(12)–O(4)–C(13)–C(14) angle shows the largest deviation from the ideal value.

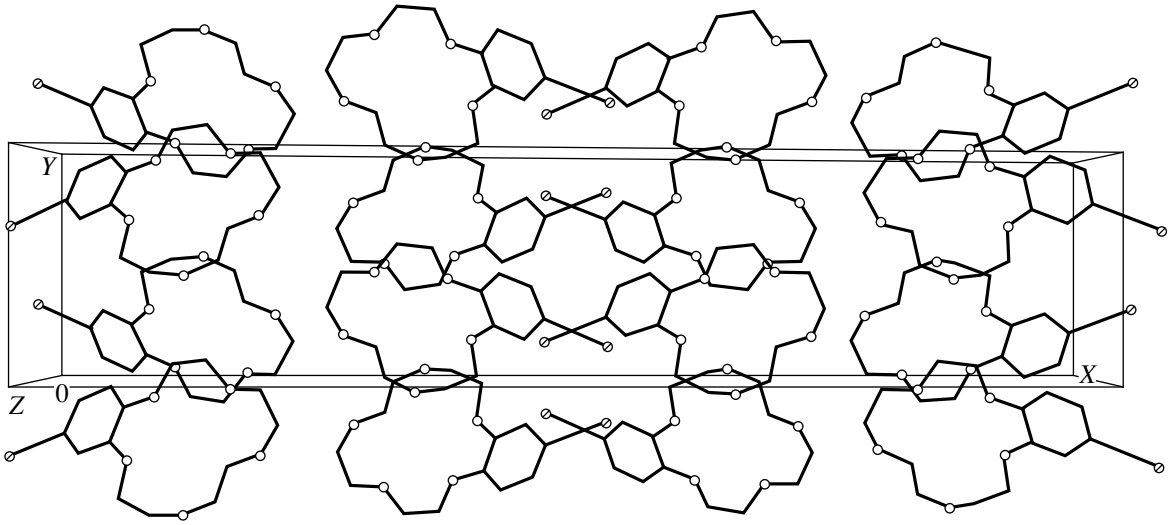

Fig. 2. Crystal structure of 4'-cyanobenzo-15-crown-5.

Analysis of the conformation of the macrocycle in benzo-15-crown-5 and its derivatives [9–12] reveals that the condensation of the macrocycle with the benzene ring causes the C(1)–C(6) bond to adopt the *cis* conformation. The conformation of the macrocycle as a whole in 4'-cyanobenzo-15-crown-5 is characterized by nine *anti* bonds, five *gauche* bonds, and one *cis* bond. The sequence of torsion angles is *a–a–g⁻–a–a–g–g⁻–a–a–g–a–g–a–a–s*.

The bond lengths and angles have the normal values. The only exception is provided by the C(11)–C(12) bond (1.369 Å), which is shorter than the commonly observed bonds (1.45–1.54 Å). This shortening can

Table 2. Torsion angles, deg

Angle	Value			
	4'-cyano-B15C5	4'-hexanoyl-B15C5	4',5'-dibromo-B15C5	Na complex of B15C5-sulfonate
C(6)–C(1)–O(5)–C(14)	166.0	−168.6	−164.3	−170.8
C(6)–O(1)–C(6)–C(1)	−175.3	173.1	169.9	172.3
O(1)–C(6)–C(1)–O(5)	2.2	0.3	−3.3	−1.3
C(6)–O(1)–C(7)–C(8)	175.4	−175.6	−167.5	−179.4
C(9)–O(2)–C(8)–C(7)	173.4	−170.0	−159.7	−170.0
O(2)–C(8)–C(7)–O(1)	−62.4	75.9	71.9	61.0
C(10)–C(9)–O(2)–C(8)	−162.8	82.4	93.1	86.1
C(11)–O(3)–C(10)–C(9)	−70.6	−87.9	−162.4	−177.5
O(3)–C(10)–C(9)–O(2)	71.2	70.3	51.3	58.3
C(12)–C(11)–O(3)–C(10)	−167.1	−150.6	174.4	−179.5
C(13)–O(4)–C(12)–C(11)	103.6	−81.2	−86.4	−86.1
O(4)–C(12)–C(11)–O(3)	−178.4	−170.3	−66.1	−60.0
C(14)–C(13)–O(4)–C(12)	−129.4	130.4	159.2	172.2
C(1)–O(5)–C(14)–C(13)	−164.7	167.4	167.3	177.1
O(5)–C(14)–C(13)–O(4)	70.8	−74.5	−68.0	−60.2

result from increased thermal vibrations of atoms or from the atomic disordering in this region. The observed decrease of the $C(sp^3)$–$C(sp^3)$ bond lengths in the macrocycle of the molecule studied is characteristic of other crown ethers as well [9–12].

The molecules in the crystal are packed in a "tail-to-tail" fashion (Fig. 2). Short intermolecular contacts are absent.

REFERENCES

1. B. A. Tashmukhamedov, A. I. Gagel'gans, A. V. Shkinev, *et al*., Bioorg. Khim. **5**, 429 (1979).
2. A. I. Gagel'gans, A. V. Shkinev, U. Z. Mirkhodzhaev, *et al*., Biol. Membr. **1**, 273 (1984).
3. U. Z. Mirkhodzhaev, V. A. Boldyrov, A. K. Tashmukhamedova, *et al*., Biofizika **34**, 235 (1989).
4. A. V. Shkinev, A. I. Gagel'gans, A. K. Tashmukhamedova, and B. A. Tashmukhamedov, Khim. Prir. Soedin., No. 2, 242 (1979).
5. U. Z. Mirkhodzhaev, V. A. Boldyrov, A. K. Tashmukhamedova, and B. A. Tashmukhamedov, Dokl. Akad. Nauk Uzb. SSR, No. 12, 36 (1986).
6. A. D. Grebenyuk and A. K. Tashmukhamedova, Dokl. Akad. Nauk Resp. Uzb., No. 6, 32 (1994).
7. G. M. Scheldrick, *SHELXS86: Program for the Solution of Crystal Structures* (Univ. of Göttingen, Göttingen, 1986).
8. G. M. Scheldrick, *SHELX76: Program for Crystal Structure Determination* (Univ. of Cambridge, Cambridge, 1976).
9. N. E. Zhukhlistova, V. I. Smirnova, Yu. V. Nekrasov, *et al*., Kristallografiya **34** (4), 874 (1989) [Sov. Phys. Crystallogr. **34** (4), 524 (1989)].
10. I. R. Hanson, Acta Crystallogr., Sect. B **34**, 1026 (1978).
11. Z. Karimov, S. A. Talipov, B. T. Ibragimov, *et al*., Kristallografiya **43** (3), 478 (1998) [Crystallogr. Rep. **43** (3), 439 (1998)].
12. Z. Karimov, S. A. Talipov, B. T. Ibragimov, *et al*., Kristallografiya **43** (3), 482 (1998) [Crystallogr. Rep. **43** (3), 443 (1998)].

Translated by I. Polyakova

Crystallography Reports, Vol. 45, No. 3, 2000, pp. 453–456. Translated from Kristallografiya, Vol. 45, No. 3, 2000, pp. 496–499.

STRUCTURES OF ORGANIC COMPOUNDS

Crystal Structure of 5-(2'-Aminophenyl)-2-Dimethylamino-1,3,4-Thiadiazole

S. T. Malinovskiĭ*, G. G. Rusu*,, N. A. Barba**, M. Z. Krimer*, and J. Lipkowski*****

** Institute of Chemistry, Academy of Sciences of Moldova, Academiei 3, Chisinau, 20-28 Moldova*

*** Moldova State University, ul. Matteevicha 60, Chisinau, 277009 Moldova*

**** Institute of Physical Chemistry, Polish Academy of Sciences, Warsaw, Poland*

Received April 16, 1998

Abstract—The crystal structure of 5-(2'-Aminophenyl)-2-dimethylamino-1,3,4-thiazole is determined by X-ray diffraction. The compound is prepared by an unusual recyclization of 3-*N*,*N*-dimethylthioureidoquinazolin-4(3*H*)-one. The crystal is monoclinic, space group $P2_1/c$, $a = 7.420(2)$ Å, $b = 10.466(5)$ Å, $c = 14.752(9)$ Å, $\beta = 109.2(4)°$, $\rho_{calcd} = 1.359$ g/cm^3, and $Z = 4$ for the $C_{10}H_{12}N_4S$ composition. The molecule consists of the thiadiazole and phenyl rings and the dimethylamine $N(CH_3)_2$ and amine NH_2 groups attached to the rings. The molecule as a whole is planar. The dihedral angle between the rings is 8.9°. The N(1) and N(4) atoms in the molecule are bound through the intramolecular interaction (2.76 Å). Molecules, which are linked in pairs by antiparallel hydrogen bonds, form a framework structure. © *2000 MAIK "Nauka/Interperiodica".*

Derivatives of 3-aminoquinazolin-4(3*H*)-one are widely used in organic synthesis and exibit a wide spectrum of physiological properties [1–3]. The thiocarbamoyl derivatives form a class of compounds that are least studied both chemically and biologically. We found that the heating of 3-*N*,*N*-dimethylthioureidoquinazolin-4(3*H*)-one (**I**) with concentrated sulfuric acid in 1,4-dioxane at 90–95°C results in a new compound, whose composition is $C_{10}H_{12}N_4S$. Based on the composition and the results of ^{1}H and ^{13}C NMR and IR spectroscopic studies, we suggested that the compound obtained is 5-(2'-aminophenyl)-2-dimethylamino-1,3,4-thiadiazole (**II**)

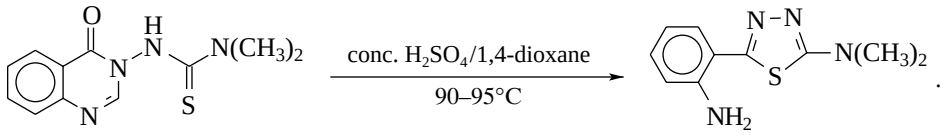

I **II**

In order to determine the structure directly and to reveal specific structural and conformational features of the compound obtained, we performed its complete X-ray diffraction study.

The experimental data were obtained from a colorless single crystal ($0.2 \times 0.3 \times 0.5$ mm in size) of an irregular shape. The crystal is monoclinic, space group $P2_1/c$, $a = 7.420(2)$ Å, $b = 10.466(5)$ Å, $c = 14.752(9)$ Å, $\beta = 109.2(4)°$, $\rho_{calcd} = 1.359$ g/cm^3, and $Z = 4$ for $C_{10}H_{12}N_4S$. The data were collected on an Enraf–Nonius Nicolet *P*3 diffractometer (CuK_α radiation, θ–2θ scan technique). The structure was solved by the direct method within the SHELX program package [4]. The calculations were performed for 2127 unique reflections with $I \geq 3\sigma(I)$.

The non-hydrogen atoms were refined in the anisotropic approximation, and the hydrogen atoms were refined isotropically. The final *R* factor was 0.051. The atomic coordinates are listed in the table.

The molecule consists of the thiadiazole (*1*) and phenyl (*2*) rings and the dimethylamine $N(CH_3)_2$ and amine NH_2 groups, which are attached to rings *1* and *2*, respectively (Fig. 1). The molecule as a whole is planar; the dihedral angle between its rings is 8.9°. The atomic deviations from the root-mean-square plane of the thiadiazole ring fall in the range 0.001–0.005 Å. In the phenyl ring, the carbon atoms are coplanar within 0.007 Å. The N(3) nitrogen atom of the dimethylamine fragment deviates from the plane of ring *1* by 0.017 Å, and the N(4) atom of the amine group deviates from the plane of ring *2* by 0.019 Å. The selected torsion angles

1063-7745/00/4503-0453$20.00 © 2000 MAIK "Nauka/Interperiodica"

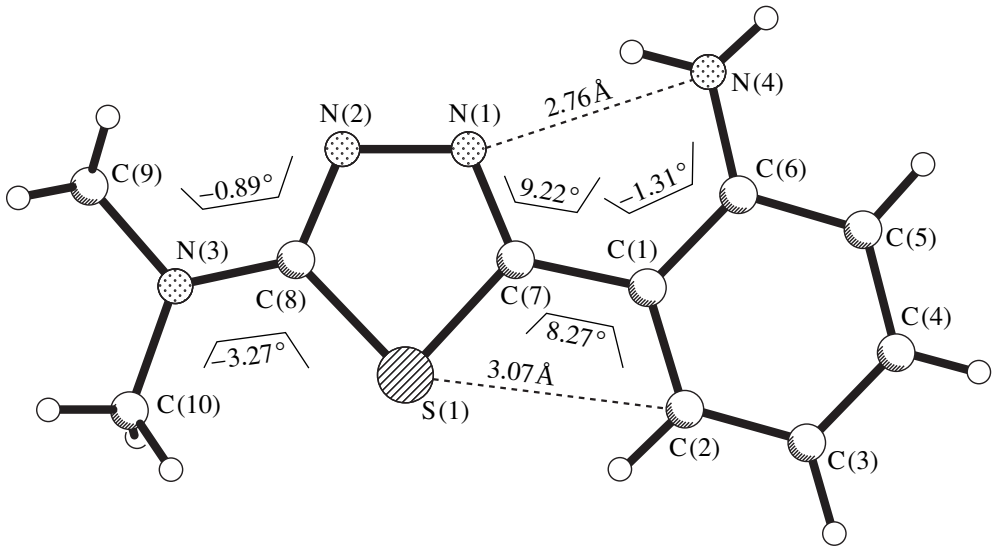

Fig. 1. Molecular structure of the $C_{10}H_{12}N_4S$ compound.

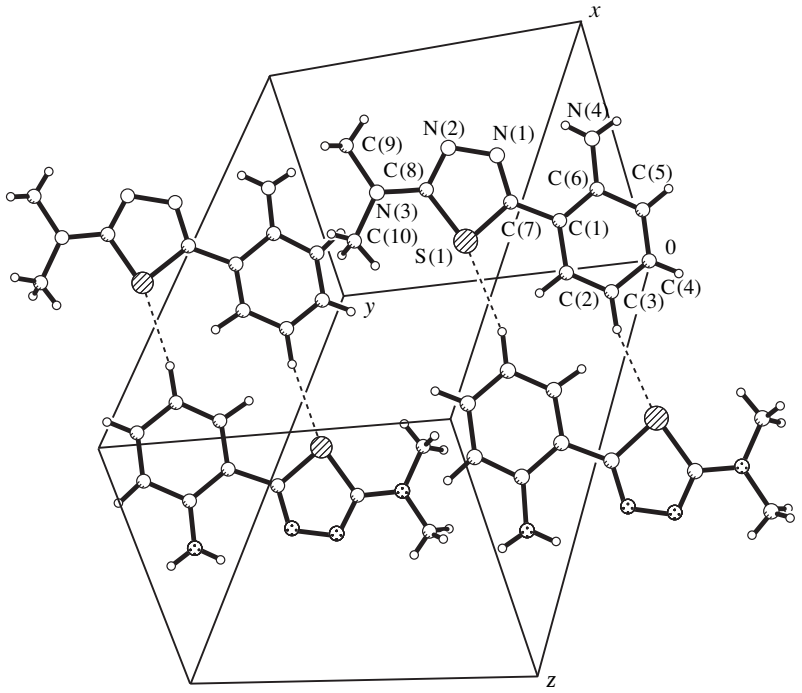

Fig. 2. A fragment of the molecular packing: arrangement of molecules in flat networks.

are shown in Fig. 1. The bond lengths and angles in the molecule agree well with the available data on the structures of organic molecules [5, 6]. A slight difference in the S–C(7) and S–C(8) bond lengths (1.738 and 1.748 Å, respectively) and the bond angle at the sulfur atom (87.1°) apparently can be explained by the electrostatic 1,4-interaction between the S and C(2) atoms (3.07 Å). The intramolecular interaction between the N(1) and N(4) atoms (2.76 Å) in the molecule can be considered as the N(4)–H··N(1) hydrogen bond [N(4)–H, 0.93 Å; N(4)··N(1), 2.09 Å; and the angle at the H atom is 154°].

The packing of the molecules in the structure is of particular interest. The intermolecular hydrogen bonds C(3)–H··S [C(3)··S, 3.60 Å; C(3)–H, 1.02 Å; S··H(C3), 2.92; and angle C(3)–H··S, 145°] link mol-

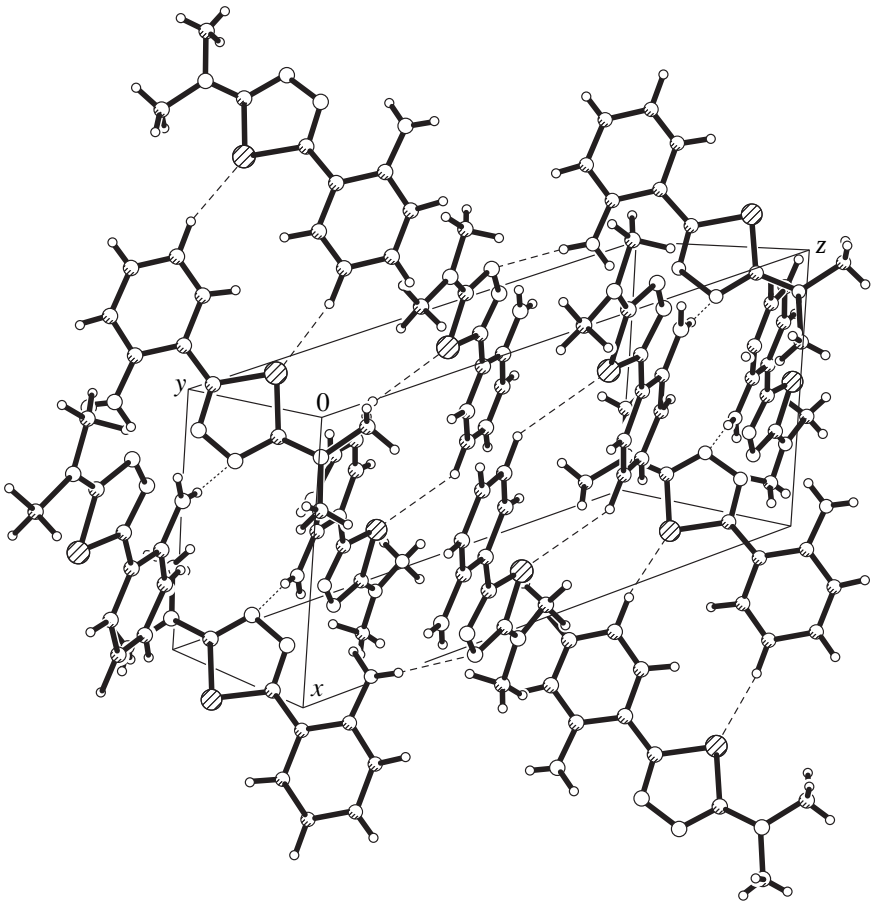

Fig. 3. Crystal structure of the $C_{10}H_{12}N_4S$ compound.

ecules into centrosymmetric dimers, which are arranged in flat networks parallel to the *xy* plane (Fig. 2). The flat networks of dimers, in turn, are interlinked by the hydrogen bonds N(2)··H–N(4) [N(2)··N(4c), 3.15 Å; N(2)··H, 2.32 Å; N(4c)–H, 0.91 Å, and angle N(4c)–H··N(2), 175°]. As a whole, the crystal structure can be considered a layered structure (Fig. 3).

Atomic coordinates ($\times 10^4$) and equivalent thermal parameters ($Å^2 \times 10^3$) for the structure

Atom	*x*	*y*	*z*	U_{eq}	Atom	*x*	*y*	*z*	U_{eq}
S(1)	8741(1)	1938(1)	4927(1)	47(1)	C(4)	4001(4)	–1590(3)	2769(2)	61(1)
N(1)	10030(2)	1239(2)	3604(1)	47(1)	C(5)	5502(4)	–1600(2)	2417(2)	58(1)
N(2)	11312(3)	2149(2)	4128(1)	50(1)	C(6)	7048(3)	–754(2)	2764(1)	47(1)
N(3)	11844(3)	3470(2)	5478(2)	64(1)	C(7)	8616(3)	1018(2)	3918(1)	39(1)
N(4)	8497(4)	–792(2)	2396(2)	69(1)	C(8)	10836(3)	2591(2)	4848(1)	46(1)
C(1)	7043(3)	120(2)	3497(1)	40(1)	C(9)	13591(5)	3971(3)	5383(2)	76(1)
C(2)	5483(3)	113(2)	3828(1)	47(1)	C(10)	11186(5)	3969(3)	6223(2)	71(1)
C(3)	3971(3)	–720(2)	3476(2)	56(1)					

Thus, the data of the X-ray diffraction analysis confirmed that, under the action of concentrated sulfuric acid, 3-*N*,*N*-dimethylthioureidoquinazolin-4(3*H*)-one undergoes recyclization with the formation of 5-(2'-aminophenyl)-2-dimethylamino-1,3,4-thiadiazole.

REFERENCES

1. K. Smith, G. A. El-Hiti, M. A. Abdo, and M. F. Abdel-Megeed, J. Chem. Soc., Perkin Trans. 1, No. 8, 1029 (1995).
2. M. F. Abdel-Megeed, M. A. Saleh, M. A. Abdo, and G. A. El-Hiti, Collect. Czech. Chem. Commun. **60**, 1016 (1995).
3. R. S. Atkinson and E. Barker, J. Chem. Soc., Perkin Trans. 1, No. 8, 819 (1995).
4. G. M. Sheldrick, in *SHELXS86: Crystallographic Computing 3*, Ed. by G. M. Sheldrick, C. Krüger, and R. Goddard (Oxford Univ. Press, Oxford, 1986), p. 175.
5. C. Byrne, J. P. James, and C. Long, J. Chem. Soc., Chem. Commun. **61**, 945 (1996).
6. M. Fettonhi, A. Bonklari, and B. El. Otmani, Acta Crystallogr. **52**, 1032 (1966).

Translated by I. Polyakova

Crystallography Reports, Vol. 45, No. 3, 2000, pp. 457–465. Translated from Kristallografiya, Vol. 45, No. 3, 2000, pp. 500–508.

Quasi-Rayleigh Waves in Sandwich Structures: Dispersion Equation, Eigenmodes, and Resonance Reflection

V. I. Alshits*, V. N. Lyubimov*, and A. Radowicz**

** Shubnikov Institute of Crystallography, Russian Academy of Sciences, Leninskiĭ pr. 59, Moscow, 117333 Russia*

*** Kielce University of Technology, Kielce, Poland*

Received October 19, 1998

Abstract—The dispersion equation for quasi-Rayleigh acoustic modes in transversely isotropic sandwich-type structures (an elastic layer between two substrates) has been obtained in the analytical form. The equation is analyzed for three types of structures—a layer between two soft substrates, a layer between a soft and a hard substrate, and a structure consisting of two contacting substrates with markedly different values of hardness. Eigenmodes are determined for all three structures. Depending on the combination of the material parameters in these structures, these eigenwaves are either Rayleigh-type waves localized at interfaces in the substrates and accompanying a Lamb wave in the interlayer (in the absence of an interlayer, forming a Stoneley wave) or the leaky modes characterized by a small imaginary addition to the phase velocity and the presence of bulk partial waves of leakage providing some energy removal from the interfaces. Without any calculations, simple criteria were established that allow one to predict the existence of a leaky mode in the given structure and the number of leakage fluxes it contains. The resonance reflection is analized for the case where the incidence angle of the wave in the substrate corresponding to the velocity v of the wave-front propagation along the interface is close to the value of the real part of the phase velocity of the leaky mode. *© 2000 MAIK "Nauka/Interperiodica".*

INTRODUCTION

As is well known [1, 2], acoustic waves propagating in the isotropy plane common for all the layers of various structures consisting of isotropic or transversely isotropic elastic layers exist as two independent families of which one is polarized in the propagation plane, and the other normally to it. It is much simpler to analyze the latter case because all the partial modes in such a wave (incident, reflected, refracted, and localized at the interface) are polarized in the same way, and the problem reduces, in fact, to the calculation of scalar amplitudes of these waves. Among the waves of this class are the so-called Love waves formed in the structure consisting of a layer on a semiinfinite substrate. The method of resonance excitation of such waves in a sandwich structure (a layer between two substrates) was suggested in [3].

An example of the waves belonging to the first family is a Lamb wave propagating in a plate and polarized in the propagation plane. Along with an infinite number of the Lamb wave-guide-type modes propagating via successive reflection of the bulk waves from the plate surface, there also exist one or two inhomogeneous or the so-called quasi-Rayleigh modes polarized in the propagation plane and transforming into a Rayleigh surface wave in the limiting transition corresponding to an infinite increase of the plate thickness in comparison with the wave length. The resonance excitation of such waves in a layer on a substrate due to a specially chosen incidence angles was considered in [4].

The resonances discussed in [3, 4] are based on the same physical concept [5, 6]. If an additional substrate with a certain hardness value and wave characteristics is added to the surfaces of the structure under consideration, the corresponding eigenwaves in these structures (the Love or the quasi-Rayleigh Lamb waves) become leaky waves and acquire some partial volume leakage components, which remove the energy into the bulk of the attached substrate. If one directs the bulk wave at the interface of this substrate in such a way that the reflected wave coincides with the wave of leakage, then the resonance excitation of the corresponding eigenmodes arises in the initial structure.

Below, we describe the study of the same phenomenon as in [4]—a sagittal polarized family of waves in a more complicated structure than that in [4]. In other words, we consider the properties of quasi-Rayleigh eigenwaves in a sandwich substrate–layer–substrate structure. We consider here three types of structures: an elastic layer between two soft substrates, a layer between soft and stiff substrates, and the limiting structure corresponding to the zeroth layer and the direct contact of two substrates with essentially different hardness. We determine the eigenwaves in these structures and establish the simple criteria for the case where the wave fields are conventional inhomogeneous waves localized at the boundaries and for the case where these waves belong to the class of leaky waves. We also analyzed possible resonance excitation of eigenwaves in the above structures.

1063-7745/00/4503-0457$20.00 © 2000 MAIK "Nauka/Interperiodica"

FORMULATION OF THE PROBLEM AND INITIAL RELATIONSHIPS

A sandwich structure intersected by the $\{x, y\}$ sagittal plane coinciding with the transverse-isotropy plane is shown in Fig. 1. An elastic layer between two substrates has the thickness $d = 2a$. We have to consider the elastic moduli of this layer, c_{11} and c_{66}, and its density ρ, the material parameters determining the velocities of the longitudinal (l) and transverse (t') bulk waves polarized in the $\{x, y\}$ plane and propagating in it:

$$v_l = (c_{11}/\rho)^{1/2}, \quad v_{t'} = (c_{66}/\rho)^{1/2}. \tag{1}$$

The wave field of elastic displacements in the layer (and also in the substrates) is a superposition of four partial waves:

$$\mathbf{u}(x, y, t) = a_l^+\mathbf{u}_l^+ + a_l^-\mathbf{u}_l^- + a_{t'}^+\mathbf{u}_{t'}^+ + a_{t'}^-\mathbf{u}_{t'}^-. \tag{2}$$

Here $a_\alpha^\pm$ ($\alpha = l, t'$) are the scalar amplitudes of the partial waves,

$$\mathbf{u}_\alpha^\pm(x, y, t) = \mathbf{u}_\alpha^{(0)\pm} e^{\mp p_\alpha k y} e^{ik(x - vt)}, \quad -a \le y \le a. \tag{3}$$

The quantities $\mathbf{u}_\alpha^{(0)\pm}$ are the polarization vectors normalized to unity, v is the reduced phase velocity defined as $v = \omega/k$, where ω is the frequency, and k is the x-component of the wave vectors that is common for all the partial waves, $k \equiv k_x$. Obviously, $k_{\alpha y}^\pm = \pm i p_\alpha k$.

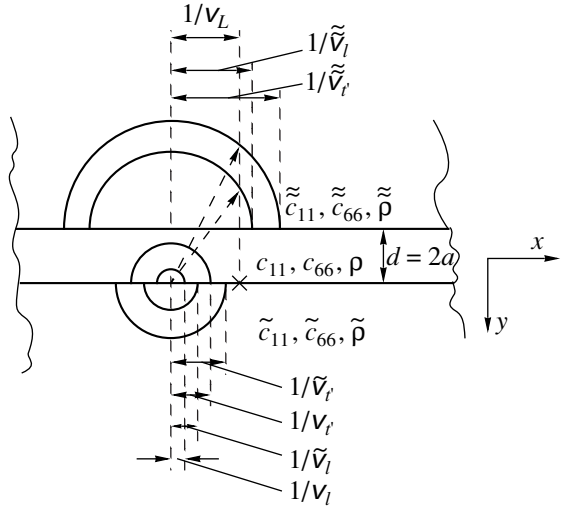

Fig. 1. Sandwich structure and its major acoustic characteristics. Semicircumferences indicate the slowness curves of bulk waves; the dashed arrows correspond to leakage fluxes in the leaky mode (the cross indicates the real part of the reciprocal velocity v_L^{-1} of this mode).

The vectors $\mathbf{u}_\alpha^\pm$ in (2) and (3) are independent solutions of the equations of motion

$$\rho\partial^2\mathbf{u}/\partial t^2 = (\nabla\hat{C}\nabla)\mathbf{u}, \tag{4}$$

where $\hat{C}$ is the elastic-moduli tensor and $\nabla = (\partial/\partial x, \partial/\partial y)$. Substituting (3) into (4) and performing some simple calculations, we arrive at

$$\mathbf{u}_l^{(0)\pm} = (1, \pm i p_l)/N_l, \quad \mathbf{u}_{t'}^{(0)\pm} = (\mp i p_{t'}, 1)/N_{t'}, \quad N_\alpha = v/v_\alpha; \tag{5}$$

$$p_\alpha = \begin{cases} (1 - v^2/v_\alpha^2)^{1/2}, & v < v_\alpha \\ -i(v^2/v_\alpha^2 - 1)^{1/2} \equiv -iq_\alpha, & v > v_\alpha. \end{cases} \tag{6}$$

The choice of the signs in (6), which was made when solving equation

$$p_\alpha^2 = 1 - v^2/v_\alpha^2, \tag{6a}$$

was dictated by the following requirement. The inhomogeneous mode (increasing with the distance from the surface) should be transformed into a homogeneous mode incident onto the surface in the transition of the velocity v through the point $v = v_\alpha$.

Now consider the wave field distribution in the substrates. In the upper and lower substrates (Fig. 1) characterized by the material constants $\tilde{c}_{11}$, $\tilde{c}_{66}$, $\tilde{\rho}$ and $\tilde{\tilde{c}}_{11}$, $\tilde{\tilde{c}}_{66}$, $\tilde{\tilde{\rho}}$, respectively, the wave fields can be described by relationships (2)–(6) with the amplitudes $a_\alpha^\pm$, polarization vectors $\mathbf{u}_\alpha^{(0)\pm}$, the parameters p_α and q_α, and the velocities v_α marked with one or two tildes, respectively.

The boundary conditions at the interfaces between the media ($y = \pm a$) are determined by the requirement of continuity of displacements and normal stress components:

$$\begin{aligned} \mathbf{u}(x, a, t) &= \tilde{\mathbf{u}}(x, a, t), \\ \mathbf{u}(x, -a, t) &= \tilde{\tilde{\mathbf{u}}}(x, -a, t), \\ \mathbf{n}[(\hat{C}\nabla)\mathbf{u}(x, y, t) - (\hat{\tilde{C}}\nabla)\tilde{\mathbf{u}}(x, y, t)]_{y = a} &= 0, \\ \mathbf{n}[(\hat{C}\nabla)\mathbf{u}(x, y, t) - (\hat{\tilde{\tilde{C}}}\nabla)\tilde{\tilde{\mathbf{u}}}(x, y, t)]_{y = -a} &= 0. \end{aligned} \tag{7}$$

Here, $\mathbf{n}$ is the normal to the boundaries under consideration. The continuity conditions (7) form a system of eight linear equations with eight unknowns—four amplitudes of the partial waves in the layer $a_\alpha^\pm$ ($\alpha = l, t'$) and four amplitudes of the waves in the substrates, $\tilde{a}_\alpha^+$ and $\tilde{\tilde{a}}_\alpha^-$, corresponding either to inhomogeneous localized modes with the real parameters $\tilde{p}_\alpha$ and $\tilde{\tilde{p}}_\alpha$, or to the reflected and refracted bulk waves that transfer the

energy from the interfaces with the imaginary parameters $\tilde{p}_\alpha$ and $\tilde{\tilde{p}}_\alpha$. In the general case, the right-hand side of this system contains four amplitudes $\tilde{a}_\alpha^-$ and $\tilde{\tilde{a}}_\alpha^+$ considered to be known. Those of the amplitudes that correspond to real $\tilde{p}_\alpha$ or $\tilde{\tilde{p}}_\alpha$ (which signifies that they are the amplitudes of nonphysical inhomogeneous modes exponentially increasing with the distance from the interface) should be taken to be zero, whereas all the other amplitudes correspond to the incident waves of the reflection problem and can be set arbitrarily. In this case, the velocity v, included as a parameter in the coefficients of the system, is determined by the angle of incidence used. The standard solution of this system has the form

$$\begin{aligned} a_\alpha^\pm &= D_\alpha^\pm(v,k)/D(v,k), \\ \tilde{a}_\alpha^+ &= \tilde{D}_\alpha^+(v,k)/D(v,k), \\ \tilde{\tilde{a}}_\alpha^- &= \tilde{\tilde{D}}_\alpha^-(v,k)/D(v,k), \end{aligned} \tag{8}$$

where the common denominator $D(v, k)$ is the determinant of the matrix of the coefficients before unknowns. The eigenwave modes of the sandwich structure studied can consist of the partial waves alone, which are localized at the interfaces, or can also include the bulk waves of leakage that transfer the energy away from the interfaces. In this formulation of the problem, the velocity v is determined from the condition of the existence of nontrivial solutions of the homogeneous system of equations

$$D(v,k) = 0. \tag{9}$$

Thus, the velocities of eigenmodes are determined by the poles of the functions that provide solution (8) of the reflection problem.

DISPERSION EQUATION FOR EIGENMODES

Dispersion equation (9) that sets the dependence of the velocity v on the wave number k (in what follows, we use the dimensionless parameter $K \equiv ka$) can be obtained in an explicit form. Omitting cumbersome transformations, we indicate here only the final result

$$D(v,k) = 4F_1(v,k) + 2F_2(v,k) + F_3(v,k) = 0, \tag{10}$$

where, the function F_1 has the form

$$F_1 = R_s R_a \tilde{f}\tilde{\tilde{f}} + (\tilde{\Gamma}\tilde{\tilde{\Gamma}})^2 \tilde{R}\tilde{\tilde{R}} f_s f_a, \tag{11}$$

and the following notation is introduced

$$\begin{aligned} R_s &= -(p_{t'}^2 + 1)\tanh p_{t'}K + 4p_l p_{t'}\tanh p_l K, \\ \tilde{R} &= (\tilde{p}_{t'}^2 + 1)^2 - 4\tilde{p}_l\tilde{p}_{t'}, \\ f_s &= -\tanh p_{t'}K + p_l p_{t'}\tanh p_l K, \\ \tilde{f} &= 1 - \tilde{p}_l\tilde{p}_{t'}, \quad \tilde{\Gamma} = \tilde{c}_{66}/c_{66}. \end{aligned} \tag{12}$$

The expressions for $\tilde{\tilde{R}}$, $\tilde{\tilde{f}}$, and $\tilde{\tilde{\Gamma}}$ are obtained from the above formulas for $\tilde{R}$, $\tilde{f}$, and $\tilde{\Gamma}$ by substituting $\tilde{p}_\alpha$ by $\tilde{\tilde{p}}_\alpha$ and $\tilde{c}_{66}$ by $\tilde{\tilde{c}}_{66}$. The transition from the functions with the subscript s to the functions with the subscript a (e.g., $R_s \longrightarrow R_a$) reduces to the substitution tanh $\longrightarrow$ cotanh.

The expression for the function F_2 in (10) can be represented in the form

$$F_2 = \tilde{\Gamma}\tilde{F}_2^R\tilde{\tilde{f}} + \tilde{\tilde{\Gamma}}\tilde{\tilde{F}}_2^R\tilde{f} + \tilde{\Gamma}\tilde{\tilde{\Gamma}}(\tilde{\Gamma}\tilde{R}\tilde{\tilde{F}}_2^f + \tilde{\tilde{\Gamma}}\tilde{\tilde{R}}\tilde{F}_2^f), \tag{13}$$

where

$$\begin{aligned} \tilde{F}_2^R &= 2\{r_s R_a\}\tilde{r} \\ &+ (N_{t'}\tilde{N}_{t'})^2(\{R_s\}p_{t'}\tilde{p}_l + \{\eta_s R_a\}p_l\tilde{p}_{t'}). \end{aligned} \tag{14}$$

The curly brackets introduced here for the sake of brevity denote the following combinations

$$\{b_s c_a\} = b_s c_a + b_a c_s, \quad \{b_s\} = b_s + b_a. \tag{15}$$

Also, in (13), we also use the notation

$$\begin{aligned} r_s &= -(p_{t'}^2 + 1)\tanh p_{t'}K + 2p_l p_{t'}\tanh p_l K, \\ \tilde{r} &= -(p_{t'}^2 + 1) + 2\tilde{p}_l\tilde{p}_{t'}, \quad \eta_s = \tanh p_l K \tanh p_{t'}K. \end{aligned} \tag{16}$$

The function $\tilde{F}_2^R$ is transformed into $\tilde{\tilde{F}}_2^R$ by marking the corresponding quantities in (14) with a tilde. Expressions for $\tilde{F}_2^f$ and $\tilde{\tilde{F}}_2^f$ are obtained from the expressions for $\tilde{F}_2^R$ and $\tilde{\tilde{F}}_2^R$ by substituting $R_{a,s}$ by $f_{a,s}$.

Finally, the last term in (10) has the form

$$F_3 = (\tilde{\Gamma}^2\tilde{R}\tilde{\tilde{f}} + \tilde{\tilde{\Gamma}}^2\tilde{\tilde{R}}\tilde{f})G + \tilde{\Gamma}\tilde{\tilde{\Gamma}}H, \tag{17}$$

where

$$\begin{aligned} G &= A + B + C, \\ A &= \{f_s R_a\}, \quad B = -N_{t'}^4\{\eta_s\}p_l p_{t'}, \quad C = 2r_s r_a, \end{aligned} \tag{18}$$

$$\begin{aligned} H &= 2(A - B + 3C)\tilde{r}\tilde{\tilde{r}} \\ &- (\tilde{N}_{t'}\tilde{\tilde{N}}_{t'})^2(A + B - C)(\tilde{p}_l\tilde{\tilde{p}}_{t'} + \tilde{p}_{t'}\tilde{\tilde{p}}_l) \\ &+ 4(N_{t'}\tilde{N}_{t'}\tilde{\tilde{N}}_{t'})^2[N_{t'}^2(p_l^2\tilde{p}_{t'}\tilde{\tilde{p}}_{t'} + p_{t'}^2\tilde{p}_l\tilde{\tilde{p}}_l) \end{aligned} \tag{19}$$

$$+\{r_s\}p_{t'}(\tilde{r}\tilde{\tilde{p}}_l\tilde{\tilde{N}}_{t'}^2+\tilde{\tilde{r}}\tilde{p}_l\tilde{N}_{t'}^2)$$
$$+\{\eta_s r_a\}p_l(\tilde{r}\tilde{\tilde{p}}_{t'}\tilde{\tilde{N}}_{t'}^2+\tilde{\tilde{r}}\tilde{p}_{t'}\tilde{N}_{t'}^2)].$$

To the eigenmodes localized in the vicinity of the layer there correspond the velocities v [the roots of dispersion equation (10)] in which all the parameters $\tilde{p}_\alpha$ and $\tilde{\tilde{p}}_\alpha$ are real. This takes place if

$$v < \min(\tilde{v}_{t'}, \tilde{\tilde{v}}_{t'}). \quad (20)$$

Of course, in the general case, dispersion equation (10) does not necessarily has real roots. Their existence depends on the relationships between the material characteristics of the media.

Another class of solutions is described by complex roots

$$v = v_L - iv'_L, \quad (21)$$

corresponding to the so-called leaky eigenwaves including the bulk partial modes (wave of leakage) that remove the energy from the layer into the bulk of one or both substrates. In fact, the solutions of type (21) have an obvious physical sense only if

$$v'_L \ll v_L, \quad (22)$$

i.e., only if the wave field in the layer decays relatively feebly—at the distance of a wave length along the interfaces. Condition (22) automatically provides low amplitude values for bulk waves of leakage. Obviously, the number of the waves of leakage is determined by the relationship between the velocities v_L, $\tilde{v}_\alpha$, and $\tilde{\tilde{v}}_\alpha$ and ranges from one to four. The latter case take place if

$$v_L > \max(\tilde{v}_l, \tilde{\tilde{v}}_l). \quad (23)$$

Below, we determine the parameters of the localized- and leaky-type eigenwaves for two different three-layer structures and a bicrystal.

LOCALIZED AND LEAKY QUASI-RAYLEIGH MODES IN SANDWICH-TYPE STRUCTURES

Plate between two soft substrates ($\tilde{\Gamma}$, $\tilde{\tilde{\Gamma}} \ll 1$). Consider a plate between two soft substrates. We assume that the elastic moduli in the substrates, $\hat{\tilde{c}}$ and $\hat{\tilde{\tilde{c}}}$, and their densities, $\tilde{\rho}$ and $\tilde{\tilde{\rho}}$, are small in comparison with the corresponding parameters of the plate. At the same time, the velocities $\tilde{v}_\alpha$ and $\tilde{\tilde{v}}_\alpha$ of the bulk waves in the substrates and the corresponding parameters $\tilde{p}_\alpha$ and $\tilde{\tilde{p}}_\alpha$ remain finite. This allows the description of the problem by two small parameters $\tilde{\Gamma} = \tilde{c}_{66}/c_{66}$ and $\tilde{\tilde{\Gamma}} = \tilde{\tilde{c}}_{66}/c_{66}$.

In the zeroth approximation (the hardness values of the substrates tend to zero and, therefore, $\tilde{\Gamma} \longrightarrow 0$ and $\tilde{\tilde{\Gamma}} \longrightarrow 0$), dispersion equation (10) is simplified to the form

$$R_s R_a = 0 \quad (24)$$

and describes a symmetric ($R_s(v) = 0$) and an antisymmetric ($R_a(v) = 0$) Lamb waves. The detailed analysis of these equations and the explicit form of the corresponding wave fields of types (2) and (3) were studied elsewhere [4]. As is well known, an antisymmetric inhomogeneous Lamb wave exists at the free boundaries of an isotropic (or transversely isotropic) plate irrespectively of the value of the wave number $K = ka$. The symmetric inhomogeneous eigenmode also exists irrespectively of the K value, but only if $c_{66}/c_{11} > 3/4$. At lower values of the c_{66}/c_{11} ratio, a threshold number K_0 arises. It limits from below the range of existence of the symmetric inhomogeneous wave: $K > K_0$. If $K < K_0$; this mode is transformed into the waveguide mode with the bulk component (or components) and propagates along the plate via a successive reflection from the surface.

At small but finite values, $\tilde{\Gamma}$, $\tilde{\tilde{\Gamma}} \ll 1$, equation (10) in the linear approximation with respect to these parameters takes the form

$$R_s R_a + \tilde{\Gamma}\tilde{F}_2^R/2\tilde{f} + \tilde{\tilde{\Gamma}}\tilde{\tilde{F}}_2^R/2\tilde{\tilde{f}} = 0. \quad (25)$$

One important remark should be made. As is well known, with an increase of the parameter K, the roots of unperturbed equation (24) (the velocities $v^{(s)}$ and $v^{(a)}$) approach (from above and from below, respectively) the velocity v_R of the Rayleigh wave and, at sufficiently high K values, become exponentially close to the velocity v_R. In this limiting case, one has to consider independent Rayleigh waves propagating in the subsurface layers of the plate. The penetration depths of these waves are considerably less than the plate thickness. Therefore at $K \gg 1$, the problem reduces to the independent influences of both substrates on the corresponding Rayleigh waves. Similar to [4], we assume that the wave number K belongs to the range, where the parameters $R_s(v^{(a)})$ and $R_a(v^{(s)})$ are not small, at least, in comparison with $\tilde{\Gamma}$ and $\tilde{\tilde{\Gamma}}$.

With due regard for the above stated, one can determine the substrate-induced perturbations in the velocities $v^{(s,a)}$:

$$v^{(s)} \longrightarrow v^{(s)} + \Delta v^{(s)}, \quad v^{(a)} \longrightarrow v^{(a)} + \Delta v^{(a)}, \quad (26)$$

$$\Delta v^{(s,a)} = -\left((\partial R_{s,a}/\partial v)^{-1} \left\{ r_{s,a}(\tilde{\Gamma}\tilde{r}/\tilde{f} + \tilde{\tilde{\Gamma}}\tilde{\tilde{r}}/\tilde{\tilde{f}}) + \frac{1}{2}N_{t'}^4[\tilde{\gamma}(p_{t'}\tilde{p}_l + \eta_{s,a}p_l\tilde{p}_{t'})/\tilde{f} + \tilde{\tilde{\gamma}}(p_{t'}\tilde{\tilde{p}}_l + \eta_{s,a}p_l\tilde{\tilde{p}}_{t'})/\tilde{\tilde{f}}] \right\} \right)_{v = v^{(s,a)}}, \quad (27)$$

where, the following notation is introduced $\tilde{\gamma} = \tilde{\rho}/\rho = \tilde{\Gamma} v_{t'}^2/\tilde{v}_{t'}^2$ and $\tilde{\tilde{\gamma}} = \tilde{\tilde{\rho}}/\rho = \tilde{\tilde{\Gamma}} v_{t'}^2/\tilde{\tilde{v}}_{t'}^2$.

At the velocities $v^{(s,a)}$ satisfying inequality (20), all four parameters $\tilde{p}_{t'}$, $\tilde{p}_l$, $\tilde{\tilde{p}}_{t'}$, and $\tilde{\tilde{p}}_l$ are real. With due regard for (12) and (16), one can readily show that the increment in velocity (27) remains real even if both or one of the parameters $p_{t'}$ and p_l are imaginary. As was indicated above, this is really observed for the symmetric wave at $K < K_0$, which, in this case, is transformed into the mode of the waveguide type. Thus, if $v^{(s,a)} < \min(\tilde{v}_{t'}, \tilde{\tilde{v}}_{t'})$, the three-layer structure has an eigenwave with the real phase velocity. This wave is formed by an inhomogeneous or waveguide-type Lamb wave in the plate and accompanies the Rayleigh-type surface modes in the substrates.

If the substrate materials are chosen in such a way that either the velocity $v^{(s)}$ or both velocities $v^{(a)}$ and $v^{(s)}$ exceed $\min(\tilde{v}_{t'}, \tilde{\tilde{v}}_{t'})$ (it should be remembered that $v^{(s)} > v^{(a)}$ in all the cases), then some of the parameters $\tilde{p}_{t',l}$ and $\tilde{\tilde{p}}_{t',l}$ become imaginary, and the corresponding increment $\Delta v^{(s,a)}$ becomes complex, i.e., corresponds to the leaky mode. The number of leakage fluxes in such a wave coincides with the number of imaginary parameters from the set $\tilde{p}_{t'}(v^{(s,a)})$, $\tilde{p}_l(v^{(s,a)})$, $\tilde{\tilde{p}}_{t'}(v^{(s,a)})$, and $\tilde{\tilde{p}}_l(v^{(s,a)})$. Thus, for the material parameters indicated in Fig. 1, the following parameters are imaginary [see (6)]:

$$\tilde{\tilde{p}}_{t'} = -i\tilde{\tilde{q}}_{t'}, \quad \tilde{\tilde{p}}_l = -i\tilde{\tilde{q}}_l. \quad (28)$$

This situation corresponds to the existence of two leakage fluxes in the upper substrate and the formation of a Rayleigh-type surface wave in the lower one. One can readily see that in the case under consideration, all the parameters in (27) (except of $\tilde{\tilde{p}}_{t'}$ and $\tilde{\tilde{p}}_l$) remain real. Therefore the separation of $\Delta v^{(s,a)}$ into the real and imaginary parts

$$\Delta v^{(s,a)} = \Delta v_L^{(s,a)} - i v'^{(s,a)}_L \quad (29)$$

is trivial.

However, we indicate here the explicit form of the imaginary velocity component $v'^{(s,a)}_L$, one of the major characteristics of the leaky mode,

$$v'^{(s,a)}_L = -\frac{1}{2}\tilde{\tilde{\gamma}}(v^{(s,a)}/v_{t'})^4 \times [(\partial R_{s,a}/\partial v)^{-1}(p_{t'}\tilde{\tilde{q}}_l + \eta_{s,a}p_l\tilde{\tilde{q}}_{t'})/\tilde{\tilde{f}}]_{v = v^{(s,a)}}. \quad (30)$$

Unfortunately, the expression for $v'^{(s,a)}_L$ is not as compact as (30) for all the combinations of possible leaky fluxes. Thus, if there are two fluxes (one for each substrate), then, in addition to the complex parameters $\tilde{p}_{t'}$ and $\tilde{\tilde{p}}_{t'}$, four more parameters become complex, namely, $\tilde{r}$, $\tilde{\tilde{r}}$, $\tilde{f}$, and $\tilde{\tilde{f}}$. However, even in this case (as in all the other cases of the combination of the imaginary or real parameters $\tilde{p}_{t',l}$ and $\tilde{\tilde{p}}_{t',l}$), the separation (27) into the real and the imaginary parts presents no essential difficulties.

A plate between the soft and the hard substrates ($\tilde{\Gamma} \ll 1$, $\tilde{\tilde{\Gamma}} \gg 1$). As earlier, consider a wave field polarized in the plane of incidence in a three-layer structure consisting of a layer between a soft and a hard substrate. In the zeroth approximation, corresponding to the limiting case $\tilde{\Gamma} \longrightarrow 0$ and $\tilde{\tilde{\Gamma}}^{-1} \longrightarrow 0$, dispersion equation (10) acquires the form

$$G(v) = 0. \quad (31)$$

The explicit form of this equation and its detailed analysis can be found in [4]. In a plate whose one surface is free, whereas the other surface is clamped, the wave field does not decompose into a system of independent symmetric and Lamb waves. According to [4], there always exists an interval $0 < K < K_0$ corresponding to the waveguide-type propagation of the eigenwave, where at least one of the partial components is a bulk wave successively reflected from the surfaces. In this range of K variation, at least one of the parameters $p_{t'}$ and p_l is imaginary. At $K > K_0$, both $p_{t'}$ and p_l parameters are real, and the eigenwave is inhomogeneous.

Substrates "perturb" equation (31) of the zeroth approximation. In the first order with respect to the parameters $\tilde{\Gamma}$ and $\tilde{\tilde{\Gamma}}^{-1}$, equation (10) takes the form

$$G + 2\tilde{\Gamma}\tilde{F}_2^f/\tilde{f} + 2\tilde{\tilde{\Gamma}}^{-1}\tilde{\tilde{F}}_2^R/\tilde{\tilde{R}} = 0. \quad (32)$$

The corresponding perturbation of the solution, $v^{(0)} \longrightarrow v^{(0)} + \Delta v$, is equal (with the same accuracy) to

$$\Delta v = -2[(\partial G/\partial v)^{-1}(\tilde{\Gamma}\tilde{F}_2^f/\tilde{f} + \tilde{\tilde{\Gamma}}^{-1}\tilde{\tilde{F}}_2^R/\tilde{\tilde{R}})]_{v = v^{(0)}}. \quad (33)$$

Similar to the previous section, the real or the complex increments in the velocity Δv are fully determined by

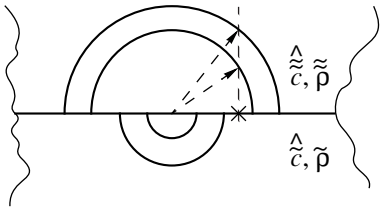

Fig. 2. The same as in Fig. 1 but for two elastic half-spaces in the absence of any layer in between.

the parameters $\tilde{p}_{t',l}$ and $\tilde{\tilde{p}}_{t',l}$ and are independent of the parameter $p_{t',l}$. At $v^{(0)} < \min(\tilde{v}_{t'}, \tilde{\tilde{v}}_{t'})$, all the $\tilde{p}_{t',l}$ and $\tilde{\tilde{p}}_{t',l}$ parameters and the increment in the velocity Δv are real, and the eigenwave is formed by an inhomogeneous or waveguide-type Lamb mode in the plate and the Rayleigh-type surface waves in the substrates.

At $v^{(0)} > \min(\tilde{v}_{t'}, \tilde{\tilde{v}}_{t'})$, the eigenwave is transformed into a leaky wave. Consider the case $v^{(0)} > \max(\tilde{v}_l, \tilde{\tilde{v}}_l)$ corresponding to the existence of four leakage fluxes (two for each substrate). In this case, $\tilde{p}_{t',l} = -i\tilde{q}_{t',l}$ and $\tilde{\tilde{p}}_{t',l} = -i\tilde{\tilde{q}}_{t',l}$, and the separation of Δv into the real and the imaginary parts, $\Delta v = \Delta v_L - iv'_L$, yields

$$\Delta v_L = -4\{(\partial G/\partial v)^{-1}[\tilde{\Gamma}\{r_s f_a\}\tilde{r}/\tilde{f} + \tilde{\tilde{\Gamma}}^{-1}\{r_s R_a\}\tilde{\tilde{r}}/\tilde{\tilde{R}}]\}_{v = v^{(0)}}, \tag{34}$$

$$v'_L = -2\{(\partial G/\partial v)^{-1}(v/v_{t'})^4 \times (\tilde{\gamma}[\{f_s\}p_{t'}\tilde{q}_l + \{\eta_s f_a\}p_l\tilde{q}_{t'}] + \tilde{\tilde{\gamma}}\tilde{\tilde{\Gamma}}^{-2}[\{R_s\}p_{t'}\tilde{\tilde{q}}_l + \{\eta_s R_a\}p_l\tilde{\tilde{q}}_{t'}])\}_{v = v^{(0)}}. \tag{35}$$

Here $\tilde{\tilde{\gamma}}\tilde{\tilde{\Gamma}}^{-2} = \tilde{\tilde{\Gamma}}^{-1}\, v_{t'}^2/\tilde{\tilde{v}}_{t'}^2$ is a small parameter.

Analyzing the wave fields in the plate on a substrate [4] with the similar polarization, we did not consider the boundary problem of a plate on a soft substrate with the clamped external surface. The trivial limiting transition $\tilde{\tilde{\Gamma}}^{-1} \longrightarrow 0$ in formulas (32)–(35), which make all the expressions twice shorter, can fill this gap.

Limiting situation $d \longrightarrow 0$: bicrystal. If the layer thickness d in a sandwich structure tends to zero, two semiinfinite substrates directly contact each other (Fig. 2). Then, cumbersome equation (10) is considerably simplified

$$\tilde{c}_{66}^2\tilde{R}\tilde{\tilde{f}} + \tilde{\tilde{c}}_{66}^2\tilde{\tilde{R}}\tilde{f} - \tilde{c}_{66}\tilde{\tilde{c}}_{66}[2\tilde{r}\tilde{\tilde{r}} + (\tilde{N}_{t'}\tilde{\tilde{N}}_{t'})^2(\tilde{p}_{t'}\tilde{\tilde{p}}_l + \tilde{p}_l\tilde{\tilde{p}}_{t'})] = 0. \tag{36}$$

Thus, we arrive at the dispersion equation for Stoneley waves (see [1, 2]).

Now, assume that one of the contacting substrates is much harder than the other. For definiteness, let $\tilde{c}_{66} \gg \tilde{\tilde{c}}_{66}$. In this limiting case, the dispersion equation in the zeroth approximation takes the form

$$\tilde{R}(v) = 0 \tag{37}$$

and describes a Rayleigh wave propagating in the lower substrate. The perturbed dispersion equation in the approximation linear with respect to the small parameter $\Gamma = \tilde{\tilde{c}}_{66}/\tilde{c}_{66}$ has the form

$$\tilde{R} - \Gamma\tilde{\tilde{f}}^{-1} \times [2\tilde{r}\tilde{\tilde{r}} + (\tilde{N}_{t'}\tilde{\tilde{N}}_{t'})^2(\tilde{p}_{t'}\tilde{\tilde{p}}_l + \tilde{p}_l\tilde{\tilde{p}}_{t'})] = 0. \tag{38}$$

The corresponding correction Δv to the velocity v_R set by this equation is

$$\Delta v = \Gamma\{(\tilde{\tilde{f}}\partial\tilde{R}/\partial v)^{-1} \times [2\tilde{r}\tilde{\tilde{r}} + (\tilde{N}_{t'}\tilde{\tilde{N}}_{t'})^2(\tilde{p}_{t'}\tilde{\tilde{p}}_l + \tilde{p}_l\tilde{\tilde{p}}_{t'})]\}_{v = v_R}. \tag{39}$$

Obviously, at $v_R < \tilde{\tilde{v}}_{t'}$, all the $\tilde{\tilde{p}}_{t',l}$ and $\tilde{p}_{t',l}$ parameters are real, and solution (39) describes the conventional Stoneley wave propagating in the bicrystal under study with a velocity $v = v_R + \Delta v$. At $\tilde{\tilde{v}}_{t'} < v_R < \tilde{\tilde{v}}_l$, the $\tilde{\tilde{p}}_{t'}$ parameter becomes imaginary, and the first wave of leakage is formed. Finally, at $v_R > \tilde{\tilde{v}}_l$, the first wave of leakage is followed by the second wave of leakage (Fig. 2). The real and the imaginary parts of the velocity increment $\Delta v = \Delta v_L - iv'_L$ acquire the form

$$\Delta v_L = 2\Gamma\{(\partial\tilde{R}/\partial v)^{-1}\tilde{r}\tilde{\tilde{r}}/\tilde{\tilde{f}}\}_{v = v_R}, \tag{40}$$

$$v'_L = \Gamma(v_R^4/\tilde{v}_{t'}^2\tilde{\tilde{v}}_{t'}^2) \times \{(\partial\tilde{R}/\partial v)^{-1}(\tilde{p}_{t'}\tilde{\tilde{q}}_l + \tilde{p}_l\tilde{\tilde{q}}_{t'})/\tilde{\tilde{f}}\}_{v = v_R}. \tag{41}$$

ON RESONANCE EXCITATION OF QUASI-RAYLEIGH WAVES IN THE STRUCTURES STUDIED

We had already considered the ideology of resonance reflection in the vicinity of the leaky eigenmodes. The principle reduces to the choice of an incidence angle for a pumping wave which provides the propagation of the reflected wave along the partial wave of leakage of the eigenwave mode in the structure. Such a "coupling" "swings" the system as a whole, i.e., provides the resonance excitation of the eigenwave. In this case, the incident wave compensating the removal of the energy from the interface by leakage fluxes provides the restoration of the steady-state energy flow along the interface, and, at the same time, also makes the phase velocity real. On the other

hand, the energy equivalence of the pumping wave to the total leakage flow, which is only a small part of the eigenwave energy, reflects the efficiency of such excitation.

To characterize the resonances under study qualitatively, consider the excitation coefficients of inhomogeneous partial waves localized at the interfaces. In the simplest situation (Fig. 2), these coefficients are the ratios of the amplitudes of inhomogeneous waves in the lower substrate and incident bulk pumping waves in the upper substrate,

$$s_{\alpha\beta}(v) = \tilde{a}_\alpha^+ / \tilde{\tilde{a}}_\beta^-. \quad (42)$$

Here $\alpha, \beta = l, t'$. In other words, the above ratio takes into account an ambiguous (double) choice of the pumping wave. According to the results obtained in [3, 4] for the simplest structures, the determination of the dependence of the coefficients $s_{\alpha\beta}(v)$ (42) on the phase velocity v set by the incidence angle of the pumping wave is a rather complicated problem, but the shape and the height of the resonance peaks of the $s_{\alpha\beta}(v)$ functions, (42), can qualitatively be estimated proceeding only from the general considerations without any complex calculations.

The shape of the resonance peak is determined from the simple universal consideration based on the well known fact that the velocities of the eigenmodes are determined by the poles of the excitation (and reflection) coefficients in the problems of wave reflection from the intefaces of any structures [see (8) and (9)]. Thus, in the vicinity of the leaky mode velocity, $v_L - iv'_L$, the excitation coefficients sought, (42), should have the form

$$s_{\alpha\beta}(v) = \frac{\eta_{\alpha\beta}}{v - v_L + iv'_L}, \quad (43)$$

where the coefficients $\eta_{\alpha\beta}$, being the smooth functions of the velocity v, can be determined at $v = v_L$.

As follows from (43), the width of the resonance peaks should be of the order of v'_L. The estimation of the heights of the resonance peaks is a more complicated problem. We have to take into account the conditions for the energy balance for energy flows of the wave fields at the interfaces. We also take into account that this peak has the same order of magnitude as that of the ratio of the amplitudes of inhomogeneous waves $\tilde{a}_\alpha^+$ and the bulk waves of leakage $\tilde{\tilde{a}}_\beta^-$ in the leaky eigenmodes [3, 4].

The initial relationship used in such estimates is the general relationship for the energy flows of the wave of elastic displacements **u** giving rise to the formation of the field of mechanical stresses $\hat{\sigma}$ [7]:

$$\mathbf{P} = -(\mathrm{Re}\hat{\sigma})\frac{\partial}{\partial t}\mathrm{Re}\mathbf{u}. \quad (44)$$

Using the above expression, one can readily estimate the order of the magnitude of the time-averaged leakage flow in a leaky eigenmode in the upper substrate

$$\tilde{\tilde{P}} \sim v_L \tilde{\tilde{c}} (\tilde{\tilde{a}}_\beta^-)^2 k_L^2. \quad (45)$$

Here $\tilde{\tilde{c}}$ is the characteristic value of the elastic moduli in the upper substrate.

On the other hand, the time-averaged energy flux in the lower substrate, where the localized wave field exists, can be estimated in the same way as in the upper substrate (45):

$$\tilde{P} \sim v_L \tilde{c} (\tilde{a}_\alpha^+)^2 k_L^2, \quad (46)$$

where $\tilde{c}$ is the characteristic value of the elastic moduli in the given medium. In the zeroth approximation (ignoring the perturbing factors considered above), this energy flux is parallel to the interface. Now, we invoke the property of an inhomogeneous wave: the time-averaged energy flux is always normal to the imaginary part of its wave vector [8]. We also take into account that perturbations give rise to an imaginary addition to the velocity v'_L, which is uniquely related to the imaginary addition to the wave-vector component parallel to the interface:

$$v_L - iv'_L = \omega/(k_L + ik'_L). \quad (47)$$

The imaginary addition k'_L makes the imaginary wave-vector components, $\mathrm{Im}\tilde{\mathbf{k}}_\alpha$, of the partial waves in the lower substrate not parallel to the interface (as was the case in the absence of perturbations). The vectors $\mathrm{Im}\tilde{\mathbf{k}}_\alpha$ deviate from the normal to the interface by the angle

$$\delta \sim k'_L/k_L \sim v'_L/v_L. \quad (48)$$

As a result, a leakage flux is also formed in the lower substrate because of the rotation of the energy flux of the wave fields in this substrate by an angle δ (48). Thus, the order of magnitude of the energy-flux component normal to the interface is

$$\tilde{P}_L \sim \delta\tilde{P} \sim v'_L \tilde{c} (\tilde{a}_\alpha^+)^2 k_L^2. \quad (49)$$

This component should be balanced by the energy leakage flux of the wave in the upper substrate. Equating (45) and (49), we arrive at the estimate of the excitation coefficients (42) at the resonance (where $v = v_L$):

$$s_{\alpha\beta}(v_L) \sim (\Gamma v_L / v'_L)^{1/2}, \quad \Gamma \sim \tilde{\tilde{c}}/\tilde{c}. \quad (50)$$

Comparing (43) and (50), we arrive at the estimate of the order of the magnitudes of the coefficients $\eta_{\alpha\beta}$:

$$\eta_{\alpha\beta} \sim s_{\alpha\beta}(v_L) v'_L \sim (\Gamma v'_L v_L)^{1/2}. \quad (51)$$

The final estimates for different cases of leaky mode formation are obtained by representing the small addi-

tions to the velocity v'_L in (50) and (51) in terms of the factors determining the perturbation.

If the upper substrate is softer than the lower one, i.e., if $\Gamma \ll 1$, we have

$$v'_L \sim \Gamma v_L. \quad (52)$$

Then, formulas (50) and (51) provide the following estimates for the height of the resonance peak and the coefficients $\eta_{\alpha\beta}$:

$$s_{\alpha\beta}(v_L) \sim 1, \quad \eta_{\alpha\beta} \sim v'_L \sim \Gamma v_L. \quad (53)$$

In this case, the height of the resonance peak is of the order of unity, whereas at the wings, where $|v - v_L| \gg v'_L$, the excitation coefficient $s_{\alpha\beta}(v)$ drops to zero.

If the resonance is excited from the harder upper substrate, where

$$v'_L \sim \Gamma^{-1} v_L \quad (54)$$

we arrive at the following estimates:

$$s_{\alpha\beta}(v_L) \sim v_L / v'_L \sim \Gamma \gg 1, \quad \eta_{\alpha\beta} \sim v_L. \quad (55)$$

Under these conditions, the resonance peak is anomalously high, whereas at the wings, the excited inhomogeneous waves have the amplitudes comparable with the amplitude of the incident pumping wave.

All these estimates are consistent with the corresponding data obtained by direct calculations in [3, 4]. Moreover, formulas (43) and (51) also adequately describe the excitation resonance of a Rayleigh wave in an anisotropic half-space (the case $\Gamma \sim 1$) because of the similar reflection in the vicinity of the leaky eigenwave [5].

In some particular cases [9, 10], where the wave number $K = kd$ lies in the range where $\exp(p_\alpha K) \gg 1$, the above simplified estimates are not sufficient for the waves in the plates on the substrates, which is seen, in particular, from the exact formulas obtained in [3, 4].

CONCLUSION

The dispersion equation is obtained in the general form. It describes the wave fields polarized in the plane of the wave propagation, which coincides with the plane of the transverse anisotropy of a three-layer structure consisting of a plate between two semiinfinite substrates. Using this equation, we managed to solve the problem of eigenwaves for two types of sandwich structures, namely, for the case where both substrates are soft and for the case where one substrate is soft, whereas the other is hard (in comparison with the plate material). In the zeroth approximation, the solution is obtained for the Lamb waves in the plate under the corresponding boundary conditions. Depending on the parameter combination, the substrates provides different perturbations of the Lamb solutions.

If the unperturbed velocity of a Lamb wave lies in the range of inhomogeneous waves in both substrates (irrespectively of their hardness), i.e., is less than the velocity of the slowest bulk wave of all the waves polarized in the symmetry planes of the substrates, then the perturbed solution is described by the superposition of the Lamb wave in the plate with the Rayleigh-type surface waves in the substrates. Although the phase velocity of these superimposed waves differs from the velocity of the unperturbed Lamb wave, it remains real.

Another situation arises if the velocity in the zeroth approximation admits the propagation of the bulk wave in at least one of the substrates. Then, the perturbation-induced variation in the phase velocity is complex, which indicates that the resulting wave belongs to the class of leaky waves. The latter waves have the bulk components which transfer the energy from the plate into the substrate (or substrates) bulk. The number of leakage fluxes can range from one to four.

A similar situation can also take place in a "limiting" structure formed by two substrates of different hardness without any layer in between. In this case, the solution in the zeroth approximation is a Rayleigh wave in a hard plate. The perturbed solutions can be of two types: a conventional Stoneley wave or a leaky wave with the leakage flux in the soft substrate.

The existence of solutions for leaky eigenwaves with weak leakage fluxes admits their resonance excitation by bulk waves incident at such angles that the velocity of the signal propagation along the surface coincides with the real part of the phase velocity in the eigensolution. As a result, the pumping flux fully compensates the leakage flux of the leaky mode, which provides the steady-state energy transfer along the interface and makes the phase velocity real.

Being a function of the phase velocity v, the shape of the resonances is characterized by the universal width of the order of an imaginary component of the leaky-wave velocity. However, there are two types of resonances which behave differently at the curve maximum and at the wings. The resonance of the first type is characterized by a high maximum, the ratio of the amplitude of the excited wave to the amplitude of the pumping wave is proportional to $\sim v_L / v'_L \gg 1$. The resonance of the second type is characterized by a high selectivity of excitation (infinitesimal signal beyond the peak of width $\sim v'_L$). The first type of the resonance is observed if the pumping wave propagates in a hard medium, whereas the excited wave propagates in a soft medium. The second type of behavior is observed if the pumping wave propagates in the soft medium, whereas the excited wave, in the hard one. This is characteristic of various sandwich structures considered in the present article and in [4], and also for the Love-type waves [3] characterized by polarization in the orthogonal plane of propagation. The universal character of these characteristics follows from the qualitative estimates made in the previous Section.

Concluding the article, we should like to emphasize that both in [3, 4] and in the present article, we restricted ourselves to the consideration of the waves

polarized either in the propagation plane or in the plane normal to it, which really takes place if the propagation plane coincides with the symmetry plane. In this connection, we should like to mention the studies of the leaky waves and the corresponding resonances in a sandwich structure [11, 12], although the physical mechanism of the leakage considered in these papers is quite different. The authors considered the mechanism related to the anisotropy of a thin ($K \ll 1$) layer on an isotropic substrate or a similar layer in the sandwich structure (with the equivalent isotropic substrates). In this case, the propagation plane does not coincide with the symmetry plane, which provides the simultaneous excitation of the modes with mutually orthogonal polarizations. Under such conditions, the waves polarized in the propagation plane are accompanied by leaky currents caused by "mixing" with the bulk partial waves polarized normally to the propagation plane. Since the leaky waves and the main wave propagate in the same medium, one has to put $\Gamma \sim 1$ in (51). This results in the fact that the resonances are of the same type as in [5], in full accord with the calculations made in [11, 12].

ACKNOWLEDGMENTS

The study was supported by the Russian Foundation for Basic Research, project no. 98-02-16077 and also by the Kielce University of Technology, Kielce, Poland.

REFERENCES

1. I. A. Viktorov, *Rayleigh and Lamb Waves: Physical Theory and Applications* (Nauka, Moscow, 1966; Plenum Press, New York, 1967).
2. I. A. Viktorov, *Sonic Surface Waves in Solids* (Nauka, Moscow, 1981).
3. V. I. Alshits, V. N. Lyubimov, and A. Radowicz, Fiz. Tverd. Tela **38** (4), 1091 (1996) [Phys. Solid State **38** (4), 604 (1996)].
4. V. I. Alshits, W. Gierulski, V. N. Lyubimov, and A. Radowicz, Kristallografiya **42** (1), 26 (1997) [Crystallogr. Rep. **42** (1), 20 (1997)].
5. V. I. Alshits and J. Lothe, Wave Motion **3**, 297 (1981).
6. V. I. Alshits, A. N. Darinskiĭ, and A. L. Shuvalov, Kristallografiya **38** (2), 22 (1993) [Crystallogr. Rep. **38** (2), 147 (1993)].
7. F. I. Fedorov, *Theory of Elastic Waves in Crystals* (Nauka, Moscow, 1965; Plenum Press, New York, 1968).
8. V. N. Lyubimov and D. G. Sannikov, Kristallografiya **23** (2), 245 (1978) [Sov. Phys. Crystallogr. **23** (2), 135 (1978)].
9. V. I. Alshits, A. S. Gorkunova, V. N. Lyubimov, and J. P. Nowacki, Kristallografiya **44** (4), 639 (1999) [Crystallogr. Rep. **44** (4), 592 (1999)].
10. V. I. Alshits, A. S. Gorkunova, V. N. Lyubimov, and R. K. Kotowskiĭ, Kristallografiya **44** (5), 858 (1999) [Crystallogr. Rep. **44** (5), 799 (1999)].
11. A. N. Darinskiĭ, Zh. Éksp. Teor. Fiz. **107** (2), 585 (1995) [JETP **80**, 317 (1995)].
12. A. N. Darinskiĭ and G. A. Maugin, Wave Motion **23**, 363 (1996).

Translated by L. Man

Crystallography Reports, Vol. 45, No. 3, 2000, pp. 466–468. Translated from Kristallografiya, Vol. 45, No. 3, 2000, pp. 509–512.

LATTICE DYNAMICS

On the Effect of Ordering on Vibrational Spectrum of Relaxor Ferroelectric $PbSc_{1/2}Ta_{1/2}O_3$ in Paraphase

S. G. Lushnikov, S. N. Gvasaliya, E. A. Rogacheva, and I. G. Siny

Ioffe Physicotechnical Institute, Russian Academy of Sciences, Politekhnicheskaya ul. 26, St. Petersburg, 194021 Russia

Received November 15, 1999

Abstract—The effect of the ordering of Sc^{3+} and Ta^{5+} ions on the behavior of the phonon subsystem in the relaxor ferroelectric $PbSc_{1/2}Ta_{1/2}O_3$ from the numerous $AB'_xB''_{x-1}O_3$ family has been studied. The nature of an additional contribution to the light-scattering spectra has been analyzed on the experimental data on Raman scattering in $PbSc_{1/2}Ta_{1/2}O_3$, $SrAl_{1/2}Ta_{1/2}O_3$, $SrAl_{1/2}Nb_{1/2}O_3$, and $BaMg_{1/3}Ta_{2/3}O_3$ compounds and inelastic neutron scattering in $PbSc_{1/2}Ta_{1/2}O_3$. It is shown that broadening of the lines in the Raman spectra of $PbSc_{1/2}Ta_{1/2}O_3$ crystals is caused by additional scattering by phonons from various points of the Brillouin zone.

INTRODUCTION

Multicomponent perovskite-like ferroelectrics with a diffuse phase transition dubbed "relaxor ferroelectrics" or "relaxors," have attracted much attention for many years. Relaxor ferroelectrics differ from the classic perovskites described by the formula ABO_3 by presence of *B*' and *B*'' ions with valence occupying crystallographically equivalent positions in the *B*-sublattice. Because of unique physical properties (such as, e.g., giant permittivity, "diffused" anomalies of many physical properties in the vicinity of the phase transition, etc.), these numerous compounds are considered as a separate family described by the general formula $AB'_xB''_{1-x}O_3$ [1].

The relaxor ferroelectric $PbSc_{1/2}Ta_{1/2}O_3$ (PST) belongs to the $AB'_xB''_{1-x}O_3$ family of perovskite-like compounds with Sc^{3+} and Ta^{5+} ions located in the positions of the *B* sublattice. The PST crystals are a model object for studying physical properties of relaxor ferroelectrics, because the degree of Sc^{3+} and Ta^{5+} order may be controlled by heat treatment [2]. A disordered PST crystal exhibits a typical relaxor behavior (a wide maximum of permittivity, appreciable frequency dispersion, etc.) and the so-called mean Curie temperature $T_C \sim 270$ K, whereas an ordered PST crystal undergoes a conventional ferroelectric phase transition with the Curie temperature $T_C \sim 300$ K [3]. The symmetry of the paraphase of PST crystals was established by the method of high-resolution neutron powder diffraction—sp. gr. *Fm*3*m* [4].

The PST vibrational spectrum was studied by the IR and Raman spectroscopy methods [5–8]. The group theoretical analysis of the PST Raman spectra in the praphase and paraphase was performed in [5], the authors checked where the consistency of the paraphase spectra with the sp. gr. *Fm*3*m* and considered in detail the high temperature transition from praphase described by the sp. gr. *Pm*3*m*. Special attention was paid to the effect of ordering on the Raman spectra and it was shown [9] that the degree of order influences the shape and the intensity of the lines of the Raman spectra. The present paper continues the study of the effect of order on the vibrational spectrum of the paraphase of the relaxor PST ferroelectric by the methods of the Raman and inelastic neutron scattering with due regard for the known and newly obtained data.

RAMAN SCATTERING IN $PbSc_{1/2}Ta_{1/2}O_3$

The Raman spectra of a PST crystal were excited by an argon laser (λ = 613.5 nm) and analyzed using a Cary-82 triple spectrophotometer. The samples were $2 \times 2 \times 1$-mm-large PST single crystals with various degree of cation order. We studied the spectra with the *X*(*ZZ*)*Y* and *X*(*ZX*)*Y* polarizations, with the *X*-, *Y*-, and *Z*-axes being parallel to the fourfold symmetry axes of the cubic unit cell.

Figure 1 shows the Raman spectra of the paraphase of PST crystals with various degrees of order. It is clearly seen that the degree of crystal order affects the spectra. A lower degree of crystal order increases the half-width and the intensity of the lines, on the spectra with the maximum values attained for spectra of the *PMN* crystals [9]. At first, it was assumed that the line widths and the other parameters of the Raman spectra of relaxor ferroelectrics depend on ordering of the *B*' and *B*'' ions in the *B*-sublattice [9]. The high-resolution electron microscopy data show the existence of nanoregions with the cation ratio *B*' : *B*'' = 1 : 1; the symmetry

1063-7745/00/4503-0466$20.00 © 2000 MAIK "Nauka/Interperiodica"

of these regions is described by the sp. gr. $Fm3m$ [10, 11]. This leads to an assumption that the Raman spectra are formed from these nanoregions, which also explains the live broadening of the experimental spectra. However, the recent studies showed that the real situation is much more complicated. For comparison, consider some other compounds of the $AB'_xB''_{1-x}O_3$ family—$SrAl_{1/2}Ta_{1/2}O_3$ (SAT), $SrAl_{1/2}Nb_{1/2}O_3$ (SAN), and $BaMg_{1/3}Ta_{2/3}O_3$ (BMT) also characterized by the presence of nanoregions with 1 : 1 or 1 : 2 ion ratios in the *B*-sublattice [12]. The Raman spectra of these compounds (Fig. 2) are quite consistent with the sp. gr. $Fm3m$ established by the method of X-ray diffraction analysis. Figure 2 illustrates the differences between the spectra of PST and other related compounds. The line half-width on the PST is about 30–50 cm^{-1}, whereas for all the other compounds it is about 2–10 cm^{-1}. Thus, it is evident that the existence of nanoregions is not responsible for such a pronounced line broadening. Neither can it be caused by anharmonicity of the crystal lattice, defects, and the other well-known mechanisms, since we consider narrow lines with half-widths of the order of 2–10 cm^{-1}. Obviously, the differences between the SAT, SAN, and BMT spectra, and the spectra of the relaxor ferroelectrics are caused by other factors. Among such obvious differences are the existence of the ferroelectric phase transition in relaxors (really observed or suppressed under normal conditions) absent in SAT, SAN, BMT, and in a number of other compounds [12]. Thus, one can assume some dynamic contributions to the Raman spectra, or a rather dynamic violation of the translational symmetry, which provides the phonon contributions to the Raman spectrum from the Γ-point that come from other points in the same Brillouin zone.

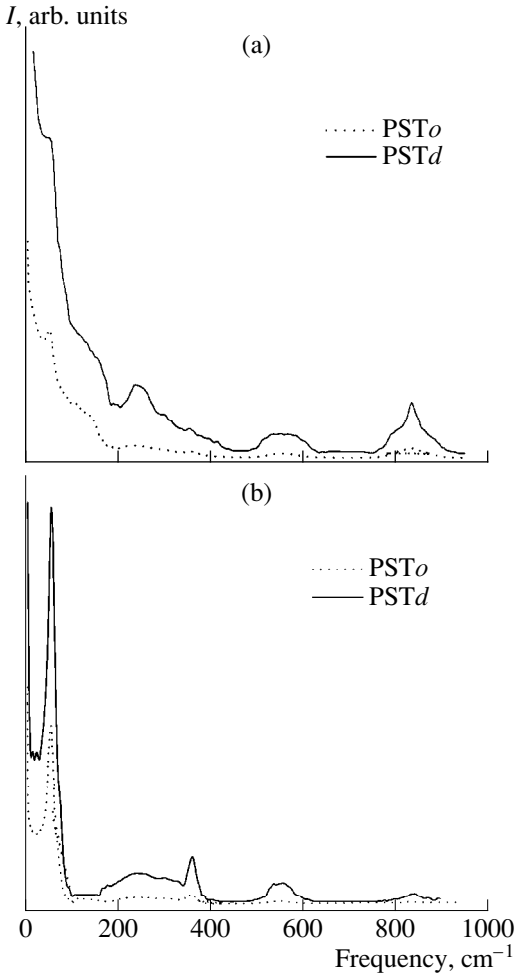

Fig. 1. Raman spectra of PST crystals with various degree of order for the (a) $X(ZZ)Y$ and (b) $X(ZX)Y$ polarizations. (PST*o*) and (PST*d*) indicate a more and a less ordered sample, respectively.

INELASTIC INCOHERENT NEUTRON SCATTERING

The experiments on inelastic neutron scattering (INS) were performed on a spectrometer with inverse geometry (designed KDSOG-M at the Joint Institute for Nuclear Research, Dubna). The samples were ordered ($s = 0.85$) and nominally disordered PST powders (120-g in weight). The degree of order was checked on a DRON-2 X-ray diffractometer by measuring the I_{001}/I_{111} intensity ration. The INS spectra were simultaneously recorded for eight scattering angles ranging from 30° to 140° in the mode of neutron energy loss, which made it possible to make measurements at low temperatures. At zero energy transfer, the resolution was 0.6 MeV. Upon subtraction of the background due to the sample holder, the spectra obtained were summed over the scattering angles for more precise averaging over momenta transferred by neutrons. Finally, the experimental data were processed in the single-phonon incoherent approximation to reconstruct the generalized density of the vibrational states $G(E)$.

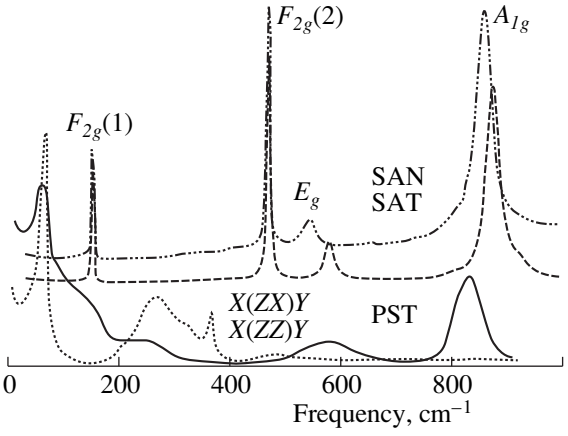

Fig. 2. Raman spectra of $PbSc_{1/2}Ta_{1/2}O_3$ (PST), $SrAl_{1/2}Ta_{1/2}O_3$ (SAT), and $SrAl_{1/2}Nb_{1/2}O_3$ (SAN). The F_{2g}, E_g, and A_{1g} modes active in the Raman spectra (sp. gr. $Fm3m$) are indicated.

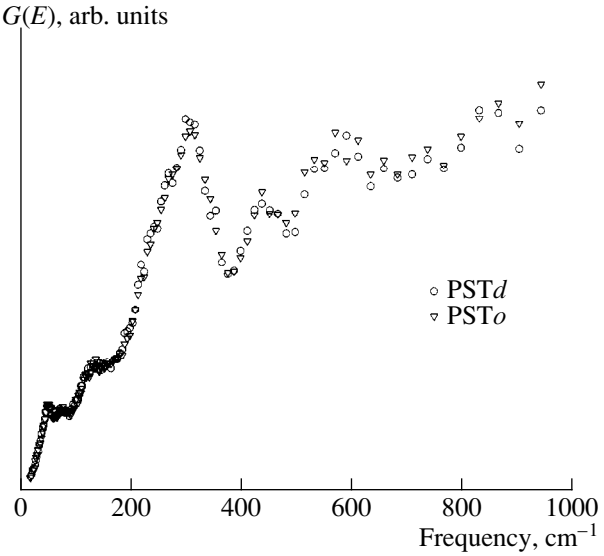

Fig. 3. The generalized density of vibrational states for ordered (PST*o*) and disordered (PST*d*) relaxor (PST) ferroelectrics at $T = 320$ K.

No multiple and multiphonon processes were taken into account [13].

Figure 3 shows generalized density of vibrational states of the ordered and disordered PST samples at the temperature $T = 320$ K (in the range of the energy transfer of 15–400 cm^{-1}, the measurement error corresponds to the dimensions of the symbols used in Fig. 3). Evidently, there are no noticeable differences in the densities of the vibrational states over all the whole energy range studied. The weakly marked discrepancy between $G(E)$ values at the transferred energies in the range higher than 400 cm^{-1} might be caused by multiphonon processes neglected in the calculation of $G(E)$ from INS data. It is well known that the generalized density of vibrational states $G(E)$ retains the characteristics of the true density of states g(E). In this connection, the coincidence of the $G(E)$ plots for ordered and disordered PST powders gives the grounds to believe that the phonon-state densities of these two compounds are equal.

CONCLUSIONS

Thus, analysis of the experimental data allows one to assume that the change in widths and intensities of the lines on the Raman spectra of the relaxor PST ferroelectrics with different degrees of order are caused by additional phonon contributions from various points of the Brillouin zone. These contributions are different for compounds with different degrees of order. Since the scattering intensity increases with the distance from the Γ-point of the Brillouin zone to the zone boundary for more disordered PST samples, the intensity of the lines on their Raman spectra should also increase. The differences in the Raman spectra are clearly seen in Fig. 1.

The cause of the appearance of the dynamic contribution from different points of the Brillouin zone is still obscure. Possibly, it comes from developed fluctuations admissible within the Tagantsev model [3].

ACKNOWLEDGMENTS

We are grateful to the staff of the Frank Laboratory of Neutron Physics of the Joint Institute for Nuclear Research and to I. L. Sashin for assistance in performing experiments on inelastic neutron scattering and to T. A. Shaplygin and N. V. Zaĭtsev for preparing and testing the samples. The study was supported by the Russian Foundation for Basic Research, project no. 99-02-18316. One of us, S. N. G., acknowledges the support of ISSEP (grant no. a99-712).

REFERENCES

1. M. E. Lines and A. M. Glass, *Principles and Applications of Ferroelectrics and Related Materials* (Oxford Univ. Press, Oxford, 1977; Mir, Moscow, 1981).
2. N. Setter and L. E. Cross, J. Mater. Sci. **15**, 2478 (1980).
3. F. Chu, N. Setter, and A. K. Tagantsev, J. Appl. Phys. **74**, 5129 (1993).
4. K. Z. Baba-Kishi, in *Proceedings of the 17th Conference on Applied Crystallography, 1998* (World Scientific, Singapore, 1998).
5. I. G. Siny and T. A. Smirnova, Fiz. Tverd. Tela **30**, 823 (1988) [Sov. Phys. Solid State **30**, 473 (1988)].
6. U. Bismayer, V. Devarajan, and P. Groves, J. Phys.: Condens. Matter. **1**, 6977 (1989).
7. I. M. Reaney, J. Petzelt, V. V. Voitsekhovskii, *et al.*, J. Appl. Phys. **76**, 2086 (1994).
8. I. G. Siny, R. S. Katiyar, and S. G. Lushnikov, *Nanophase and Nanocomposite Materials II. Symposium Mater. Res. Soc., Pittsburgh, 1997.*
9. I. Siny and C. Boulesteix, Ferroelectrics **96**, 119 (1989).
10. C. Boulesteix, C. Caranoni, C. Z. Kang, *et al.*, Ferroelectrics **107**, 241 (1990).
11. L. A. Bursill, J. L. Peng, H. Qian, and N. Setter, Physica B **205**, 305 (1995).
12. I. G. Siny, R. Tao, R. S. Katiyar, *et al.*, J. Phys. Chem. Solids **59**, 181 (1998).
13. S. N. Gvasaliya, S. G. Lushnikov, I. G. Siny, *et al.*, Physica B (in press).

Translated by A. Zolot'ko

Crystallography Reports, Vol. 45, No. 3, 2000, pp. 469–472. Translated from Kristallografiya, Vol. 45, No. 3, 2000, pp. 513–517.

PHASE TRANSITIONS

Study of Phase Transitions and the Incommensurate Phase in $ACBX_4$ Crystals by the Monte Carlo Method

V. I. Zinenko and N. G. Zamkova

Kirenskiĭ Institute of Physics, Siberian Division of the Russian Academy of Sciences, Krasnoyarsk, 660036 Russia

Received September 12, 1996; in final form, July 20, 1998

Abstract—The statistical model of successive phase transitions in the family of crystals described by the general formula $ACBX_4$ has been studied. It is assumed that tetrahedral BX_4 groups in the disordered tetragonal phase can be located in four equally probable equilibrium positions. Five representatives with different sequences of phase transitions in this family of crystals are considered. The effective equilibrium constants of interactions between tetrahedral groups are calculated within the framework of the electrostatic model. The corresponding phase diagrams and the thermodynamic characteristics of the phase transitions are studied by the Monte Carlo method. The experimental data provided the establishment of the sequence of phase transitions in Rb_2ZnCl_4 and K_2SeO_4 crystals with the formation of an intermediate incommensurate phase. The character of the structure modulation in this phase is established. The calculated thermodynamic characteristics of the phase transitions agree quite well with the experimental data for all the crystals under consideration. © *2000 MAIK "Nauka/Interperiodica".*

INTRODUCTION

A family of crystals with the general formula $ACBX_4$ (*A* and *C* are alkali metals and BX_4 are tetrahedral SO_4, SeO_4, CrO_4, $ZnCl_4$, etc. groups) have attracted attention for many decades. The interest in these compounds is associated with the fact that, depending on the chemical composition and the external conditions, they show a large variety of structural phase transitions with unusual physical characteristics. Some crystals of this family also have incommensurate phases, whose study is of great interest for solid state physics. The $ACBX_4$ compounds were repeatedly studied and the information about their structures, phase diagrams, and physical properties can be found, e.g., in [1] and in the review articles [2, 3] and the references given there.

It should be emphasized that all the structures of these compounds studied by now have one common property—they all are the derivatives of a highly symmetric hexagonal phase described by the sp. gr. $P6_3/mmm$ (D_{6h}^4). An important characteristic of this hexagonal phase is the distribution of BX_4 tetrahedra over several equilibrium positions. Thus, it was natural to assume that the distorted structures observed are formed due to phase transitions provided by homogeneous and inhomogeneous ordering in these crystals.

The Rb_2ZnCl_4 (RZC), $CsLiSO_4$ (CLS), and $CsLiCrO_4$ (CLC) crystals are characterized by the β-K_2SO_4 (KS) structure with four molecules in the orthorhombic unit cell (sp. gr. *Pnam*). At the temperature of 302 K, the RZC crystals experience a phase transition into the incommensurate phase with the modulation vector $\mathbf{q} = (1 - \delta)\mathbf{c}^*/3$, where $\mathbf{c}^*$ is the first reciprocal-lattice vector directed along the sixfold axis. It should be emphasized that the δ-values determining the long-wavelength modulation inside the incommensurate phase in Rb_2ZnCl_4 and K_2SeO_4 are rather low. With further crystal cooling, δ decreases and completely disappears at 189 K, and the system is transformed into (locked-into) the ferroelectric commensurate phase described by the sp. gr. $Pna2_1$, where the pseudosixfold axis disappears and the unit cell contains 12 molecules. With still further cooling, the RZC undergoes one more phase transition at 74 K and becomes monoclinic, but its space group has not been established as yet. Being cooled, the CLS and CLC crystals undergo only one phase transition into the monoclinic phase, sp. gr. $P2/n$ occurring at the constant unit-cell volume. On the other hand, the KS and K_2SeO_4 (KSe) crystals at high temperatures possess a disordered hexagonal phase (sp. gr. $P6_3/mmm$) and at the temperatures 860 and 745 K, respectively, undergo the transition to the orthorhombic phase (sp. gr. *Pnam*). With further cooling, KSe undergoes the same phase transitions as RZC, whereas, according to [4], KS undergoes no more phase transitions and is described by $P2/n$ up to the temperature T = 0 K. However, according to [5], at T = 60 K it undergoes the transition into a phase, whose structure has not been established as yet.

Below, we describe our study of the model of phase transitions in the $ACBX_4$ family. The model is based on the assumptions that these crystals have a hexagonal parental phase described by the sp. gr. $P6_3/mmm$ and that the sequence of phase transitions observed is

1063-7745/00/4503-0469$20.00 © 2000 MAIK "Nauka/Interperiodica"

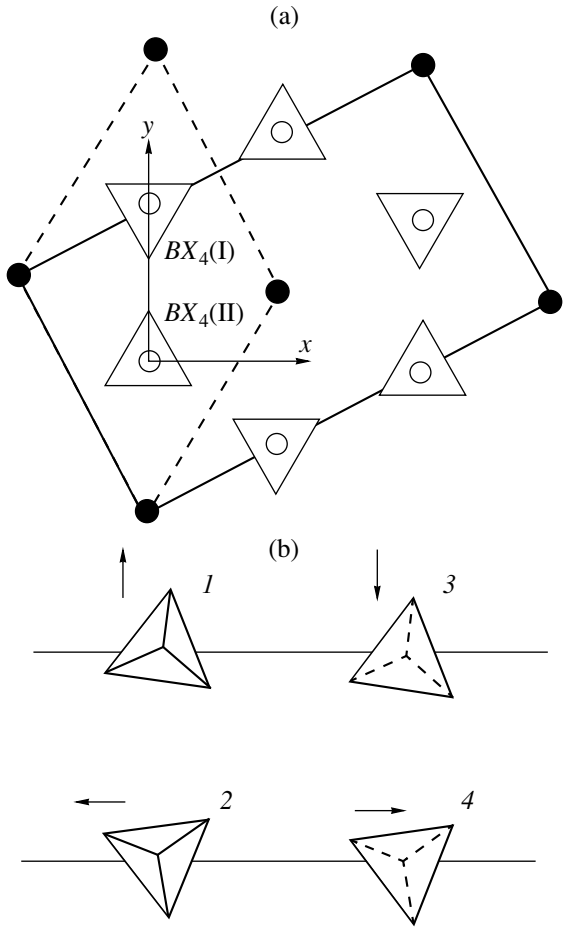

Fig. 1. (a) Rb_2ZnCl_4 structure in the phase described by the sp. gr. D_{6h}^4 projected onto the plane normal to the sixfold axis and (b) (*1–4*) the positions of $ZnCl_4$-tetrahedra in this phase.

caused by ordering of BX_4 tetrahedra over four equally probable equilibrium positions in the structure.

MODEL. CALCULATION OF THE INTERACTION CONSTANTS. STUDY OF PHASE DIAGRAM

The projection of the hexagonal $ACBX_4$ structure is shown in Fig. 1a. The effective interaction constants and the thermodynamic characteristics were calculated for the model under the assumption that the BX_4 tetrahedra in the hexagonal phase are statistically distributed over four equilibrium positions (*1–4*) [6] (Fig. 1b). The interaction constants are calculated within the framework of the electrostatic model.

Table 1. Lattice parameters used in calculating effective interaction constants

Crystal	a_0, Å	c_0, Å	α_A, Å^3	α_C, Å^3	$I_3 \times 10^{-45}$, C m^3
CLS	5.46	8.82	0.39	0.06	11.8
CLCr	5.68	8.90	0.39	0.06	18.2
RZC	7.30	10.58	0.9	1.29	27.9
KSe	6.14	8.90	0.6	0.24	17.0
KS	5.94	8.61	1.2	0.14	17.2

The detailed calculation of the interaction matrices were considered in [7]. Here, we consider only the results of these calculations. Table 1 lists the unit-cell parameters of the hexagonal phase (which is a hypothetical phase for RbZC, CLS, and CLC and the real one for KS and KSe) used in these calculations.

Calculating the octupole–dipole interactions, we took into account the interactions between BX_4 tetrahedra and metal atoms from the first (*A*-type) and the second (*C*-type) coordination spheres. The dipole–dipole interactions were calculated by the Ewald method. Integration over the **q** space was performed by the Gauss method. The polarizabilities are also indicated in Table 1. They were chosen from the condition that, at low temperatures, the experimentally observed phase should have the lowest energy.

The octupole moments of the BX_4 of the I_3 groups were fitted using the experimental temperatures of high-temperature transition in the crystals (Table 1). The effective interaction constants $V_{ij}^{\mathrm{I,I}}(R) = V_{ij}^{\mathrm{II,II}}(R)$ and $V_{ij}^{\mathrm{I,II}}(R)$ were calculated within 19 coordination spheres up to $R = 2c_0$. The interaction constants oscillate both in sign and amplitude with the distance, thus indicating an essential competition between various interactions.

The thermodynamic properties of the model were studied by the conventional Monte Carlo method used for Ising-type models [8, 9]. We considered two types of boundary conditions: periodic boundary conditions and the boundary conditions with phantom spins.

We also made an attempt to use free boundary conditions, but in this case the system rapidly returned to metastable states (even at rather high temperatures) and could not be taken away from these states at any reasonable number of steps of the Monte Carlo method. This is explained by the fact that, due to a large number of interactions, even for large lattices, too many spins are still free, and the competition of these interactions makes the system unstable. The calculations were performed on $(16 \times 16 \times 24)$ and $(24 \times 24 \times 48)$ three-dimensional hexagonal nets.

Table 2 lists the calculated and the experimental temperatures of successive transitions in the crystals. It should be emphasized that the calculated temperature of the transition from the hexagonal to the orthorhombic phases ($T_{c1} \approx 700$, 770, and 1400 K for RZC, CLS, and CLC, respectively) considerably exceeds the decomposition temperature, and therefore these transitions could never be observed in these crystals. The calculated transition temperatures agree with the corre-

Table 2. Phase symmetries and the temperatures of successive phase transitions in $ACBX_4$ crystals

CLS	D_{6h}^4 ($z = 2$)	$\xrightarrow{770\text{ K }(-)^*}$	D_{2h}^{16} ($z = 4$)	$\xrightarrow{202\text{ K }(202\text{ K})}$	C_{2h}^5 ($z = 4$)				
CLCr	D_{6h}^4 ($z = 2$)	$\xrightarrow{1400\text{ K }(-)}$	D_{2h}^{16} ($z = 4$)	$\xrightarrow{370\text{ K }(427\text{ K})}$	C_{2h}^5 ($z = 4$)				
KS	D_{6h}^4 ($z = 2$)	$\xrightarrow{860\text{ K }(860)}$	D_{2h}^{16} ($z = 4$)	$\xrightarrow{76\text{ K }(?)}$	C_{2h}^5 ($z = 16$)				
RZC	D_{6h}^4 ($z = 2$)	$\xrightarrow{700\text{ K }(-)}$	D_{2h}^{16} ($z = 4$)	$\xrightarrow{302\text{ K }(302\text{ K})}$	J	$\xrightarrow{200\text{ K }(192\text{ K})}$	C_{2v}^9 ($z = 12$)		
KSe	D_{6h}^4 ($z = 2$)	$\xrightarrow{745\text{ K }(745)}$	D_{2h}^{16} ($z = 4$)	$\xrightarrow{177\text{ K }(129\text{ K})}$	J	$\xrightarrow{115\text{ K }(93\text{ K})}$	C_{2v}^9 ($z = 12$)		

* The experimental temperatures are indicated above the arrows in parentheses.

sponding experimental data [10–12]. The phase-transition temperature were determined from the Monte Carlo peaks of the temperature dependence of heat capacity (Fig. 2). The determination of the "lock-in temperature" was somewhat hindered because the heat-capacity data for the incommensurate phase are characterized by a considerable scatter (Fig. 2), which remains almost the same with an increase of the lattice dimension. Therefore, the lock-in temperature was determined from the inflection of the temperature dependence of the internal energy.

Consider the incommensurate phase in RZC and KSe. Its structure is spatially modulated along the pseudohexagonal axis with the temperature-dependent modulation vector. As follows from the Monte Carlo data, ordering of BX_4-tetrahedra in the layers normal to the sixfold axis occurs in the same way irrespectively of the temperature, including the temperature range of the modulated phase. However, inside this phase, the degrees of tetrahedra ordering in the layers are different. The long-wave modulation inside the incommensurate phase depends on the temperature, which is especially well seen if one uses the boundary conditions with phantom spins and the system "chooses" the modulation period itself. Thus, the periodic boundary conditions at all the temperatures force the system to accept their period.

To determine the temperature dependence of the modulation period, we calculated the structure factor $S(\mathbf{q})$ in terms of the correlation function $G_{11}(\mathbf{R})$

$$S(\mathbf{q}) = \sum_{\substack{\mathbf{R} \\ n\times n\times n_1}} G_{11}(\mathbf{R})\exp(i\mathbf{qR}),$$
$$G_{11}(\mathbf{R}) = \sum_{i=1} C_1(\mathbf{r}_i)C_1(\mathbf{r}_i - \mathbf{R}). \quad (1)$$

DISCUSSION. COMPARISON WITH EXPERIMENT

The temperature dependences of heat capacity for CLS, KSe, and RZC obtained from the Monte Carlo data are shown in Fig. 2. Solid line indicates the experimental dependence of heat capacity. The agreement between the calculated and experimental dependences is quite satisfactory including the region of existence of the modulated phase, where, as was already indicated, the Monte Carlo data are characterized by a considerable scatter.

The structures of the modulated RZC and KSe phases were determined in [13, 14]. It was shown that

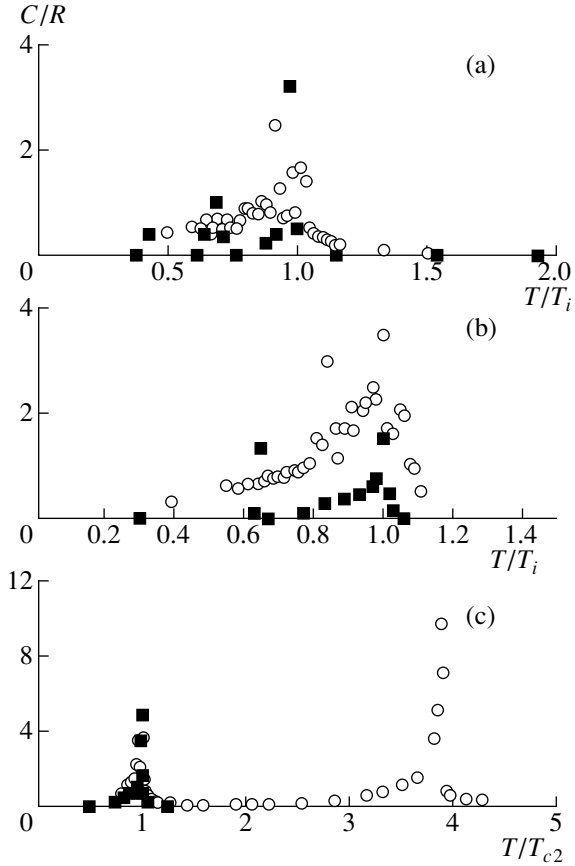

Fig. 2. Temperature dependences of heat capacity for (a) KSe, (b) RZC, and (c) CLS. The Monte Carlo data (circles) are compared with the experimental data [10–12] (squares). T_i is the temperature of transition into the incommensurate phase, T_{c2} is the temperature of transition into the monoclinic phase, and R is the universal gas constant.

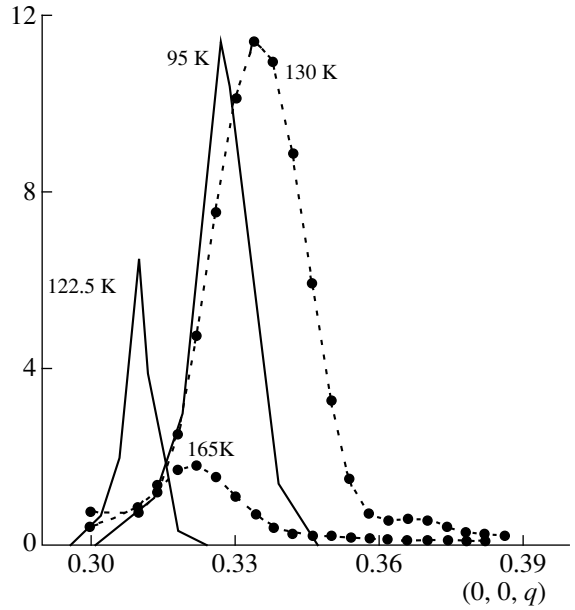

Fig. 3. Profile of the first X-ray satellite along the (0, 0, q) direction for KSe. The Monte Carlo data are indicated by the dashed curves (the boundary conditions with phantom spins), the solid lines show the experimental data [13, 14].

the structure modulation was determined mainly by the nonuniform rotation of BX_4-tetrahedra toward the pseudosixfold axis and is of the long-wavelength nature. Qualitatively, the long wavelength modulation of the structure obtained by the Monte Carlo method qualitatively agrees with the corresponding experimental data.

The temperature dependence of the modulation-vector magnitude in the incommensurate RZC and KSe phases was studied in [13, 14]. Figure 3 shows the experimental and calculated (by the Monte Carlo method) intensities at different temperatures of the modulated phase. Obviously, the agreement between the calculated and the experimental dependences is only qualitative. The peak of the experimental intensity curve is considerably narrower than that of the calculated one.

As was indicated in the introduction, at low temperatures, RZC and KSe undergo one more transition—the transition to the monoclinic phase whose structure has not been determined as yet. Using the molecular-dynamics method [15] and the constants of the inter- and intramolecular interactions determined from the first principles, Lu and Hardy [15] determined the structure of this phase (sp. gr. $C1c1$) with 48 molecules per unit cell. The Monte Carlo method becomes invalid at low temperatures, and, therefore, the transition to the monoclinic phase could not have been studied. In KSe, the phase described by the sp. gr. $C1c1$ is characterized by an energy close to that of the ferroelectric phase; and lowering of the temperature can give rise to the transition into this phase. However, the energy of this phase for RZC calculated for the finite lattice at $T = 0$ [15] was considerably higher than the energies of several other phases with other types of ordering of $ZnCl_4$-tetrahedra. Therefore it is hardly probable that this phase can really be formed in RZC at low temperatures.

In conclusion, indicate the main results obtained. The model calculated with due regard for the interaction constant between the BX_4 tetrahedra in the electrostatic approximation adequately describes the sequence of phase transitions in $ACBX_4$ crystals, including the transition into the intermediate modulated phase. The calculation of the transition temperatures and the thermodynamic characteristics agree quite well with the corresponding experimental data. In K_2SO_4, a low-temperature transition is revealed, and the symmetry of the low-temperature phase is determined.

ACKNOWLEDGMENTS

The study was supported by the Russian Foundation for Basic Research, project no. 97-02-16277.

REFERENCES

1. K. S. Aleksandrov and B. V. Beznosikov, *Structural Phase Transitions in Crystals* (Nauka, Novosibirsk, 1993).
2. H. Z. Cummins, Phys. Rep. **185**, 211 (1990).
3. W. Eysel, *Structuren und kristallochemische Verwandschaft bei Vergbindungen $A(BX_4)$ und $A_2(BX_3)$*, Dissertation, Aachen University (1975).
4. K. Gesi, Y. Tominaga, and H. Urabe, Ferroelectrics Lett. Sect. **44** (5), 71 (1982).
5. K. Ojima, Y. Nishihara, and A. Sawada, Acta Crystallogr., Sect. B: Struct. Sci. **51** (2), 287 (1995).
6. V. I. Zinenko and D. Kh. Blat, Fiz. Tverd. Tela **20**, 3539 (1978) [Sov. Phys. Solid State **20**, 2047 (1978)].
7. N. G. Zamkova and V. I. Zinenko, Fiz. Tverd. Tela **34**, 2735 (1992) [Sov. Phys. Solid State **34**, 1464 (1992)].
8. K. Binder, *Monte Carlo Methods in Statistical Physics*, Ed. by K. Binder (Springer, Heidelberg, 1979).
9. D. P. Landau, Phys. Rev. B **13**, 2997 (1976).
10. K. S. Aleksandrov, L. I. Zherebtsova, A. I. Kruglik, *et al.*, Fiz. Tverd. Tela **23**, 3673 (1981).
11. K. Nomoto, T. Atake, B. K. Chaudhuri, and H. Chihara, J. Phys. Soc. Jpn. **52**, 3475 (1983).
12. K. Aiki, K. Hukuda, and H. Koga, J. Phys. Soc. Jpn. **28**, 389 (1970).
13. H. Mashiyama, S. Tanisaki, and K. Hamano, J. Phys. Soc. Jpn. **51**, 2538 (1982).
14. M. Iizumi, J. D. Axe, and G. Shirane, Phys. Rev. B **15**, 4392 (1977).
15. H. M. Lu and I. R. Hardy, Phys. Rev. B **42**, 8339 (1990).

Translated by L. Man

Crystallography Reports, Vol. 45, No. 3, 2000, pp. 473–478. Translated from Kristallografiya, Vol. 45, No. 3, 2000, pp. 518–524.

Order Parameter in the Quasicrystal–Crystal Transformation

S. B. Roshal and I. V. Lebedyuk

Physics Faculty, Rostov State University, ul. Zorge 5, Rostov-on-Don, 344090 Russia

Received February 24, 1998; in final form, April 19, 1999

Abstract—Some aspects of the relationship between quasicrystal and crystal structures not considered earlier are discussed. It is shown that the atomic positions in a quasicrystal lattice are intermediate between the positions of periodic incommensurate crystal lattice. For the octagonal symmetry, two such generating lattices can be square and equal to one another. Then any quasicrystal position lies exactly between two crystal positions in different lattices. The classical (phason) mechanism of the quasicrystal–crystal phase transition is interpreted as a relative homogeneous deformation of generating crystal lattices leading to the commensurability of these lattices. The order parameter of such a transition is defined. *© 2000 MAIK "Nauka/Interperiodica".*

INTRODUCTION

For more than 20 years, the nonperiodic structures characterized by the long-range order are described in terms of the multidimensional crystallography, which considers these structures to be periodic in a space of the dimension equal to the minimum number of vectors which provide the expansion of any reciprocal-space vector of an incommensurate structure with integral coefficients. Prior to discovery of quasicrystals in 1984 [1], the *n*-dimensional crystallography was only used as a method to describe incommensurate structures. For any modulated structure, it was possible to determine the average crystal structure and the system of density waves modulating this structure. For a quasicrystal, it is impossible to choose a 3*D*-periodical subsystem of strong Bragg reflections and, as a consequence, to determine the average crystal structure with small distortions, which can form a quasicrystal. Therefore, quasicrystal structures differ much more pronouncedly from crystal structures than the modulated or the composite structures [2]. The possible mechanism of the quasicrystal–crystal phase transformation has been actively discussed since 1985 [3, 4].

The present study had the aim to illustrate the close relation of crystal and quasicrystal structures and to determine the physical nature of the order parameter at the corresponding phase transition. With this aim, the specific features of quasicrystal order are discussed and various modes of distortion of the ideal octagonal networks into imperfect periodical structures are considered. The choice of the octagonal symmetry to illustrate the specific features of the quasicrystal order and properties of quasicrystal–crystal phase transition was dictated by the fact that the orientational symmetry in this transition changes by a factor of 2.

THE SIMPLEST IDEAL OCTAGONAL NETWORK AS THE AVERAGE OF TWO SQUARE LATTICES

For a two-dimensional octagonal quasicrystal, one can select four reciprocal-space basis vectors in the form [5]

$$\begin{aligned} \mathbf{e}_1 &= \langle P0 \rangle, \ \mathbf{e}_2 = \langle QQ \rangle, \\ \mathbf{e}_3 &= \langle 0P \rangle, \ \mathbf{e}_4 = \langle -QQ \rangle, \end{aligned} \tag{1}$$

where $P/Q = \sqrt{2}$.

The phase space, hereafter denoted as E, is determined as a space of four variables: $n_i = \mathbf{e}_i\mathbf{R}$, where $\mathbf{R}$ is a radius-vector. The density function of a quasicrystal can be expanded in a Fourier series in harmonics, i.e., the density waves with the wave vectors which are the linear combinations of vectors (1) with integral coefficients. Formally, this density function can be considered not as a function of radius-vector, but as that of independent variables n_i and is invariant with respect to the operations of the symmetry group that is a direct product of the point group C_{8v} and the subgroup of four-dimensional translations. Each of the latter translations corresponds to the change in the corresponding phase (i.e., to the change of the variable n_i for a number multiple to 2π). Since the variables n_i show the linear dependences, the density function of the quasicrystal, being the function of the radius-vector, is determined on the plane of the phase space denoted as $E_{\|}$. All the translations of the phase space bring this plane into coincidence with other equivalent planes. If the section of the phase space is rational and close to $E_{\|}$, some of the translations bring the section plane into coincidence with itself and correspond to the crystal translations of the structure known as an approximant of a quasicrystal. If the atomic positions in the real space are assumed to be points, the density function in the phase space can be represented by two-dimensional limited atomic

1063-7745/00/4503-0473$20.00

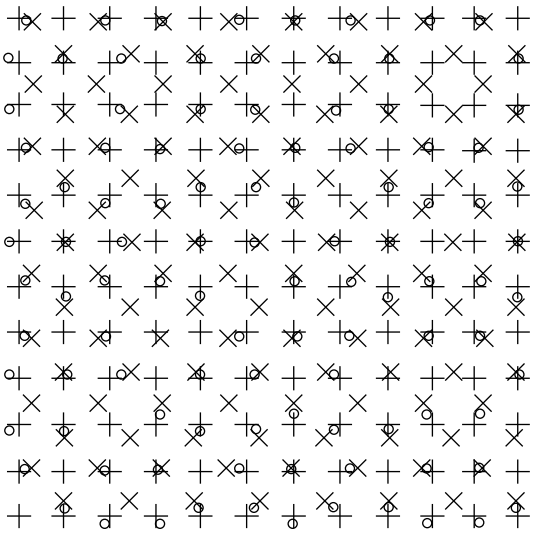

Fig. 1. Octagonal quasicrystal network. Crosses and oblique crosses indicate the sites of the generating lattices. Circles indicate lattice positions.

planes [6]. The probability of occupation of these positions can depend on the coordinate of the point at which the atomic plane intersects $E_{\parallel}$. The simplest model is that of a quasicrystal whose density function can be modeled in the phase space by the planar atomic planes of one type passing through the centers or the vertices of all cells of the phase space. The symmetry group of such atomic planes is C_{8v} or has even higher symmetry. A similar model was also used to describe a quasicrystalline state in $Mn_{12}Si_5$ [5, 7]. In this case, each of N positions in the quasicrystal lattice can be described with the aid of four half-integral indices n_1, n_2, n_3, and n_4 corresponding to the ordinal number of the atomic plane in the phase space intersected by $E_{\parallel}$. The coordinates of this position are set by the following expressions:

$$\begin{aligned} x^N &= \{Pn_1 + Q(n_2 - n_4)\}/(P^2 + 2Q^2), \\ y^N &= \{Pn_3 + Q(n_2 + n_4)\}/(P^2 + 2Q^2) \end{aligned} \tag{2}$$

under the condition that the vector with the components

$$\begin{aligned} x_\perp^N &= \{2Qn_1 - P(n_2 - n_4)\}/(2PQ), \\ y_\perp^N &= \{2Qn_3 - P(n_2 + n_4)\}/(2PQ) \end{aligned} \tag{3}$$

lies within this atomic plane. Expressions (2) and (3) can be readily obtained since they are the basis vectors of two two-dimensional vector representations of the group C_{8v}. Let us discuss the crystallogeometrical meaning of (2) and (3). Consider two square lattices with the occupied cell centers (with the coordinates 0.5, 0.5) rotated by 45° with respect to each other around the common fourfold axis passing trough the same origin of coordinates. We choose the lengths of the main lattice periods in such a way that the vectors $\mathbf{e}_1$, $\mathbf{e}_2$ and $\mathbf{e}_3$, $\mathbf{e}_4$ are the reciprocal-space vectors and the vectors $\mathbf{a}_1$, $\mathbf{a}_3$ and $\mathbf{a}_2$, $\mathbf{a}_4$ are the direct-space vectors of the first and the second lattices, respectively. All the vectors have the same length, $|\mathbf{a}_i| = 1/P$. Moreover, $\mathbf{a}_i \parallel \mathbf{e}_i$. Then, one can transform the expressions (2) and (3) to the form

$$\begin{aligned} \mathbf{R}^N &= (n_1\mathbf{a}_1 + n_3\mathbf{a}_3 + n_2\mathbf{a}_2 + n_4\mathbf{a}_4), \\ \mathbf{R}_\perp^N &= (n_1\mathbf{a}_1 + n_3\mathbf{a}_3 - n_2\mathbf{a}_2 - n_4\mathbf{a}_4). \end{aligned} \tag{4}$$

Relationships (4) show that the positions of the octagonal quasicrystal lattice are located between the neighboring positions of two square lattices rotated with respect to one another (Fig. 1). Similarly, the vectors $\mathbf{R}_\perp^N$ of the perpendicular space can be interpreted as the vectors connecting the positions in these lattices. The probability of occupation of the positions of the octagonal network is a function of $\mathbf{R}_\perp^N$ with the symmetry C_{8v} or higher. The lattices (or the structures) whose averaging leads to the formation of a quasilattice are called the generating lattices. If a set of vectors $\mathbf{R}_\perp^N$ (4) "sweeps away" the region lying inside a regular octagon with the distances between the opposite edges equal to $1/P$, then one position in a quasicrystal is formed by the nearest pair of the positions in the crystal. The concentration of empty positions in each sublattices $\geq 1/(3 + 2\sqrt{2})$. For a given quasicrystal network, the generating lattices can also be other lattices, for example, square lattices larger or smaller by a factor of $(1 + \sqrt{2})$ (the coefficient of self-similarity of the octagonal network).

Thus, the quasicrystal order can be considered as the average of two incommensurate crystal orders. However, similar to the fact that the same crystal lattice can be set by two different sets of basis vectors, the quasicrystal order can be set by the averaging of two or more generating crystal orders. For example, a simple icosahedral quasicrystal network can be obtained by averaging five equivalent fcc or two primitive cubic networks with their lattice parameters being related the "golden mean" $(\sqrt{5} + 1)/2$, provided that all the additional simple conditions for incorporating the positions into a resulting lattice are fulfilled. Here, one can invoke the following analogy. It is well known that, if in the phase transition from a highly symmetric phase to a low-symmetric phase, there are no specific conditions providing formation of single domains, then the average symmetry upon the transition remains unchanged. Therefore, if the deformation contribution into the structure distortion during the group–subgroup phase transition is taken into account appropriately, the structure formed by the averaging of all domains, including the orientational and translational ones, will coincide with the structure of highly symmetric phase. In our case, square networks rotated by 45° with respect to one

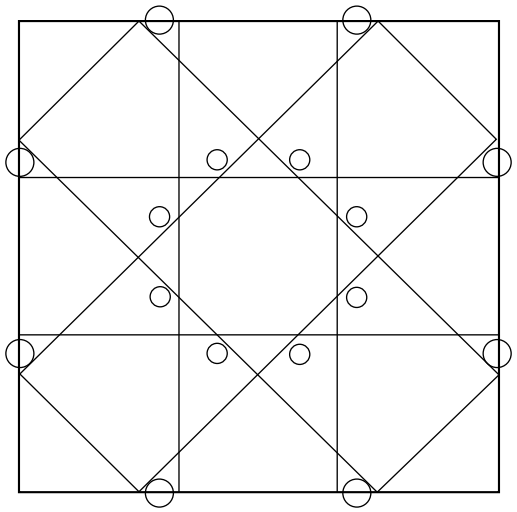

Fig. 2. Structure of the simplest approximant.

another can be considered as two types of domains forming, upon averaging, an octagonal network.

MECHANISM AND ORDER PARAMETER OF THE QUASICRYSTAL–APPROXIMANT PHASE TRANSITION

None of the known quasicrystal–crystal phase transitions provides the transformation into one of the generating structures. Any small deformation providing their mutual commensurability is energetically more advantageous. Let us analyze this mechanism of phase transition considering the following example. We assume that the crystalline state of the approximant corresponds to the ratio $P/Q = 3/2$ in (1), whence it follows that the basic periods of the first generating lattice can be written as $\mathbf{a}_1 = \langle 1/3, 0\rangle$, $\mathbf{a}_3 = \langle 0, 1/3\rangle$, and those of the second one as $\mathbf{a}_2 = \langle 1/4, 1/4\rangle$, $\mathbf{a}_4 = \langle 1/4, 1/4\rangle$. Figure 2 shows the structure of the simplest approximant whose primitive cell corresponds to a square shown by solid lines. The points of the first square lattice with the periods $\mathbf{a}_1$ and $\mathbf{a}_3$ correspond to the intersection of the horizontal and vertical lines, whereas the points of the second lattice coincide with the points of intersections of the inclined lines. Two types of the positions of the approximant, fourfold and eightfold positions, correspond to the vertices of the larger and the smaller octagons and are located approximately between the adjacent points of the generating lattices. It is seen from Fig. 2 that the approximant is formed as a result of the homogeneous isotropic deformation of the generating lattices with respect to one another. The transition into the crystal phase corresponds here to a small but finite deformation satisfying the requirement of commensurability of the lattices. The order parameter of this transition can be obtained from the components of the deformation tensors of the generating structures that are transformed into one another by the symmetry operations of the group C_{8v}. However, for the icosahedral symmetry this approach is too complicated (one has to use 30 functions corresponding to the components of five deformation tensors to obtain the order parameter). On the other hand, the thus obtained order parameter cannot be used, e.g., to describe a small relative rotations of the generating lattices, which can also lead to mutual commensurability of these lattices.

One can avoid these complications in the attempt to describe complex deformation during the quasicrystal–crystal transition in the reciprocal space. It seems to be reasonable, first, to classify such deformations, and only then to determine those of them that provide lattice commensurability. First, consider how the octago-

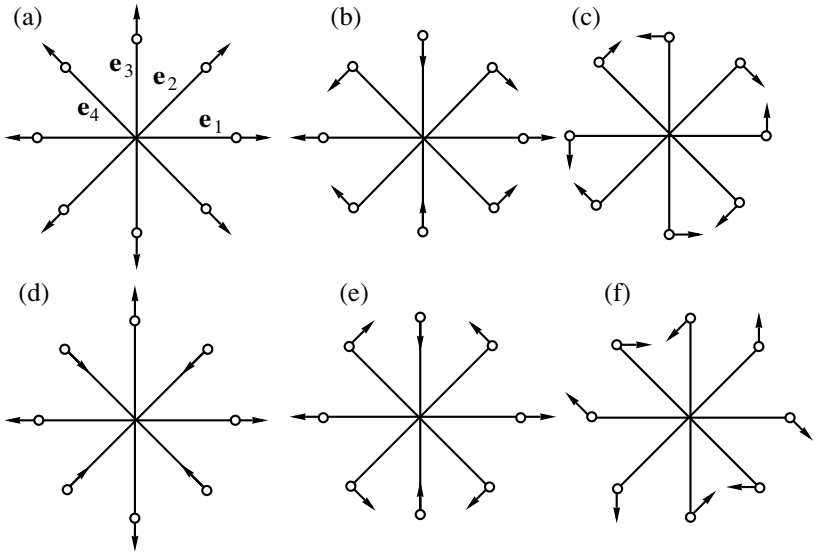

Fig. 3. All the possible "irreducible" deformations of the reciprocal-space basis vectors of a two-dimensional octagonal quasicrystal.

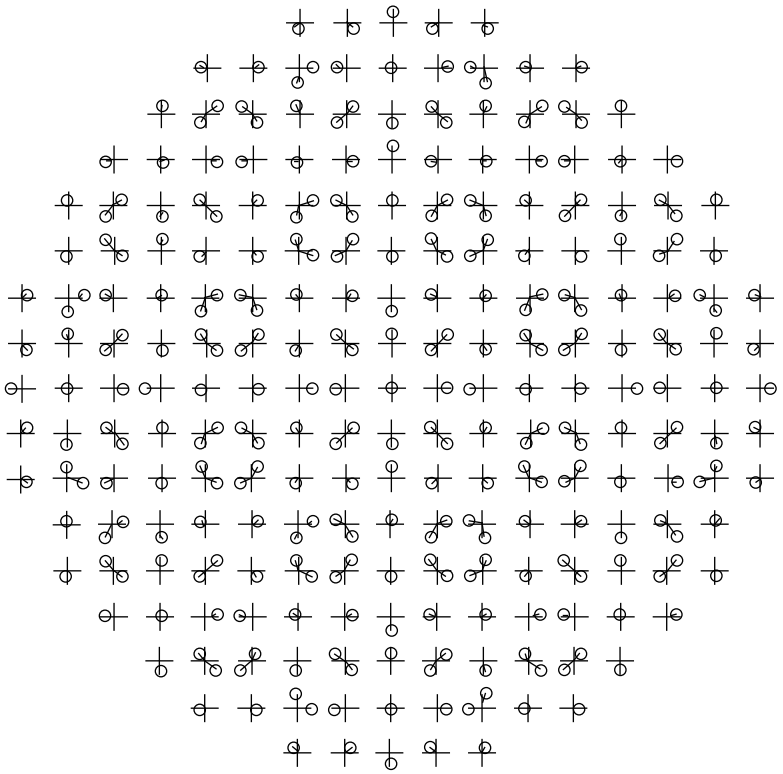

Fig. 4. Displacements of the reciprocal-space points during the transition of a quasicrystal to the approximant.

nal quasicrystal density function of the general type loses its symmetry at the arbitrary changes of the basis vectors in reciprocal space (1). These distortions can be classified using the irreducible representations of the point group C_{8v}. All such "irreducible" distortions are illustrated by Fig. 3. Figures 3a and 3b show changes in reciprocal-space basis vectors for a two-dimensional octagonal crystal in the case of homogeneous deformation. For a three-dimensional crystal structure, one can construct six linear combinations from nine components of three vectors corresponding to the changes in the basis vectors (of the direct or the reciprocal space), that are transformed by the same representations as the components of the deformation tensor. Three remaining combinations correspond to the rotation of the structure as a whole. For a quasicrystal lattice (the number of the components of the reciprocal-space basis exceeds the dimension of the physical space), the linear but inhomogeneous deformations of the reciprocal space can exist that are also transformed by the representations of the point group of a quasicrystal. The changes in basis vectors of the reciprocal space of the quasicrystal corresponding to these deformations are shown in Figs. 3c–3f. In the first two cases, the symmetry C_{4v} is preserved. Figure 3d (the direct space) should be interpreted as a deformation of isotropic compression of one generating lattice and expansion of the other lattice. Figure 3c corresponds to lattice rotation with respect to one another. In both cases, the transition into a crystalline state results in certain strain values. It should be emphasized that the deformation of one generating lattice with respect to the other as a whole should be accompanied by atomic hoppings, the so-called phasons. At such deformations, the pairs of nearest crystal positions generating one quasicrystal position are "split," which results in the disappearance of some quasicrystal positions and the formation of some new ones. The displacement of positions in the reciprocal space of a quasicrystal during its transition into a crystal (Fig. 3c) was observed experimentally in the Cr–Ni–Si system and was interpreted as a motion of projections of the points of the four-dimensional space during certain homogeneous (phason) deformation [8]. Figure 4 shows a field of displacements of the points of the reciprocal space providing an essential contribution to the density function of a quasicrystal during its transition into a crystal for the case depicted in Fig. 3d. The initial coordinates of the reciprocal space point (n_1, n_2, n_3, n_4) of a quasicrystal are given by the expression

$$k_x = Pn_1 + Q(n_2 - n_4),$$
$$k_y = Pn_3 + Q(n_2 + n_4),$$

where $P/Q = \sqrt{2}$ and P is equal to the basis-vector magnitude of the reciprocal space of the quasicrystal. The displacements of reciprocal-space points proportional

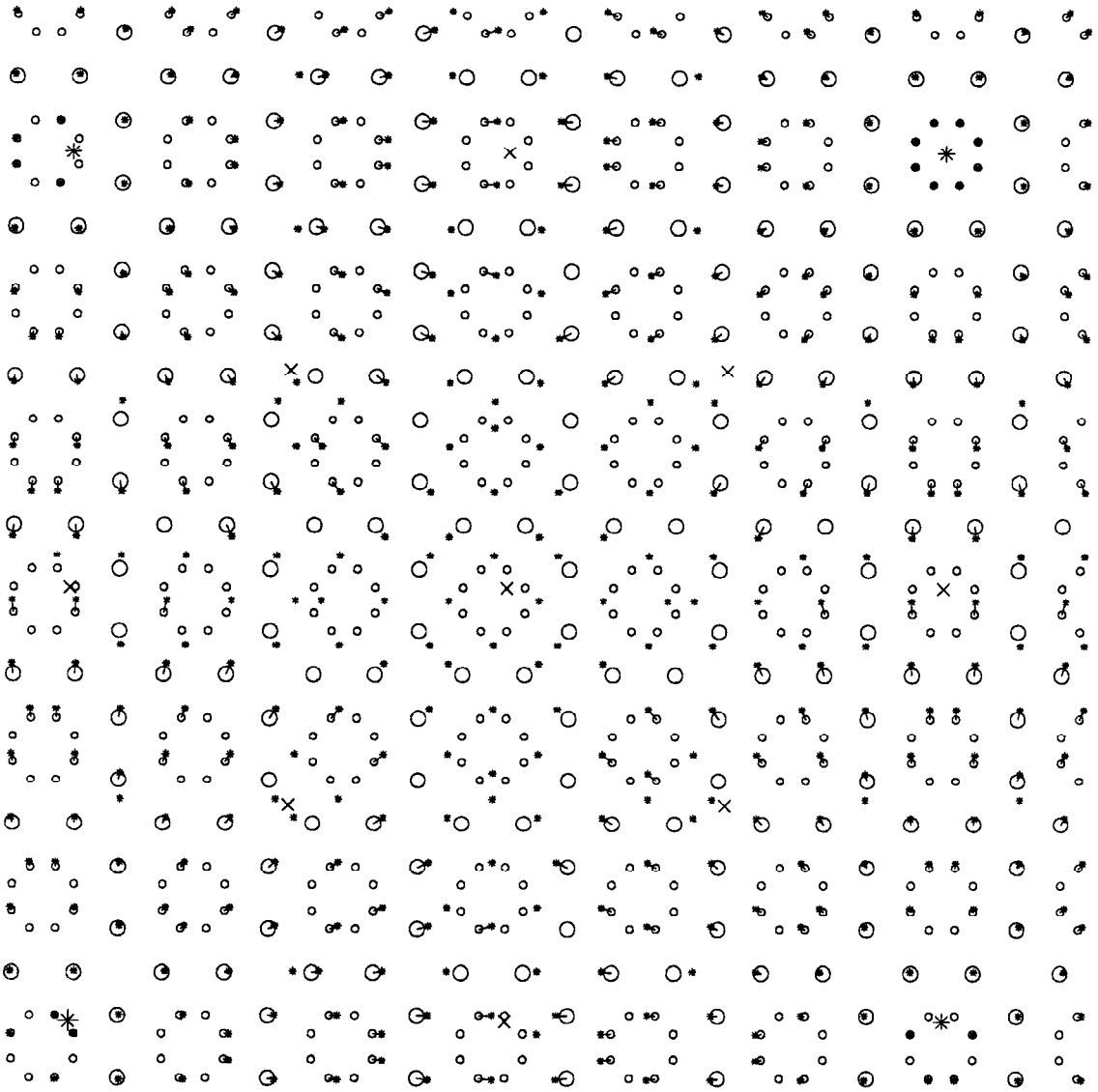

Fig. 5. The arrangement of the sites in the quasicrystal and the approximant with due regard for the contribution of the full-symmetry (homogeneous and isotropic) deformation of the reciprocal space. The positions of the octagonal network are indicated by small asterisks, the positions of atoms in the approximant structure are shown by large (fourfold position) and small (eightfold position) circles.

to the change of basis vectors (Fig. 3d) are set as

$$\begin{aligned} \Delta k_x &= \alpha P(n_1 - (n_2 - n_4)/\sqrt{2}), \\ \Delta k_y &= \alpha P(n_1 - (n_2 + n_4)/\sqrt{2}), \end{aligned} \tag{5}$$

where α is proportionality coefficient.

Expressions (5) at $\alpha = 1$ coincide with the expressions for the vector components in the so-called perpendicular reciprocal space. It is well known that the considerable structure amplitudes of the quasicrystal density function can correspond only to those (n_1, n_2, n_3, n_4) values for which the magnitude of the vector perpendicular to the reciprocal space is small [9]. Therefore, all the strong reflections are displaced insignificantly during the quasicrystal–crystal transition; some moderate and weak reflections merge together, whereas the corresponding structure amplitudes are summed up. The quantity P in (5) is taken out of parentheses to make α a dimensionless quantity. Thus, from the above stated, it becomes clear that α, which is transformed by the one-dimensional representation of the group C_{8v}, is a measure of such a distortion of the quasicrystal structure (linear inhomogeneous deformation) which provides the occurrence of the transition into a crystal approximant. The coefficient α plays the role of a specific order parameter. In this approach, the crystal phase becomes a limiting phase [10, 11] because to an approximant there corresponds a fixed value of the

order parameter, $\alpha = (17 - 12\sqrt{2})$. In the similar way, one can also define the order parameter for the quasicrystal–crystal phase transition for any symmetry of a quasicrystal. The attempts to introduce the measure of a distortion of the quasicrystal structure during its transition into a crystal structure have repeatedly been made. Thus, in [12], the order parameter is defined in terms of tangents of rotation angles of the physical space in the phase space. Most often, the order parameter is not considered as a quantity possessing symmetry properties, and the transformation is characterized by linear (phason) homogeneous deformations of a multidimensional phase space (see, e.g., [8]). The first method does not take into account the symmetry of the order parameter at all. The second method makes the construction of a thermodynamic model of the transition very difficult as well as the allowance for the interactions of the order parameter with external fields, such as, e.g., the stress field.

In [7, 13], the system of rational planes translation-equivalent in the phase space was considered, which corresponds to the equivalent approximants displaced in the vicinity of the sites of the so-called *T*-lattice, with respect to one another in the physical space. It was shown that the density function of a quasicrystal, ρ_q, can be approximated by the density function of the approximant, ρ_c. Figure 5 illustrates the correspondence of an ideal quasicrystal structure to a perfect approximant of the $P/Q = {}^3/_2$ type. The crosses in Fig. 5 depict the points of the *T*-lattice. The basic periods $\mathbf{t}_1$ and $\mathbf{t}_2$ of the *T*-lattice are obtained from (1) as

$$\mathbf{t}_1 = \langle 1/d, 1/d\rangle, \quad \mathbf{t}_2 = \langle 1/d, -1/d\rangle,$$

where $d = (4 - 3\sqrt{2})P$. The role of an order parameter in the phase transition can be played by the homogeneous isotropic deformation in the reciprocal space. In this case, a quasiperiodic structure is projected along the direction not coinciding with $E_\perp$ in the phase space onto the crystal structure. Figure 5 corresponds to the case where the structure is projected made along the rational direction close to $E_\perp$ in phase space. The positions of the reflections $\langle 22\rangle$ and $\langle -22\rangle$ of the approximant in this case coincide with the positions of the quasicrystal reflections $\langle 0100\rangle$ and $\langle 0001\rangle$, respectively. In the direct space, the corresponding generating lattice is not distorted during the transition. The regions in which the structures of an approximant and a quasicrystal are locally similar (the centers of these regions are shown by eight-ray asterisks) are repeated with the periods $\mathbf{t}_1^c$ and $\mathbf{t}_2^c$ (within the accuracy of homogeneous isotropic deformation)

$$\mathbf{t}_1^c = 2(\mathbf{t}_1 + \mathbf{t}_2), \quad \mathbf{t}_2^c = 2(\mathbf{t}_1 - \mathbf{t}_2),$$

where $\mathbf{t}_1$ and $\mathbf{t}_2$ are the periods of the *T*-lattice. The average displacements of the positions at such deformation are smaller, so that this mechanism seems to be more favorable. The participation of the homogeneous deformation of the reciprocal space in the mechanism of a phase transition can be established experimentally by measuring the displacements of the reflections upon the transformation and determining independently the jump in the volume or density of the substance upon the transition.

CONCLUSIONS

The quasicrystal order can be considered as a result of the averaging of several incommensurate generating crystal orders. The description of the mechanism of the quasicrystal–crystal transition with the aid of the deformation of a multidimensional space, which is traditional for the *n*-dimensional crystallography, can be interpreted as the relative deformation (strain) of the generating structures in the real physical space. The order parameter of the quasicrystal–crystal transition is obtained from the displacements of the basis-vector components in the reciprocal space of a quasicrystal and is, in fact, a linear inhomogeneous deformation which is transformed by the irreducible representation of the point group of a quasicrystal.

ACKNOWLEDGMENTS

This study was supported by the Russian Foundation for Basic Research, project no. 97-02-17875.

REFERENCES

1. D. Shechtman, I. Blech, D. Gratias, and J. W. Cahn, Phys. Rev. Lett. **53**, 1951 (1984).
2. E. Makovicky and B. G. Hyde, Struct. Bonding (Berlin) **46**, 101 (1981).
3. M. Duneau and A. Katz, Phys. Rev. Lett. **54**, 2688 (1985).
4. V. Elser and C. L. Henley, Phys. Rev. Lett. **55**, 2883 (1985).
5. S. B. Roshal, V. P. Dmitriev, V. L. Lorman, and V. Toledano, Fiz. Tverd. Tela (St. Petersburg) **34** (1), 237 (1995) [Phys. Solid State **37** (1), 130 (1995)].
6. V. Elser, Acta Crystallogr. Sect. A: Found. Crystallogr. **42**, 36 (1986).
7. S. B. Rochal, V. P. Dmitriev, V. L. Lorman, and V. Toledano, Phys. Lett. A **220**, 111 (1996).
8. Z. H. Mai, L. Xu, N. Wang, *et al.*, Phys. Rev. B: Condens. Matter **40**, 12183 (1989).
9. T. C. Lubensky, J. E. S. Socolar, P. J. Steinhardt, *et al.*, Phys. Rev. Lett. **57**, 1440 (1986).
10. V. P. Dmitriev, S. B. Rochal, Yu. M. Gufan, and V. Toledano, Phys. Rev. Lett. **60** (19), 1958 (1988).
11. V. P. Dmitriev, S. B. Rochal, Yu. M. Gufan, and V. Toledano, Phys. Rev. Lett. **62** (21), 2495 (1989).
12. M. Torres, in *Materials of the International Workshop on Methods of Structure Analysis of Modulated Structures and Quasicrystals, Lekeitio*, Ed. by J. M. Pérez-Mato, F. J. Zuniza, *et al.* (World Scientific, Singapore, 1991).
13. S. B. Roshal, Kristallografiya **42** (5), 780 (1997) [Crystallogr. Rep. **42** (5), 714 (1997)].

Translated by A. V. Zalesskii

Crystallography Reports, Vol. 45, No. 3, 2000, pp. 479–481. Translated from Kristallografiya, Vol. 45, No. 3, 2000, pp. 525–527.

Structure and Some Physical Properties of $K_2Ni(SO_4)_2 \cdot 6H_2O$ Crystals

A. Pietrashko*, Z. B. Perekalina, L. V. Soboleva**, and L. F. Kirpichnikova****

** Institute of Low Temperature and Structure Research, Polish Academy of Sciences, Ocolna 2, Wroclaw, 50-950 Poland*

*** Shubnikov Institute of Crystallography, Russian Academy of Sciences, Leninskiĭ pr. 59, Moscow, 117333 Russia*

Received November 3, 1999

Abstract—The data obtained from the analysis of the solubility phase diagrams have been used in growth of $K_2Ni(SO_4)_2 \cdot 6H_2O$ crystals. The X-ray diffraction studies of the crystals grown showed that, at room temperature, the crystals belong to the diffraction class 2/*m*. The crystal structure is similar to the structures of the Tutton salts. The study of the absorption spectra and the differential scanning calorimetry (DSC) revealed a pronounced anomaly in the vicinity of 45–46°C, which seems to be associated with the structural changes in the crystal. © *2000 MAIK "Nauka/Interperiodica".*

The crystals of double sulfates hexahydrates of the composition $K_2Ni(SO_4)_2 \cdot 6H_2O$ (KNSH) belong to the family of the Tutton salts [1] described by the general formula $M_2^{1+}M^{2+}(XO_4)_2 \cdot 6H_2O$, where M^+ is an alkali metal or ammonium, M^{2+} is a bivalent metal, and $XO_4 = SO_4$ or SeO_4. These compounds form an isostructural series and belong to the monoclinic system. The crystals of some Tutton salts undergo phase transitions. Thus, $NH_4Cu(SO_4)_2 \cdot 6H_2O$ crystals at 67°C undergo the transition from the phase described by the sp. gr. $P2_1/a$ to the phase described by the sp. gr. *Pmnm* accompanied by partial dehydration and the transformation of hexahydrate into dihydrate [2]. The neutron diffraction studies [3] showed that KNSH crystals belong to the monoclinic class 2/*m*. Unfortunately, the structures of these crystals are studied insufficiently and their properties almost not at all. We aimed to determine the structure of $K_2Ni(SO_4)_2 \cdot 6H_2O$ crystals and to study their spectroscopic, calorimetric, and dielectric properties.

Soboleva [4] analyzes the solubility phase diagram of the ternary K_2SO_4–$NiSO_4$–H_2O system and determined the optimum crystallization conditions for KNSH growth. She grew KNSH crystals by the method of temperature decrease.

The structural studies were performed on an automatic KUMA KM4 diffractometer (CuK_α-radiation, graphite monochromator). The experimental data obtained were processes by the program SHELX-97 to $R = 00155$. It was established that KNSH crystals are monoclinic (sp. gr. $P2_1/c$) with the unit-cell parameters $a = 6.1250$ Å, $b = 12.159$ Å, $c = 8.980$ Å, $\beta = 105.06°$,

Atomic coordinates ($\times 10^4$) and parameters of atomic thermal vibrations B_{ef} ($Å^2 \times 10^3$) for KNSH crystals at 20°C

Atom	*x*/*a*	*y*/*b*	*z*/*c*	B_{ef}
K(1)	6572(1)	1544(1)	3658(1)	31(1)
S(1)	7263(1)	8650(1)	4118(1)	19(1)
O(11)	6184(1)	9386(1)	2835(1)	25(1)
O(12)	9483	8248	3944	28(1)
O(13)	5745(1)	7703(1)	4095(1)	33(1)
O(14)	7552(1)	9252(1)	5564(1)	40(1)
Ni(1)	0	0	0	16(1)
O(1)	3014(1)	668(1)	4(1)	23(1)
O(2)	1629(1)	−1109(1)	1675(1)	24(1)
O(3)	−355(1)	1126(1)	1664(1)	23(1)
H(11)	3228(23)	600(11)	–781(16)	38(3)
H(12)	3322(26)	1363(13)	271(17)	54(4)
H(21)	2866(25)	−874(12)	2100(17)	45(4)
H(22)	938(23)	−1252(12)	2349(16)	39(3)
H(31)	474(27)	1011(14)	2547(19)	58(4)
H(32)	−68(21)	1742(10)	1425(14)	28(3)

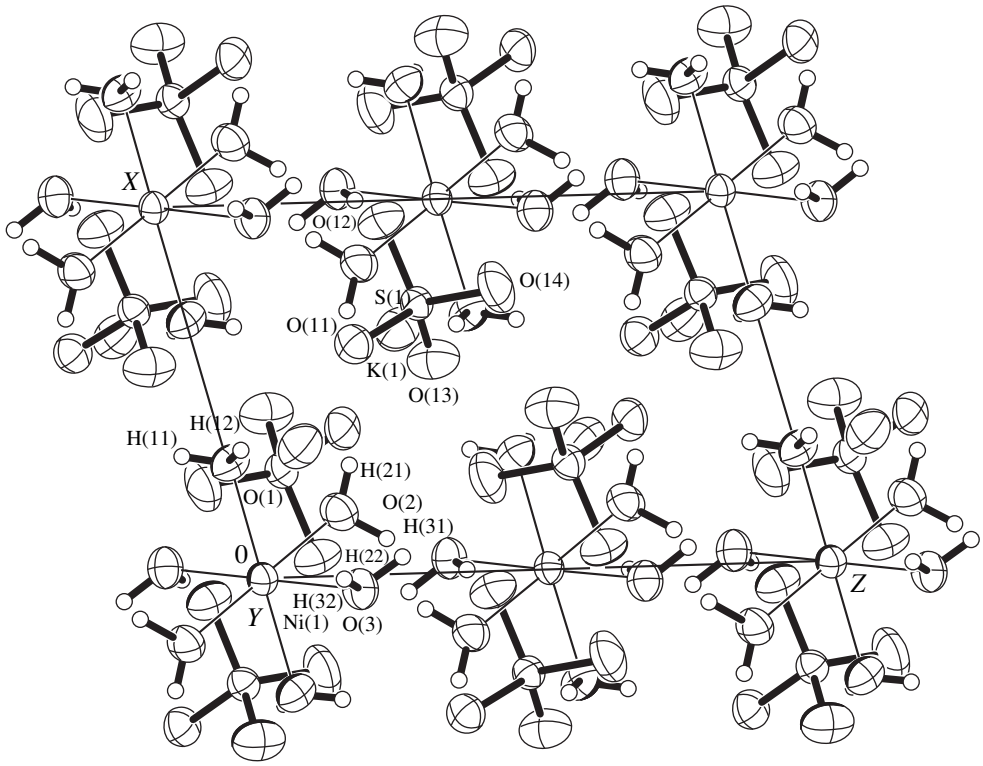

Fig. 1. Projection of the KNSH structure onto the (010) plane.

$V = 645.8$ Å^3, $Z = 2$, $d_{obs} = 2.248$ mg/m^3. Table lists the coordinates and the thermal parameters of atoms. Figure 1 shows the crystal structure determined. The X-ray diffraction analysis confirmed the chemical composition of the KNSH crystals and showed that their structure is built by potassium ions and complex $[Ni \cdot 6H_2O]$ to sulfate ions $[SO_4]$ cations located at the center of inversion and linked by a system of hydrogen bonds.

The differential scanning calorimetry (DSC) measurements of KNSH crystals were performed on a Netsch DSC-200 setup. The specimen was heated at a rate of 0.2°C/min. The measurements revealed an anomaly in the vicinity of 45–46°C (Fig. 2), which indicates the dependence of the KNSH properties on temperature in the vicinity this temperature. The dielectric measurements over a wide range of crystal temperatures showed that the KNSH crystals possess no ferroelectric or ferroelastic properties. The studies of the absorption spectra in a polarized light were performed on a Hitachi spectrophotometer with the special attachment in the temperature range from 20 to 120°C. The crystal plates were oriented in such a way that the twofold axis of the crystal in the plate was parallel to the polarization plane of the incident light. Analyzing the temperature dependences obtained, we considered the band of the most uniform absorption with the maximum at 390 nm (25000 cm^{-1}), according to [5], this band corresponds to the spin-allowed $^3Ag_{2g}(F)$–$^3T_{ig}(P)$ transition. Our measurements show (Fig. 3) that, with an increase in the temperature, the absorption band shifts to the long-wave length range of the spectrum, whereas the position of the short-wave length edge remains unchanged. Thus, a nonuniform broadening of the absorption band was observed. To study the changes in the absorption-spectra, we constructed the temperature dependences of the wavelength of the absorption maximum (Fig. 4, *a*) and the optical density (Fig. 4, *b*). It is seen that at the temperature of 45–46°C, the temperature dependences show clearly pronounced changes. These changes cannot be explained only by

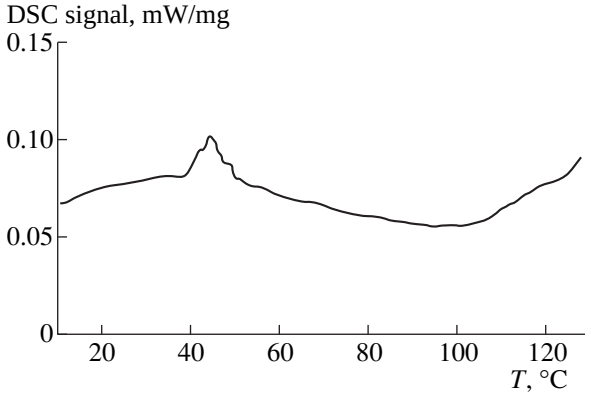

Fig. 2. Differential scanning calorimetry curve for KNSH crystals.

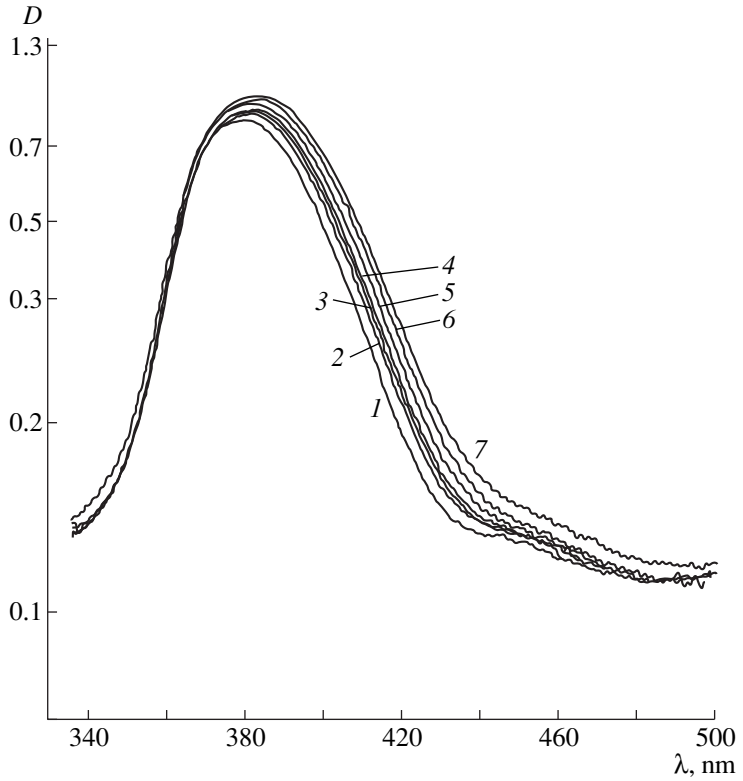

Fig. 3. Absorption spectra of KNSH crystals at various temperatures: (*1*) 22, (*2*) 45.5, (*3*) 56.5, (*4*) 67, (*5*) 90, (*6*) 108.5, and (*7*) 116.5°C.

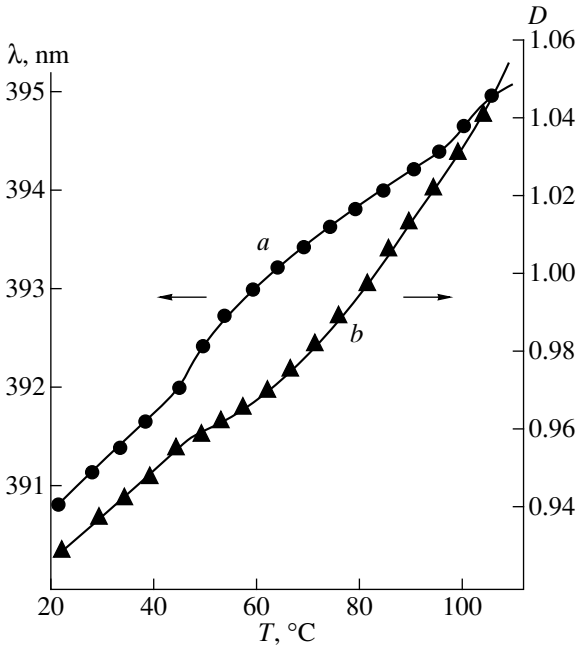

Fig. 4. *a*, temperature dependences of the absorption-maximum position (wavelength) and *b*, the optical absorption density for the KNSH crystals.

the change in the contribution of normal vibrations to the absorption intensity characteristic of this band. These changes should also be associated with some structural rearrangements occurring in this temperature range. Thus, the nature of the anomalies observed by the methods differential scanning calorimetry and spectroscopy is still unclear and requires further X-ray studies in the above temperature range.

ACKNOWLEDGMENTS

The study was supported by the Russian Foundation for Basic Research (project no. 97-02-16372).

REFERENCES

1. A. N. Winchell and H. Winchell, *The Microscopical Characters of Artificial Inorganic Solid Substances: Optical Properties of Artificial Minerals*, 3rd ed. (Academic Press, New York, 1964; Mir, Moscow, 1967).
2. G. Browmik, Indian J. Phys. **43**, 43 (1960).
3. P. G. Hodgeson, J. Whitnalls, C. H. Kennar, and F. H. Moor, Struct. Commun. **4**, 713 (1975).
4. L. V. Soboleva, Neorg. Mater. **31**, 614 (1995).
5. C. J. Ballhausen, *Introduction to Ligand Field Theory* (McGraw-Hill, New York, 1962; Mir, Moscow, 1964).

Translated by L. Man

Crystallography Reports, Vol. 45, No. 3, 2000, pp. 482–486. Translated from Kristallografiya, Vol. 45, No. 3, 2000, pp. 528–533.

Effect of Ionizing Radiation on Energy-Barrier Distribution for Domain Walls in Ferroelectrics

V. V. Gladkiĭ, V. A. Kirikov, and E. S. Ivanova

Shubnikov Institute of Crystallography, Russian Academy of Sciences, Leninskiĭ pr. 59, Moscow, 117333 Russia

Received November 16, 1998

Abstract—A precision study of slow polarization in a polydomain ferroelectric has been performed on an example of triglycine sulfate samples in weak electric fields prior to and upon their γ-irradiation at doses of 0.2 and 0.3 Mrad. It is shown that in all the cases, relaxation obeys the universal temporal power law. The phenomenological analysis of the experimental data was performed in the approximation of noninteracting relaxation centers (nuclei), which provided the restoration of the spectra of potential barrier distribution for domain walls in the crystal. The transformation of the spectrum of a γ-irradiated ferroelectric indicates the simultaneous formation of new small and gigantic barriers in the crystal. *© 2000 MAIK "Nauka/Interperiodica".*

INTRODUCTION

Ferroelectrics subjected to ionizing irradiation have repeatedly been studied [1–3]. One of the major conclusions made from these experiments is that irradiation at low doses gives rise to the formation of small domains with polarization opposite to the polarization of their environment. In other words, the number of domain walls increases [3, 4] and, at doses exceeding some critical value, domain walls are pinned in their positions because of higher energy barriers and, thus, stabilize the domain structure [1–3]. As a result, all the physical properties sensitive to the domain structure undergo considerable changes. In particular, the electric polarization and the dielectric constant increase at low irradiation doses (radiation annealing) and decrease at high ones. In this case, the dielectric hysteresis shows characteristic distortions because of a drastic increase of structure-relaxation time in an electric field [1–3].

All the parameters of irradiated ferroelectrics determined by the standard methods give only partial information on the domain structure, because at high measuring-field frequencies (~10 Hz and higher) [3], the slow processes characteristic of many inhomogeneous materials with a long-living metastable state do not participate in polarization. Moreover, these parameters characterize only the electric response to the external field, which is averaged over the volume of an essentially inhomogeneous material. Therefore, many conclusions on the changes in the structural properties of crystals upon their irradiation based on the electric measurements are only of a qualitative nature.

Below, we report the study of polarization of a ferroelectric irradiated in a weak electric field on an example of triglycine sulfate (TGS) samples. The measurements were made by the method of dielectric spectroscopy at infralow frequencies, which allowed the observation of slow relaxation processes. The experimental data obtained were used to restore the spectra of relaxation-time distribution of the domain structure or the energy-barriers distribution of domain walls and provided their evaluation and comparison with the similar characteristics of unirradiated TGS crystals.

EXPERIMENTAL

Electric polarization of TGS crystals was measured with the use of a bridge with unequal shoulders by the compensation electrometric method, which provided the detection of small charge variations on the sample surface. The zero-indicator was a V7-29 electrometer with the maximum voltage sensitivity 0.1 mV and the charge sensitivity (at the optimum choice of the scheme elements) $\sim 10^{-8}$ μC. The voltage compensation in the bridge diagonal and polarization were automatically measured with the aid of an electronic system, which also provided the viewing of the curves of polarization versus the electric field and time on a monitor screen of an IBM PC computer. The system and its operation are described in detail elsewhere [5].

The γ-radiation from a Co^{60} source had the power ~700 R/s in the irradiation zone. The samples were $4 \times 5 \times 1$ mm large rectangular plates cut normally to the polar *Y*-axis. The large faces of the plates were polished and coated with silver-paste electrodes. The error in the temperature stabilization did not exceed 0.03 K.

The electric field polarizing the crystal was less intense than the coercive field, so that only slow relaxation processes in the domain structure were taken into account (the thermally activated processes proceeded through the energy barriers of domain walls). The coercive field was evaluated from the measurements of qua-

1063-7745/00/4503-0482$20.00

sistatic loops of dielectric hysteresis under a slow stepwise variation of the field. One loop was measured for ~1.5 h.

RESULTS AND DISCUSSION

Under the conditions of slow variation of the domain structure and polarization, the relaxation centers (nuclei) are independent from one another, and it is therefore possible to assume that their contribution to the total polarization P is additive. Then, the following equation is valid for the dimensionless quantity $y(t) = (P_e - P(t))/(P_e - P_0)$ (where P_e is the equilibrium polarization, $P(t)$ is the polarization at the moment t, and P_0 is the initial polarization at $t = 0$):

$$y(t) = \int_0^\infty f(\tau)\exp(-t/\tau)d\tau. \quad (1)$$

Here $f(\tau)$ is the normalized distribution function of local relaxation times τ for nuclei, $\int_0^\infty f(\tau)d\tau = 1$.

The $f(\tau)$ distribution can readily be determined if the analytical expression for the function $y(t)$, which describes the experimental data, is known, because $y(t)$ and $\tau^2 f(\tau)$ are the Laplace transform and the initial integral Laplace transformation, respectively. As was the case in [5], for all the crystals studied, this function is satisfactorily described by the power law

$$y(t) = 1/(1 + t/a)^n. \quad (2)$$

Here a and n are the free parameters characterizing the relaxation processes in each sample, and the distribution $f(\tau)$ has the form [6]

$$f(\tau) = \{a^n/\Gamma(n)\}(1/\tau)^{n+1}\exp(-a/\tau), \quad (3)$$

where $\Gamma(n)$ is the gamma-function.

The relaxation time τ and the potential barrier U for the domain wall are related by the Arrhenius law $\tau = \tau_0\exp(U/kT)$, where τ_0 is the kinetic coefficient, i.e., $U = kT\ln(\tau/\tau_0)$ is the quantity proportional to $\ln\tau$. Therefore, it is sometimes more convenient to construct the following dimensionless function using the experimental data:

$$g(\tau) = \tau f(\tau) = (1/\Gamma(n))(a/\tau)^n\exp(-a/\tau). \quad (4)$$

This function characterizes the distribution density $\ln\tau$, i.e., reproduces the shape of the barrier distribution U in the sample. Then $g(\tau)d(\ln\tau)$ singles out the region of the spectrum $g(\tau)$ with the width $d(\ln\tau) = dU/kT$.

When analyzing the experimental data, we assumed that the equilibrium value of P_e in (1) is equal to the spontaneous polarization P_s ($P_e = P_s$). This assumption seems to be quite justified, because for crystals with strictly defined coercive field (such as TGS crystals) it coincides with the general concepts of the specific features of a ferroelectric polarization in a weak electric field [7].

The dependences $P(t)$ and $y(t)$ were approximated by the least squares method using the standard programs. The experimental errors in the determination of the parameters a and n and the spectra $f(\tau)$ and $g(\tau)$ can be readily determined by differentiating (2), (3), and (4) with respect to a and n:

$$\left|\frac{\delta a}{a}\right| = \frac{1 + t/a}{n(t/a)}\left|\frac{\delta y}{y}\right|, \quad \left|\frac{\delta n}{n}\right| = \frac{1}{n\ln(1 + t/a)}\left|\frac{\delta y}{y}\right|. \quad (5)$$

It is seen from (5) that the accuracy of the estimates are higher for a longer time of measurements and that $\left|\frac{\delta a}{a}\right| \longrightarrow \left|\frac{\delta y}{y}\right|$ and $\left|\frac{\delta n}{n}\right| \longrightarrow 0$ at $t \longrightarrow \infty$.

The experimental $P(t)$ and $y(t)$ dependences for two TGS samples (prior to and upon γ-irradiation) are shown by circles in Fig. 1, whereas the dependences calculated by formula (2) are shown by solid lines. It is seen that these data agree quite well (the deviation of the experimental $\left|\frac{\delta y}{y}\right|$ values from the calculated ones does not exceed 0.005). The first sample was irradiated at a dose of 0.2 Mrad (Fig. 1a), the second, at a dose of 0.3 Mrad (Fig. 1b). The relaxation parameters a and n used in formula (2) in all the cases are listed in table. It is seen from Fig. 1 that irradiation of crystals even at low doses essentially decreases the time-averaged rate of polarization relaxation. A decrease of this rate is especially pronounced upon irradiation at a dose of 0.3 Mrad. Therefore, in this case, relaxation was recorded in a more intense polarizing field than for a non-irradiated sample (Fig. 1b, table).

The continuous spectra of the $f(\tau)$ and $g(\tau)$ distributions calculated from the experimentally determined parameters a and n by formulas (3) and (4) are shown in Fig. 2. The $f(\tau)$ spectra constructed on the logarithmic scale of relaxation times τ have the bell shape. For both non-irradiated crystals, the parameters are rather close [the maximum of f_{max}, the spectrum width $\Delta\tau$, the area $S \sim f_{max}\Delta\tau/2$ under the curve $f(\tau)$, but for the second sample (Fig. 2b), the spectrum is somewhat displaced toward lower τ values in comparison with the first sample (Fig. 2a). The width $\Delta\tau = \tau_2 - \tau_1$, the maximum τ_2 and the minimum τ_1 τ values, the range of the barrier-energy $\Delta U = kT\ln(\tau_2/\tau_1)$ distribution, and the area S were determined at the level $f(\tau) = 0.1f_{max}$. It is important that for both samples the area is close to unity, $S \sim 0.9$, i.e., that the spectra of non-irradiated samples in Fig. 2 include almost the complete set of relaxation times τ.

The maxima of the $f(\tau)$ spectra of irradiated samples are broader and displaced toward lower τ values in comparison with those of non-irradiated samples. At first glance, one can get an erroneous idea that irradia-

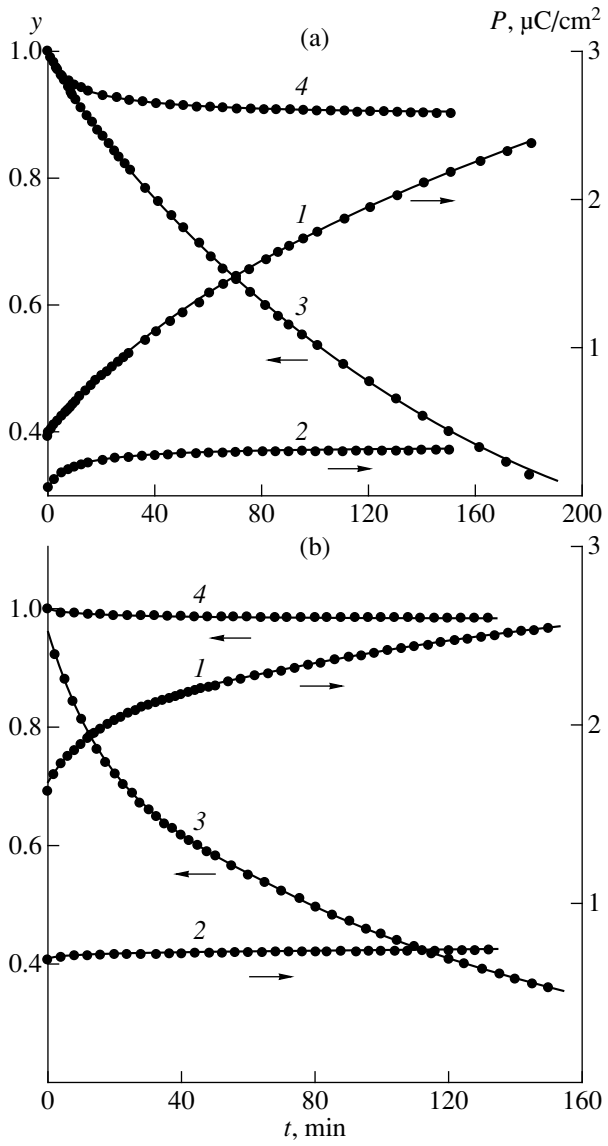

Fig. 1. (*1*, *2*) Polarization *P* and (*3*, *4*) dimensionless quantity $y = (P_s - P)/(P_s - P_0)$ as functions of time *t* for two TGS samples at $T = 20°C$. (*1*, *3*) non-irradiated samples, (*2*, *4*) samples irradiated at a dose (a) 0.2 and (b) 0.3 Mrad. Polarizing field *E*: (*1*, *3*) (a) 56, (b) 17, and (*2*, *4*) 260 V/cm. Circles denote the experimental data, solid lines indicate the data calculated by formula (2) with the values of the relaxation-parameters *a* and *n* indicated in table.

tion increases the average rate of structure relaxation. But, in fact, the areas *S* between the curves $f(\tau)$ and the straight line $f(\tau) = 0.1$, $f_{max} = \text{const}$ are much less than unity (~0.09 at a dose of 0.2 Mrad and ~0.02 at a dose of 0.3 Mrad) and therefore the largest parts of the sample (~0.91 and ~0.98 of the sample volume, respectively) have a considerably higher τ values at the "wings" of the $f(\tau)$ distributions, which can hardly be distinguished on the scale of Fig. 2. The parameters of all the $f(\tau)$ spectra are indicated in table.

The $g(\tau)$ spectra are the most informative for the analysis (Figs. 2c, 2d). It is seen that the spectrum of the irradiated sample acquires quite different shape and becomes asymmetric, shows a relatively fast increase of *g*, attains the maximum g_{max}, and then very slowly decreases at high τ. With an increase of the irradiation dose (Fig. 2d), the *g* spectrum is shifted to the right, and the slope of *g* to the abscissa becomes even smaller, which indicates that the fraction of the regions with relatively low barrier energies *U* reduces, whereas the fraction of the regions with high *U* energies increases. If the sample irradiated at a dose of 0.3 Mrad was polarized in a less intense electric field, *E*, the segregation of the low and high barriers in the sample would have been even more pronounced so that the *g* spectrum would have been transformed into a "step" with a very low $dg/d\tau$ value at high τ values (because, it is well known, that less intense *E* fields result in the shift of the whole *g* spectrum of the crystal toward high τ values [5]). Consider the slow variations of *g* in Figs. 2c, 2d at high τ values using formula (4). At $\tau = 10^7$, 10^{10}, and 10^{15} min, the relative decrease in g/g_{max} equals 0.80, 0.67, and 0.54 at a dose of 0.2 Mrad and 0.96, 0.92, and 0.87 at a dose of 0.3 Mrad, respectively. Such an interpolation of the experimental data indicate the existence of gigantic τ values in the *g* spectra of irradiated crystals.

It should be emphasized that we used only relatively low doses of γ-radiation, which usually cause only slight changes in the traditionally measured crystal characteristics, which then are averaged over the sample [3]. The insets in Figs. 2c, 2d show the quasistatic hysteresis loops for nonirradiated and irradiated samples. It is seen that unlike the *g* spectra, the loops are only slightly changed upon irradiation: at a dose of 0.2 Mrad, they are almost unchanged (one observes only a slight unipolarity, Fig. 2c); at a dose of 0.3 Mrad, the coercive field increases and the middle part of the loop becomes somewhat narrower (Fig. 2d), which, with a further increase of the dose, should provide the formation of a "double" hysteresis loop [1–3].

The main characteristics of the spectra agree with the well-known data on the macroscopic properties of the irradiated crystals. Thus, the short relaxation times for the spectra of the crystals irradiated at low doses can be associated with formation of new small domains [4], which increase the domain-wall density and, therefore, make an additional contribution to the dielectric constant [3]. The stabilization of the domain structure and a decrease of the electric response of the crystal in alternating fields at high irradiation doses seems to be the consequence of a drastic increase of the fraction of high barriers for domain walls and the gigantic relaxation times τ.

The empiric power law for relaxation [2] seems to be a universal law for inhomogeneous systems with the long-living metastable states. This law is satisfactorily fulfilled for the slow polarization of TGS crystals with

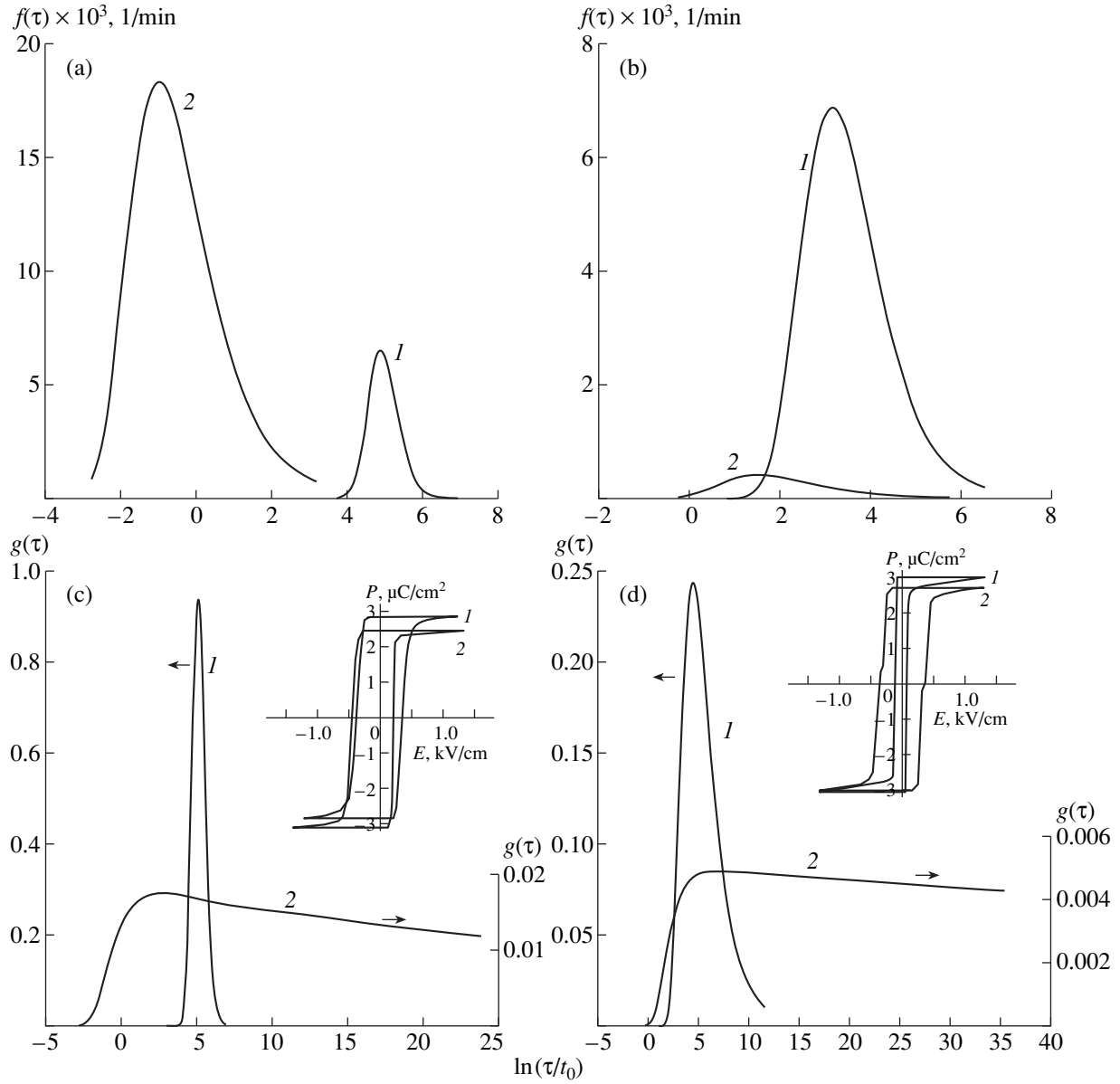

Fig. 2. The (a, b) $f(\tau)$ and (c, d) $g(\tau)$ spectra (*1*) prior to and (*2*) upon γ-irradiation of TGS crystals at a dose (a, c) 0.2 and (b, d) 0.3 Mrad. The spectra were calculated by formulas (3) and (4) with the parameters determined from the experimental data shown in Fig. 1, $t_0 = 1$ min. In the insets: quasistatic loops of dielectric hysteresis (*1*) prior to and (*2*) upon irradiation.

different states of the domain structure and the surface [5], for the dielectric constant of mixed $K_{(1-x)}Li_xTaO_3$ crystals in the glassy state [8] and, as we showed, for slow thermoactivated polarization of other polydomain ferroelectrics. The universal nature of this law is also confirmed by the fact that some laws recorded earlier are only the particular cases of this universal law. Thus, at $t \gg a$, the law described by (2) coincides with the power law $y \sim 1/t^n$ observed for large relaxation times in dielectrics [9, 10]; at $n \ll 1$, it coincides with the logarithmic law $y \sim 1 - n\ln(1 + t/a)$ characteristic of numerous inhomogeneous systems with slow relaxation and, in particular, for magnetic [11] and dielectric [12, 13] systems. One can readily show that, unlike the data for unirradiated crystals, the experimental data for irradiated crystals can approximately be represented by a logarithmic temporal law with the distribution function g [because of low n values ($n \ll 1$, see table)]. This distribution function is equal to zero at $\tau < \tau_{min}$ and $\tau > \tau_{max}$ and is constant in the range $\tau_{min} < \tau < \tau_{max}$ [11, 12]. In many respects, this function reminds the distribution g corresponding to power law (2) in Figs. 2c, 2d. The answer to the question of which relaxation law and which distribution function τ should be used in the analysis of the experimental data depends on the accu-

Parameters of the spectrum of the relaxation-time distribution $f(\tau)$ for a TGS crystal prior to and upon its γ-irradiation

Sample	Dose, Mrad	E, V/cm	a, min	n	τ_1, min	τ_2, min	τ_m, min	ΔU, eV	S
1	0	56	900 ± 2	5.7 ± 0.1	65 ± 0.3	350 ± 1.6	134 ± 0.6	0.04 ± 0.002	0.9
	0.2	56	0.4 ± 0.05	0.019 ± 0.004	0.1 ± 0.01	9.5 ± 1.3	0.38 ± 0.05	0.12 ± 0.007	0.09
2	0	17	34 ± 0.2	0.502 ± 0.001	5.79 ± 0.02	260 ± 1	23 ± 0.1	0.1 ± 0.007	0.9
	0.3	260	4.5 ± 2.3	0.005 ± 0.0007	1.0 ± 0.5	117 ± 52	4.5 ± 2.3	0.12 ± 0.007	0.02

racy of the measured relaxation parameters, which considerably decreases at low n [see formulas (5)].

It can also be shown that, within quite a long period of time, relaxation follows the well-known empiric Kohlrausch law $y \sim \exp(-t/\tau)^\beta$ [14], where τ is a certain average relaxation time and $\beta < 1$. However, the power law described by (2) is more advantageous at short times, because, first, the derivative dy/dt for the Kohlrausch law is infinite at $t = 0$, whereas for (2), this derivative is finite in full accord with the experimental data, and, second, formula (2) takes into account the idea about the existence of the spectrum of relaxation time τ and a simple distribution function of τ.

CONCLUSION

The data obtained for slow kinetics of nonequilibrium polarization of a polydomain ferroelectric illustrate the possibilities provided by the method of electric measurements used, which can be called the precision infralow frequency dielectric spectroscopy. The lower frequency boundary of the method is about 10^{-5} Hz or even lower. Unlike the traditionally measured macroscopic properties (which are the characteristics averaged over the sample volume), the infralow frequency spectra provide detailed quantitative information on the fine details of the energy distribution of the potential barriers for domain walls in crystals and its changes. The spectrum parameters are the dynamic characteristics of a ferroelectric, which are rather sensitive to the variations in its domain and defect structures and, in particular, to those induced by ionizing radiation. Thus, these spectra show that even irradiation at low γ-irradiation doses gives rise to the formation of new relaxation centers (nuclei) with low barriers and to a drastic increase of pronounced barriers for domain walls with gigantic relaxation times. A further increase of the irradiation dose rapidly displaces the spectrum of barrier-energy distribution toward higher values, which is consistent with the known characteristics of the behavior of physical properties. The reconstruction of the spectra of barrier-energy distribution from the experimental data is rather simple because of the temporal power law of relaxation seems to be universal for a large class of inhomogeneous materials with various rates of their approaching to the thermodynamic equilibrium.

ACKNOWLEDGMENTS

The authors are grateful to N.V. Belugina for her help in preparation of the samples and discussion of their domain structure.

The study was supported by the Russian Foundation for Basic Research, project no. 96-02-18456.

REFERENCES

1. M. E. Lines and A. M. Glass, *Principles and Applications of Ferroelectrics and Related Materials* (Oxford Univ. Press, Oxford, 1977; Mir, Moscow, 1981).
2. G. A. Smolenskiĭ, V. A. Bokov, V. A. Isupov, *et al.*, *Ferro- and Antiferroelectrics* (Nauka, Leningrad, 1971).
3. E. V. Peshikov, *Effect of Radiation on Ferroelectrics* (FAN, Tashkent, 1972).
4. V. A. Yurin, N. V. Belugina, V. A. Meleshina, *et al.*, Izv. Akad. Nauk SSSR, Ser. Fiz. **35** (9), 1927 (1971).
5. V. V. Gladkiĭ, V. A. Kirikov, S. V. Nekhlyudov, and E. S. Ivanova, Fiz. Tverd. Tela **39** (11), 3181 (1997) [Phys. Solid State **39** (11), 1829 (1997)].
6. V. A. Ditkin and A. P. Prudnikov, *Handbook on Operational Calculus* (Vysshaya Shkola, Moscow, 1965).
7. L. D. Landau and E. M. Lifshitz, *Course of Theoretical Physics. Vol. 8. Electrodynamics of Continuous Media* (3rd ed., Nauka, Moscow, 1982; 2nd ed., Pergamon Press, Oxford, 1981).
8. F. Alberici, P. Doussineau, and A. Levelut, J. Phys. I **7** (2), 239 (1997).
9. A. K. Jonscher, in *Dielectric Relaxation in Solids* (Chelsea Dielectric, London, 1983), p. 380.
10. H. Z. Cummins, Phys. Rep. **185** (5–6), 211 (1990).
11. S. Krupicka, *Physik der Ferrite und der verwandten magnetischen Oxide* (Academia, Praha, 1973; Mir, Moscow, 1976).
12. V. V. Gladkiĭ, V. A. Kirikov, and E. S. Ivanova, Zh. Éksp. Teor. Fiz. **110**, 298 (1996) [JETP **83**, 161 (1996)].
13. V. V. Gladkiĭ, V. A. Kirikov, and E. S. Ivanova, Kristallografiya **43** (4), 710 (1998) [Crystallogr. Rep. **43** (4), 661 (1998)].
14. A. K. Jonscher, Nature **267**, 673 (1977).

Translated by L. Man

Crystallography Reports, Vol. 45, No. 3, 2000, pp. 487–492. Translated from Kristallografiya, Vol. 45, No. 3, 2000, pp. 534–540.

Light Propagation in Stratified Chiral Media. The 4 × 4 Matrix Method

O. V. Ivanov and D. I. Sementsov

Ulyanovsk State University, Ulyanovsk, 432700 Russia

Received May 29, 1997; in final form, April 2, 1999

Abstract—Propagation of electromagnetic waves in stratified bianisotropic chiral structures is described by the 4×4 matrix method. At arbitrary layer parameters, the amplitude and the polarization characteristics (intensity, polarization azimuth, and ellipticity) of reflected and transmitted electromagnetic waves are studied as functions of the angle of the wave incidence onto the structure. *© 2000 MAIK "Nauka/Interperiodica".*

INTRODUCTION

Recently, we have evidenced the fast development of the theory of electromagnetic waves (EMW) propagation in bianisotropic chiral media, such as composite materials, liquid crystals, and other optically active substances [1]. Chiral media exhibit two basic properties: the optical activity (difference of phase velocities for the left- and right-handed circular polarizations) and chiral dichroism. Within the microwave range, such media are formed by the inclusion of metallic or ceramic helicoids into a dielectric matrix [2, 3]. Within the optical range, the role of such helicoids can be played by molecules possessing no mirror symmetry [4]. These properties are inherent in cholesteric and smectic liquid crystals, which, despite the appreciable differences in the properties and structures, have one common characteristic—they are all formed by molecules possessing the left- or right-hand symmetry (chiral molecules) and spatially periodic with the period usually lying within the optical range [5, 6]. Similar phenomena can also be obtained by using helicoid swastika or Ω like inclusions [7, 8]. In the general case of arbitrary orientations of the anisotropy axes, the symmetry axis of the stratified structure and the propagation directions, the analysis of the characteristics of EMW propagation in bianisotropic chiral media is an important but rather complicated problem. Today, a number of particular problems of electrodynamics of bianisotropic and chiral media has been solved. The studies in this field are progressing rapidly [9–12].

Below, the propagation of electromagnetic waves in chiral structures is described by the method of 4×4 matrices, which is efficient for any kind of anisotropy and number of layers. Vanous modifications of this method are used to describe the EMW propagation in media with the anisotropy of different nature, in particular, in dielectric, magnetic and liquid–crystal structures [13, 14]. In the majority of publications, the authors restricted themselves to the consideration of particular cases of chirality and the simplest stratified structures. Below, such cases are considered as particular cases of the general method. In these cases the parameters of the reflected and the transmitted EMWs (intensity, polarization azimuth, and ellipticity) are determined.

4 × 4 PERMITTIVITY MATRIX

Consider a medium composed of anisotropic chiral layers parallel to the *XY*-plane, with the *Z*-axis coinciding with the symmetry axis of the structure. Let a plane monochromatic EMW with the wave vector **k**, parallel to *XZ*-plane propagate in this medium. Then, the electric and the magnetic fields of the wave, **E**, **D**, **H**, and **B**, are proportional to $\exp[i(\omega t - k_x x)]$, and the Maxwell equations have the form

$$\nabla \mathbf{E} = -ik_0 \mathbf{B}, \quad \nabla \mathbf{H} - ik_0 \mathbf{D}, \tag{1}$$

where $\nabla = \left(-ik_x, 0, \frac{\partial}{\partial z}\right)$, $k_0 = \omega/c$, ω is frequency, and *c* is the velocity of light in vacuum. To describe the bianisotropic chiral medium in the general form, we write the material equations as [15]:

$$\mathbf{D} = \hat{\varepsilon}\mathbf{E} - \hat{\alpha}\mathbf{H}, \quad \mathbf{B} = \hat{\mu}\mathbf{H} + \hat{\beta}\mathbf{E}. \tag{2}$$

The above equations include four tensors—those of dielectric $\hat{\varepsilon}$, magnetic $\hat{\mu}$, and magnetooptical $\hat{\alpha}$ and $\hat{\beta}$ permittivities, which relate the strengths of the electric and magnetic fields with the electric and magnetic inductions. Substituting (2) into (1), we arrive at the following system of equations:

$$\begin{aligned} E_y' &= ik_0(\hat{\mu}\mathbf{H} + \hat{\beta}\mathbf{E})_x, \quad H_y' = -ik_0(\hat{\varepsilon}\mathbf{E} + \hat{\alpha}\mathbf{H})_x, \\ E_x' &= -ik_0[(\hat{\mu}\mathbf{H} + \hat{\beta}\mathbf{E})_y + n_x E_z], \\ H_x' &= ik_0[(\hat{\varepsilon}\mathbf{E} + \hat{\alpha}\mathbf{H})_y - n_x H_z], \end{aligned} \tag{3}$$

1063-7745/00/4503-0487$20.00 © 2000 MAIK "Nauka/Interperiodica"

$$n_x E_y = (\hat{\mu}\mathbf{H} + \hat{\beta}\mathbf{E})_z, \quad n_x H_y = -(\hat{\varepsilon}\mathbf{E} + \hat{\alpha}\mathbf{H})_z,$$

where prime denotes differentiation with respect to z and $n_x = k_x/k_0$. Excluding the field components E_z and H_z parallel to the structure axis and introducing the vector $\mathbf{g} = (E_x, -E_y, H_x, H_y)$, having four tangential field components, we can represent the system (3) of the wave equations for planar layered medium in terms of the following differential matrix equation:

$$\mathbf{g}' = -ik_0\hat{G}\mathbf{g}, \tag{4}$$

where, the matrix $\hat{G}$ of the dimension 4×4 is determined by the local properties of the medium, i.e., has the same form in both homogeneous and inhomogeneous media and contains no differential operators. It is constructed using four permittivity tensors and allows the most general consideration of bianisotropic and chiral properties of the medium. In order to write the $\hat{G}$ matrix in the most concise form, introduce the following notation:

$$\mathscr{E}_{ij} = \begin{vmatrix} \varepsilon_{ij} & \varepsilon_{iz} & \alpha_{iz} \\ \varepsilon_{zj} & \varepsilon_{zz} & \alpha_{zz} \\ \beta_{zj} & \beta_{zz} & \mu_{zz} \end{vmatrix}, \quad \mathscr{M}_{ij} = \begin{vmatrix} \mu_{ij} & \beta_{iz} & \mu_{iz} \\ \alpha_{zj} & \varepsilon_{zz} & \alpha_{zz} \\ \mu_{zj} & \beta_{zz} & \mu_{zz} \end{vmatrix},$$

$$\mathscr{A}_{ij} = \begin{vmatrix} \alpha_{ij} & \varepsilon_{iz} & \alpha_{iz} \\ \alpha_{zj} & \varepsilon_{zz} & \alpha_{zz} \\ \mu_{zj} & \beta_{zz} & \mu_{zz} \end{vmatrix}, \quad \mathscr{B}_{ij} = \begin{vmatrix} \beta_{ij} & \beta_{iz} & \mu_{iz} \\ \varepsilon_{zj} & \varepsilon_{zz} & \alpha_{zz} \\ \beta_{zj} & \beta_{zz} & \mu_{zz} \end{vmatrix},$$

$$e_{ij} = \begin{vmatrix} \varepsilon_{ij} & \alpha_{iz} \\ \beta_{zj} & \mu_{zz} \end{vmatrix}, \quad m_{ij} = \begin{vmatrix} \mu_{ij} & \beta_{iz} \\ \alpha_{zj} & \varepsilon_{zz} \end{vmatrix}, \quad d = \begin{vmatrix} \varepsilon_{zz} & \alpha_{zz} \\ \beta_{zz} & \mu_{zz} \end{vmatrix},$$

$$a_{iz} = \begin{vmatrix} \alpha_{iz} & \varepsilon_{iz} \\ \alpha_{zz} & \varepsilon_{zz} \end{vmatrix}, \quad a_{zj} = \begin{vmatrix} \alpha_{zj} & \alpha_{zz} \\ \mu_{zj} & \mu_{zz} \end{vmatrix},$$

$$b_{iz} = \begin{vmatrix} \beta_{iz} & \mu_{iz} \\ \beta_{zz} & \mu_{zz} \end{vmatrix}, \quad b_{zj} = \begin{vmatrix} \beta_{zj} & \beta_{zz} \\ \varepsilon_{zj} & \varepsilon_{zz} \end{vmatrix},$$

where $i, j = x, y$, and $|A|$ is the determinant of the matrix A. Now, the matrix $\hat{G}$ can be represented as a sum of three terms proportional to different powers of n_x:

$$\hat{G} = \frac{1}{d}\begin{pmatrix} \mathscr{B}_{yx} & -\mathscr{B}_{yy} & \mathscr{M}_{yx} & \mathscr{M}_{yy} \\ \mathscr{B}_{xx} & -\mathscr{B}_{xy} & \mathscr{M}_{xx} & \mathscr{M}_{xy} \\ -\mathscr{E}_{yx} & \mathscr{E}_{yy} & -\mathscr{A}_{yx} & -\mathscr{A}_{yy} \\ \mathscr{E}_{xx} & -\mathscr{E}_{xy} & \mathscr{A}_{xx} & \mathscr{A}_{xy} \end{pmatrix}$$

$$+ \frac{n_x^2}{d}\begin{pmatrix} 0 & \alpha_{zz} & 0 & -\mu_{zz} \\ 0 & 0 & 0 & 0 \\ 0 & -\varepsilon_{zz} & 0 & \beta_{zz} \\ 0 & 0 & 0 & 0 \end{pmatrix} \tag{5}$$

$$- \frac{n_x}{d}\begin{pmatrix} e_{zx} & m_{yz} - e_{zy} & a_{zx} & a_{zy} + b_{yz} \\ 0 & m_{xz} & 0 & b_{xz} \\ b_{zx} - a_{yz} - b_{zy} & m_{zx} & m_{zy} - e_{yz} & \\ 0 & a_{xz} & 0 & e_{xz} \end{pmatrix}.$$

For a homogeneous medium, $\hat{G}$ is independent of the z-coordinate, and the solution of matrix equation (4) is the superposition of the eigenwaves

$$\mathbf{g} = \sum a_j \mathbf{g}_j \exp(-ik_{zj}z), \quad j = 1, \ldots, 4, \tag{6}$$

where a_j are waves amplitudes corresponding to the eigenvectors $\mathbf{g}_j$ of the $\hat{G}$ matrix. The eigenvalues $n_{zj} = k_{zj}/k_0$ of this matrix are the roots of the dispersion equation

$$\det(\hat{G} - n_z\hat{I}) = 0, \tag{7}$$

where $\hat{I}$ is the unit matrix. In general case, it follows from (6) and (7) that there are four eigenvalues with different polarizations, propagation directions, and refractive indices $n_j = \sqrt{n_x^2 + n_{zj}^2}$ quartic in n_{zj} and defined by equation (7).

If the medium is homogeneous along the z-axis, the study of EMW propagation is reduced to the solution of the boundary–value problem: the medium is divided into thin layers, whose boundaries lie in the XY plane and the material parameters are constant within each layer.

PLANAR LAYERED STRUCTURE

Consider EMW propagation in a planar layered medium. The tangential components of the electric- and magnetic-fields strengths or, which is equivalent, the four-component vector $\mathbf{g}$, should be continuous across the boundaries of the adjacent layers. Let the superposition of the eigenwaves with the amplitudes $a_j^{(n)}$ be incident onto the boundary between the nth and $(n + 1)$th layers. For the wave entering the $(n + 1)$th layer, the amplitudes obtained from the continuity conditions for the $\mathbf{g}$ vector components at the boundary are determined by the matrix equation:

$$a_i^{(n+1)} = M_{ij}^{(n)} a_j^{(n)}, \tag{8}$$

where the elements of propagation matrix $\hat{M}^{(n)}$ at the nth boundary have the form

$$M_{ij}^{(n)} = \tilde{\mathbf{g}}_i^{(n+1)}\mathbf{g}_j^{(n)}. \quad (9)$$

Here, $\tilde{\mathbf{g}}_i^{(n)}$ are the vectors complementary to $\mathbf{g}_j^{(n)}$, i.e., the vectors satisfying the condition $\tilde{\mathbf{g}}_i^{(n)}\mathbf{g}_j^{(n)} = \delta_{ij}$. The EMW propagation through the homogeneous nth layer, with no account for the boundary, is described by the diagonal $\hat{T}^{(n)}$ matrix with the elements

$$T_{ij}^{(n)} = \delta_{ij}\exp(-ik_{zj}^{(n)}l_n), \quad (10)$$

where l_n is the thickness of the nth layer. For the system consisting of p layers, the resultant propagation matrix is the product of the propagation matrices for particular boundaries and layers

$$\hat{M} = (\hat{M}^{(p)}\hat{T}^{(p)})(\hat{M}^{(p-1)}\hat{T}^{(p-1)})\ldots(\hat{M}^{(1)}\hat{T}^{(1)})\hat{M}^{(0)}. \quad (11)$$

The amplitude of the transmitted wave is given by

$$\mathbf{a}^{(p)} = \hat{M}\mathbf{a}^{(0)}. \quad (12)$$

Let us mark the eigenwaves propagating in the forward direction with subscripts 1 and 2 ($n_z > 0$), and those propagating in the backward direction, with 3 and 4 ($n_z < 0$). The waves with subscripts 1, 3 and those with subscripts 2, 4 have the same polarization. Now, introduce the matrix $\hat{N} = \hat{M}^{-1}$ inverse with respect to $\hat{M}$ and write down the corresponding elements of reflection and transmission matrices of the layered structure:

$$\begin{aligned}
r_{11} &= \left.\frac{a_3^{(0)}}{a_1^{(0)}}\right|_{a_2^{(0)}=0} = \frac{L_{31}^{22}}{L_{11}^{22}}, \quad r_{12} = \left.\frac{a_4^{(0)}}{a_1^{(0)}}\right|_{a_2^{(0)}=0} = \frac{L_{41}^{22}}{L_{11}^{22}},\\
r_{21} &= \left.\frac{a_3^{(0)}}{a_2^{(0)}}\right|_{a_1^{(0)}=0} = \frac{L_{32}^{11}}{L_{11}^{22}}, \quad r_{22} = \left.\frac{a_4^{(0)}}{a_2^{(0)}}\right|_{a_1^{(0)}=0} = \frac{L_{42}^{11}}{L_{11}^{22}},\\
t_{11} &= \left.\frac{a_3^{(p)}}{a_1^{(0)}}\right|_{a_2^{(0)}=0} = \frac{N_{22}}{L_{11}^{22}}, \quad t_{12} = \left.\frac{a_4^{(p)}}{a_1^{(0)}}\right|_{a_2^{(0)}=0} = \frac{N_{21}}{L_{11}^{22}},\\
t_{21} &= \left.\frac{a_3^{(p)}}{a_2^{(0)}}\right|_{a_1^{(0)}=0} = -\frac{N_{12}}{L_{11}^{22}}, \quad t_{22} = \left.\frac{a_4^{(p)}}{a_2^{(0)}}\right|_{a_1^{(0)}=0} = \frac{N_{11}}{L_{11}^{22}}.
\end{aligned} \quad (13)$$

Above, we used the notation $L_{ij}^{kl} = N_{ij}N_{kl} - N_{il}N_{kj}$.

In semi-infinite media, labelled with subscripts "0" and "p," separated by the layered structure, the vectors $\mathbf{g}_j$ are normalized in such a way that the energy fluxes corresponding to each wave are equal (e.g., $|\mathbf{S}_j| = |\mathbf{E}_j \times \mathbf{H}_j^* + \mathbf{E}_j^* \times \mathbf{H}_j| = 1$). Then the quantities $|r|^2 = |r_{j1}|^2 + |r_{j2}|^2$ and $|t|^2 = |t_{j1}|^2 + |t_{j2}|^2$ determine the ratios of energy fluxes of the reflected and the transmitted waves to that of the incident wave. Other types of normalization are also possible, e.g., such that r and t would be the ratios of the amplitudes of the corresponding fields. In intermediate layers, normalization is not necessary, because no determination of the eigenwave amplitudes is required.

The method under consideration is a unified approach to the problem of EMW propagation in planar layered structures. It allows the consideration of various problems of electro- and magnetooptics, including the optics of bianisotropic and chiral media.

APPLICATION OF THE METHOD TO SIMPLEST CHIRAL STRUCTURES

1. Bianisotropic medium. For an isotropic medium, $\hat{\varepsilon}$, $\hat{\mu}$, $\hat{\alpha}$, and $\hat{\beta}$ are the diagonal tensors of the type $\varepsilon_{ij} = \varepsilon\delta_{ij}$, so that the $\hat{G}$ matrix acquires the simple form

$$\hat{G} = \begin{pmatrix} 0 & s\alpha-\beta & 0 & \mu(1-s) \\ \beta & 0 & \mu & 0 \\ 0 & \varepsilon(1-s) & 0 & s\beta-\alpha \\ \varepsilon & 0 & \alpha & 0 \end{pmatrix}, \quad s = \frac{n_x^2}{\varepsilon\mu-\alpha\beta}. \quad (14)$$

Then, the solution of dispersion equation (7) yields the following eigenvalues of the $\hat{G}$ matrix:

$$\begin{aligned} n_z^{\pm} = \Big[&\varepsilon\mu(1-s) + \frac{1}{2}[\alpha(s\beta-\alpha) + \beta(s\alpha-\beta)] \\ &\pm i(\alpha-\beta)\sqrt{\varepsilon\mu - (\alpha+\beta)^2/4}\Big]^{1/2}. \end{aligned} \quad (15)$$

Using the expressions for $n_z^{\pm}$, we can determine the refractive indices of the eigenwaves as:

$$n_{\pm} = \sqrt{\varepsilon\mu - (\alpha+\beta)^2/4} \pm i(\alpha-\beta)/2. \quad (16)$$

The eigenvalues of the $\hat{G}$ matrix, determined from the equation $(\hat{G} - n_z\hat{I})\mathbf{g}^{(c)} = 0$, have the following components:

$$\begin{aligned} &\mathbf{g}^{(c)} \\ &= (n_z^{\pm}(n_{\pm} \mp i\alpha), \pm i\varepsilon\mu + \beta(n_{\pm} \mp i\alpha), \pm i\varepsilon n_z^{\pm}, \varepsilon n_{\pm}). \end{aligned} \quad (17)$$

The above vectors specify the eigenwaves of the biisotropic medium, which are the left-hand (upper signs) or right-hand (lower signs) polarized waves propagating in the forward ($n_z^{\pm} > 0$) or the backward ($n_z^{\pm} < 0$) directions.

Introducing the parameters of nonreciprocity $\chi = (\alpha+\beta)/2$ and chirality $\kappa = i(\alpha-\beta)/2$ instead of magnetoelectric permittivities, we obtain the refractive indices for the eigenwaves in the medium in the form: $n_{\pm} = \sqrt{\varepsilon\mu - \chi^2} \pm \kappa$. With due regard of complexity of

the introduced parameters ($\chi = \chi' + i\chi''$, $\kappa = \kappa' + i\kappa''$), the above relations lead to two general types of biisotropic non-absorbing media. For such media, the imaginary part of the chirality parameter is zero, while either imaginary or real part of the nonreciprocity parameter has nonzero value. The dependence of the refractive indices of eigenwaves on nonreciprocity for two types of media is quite different. For the first type ($\chi'' = 0$) the refracting index monotonically decreases; for the second type ($\chi' = 0$), the value of $n_\pm$ monotonically increases.

2. Reflection from the dielectric–chiral medium interface. Let a wave from dielectric with material parameters ε_0, μ_0 be incident onto the plane interface with a semi-infinite chiral medium. For an isotropic dielectric, all the waves irrespectively of their polarization are eigenwaves; therefore, we may resolve the field into the *p*- and *s*-polarized waves, for which the vector **g** has the components

$$\mathbf{g}_p^{(0)} = (\pm\sigma_0, 0, 0, \eta_0), \quad \mathbf{g}_s^{(0)} = (0, 1, \pm\eta_0\sigma_0, 0),$$

where $\sigma_0 = \sqrt{1 - n_x^2/\varepsilon_0\mu_0}$, $\eta_0 = \sqrt{\varepsilon_0/\mu_0}$, and the signs "±" correspond to two opposite directions of wave propagation. According to (9), the propagation matrix $M_{ij}^{(0)}$ at the boundary between the media can be written as $M_n^{(0)} = \tilde{\mathbf{g}}_i^{(c)}\mathbf{g}_j^{(0)}$, then the $N_{ij} = \tilde{\mathbf{g}}_i^{(0)}\mathbf{g}_j^{(c)}$ matrix has the form

$$\hat{N} = \begin{pmatrix} \eta_0 & 0 & 0 & \sigma_0 \\ 0 & \eta_0\sigma_0 & 1 & 0 \\ -\eta_0 & 0 & 0 & \sigma_0 \\ 0 & \eta_0\sigma_0 & -1 & 0 \end{pmatrix} \times \begin{pmatrix} n_z^+(n_+ - i\alpha) & n_z^-(n_- + i\alpha) & -n_z^+(n_+ - i\alpha) & -n_z^-(n_- + i\alpha) \\ i\varepsilon\mu + \beta(n_+ - i\alpha) & -i\varepsilon\mu + \beta(n_- + i\alpha) & i\varepsilon\mu + \beta(n_+ - i\alpha) & -i\varepsilon\mu + \beta(n_- + i\alpha) \\ i\varepsilon n_z^+ & -i\varepsilon n_z^- & -i\varepsilon n_z^+ & i\varepsilon n_z^- \\ \varepsilon n_+ & \varepsilon n_- & \varepsilon n_+ & \varepsilon n_- \end{pmatrix}. \tag{18}$$

Using of (13) and (18), one may find the coefficients of the EMW reflection from the interface between the dielectric and chiral media. For normal incidence, these coefficients for the *s*- and *p*-polarized waves are

$$r_{pp} = -r_{ss} = \frac{\eta^2 - \eta_0^2}{\eta^2 + \eta_0^2 + 2\eta\eta_0\gamma}, \qquad r_{ps} = r_{sp} = \frac{2\chi\eta\eta_0/\sqrt{\varepsilon\mu}}{\eta^2 + \eta_0^2 + 2\eta\eta_0\gamma}, \tag{19}$$

where $\gamma = \sqrt{1 - \chi^2/\varepsilon\mu}$ an $\eta = \sqrt{\varepsilon/\mu}$. Thus, the characteristics of reflected wave are independent of the medium chirality specified by the parameter κ but are essentially dependent on the nonreciprocity parameter χ. The polarization characteristics of the reflected wave, i.e., polarization azimuth θ_r and ellipticity angle E_r, are obtained from the relationship

$$\tan(\theta_r - iE_r) = \frac{r_{ps}}{r_{pp}} = \frac{2\chi\eta\eta_0/\sqrt{\varepsilon\mu}}{\eta^2 - \eta_0^2}. \tag{20}$$

At low values of the nonreciprocity parameter ($|\chi| \ll 1$), they have the form

$$\theta_r = \frac{2\chi'\sqrt{\varepsilon_0\mu_0}}{\varepsilon\mu_0 - \varepsilon_0\mu}, \quad E_r = \frac{2\chi''\sqrt{\varepsilon_0\mu_0}}{\varepsilon\mu_0 - \varepsilon_0\mu}. \tag{21}$$

For a non-absorbing chiral medium, either the rotation of the polarization plane (the medium of the first type) or the ellipticity (the medium of the second type) of the reflected radiation can take place.

For an oblique EMW incidence onto the interface between two media, we obtain in the first approximation in small parameters κ and χ:

$$r_{pp} = \frac{\eta\sigma_0 - \eta_0\sigma}{\eta\sigma_0 + \eta_0\sigma},$$

$$r_{ps} = \frac{2\eta\eta_0\sigma_0(\chi\sigma^2 + i\kappa(\sigma^2 - 1))}{\sigma\sqrt{\varepsilon\mu}(\eta_0\sigma_0 + \eta\sigma)(\eta\sigma_0 + \eta_0\sigma)}, \tag{22}$$

$$r_{sp} = \frac{2\eta\eta_0\sigma_0(\chi\sigma^2 - i\kappa(\sigma^2 - 1))}{\sigma\sqrt{\varepsilon\mu}(\eta_0\sigma_0 + \eta\sigma)(\eta\sigma_0 + \eta_0\sigma)},$$

$$r_{ss} = \frac{\eta_0\sigma_0 - \eta\sigma}{\eta_0\sigma_0 + \eta\sigma},$$

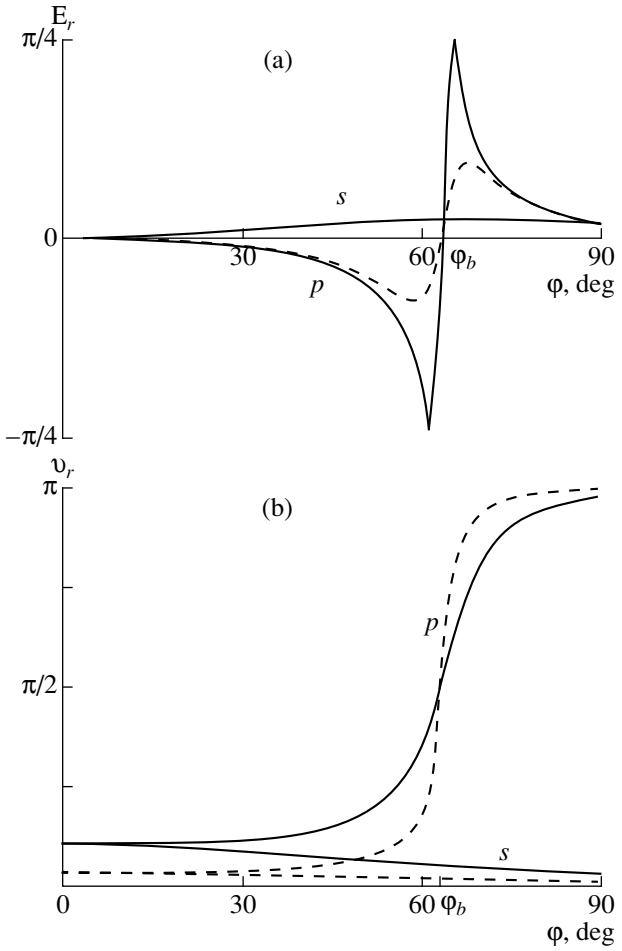

Fig. 1. (a) Ellipticity angle E_r and (b) polarization azimuth θ_r as functions of the incidence angle φ of *p*- and *s*-polarized reflected wave: (a) $\kappa = 0.1$, $\chi = 0$ (solid curve), $\chi = 0.04$ (dashed curve); (b) $\kappa = 0$, $\chi = 0.06$ (solid curve), $\chi = 0.02$ (dashed curve).

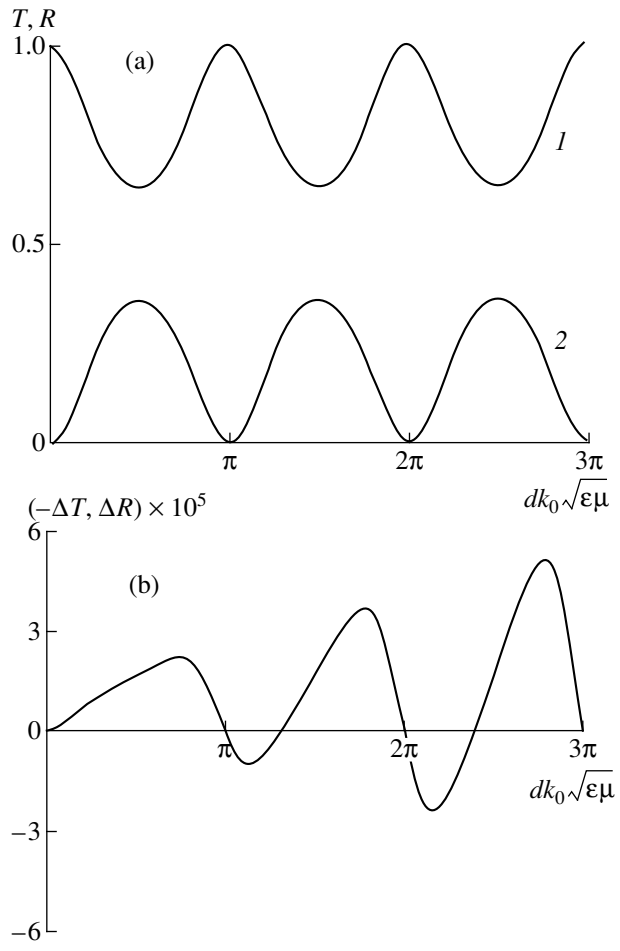

Fig. 2. Power transmittance *T* (a, curve *1*) and reflectance *R* (a, curve *2*) versus chiral layer thickness at $\chi = 0.01$ and (b) their variations, ΔT and ΔR, with respect to the dielectric layer with the same permittivities and $\chi = 0$.

where $\sigma = \sqrt{1 - s}$. In this approximation, r_{pp} and r_{ss} are of the standard form, i.e. coincide with the well-known expressions for reflection of an electromagnetic wave from the interface between two dielectrics. The polarization characteristics of the reflected wave depend on both nonreciprocity and chirality of biisotropic medium. Figure 1a shows the ellipticity and Fig. 1b the polarization azimuth of the reflected wave as a function of the angle of incidence φ at the interface between the dielectric and chiral media with $\varepsilon = 4$ and $\mu = 1$. The curves are obtained at various values of the nonreciprocity and chirality parameters. The dependence $E_r(\varphi)$ is plotted for the medium with chirality $\kappa = 0.1$ and nonreciprocity $\chi = 0$ (solid curve) and $\chi = 0.04$ (dashed curve). The dependence $E_r(\varphi)$ is plotted for the medium with chirality $\kappa = 0$ and $\chi = 0.06$ (solid curve) and $\xi = 0.02$ (dashed curve). If the incident wave is *s*-polarized, the polarization characteristics of the reflected wave are almost independent of the incidence angle. For a *p*-polarized incident wave, the changes in θ_r and E_r are most pronounced near the angle φ close to the Brewster angle φ_b. At $\varphi = \varphi_b$, the reflected *p*-wave is linearly polarized with the polarization plane being rotated by angle of $\pi/2$ with respect to that of the incident wave. On departure of φ from φ_b-value the ellipticity angle first rapidly increases (at $\chi = 0$ it reaches the value $\pi/4$, i.e., the wave becomes circularly polarized) and then gradually decreases and becomes almost zero, at the normal and the grazing incidence. When the incidence angle φ attains the value of the Brewster angle, the polarization plane of the reflected *p*-wave is rotated by an angle close to 180°. This rotation occurs the slower, the higher the nonreciprocity of the medium.

Typical values of the chirality parameter κ normalized to the refractive index $\sqrt{\varepsilon\mu}$ for natural and synthesized biisotropic media range from 0.05 to 0.3. The nonreciprocity effect observed in Cr_2O_3 natural crystals is much weaker, the corresponding parameter for these crystals is also lower, $\chi \approx 10^{-5}$ [16]. For a clearer repre-

sentation of the nonreciprocity effects, we use higher values of this parameter.

3. Chiral layer in dielectric. To find the reflectance and transmittance of an EMW in a layer of thickness d in a dielectric with the material parameters ε_0 and μ_0, we represent the resultant propagation matrix (11) as the product of transmission matrices for the first interface, layer, and second interface:

$$\hat{M} = \hat{M}_0^{-1}\hat{T}\hat{M}_0, \quad T_{ij} = \delta_{ij}\exp(-ik_0 n_{zj} d). \qquad (23)$$

Using this relationship and formula (13), we can obtain the expressions for amplitude coefficients of reflection and transmission for an EMW normally incident onto the layer:

$$\begin{aligned} t_{pp} &= t_{ss} = (2/D)\eta\eta_0\gamma\cos(\kappa k_0 d), \\ t_{ps} &= -t_{sp} = (2/D)\eta\eta_0\gamma\sin(\kappa k_0 d), \\ r_{pp} &= -r_{ss} = (1/D)i(\eta^2 - \eta_0^2)\sin(dk_0\gamma\sqrt{\varepsilon\mu}), \\ r_{ps} &= r_{sp} = (1/D)2i\eta\eta_0\frac{\chi}{\sqrt{\varepsilon\mu}}\sin(dk_0\gamma\sqrt{\varepsilon\mu}), \end{aligned} \qquad (24)$$

$$\begin{aligned} D &= 2\eta\eta_0\gamma\cos(dk_0\gamma\sqrt{\varepsilon\mu}) \\ &+ i(\eta^2 + \eta_0^2)\sin(dk_0\gamma\sqrt{\varepsilon\mu}). \end{aligned}$$

In this case, the ratio r_{ps}/r_{pp}, determining the polarization characteristics of the reflected wave, coincides with the analogous expression (20) for the interface between two semi-insinite media. Polarization characteristics of the transmitted wave linearly depend on the layer thickness and are determined by the chirality parameter, namely, $\theta_t - i\mathrm{E}_t = \kappa k_0 d$. For non-absorbing medium ($\kappa'' = 0$), the transmitted wave shows only the rotation of the polarization plane by the angle $\theta_t = \kappa' k_0 d$. Figure 2 presents dependences of the transmittance $T = |t_{pp}|^2 + |t_{ps}|^2$ and reflectance $R = |r_{pp}|^2 + |r_{ps}|^2$ on the layer thickness (Fig. 1a), and also their variations $\Delta T = T(\chi) - T(0)$ and $\Delta R = R(\chi) - R(0)$ (Fig. 1b) due to medium nonreciprocity. For a non-absorbing medium, the total energy of the reflected and transmitted waves is conserved, with ΔT being equal to $-\Delta R$.

CONCLUSIONS

The above solutions and their analysis demonstrate the efficiency and versatility of the method based on the reduction of the Maxwell equations for plane EMW propagating in a layered bianisotropic medium, to the matrix first-order differential equation for a four-component vector, with the tangential field components. The method proposed can be used for determining the intensity and polarization characteristics of transmitted and reflected EMWs for continuous inhomogeneous chiral structures and structures with an arbitrary number of uniform layers.

REFERENCES

1. I. V. Lindell, A. H. Sihvala, S. A. Tretyakov, and A. J. Vitanen, *Electromagnetic Waves in Chiral and Bi-isotropic Media* (Artech House, London, 1994).
2. T. Guire, V. K. Varadan, and V. V. Varadan, IEEE Trans. Electromagn. Compat. **32** (4), 300 (1990).
3. R. Ro, V. K. Varadan, and V. V. Varadan, IEE Proc., Part H: Microwaves, Antennas Propag. **139** (5), 441 (1992).
4. F. I. Fedorov, *Theory of Gyrotropy* (Nauka i Tekhnika, Minsk, 1976).
5. V. A. Belyakov, *Diffraction Optics of Periodic Media of Complicated Structure* (Nauka, Moscow, 1988).
6. L. M. Blinov and V. G. Chigrinov, *Electrooptic Effects in Liquid Crystal Materials* (Springer, New York, 1996).
7. M. M. I. Saadoun and N. Engheta, Microwave Opt. Technol. Lett. **5** (4) 184 (1992).
8. L. R. Arnaut and L. E. Davis, in *Proceedings of ICEAA* (Turin, Italy, 1995), p. 381.
9. S. B. Borisov, N. N. Dadoenkova, and N. L. Lyubchanskiĭ, Opt. Spektrosk. **74** (6), 1127 (1993) [Opt. Spectrosc. **74** (6), 670 (1993)].
10. M. P. Silverman and J. Badoz, J. Opt. Soc. Am. A **7**, 1163 (1990).
11. M. P. Silverman and J. Badoz, J. Opt. Soc. Am. A **11**, 1894 (1994).
12. O. V. Ivanov and D. I. Sementsov, Kristallografiya **41** (5), 791 (1996) [Crystallogr. Rep. **41** (5), 749 (1996)].
13. V. V. Zheleznyakov, V. V. Kocharovskiĭ, and V. V. Kocharovskiĭ, Usp. Fiz. Nauk **141** (2), 257 (1983) [Sov. Phys. Usp. **26** (10), 877 (1983)].
14. C. Oldano, P. Allia, and L. Trossi, J. Phys. (France) **46**, 573 (1985).
15. A. J. Kong, *Electromagnetic Wave Theory* (Wiley, New York, 1986).
16. S. A. Tret'yakov, Radiotekh. Élektron. (Moscow) **39**, 1457 (1994).

Translated by A. Zolot'ko

Crystallography Reports, Vol. 45, No. 3, 2000, pp. 493–500. Translated from Kristallografiya, Vol. 45, No. 3, 2000, pp. 541–548.

LIQUID CRYSTALS

Lyotropic Nematogenic System Potassium Laurate–1-Decanol–Water: Method of Synthesis and Study of Phase Diagrams

V. V. Berejnov*,, V. Cabuil**, R. Perzynski***, Yu. L. Raikher*, S. N. Lysenko****, and V. N. Sdobnov*****

** Institute of Mechanics of Continuous Media, Ural Division, Russian Academy of Sciences, Perm, 614013 Russia*

*** Laboratoire de Physicochimie Inorganique, Université Paris VI, France*

**** Laboratoire des Milieux Désordonnés et Hétérogène, Université Paris VI, France*

***** Institute of Technical Chemistry, Ural Division, Russian Academy of Sciences, Perm, 614013 Russia*

****** Perm State University, Perm, 614005 Russia*

Received March 2, 1999

Abstract—The results of the study of the potassium laurate–1-decanol–water lyotropic composition are presented. The procedure of preparation of micellar solutions provides the good reproducibility of the phase diagrams. The configurations of the domains of the liquid crystal order are constructed on the concentration plane at the constant temperature as well as the temperature sections (T, $C_{1\text{-decanol}}$) (at the constant ratio of potassium laurate to water) and (T, C_{water}) (at the constant ratio of potassium laurate to 1-decanol). The liquid-crystal phases observed are described. *© 2000 MAIK "Nauka/Interperiodica".*

INTRODUCTION

As is well known [1, 2], mesogenic systems, i.e., compounds that can form liquid crystal phases, are divided into two classes—thermotropic and lyotropic. The division reflects the fundamental distinctions, which can be traced even at the level of the elementary structural units. For thermotropics, such a unit is a molecule, whereas for lyotropics, it is an associate of molecules called a *micelle*. The complexity of the structural units makes a lyotropic a complex compound as a whole. Because of the relatively low energy of the shape-forming bonds, micelles are very sensitive to the composition and the external conditions (they change their shape and size).

To identify the systems of such type, de Gennes [3] even has purposely introduced the term *soft matter*. In turn, the Mesoscopic transformations occurring in soft matter, influence the symmetry of the implemented order [4], the macroscopic parameters of the material [5], etc.

The chemical aspect of the synthesis of a thermotropic liquid crystal reduces to the requirement to synthesize the material with a sufficiently high purity grade, whereas for the synthesis of lyotropic (micellar) systems, the composition of the mixture used is also a key factor, because the domain of liquid crystal order on the ternary phase diagram is rather small, whereas its position is sensitive to the effect of impurities. At present, a number of nematogenic lyotropic compositions are known [6]. They posses rather interesting properties, namely, the existence of several nematic-phase modifications [7], the occurrence of the second-order isotropic $\longleftrightarrow$ nematic transitions [8, 9], very low light scattering in the visible range, and the ability to keep dispersed particles in the composition [9, 10].

The present paper is devoted to the study of the nematogenic system potassium laurate (KL)–1-decanol–water. The choice of the composition was dictated by the fact that it is the most well known [6] phase and, at the same time, is far from being exhaustively studied. Moreover, the known experimental results [7, 11, 12] are inconsistent.

The article consists of sections three. First, the necessary requirements to chemical purity and the aggregate state of each component are formulated. The second section describes the method of the composition preparation and the studies of liquid-crystal states proper. We found the method for mixing the components that provides the synthesis of lyotropic solutions with well reproducible physicochemical properties. And finally, the phase diagrams constructed are discussed in Section 3.

1. PREPARATION OF LYOTROPIC KL–1-DECANOL–WATER SOLUTIONS

1.1. Potassium laurate. The main component of the composition, potassium laurate (KL), was synthesized from the following commercial products: (1) lauric acid, LA (*Fluka*) with M_r = 200.32 g/mol and the nom-

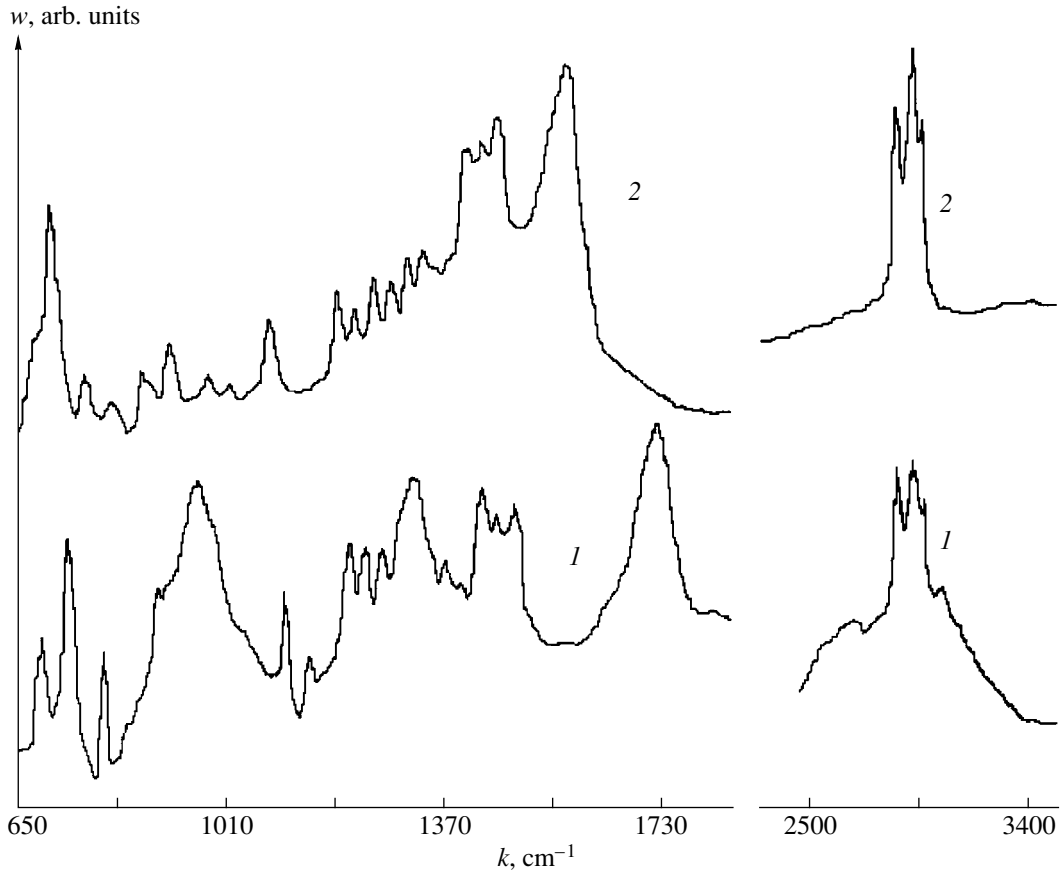

Fig. 1. IR spectra of (*1*) lauric acid and (*2*) KL in the crystalline state.

inal content of the main product not less than 99% and (2) potassium hydroxide (KOH) (*Prolabo*) with M_r = 56.11 g/mol and the nominal content of the main product not less than 86%. The total content of other alkali metals did not exceed 1%.

The lauric acid solution in a 50% water–alcohol medium was neutralized with the aqueous KOH solution (~9*M*) until the attainment of pH of 10.8–10.9. The dried product was a white crystalline substance.

The purity of potassium laurate was checked by recording IR spectra on a UR-20 spectrometer. The comparison of the LA and KL, absorption spectra (Fig. 1) shows that the main difference is caused by the absence of a hydrogen atom in a KL molecule. The carboxyl group of LA gives an intense peak due to nonsymmetric valence vibrations in the range 1650–1725 cm^{-1} [13]. The absorption spectrum of potassium laurate shows the shift of this maximum observed due to the appearance of a heavy potassium atom. Another essential difference in the spectra consists in disappearance of the bands due to deformation vibrations of the hydroxyl group in the ranges 850–960 and 1240–1300 cm^{-1} and the valence vibration band in the range 2500–3400 cm^{-1} [13–15]. Thus, the absence of hydroxyl bands in the spectrum can serve an indicator of the purity of potassium laurate from the lauric acid.

1.2. Components. The components for preparing the ternary system the components were water, 1-decanol, and an aqueous solution of potassium laurate. Water was purified by single distillation and had the pH ~ 6. The commercial chemical 1-decanol (*Fluka*) with M_r = 158.3 g/mol with the nominal content of the main product not less than 99%. The potassium laurate aqueous solution was prepared preliminary by dissolving crystalline KL in water at the temperature 80–100°C until the attainment of the concentration of ≥35 wt % and then was cooled down to 22°C. It should be emphasized that, unlike the previous studies [7, 8, 11, 12], we excluded the solid KL from the set of components used, because it is difficult to control *in situ* its complete dissolution.

1.3. Method of mixing. The components were always mixed at room temperature. To prepare a sample of the composition corresponding to the given point on the ternary phase diagram, the calculated component amounts (KL, 1-decanol, and water) were placed into the mixing vessel. Upon pouring each portion of water, the vessel was sealed and weighed with an accuracy of 10 μg on an electronic scale (*Mettler*). This pro-

vided a more accurate determination of the mixture composition than the use of the volume dosage of liquid components. The weighing procedure continued within 5–10 s. The mixing vessels were 9 ml-test tubes of the volume with tight silicone covers. The preparation in the tube occupied a volume not exceeding 3–4 ml.

Components were stirred for 60–100 min in the closed mixing vessels by a vibromixer at a frequency of 10–20 Hz. To remove the stable foam, the mixture in the mixing vessel was centrifuged for 1–3 min at the rotational velocity of 1000–2000 rev/min, which restored the solution homogeneity. The small amount of highly dispersed foam at the free surface did not hinder any further work.

The compounds obtained were used to study of the behavior of the phases in the ternary system KL–1-decanol–water at 20 ± 1°C. The results obtained are summarized in the phase diagram shown in Fig. 2.

The sections of the concentration phase diagram and its temperature sections (the concentration–temperature diagrams) were obtained as follows. First, the solution of the composition corresponding to the initial, point of the diagram was prepared. The mixing vessels were 50 ml glasses. They were filled up to 3/4 of their volumes, closed with screw Teflon tops, and the content was homogenized as described above.

The solution prepared was poured into 8 to 10 9 ml-test tubes, which were preliminarily carefully weighted. This procedure provided the identity of the starting material for all 8–10 points on the sections of the phase diagram to be studied. The filled tubes were weighted and an appropriate portion of the admixture–components was introduced, and the tube was weighted anew in order to determine the amount of admixture and to calculate the composition of the final mixture. Then, the material in tubes was homogenized by stirring and the subsequent centrifuging.

The addition of 1-decanol resulted in the formation of a number of mixtures with the constant water/KL ratio and various content of 1-decanol (Sections 1, 2, and 3 in Fig. 2). The addition of water resulted in the mixtures with the constant KL/1-decanol ration but variable water content (Section 4 in Fig. 2). Similar sets of solutions were also used to study the behavior of various phases as function of temperature.

Consider the lyotropic compositions obtained. The solutions formed in mixing vessels under the above conditions were homogeneous transparent liquids occupying the whole sample volume. Each of the observable phases existed for not less than six months. Upon five months, the samples showed no noticeable changes in the phase diagrams.

The laboratory practice of synthesizing KL and the final product, the lyotropic nematogenic composition, provided the formulation of the conditions necessary for obtaining the lyotropic nematics with reproducible phase diagrams. The content of unreacted lauric acid in

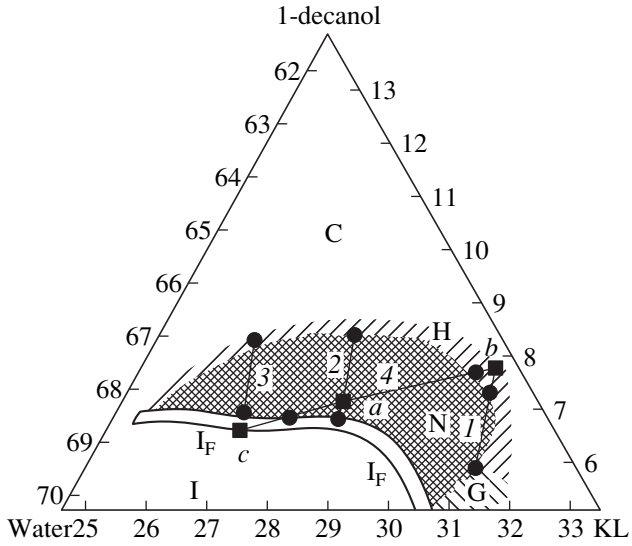

Fig. 2. KL–1-decanol–water concentration plane. (For notation see the text.) The hatched domain represents the phase N; the fluctuation zone I_F is represented by a light band along the boundary of the I ⟷ N transition. The slanted hatching indicates the phase H; the crossed lines, the region of phase G. The indicated plane for the phase space (*T*, PL, 1-decanol, and water) is the section at $T = 20 \pm 1$°C. Each of the segments *1–4* is the trace of the two-dimensional section, namely: (*1*) (T, $C_{1\text{-decanol}}$) at $C_{water}/C_{KL} = 2.08$, (*2*) 2.28, (*3*) 2.51, (*4*) (T, C_{water}) at $C_{KL}/C_{1\text{-decanol}} = 4.10$. Circles denote the boundaries of the domain of the nematic phase. Squares are the reference points: point *a* (28.4, 7.0, 64.6) is common for sections *2* and *4*, point *b* (30.6, 7.6, 61.8) is common for sections *1* and *4*, and point *c* (26.7, 6.6, 66.7) is common for sections *3* and *4*. The coordinates of the points correspond to the sequence KL, 1-decanol, water.

the KL should not exceed 1 wt %, the pH of the solutions obtained at the liquid crystal concentrations used (KL ~ 25–33 wt %) should the range within 10.4–10.8. The IR spectroscopy control should be used at all stages of the synthesis.

2. PHASE DIAGRAMS OF LYOTROPIC SOLUTIONS IN THE VICINITY OF THE NEMATIC DOMAIN

2.1. Equipment and materials. The lyotropic solution was poured out either into 1 ml-cylindrical glass test tubes closed with a polyethylene cover or into flat 0.1 mm-thick and 2.0 mm-wide capillaries (*Vitro Dynamic*) placed onto slides carefully sealed up with molten paraffin. Then, these preparations were coated with several layers of the transparent water-repellent varnish.

Each of the solution samples (corresponding to one point on the concentration diagram) consisted of three identical test tubes or 4–6 capillaries necessary for studying the conditionally reversible phase transformations (see Sect. 3.4). The phases were identified visually on a crystallographic polarizing microscope

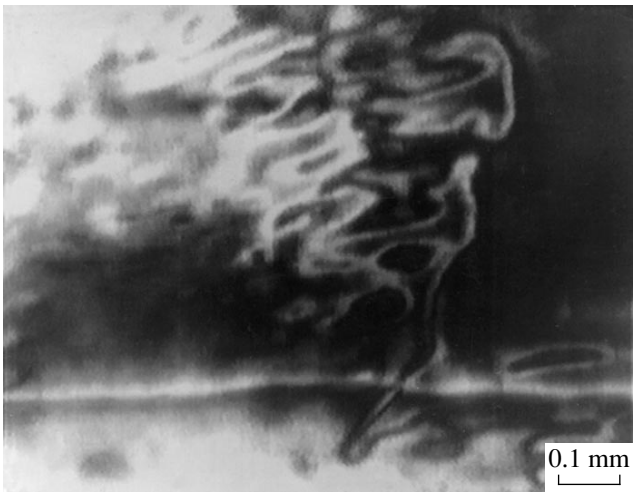

Fig. 3. Marble texture characterizing the nematic order. It is observed for all the solutions within the domain N on the phase diagram.

(POLAM R-11, LOMO) adjusted to observe the meniscuses in inclined tubes and determine the sign of the optical anisotropy [16]. The fast control the solutions was made in crossed polarizers.

2.2. Methods of phase observations. A number of tubes with preparations corresponding to a given concentration section were placed into a thermostat and were kept there for about 40 min until thermal equilibrium was reached. The preparation stop showing any visual changes, which indicated the attainment of the phase equilibrium. Each tube was taken out of the thermostat for about 1 min for the identification of the phase type in a microscope. A special device allowed the fixation of the test tube at an angle of 10°–25° to the direction of observation. A meniscus edge was located between the crossed polarizers, thus providing the configuration of a wedgelike layer with a free boundary which yields sufficient information for phase identification (the criterion of the phase identification is considered below). The meniscus of the isotropic phase was black. The nematic phase showed the characteristic texture typical of this state (Fig. 3). The meniscus in the state G-1 appears as the suspension of colored droplets against the background of isotropic medium (Fig. 4). The meniscus in the states H and C showed the smectic-like texture (Fig. 5).

The above phases and states could be also reliably identified visually in the polarized light. For the qualitative identification phase identification we used the polarization cell with crossed polaroids.

Special observations were performed to understand the effect of temperature variation on the phase organization of the solutions under study. For about one minute, no phase changes were recorded. This allows us to conclude that short abrupt changes in the thermal mode produce no effect on the phase state of the solution.

Some solutions were studied in the "classic" way as well [1, 2]. A flat capillary was filled with the preparation. Then the sign and the symmetry of the orientational order were determined by the conventional methods [16]. Being rather laborious, this procedure was employed only for a limited number of the samples, whose composition corresponded to the characteristic points of the phase diagram.

2.3. Phases and heterogeneous states of lyotropic solutions. The state of the solution is considered to be equilibrium, if it shows no apparent changes for a long period of time (several months). The phase diagram constructed from the data measured at 20°C is shown in Fig. 2. The lines, representing the domain boundaries

Fig. 4. Emulsion of flat liquid-crystal droplets in an isotropic medium which characterizes the G-1 state.

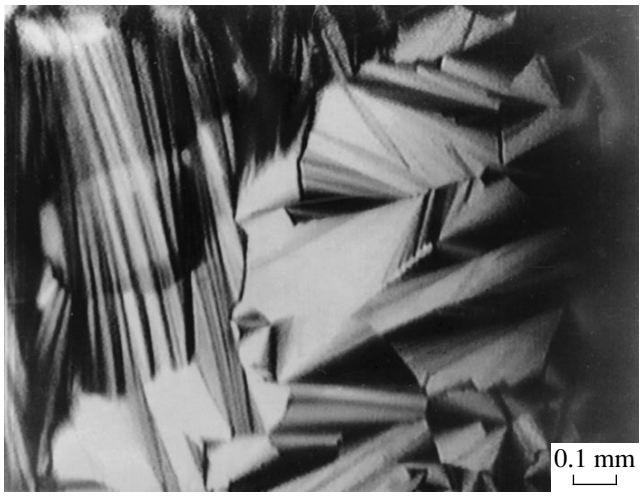

Fig. 5. Texture corresponding to the H domain (presumably, the hexagonal mesophase); on the phase diagrams, this zone is shown by slanted hatching.

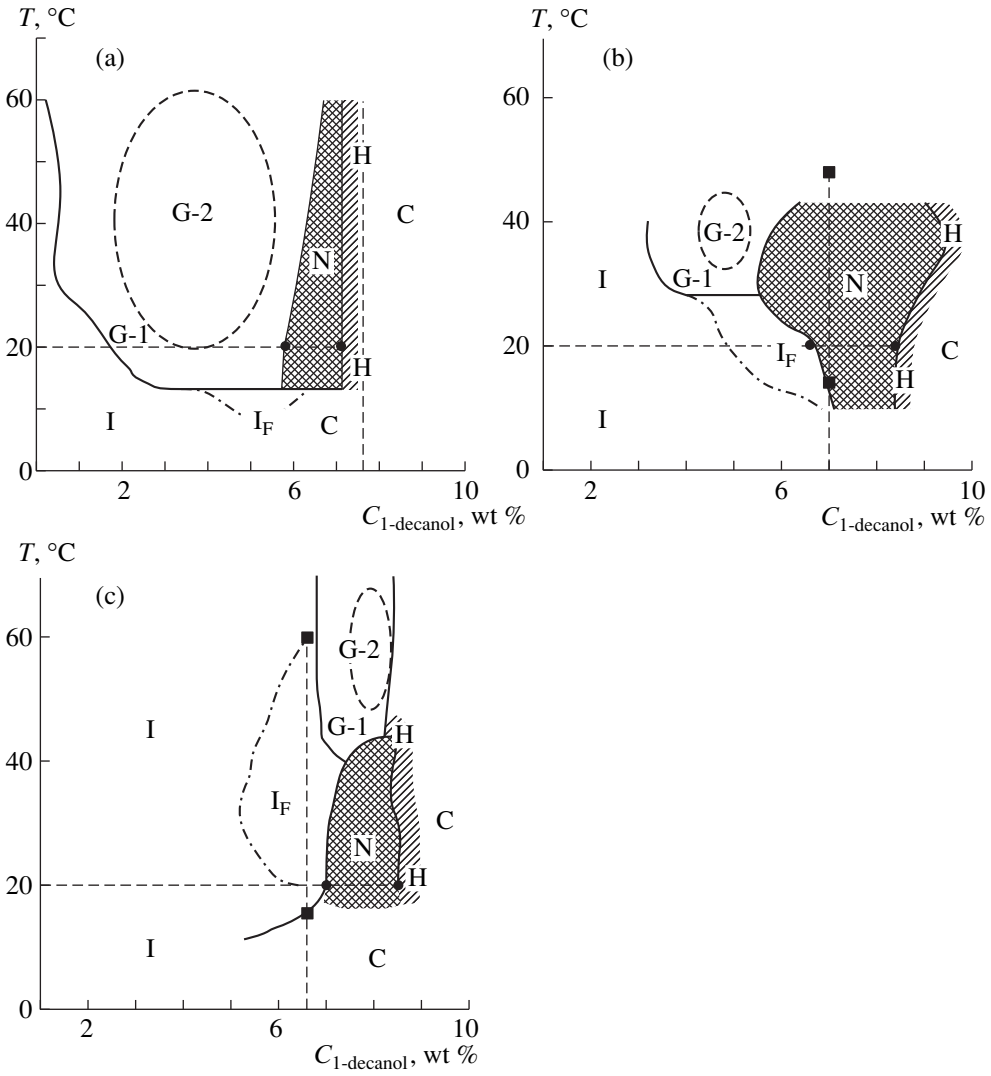

Fig. 6. Phase diagram in the coordinates (T, $C_{1\text{-decano}}$) for C_{water}/C_{KL} = 2.02 (a), 2.28 (b) and 2.51 (c). Notation see Fig. 2.

are drawn using the data analyzed for more than 300 samples. Figure 2 shows only eight of these points (black circles). Straight lines *1–4*, connecting the pairs of these points are the projections of the experimentally studied temperature sections of the phase diagram. The phase-diagram sections by the planes (T, $C_{1\text{-decanol}}$) and (T, C_{water}) are shown in Figs. 6 and 7, respectively.

The temperature–concentration region studied has five clearly seen states.

The isotropic phase (I) is located in the region of low concentrations <4 wt % of 1-decanol and <30 wt % of KL (T = 22°C). The solution consists of a transparent optically isotropic liquid, with the viscosity being of the same order of magnitude that the viscosity of water.

The nematic phase (N) is located in the domain having a complicated shape (Fig. 2) and, occupies mainly the regions with 5–8 wt % of decanol and 25–32 wt % of KL (T = 22°C). The solution is a transparent optically anisotropic liquid, with the viscosity of the order of magnitude the viscosity of glycerol. The solution in test tubes (thick samples) provides complete depolarization of light; whereas the solution in capillaries and meniscus edge (thin samples) exhibits the structure typical of nematics (Fig. 3). The measurements on oriented samples indicate the positive sign of the optical anisotropy and the uniaxial symmetry of the solution in the state of mechanical equilibrium (i.e., in the absence of hydrodynamic perturbations). The comparison of the defects observed with those known for lyotropic liquid crystals [6] showed that the textures formed in our system at 18–22°C correspond to a lyotropic nematic with the discotic structure-forming units. At the temperatures over the range 30–40°C, we also observed in some samples the formation of defects typical of the nematic calamitic structure.

The hexagonal state (H). The domain of the hexagonal state H (Fig. 2) is a narrow stripe above the domain

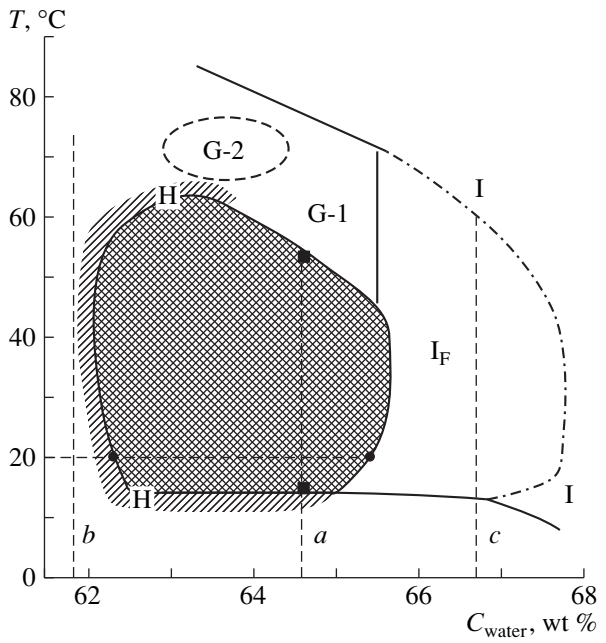

Fig. 7. Phase diagram in the (T, C_{water}) coordinates for $C_{KL}/C_{1\text{-decanol}} = 4.10$. For notation see Fig. 2.

of the nematic phase. The aggregate state resembles swollen soap showing no flowability. In a polarized light, thick layers have a white color. The liquid-crystal texture of the thin oriented layers (Fig. 5) is similar to that formed in hexagonal lyotropic phases [17]. The 1-decanol concentrations for such textures lie within a rather narrow (0.5%) range.

The gellike state (G). The domain of the gelike state is adjacent to those of the isotropic and the nematic states and also to those of the polycrystal and hexagonal structures. Near the boundary with the isotropic phase (denoted as G-1), the sample is a suspension of optically anisotropic droplets within the isotropic medium (Fig. 4). The droplets are anisometric they have mainly disklike shape and are characterized by concentric color rings in the polarized light. The extinction of the fringes in a polarizing microscope indicates the uniaxial optical anisotropy of the droplet substance. In the unpolarized light, thick layers of the G-1 emulsion are turbid. This inhomogeneous system is rather stable.

In the middle of the domain, there is the state denoted on the phase diagrams as G-2. Here, the sample loses fluidity and, rheologically, is very similar to the H phase. The polarization–optical experiments with the thin layers of the G-2 gel revealed no appreciable tendency to orientation. In unpolarized light, the thick specimens are of turbid white color. Close to the boundary with the nematic domain, the system restores its fluidity.

The polycrystalline phase (C). The domain of this phase is adjacent to those of the isotropic, hexagonal, and gellike states. It is determined from the observations on thin layers and looks like the accumulation of numerous small polydomain regions. Inside these regions, the sign of the optical anisotropy can vary, which may be explained by the presence of spherulites and similar formations. The phase C is characterized by the absence of the large-scale structures similar to those observed in the H phase. The aggregate state resembles a swollen soap. Thick layers are of white color in both polarized and unpolarized light.

2.4. Phase transitions. Studying the transition between the isotropic and the nematic phases, we established two types of such transitions, which is most clearly seen on in the (T, $C_{1\text{-decanol}}$) diagrams at the constant KL/water ratio.

The transition from the isotropic to the nematic phase may occur either through the intermediate gel state (for example, at $T = 35°C$, see Fig. 6b) or directly (for example, at $T = 20°C$). The transitions themselves occur qualitatively differently. In particular, in the phase transformation I ⟶ G ⟶ N, the isotropic one-phase solution, first, laminates to give the stable emulsion (its morphology is illustrated by Fig. 4). With addition of 1-decanol, the droplets of the new optically anisotropic phase gradually increase in size and number. It should be pointed out that the method of the texture analysis used does not allow the reliable determination of a type of the droplet-forming mesophase. Moving along the $C_{1\text{-decanol}}$ axis, we arrive at the G-2 region, where, most likely, the essential restructuring takes place. The G-1 phase is a liquid, whereas the G-2 phase is a gel with a considerable shear stress. With the further increase of the 1-decanol concentration (approaching the nematic-domain boundary) the system restores its fluidity. The transition to the nematic phase occupying the whole sample volume proceeds within a very narrow temperature or concentration range. The actual width of the transition zones appeared to be less than the accuracy of our measurements. Hence, the boundary between the domains of the G and H states is shown by a line in Figs. 6 and 7.

The G ⟶ N transition may occur with the changes in both concentration (1-decanol and/or water) and temperature. Our observations indicate the possibility of the reversible N ⟶ G ⟶ N transformation depends on the "penetration depth" into the state G. If, the transformation results in the gel state, then it is impossible to return to the nematic state using only the temperature variation. However, repeating the mixing, one can again observe the nematic state at the given temperature. If the system preserves its fluidity, then the nematic state is restored with a decrease of the temperature. In our opinion, the possibility of reversible N ⟶ G ⟶ N transformation indicates that the nematic is a true phase and not a metastable state. The seeming irreversibility of the N ⟶ G-2 transition (with respect to the temperature) is associated solely with the kinetic difficulties of restructuring.

Another scenario of the I ⟷ N transition involves no droplet formation and the transformation occurs between the homogeneous states. Of particular interest is the pattern of the pretransitional phenomena. An isotropic solution located rather closely to the nematic-domain boundary responds to the small mechanical disturbances (vibration) by the formation of macroscopic regions with the uniaxial optical anisotropy, i.e., with giant orientational fluctuations. In the light transmitted through crossed polaroids, a slight shaking of the test tube results in a *bright light flash* against the black (in the equilibrium) background. The intensity of the response noticeably increases with an approach to the boundary of the I ⟷ N transition irrespective of whether it is caused by the change in temperature or concentration. This "fluctuation" interval is denoted by I_F in Figs. 6 and 7. A similar phenomenon was also reported for the lyotropic system sodium dodecyl sulfate–1-decanol–water [11].

Visually, the N ⟷ H transition and I ⟷ G-1 the transition are quite similar. The former transition is also reversible. Each time, the formation of a new phase starts from the appearance of the nucleation centers, which looks like the regions with smectic-like (lamellar) order.

3. DISCUSSION AND CONCLUSIONS

Nematic order in a lyotropic system is a fine effect [1]. This is indicated by the narrow region of the nematic domain in Fig. 2 in comparison with the entire concentration plane and the strong dependence of the polymorphism on the conditions of the compound preparation. In the Sections 1 and 2, a number of rules was formulated, whose thorough fulfillment provided the preparation of lyotropic compounds with the reproducible phase diagrams. The reproduced properties were observed at both concentration and temperature variations. Because of pronounced orientational–optical effects, the liquid crystal phases and transitions between them can readily be observed even using a simple polarization cell.

The study of the systems prepared provided: (1) the precise localization of the nematic phase N in the three-dimensional space of the thermodynamical variables of the system (the temperature and the concentrations of any two components), (2) the demonstration of the possibility of the first- and the second-order I ⟷ N phase transitions and the establishment of the qualitative differences between them, (3) the determination of the two-phase domain (G), in which the system has the form either of a gel or an emulsion, and the study of its morphology, (4) the demonstration of the fact that, in addition to the temperature and partial concentrations, an important parameter characterizing the state of the lyotropic solution is also pH.

The present study is the first one, which considers the problem of reproducibility (and, thus also, the possible standardization) of the properties of the lyotropic solutions. As far as we know, all the preceding publications [7, 8, 11, 12] implied the reproducibility as a natural fact, because none of them had any detailed description of the synthesis of a lyotropic system. At the same time, the experimental results reported by various authors are inconsistent. Thus, comparing the representative points of the ternary diagrams of the systems KL–1-decanol–water, the data of [7, 8, 12] differ within 1 wt %. With the widths of the phase domains under discussion ranging from 0.1 to 1 wt %, this contradiction seems to be quite serious.

The above quantitative approach to the synthesis of the lyotropic system KL–1-decanol–water opens the way for studying the nematic state, for which many serious problems should be solved. For example, until now the problem of the "fine structure" of this phase remains open. Thus it was concluded [7, 18] that the nematic domain (N) has several modifications which are characterized by different micelle shapes. These are the discotic N_d, the calamitic N_c, and biaxial N_{bx} phases with the elementary units in the shape of a disk, a cylinder, and a biaxial ellipsoid or a parallelepiped, respectively.

Studying the existence domain of the nematic phase, we found out the transitions through its external borders are of a complicated nature (see diagrams in Figs. 2, 6, and 7). In particular, either the transformation from the isotropic to the nematic state can be implemented only by the mechanism with obvious features of the *first-order* transition, the phases N and I, are separated by a rather wide domain G, where both these phases coexist or else the I ⟷ N transition occurs, which is very close to *second*-order phase transition and is accompanied by a drastic increase in the orientation fluctuations with an approach to the boundary (region I_F in Figs. 2, 6, and 7). The character of the transition changes at the point of intersection of the boundaries of the I, G, and N domains. It should also be indicated that not far from the point indicated, above in the phase N the conoscopic observations showed the biaxiality. Although all the biaxial textures were formed under the action of mechanical perturbations and then relaxed to the uniaxial configuration, their formation signifies that it is in the vicinity of the intersection point mentioned above that the lines separating the still hypothetical N_d, N_c, and N_{bx} phases pass.

It is worth noting to indicate some characteristic features of the two-phase domain G that separates the nematic and the isotropic phases. In particular, the "entering" into this domain from the side of any of the homogeneous phases results in an abrupt phase segregation. In our observations at the spacial resolution not exceeding 10^{-2} cm at the time scale of ≥1s, the appearance of droplets (Fig. 4) was observed at once in the amounts comparable with the volume of the initial homogeneous phase. This fact points to the unconventional shape of the spinodal in our system. So far, we do

not have enough data for a detailed description of the domain G and the constituting states (their division into G-1 and G-2 only reflects the difference in their rheologies). The detailed study of this domain is the objective of future studies.

In this connection, it should be indicated that the kinetic effects substantially hinder the implementation of the "cyclic" transition N ⟶ G ⟶ N with respect to temperature. As an example, consider Fig. 3c. Heating of the nematic to the temperatures characteristic of the region G-2 does not directly lead to gel formation. The gel is formed with a time lag of 5–10 min. Prior to gel formation, a decrease of the temperature "returns" the "overheated" nematic to the domain N. If the gel had enough time to be formed, a decrease in the temperature provides only the "freezing" of this state and the time necessary for the return to the nematic state, indefinitely increases. Thus, the supercooled gel, being, in fact, metastable, behaves in practice as the stable one.

ACKNOWLEDGMENTS

The study was supported in part by the Program Le Réseau Formation—Recherché of the Ministry of Higher Education of France, project no. 96P0079, and the Russian Foundation for Basic Research, project no. 98-02-16453). V. V. Berejnov acknowledges the support of the Federal Program *Integration* (Western Ural), project no. 97-06).

REFERENCES

1. P. G. de Gennes and J. Prost, *The Physics of Liquid Crystals*, 2nd ed. (Clarendon, Oxford, 1993).
2. A. S. Sonin, *Introduction to Physics of Liquid Crystals* (Nauka, Moscow, 1983).
3. P.G. de Gennes, Rev. Mod. Phys. **64**, 645 (1992).
4. G. J. Tiddy, Phys. Rev. **57**, 1 (1980).
5. K. Shinoda, T. Nakagava, B. Tamamushi, and T. Isemura, *Colloidal Surfactants. Some Physicochemical Properties* (Academic, New York, 1963).
6. A. S. Sonin, Usp. Fiz. Nauk **153**, 875 (1987).
7. L. J. Yu and A. Saupe, Phys. Rev. Lett. **45**, 1000 (1980).
8. Y. Hendrix and J. Gharvolin, J. Phys. II **42**, 1427 (1981).
9. V. Berejnov, Yu. Raikher, V. Cabuil, *et al.*, J. Colloid Interface Sci. **199**, 215 (1998).
10. L. Liebert and A. Martinet, J. Phys. II **40**, L363 (1979).
11. Y. Hendrix, J. Charvolin, M. Rawiso, *et al.*, J. Phys. Chem. **87**, 3991 (1983).
12. A. M. Figueiredo Neto, L. Liebert, and Y. Galerne, J. Phys. Chem. **89**, 3737 (1985).
13. K. Nakanishi, *Infrared Absorption Spectroscopy* (Nancodo, Tokyo, 1965).
14. R. G. Sinklair, A. F. Mckay, and R.N. Jones, J. Am. Chem. Soc. **74**, 2571 (1952).
15. R. N. Jones, A. F. McKay, and R. G. Sinklair, J. Am. Chem. Soc. **74**, 2575 (1952).
16. N. H. Hartshorne and A. Stuart, *Crystals and the Polarizing Microscopy*, 4th ed. (Edward Arnold, London, 1970).
17. P. Oswald and M. Kleman, J. Phys. II **42**, 1461 (1981).
18. A. M. Figueiredo Neto, Braz. J. Phys. **22**, 85 (1992).

Translated by A. Zolot'ko

Crystallography Reports, Vol. 45, No. 3, 2000, pp. 501–509. Translated from Kristallografiya, Vol. 45, No. 3, 2000, pp. 549–557.

LIQUID CRYSTALS

Nematic–Isotropic Phase Transition in Polar Liquid Crystals. 1. Statistical Theory

A. V. Emel'yanenko* and M. A. Osipov**

** Physics Faculty, Moscow State University, Vorob'evy gory, Moscow, 119899 Russia*

*** Shubnikov Institute of Crystallography, Russian Academy of Sciences, Leninskiĭ pr. 59, Moscow, 117333 Russia*

Received April 29, 1998; in final form, April 12, 1999

Abstract—The theory of transition from the nematic to the isotropic phase for liquid crystals in the system of rodlike particles with large longitudinal dipoles has been developed with due regard for the equilibrium between monomers and antiparallel molecular pairs—dimers. The order parameters of monomers and dimers are determined as well as the dimer fraction. It is shown that, in accordance with the results obtained earlier, for low values of dipole moments, the temperature of the nematic–isotropic phase transition increases with an increase of the dipole moment. However, for large dipoles, the transition temperature starts decreasing with an increase of the dipole moment because of higher dimer concentration. This provides the interpretation of the recent computer simulation, which showed a destabilization of the nematic phase in the system of rigid rods with pronounced central dipoles. The temperature dependence of the dimer fraction is also studied. The qualitative relation between the sign of the jump in the dimer fraction at the transition point and the effect of dimerization on the transition temperature are established. © *2000 MAIK "Nauka/Interperiodica".*

1. INTRODUCTION

Many of the well known nematic crystals consist of polar molecules. Constant dipoles improve the electrooptical properties of liquid-crystalline materials and their chemical stability. As is well known, the physical properties of polar liquid crystals are essentially different from those of nonpolar liquid crystals. In particular, strongly polar liquid crystals can form reentrant and other complicated smectic phases [1–3].

The effect of molecular dipoles on the nematic phase has been studied insufficiently. However, there are some experimental data on the influence of molecule polarity on the nematic–isotropic phase transition. Some interesting effects were observed in mixtures of the polar and nonpolar nematics, where the transition temperature is a nonlinear function of the relative component concentration [4, 5]. No such phenomena were observed in mixtures of nonpolar nematics.

At the microscopic level, such effects are explained by the fact that antiparallel molecules form dimers. The existence of such dimers is confirmed by X-ray scattering data [6, 7] and measurements of the dielectric constant [8]. Of course, these dimers are not stable particles, but one can consider the dynamic equilibrium between monomers and dimers. The coexistence of dimers and monomers is a characteristic feature of strongly polar nematics and therefore should be taken into account in the molecular theory describing the nematic–isotropic phase transition.

The effect of constant molecular dipoles on the nematic–isotropic phase transition was considered in several theoretical studies [9–12], most of which were devoted to systems of rigid spherocylinders or ellipsoids with constant dipoles. Phase transition in such systems occur as a result of the changes in the particle concentrations at a constant temperature. Recent studies showed [9–11] that central dipoles stabilize the nematic phase. Some qualitative results were obtained in the studies of polar thermotropic nematics [12]. It was shown that, in the approximation of a two-particle cluster, the transition temperature rapidly increases with an increase of the dipole moment.

However, the above results are inconsistent with computer experiments [13, 14]. Computer simulation indicates either a destabilization of the nematic phase by constant dipoles [13] or the absence of any essential effect of constant dipoles on the nematic–isotropic phase transition [14].

The inconsistent data obtained in the statistical theory and computer experiments are explained by the insufficient accuracy of the theory. The theoretical studies of polar nematics are based on the Onsager theory [9, 10] or on the two-particle cluster approximation used to construct of the lattice model [11]. In the cited studies, the orientational correlations were taken into account, but the results obtained are applicable only to weak dipoles. For strong dipoles, the results becomes insufficiently accurate owing to strong translational correlations resulting in dimer formation. The free energy in the Onsager theory depends mainly on the second-order virial coefficient, whereas in the case of strong dipoles, this coefficient is determined by large value of the factor $\exp(d^2/kTR_0^3) \gg 1$, where R_0 is the minimum intermolecular distance. Higher order virial

1063-7745/00/4503-0501$20.00 © 2000 MAIK "Nauka/Interperiodica"

coefficients also include this factor. Moreover, with an increase of the dipole moment, they increase even faster than the second-order virial coefficient. As a result, the virial series becomes divergent.

Below, this problem is solved with the aid of dimers introduced into consideration and the subsequent evaluation of the dynamic equilibrium between these dimers and monomers. The molecular configuration possessing the minimum energy (the main difficulty encountered in this approach) is taken into account by the saddle-point method.

2. STATISTICAL THEORY OF NEMATIC ORDER IN THE SYSTEM CONSISTING OF MONOMERS AND DIMERS

Consider a system of strongly polar molecules as a mixture of monomers and dimers with the densities ρ_1 and ρ_2, respectively. In the nematic phase, these monomers and dimers are also characterized by the orientational distribution functions $f^{(1)}(\mathbf{a}\cdot\mathbf{n})$ and $f^{(2)}(\mathbf{a}\cdot\mathbf{n})$, where the unit vector $\mathbf{a}$ is directed along the long axis of the particle. The free energy of such a mixture is a functional of the densities $\rho_i(\mathbf{a}) = \rho_i f^{(i)}(\mathbf{a}\cdot\mathbf{n})$, where $i = 1, 2$. Taking into account only the direct pair correlations between the particles, we can write the free energy as [15]

$$\begin{aligned}\frac{\Phi}{NkTV}F &= \int\rho_1(\mathbf{a}_1)\{\ln[\rho_1(\mathbf{a}_1)\Lambda^3]-1\}d^2\mathbf{a}_1 \\ &+\int\rho_2(\mathbf{a}_1)\{\ln[\rho_2(\mathbf{a}_1)\Lambda^3]-1\}d^2\mathbf{a}_1 \\ &-\frac{1}{2}\int\rho_1(\mathbf{a}_1)\rho_1(\mathbf{a}_2)C_{11}(1,2)d^2\mathbf{a}_1d^3\mathbf{R}_{12}d^2\mathbf{a}_2 \\ &-\int\rho_1(\mathbf{a}_1)\rho_2(\mathbf{a}_2)C_{12}(1,2)d^2\mathbf{a}_1d^3\mathbf{R}_{12}d^2\mathbf{a}_2 \\ &-\frac{1}{2}\int\rho_2(\mathbf{a}_1)\rho_2(\mathbf{a}_2)C_{22}(1,2)d^2\mathbf{a}_1d^3\mathbf{R}_{12}d^2\mathbf{a}_2-\rho_2\frac{E_0}{kT},\end{aligned} \quad (1)$$

where N is the number of molecules, V is the molecular volume, $\Phi = \rho_0 V$ is the volume fraction of molecules in the system, Λ is the de Broglie wave number, $\mathbf{R}_{12}$ is the intermolecular vector, and $C_{ij}(1, 2)$ ($i, j = 1, 2$) are the effective direct correlation functions of the particles of the kinds i and j.

The last term in equation (1) describes the internal energy of dimers. Here E_0 is the binding energy of a dimer corresponding to the configuration of two constituent molecules in which the interaction potential between the molecules has the principal minimum. The dimer energy is given by the formula

$$\begin{aligned}E_0 &= \ln\left\{\frac{1}{4\pi\Lambda^3}\int\theta(\mathbf{R}_{12}-\boldsymbol{\xi}_{12})\right. \\ &\left.\times\left[\exp\left(-\frac{U_{dd}(1,2)}{kT}\right)-1\right]d^2\mathbf{a}_1d^3\mathbf{R}_{12}d^2\mathbf{a}_2\right\},\end{aligned} \quad (2)$$

where $\theta(\mathbf{R}_{12} - \boldsymbol{\xi}_{12})$ is the stepwise function describing the steric effects. If the molecules penetrate one another, the function equals zero, $\theta(\mathbf{R}_{12} - \boldsymbol{\xi}_{12}) = 0$, otherwise it equals unity, $\theta(\mathbf{R}_{12} - \boldsymbol{\xi}_{12}) = 1$. The potential $U_{dd}(1, 2)$ describes the energy of the dipole–dipole interaction

$$U_{dd}(1,2) = \frac{1}{R_{12}^3}\left[\mathbf{d}_1\cdot\mathbf{d}_2-\frac{3(\mathbf{d}_1\cdot\mathbf{R}_{12})(\mathbf{d}_2\cdot\mathbf{R}_{12})}{R_{12}^2}\right], \quad (3)$$

where $\mathbf{d}$ is the molecular dipole.

For considerable values of the dipole moment, the effective binding energy E_0 is determined mainly by the energy of the dipole–dipole interaction for the most probable configuration of two polar molecules.

Below, we consider a simple model of a polar molecule represented by a spherocylinder with the longitudinal central dipole. For long spherocylinders, such a dimer consists of two parallel neighboring monomers with antiparallel dipoles. The binding energy of such a dimer depends on the value of $-k(d^*)^2$, which describes the dipole–dipole interaction in the antiparallel configuration, where $d^* = d/\sqrt{kD^3}$ is the reduced dipole moment. It should be noted that the effective binding energy given by (2) also depends on the configurations determined by thermal fluctuations [16]. The calculation of E_0 is considered in detail in Appendix B. Here, we only give the result obtained for $E \equiv \rho\Lambda^3\exp(E_0/kT)$:

$$E = \frac{2\pi^2\Phi D^3}{3V}\sqrt{\frac{\pi}{3}}(d^*/\sqrt{T})^{-5}\exp(d^*/\sqrt{T})^2. \quad (4)$$

The free energy given by (1) is a functional of two densities, ρ_1 and ρ_2. However, these densities are not independent, because the total density of all the molecules (monomers or dimers) is fixed. This fact is described by the law

$$\int[\rho_1(\mathbf{a}) + 2\rho_2(\mathbf{a})]d^2\mathbf{a} = \rho_0, \quad (5)$$

where ρ_0 is the total density of all the molecules.

Minimizing free energy (1) with respect to the variables ρ_1 and ρ_2 under condition (5), we arrive at the fol-

lowing system of equations for these variables:

$$\begin{cases} \ln\rho_1(\mathbf{a}_1) - \int \rho_1(\mathbf{a}_2) C_{11}(1,2) d^3\mathbf{R}_{12} d^2\mathbf{a}_2 \\ - \int \rho_2(\mathbf{a}_2) C_{12}(1,2) d^3\mathbf{R}_{12} d^2\mathbf{a}_2 = \lambda^* \\ \ln\rho_2(\mathbf{a}_1) - \int \rho_2(\mathbf{a}_2) C_{22}(1,2) d^3\mathbf{R}_{12} d^2\mathbf{a}_2 \\ - \int \rho_1(\mathbf{a}_2) C_{12}(1,2) d^3\mathbf{R}_{12} d^2\mathbf{a}_2 \ln\left[\frac{E}{\rho\Lambda^3}\right] = 2\lambda^*, \end{cases} \quad (6)$$

where the parameter λ^* is determined from equation (5).

Equations (6) can be rewritten in a more convenient form:

$$\begin{cases} p f^{(1)}(\mathbf{a}_1 \cdot \mathbf{n}) \\ = \lambda \exp\left\{ p A_{11}(\mathbf{a}_1 \cdot \mathbf{n}) + \frac{1-p}{2} A_{12}(\mathbf{a}_1 \cdot \mathbf{n}) \right\} \\ \frac{1-p}{2} f^{(2)}(\mathbf{a}_1 \cdot \mathbf{n}) \\ = E\lambda^2 \exp\left\{ p A_{12}(\mathbf{a}_1 \cdot \mathbf{n}) + \frac{1-p}{2} A_{22}(\mathbf{a}_1 \cdot \mathbf{n}) \right\}, \end{cases} \quad (7)$$

where $p = \rho_1/\rho_0$ is the molar fraction of monomers, and the quantities A_{ij} ($i, j = 1, 2$) are the corresponding effective one-particle potentials given by the formulas

$$A_{ij}(\mathbf{a}_1 \cdot \mathbf{n}) = \frac{\Phi}{V} \int f^{(j)}(\mathbf{a}_2 \cdot \mathbf{n}) \times C_{ij}(\mathbf{a}_1, \mathbf{R}_{12}, \mathbf{a}_2) d^3\mathbf{R}_{12} d^2\mathbf{a}_2 \quad (8)$$

and $\lambda = \exp\lambda^*/(\rho\Lambda^3)$. The equation for the parameter λ is obtained by integrating each equation of system (7) with respect to $\mathbf{a}_1$:

$$I_1\lambda + 2I_2 E\lambda^2 = 1, \quad (9)$$

where

$$I_1 = \int \exp\left\{ p A_{11} + \frac{1-p}{2} A_{12} \right\} d^2\mathbf{a}_1, \quad (10)$$

$$I_2 = \int \exp\left\{ \frac{1-p}{2} A_{22} + p A_{21} \right\} d^2\mathbf{a}_1. \quad (11)$$

The positive root of equation (9) is

$$\lambda = \frac{\sqrt{I_1^2 + 8EI_2} - I_1}{4EI_2}. \quad (12)$$

Now, we can obtain the equations for the order parameters S_1 and S_2 of the monomers and dimers in terms of the generalized Maier–Saupe theory. With this aim, we have to expand the one-particle potentials $A_{ij}(\mathbf{a} \cdot \mathbf{n})$ into Legendre polynomials and retain only the first two terms,

$$A_{ij}(\mathbf{a} \cdot \mathbf{n}) = A_0^{ij} + A_2^{ij} S_j P_2(\mathbf{a} \cdot \mathbf{n}) + \ldots . \quad (13)$$

As a result, we arrive at the following equations for the order parameters S_j ($j = 1, 2$):

$$\begin{cases} S_j = \frac{1}{I_j^a} \int_{-1}^{1} P_2(x) \\ \times \exp\left\{ \left[A_2^{1j} p S_1 + A_2^{2j} \frac{1-p}{2} S_2 \right] P_2(x) \right\} dx \\ p = \frac{\sqrt{I_1^2 + 8EI_2} - I_1}{4EI_2} I_1, \end{cases} \quad (14)$$

where

$$I_J^a = \int_{-1}^{1} \exp\left\{ \left[A_2^{1j} p S_1 + A_2^{2j} \frac{1-p}{2} S_2 \right] P_2(x) \right\} dx, \quad (15)$$

$$I_j = I_j^a \exp\left\{ A_0^{1j} p + A_0^{2j} \frac{1-p}{2} \right\}. \quad (16)$$

The coefficients $A_{0,2}^{ij}$ ($i, j = 1, 2$) depend on the temperature and structure of the molecules under study.

3. DISPERSION AND ELECTROSTATIC INTERACTIONS BETWEEN MONOMERS AND DIMERS

The system of equations for the order parameters S_1 and S_2 and the monomers fraction p can be solved numerically if the coefficients A_0^{ij} and A_2^{ij} are known. These coefficients are the moments of the effective direct correlations functions $C_{ij}(1, 2)$.

In the generalized theory of a mean field, the functions $C_{ij}(1, 2)$ are expressed in a simple analytical form

$$C_{ij}(1,2) = -\Theta(\mathbf{R}_{12} - \boldsymbol{\xi}_{12}) \frac{U_{ij}(1,2)}{kT}, \quad (17)$$

where $U_{ij}(1, 2)$ are the potentials of intermolecular interactions averaged over all the orientations of the short axes $\mathbf{b}_1$ and $\mathbf{b}_2$ of both interacting particles and $(\mathbf{a}_i \cdot \mathbf{b}_i) = 0$, $i = 1, 2$.

In this study, we take into account the dispersion interaction between the particles of any kind (monomers and dimers) and also the electrostatic dipole–dipole interactions between the monomers. A dimer consisting of two monomers possesses an effective quadrupole, which results in the occurrence of dipole–quadrupole and the quadrupole–quadrupole interactions in the system. However, these are relatively weak

short-range interactions, which can be neglected in the following consideration.

Thus, the interactions between monomers can be written in the form

$$U_{11}(1, 2) = U_{11}^{disp}(1, 2) + U_{11}^{dd}(1, 2), \quad (18)$$

where $U_{11}^{disp}(1, 2)$ is the energy of the dispersion interaction and $U_{11}^{dd}(1, 2)$ is the dipole–dipole potential.

It should be indicated that, upon averaging, the electrostatic interaction in equation (8) disappears. Thus, the electrostatic interactions provide no contribution to the free energy in the approximation of the mean field. It is possible to improve this approximation by considering the dipole–dipole interactions within the second-order virial approximation. In this case, the direct correlation functions can be written in the following way:

$$\begin{cases} C_{11}(1, 2) = -\theta(\mathbf{R}_{12} - \boldsymbol{\xi}_{12}) \\ \times \left[\frac{1}{kT} U_{11}^{disp}(1, 2) - \frac{1}{2}\left(\frac{1}{kT} U_{11}^{dd}\right)^2 \right] \\ C_{i2}(1, 2) = -\theta(\mathbf{R}_{12} - \boldsymbol{\xi}_{12}) \frac{1}{kT} U_{i2}^{disp}(1, 2), \quad i = 1, 2. \end{cases} \quad (19)$$

The dispersion interactions in (19) are considered in the mean-field approximation, whereas the dipole–dipole interactions between the monomers are considered in the second-order virial approximation. In (19), we neglected the dipole–quadrupole interactions between monomers and dimers and the quadrupole–quadrupole interactions between the dimers.

The quantity A_{11} consists of the dispersion and the dipole–dipole terms.

$$A_{11} = A_{11}^{disp} + A_{11}^{es}. \quad (20)$$

The quantities A_{ij}^{disp} and A_{11}^{es} can be expanded into Legendre polynomials

$$A_{ij}^{disp}(\mathbf{a}_1 \cdot \mathbf{n}) = J_0^{ij} + J_2^{ij} S_j P_2(\mathbf{a}_1 \cdot \mathbf{n}) + \ldots, \quad (21)$$

$$A_{11}^{es}(\mathbf{a}_1 \cdot \mathbf{n}) = J_0^{es} + J_2^{es} S_1 P_2(\mathbf{a}_1 \cdot \mathbf{n}) + \ldots. \quad (22)$$

Then, in accordance with formula (13), we arrive at

$$\begin{cases} A_{0,2}^{11} = J_{0,2}^{11} + J_{0,2}^{es} \\ A_{0,2}^{i2} = J_{0,2}^{i2}, \quad i = 1, 2. \end{cases} \quad (23)$$

The coefficients of the dipole–dipole interactions, J_0^{es} and J_2^{es}, are estimated in Appendix A. The coefficients of the dispersion interactions, J_0^{ij} and J_2^{ij}, depend on the structure of the molecules and can be estimated in the similar way within the framework of the chosen molecular model. In [17], the coefficients of dispersion interactions are determined within the framework of the so-called block model in which a molecule is represented by a chain of spherical blocks interacting according to the Lennard–Jones law. In this study, we invoke the results obtained in [17].

4. DISCUSSION OF RESULTS

In order to describe the temperatures dependences of the order parameters S_1 and S_2 and the monomer fraction p, we solved numerically system of equations (14). The system has two sets of solutions. One of these set ($S_1 = 0$, $S_2 = 0$, and $p = p_0$) corresponds to the isotropic phase, whereas the other (S_1, S_2, and p) corresponds to the nematic phase. The phase transition takes place if the free energy $F(S_1, S_2, p)$ has a value lower than $F(0, 0, p_0)$. The numerical value of the free energy was calculated by the formula

$$\begin{aligned} \frac{F}{NkT} &= \frac{1}{2}(A_0^{11} + A_2^{11} S_1^2) p^2 \Phi \\ &+ \frac{1}{2}(A_0^{22} + A_2^{22} S_2^2)\left(\frac{1-p}{2}\right)^2 \Phi \\ &+ (A_0^{12} + A_2^{12} S_1 S_2) p \frac{1-p}{2} \Phi \\ &+ p \ln \frac{p}{I_1} + \frac{1-p}{2} \ln \frac{\left(\frac{1-p}{2}\right)}{EI_2} - \frac{1+p}{2} + \ln \frac{\Lambda^3 \Phi}{V}, \end{aligned} \quad (24)$$

obtained from the above calculations. In particular, all the three equations of system (14) can be obtained from formula (24) by independent minimization of the free energy with respect to the variables S_1, S_2, and p.

Thus, the $S_1(T)$, $S_2(T)$, and $p(T)$ curves have jumps at the transition point, whereas the transition point itself is dependent on the dipole-moment value. The dependence of the transition temperature T_{NI} on the squared reduced moment, $(d^*)^2$, is shown in Fig. 1. In our calculations, we used the coefficient of the dispersion interactions calculated within the block model and the axial ratio $L/D = 5$ (as in [13]) and $\Phi = 0.3$. The dashed line in Fig. 1 shows the corresponding curve calculated without the allowance for dimerization.

For weak dipoles, the transition temperature increases with an increase of the dipole moment in both cases, which is determined by an increase of the effective orientational interactions between monomers caused, in turn, by an increase of the dipole–dipole interactions between these monomers. Since the number of dimers in this region is rather small (see the temperature dependence of the monomer fraction p for $(d^*)^2 = 2500$ K, curve *1* in Fig. 2), they can only slightly affect the system behavior.

At the same time, for strong dipoles, the number of dimers is considerably higher (curve *3* in Fig. 2), which results, first, in a decelerated rise of the $T_{N1}(d^*)^2$ curve,

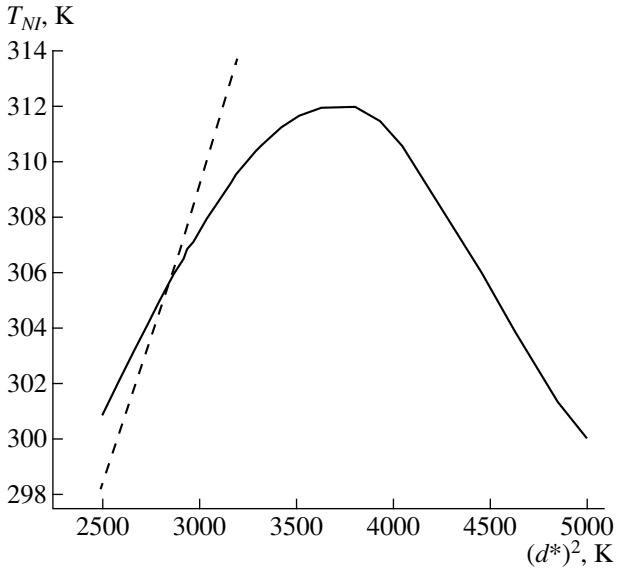

Fig. 1. Dependence of the transition temperature on the squared reduced dipole moment. The dashed line shows the corresponding dependence obtained without the allowance for dimers, $L/D = 5$, $\Phi = 0.3$.

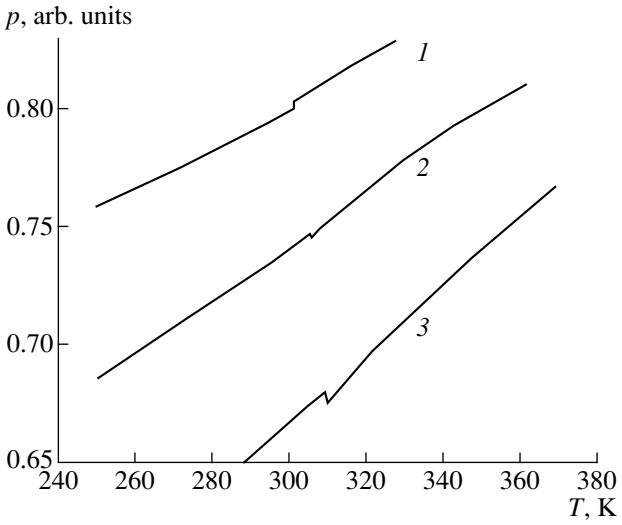

Fig. 2. Temperature dependence of the monomer fraction. The squared reduced dipole moment is (*1*) 2500, (*2*) 2850, and (*3*) 3200 K.

and then also in a decrease of the transition temperature, with an increase of the dipole moment. This is explained by the fact that, unlike monomers interacting with their own dipoles, the dimers show no noticeable electrostatic interactions. Since the initial rise of the $T_{NI}(d^*)^2$ curve in Fig. 1 is explained mainly by an increase of the dipole–dipole interactions, the decrease in the number of monomers (because of an increase in the number of dimers) results in decay of the $T_{NI}(d^*)^2$ curve (Fig. 1).

It is characteristic that even in the region of weak dipoles, an increase of the transition temperature is slower than was predicted by the theory, which neglected dimerization. This in turn makes it possible to interpret the results of the computer simulation of which some indicate destabilization of the nematic phase in strongly polar liquids [13], whereas other results indicate that the central molecular dipoles do not affect the nematic–isotropic phase transition at all [14].

It should be emphasized that at low values of the dipole moment (see the left-hand part of Fig. 1), the transition temperature is higher than the transition temperature obtained without the allowance for dimerization. This indicates that in the case of weak dipoles, dimers stabilize the nematic phase. Such a situation is obtained within the framework of the block model, in which a dimer seems to have a more mesogenic shape than a monomer. In the absence of another, more important, factor—electrostatic interactions—the shape plays the decisive role, which results in the fact that the solid curve in the left-hand side of Fig. 1 runs above the dashed curve.

At a certain value of $(d^*)^2$, the effect of electrostatic interactions is balanced by the shape effect. At this point, henceforth called the balance point for sake of brevity, the solid and the dashed curves in Fig. 1 intersect one another. The point of their intersection is unique because, at this point, dimers produce no effect on the system, and the latter behaves as if there were no dimers at all.

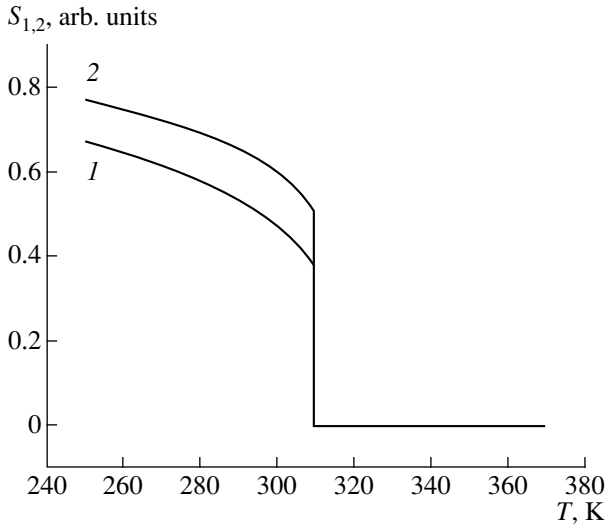

Fig. 3. Temperature dependence of the order parameters for (*1*) monomers and (*2*) dimers. The squared reduced dipole moment equals 3200 K.

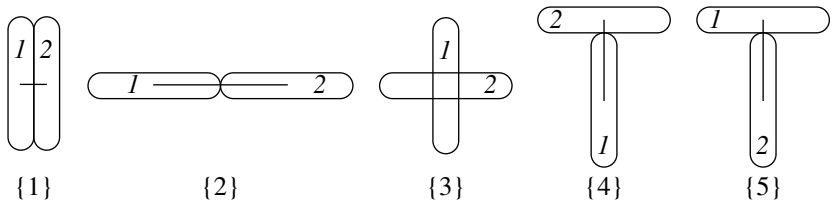

Fig. 4. Five relative monomer orientations providing the determination of the minimum distance and X between monomers, $\xi_{\{n\}}$: $\xi_{\{1\}} = \xi_{\{3\}} = 1$; $\xi_{\{2\}} = q$; $\xi_{\{4\}} = \xi_{\{5\}} = \frac{q+1}{2}$, where $q \equiv L/D_{\text{eff}}$ is the effective axial ratio and $\{n\}$ indicates the ordinal number of the orientation.

Consider the behavior of the system of monomers and dimers in the vicinity of the balance point in Fig. 1. Curve *1* in Fig. 2 represents the temperature dependence of the monomer fraction p at the point $(d^*)^2 = 2500$ K lying on the left of the balance point. It is seen from Fig. 2, that at the transition point, the monomer fraction has an upward jump, which indicates that it is more favorable for dimers to be in the ordered phase, which is quite consistent with the above statement that, in this region, dimers are more mesogenic.

Curve *3* in Fig. 2 represents the temperature dependence of the monomer fraction p at the point $(d^*)^2 = 3200$ K lying on the right of the balance point. It is seen that, in this case, the monomer fraction has a downward jump, which indicates that it is more favorable for dimers to be in the isotropic phase. This confirms the fact that, on the right of the balance point, dimers are less mesogenic than monomers.

At the balance point proper, p displays no jump at all. The corresponding temperature dependence of the monomer fraction at the balance point $(d^*)^2 = 2850$ K is represented by curve *2* in Fig. 2. Thus, at this point, dimers do no affect the thermodynamic properties of the system at all.

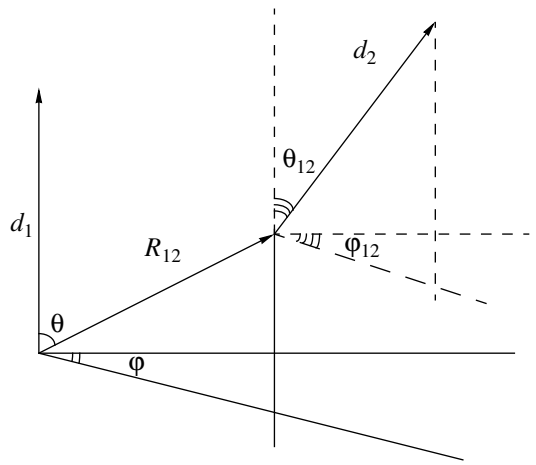

Fig. 5. Local coordinate system with the z-axis parallel to the dipole moment d_1 of one of the spherocylinders forming a dimer. This system was used to estimate the dimer energy in Appendix B.

Figure 3 shows the temperature dependence of the order parameters S_1 and S_2 of monomers and dimers at the point $(d^*)^2 = 3200$ K. It is seen that the allowance for dimers does not essentially influence the behavior of the order parameter, which decreases with the temperature as in the conventional Maier–Saupe theory. However, the transition point is sensitive to the balance between monomers and dimers (Fig. 1).

The above results clearly show the following tendency. The transition temperature, even for weak dipoles, increases much slower than in the theory neglecting dimerization, whereas for strong dipoles it even decreases. Therefore, with an increase of the dipole moment of the molecule, the range of the variations of the transition temperature becomes narrower than it was indicated in the previous theoretical studies [12]. As has already been indicated, this is consistent with the results obtained in computer experiments [13, 14]. The data obtained in the present study are also consistent with the pronounced effect of constant molecular dipoles on the transition to the smectic phase.

The method used in the present study is also applicable to the transitions of the polar systems to various smectic phases and the studies of liquid-crystalline ordering in polymer systems with constant dipoles.

The above theory describes the phase transition from the nematic to the isotropic phase in strongly polar thermotropic liquid crystals. This theory can also be used to develop a theory of phase transitions in strongly polar lyotropic systems.

APPENDIX A

DIPOLE–DIPOLE INTERACTIONS OF MONOMERS

Let us determine the coefficients of dipole–dipole interactions. In our model, a dipole is located in the center of a molecule parallel to its long axis.

Expand the effective dipole–dipole potential into Legendre polynomials and retain only two first terms:

$$A_{11}^{es}(\mathbf{a}_1\cdot\mathbf{n}) = \frac{\Phi}{2V(kT)^2}\int f^{(1)}(\mathbf{a}_2\cdot\mathbf{n})\theta(\mathbf{R}_{12}-\boldsymbol{\xi}_{12}) \times[U_{11}^{dd}(1,2)]^2 d^3\mathbf{R}_{12}d^2\mathbf{a}_2 = J_0^{es} + J_2^{es}S_1P_2(\mathbf{a}_1\cdot\mathbf{n}) + \ldots, \quad \text{(A1)}$$

where the potential of the dipole–dipole interaction is set by formula (3).

Consider, first, the integral taken over the intermolecular vector $\mathbf{R}_{12}$ in formula (A1). The integral over the absolute value of R_{12} can be taken directly, and, therefore, we obtain

$$A_{11}^{es} = \frac{\Phi d^4}{6V(kT)^2}\int f^{(1)}(\mathbf{a}_2\cdot\mathbf{u})[(\mathbf{a}_1\cdot\mathbf{a}_2) - 3(\mathbf{a}_1\cdot\mathbf{u})(\mathbf{a}_2\cdot\mathbf{u})]^2\xi_{12}^{-3}(\mathbf{a}_1,\mathbf{u},\mathbf{a}_2)d^2\mathbf{u}d^2\mathbf{a}_2, \quad \text{(A2)}$$

where $\mathbf{u} = \mathbf{R}_{12}/|R_{12}|$. In formula (A2), the minimum distance between the centers of two molecules, $\xi_{12}(\mathbf{a}_1, \mathbf{u}, \mathbf{a}_2)$, depends on the relative orientations of the contacting molecules. It is impossible to calculate the function ξ_{12} analytically even for the simplest molecular model. However, similar to [18], one can use the interpolating expressions, which can be obtained in the following way.

First, expand ξ_{12}^{-3} into a series in the complete system of spherical invariants and retain only several terms of the expansion

$$\xi_{12}^{-3} = D_{\text{eff}}^{-3}\Big\{\alpha + \beta_1P_2(\mathbf{a}_1\cdot\mathbf{u}) + \beta_2P_2(\mathbf{a}_2\cdot\mathbf{u}) + \gamma P_2(\mathbf{a}_1\cdot\mathbf{a}_2) + \delta\Big[\frac{9}{2}(\mathbf{a}_1\cdot\mathbf{u})(\mathbf{a}_2\cdot\mathbf{u})(\mathbf{a}_1\cdot\mathbf{a}_2) - \frac{3}{2}(\mathbf{a}_1\cdot\mathbf{u})^2 - \frac{3}{2}(\mathbf{a}_2\cdot\mathbf{u})^2 - \frac{3}{2}(\mathbf{a}_1\cdot\mathbf{a}_2)^2 + 1\Big]\Big\}. \quad \text{(A3)}$$

Now, in order to exclude the integration domain in which two molecules should be considered as a dimer (and not as independent monomers), introduce the effective diameter of the molecule, $D_{\text{eff}} = 1.62\,D$.

Substituting (A3) into (A2), we arrive at the expressions for J_0^{es} and J_2^{es}

$$J_0^{es} = \frac{4}{9}\pi\frac{\Phi D_{eff}^3}{V}\frac{(d^*)^4}{T^2} \times\Big[\alpha + \frac{1}{5}\beta_1 + \frac{1}{5}\beta_2 + \frac{1}{25}\gamma - \frac{1}{25}\delta\Big], \quad \text{(A4)}$$

$$J_2^{es} = \frac{4}{9}\pi\frac{\Phi D_{eff}^3}{V}\frac{(d^*)^4}{T^2} \times\Big[\frac{1}{5}\alpha + \frac{1}{7}\beta_1 + \frac{1}{7}\beta_2 + \frac{37}{35}\gamma + \frac{101}{245}\delta\Big]. \quad \text{(A5)}$$

Now, consider five coefficients, α, β_1, β_2, γ, and δ in formulas (A4) and (A5) as free parameters [19] and stipulate that expression (A3) for ξ_{12}^{-3} coincide with the exact result for five orientations of two molecules shown in Fig. 4.

Now, using the quantities $\xi_{\{n\}}$ (Fig. 4), we arrive at the following expressions for the coefficients in formulas (A4) and (A5):

$$\begin{cases} \alpha = \frac{2}{9}\Big\{2 + \frac{1}{2}q^{-3} + 2[(q+1)/2]^{-3}\Big\} \\ \beta_i = \frac{2}{9}\{-2 + q^{-3} + [(q+1)/2]^{-3}\}, \quad i = 1, 2 \\ \gamma = \delta = \frac{2}{9}\{1 + q^{-3} - 2[(q+1)/2]^{-3}\}. \end{cases} \quad \text{(A6)}$$

APPENDIX B

DIMER ENERGY

A dimer is built by two molecules located in the vicinity of the minimum of the energy of interaction between these molecules. The configuration with the minimum energy for a pair of spherocylinders with longitudinal dipoles is obtained for neighboring dipoles having the antiparallel orientations.

The total energy of all the dipoles (see Sect. 2) equals

$$E = \frac{1}{4\pi}\rho\int\theta(\mathbf{R}_{12}-\boldsymbol{\xi}_{12}) \times\Big[\exp\Big(-\frac{U_{dd}(1,2)}{kT}\Big) - 1\Big]d^2\mathbf{a}_1d^3\mathbf{R}_{12}d^2\mathbf{a}_2. \quad \text{(B1)}$$

Since the dipole–dipole interactions are polar and, thus, on the average, equal zero, we cannot use the mean-field approximation when calculating E. At the same time, the dimer energy shows the well pronounced principal maximum and therefore can be estimated by the saddle-point method.

The dipole–dipole interaction in formula (B1) is determined by the expression

$$U_{dd}(1,2) = \frac{1}{R_{12}^3}\Big[\mathbf{d}_1\cdot\mathbf{d}_2 - \frac{3(\mathbf{d}_1\cdot\mathbf{R}_{12})(\mathbf{d}_2\cdot\mathbf{R}_{12})}{R_{12}^2}\Big]. \quad \text{(B2)}$$

Now, introduce a cylindrical coordinate system in which the polar axis is directed along the dipole moment of one of the two molecules forming a dimer (Fig. 5). In this coordinate system, the vectors in formula (B2) have the following coordinates

$$\mathbf{d}_1 = d\begin{pmatrix}0\\0\\1\end{pmatrix}, \quad \mathbf{d}_2 = d\begin{pmatrix}\sin\theta_{12}\cos\varphi_{12}\\ \sin\theta_{12}\sin\varphi_{12}\\ \cos\theta_{12}\end{pmatrix},$$

$$\mathbf{R}_{12} = R_{12}\begin{pmatrix}\sin\theta\cos\varphi\\ \sin\theta\sin\varphi\\ \cos\theta\end{pmatrix}.$$

In the vicinity of the energy minimum, we can write:

$$\sin\theta_{12} \approx (\pi - \theta_{12}), \quad \cos\theta_{12} \approx -1 + (\theta_{12} - \pi)^2,$$

$$\sin\theta \approx 1 - \left(\theta - \frac{\pi}{2}\right)^2, \quad \cos\theta \approx \left(\frac{\pi}{2} - \theta\right),$$

$$R_{12} \approx D(1 + \xi),$$

where $\theta_{12} \longrightarrow \pi$, $\theta \longrightarrow \frac{\pi}{2}$, $\xi \longrightarrow 0$.

Now, retaining in (B2) only the terms $\sim(\theta_{12} - \pi)^i\left(\theta - \frac{\pi}{2}\right)^j \xi^k$, where $i + j + 2k \le 2$, we have

$$U_{dd} \approx -\frac{d^2}{D^3}\left[1 - 3\xi - (\theta_{12} - \pi)^2 - 3\left(\theta - \frac{\pi}{2}\right)^2 + 3(\theta_{12} - \pi)\left(\theta - \frac{\pi}{2}\right)\cos(\varphi_{12} - \varphi)\right]. \quad \text{(B3)}$$

Introducing the notation $\mu = \frac{d^2}{kTD^3}$, we can rewrite (B1), with due regard of the above stated, in the following form:

$$E \approx \rho D^3 \int_0^\infty d\xi \int_0^\pi d\theta \sin\theta \int_0^\pi d\theta_{12} \sin\theta_{12} \int_0^{2\pi} d\varphi_{12} \int_0^{2\pi} d\varphi$$

$$\times \exp\left\{\mu\left[1 - 3\xi - (\theta_{12} - \pi)^2 - 3\left(\theta - \frac{\pi}{2}\right)^2 + 3(\theta_{12} - \pi)\left(\theta - \frac{\pi}{2}\right)\cos(\varphi_{12} - \varphi)\right]\right\}$$

$$\approx 2\pi\rho D^3 \frac{1}{3\mu} e^\mu \int_0^\pi d\theta \sin\theta \int_0^\pi d\theta_{12} \sin\theta_{12} \int_0^{2\pi} d\varphi$$

$$\times \exp\left\{\mu\left[-(\theta_{12} - \pi)^2 - 3\left(\theta - \frac{\pi}{2}\right)^2 + 3(\theta_{12} - \pi)\left(\theta - \frac{\pi}{2}\right)\cos\varphi\right]\right\}$$

$$= 4\pi^2\rho D^3 \frac{1}{3\mu} e^\mu \int_0^\pi d\theta \sin\theta \int_0^\pi d\theta_{12} \sin\theta_{12}$$

$$\times \exp\left\{\mu\left[-(\theta_{12} - \pi)^2 - 3\left(\theta - \frac{\pi}{2}\right)^2\right]\right\}$$

$$\times J_0\left[3i\mu(\theta_{12} - \pi)\left(\theta - \frac{\pi}{2}\right)\right],$$

where J_0 is the zeroth-order Bessel function. We assume that $J_0\left[3i\mu(\theta_{12} - \pi)\left(\theta - \frac{\pi}{2}\right)\right] \approx 1$. Then

$$E \approx 4\pi^2\rho D^3 \frac{1}{3\mu} e^\mu \int_0^\pi d\theta_{12} \sin\theta_{12} \exp[-\mu(\theta_{12} - \pi)^2]$$

$$\times \int_0^\pi d\theta \sin\theta \exp\left[-3\mu\left(\theta - \frac{\pi}{2}\right)^2\right]$$

$$\approx \pi^2\rho D^3 \frac{4}{3\mu} e^\mu \int_0^\pi d\theta_{12}[\pi - \theta_{12}] \exp[-\mu(\theta_{12} - \pi)^2]$$

$$\times \int_0^\pi d\theta \left[1 - \left(\theta - \frac{\pi}{2}\right)^2\right] \exp\left[-3\mu\left(\theta - \frac{\pi}{2}\right)^2\right] \quad \text{(B4)}$$

$$\approx \pi^2\rho D^3 \frac{4}{3\mu} e^\mu \int_0^\infty x \exp[-\mu x^2] dx \int_{-\infty}^\infty \exp[-3\mu y^2] dy$$

$$= \frac{2\pi^2\Phi D^3}{3\mu^2 V}\sqrt{\frac{\pi}{3\mu}} e^\mu.$$

Formula (B4) yields the correct value of E if $\mu = (d^*)^2/T > 1$. As is seen from Fig. 1, the temperature range studied satisfies this condition.

ACKNOWLEDGMENTS

The authors are grateful to A. R. Khokhlov and other scientists of the Department of Physics of Polymers and Crystals of the Physics Faculty of Moscow State University and to S. A. Pikin for their valuable

help. The study was supported by the INTAS within the Program for Research of the International Center of Fundamental Physics in Moscow, project no. 96-0457.

REFERENCES

1. P. E. Cladis, Phys. Rev. Lett. **35**, 48 (1975).
2. F. Hardouin, A. M. Levelut, and G. Sigaud, J. Phys. (Paris) **42**, 71 (1981).
3. J. Prost, Adv. Phys. **33**, 46 (1984).
4. B. K. Vaĭnshteĭn and I. G. Chistyakov, in *Problems of Modern Crystallography* (Nauka, Moscow, 1975), p. 12.
5. W. H. de Jeu, *Structural Incommensurability in Crystals, Liquid Crystals, and Quasi-Crystals*, Ed. by J. F. Scott (Plenum, New York, 1986).
6. G. J. Brownsey and A. J. Leadbetter, Phys. Rev. Lett. **44**, 1608 (1980).
7. V. F. Petrov, M. F. Grebenkin, and B. I. Ostrovskii, Kristallografiya **33** (5), 1194 (1988) [Sov. Phys.–Crystallogr. **33** (5), 708 (1988)].
8. J. J. Penchev and J. N. Dozov, Mol. Cryst. Liq. Cryst. Sci. Technol., Sect. A **73**, 267 (1981).
9. A. Perera and G. N. Patey, J. Chem. Phys. **89**, 5861 (1988).
10. A. G. Vanakaras and D. J. Photinos, Mol. Phys. **85**, 1089 (1995).
11. C. Vega and S. Lago, J. Chem. Phys. **100**, 6727 (1994).
12. M. A. Osipov and A. Yu. Simonov, Khim. Fiz. **8** (7), 992 (1989).
13. S. C. McGrother, A. Gil-Villegas, and G. Jackson, J. Phys. C: Solid State Phys. **8**, 9649 (1996).
14. K. Satoh, Sh. Mita, and Sh. Kondo, Liq. Cryst. **20** (6), 757 (1996).
15. M. A. Osipov, in *Handbook of Liquid Crystals*, Ed. by J. Goodby *et al.* (Wiley, Berlin, 1998).
16. P. C. Jordan, Mol. Phys. **25** (4), 961 (1973).
17. A. V. Emel'yanenko and M. A. Osipov, Kristallografiya **45** (3), 558 (2000) [Crystallogr. Rep. **45** (3), 510 (2000)].
18. B. W. van der Meer and G. Vertogen, *Molecular Physics of Liquid Crystals*, Ed. by G. R. Luckhurst and G. W. Gray (Academic, New York, 1979).
19. L. Blum and A. J. Torruella, J. Chem. Phys. **56**, 303 (1972).

Translated by L. Man

Crystallography Reports, Vol. 45, No. 3, 2000, pp. 510–514. Translated from Kristallografiya, Vol. 45, No. 3, 2000, pp. 558–563.

LIQUID CRYSTALS

Nematic–Isotropic Phase Transition in Polar Liquid Crystals. 2. Role of Dispersion Interactions

A. V. Emel'yanenko* and M. A. Osipov**

** Physics Faculty, Moscow State University, Vorob'evy gory, Moscow, 119899 Russia*

*** Shubnikov Institute of Crystallography, Russian Academy of Sciences, Leninskiĭ pr. 59, Moscow, 117333 Russia*

Received April 29, 1998

Abstract—The present study furthers the development of the theory of the nematic–isotropic phase transition in the system of rodlike particles with large longitudinal dipoles. The effect of dispersion interactions between single molecules (monomers) and molecular pairs (dimers) on the transition temperature is considered. The crucial point of the approach used is existence of dimers in the system. Dispersion interactions are estimated within the framework of the model in which molecules consist of spherical blocks interacting according to the Lennard–Jones law. The direct pair-correlation functions are approximated by spherical invariants forming a complete system of functions. Then, these correlation functions are varied in order to study the behavior of the phase-transition temperature depending on the choice of the molecular model. It is shown that, depending on the molecule shapes, dimers can either destroy or stabilize the nematic order. It is also shown that the presence of dimers in the system decelerates an increase of the transition temperature (and, in many instances, can even reduce it) with an increase in the value of the molecular dipole. © *2000 MAIK "Nauka/Interperiodica".*

1. INTRODUCTION

In the first part of this article [1], we studied the effect of constant molecular dipoles on the transition from the nematic to the isotropic phase. Unlike in previous theoretical studies [2–5], we took into account the formation of dimers—molecular pairs with antiparallel dipoles. As a result, we established that dimers produce a strong effect on the behavior of liquid-crystalline system and, at large values of the dipole moments, destroy the nematic order. These results provide the qualitative interpretation of the data of computer simulation [6, 7].

In the first part of this article [1], we derived a system of equations for the equilibrium values of the order parameters S_1 and S_2 of monomers and dimers and for the monomer fraction p, [equations (14) in [1]]. Their numerical solution yields the temperature dependences of these quantities. Equations (14) include the parameters of the quantity A_{ij}, which, in turn, are determined by the effective dispersion and electrostatic interactions in formula (23) in [1]. Appendix A in [1], gives the estimates of the electrostatic dipole–dipole interactions between monomers (formulas (A4) and (A5) for coefficients J_0^{es} and J_2^{es} in [1]). Electrostatic interactions between monomers and dimers are weak short-range interactions which, within the approach used, could be ignored.

However, in [1] we did not determine the coefficients of dispersion interactions, J_0^{ij} and J_2^{ij}. Nevertheless, the relationships between these coefficients for particles of different kinds (monomers and dimers) would considerably influence the system behavior. In particular, the range of the values of a molecular dipole in which dimers either stabilize or, on the contrary, destroy the nematic order is strongly dependent on the J_2^{22}/J_2^{11} ratio. The coefficients of the dispersion interactions within the so-called block model of a molecules are estimated in Section 2. The consequences of the variations in these coefficients are considered in Section 3.

2. DISPERSION INTERACTIONS WITHIN THE FRAMEWORK OF THE BLOCK MODEL

In order to estimate the coefficients J_0^{ij} and J_2^{ij}, consider the block model of a molecule [8–10] in which a monomer consists of five spherical blocks (Fig.1a), whereas a dimer consists of ten blocks (Fig. 1b).

Each block of a particle (a monomer or a dimer) interacts with each block of another particle according to the Lennard–Jones law, $\varepsilon_0[(D/r)^{12} - (D/r)^6]$, where D is the block diameter. The total potential of all the interactions between the particles, U_{ij}^{disp} (i, j = 1, 2), includes the double sum taken over all the corresponding blocks of both particles.

Expand the effective dispersion one-particle potentials A_{ij}^{disp} into Legendre polynomials and retain only the two first terms, (see formula (8) and formula (17)

1063-7745/00/4503-0510$20.00 © 2000 MAIK "Nauka/Interperiodica"

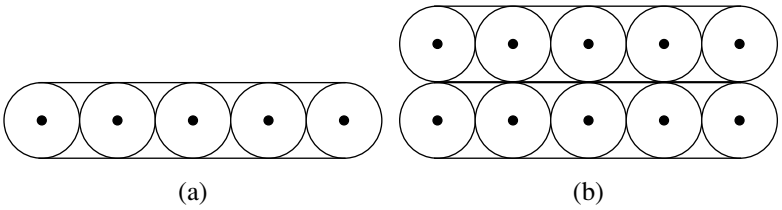

Fig. 1. Block model of a molecule: (a) a monomer, (b) a dimer.

for the correlation functions C_{ij} in [1]):

$$A_{ij}^{disp}(\mathbf{a}_1\cdot\mathbf{n}) = -\frac{\Phi}{4\pi VkT}\int f^{(j)}(\mathbf{a}_2\cdot\mathbf{n})\theta(\mathbf{R}_{12}-\boldsymbol{\xi}_{12}) \times U_{ij}^{disp}(1,2)d^3\mathbf{R}_{12}d^2\mathbf{a}_2d^2\mathbf{b}_2 = J_0^{ij} + J_2^{ij}S_jP_2(\mathbf{a}_1\cdot\mathbf{n}) + \ldots. \quad (1)$$

With this aim, take the integral, first, over the absolute values of R_{12} and then along the short axis $\mathbf{b}_2$ in (1) and introduce the following functions

$$Y_{ij}(\mathbf{a}_1,\mathbf{u},\mathbf{a}_2) \equiv -\frac{1}{4\pi D^3k} \times\int\theta(\mathbf{R}_{12}-\boldsymbol{\xi}_{12})U_{ij}^{disp}(1,2)R_{12}^2dR_{12}d^2\mathbf{b}_2. \quad (2)$$

Then, we arrive at the expression

$$A_{ij}^{disp}(\mathbf{a}_1\cdot\mathbf{n}) = \frac{\Phi D^3}{VT}\int f^{(j)}(\mathbf{a}_2\cdot\mathbf{n})Y_{ij}(\mathbf{a}_1,\mathbf{u},\mathbf{a}_2)d^2\mathbf{u}\,d^2\mathbf{a}_2. \quad (3)$$

The functions $Y_{ij}(\mathbf{a}_1,\mathbf{u},\mathbf{a}_2)$ depend on the orientations of the long axes of the particles and the orientations of the intermolecular vectors. We use here the same interpolating expression for Y_{ij} as for the dipole–dipole interaction in [1] (see also [11]):

$$Y_{ij}(\mathbf{a}_1,\mathbf{u},\mathbf{a}_2) = \alpha_{ij}' + (\beta_1')_{ij}P_2(\mathbf{a}_1\cdot\mathbf{u}) + (\beta_2')_{ij}P_2(\mathbf{a}_2\cdot\mathbf{u}) + \gamma_{ij}'P_2(\mathbf{a}_1\cdot\mathbf{a}_2) + \delta_{ij}'\left[\frac{9}{2}(\mathbf{a}_1\cdot\mathbf{u})(\mathbf{a}_2\cdot\mathbf{u})(\mathbf{a}_1\cdot\mathbf{a}_2) - \frac{3}{2}(\mathbf{a}_1\cdot\mathbf{u})^2 - \frac{3}{2}(\mathbf{a}_2\cdot\mathbf{u})^2\ \frac{3}{2}(\mathbf{a}_1\cdot\mathbf{a}_2)^2 + 1\right]. \quad (4)$$

Substituting (4) into (3), we arrive at the following expressions for the coefficients J_0^{ij} and J_2^{ij}:

$$J_0^{ij} = 4\pi\frac{\Phi D^3}{V}\frac{1}{T}\alpha_{ij}', \quad (5)$$

$$J_2^{ij} = 4\pi\frac{\Phi D^3}{V}\frac{1}{T}\gamma_{ij}'. \quad (6)$$

We consider here the coefficients α_{ij}' and γ_{ij}' in (5) and (6) as free parameters [12] and require that expression (4) would be valid for five orientations of the long axes $\mathbf{a}_1$ and $\mathbf{a}_2$ with respect to the orientation of the vector $\mathbf{u}$ (see Fig. 4 in [1]). Thus, we obtain for α_{ij}' and γ_{ij}':

$$\begin{cases}\alpha_{ij}' = \frac{2}{9}\left(Y_1^{ij} + \frac{1}{2}Y_2^{ij} + Y_3^{ij} + Y_4^{ij} + Y_5^{ij}\right)\\ \gamma_{ij}' = \frac{2}{9}(2Y_1^{ij} + Y_2^{ij} - Y_3^{ij} - Y_4^{ij} - Y_5^{ij}).\end{cases} \quad (7)$$

In order to determine the coefficients Y_n^{ij}, where the subscript n indicates the ordinal number of the long-axis orientation in Fig. 4 in [1], one has to take the integral over the vector $\mathbf{b}_2$ in (2) for each of the five orientations. Introduce the functions $Z_n^{ij}(\mathbf{b}_1,\mathbf{u},\mathbf{b}_2)$ which are equivalent to the integrals taken over the intermolecular distances for each fixed orientation n of the long axes:

$$Z_n^{ij}(\mathbf{b}_1,\mathbf{u},\mathbf{b}_2) \equiv \frac{1}{D^3k} \times\int\theta(\mathbf{R}_{12}-\boldsymbol{\xi}_{12})U_{ij}^{disp}(1,2)R_{12}^2dR_{12}. \quad (8)$$

The functions Z_n^{ij} are independent of the vectors $\mathbf{a}_1$ and $\mathbf{a}_2$, because the latter are fixed. Thus, we obtain

$$Y_n^{ij} = \frac{1}{4\pi}\int Z_n^{ij}(\mathbf{b}_1,\mathbf{u},\mathbf{b}_2)d^2\mathbf{b}_2. \quad (9)$$

If the interacting particles are monomers ($i = 1$ and $j = 1$), then the integration in (9) yields

$$Y_n^{11} = Z_n^{11}. \quad (10)$$

In the present study, we obtained the Z_n^{11} values by performing the numerical integration of the block potential over the distances R_{12} between the centers of monomers using the expression (8) for each of n orientations shown in Fig. 4 in [1].

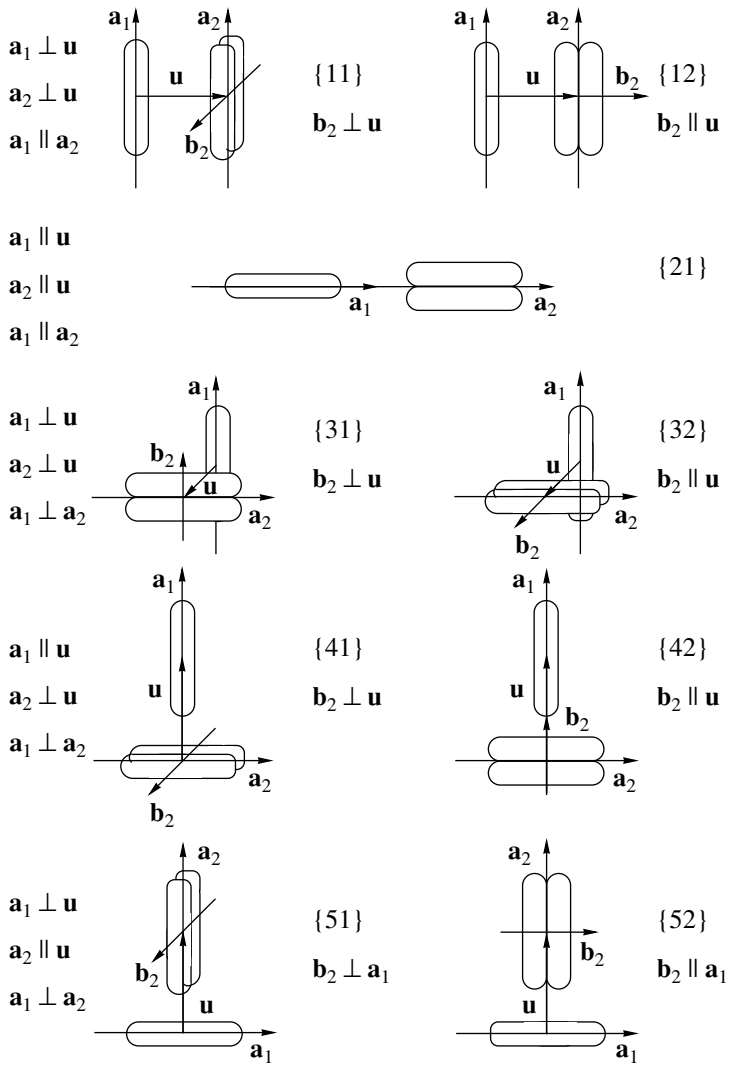

Fig. 2. Nine relative orientations of a monomer and a biaxial dimer used for calculating nine Z_{nm}^{12} coefficients by formula (14). Figures in parentheses indicate the ordinal number of the orientation $\{nm\}$.

For interacting monomers and dimers ($i = 1, j = 2$), the value of Z_n^{12} depends on the orientation of the short dimer axis $\mathbf{b}_2$. This dependence cannot be obtained analytically. In order to estimate the integral in (9), we have to approximate $Z_n^{12}(\mathbf{b}_1, \mathbf{u}, \mathbf{b}_2)$ by polynomials,

$$\begin{cases} Z_n^{12} = \alpha_n^{12} + \beta_n^{12} P_2(\mathbf{b}_2 \cdot \mathbf{u}), \quad n = 1, 3, 4 \\ Z_2^{12} = \alpha_2^{12} \\ Z_5^{12} = \alpha_5^{12} + \beta_5^{12} P_2(\mathbf{b}_2 \cdot \mathbf{a}_1). \end{cases} \tag{11}$$

Substituting (11) into (9), we have

$$Y_n^{12} = \alpha_n^{12}. \tag{12}$$

The free parameters for Z_n^{12} in (11) can be obtained from the condition that these expressing are valid for nine orientations of the monomer and the dimer shown in Fig. 2. Then we obtain for α_n^{12}:

$$\begin{cases} \alpha_n^{12} = \frac{1}{3}(2Z_{n1}^{12} + Z_{n2}^{12}), \quad n = 1, 3, 4, 5 \\ \alpha_2^{12} = Z_{21}^{12}. \end{cases} \tag{13}$$

The quantities Z_{nm}^{12} with the double subscript $\{nm\}$ indicating the number of the particle orientation (Fig. 2) are also obtained by the numerical integration of the block potential over the distance R_{12} between the monomer and the dimer centers for each of the $\{nm\}$ orientations (Fig. 2) using the following expression

$$Z_{nm}^{12} = \frac{1}{D^3 k} \int \theta(\mathbf{R}_{12} - \boldsymbol{\xi}_{12}) U_{12}^{disp}(1, 2) R_{12}^2 dR_{12}. \tag{14}$$

The same procedure can also be applied to two dimers ($i = 2, j = 2$) with the only difference—the polynomials $P_2(\mathbf{b}_1 \cdot \mathbf{u})$ and $P_2(\mathbf{b}_1 \cdot \mathbf{b}_2)$ are added to the interpolating expressions for Z_n^{22} [see the analogous expressions (11) for Z_n^{12}]. Therefore, instead of the use of nine orientations shown in Fig. 2, we estimated the interpolation coefficients for Z_n^{22} with the use of 16 orientations at different directions of the vector $\mathbf{b}_1$. Similar to the case of a monomer and a dimer, the value of Y_n^{22} for two dimers is determined only by the free coefficients α_n^{22} in the expansion for Z_n^{22}:

$$Y_n^{22} = \alpha_n^{22}. \quad (15)$$

The Y_n^{11}-values in formula (10), the Y_n^{12}-values in formula (12), and the Y_n^{22}-values in formula (15) were substituted for the coefficients α_{ij}' and γ_{ij}' into (7), and those, in turn, were substituted for the coefficients of dispersion interaction J_0^{ij} and J_2^{ij} in expressions (5) and (6). In the numerical integration of the potential, we put $\varepsilon_0/k = 5350$. As a result, we obtained the coefficients J_0^{ij} and J_2^{ij} for the block model which are listed in table.

3. MAJOR RESULTS AND CONCLUSIONS

The coefficients of dispersion interaction given in table were obtained for the block model and were used to estimate the effective one-particle potentials, see formula (23) in [1]. At such a choice of the coefficients $J_{0,2}^{ij}$, the numerical solution of system (14) from [1] with respect to the order parameters S_1 and S_2 and the monomer fraction p yields the temperature T dependences of these quantities for any fixed value of the dipole moment. The dependence of the transition temperature on the squared reduced dipole moment for the block model is shown by curve *1* in Fig. 3. The dashed line in Fig. 3 corresponds to the solution of the first equation of the system in which p equals unity (the case of the dimer absence). The comparative analysis of the behavior of the solid and dashed curves in Fig. 3 shows the possibilities provided by the allowance for dimerization. On the left of the intersection point of these curves in Fig. 3 (the balance point), dimers stabilize the nematic phase, whereas on the right of the balance point, they destroy it. (For more details see [1]). At the balance point proper, dimers produce no effect on the system behavior at all.

In order to understand in which way the choice of the molecular model influences the behavior of the temperature of the nematic–isotropic phase transition of the system consider the variation in the anisotropic coefficients of the dispersion interaction. We vary these coefficients in accordance with their values listed in table. We do not vary the isotropic coefficients, because they only slightly affect the transition temperature (and only via the monomer fraction p). For comparison, in the conventional Maier–Saupe theory, the isotropic coefficient in the expansion of the one-particle potential into Legendre polynomials does not affect the system behavior. New anisotropic coefficients are chosen in such a way that the J_2^{22}/J_2^{11} ratio exceeds this ratio for the initial block model. Thus, anisotropic interactions of dimers become more pronounced than anisotropic interactions of monomers. In this case, dimers become slightly more mesogenic than in the initial model. The corresponding dependence of the transition temperature on the squared reduced dipole moment is shown by curve *2* in Fig. 3. First, it is seen that the region where dimers are more mesogenic than monomers is broadened (the balance point is shifted to the right). Second, on the right of the balance point, where monomers are more mesogenic than dimers, the dimers destroy the nematic order to a lesser degree than in the block model (the difference between the solid and dashed lines is much less). Moreover, at the point where curve *2* in Fig. 3 attains its maximum, the num-

Coefficients of disperse interactions, $\tilde{J}_{0.2}^{ij} \equiv T J_{0.2}^{ij}$

Calculated coefficient	$\tilde{J}_0^{11}$	$\tilde{J}_0^{12}$	$\tilde{J}_0^{22}$	$\tilde{J}_2^{11}$	$\tilde{J}_2^{12}$	$\tilde{J}_2^{22}$
Block model	2100	4130	6580	1230	1990	2690
Upon variation	2100	4130	6580	1110	1990	2840

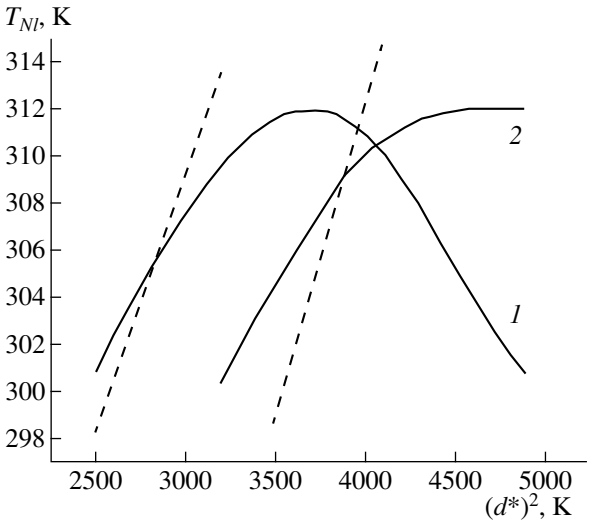

Fig. 3. Dependence of the transition temperature on the squared reduced dipole moment (*1*) for the block model and (*2*) upon the variation of the interaction coefficients, $L/D = 5$, $\Phi = 0.3$. Dashed lines indicate the correspondent dependences obtained without the allowance for dimer existence.

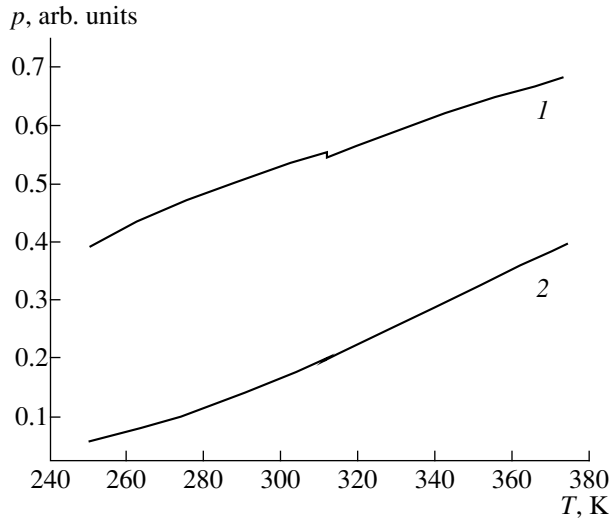

Fig. 4. Temperature dependence of the monomer fraction (*1*) for the block model; (*2*) upon the variation of the interaction coefficients. In both cases, the values of the molecular dipole correspond to the maximum transition temperature.

ber of monomers becomes so small that they can only insignificantly affect the system behavior. Therefore curve *2* attains the saturation. It should be indicated that assuming that dimers do not interact electrostatically so that their total interaction is independent of the value of the molecular dipole, one arrives to the same situation. Figure 4 shows the temperature dependence of the monomer fraction p for the dipole moment corresponding to the maximum in Fig. 3. Curve *1* in Fig. 4 corresponds to the coefficients of disperse interactions obtained within the framework of the block model and curve *2*, to the coefficients upon their variation. It is seen that in the second case, the number of monomers is considerably lower than in the first one.

All the above stated leads to the conclusion that dimer formation results in a decrease of the temperature nematic–isotropic phase transition with an increase of the dipole moment only if the anisotropy of dimer interactions is rather weak (curve *1* in Fig. 3). To the right from the balance point, dimers, always being less anisotropic than monomers, can still make the temperature decrease barely noticeable or even unobservable (curve *2* in Fig. 3). The situation is determined by the choice of the molecular model most adequately describing the type of the molecule. Possibly, these considerations can explain the fact [6] that computer simulation of polar systems indicates the temperature decrease for stronger dipoles, whereas in [7], it was stated that molecular dipoles do not affect the transition temperature at all. In any case, the allowance for dimerization is very important for this approach, because the results of the above studies show only a feebly marked increase of the transition temperature with an increase of the dipole moment in comparison with its increase observed without allowance for dimerization.

ACKNOWLEDGMENTS

The authors are grateful to A. R. Khokhlov and other researches of the Department of Physics of Polymers and Crystals of the Physics Faculty of the Moscow State University and S. A. Pikin for valuable help in their work. This study was supported by the INTAS within the program of the International Center of Fundamental Physics in Moscow, project no. 96-0457.

REFERENCES

1. A. V. Emel'yanenko and M. A. Osipov, Kristallografiya **45** (3), 549 (2000) [Crystallogr. Rep. **45** (3), 501 (2000)].
2. A. Perera and G. N. Patey, J. Chem. Phys. **89**, 5861 (1988).
3. A. G. Vanakaras and D. J. Photinos, Mol. Phys. **85**, 1089 (1995).
4. C. Vega and S. Lago, J. Chem. Phys. **100**, 6727 (1994).
5. M. A. Osipov and A. Yu. Simonov, Khim. Fiz. **8** (7), 992 (1989).
6. S. C. McGrother, A. Gil-Villegas, and G. Jackson, J. Phys. C: Solid State Phys. **8**, 9649 (1996).
7. K. Satoh, Sh. Mita, and Sh. Kondo, Liq. Cryst. **20** (6), 757 (1996).
8. K. Singer, A. Taylor, and J. V. L. Singer, Mol. Phys. **33**, 1757 (1977).
9. S. Murad, D. J. Evans, and K. E. Gubbins, Mol. Phys. **37**, 725 (1979).
10. D. J. Tildseley, W. B. Streett, and W. A. Steele, Mol. Phys. **39**, 1169 (1980).
11. B. W. van der Meer and G. Vertogen, *Molecular Physics of Liquid Crystals*, Ed. by G. R. Luckhurst and G. W. Gray (Academic, New York, 1979).
12. L. Blum and A. J. Torruella, J. Chem. Phys. **56**, 303 (1972).

Translated by L. Man

Crystallography Reports, Vol. 45, No. 3, 2000, pp. 515–518. Translated from Kristallografiya, Vol. 45, No. 3, 2000, pp. 564–567.

SURFACE

Influence of the Surface on the Properties of Macro- and Nanocrystals

V. P. Bokarev

Research Institute of Molecular Electronics, Moscow, Russia

e-mail: vpb@mikron.zgrad.su; bokarev@mikron.ru

Received May 20, 1998

Abstract—The influence of the surface energy on the properties of macro- and nanocrystals has been considered. It is shown that the properties of small crystals (several microns and less) depend on their dimensions, which is explained by an increase of the number of surface atoms in the total number of all the atoms in a crystal. On the basis of the energy criterion of crystalline substance amorphization, a formula relating the surface energy of a crystal to its crystal-lattice parameters is derived. The surface energies of elemental crystals are calculated. It is assumed that anisotropy in contact-melting temperature of single crystals can be observed experimentally. *© 2000 MAIK "Nauka/Interperiodica".*

The surface, being an unavoidable defect of a crystal, influences its physical and chemical properties. The surface is the site of occurrence of various chemical and catalytic reactions, it influences the chemical and catalytic activity, adsorption ability, and sintering temperature of powder-like substances. The surface state determines the mechanical properties of crystalline materials and the most important properties of semiconductor devices based on the use of single-crystal surfaces.

At the present, the effect of the surface on the properties of nanocrystals (in which the number of surface atoms is comparable with the number of atoms in the bulk) has been studied in detail. The formulas relating the properties of nanocrystals with their linear dimensions are derived with due regard of the surface-energy contribution into the chemical potential of a nanocrystal. Thus, according to the Gibbs–Thomson equation, a spherical nanocrystal melts at a lower temperature [1]:

$$T(R) = T(\infty) - 2\sigma T(\infty)/L\rho R,$$

where $T(R)$ is the melting point of a nanocrystal of the radius R, σ is the specific surface energy of the crystal–melt interface, L is the latent heat of melting, and ρ is the material density.

Earlier [2], we formulated the energy criterion of crystalline substance amorphization, according to which amorphization starts at the moment when the heat content in a crystal attains (no matter in which way) the value [2]:

$$Q = \int_0^{T_m} c_p dT,$$

where c_p is the heat capacity and T_m is the melting point of the crystalline substance under consideration.

Using this criterion, we calculated the limiting dimensions of inorganic and metal nanocrystals at an arbitrary temperature, $T < T_m$, beginning from which the material undergoes amorphization, and also the decrease in the melting point of nanocrystals as a function of their dimensions [2]. It should be indicated that the formula derived contained not the latent melting heat of the crystal, L, which characterizes the structure rearrangement during the transformation of a crystal into a liquid, but the heat content at the melting point, Q, i.e., the thermal energy accumulated in the crystal by the moment of its melting. It is clear that it is the heat Q that initiates the onset of the phase transformation of a crystal into a liquid.

The dependence of the crystal properties on its dimensions is clearly seen from the change of the average coordination number (c.n.) in crystals with a decrease of their dimensions. We derived the formulas relating the change in the coordination number (c.n.) of nanocrystals and their linear dimension l for the simplest cubic structures with the lattice parameters a [3, 4]:

$$\text{c.n.}(Pm3m, Z = 1) = 6\frac{l/a}{l/a + 1},$$

$$\text{c.n.}(Im3m, Z = 2) = 16\frac{(l/a)^3}{(l/a + 1)^3 + (l/a)^3},$$

$$\text{c.n.}(Fm3m, Z = 4) = 48\frac{(l/a)^3}{(l/a + 1)^3 - 3(l/a)^2(l/a + 1)},$$

$$\text{c.n.}(Fd3m, Z = 4) = 32\frac{(l/a)^3}{(2l/a + 1)^3 - 3(l/a)^2(2l/a + 1)}.$$

1063-7745/00/4503-0515$20.00

The calculations performed by these formulas show considerable changes in the physical and chemical properties of nanocrystals observed to submicron dimensions [3].

A similar dependence was also obtained for column-type crystalline elements on a single-crystal substrate. Such elements are used in silicon technologies for manufacturing large-scale integrated (LSI) circuits with submicron elements. Such calculations for silicon columns were performed by the formula [5]

$$\text{c.n.(Si)} = 2\frac{16l^2h/a^3 + 2l^2/a^2 + 2l/a + 1}{8l^2h/a^3 + 2l^2/a^2 + 4lh/a^2 + 2l/a + h/a + 1},$$

where l is the width and h is the height of a single-crystal column.

The calculations showed that physical and chemical properties depend on element dimensions to the linear dimensions of the order of 0.25 μm. The influence of the dimensions on the physical and chemical properties of a 0.25 μm-wide column is comparable with the effect of vacancies with a concentration exceeding 10^{19} cm^{-3} [5]. With due regard for the fact that the equilibrium vacancy concentration at the melting point does not exceed 10^{16} cm^{-3} and that some of these vacancies are electrically active centers, the importance of the allowance for the variation of silicon properties on submicron dimensions of the crystalline elements of large-scale integrated circuits becomes quite obvious.

Thus, the effect of the surface on the properties of a nanocrystal is confirmed both experimentally and theoretically (thermodynamic calculations). For macrocrystals, many of the above effects become negligible already at micron dimensions of the crystal. However, irrespectively of the crystal dimension, the surface has the determining effect on such crystal properties as catalytic activity, adsorption ability, mechanical strength, and melting. The catalytic and adsorption properties at the surface and mechanical properties of crystals important for science and technology have repeatedly been considered in various publications. The relation of these properties to the energy and the physical state of the surface is obvious. At the same time, the effect of the surface on crystal melting which is not that obvious.

It was shown that thermal vibrations of surface atoms occurring normally to the crystal surface are more pronounced (by 50–100%) than in the bulk [6]. Therefore, proceeding from the Lindemann criterion (according to which a crystal starts melting when the root-mean-square deviations of the atoms attain a value of about 25% of the lattice constant), Zangwill assumed [7] that crystal starts melting on the surface at a temperature considerably lower than the melting point in the bulk and then "propagates" from layer to layer over the whole crystal bulk. Even earlier, Ubbelohde [8] assumed that if the surface energy of the crystal is anisotropic, melting on different faces would start at different temperatures. However, this assumption was not confirmed experimentally. The existence of this effect would have contradicted the assumption that the melting process is a first-order phase transition, because the anisotropy of the melting point of the crystal would have resulted in a diffuse phase transformation with respect to temperature. In the present study, the question which crystal layer passes into the melt under the effect of the surface energy was not considered. At the same time, the fact of the surface-energy effect on the melting process in a macrocrystal was recorded.

It is also possible to assume that crystal melting at various faces starts at the same temperature. But then the layers of different thicknesses should pass into the melt per unit time. The thicknesses of such layers are proportional to the thickness of the first coordination sphere of atoms (or molecules, in the case of molecular crystals) along the given direction [9]. Similar to [7, 8], the melting of the surface layer is initialed by an excessive energy in such a layer stored in the form of the surface energy [9]. Using the energy criterion of crystalline-substance amorphization [2], we derived the formula relating the specific free surface energy of the crystal (σ_{hkl}) on the (hkl) planes and the thickness of the first coordination sphere (l_{hkl}) along the [hkl] direction:

$$\sigma_{hkl} = (\rho l_{hkl}/M)\int_0^{T_m} c_p dT, \qquad (1)$$

where ρ is the density of the crystalline substance and M is the mass of atoms (molecules) occupying the crystal-lattice points [9]. The above formula allows one to take into account the anisotropy in the surface energy of crystals. For crystalline metals, the relation between l_{100}, l_{110}, and l_{111} is determined by the spatial arrangement of atoms within the first coordination sphere and, for cubic crystals, has the form:

for primitive lattices, $l_{100} = 2a$; $l_{110} = a\sqrt{2}$, and $l_{111} = 2a/\sqrt{3}$;

for body-centered lattices $l_{100} = a$; $l_{110} = a\sqrt{2}$, and $l_{111} = a/\sqrt{3}$;

for face-centered lattices $l_{100} = a$; $l_{110} = a/\sqrt{2}$, $l_{111} = 2a/\sqrt{3}$.

Table lists the specific surface energies of metal and nonmetal simple crystals calculated by formula (1) and, for comparison, also the values from [10–18]. It is seen that the calculated surface energies only slightly differ from the experimentally obtained ones and the values calculated with the invocation of other theoretical approaches and thus confirm our approach to the description of the beginning of melting [9]. This is also confirmed by the qualitative correlation of the surface-energy ratios $\sigma_{100}/\sigma_{110}$ for tungsten and copper crystals

Specific free surface energies of elemental crystals calculated by formula (1) and the known experimental data

Element	*hkl*	σ_{hkl}, mJ/m^2 (calculated data)	σ_{hkl}, mJ/m^2 (known data)	Element	*hkl*	σ_{hkl}, mJ/m^2 (calculated data)	σ_{hkl}, mJ/m^2 (known data)
H	0001	11.1		As	100	1710	
He	100	1.76		Se	100	752	
Li	100	304		Br	100	110	
Li	110	430	377 [10]	Kr	111	56.8	52.8 [12]
Li	111	180		Rb	110	143	75 [10]
Be	0001	1840	1500 [11]	Sr	100	518	303 [10]
B	100	2820		Y	0001	1285	
C	0001	2168		Zr	0001	2017	
N	0001	43.6		Nb	110	2646	1927 [10]
O	100	100		Mo	100	2306	2240 [10]
F	100	124		Tc	0001	2990	
Ne	100	16.3		Ru	0001	3200	
Ne	110	11.5		Rh	100	2560	2610 [10]
Ne	111	18.8	19.7 [12]	Pd	100	2090	1685 [10]
Na	100	189	171 [10]	Ag	100	1246	1140 [16]
Na	110	267		Ag	110	881	
Na	111	109		Ag	111	1439	
Mg	0001	867	728 [10]	Cd	0001	668	650 [18]
Al	100	921	964 [10]	In	100	336	
Al	110	651		Sn	100	488	765 [10]
Al	111	1063		Sb	100	1130	
Si	100	1530		Te	0001	543	520 [10]
Si	110	2164		I	100	195	
Si	111	1767	1240 [13]	Xe	100	57.0	
S	001	75.8		Xe	110	40.3	
Cl	100	75.2		Xe	111	65.8	62.11 [12]
Ar	111	44.3	43.2 [12]	Cs	100	85	
K	100	124	105 [10]	Ba	100	365	
Ca	100	630		La	0001	900	
Sc	0001	1584		Ce	100	724	
Ti	0001	2226		Pr	0001	930	
V	100	1961	1878 [10]	Nd	0001	1025	
Cr	100	2017	1591 [10]	Pa	100	1390	
Mn	100	1502		Pa	001	1150	
Fe	100	1832	1940 [15]	Th	100	1380	
Co	100	2317	1368 [10]	U	001	1544	
Ni	100	2405	1440 [10]	Np	100	1210	
Cu	100	1686	1500 [14]	Np	001	840	
Zn	0001	953	770 [17]	Pm	0001	1030	
Ga	100	303		Tb	0001	1326	
Ge	100	1175		Dy	0001	1408	
Sm	100	747		Re	0001	4460	
Eu	100	472		Os	0001	4210	
Gd	100	1182		Ir	100	3090	
Gd	0001	1683		Pt	100	2280	2480 [10]
Ho	0001	1415		Pt	110	1612	
Er	001	1510		Pt	111	2633	
Tm	0001	1500		Au	100	1360	1250 [16]
Yb	100	610		Hg	100	283	
Lu	0001	1623		Tl	100	343	
Hf	0001	2130	1553 [10]	Pb	100	430	546 [10]
Ta	100	2530	2388 [10]	Bi	100	595	
W	100	3020	2455 [10]	Po	100	416	

measured experimentally and calculated by formula (1). The corresponding ratios determined experimentally for W and Cu are equal to 0.926 and 1.2, whereas those calculated by formula (1) are equal to 0.707 and 1.414, respectively. To simplify the calculations, we neglected the temperature dependences of σ_{hkl}, ρ, l_{hkl}, and c_p, because they can only slightly affect the results obtained [9].

It follows from (1) that with the change of the surface energy on one of the crystal faces, the melting temperature of the crystal on the face under consideration also changes. In other words, under certain conditions, it is possible to observe the anisotropy of the meting point in the crystal. For example, the anisotropy can be observed during adsorption of impurities on one of the crystal faces, chemically interacting with the impurities. Under the conditions of crystal heating, these impurities can melt and form a chemical compound at the temperature lower that the melting point of the crystal. Moreover, the anisotropy in the melting point is also observed in contact melting of crystals forming a eutectics. This phenomenon was repeatedly observed, but was interpreted somewhat differently. Thus, Savintsev [19] showed that melting of zinc single crystal wrapped into a foil of the eutectic cadmium–lead alloy takes place only along the basis zinc faces. Earlier [8], it was indicated that some faces of some metal single crystals of some metals are not wet with melt. It was explained by selective impurity adsorption on these faces.

All the above stated facts prove that studying physical and chemical properties of nano- and macrocrystals, one has necessarily to take into account the properties of the crystal surfaces such as, e.g., the specific surface energy.

REFERENCES

1. R. Laudise and R. Parker, *The Growth of Single Crystals; Crystal Growth Mechanisms: Energetics, Kinematics and Transport* (Prentice-Hall, New York, 1970; Mir, Moscow, 1974).
2. S. S. Batsanov and V. P. Bokarev, Izv. Akad. Nauk SSSR, Neorg. Mater. **16**, 1650 (1980).
3. V. P. Bokarev, Izv. Akad. Nauk SSSR, Neorg. Mater. **22**, 347 (1986).
4. S. S. Batsanov and V. P. Bokarev, Izv. Akad. Nauk SSSR, Neorg. Mater. **23**, 1054 (1987).
5. V. P. Bokarev and M. Yu. Vakhrushev, Mikroélektronika **21**, 66 (1992).
6. B. A. Nesterenko and O. V. Snitko, *Physical Properties of Atomically Pure Surface* (Naukova Dumka, Kiev, 1983).
7. A. Zangwill, *Physics at Surfaces* (Cambridge Univ. Press, Cambridge, 1988; Mir, Moscow, 1990).
8. A. R. Ubbelohde, *Melting and Crystal Structure* (Clarendon, Oxford, 1965; Mir, Moscow, 1969).
9. V. P. Bokarev, in *Proceedings of Interbranch Council on Complex Problems of the Russian Academy of Sciences, Moscow, 1995* (Ekaterinburg, 1995), p. 67.
10. *Properties of Chemical Elements. Part 1. Physical Properties*, 2nd ed. (Metallurgiya, Moscow, 1976), Chap. 1.
11. G. Caglioti, G. Rizzi, and J. C. Bilello, J. Appl. Phys. **42** (11), 4271 (1971).
12. G. C. Benson and T. A Claxton, Phys. Chem. Solids **25**, 367 (1964).
13. J. J. Gilman, J. Appl. Phys. **31** (12), 2208 (1960).
14. M. T. Lilburne, J. Mater. Sci. **5** (4), 351 (1970).
15. A. Kelly, W. R. Tyson, and A. H. Cottrell, Philos. Mag., No. 15, 567 (1967).
16. H. Udin, A. Shuler, and J. Wullf, J. Met. **1**, 186 (1949).
17. D. W. G. White, Trans. Metall. Soc. AIME **236**, 796 (1966).
18. V. I. Likhtman, I. A. Andreeva, L. S. Bryukhanova, and E. D. Shchukin, Fiz.-Khim. Mekh. Mater. **5** (4), 433 (1969).
19. P. A. Savintsev and L. Ya. Kalachnikova, Izv. Tomsk. Politekh. Inst. **68**, 195 (1951).

Translated by L. Man

Crystallography Reports, Vol. 45, No. 3, 2000, pp. 519–523. Translated from Kristallografiya, Vol. 45, No. 3, 2000, pp. 568–572.

CRYSTAL GROWTH

Alternation of the Flows of Liquid Components under Asymmetric Temperature Oscillations

V. Yu. Gershanov, S. I. Garmashov, A. V. Beletskaya, and A. R. Minyaev

Rostov State University, pr. Stachki 194, Rostov-on-Don, 344104 Russia

e-mail: vgersh@jeo.ru

Received July 28, 1997; in final form, July 27, 1999

Abstract—The mass transfer in a cylindrical inclusion of the melt with a rectangular cross-section in an anisotropic crystal in a nonstationary thermal field has been analyzed with due regard for the nonlinear solid–liquid interfacial kinetics. The possibility of the existence of a new effect is substantiated—alternation of the direction of the flows of liquid components depending on the rate of temperature variation. It is shown that the inclusion shape can be controlled by changing the shape of the temperature oscillations. © *2000 MAIK "Nauka/Interperiodica".*

INTRODUCTION

Migration of liquid inclusions in an anisotropic solid [1] is of interest as a method for studying of the mechanism and the kinetics of crystallization, diffusion in high-temperature melts, and the segregation coefficients of the components [2]. Moreover, the study of thermal migration is a promising method of semiconductor technology, which provides the formation of doped regions of complicated geometries in the substrate bulk and, thus, can be used for the manufacturing new semiconductor devices and large-scale integrated circuits. The possibilities of thermomigration as a research method are determined by understanding of the mechanism of mass transfer. In terms of technology, the control of the shape of migrating inclusions is very important, because it is the inclusion shape that determines the dimensions and the shape of the recrystallized doped regions in the bulk of the semiconductor substrate.

Small characteristic size of liquid-phase layers (<100 μm) and, in the general case, the nonlinear boundary conditions for the mass transfer equations provide a high sensitivity of the thermomigration process to deviations of thermal conditions from the stationary ones [3]. In the case of a non-one-dimensional mass transfer characteristic of the discrete liquid-phase inclusions inside an nonuniformly heated anisotropic solid material, the deviation from the stationary conditions should result not only in the change of the migration velocity (as is the case of planar inclusions [3]), also to the change in the inclusions shape because of the anisotropy of growth and dissolution kinetics.

The goal of this paper is to demonstrate the possibility of controlling the shape of liquid inclusions under the nonstationary thermal conditions.

MODEL

The rigorous approach to the description of the mass transfer in limited liquid-phase inclusions in an anisotropic medium requires the allowance for step motion from the "reentrant angles" and the capillary effects caused by the tendency of the system to have the minimum free energy. The solution of this problem can be obtained only by numerical modeling of the mass transfer on a computer. However, at the first stage of the study, the analytical solution of the problem can be obtained for a simplified model, which can also be used for the qualitative analysis of the above effects.

Consider a cylindrical inclusion of the composition *A–B* having a rectangular cross section in a uniformly heated anisotropic crystal (Fig. 1) consisting of mainly the substance *A* with the substance *B* being a solvent. The phase diagram of the system *A–B* is assumed to be known with the slope of the liquidus line $a_{c(h)} = dT/dC$ being equal to m.

The dimensions l_x and l_y of the inclusion (Fig. 1) are assumed to be rather small, so that one cannot neglect the effect of the solid–liquid interfacial kinetics on the mass transfer in the liquid-phase bulk [2], on the one hand, but can neglect the convective stirring of the liquid phase [4]. For simplicity, the segregation coefficient of the solvent *B* in the *A–B* system is assumed to be zero.

Two interfaces (parallel to the axis x, Fig. 1) are assumed to be singular and the growth and dissolution processes at these interfaces are assumed to proceed by the mechanism of two-dimensional nucleation. For further simplification, we assume that supersaturations necessary for formation and dissolution of nuclei have the same absolute values equal to ΔC. Two other interfaces are assumed to be nonsingular, and therefore the growth and dissolution processes at these interfaces are assumed to proceed by the normal growth mechanism.

1063-7745/00/4503-0519$20.00

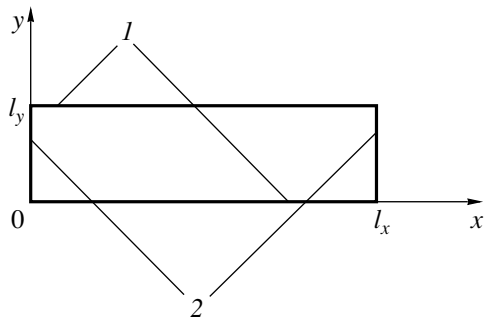

Fig. 1. Cross section of the cylindrical liquid inclusion considered in the model: (*1*) singular interfaces; (*2*) nonsingular interfaces.

Let the crystal temperature be decreased at a rate of $a_c < 0$. Now, calculate the flows of the substance *A* to the interfaces of different types. The mass transfer in the system can be described by the following two-dimensional diffusion equation:

$$\frac{\partial C(x, y, t)}{\partial t} = D\left(\frac{\partial^2 C(x, y, t)}{\partial x^2} + \frac{\partial^2 C(x, y, t)}{\partial y^2}\right), \quad (1)$$

where $C(x, y, t)$ is the concentration of the substance *A* at the point with coordinates *x, y* at a moment *t* and *D* is the coefficient of mutual diffusion in the *A*–*B* system.

If the temperature variations occur at a constant rate and for a rather long time, the distribution of supersaturations $\delta C(x, y)$ of the substance *A* in the liquid-phase bulk measured from the equilibrium concentration $C_e(t)$ becomes time-independent. Then equation (1) can considerably be simplified. It should be emphasized that the equilibrium concentration $C_e(t)$ in our model does not depend on the coordinate (because of the absence of a temperature gradient) and is determined from the liquidus line of the phase diagram of the *A*–*B* system without taking into account the capillary effects.

The concentration of the substance *A* in the liquid phase can be represented as a sum of supersaturations and equilibrium concentrations,

$$C(x, y, t) = \delta C(x, y) + C_e(t)$$
$$= \delta C(x, y) + C_e(0) + a_c t/m.$$

Then equation (1) can be rewritten as

$$\frac{\partial^2 \delta C(x, y)}{\partial x^2} + \frac{\partial^2 \delta C(x, y)}{\partial y^2} = \frac{a_c}{mD}. \quad (2)$$

Such a transformation of equation (1) to (2) is justified if the duration of the process of crystal cooling considerably exceeds the time of supersaturation relaxation in the liquid inclusion due to diffusion, τ_r. The relaxation time for a liquid–phase volume of the selected shape depends on the cross section dimensions l_x and l_y, and, if $l_x > l_y$, can be estimated as $\tau_r = l_x^2/(\pi^2 D)$. (If all the interfaces were nonsingular, one had to choose as the characteristic dimension the smaller dimension from l_x and l_y. However, our analysis showed that if there are some singular interfaces, one had to use a more severe constrain.). At $l_x \approx 3 \times 10^{-3}$ cm and $D = 10^{-4}$ cm^2/s, equation (2) is valid only for $t \gg 10^{-2}$ s.

It is natural that the maximal supersaturation in the liquid phase increases with an increase of the cooling rate. Until the maximal supersaturation δC_{max} does not exceed the critical supersaturation for the formation of two-dimensional nuclei on singular interfaces, ΔC, and the flows to these interfaces should be equal to zero. Therefore the derivatives of the supersaturation along the direction perpendicular to these interfaces appear to be equal to zero,

$$\left.\frac{\partial(\delta C(x, y))}{\partial y}\right|_{y = 0, l_y} = 0.$$

Thus, at low cooling rates (the corresponding criterion is derived below), the problem is reduced a one-dimensional one ($\delta C(x, y) = \delta C_1(x)$), and equation (2) can be replaced by an ordinary differential equation

$$\frac{d^2(\delta C_1(x))}{dx^2} = \frac{a_c}{mD}. \quad (3)$$

Supersaturations at rough (nonsingular) interfaces (at any mass flows) are assumed to be zero

$$\delta C(0, y) = \delta C_1(0) = 0, \quad (4)$$

$$\delta C(l_x, y) = \delta C_1(l_x) = 0. \quad (5)$$

Integrating equation (3) describing the supersaturation distribution along the *x*-axis with due regard for conditions (4) and (5) at rough interfaces, we have (Fig. 2)

$$\delta C_1(x) = a_c x(x - l_x)/(2mD). \quad (6)$$

The maximum supersaturation (at $x = l_x/2$) is

$$\delta C_1(l_x/2) = -a_c l_x^2/(8mD).$$

To justify the transition to a one-dimensional problem, it is necessary that this supersaturation would not exceed the critical supersaturation for nucleation of crystal layers, ΔC, whence the condition of low cooling rate can be written in the form

$$a_c \geq a_0 = -8D\Delta Cm/l_x^2, \quad (7)$$

where a_0 is a certain critical value of temperature variation. In what follows, the rates of temperature variations satisfying condition (7) are referred to as low rates.

At high cooling rates, i.e., at $a_c \ll a_0$, the supersaturations at singular interfaces are assumed to be equal to ΔC:

$$\delta C(x, 0) = \Delta C, \quad (8)$$

$$\delta C(x, l_y) = \Delta C. \quad (9)$$

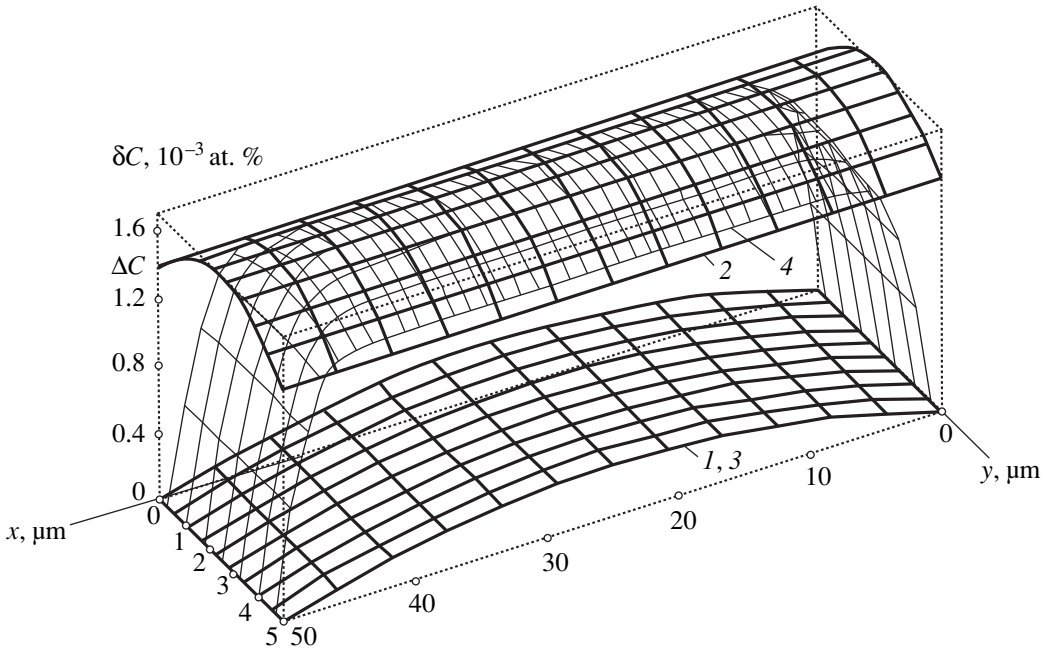

Fig. 2. Distribution of supersaturations in the liquid phase at the constant cooling rate $a_c = -0.1$ (*1*, *3*); –10 K/s (*2*, *4*). (*1* and *2*) are the analytical solutions of equations (6) and (11), respectively; (*3* and *4*) are the numerical solutions of equation (1).

At high cooling rates for the selected dimensions of the liquid phase ($l_x \gg l_y$), the problem again reduces to the one-dimensional one (within an accuracy of edge effects).

If temperature variations occur for a rather long time, $t \gg l_y^2/(\pi^2 D) - \Delta C m/a_c$, equation (2) becomes a one-dimensional equation along the coordinate *y*:

$$\frac{d^2(\delta C_2(y))}{dy^2} = \frac{a_c}{mD}, \qquad (10)$$

where $\delta C_2(y) = \delta C(x, y)$ at the boundary conditions (8) and (9). The supersaturation distribution obtained by integrating equation (10) has the form (see Fig. 2)

$$\delta C_2(y) = a_c y(y - l_y)/(2mD) + \Delta C. \qquad (11)$$

The supersaturation distributions (6) and (11) are qualitatively different (Fig. 2). In the first case, at low cooling rates, the flows of the substance *A* are directed to the nonsingular interfaces. In the second case, the flows are directed to the singular interfaces. The alternation of flows is caused by the changes in the cooling rate.

The results obtained can be readily extended to the case of a temperature increase occurring at a constant rate. In this case, one has to change the cooling rate $a_c < 0$ and the critical growth supersaturation ΔC to the rate of temperature increase $a_h > 0$ and the critical supersaturation for the nucleation of dissolution layers $-\Delta C$, respectively (in the general case, the absolute values of the critical supersaturations necessary for growth and dissolution can be different. The assumption about their equality is made here only to simplify the mathematical form of the final results).

Now, discuss the effect of temperature oscillations on the shape of the liquid-inclusion cross section. For symmetrical temperature oscillations (the rate of temperature variations is low, i.e., condition (7) is fulfilled), the singular interfaces remain immobile, while the nonsingular interfaces oscillate about their initial positions. If the temperature variations occur at a high rate, only singular interfaces can oscillate about their equilibrium positions (provided that the edge effects are neglected).

The situation is qualitatively different, if the shape of the temperature oscillations is asymmetric. Let the system temperature oscillate with a small amplitude, with the absolute value of the heating rate a_h being different from the cooling rate $|a_c|$. Then, the time of the temperature increase τ_h is different from the time of the temperature decrease τ_c, and the condition for the constancy of average temperature of the system has the form:

$$a_h \tau_h = |a_c| \tau_c. \qquad (12)$$

Now, calculate the flow of the substance *A* to the singular interfaces averaged over the period of the temperature oscillations,

$$\langle J_y \rangle = (J_y^h \tau_h + J_y^c \tau_c)/(\tau_h + \tau_c), \qquad (13)$$

where J_y^h and J_y^c are the steady-state flows to the singular interfaces during heating and cooling,

respectively.

$$J_y^{h(c)} = \left(-D\frac{d\delta C_2(y)}{dy}\bigg|_{y=0,\,l_y}\right)l_x.$$

The average flow to the nonsingular interfaces has the same absolute value but the opposite sign.

Consider the case of fast heating $|a_h| > |a_0|$ and slow cooling $|a_c| < |a_0|$. Since during slow heating, there is no flow to the singular interfaces, expression (13) takes the form

$$\langle J_y\rangle = \pm a_h l_y l_x \tau_h/(2m(\tau_h + \tau_c)),$$

where the upper sign of the fraction refers to the flow to the interface $y = 0$, whereas the lower sign, to the flow to the interface $y = l_y$.

For the inverse ratio of the heating and the cooling rates, the averaged flow to the corresponding singular interface change the sign to the opposite one, because the quantities a_h and a_c have different signs,

$$\langle J_y'\rangle = \pm a_c l_y l_x \tau_c/(2m(\tau_h + \tau_c)).$$

In accordance with (12), $\langle J_y\rangle$ and $\langle J_y'\rangle$ have the same absolute values.

If $a_h > |a_c|$, the singular interfaces are dissolved at average absolute rates

$$\langle V\rangle = a_h l_y \tau_h/(2m(C_S - C_L)(\tau_h + \tau_c)),$$

where $(C_S - C_L)$ is the difference between the concentrations of growth substance in the solid and the liquid phases. The liquid-phase dimension l_y increases by

$$\delta l_y = 2\langle V\rangle(\tau_h + \tau_c) = a_h l_y \tau_h/(m(C_S - C_L)),$$

whereas the l_x dimension decreases by δl_x, in accordance with the condition of the constancy of the average liquid-phase volume

$$\delta l_x = a_h l_x \tau_h/(m(C_S - C_L)).$$

At the inverse ratio of the rates of temperature changes, the signs of the flows and of the dimension variations change to the opposite ones.

DISCUSSION OF THE RESULTS

First of all, it should be noted that, depending on the rate of the temperature change, the directions of liquid-phase component flows also change. At low cooling rates, the flows of the substance *A* are directed to the nonsingular interfaces, whereas at high rates, the flows are directed to the singular interfaces. With an increase of the temperature, the flows change their signs to the opposite ones. The effect of flow alternation depending on the heating rate is still observed. Let us estimate the critical rate of the temperature variation a_0 at which the flow alternation should occur. The coefficient of mutual diffusion in the droplet liquids (melts and solutions of metals and semiconductors) is of the order of $10^{-4} \times 10^{-5}$ cm^2/s [5]. The supersaturation ΔC necessary for the formation of a critical two-dimensional nucleus in the Si–(Si + Al) system at the temperature 1000 K estimated from data [6] equals 1.4×10^{-3} at. %. The slope of the liquidus line is $m \cong 10$ K/(at. %). Then at $l_x = 3 \times 10^{-3}$ cm, the critical rate of the temperature variation a_0 is of the order of 1 K/s. The amplitude of temperature oscillations for the heating time 1 s is of the order of 1 K. The attainable rates of pulse heating strongly exceed the value of 1 K/s. The maximum cooling rate depends on the experimental conditions. During cooling by radiation into a vacuum one can readily obtain the cooling rate of the same order of magnitude.

If the absolute values of the heating and the cooling rates are less than $|a_0|$, the singular interfaces remain immobile, whereas the nonsingular ones oscillate about the equilibrium position.

At slow cooling ($|a_c| < |a_0|$) and at fast heating ($|a_h| > |a_0|$), the inclusion cross section is somewhat rounded-off (the singular facets decrease in size). In the opposite situation, the cross section is flattened (the singular facets increase in size). For heating and cooling rates exceeding the critical value, the singular interfaces should oscillate about their equilibrium positions, whereas the nonsingular interfaces (within the framework of our model) should remain immobile.

Naturally, the above assumptions essentially simplify the problem under consideration. However, there are a number of factors that cannot be taken into account within an analytical model, but it can be made by the methods of numerical computer modeling. Since the singular interfaces have the limited dimensions, the concentration distribution has the extremum in the middle part, which should distort their planar character and give rise to the formation of steps, whose motion was neglected in the simplified model. The motion of steps from the reentrant angles on the growth stage was not taken into account either. Moreover, the true dependences of the rates of interfacial processes on supersaturations have a more complicated form than the modeled ones [2]. However, all these shortcomings cannot essentially distort the results obtained. The numerical modeling of mass transfer under the conditions of nonsymmetric temperature oscillations confirms the results obtained for the analytical model. The refinement is mainly associated with the manifestation of the edge effects (Fig. 2) and the loss of the inclusion-shape stability—separation of a part of the liquid phase from the inclusion edges under the condition of not too slow temperature decrease.

The the rectangular shape of the cross-section of the inclusion used in the simplified approach and the two-dimensional character of the problem are not the necessary conditions of such consideration. In the three-dimensional case, at the existence of two types of interfaces (singular and nonsingular) under the conditions

of asymmetric temperature oscillations, the inclusion shape should change. If the heating rate exceeds the cooling rate, the dimensions of singular regions of the interface should decrease, whereas the tendency of the system to have the minimum surface energy should lead to rounding-off of the inclusion shape. For the inverse ratio of the heating and the cooling rates, the inclusion should be faceted with singular facets.

REFERENCES

1. W. G. Pfann, *Zone Melting* (Wiley, New York, 1966; Mir, Moscow, 1970).
2. W. A. Tiller, J. Appl. Phys. **34** (9), 2757 (1963).
3. V. Yu. Gershanov and S. I. Garmashov, Kristallografiya **37** (1), 34 (1992) [Sov. Phys.–Crystallogr. **37** (1), 14 (1992)].
4. V. G. Levich, *Physical–Chemical Hydrodynamics* (Fizmatgiz, Moscow, 1959).
5. D. A. Frank-Kamenetskiĭ, *Diffusion and Heat Transfer in Chemical Kinetics* (Nauka, Moscow, 1987).
6. V. Yu. Gershanov, L. Z. Golovanova, and N. I. Nikitin, in *Proceedings of VI International Conference on Crystal Growth* (Moscow, 1980), Vol. 2, p. 10.

Translated by V. Tokarev

Crystallography Reports, Vol. 45, No. 3, 2000, pp. 524–526. Translated from Kristallografiya, Vol. 45, No. 3, 2000, pp. 573–575.

CRYSTAL GROWTH

Luminescence Effects Accompanying $Ba(BrO_3)_2 \cdot H_2O$ Crystallization from Solution

N. K. Tolochko, A. Z. Myal'dun, V. A. Yanusov, and N. V. Sobolenko

Institute of Technical Acoustics, Belarussian Academy of Sciences, pr. Lyudnikova 13, Vitebsk, 210717 Belarus

Received May 12, 1999

Abstract—Kinetics of the $Ba(Br_2O_3)_2 \cdot H_2O$ precipitation from aqueous solution and the accompanying luminescence effects are studied. Specific features of appearance of luminescence during grinding of $Ba(Br_2O_3)_2 \cdot H_2O$ crystals are also examined. The origin of luminescence effects is interpreted as the result of electric discharge accompanying cracking of crystals during their growth or grinding. © *2000 MAIK "Nauka/Interperiodica".*

INTRODUCTION

The effect of light emission during crystallization from solutions or melts has been known for quite a long time. However, the mechanism of this phenomenon is explained only hypothetically. In particular, it was assumed that luminescence results from synchronized elementary adsorption events at the growth front [1, 2], that a part of the latent crystallization heat can be converted into the photons energy of the characteristic spectrum [3]; that the light emission can be caused by cavitation during fast melt solidification [4–6], or due to charge distribution between the phases [7–9], or due to formation and motion of charged dislocations [10].

Most of the above cited studies provide no information on the crystallization kinetics. Below, we compare the temporal characteristics of the luminescence effects with the precipitation kinetics for $Ba(Br_2O_3)_2 \cdot H_2O$ crystallized from an aqueous solution.

EXPERIMENTAL

Crystallization experiments were conducted in thermostated glass vessels. The solution temperature was controlled by an UH-4 water ultrathermostat within ±0.1°C. In the course of experiments, the temperature was lowered from 90 to 25–30°C at a rate of 0.25–1.0 °C/min according to a linear low. The saturation temperature of all the solution was $T_{sat} \approx 87$°C.

For measuring the precipitation rate, 75-ml solution batches poured in to a glass tube (15 mm in diameter) with a narrow branch tube (8 mm in diameter) in the lower part for the crystalline precipitate were used. The thickness h of the precipitate layer accumulated in the branch tube was periodically measured during solution cooling in the light. The quantity h was used as a measure of the crystallized material.

The Figure shows typical plots of the thickness h of the precipitate layer and the precipitation rate (dh/dt) as functions of the solution temperature T and time t for the cooling rate $dT/dt = 0.5$°C/min. The moment of the attainment the saturation temperature T_{sat} is taken to be the origin. The first crystals appeared in 14 min at T = 80°C. Beginning with this moment, the total amount of the precipitate increases first rapidly and then at a lower rate. On covling, the precipitation rate reaches the peak value of 0.85 mm/min within 25-min upon the attainment of the saturation temperature, at T = 74°C, and then decreases almost exponentially. The most intense precipitation is observed in the vicinity of the maximum of the dh/dt curve, (80–62°C).

In the studies of luminescence of the crystallization solution, a glass bulb with the solution (60 ml) was placed into in a light-protected chamber together with a FEU-85 photomultiplier. The signal from the photomultiplier was transmitted through an amplifier to an S8-17 storing oscillograph with an EN3001-3 plotter. We recorded the number n of light pulses emitted per unit time by on a solution cooled in the same mode as in experiments on crystallization.

The dependences of n on T and t measured at $dT/dt = 0.5$°C/min were compared with the dh/dt curve (figure). It is seen that luminescence is observed with a certain delay and not simultaneously with precipitation—28 minutes upon the attainment of the saturation temperature at T = 73°C, when the first precipitated crystals are sufficiently large. Initially weak luminescence gradually becomes more intense and the attains

1063-7745/00/4503-0524$20.00

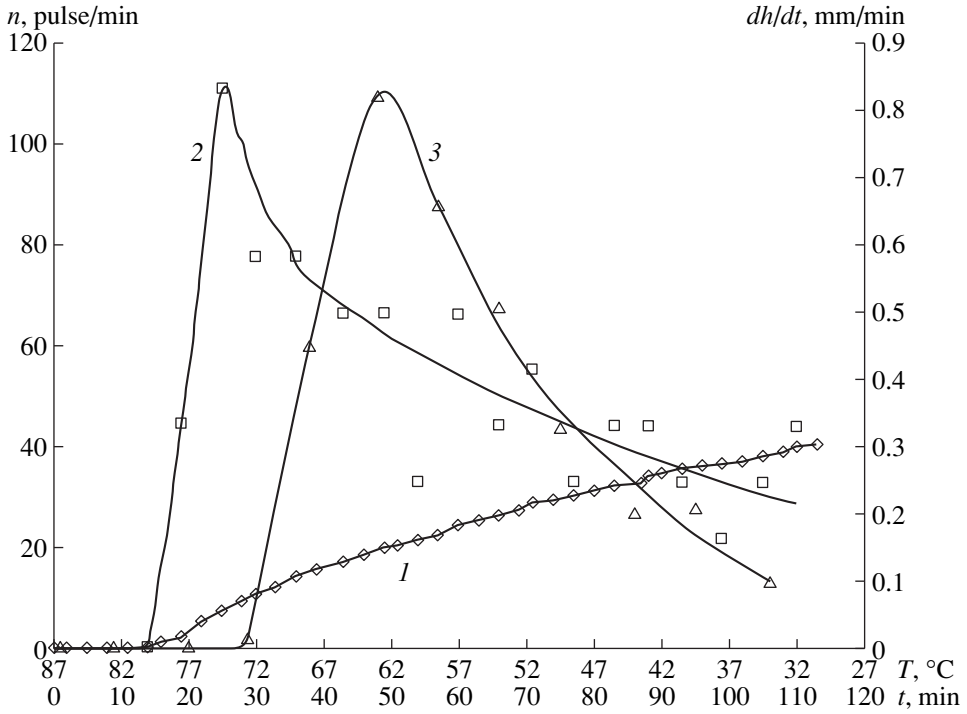

The thickness h of the precipitate layer (*1*), the precipitation rate dh/dt (*2*), and the number n of light pulses per minute (*3*) as functions of time and the solution temperature during cooling of the solution at a rate of 0.5°C/min.

its maximum intensity (the maximum signal amplitude and the highest pulse frequency of $n = 110$ pulse/min at the moment $t = 50$ min and at the temperature $T = 62$°C. Later on, the luminescence intensity decreases and one observes single pulses of ~5 μs duration and sometimes, multiperiod pulses (probably, several superimposed pulses).

In addition, we visually observed luminescence during crystallization in the solution bulk or during crystal grinding in a dark room. To enhance the luminescence, we used a bulb of a larger volume (550 ml).

The solution weak luminescence was observed as a series of relatively weak flashes of the bluish color close to the bulb bottom (i.e., close to the precipitated crystals) and only occasionally in the solution bulk. No luminescence was observed during stirring of solutions with the precipitated crystals, or during grinding crystal of dry powder or powder prepared earlier and powed into a saturated solution. At the same time, we observed luminescence during grinding of the precipitate in its mother solution.

DISCUSSION OF RESULTS

The fact that luminescence is observed only upon a certain time after the beginning of precipitation can be explained by a gradual accumulation of defects in the crystals leading to their cracking. The absence of luminescence in the stirred solution with the precipitate can be explained by insufficient intensity of crystal collisions that can cause crystal cracking. The absence of any luminescence during grinding of a dry powder or a powder prepared earlier and then poured into the saturated solution may be associated with screening of charges on the surfaces of crystals in the air due to gas absorption.

CONCLUSION

The results obtained show that luminescence accompanying crystal precipitation from solutions is associated with the processes occurring during crystals growth rather than with the processes occurring during their nucleation. The most probable mechanism of luminescence appearance is the accumulation of defects in growing crystals giving rise to their cracking, which, in turn, gives rise to the potential difference between the crack sides followed by an electric discharge.

REFERENCES

1. V. K. Bykhovskiĭ, Kristallografiya **18**, 915 (1973).
2. V. K. Bykhovskiĭ and V. R. Yampol'skiĭ, in *Proceedings of Fifth All-Union Conference on Crystal Growth*, Tbilisi, USSR (1977), Vol. 1, p. 173.

3. A. N. Mestvirishvili and M. E. Perel'man, in *Proceedings of Fifth All-Union Conference on Crystal Growth* (Tbilisi, USSR, 1977), Vol. 1, p. 187.
4. E. S. Omarov, in *Proceedings of Second All-Union Conference on Modeling of Crystal Growth* (Riga, USSR, 1987), Vol. 2, p. 249.
5. L. G. Kachurin, S. Kolev, and V. F. Psalomshchikov, Dokl. Akad. Nauk SSSR **267**, 347 (1982).
6. V. V. Sobolev, Izv. Akad. Nauk SSSR, Metally, No. 1, 79 (1986).
7. S. Maskarenas and L. G. Freitas, J. Appl. Phys. **31**, 1684 (1960).
8. D. P. Shumov, V. A. D'yakov, and A. L. Aleksandrovskiĭ, in *Proceedings of Sixth All-Union Conference on Crystal Growth* (Yerevan, USSR, 1985), Vol. 1, p. 284.
9. R. G. Manucharyan and O. G. Nalbandyan, in *Proceedings of Second All-Union Conference on Modeling of Crystal Growth* (Riga, USSR, 1987), Vol. 2, p. 384.
10. A. M. Trokhan, A. I. Lapshin, and O. I. Gudzenko, Dokl. Akad. Nauk SSSR **275**, 83 (1984).

Translated by A. Mel'nikova